frontiers | Research Topics

Arctic amplification: Feedback process interactions and contributions

Edited by
Patrick Charles Taylor, Peter L. Langen and Ivy Tan

Published in
Frontiers in Earth Science

ISSN 1664-8714
ISBN 978-2-83251-753-6
DOI 10.3389/978-2-83251-753-6

About Frontiers

Frontiers is more than just an open access publisher of scholarly articles: it is a pioneering approach to the world of academia, radically improving the way scholarly research is managed. The grand vision of Frontiers is a world where all people have an equal opportunity to seek, share and generate knowledge. Frontiers provides immediate and permanent online open access to all its publications, but this alone is not enough to realize our grand goals.

Frontiers journal series

The Frontiers journal series is a multi-tier and interdisciplinary set of open-access, online journals, promising a paradigm shift from the current review, selection and dissemination processes in academic publishing. All Frontiers journals are driven by researchers for researchers; therefore, they constitute a service to the scholarly community. At the same time, the *Frontiers journal series* operates on a revolutionary invention, the tiered publishing system, initially addressing specific communities of scholars, and gradually climbing up to broader public understanding, thus serving the interests of the lay society, too.

Dedication to quality

Each Frontiers article is a landmark of the highest quality, thanks to genuinely collaborative interactions between authors and review editors, who include some of the world's best academicians. Research must be certified by peers before entering a stream of knowledge that may eventually reach the public - and shape society; therefore, Frontiers only applies the most rigorous and unbiased reviews. Frontiers revolutionizes research publishing by freely delivering the most outstanding research, evaluated with no bias from both the academic and social point of view. By applying the most advanced information technologies, Frontiers is catapulting scholarly publishing into a new generation.

What are Frontiers Research Topics?

Frontiers Research Topics are very popular trademarks of the *Frontiers journals series*: they are collections of at least ten articles, all centered on a particular subject. With their unique mix of varied contributions from Original Research to Review Articles, Frontiers Research Topics unify the most influential researchers, the latest key findings and historical advances in a hot research area.

Find out more on how to host your own Frontiers Research Topic or contribute to one as an author by contacting the Frontiers editorial office: frontiersin.org/about/contact

Arctic amplification: Feedback process interactions and contributions

Topic editors

Patrick Charles Taylor — Langley Research Center, National Aeronautics and Space Administration, United States

Peter L. Langen — Aarhus University, Denmark

Ivy Tan — McGill University, Canada

Citation

Taylor, P. C., Langen, P. L., Tan, I., eds. (2023). *Arctic amplification: Feedback process interactions and contributions*. Lausanne: Frontiers Media SA.

doi: 10.3389/978-2-83251-753-6

Table of contents

frontiers | Frontiers in Earth Science

TYPE Editorial
PUBLISHED 10 February 2023
DOI 10.3389/feart.2023.1140871

OPEN ACCESS

EDITED AND REVIEWED BY
Hayley Jane Fowler,
Newcastle University, United Kingdom

*CORRESPONDENCE
Patrick C. Taylor,
patrick.c.taylor@nasa.gov

SPECIALTY SECTION
This article was submitted to Interdisciplinary Climate Studies, a section of the journal Frontiers in Earth Science

RECEIVED 09 January 2023
ACCEPTED 02 February 2023
PUBLISHED 10 February 2023

CITATION
Taylor PC, Langen PL and Tan I (2023), Editorial: Arctic amplification: Feedback process interactions and contributions. *Front. Earth Sci.* 11:1140871. doi: 10.3389/feart.2023.1140871

Editorial: Arctic amplification: Feedback process interactions and contributions

Patrick C. Taylor[1]*, Peter L. Langen[2] and Ivy Tan[3]

[1]NASA Langley Research Center, National Aeronautics and Space Administration, Hampton, VA, United States, [2]Department of Environmental Science, IClimate, Aarhus University, Roskilde, Denmark, [3]Department of Atmospheric and Oceanic Sciences, McGill University, Montreal, QC, Canada

KEYWORDS

arctic amplificaiton, arctic climate change, climate feedback, arctic sea ice, arctic physical processes

Editorial on the Research Topic
Arctic amplification: Feedback process interactions and contributions

The Arctic is a system in transition. In recent decades, we have witnessed rapid and unprecedented changes within the Arctic that represent an early warning sign of global climate change. Observed rapid Arctic climate change is considered indicative of a broader phenomenon called Arctic Amplification. Arctic Amplification is most clearly described as greater surface warming in the Arctic relative to the rest of the globe (roughly 2–4 times faster) in response to increased CO_2 and is accompanied by other changes to the Arctic system, most visibly reductions in the snow and ice cover. Despite the early awareness of this fundamental feature of the Arctic for more than 100 years (e.g., Arrhenius 1896), projections of the Arctic climate system response to increased CO_2 are more uncertain than in any other region.

The evolution of the Arctic climate, and hence the uncertainty in its projected change, is of great societal relevance. The Arctic system affects the global climate through its influences on sea level, atmosphere and ocean circulation patterns, carbon storage and release, and extreme events. The societal relevance of the uncertainty in the Arctic warming rate is exemplified by considering the 2°C Paris Climate Agreement warming target. A 2°C global warming, considering present uncertainty levels, results in an Arctic warming range from + 3.5 to + 7.5°C. Substantially different degrees of land ice melt and permafrost thaw are expected for a +3.5 vs. a +7.5°C warming. Key to reducing this uncertainty in Arctic Amplification is improving our understanding of the processes driving Arctic Amplification.

The aim of this Research Topic is to focus research efforts on how local and remote atmosphere, land, ocean, sea ice, and coupled physical processes drive Arctic Amplification. By bringing together current understanding from multiple perspectives in a manner that elucidates the influence of coupled processes, this Research Topic aims to accelerate advances in our understanding of Arctic Amplification and make progress towards reducing uncertainty in climate projections. This Research Topic contains original research and review articles that expand our knowledge of Arctic Amplification.

Radiative climate feedback analysis is a key area discussed within this Research Topic as it is a critical tool for understanding Arctic Amplification. Sledd and L'Ecuyer present original research describing the interplay between the sea ice and clouds as it pertains to the ice-albedo feedback. Their findings indicate that not only do clouds influence the magnitude of the ice-albedo feedback, but they also change the ability to detect the emergence of the

feedback above natural variability. Hahn et al. apply radiative feedback kernels to investigate the hemispheric asymmetry in observed and projected polar amplification in contemporary climate models. This original research reveals differences between the importance of poleward heat transport contribution to Arctic and Antarctic Amplification.

Contributions from Huang et al. and Sejas et al. discuss the shortcomings associated with current methods in quantifying radiative feedbacks. Huang et al. investigate the fidelity of linear radiative feedback methods for quantifying high-latitude feedbacks and demonstrate the need to apply non-linear methods when quantifying Arctic feedbacks. Sejas et al. tackle the inherent differences between the top-of-atmosphere and surface perspectives for quantifying climate feedbacks. This article demonstrates that the discrepancies between these perspectives are linked to the definition of the top-of-atmosphere lapse rate feedback.

Another major theme of this Research Topic is the importance of remote processes and local feedback interactions. Contributions from Finocchio and Doyle and Hendersen et al. provide perspectives on the connections between the global atmospheric circulation and high-latitude climate. Finocchio and Doyle shed light on the seasonal variations of the impacts of cyclones on sea ice loss. Their results indicate that early melt season cyclones tend to reduce sea ice melt whereas late melt season cyclones tend to enhance sea ice loss. This difference is tied to seasonal variations in cyclone properties and to differences in the surface properties. Hendersen et al. review the local and remote drivers of Arctic Amplification focusing on the role of high-latitude atmospheric blocking, poleward moisture transport, and tropical-high latitude sub-seasonal teleconnections. This review stresses the importance of capturing tropical-to-Arctic teleconnections to understanding Arctic Amplification.

Many papers within the Research Topic highlight the importance of Arctic surface characteristics to the future evolution of the Arctic. Holland and Landrum do this by analyzing the emergence of forced climate change in Arctic sea ice across seven coupled climate model large ensembles. Boisvert et al. demonstrate the importance of surface properties through their investigation of the surface turbulent fluxes across contemporary climate models finding some promising observational constraints on Arctic climate change and key biases.

Lastly, Taylor et al. contribute a comprehensive review of the processes that have been studied as contributing factors to Arctic Amplification. The review provides two key outcomes. First, Taylor et al. construct a conceptual model of Arctic Amplification containing five fundamental processes. Second, the review closes with a set of recommendations for actions needed to reduce uncertainty in future Arctic Amplification. Clear from this review is the need to account for local feedback and remote process interactions within the context of the annual cycle to constrain projected Arctic Amplification.

In the decade or so since the emergence of Arctic Amplification in observations, our understanding of Arctic Amplification has evolved considerably. Our scientific perspectives have changed from considering Arctic Amplification as the consequence of primarily a single feedback process, namely, the surface albedo feedback, to acknowledging it as the result of an interplay between the atmosphere, ocean, and sea ice at high and low latitudes. The articles within this Research Topic further demonstrate Arctic Amplification as a coupled atmosphere-ocean-sea ice process. While this Research Topic actually raises more questions than it solves, it advances our understanding of Arctic Amplification by crystalizing the notion that focusing scientific attention on measuring, modeling, and understanding cross-scale energy exchanges between the atmosphere, ocean, and sea ice is fundamental to reducing uncertainty in projections of Arctic climate change.

Author contributions

PT, PL, and IT contributed to the draft and editing of this work.

Conflict of interest

The authors declare that the research was conducted in the absence of any commercial or financial relationships that could be construed as a potential conflict of interest.

Publisher's note

Reference

Arrhenius, S. (1896). Xxxi. On the influence of carbonic acid in the air upon the temperature of the ground. *Lond. Edinb.* 41, 237–276. doi:10.1080/14786449608620846

frontiers in Earth Science

REVIEW
published: 01 July 2021
doi: 10.3389/feart.2021.709896

Local and Remote Atmospheric Circulation Drivers of Arctic Change: A Review

Gina R. Henderson[1], Bradford S. Barrett[2], Lori J. Wachowicz[3], Kyle S. Mattingly[4], Jonathon R. Preece[3] and Thomas L. Mote[3]*

[1]Oceanography Department, United States Naval Academy, Annapolis, MD, United States, [2]Air Force Office of Scientific Research, Arlington, VA, United States, [3]Department of Geography, University of Georgia, Athens, GA, United States, [4]Institute of Earth, Ocean, and Atmospheric Sciences, Rutgers, the State University of New Jersey, Newark, NJ, United States

Arctic Amplification is a fundamental feature of past, present, and modelled future climate. However, the causes of this "amplification" within Earth's climate system are not fully understood. To date, warming in the Arctic has been most pronounced in autumn and winter seasons, with this trend predicted to continue based on model projections of future climate. Nevertheless, the mechanisms by which this will take place are numerous, interconnected. and complex. Will future Arctic Amplification be primarily driven by local, within-Arctic processes, or will external forces play a greater role in contributing to changing climate in this region? Motivated by this uncertainty in future Arctic climate, this review seeks to evaluate several of the key atmospheric circulation processes important to the ongoing discussion of Arctic amplification, focusing primarily on processes in the troposphere. Both local and remote drivers of Arctic amplification are considered, with specific focus given to high-latitude atmospheric blocking, poleward moisture transport, and tropical-high latitude subseasonal teleconnections. Impacts of circulation variability and moisture transport on sea ice, ice sheet surface mass balance, snow cover, and other surface cryospheric variables are reviewed and discussed. The future evolution of Arctic amplification is discussed in terms of projected future trends in atmospheric blocking and moisture transport and their coupling with the cryosphere. As high-latitude atmospheric circulation is strongly influenced by lower-latitude processes, the future state of tropical-to-Arctic teleconnections is also considered.

Keywords: blocking, greenland, arctic amplification, moisture intrusions, intraseasonal

OPEN ACCESS

Edited by:
Peter L. Langen,
Aarhus University, Denmark

Reviewed by:
Hyo-Seok Park,
Hanyang Universiy, South Korea
Qinghua Ding,
University of California, Santa Barbara, United States

****Correspondence:***
Gina R. Henderson
ghenders@usna.edu

Specialty section:
This article was submitted to Cryospheric Sciences, a section of the journal Frontiers in Earth Science

Received: *14 May 2021*
Accepted: *22 June 2021*
Published: *01 July 2021*

Citation:
Henderson GR, Barrett BS, Wachowicz LJ, Mattingly KS, Preece JR and Mote TL (2021) Local and Remote Atmospheric Circulation Drivers of Arctic Change: A Review. Front. Earth Sci. 9:709896. doi: 10.3389/feart.2021.709896

INTRODUCTION: ARCTIC AMPLIFICATION–LOCAL AND REMOTE CAUSES

Arctic-amplified near-surface atmospheric warming is a fundamental feature of past climate warming periods, present-day warming trends, and modeled future changes to the Earth's climate system. However, the causes of this "Arctic amplification" are not fully understood (Serreze and Barry, 2011). Amplified Arctic warming has been most pronounced during autumn and winter, and model simulations project this will remain the case in future warming scenarios (Serreze and Francis, 2006; Lu and Cai, 2009; Serreze et al., 2009; Screen and Simmonds, 2010; Bintanja and van der Linden, 2013; Cohen et al., 2014; Dai et al., 2019). A number of interconnected physical processes, occurring within and external to the Arctic and with distinct seasonal variability, have been identified as contributing to Arctic amplification (Taylor et al., 2013; Yoshimori et al.,

2014a; Kim and Kim, 2017; Lang et al., 2017; Goosse et al., 2018; Park et al., 2018; Stuecker et al., 2018; Ding et al., 2019).

The earliest-identified cause of enhanced warming is the ice-albedo (or surface-albedo) feedback, whereby some initial warming reduces polar ice and snow cover and causes a greater fraction of incoming solar radiation to be absorbed, which further accelerates warming and albedo reduction (Budyko, 1969; Cess et al., 1991; Serreze et al., 2009). Other local feedback processes that may contribute to enhanced warming in the absence of extra-Arctic influence include the lapse rate and Planck feedbacks (Manabe and Wetherald, 1975; Crook et al., 2011; Pithan and Mauritsen, 2014; Hahn et al., 2020; Previdi et al., 2020), as well as cloud and water vapor feedbacks (Graversen and Wang, 2009; Cox et al., 2015; Kay et al., 2016; Södergren et al., 2018; Huang et al., 2019; Feldl et al., 2020; Middlemas et al., 2020) in an atmosphere moistened by sea ice decline (Boisvert et al., 2015; Jun et al., 2016; Taylor et al., 2018; Rinke et al., 2019b). Extra-Arctic processes, in particular changes to large-scale atmospheric and oceanic circulation and related changes in poleward atmospheric moist and dry static energy transport (e.g., Yang et al., 2010; Alexeev and Jackson, 2013; Zhang et al., 2013; Graversen and Burtu, 2016; Gong et al., 2017; Yoshimori et al., 2017), also contribute to Arctic amplification and are entangled with intra-Arctic feedbacks in complex ways. For example, cyclones facilitating poleward warm, moist air from lower latitudes may induce an initial retreat of sea ice, which strengthens the local ice-albedo feedback. This in turn amplifies the lapse rate feedback, which can be understood as a manifestation of accentuated lower-tropospheric warming dictated by the surface temperature change (Boeke et al., 2021). Feldl et al. (2020) and Boeke et al. (2021) argue that Arctic amplification should be attributed to the physical processes that establish the nonuniform vertical warming profile producing the lapse rate feedback, rather than the lapse rate feedback per se.

Given this debate, in this review, we focus on several of the key processes important to the ongoing discussion on Arctic amplification, focusing primarily on processes in the troposphere associated with blocking, moisture transport, and subseasonal influences. Our focus in the next sections is as follows: first, we review atmospheric blocking, including its definition, current challenges to identify present and future blocking, its relationship with moisture transport in the Arctic, and the impacts from Arctic blocking and moisture intrusions. We then review tropical-to-high latitude teleconnections that exert critical control on Arctic processes on the subseasonal time scale, both in the atmosphere and cryosphere. We conclude the review with a forward-looking assessment of how these interrelated topics are expected to evolve in future climate.

ARCTIC CIRCULATION FEATURES: BLOCKING, MOISTURE TRANSPORT, AND COUPLING WITH THE CRYOSPHERE

Blocking Definition, Identification, and Northern Hemisphere Climatology

Blocking is broadly defined as a quasi-stationary anomalous anticyclonic circulation pattern which disrupts the eastward propagation of cyclones and other systems (AMS American Meteorological Society, 2020). The formation of a blocking flow pattern results from disruption of the background flow interactions with Rossby wave dynamics (Woollings et al., 2018 and references therein). Mechanisms contributing to the building and maintenance of blocked systems can include moist-thermodynamic processes during cyclogenesis and transient eddies (e.g., Pfahl et al., 2015; Steinfeld and Pfahl, 2019). More recently, blocking has been described by the column budget of Local Wave Activity, using an analogy to traffic congestion (Nakamura and Huang 2018). Direct meteorological impacts of long-lived blocks vary seasonally, primarily resulting in extreme heat and cold airmasses (e.g., Brunner et al., 2018; Schaller et al., 2018), as well as increased advection of heat and moisture along the periphery of the anticyclones (e.g., Barrett et al., 2020; Mattingly et al., 2018) (**Figure 1**). In the high latitudes, environmental consequences can include significant loss of sea ice and ablation of land ice, as discussed in detail in *Tropical-High Latitude Subseasonal Teleconnections* (e.g., McLeod and Mote, 2016; Tedesco et al., 2016; Wernli and Papritz, 2018).

The broad definition of blocking has led to a variety of different methodological considerations for quantifying blocking and its impacts in the mid- and high-latitudes, particularly regarding spatial and temporal constraints and the dynamic considerations, as explained further in Woollings et al., 2018. The definition of atmospheric blocking has changed over time, resulting in a variety of different blocking identification methods used today. The earliest blocking detection studies, such as Rex (1950), defined blocking as a split jet over a 45° longitudinal span and persisting for 10 or more days. This definition was later revised to include shorter minimum durations, inclusion of latitudinal ranges, geopotential height anomaly thresholds, or a combination of these (e.g., Geb 1966; Charney et al., 1981; Treidl et al., 1981; Lejenas and Øakland, 1983). This has resulted in several papers highlighting advantages and disadvantages of differing methods (Barnes et al., 2012; Woollings et al., 2018; Wachowicz et al., 2021). While we do not intend to detail each separate metric available nor provide an exhaustive list, we briefly discuss some metrics below.

Geopotential Height-Based Indices

Geopotential height-based blocking identification methods are most common, given that geopotential height data is almost universally available in atmospheric reanalysis products and climate model intercomparisons. Consequently, metrics measuring the reversal of the 500-hPa height gradient (e.g., Lejenas and Øakland, 1983; Tibaldi and Molteni, 1990) are most common (**Figure 2A**). These methods use a constant reference latitude (e.g., 60° N) about which the gradient is computed (Tibaldi and Molteni, 1990), but these approaches may mischaracterize blocking in some regions (Pelly and Hoskins, 2003; Dunn-Sigouin and Son, 2013).

Other height-based metrics calculate regional average geopotential height, such as the Greenland Blocking Index (GBI) (**Figure 2B**) (e.g., Fang 2004; Hanna et al., 2014; Hanna et al., 2016) and Alaska Blocking Index (McLeod et al., 2018), where positive regional anomalies typically indicate blocking

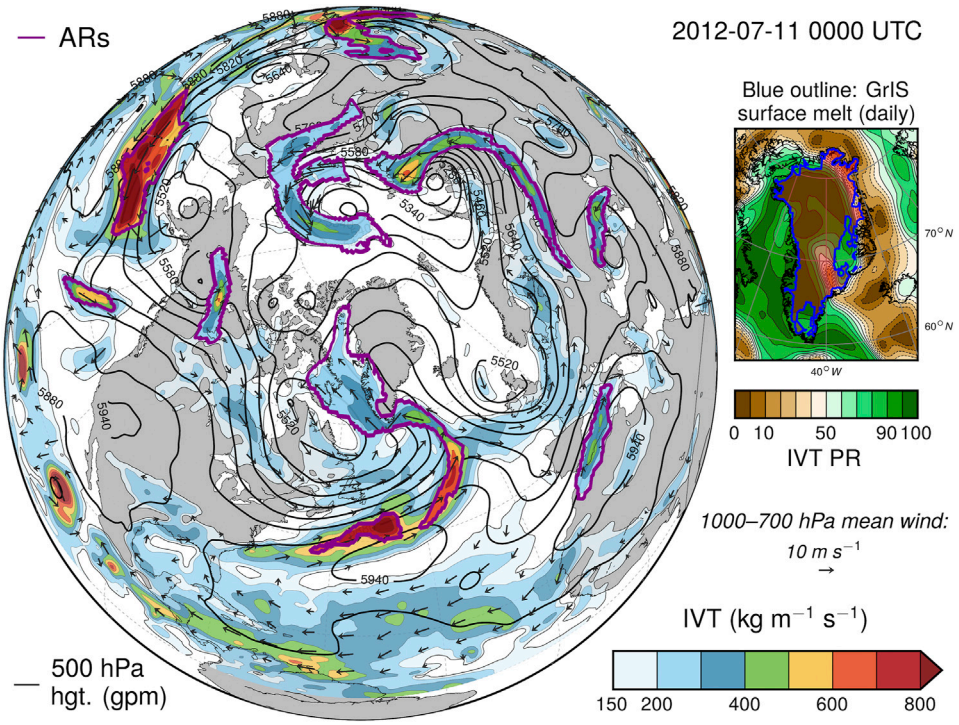

FIGURE 1 | Example of atmospheric rivers detected using MERRA-2 data at July 11, 2012 0000 UTC. Purple outlines identify features classified as atmospheric rivers based on the criteria outlined in Mattingly et al. (2018); Table 1.

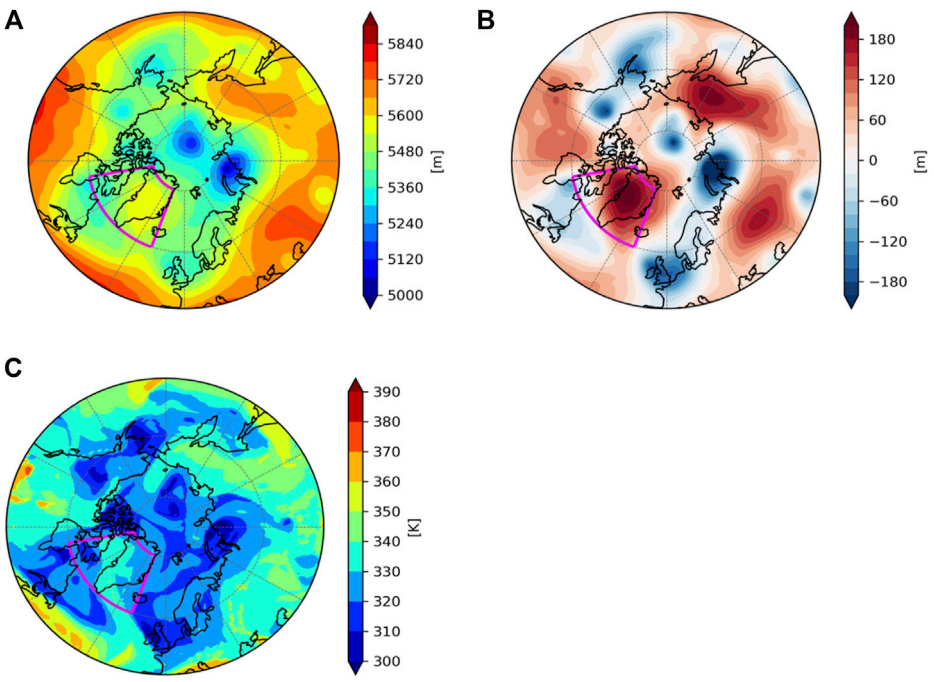

FIGURE 2 | A Greenland blocking event on July 11, 2012 seen in **(A)** 500 hPa height, **(B)** 500 hPa height anomalies compared with the 1981–2010 JJA climatology, and **(C)** potential temperature at 2PVU. The box corresponds to the spatial extent of the GBI boundary, from Wachowicz et al. (2021).

conditions. While computationally straightforward, this anomaly type of method may be sensitive to long-term increases in geopotential heights due to climate change (Christidis and Stott, 2015), and may require detrending of the height field prior to calculation (Hanna et al., 2018a; Wachowicz et al., 2021). Similarly, the method described in Dunn-Sigouin and Son, 2013–based on methods from Barriopedro et al. (2010) and Dole and Gordon (1983)–calculates and tracks geopotential height anomalies, which reduces errors in blocking classification that occur when using a constant, reference latitude. Both height reversal and anomaly methods have various spatial, temporal, and amplitude constraints that vary by study, particularly regarding what constitutes instantaneous, regional, and sector blocking events and episodes (e.g., Tibaldi and Molteni, 1990; Dunn-Sigouin and Son, 2013).

PV-Θ -Based Indices

Methods employing a potential vorticity-potential temperature (PV-Θ) approach, which generally follow from Pelly and Hoskins (2003), identify instances of a reversal in the meridional potential temperature (Θ) gradient on a constant PV surface (**Figure 2C**). An advantage to these methods stems from theory in that Θ is conserved in the absence of diabatic processes (Hoskins et al., 1985; Hoskins 1997). These methods (e.g., Pelly and Hoskins, 2003; Tyrlis and Hoskins, 2008) consider the climatology of annual transient eddy kinetic energy (TEKE) in establishing a reference latitude, which varies with longitude. Moreover, the use of seasonal TEKE may better identify blocking in some regions (Tyrlis and Hoskins, 2008; Masato, et al., 2012; Wachowicz et al., 2021). This method has been adapted to examine Rossby wave breaking characteristics from blocking (e.g., Masato et al., 2012; Masato et al., 2013a; Woollings et al., 2018).

Despite their theoretical advantages, shortcomings of these methodologies include primarily the lack of isentropic variables, primarily in global climate model (GCM) output. As a consequence, others have been able to successfully apply somewhat similar techniques to 500-hPa data to examine blocking in these datasets (e.g., Barnes et al., 2012; Barnes, et al., 2014; Masato et al., 2013b; Simpson et al., 2020). Barnes et al. (2012) report that there is systematically little difference in blocking representation in climate models when comparing the methods, including Tibaldi and Molteni (1990) and Pelly and Hoskins (2003).

While the geographical distribution and frequency of blocking may vary depending on the blocking metric used, some common themes do emerge. Broadly, blocking activity is greatest along the climatological storm tracks—e.g., over the North Atlantic and Pacific Basins or over Asia (Lejenas and Øakland, 1983; Tibaldi and Molteni, 1990; Pelly and Hoskins, 2003). Depending on the method used, blocking occurs over preferred regions including Greenland, Europe, the Central Arctic, Ural-Siberia, and the North Pacific (e.g., Barnes et al., 2014; Horton et al., 2015; Woollings et al., 2018). Furthermore, application of these metrics typically shows blocking to be most common in winter and early spring and least common in summer due to climatological cyclone frequency (Woollings et al., 2018; Lupo 2020).

Stationary and transient eddies within Rossby waves increase poleward moisture and heat transport, and act to enhance upper-level ridges (Franzke et al., 2011; Baggett et al., 2016; Zhang and Wang, 2018; Steinfeld and Pfahl, 2019), leading to blocking conditions over a region (Kim and Kim, 2017; Yang and Magnusdottir, 2017). Rossby wave breaking and diabatic processes, such as latent heat release from moisture transport, can both play an effective role in generating and maintaining blocks (e.g., Masato et al., 2013a; Woollings et al., 2018; Luo et al., 2019; Steinfeld and Pfahl, 2019; Steinfeld et al., 2020). Though the average measured duration of blocking events is dependent on identification methodology, identification efforts indicate that individual blocking events typically last 4 to 9 or more days (Pelly and Hoskins, 2003; Tyrlis and Hoskins, 2008; Lupo et al., 2019). We direct the reader to Lupo (2020) for a more detailed description of specific climatological characteristics of Northern Hemisphere blocks. However, understanding high-latitude moisture transport pathways in more detail is required to fully quantify the impact of blocking within the Arctic climate system and these connections to Arctic amplification more broadly.

Arctic Moisture Transport Pathways and Climatology

The geographical setting of the Northern Hemisphere high latitudes—with oceanic "gateways" in the Atlantic and Pacific sectors opening to the partially confined Arctic Ocean basin, at the downstream terminus of major extratropical storm tracks—facilitates the coupling of Arctic climate with lower-latitude processes. One of the primary ways lower-latitude processes affect the Arctic is through direct poleward heat and moisture fluxes in the atmosphere, which act to partially offset the global radiative imbalance between the tropics and poles (Trenberth and Solomon, 1994; Overland et al., 1996). The major pathways for meridional sensible and latent energy transport into the Arctic are through the North Atlantic (including the Fram Strait and Barents-Kara seas to the east of Greenland and the Labrador Sea/Baffin Bay pathway to the west of Greenland), North Pacific, and Siberian sectors (Sorteberg and Walsh, 2008; Woods et al., 2013; Woods et al., 2017; Dufour et al., 2016; Vázquez et al., 2016; Xu et al., 2020; Mewes and Jacobi, 2019; Mewes and Jacobi, 2020). Most prior studies have focused on meridional moisture rather than sensible heat transport, and have found that moisture transport into the Arctic is greatest during summer and minimized during winter (Dufour et al., 2016). During winter (DJF), poleward moisture transport is mainly confined to the Barents-Kara seas and, to a lesser extent, the Labrador/Baffin Bay and North Pacific transport pathways (Naakka et al., 2019; Nygård et al., 2020). During summer (JJA), mean moisture transport is directed poleward through the North Pacific, Siberian, and Labrador/Baffin Bay pathways, with moisture transport in the North Atlantic sector tending to be diverted zonally over Eurasia and onward into the Siberian pathway (Naakka et al., 2019 - see their **Figure 1**). Spring (MAM) and autumn (SON) exhibit a mixture of winter and summer characteristics, likely because these averaging periods

capture transitions between the maximally frozen and thawed Arctic seasons (Tilinina et al., 2014; Dufour et al., 2016).

Moisture transport into the Arctic does not occur in a temporally uniform manner, but rather is primarily accomplished through intense, short-lived events that are typically linked to cyclones (Sorteberg and Walsh, 2008; Dufour et al., 2016; Rinke et al., 2017; Villamil-Otero et al., 2018; Fearon et al., 2020) and Rossby wave breaking (Liu and Barnes, 2015). These events are often termed "moisture intrusions" (e.g., Doyle et al., 2011; Woods et al., 2013; Woods et al., 2017; Johansson et al., 2017; Yamanouchi, 2019; Ali and Pithan, 2020) and may resemble the narrow "atmospheric rivers" found in the mid-latitudes (Hegyi and Taylor, 2018; Komatsu et al., 2018; Nash et al., 2018; Vázquez et al., 2018).

Greenland Blocking: Impacts on Ice Sheet Surface Mass Balance and Relationships With Moisture Transport

Research efforts during the era of Arctic amplification have placed specific attention on atmospheric blocking and associated moisture transport over Greenland due to its impact on the surface mass balance (SMB) of the Greenland Ice Sheet (GrIS). Greenland blocking events encourage surface melt through a variety of mechanisms that will be discussed below and, as such, are strongly associated with increased GrIS surface melt and runoff over synoptic to decadal timescales (Hanna et al., 2013; Häkkinen et al., 2014; Hermann et al., 2020). This amplified runoff from the ice sheet can impact the climate system in several ways, including through contributions to global sea level rise. GrIS mass loss has contributed approximately 14 mm of sea level rise since the 1970s (Mouginot et al., 2019)–exceeding the upper end of estimates from GCM projections (Slater et al., 2020)–while continued runoff is expected to contribute from 5 to over 30 cm by the end of the century, and complete melt of the ice sheet would raise sea level by over 7 m (Aschwanden et al., 2019).

From a synoptic perspective, Greenland blocking events encourage melt by transporting moist, potentially warm air from unusually low latitudes poleward within the amplified ridge of the blocking anticyclone (Oltmanns et al., 2019; Steinfeld and Pfahl, 2019; Hermann et al., 2020), causing widespread, positive surface temperature anomalies across the ice sheet (Hanna et al., 2014; McLeod and Mote, 2016) (**Figure 2**). Advection from lower latitudes is greatest along the upstream side of the ridge. A common pattern involves southerly winds tracking the western coast of Greenland and curving anticyclonically to the north of the high-pressure center, transporting warm, moist air poleward through the Labrador Sea/Baffin Bay pathway (Baggett and Lee, 2019; Akers et al., 2020) described in *Arctic Moisture Transport Pathways and Climatology* (see **Figure 1**). This results in onshore flow over the ice sheet—a synoptic setting conducive to meltwater production (Mote, 1998b; Fettweis et al., 2011; Fettweis et al., 2013; McLeod and Mote, 2016). This transport of warm, moist air from lower latitudes along with the associated cloud cover anomalies produce widespread surface melt via a spatially varying surface energy balance (SEB) response (Cullather and Nowicki, 2018). However, this exact blocking and moisture transport pattern is not observed during all major GrIS melt events, and the most recent such event in July 2019 involved an unusual blocking pattern transiting westward from Europe to Greenland (Cullather et al., 2020).

The strong advection of heat and moisture during Greenland blocking plays a crucial role in augmenting melt over the steep margins of the ice sheet by mixing warm, moist air to the surface from above the stable boundary layer that typifies the near surface atmosphere, thus enhancing sensible and latent heat flux and increasing the net SEB (Duynkerke and van den Broeke, 1994; van den Broeke and Gallée, 1996; Mattingly et al., 2020). Turbulent heat flux associated with Greenland blocking has been shown to dominate the SEB response during intense melt across much of the ablation zone (Fausto et al., 2016a; Fausto et al., 2016b).

The cloud-radiative effects associated with Greenland blocking are reflective of the interaction between the large-scale synoptic setting and the topography of the ice sheet. As the flow is directed inland to the north of the high-pressure center, anomalously warm and moist air ascends the windward side of the ice sheet, cooling adiabatically (Hahn et al., 2020). This generates an increase in cloud cover and attendant downward longwave radiation while reducing incoming shortwave radiation over northern Greenland and higher elevations of the ice sheet (Hahn et al., 2020; Ward et al., 2020). Conversely, the southern part of the ice sheet is more frequently embedded within the ridge and, consequently, experiences cloud-suppressing subsidence that causes a reduction in downwelling longwave radiation and an increase in incoming shortwave radiation (Hofer et al., 2017; Noël et al., 2019; Hahn et al., 2020; Ward et al., 2020).

The importance of these cloud-radiative effects to the SEB varies geographically as dictated by surface albedo. In locations of high surface albedo, such as northern Greenland and the high-elevation accumulation zone, the SEB is resilient to changes in incoming shortwave radiation and, rather, longwave cloud-radiative effects dominate (Wang B. et al., 2018, Wang et al., 2019; Lenaerts et al., 2019 and references therein). In locations of lower surface albedo, such as southern Greenland and the low-elevation ablation zone, there is a greater sensitivity to changes in incoming shortwave radiation and, consequently, shortwave cloud-radiative effects dominate (Wang W. et al., 2018, Wang et al., 2019; Lenaerts et al., 2019 and references therein; Izeboud et al., 2020). This physical framework explains the seemingly disparate observational results showing that suppressed cloud cover over southern Greenland during frequent blocking events drives GrIS mass loss (Hofer et al., 2017) while also pointing to the critical role of moisture transport and the presence of low-level clouds in generating surface melt at high elevations during extensive melt events (Nghiem et al., 2012; Bennartz et al., 2013; Neff et al., 2014; Van Tricht et al., 2016; Gallagher et al., 2018; Tedesco and Fettweis, 2020).

The impact of each radiative term on the SEB is further complicated by the fact that the surface albedo of the ice sheet is not static with time. In what is referred to as the ice-albedo feedback, surface melt lowers albedo of ice sheet, first by accelerating snow metamorphism, then, in locations of seasonal snowpack, by uncovering lower-albedo glacial ice

(Tedesco et al., 2011; Box et al., 2012; Lenaerts et al., 2019 and references therein). Consequently, the influence of incoming shortwave radiation on the SEB increases following Greenland blocking onset (Tedesco et al., 2011; Tedesco et al., 2013; Tedesco et al., 2016) and the efficacy of shortwave cloud radiative effects is maximized at the heart of the melt season (Wang et al., 2019).

A related mechanism whereby Greenland blocking impacts the GrIS is by inhibiting snowfall that would otherwise act to increase both accumulation and surface albedo, thus driving below-normal SMB across portions of the ice sheet that are located within the ridge (Tedesco et al., 2011; Box et al., 2012; Tedesco and Fettweis, 2020). However, the anomalous moisture transport that accompanies Greenland blocking (e.g., Barrett et al., 2020; see also **Figure 1**) can also cause significant positive SMB anomalies in some situations. Mattingly et al. (2018) show that while strong moisture transport to western Greenland during the melt season is associated with increased melt in the ablation zone, these losses are partially compensated by snowfall in the accumulation zone, while anomalous moisture transport during non-summer months typically produces anomalous snowfall throughout the GrIS, especially in southeast Greenland. This demonstrates that the orientation of blocking anticyclones relative to the topography of the GrIS and their seasonal timing exert critical controls on SMB response.

Arctic Moisture Intrusions: Impacts on Sea Ice and Relationships With Blocking

Numerous studies have found that Arctic moisture intrusions cause sea ice melt or impeded growth. During the cold season, moisture intrusions trigger transitions from the "radiatively clear" to "opaquely cloudy" atmospheric states observed in Arctic field campaigns (Stramler et al., 2011; Woods and Caballero, 2016; Graham et al., 2017b; Cohen et al., 2017; Kayser et al., 2017; Ali and Pithan, 2020). Downwelling longwave radiation is enhanced by anomalous cloud cover and elevated water vapor amounts during subsequent days, which, along with the insulating effect of enhanced snow accumulation during the storms, reduces sea ice growth and may cause the sea ice edge to retreat (Park et al., 2015b; Merkouriadi et al., 2017; Merkouriadi et al., 2020; Persson et al., 2017; Graham et al., 2019). During summer, cyclones are less intense and the warming effect of moisture intrusions may be tempered by their associated negative shortwave cloud radiative effect, but episodes of warm, moist air advection have nevertheless been shown to force sea ice melt (Graversen et al., 2011; Rinke et al., 2019a), with case studies demonstrating the formation of a moist inversion and fog layer over sea ice that enhances downwelling longwave radiation and turbulent heat flux (Tjernström et al., 2015; Tjernström et al., 2019; You et al., 2020). Synoptic storms and moisture intrusions have been found to coincide with the initial melt of sea ice in early summer (Persson, 2012; Else et al., 2014; Hegyi and Deng, 2017) and the period of rapid warming during the Arctic springtime transition (Long and Robinson, 2017). Several studies have found correlations between enhanced winter and spring poleward moisture transport, increased longwave radiation from cloud cover, earlier sea ice melt onset, and decreased sea ice cover during the subsequent September annual minimum (Kapsch et al., 2013; Kapsch et al., 2014; Kapsch et al., 2016; Kapsch et al., 2019; Park et al., 2015a; Cox et al., 2016; Mortin et al., 2016; Cao et al., 2017), although Choi et al. (2014) and Sedlar (2018) find that absorbed shortwave radiation absorption likely plays an important preconditioning role in spring and early summer as well. Winter and spring moisture intrusions are most frequent through the Atlantic sector of the Arctic (Yang and Magnusdottir, 2017; Messori et al., 2018; Hao et al., 2019; Hong et al., 2020; Papritz and Dunn-Sigouin, 2020).

The frequent recent occurrence of atmospheric blocking patterns alongside moist intrusions and warm extremes in the Atlantic and Pacific sectors shows that these circulation features are often closely related, and that blocking also influences sea ice evolution. Anticyclonic flow patterns over the Arctic have been linked to anomalously low summer minimum sea ice extent (Ogi and Wallace, 2012; Bellefamme et al., 2015; Ding et al., 2017; Wernli and Papritz, 2018; Rinke et al., 2019a), to extreme early sea ice melt in the Baffin Bay–Davis Strait–Labrador Sea sector in spring 2013 (Ballinger et al., 2018), and to negative sea ice extent anomalies around Alaska in all seasons (McLeod et al., 2018).

Several recent studies have detailed the complex circulation features and thermodynamic processes that produce episodes of extreme Arctic warmth, including interactions between cyclones, blocking, and moisture transport as well as the coupling between transport from lower latitudes and intra-Arctic thermodynamic processes. Papritz and Dunn-Sigouin (2020) analyzed a climatology of all extreme moisture transport events during winter, finding that planetary-scale anticyclones and synoptic-scale cyclones interact to produce the most extreme events, as blocks deflect the tracks of cyclones poleward and establish a strong poleward transport in the interaction zone between the block and upstream cyclones. During summer, Wernli and Papritz (2018) found that episodic upper-level Arctic anticyclones enhance sea ice reduction, and that extratropical cyclones injecting extratropical air masses with low potential vorticity into the Arctic are responsible for the formation of these anticyclones (in agreement with the extratropical-to-polar transport along moist isentropes described by Laliberté and Kushner (2014)). Binder et al. (2017) examined the dynamic and thermodynamic evolution of a winter 2015–16 extreme Arctic warm event in detail, finding that three air streams with distinct origins and warmed by different processes contributed to the warm episode: warm low-level air of subtropical origin, initially cold low-level air of polar origin heated by surface fluxes, and descending air heated by adiabatic compression. These airstreams were transported poleward by a low-level jet positioned between an anticyclone and a series of cyclones, with further warming by latent heating in a region of continuous warm conveyor belt ascent into the upper part of the anticyclone. Papritz (2020) extended this type of Lagrangian air mass evolution analysis to all Arctic lower-tropospheric warm (and cold) extreme events and found that blocking plays a critical role in generating warm extremes in both summer and winter. Subsidence from the Arctic middle

troposphere in blocking anticyclones was found to be the most important warming process, with anomalous blocking in the Barents, Kara, and Laptev Seas favoring warm extremes during winter and blocks located in the high Arctic during summer, when subsidence within blocks is particularly important for warming. Poleward transport of already warm air masses contributes around 20% to warming during both summer and winter, while about 40% of the air masses originate from the Arctic during winter and are heated diabatically by ocean-atmosphere fluxes in marine cold air outbreaks.

These recent studies expand upon and complicate the traditional view that cyclonic moisture intrusions directly transport already warm, moist air from lower latitudes to warm the Arctic and impact sea ice. It instead appears likely that lower latitude atmospheric processes contribute to Arctic warm events through complex planetary- and synoptic-scale dynamics that involve two-way interactions between the Arctic and lower latitudes in response to initial extratropical forcing, with critical contributions to final warming from intra-Arctic coupling between ocean and land surfaces, the atmospheric boundary layer, and the middle and upper troposphere. A further question concerns the vertical distribution of moisture transport in the Arctic atmosphere and its impact on amplification and near-surface warming. Corridors of direct moisture advection from the mid-latitudes to the Arctic tend to ascend from the surface to the middle troposphere along moist isentropes (Laliberté and Kushner, 2014; Wernli and Papritz, 2018; Hao et al., 2021), and Feldl et al. (2020) find that greater warming and moistening of the upper troposphere does not directly contribute to Arctic amplification as it does not affect the near-surface lapse rate feedback. However, transport of moist air masses from the mid-latitude near-surface layer to the Arctic middle and upper troposphere likely still contributes to Arctic warming indirectly, as latent heat release aids the formation of blocking anticyclones (Pfahl et al., 2015; Grams and Archambault, 2016; Zhang and Wang, 2018; Sánchez et al., 2020) that deflect cyclones poleward (Papritz and Dunn-Sigouin, 2020) and warm the lower troposphere through subsidence (Laliberté and Kushner, 2014; Ding et al., 2017; Wernli and Papritz, 2018; Papritz, 2020).

Further research is needed to clarify the complex interrelationships between cyclone-driven moisture intrusions, blocking, and sea ice in a rapidly changing Arctic, along with the contribution of these phenomena to overall Arctic amplification. These investigations should address the seasonality of cyclonic moisture intrusions and blocking and their role in Arctic warming, as Arctic-amplified warming is most pronounced during winter, while the warming contribution of subsidence within anticyclones is maximized during the summer according to Papritz (2020). Arctic blocking is less studied than in the mid-latitudes, and future studies should ensure that any blocking detection algorithms employed in this emerging area of research are suitable to detect Arctic blocks, which are generally weaker than their mid-latitude counterparts and may not be detected by geopotential height-based algorithms (see *Blocking Definition, Identification, and Northern Hemisphere Climatology*), that require poleward westerlies (Tyrlis et al., 2020). The vertical structure of moisture transport should be carefully examined in relation to blocking and influences on warming, as Arctic moistening in lower levels likely contributes directly to the lapse rate feedback, while middle- and upper-tropospheric moisture transport may contribute to warming through more indirect pathways including latent heat release and blocking development, and/or may act to dampen Arctic amplification due to a negative upper-level lapse rate feedback (Feldl et al., 2020; Hao et al., 2021). The relative importance of and relationships between lower-latitude and within-Arctic processes during Arctic warming events should also be further investigated. Recent studies reviewed here show that a large proportion of air masses originate from within the Arctic during these warm events, but the thermodynamic processes occurring within local and remote air masses to produce warming are linked to extra-Arctic atmospheric circulation features, thus the interactions between variability in the extratropical storm tracks and Arctic circulation extremes are an important avenue for future research. These questions regarding local and remote drivers of episodes of anomalous Arctic warming mirror the broader debate over local and remote influences on Arctic amplification, and future research should assess the overall significance of remotely forced cyclonic moisture intrusions and blocking to Arctic-amplified warming, including their interactions with mechanisms that have traditionally been conceptualized as intra-Arctic processes such as the ice-albedo, lapse rate, and cloud and water vapor feedbacks.

TROPICAL-HIGH LATITUDE SUBSEASONAL TELECONNECTIONS

Intraseasonal Influences on Extratropical Rossby Waves

In order to understand the potential future evolution of high-latitude circulation and its association with Arctic amplification, it is critical to understand lower-latitude and tropical processes. Tropical upper-tropospheric heating produced by thunderstorms in the convectively active region of the leading mode of atmospheric subseasonal variability, the Madden–Julian Oscillation (MJO; Madden and Julian, 1971; Madden and Julian, 1972; Madden and Julian, 1994), has been found to be an effective source of Rossby wave generation to the extratropics and Arctic (Hoskins and Karoly, 1981; Sardeshmukh and Hoskins, 1988; Bladé and Hartmann, 1995; Jin and Hoskins, 1995; Hendon and Salby, 1996). To generate these Rossby waves, diabatic heating produced by MJO deep convection leads to a divergent component of the upper-tropospheric tropical and subtropical wind field. That divergent wind then advects absolute vorticity toward the poles and leads to the formation of a wave train (Kiladis and Weickmann, 1992; Knutson and Weickmann, 1987; Sardeshmukh and Hoskins, 1988; Hendon and Salby, 1994; Higgins and Mo, 1997; Matthews et al., 2004; L'Heureux and Higgins, 2008; Lin et al., 2009; Seo and Son, 2012; Riddle et al., 2013) that can be traced (Seo and Lee, 2017; Barrett, 2019). The Rossby wave train's subtropical origins depend on the

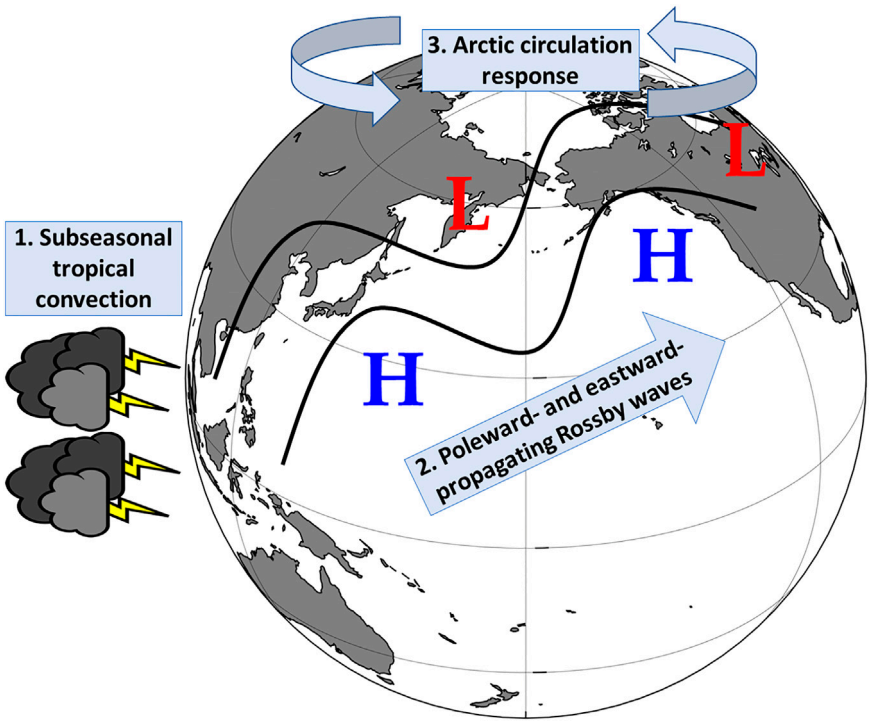

FIGURE 3 | Schematic representing the sequence of processes by which subseasonal tropical convection can influence the poleward and eastward propagation of Rossby waves, resulting in an Arctic circulation response.

longitude of the MJO convection, and the origin of the wave train can move east, in tandem with the diabatic heating source (Johnson and Feldstein, 2010; Hamill and Kiladis, 2014; Stan et al., 2017). The Rossby wave source region can extend across nearly the entire tropical Indian Ocean and the Pacific Ocean west of 180° (Lukens et al., 2017), and that allows the MJO to modulate tropical cyclones in the Atlanitc Ocean (Barrett and Leslie, 2009). One proposed physical mechanism for Rossby wave generation is as follows: when the MJO convection is over the Indian Ocean, horizontal convergence in the tropics and the advection of absolute vorticity in the subtropics develops a cyclonic anomaly over southeast Asia. As MJO convection moves eastward, a Rossby wave train departs the subtropics in the exit region of the subtropical Pacific jet (Lukens et al., 2017). Another proposed physical mechanism for Rossby wave generation involves modulation of the local Walker and Hadley cell circulations (Schwendike et al., 2014) over the Pacific. The subtropical jet over the Pacific is enhanced in regions of anomalous upper-tropospheric (anticyclonic; Roundy, 2012) divergence located poleward of MJO convection (Matthews and Kiladis, 1999; Moore et al., 2010). This jet shifts eastward with the MJO propagation, and regions of enhanced convection strengthen the local Hadley circulation, and as upper-tropospheric flow accelerates poleward due to pressure gradient forces, geostrophic adjustments yield troughing downstream of ridging, thereby producing midlatitude Rossby waves that propagate poleward across the Pacific Ocean in both the Northern and Southern Hemispheres (Schwendike et al., 2021).

Because of this important influence, predicting the future state of high-latitude circulation, precipitation, temperature, and cryosphere (snow and ice) depends on the correctly capturing the temporal evolution and geographical distribution of tropical convection of the MJO (Jones et al., 2004; Marshall et al., 2011; Riddle et al., 2013; Rodney et al., 2013; Goss and Feldstein, 2015; Tseng et al., 2018; Lin and Brunet, 2018; Zheng et al., 2019; Zheng and Chang, 2019; Zheng and Chang, 2020; Tseng et al., 2020). Indeed, the broader topic of polar amplification of surface temperature and precipitation has been linked to poleward-propagating Rossby waves excited by MJO-related tropical convection (**Figure 3**) (Lee et al., 2011). Furthermore, there is evidence that many of the blocked atmospheric circulations in the Arctic that were reviewed in *Blocking Definition, Identification, and Northern Hemisphere Climatology* are have connections to tropical convection on the subseasonal time scale (Henderson et al., 2016; Henderson and Maloney 2018), and even the moisture pathways and atmospheric rivers reviewed in *Blocking Definition, Identification, and Northern Hemisphere Climatology* and *Arctic Moisture Intrusions: Impacts on Sea Ice and Relationships With Blocking* may also have connections to the MJO on the subseasonal time scale (Mundhenk et al., 2016).

It remains an open question whether the extratropical Rossby wave train depends more on characteristics of the source region or either the tropical or extratropical flow (Roundy, 2021). Regardless, the Rossby wave response seems to be strongest

when the MJO diabatic heating structure resembles a dipole but with asymmetries that are not yet fully understood (Lin and Brunet, 2018). Moreover, stronger MJO events do not necessarily produce stronger extratropical responses or in the same location as weaker MJO events (Lafleur et al., 2015). Another uncertainty comes in the timing of the lagged response, with studies suggesting the lag can be anywhere from 1 to 3 weeks (Higgins et al., 2000; Lin and Brunet, 2009; Riddle et al., 2013; Rodney et al., 2013; Schreck et al., 2013; Matsueda and Takaya, 2015; Seo et al., 2016; Hu et al., 2019).

Approximately 30% of the variability of the subseasonal upper-tropospheric extratropical circulation can be linked with MJO-induced teleconnections (**Figure 3**) (Matthews et al., 2004; Seo and Son, 2012; Seo et al., 2016). One of the critical consequences of the diabatic heating of the MJO is that it is able to produce long-lasting responses in the high latitudes that last much longer than their tropical forcing (Matthews et al., 2004; Kim et al., 2006; Branstator, 2014; Franzke et al., 2019). This suggests the low-frequency evolution of the MJO in the future will affect many of the processes responsible for Arctic amplification. One other important open question regarding MJO-linked Rossby waves centers on seasonality. There is much research that suggests the MJO is strongest in extended boreal winter (November-May; see reviews by Zhang, 2005 and Zhang et al., 2013). However, in extended boreal summer months (June-September), the tropical intraseasonal oscillation exhibits multiple propagation characteristics: east and north over the Indian monsoon region (Murakami and Nakazawa, 1985; Hartmann and Michelsen, 1989; Gadgil and Srinivasan, 1990) and northwest over the western North Pacific Ocean (Murakami, 1980; Lau and Chan, 1986; Chen and Murakami, 1988). This change in propagation has led to the MJO being referred to as the boreal summer intraseasonal oscillation (BSISO; Krishnamurti and Subrahmanyam, 1982; Yasunari, 1979). The ability of the BSISO to act as a Rossby wave source into the midlatitudes remains significantly understudied when compared to the MJO (Wang et al., 2020a; Wang et al., 2020b). Thus, studies of Arctic amplification in summer months should also consider the teleconnected influence from the BSISO in the tropics, just as studies of Arctic amplification in winter should consider the influence from the tropical MJO.

Despite the remaining questions on the seasonality and strength of the MJO-driven Rossby wave trains, it is very clear that the MJO modulates a wide range of weather phenomena located in the tropics, the mid-latitudes and even in the high latitudes.

Subseasonal Influence on Mid-to-High Latitude Circulation and Surface Variables

In addition to the Rossby wave pathways discussed in *Intraseasonal Influences on Extratropical Rossby Waves*, another primary way by which the MJO influences surface variables is by strongly modulating the extratropical North Atlantic Oscillation (NAO) and Pacific–North American (PNA) pattern. The PNA and NAO are two of the leading modes of Northern Hemisphere extratropical variability (Blackmon et al., 1984; Hurrell et al., 2001). Over the Pacific, the PNA pattern has been found to be related to the MJO. The MJO's modulation of the PNA pattern is caused by two Rossby wave sources: a negative source north of MJO-enhanced convection over the Indian Ocean and a positive source north of the MJO-enhanced convection over the western Pacific Ocean (Seo and Lee, 2017). When the MJO convection is in the Pacific Ocean, it tends to excite the positive PNA phase, which translates into above-normal geopotential heights over western North American, below-normal heights over eastern North America (Higgins and Mo, 1997; Mori and Watanabe, 2008; Franzke et al., 2011), and colder-than-normal temperatures over the northeastern United States (Leathers et al., 1991).

Flatau and Kim (2013) noted that the MJO forces the annular modes (the AO and NAO) on intraseasonal time scales. The MJO and NAO have a statistically significant time-lagged relationship. Between 7 and 10 days after MJO convection is over the Indian Ocean (phases 2–3), the probability of a positive NAO is increased significantly from the background climatology. Similarly, between 7 and 10 days after MJO convection is over the western Pacific Ocean (phases 6–7), the probability of a negative NAO is increased significantly (Cassou, 2008; Lin et al., 2009; Yadav and Straus, 2017). This pathway, called by Barnes et al. (2019) the "tropospheric pathway", is one way that the MJO can influence the NAO. Another mechanism is via the polar stratosphere, and that is not reviewed here, beyond noting that the tropospheric pathway may depend on the prevailing direction of tropical stratospheric winds of the quasi-biennial oscillation (QBO) (when QBO is westerly, the MJO-NAO tropospheric pathway is more robust; Barnes et al., 2019; Feng and Lin, 2019). A positive NAO is associated with anomalous ridging over the eastern United States and North Atlantic Ocean and thus with warmer surface air temperatures and less precipitation (Hurrell et al., 2001; Hurrell et al., 2003). Conversely, a negative NAO is associated with anomalous troughing over the eastern United States and North Atlantic Ocean and thus colder surface air temperatures and more precipitation. Thus, above-average surface temperatures and below-normal precipitation can be expected over the eastern United States after MJO convection is over the Indian Ocean. Similarly, colder temperatures and above-normal precipitation can be expected after MJO convection is over the western Pacific Ocean.

The MJO's impacts on surface weather can be explained by the extratropical circulation anomalies forced by the tropical MJO convection (**Figure 3**). Zheng et al. (2018) noted that impacts on extratropical sea-level pressure, and thereby cyclone activity, may be greatest over the eastern North Pacific, the southeastern United States, Canada, and the north-central Atlantic Ocean. Temperature impacts, however, could be more significant over the eastern U.S. (Zheng and Chan, 2019). The anomalies in pressure and temperature have been definitively linked to the Rossby wave trains excited by the MJO, given that the upper-tropospheric circulation anomalies are equivalent barotropic (Zheng and Chan, 2019), thereby allowing any enhancement or suppression of the wind field to cause temperature advection. Zheng and Chan (2019) conclude: "the upper-level Rossby wave

train is very important as it connects the MJO and extratropical surface weather anomalies."

One of the most important ways in which the MJO's influence extends to the Northern Hemisphere high latitudes is via its influence on surface air temperature (Lin and Brunet 2009; Yao et al., 2011; Yoo et al., 2011; Yoo et al., 2012; Zhou et al., 2012; Rodney et al., 2013; Johnson et al., 2014; Yoo et al., 2014; Lin 2015; Oliver 2015) and precipitation (Bond and Vecchi 2003; Jeong et al., 2008; Lin et al., 2010; Becker et al., 2011; He et al., 2011; Baxter et al., 2014; Jones and Carvalho 2014). Vecchi and Bond (2004) found that geopotential height, specific humidity, and surface air temperature in the Arctic varied by phase of the MJO, while Lin and Brunet (2009) confirmed a similar response of surface air temperature in Canada. Modulation of the Arctic atmosphere specifically, by phase of MJO has also been documented (L'Heureux and Higgins 2008; Yoo et al., 2011), while Yoo et al. (2012) further confirmed the MJO-driven, poleward propagating wave train drove changes in the Arctic overturning circulation, heat flux, and downward infrared radiation. Barrett et al. (2015), Klotzbach et al. (2016), Henderson et al. (2017), and Barrett (2019) noted that the MJO's influence on circulation and temperature extends to snowfall, and that for the eastern parts of North America, snowfall, snow depth change, and snow water equivalent change all tended to be above normal (or snowier) after MJO convection in phases 8 and 1. This relationship between the MJO and NAO appears to be strongest when the El Niño–Southern Oscillation (ENSO) is in negative (La Niña) phase (Roundy et al., 2010), and as discussed above, when the stratospheric QBO is in its easterly phase (Yoo and Son, 2016).

In addition to documented relationships between MJO and high-latitude temperature and precipitation tendencies via modulation of large-scale circulation, the MJO's influence has already been found to extend to Arctic sea ice (Henderson et al., 2014), by projecting onto the Arctic atmosphere in both boreal winter and summer seasons. Indeed, sea ice concentration is lower in both the Barents and Kara Seas one to two weeks after convection over the Maritime Continent, as a result of stationary wave interference and subsequent Arctic warming (Goss et al., 2016). Variability in sea ice concentration by phase of MJO was supported by corresponding lower troposphere atmospheric anomalies, with evidence of sea ice modulation occurring regionally. Daily changes in Northern Hemisphere (NH) spring snow depth by phase of MJO was explored by Barrett et al. (2015), with statistically significant depth anomalies found in March, april and May for both North America and Eurasia. In October, correlations between patterns of snow water equivalent (SWE) variability over Eurasia and mid-tropospheric geopotential heights were largest during MJO phases 4–7, indicating that tropical convection anomalies over the Indian Ocean and Maritime continent had the most impact on October circulation and snow variability (Henderson et al., 2017). These studies therefore provide additional evidence for connections between the tropics and the extratropics on subseasonal timescales.

FUTURE IMPLICATIONS FOR BLOCKING, MOISTURE TRANSPORT, SUBSEASONAL VARIABILITY, AND ARCTIC AMPLIFICATION

Arctic Amplification & Northern Hemisphere Blocking

There are several working hypotheses for how Arctic Amplification may influence mid-latitude weather extremes, and we refer the reader to existing reviews of the subject for a more thorough examination of the mechanisms behind both winter (Cohen et al., 2014; Cohen et al., 2020) and summer (Coumou et al., 2018) circulation response to Arctic change. Here, we briefly summarize some of these theoretical frameworks as they pertain to blocking. One prominent hypothesis to explain changes in mid-to high-latitude atmospheric circulation follows from the observation that Arctic amplification weakens the near-surface meridional temperature gradient, thus reducing the strength of the jet stream aloft (Francis and Vavrus, 2012; Francis and Vavrus, 2015; Cvijanovic and Caldeira, 2015; Deser et al., 2015; Vavrus et al., 2017). It is proposed that, under a weaker jet, Rossby waves become more amplified, and their westward progression slows, creating conditions that are conducive to blocking (Francis and Vavrus, 2012). It has also been argued that changes in snow cover or sea ice extent can exert an influence on blocking by altering the stationary wave pattern, thus bringing the background state of the atmosphere in certain regions closer to blocked conditions (Matsumura and Yamazaki, 2011; Wu et al., 2013; Cohen et al., 2014; Kim et al., 2014; Nakamura and Huang, 2018). Regarding winter circulation response, research efforts have also placed focus on a stratospheric pathway, where reduced sea ice along the Siberian coast may work in concert with increased snow cover over Eurasia in fall to elicit an increase in the upward propagation of Rossby waves that then disrupts the stratospheric polar vortex and exerts a downward influence on the troposphere, causing a negative AO by late winter (Cohen et al., 2007; Kim et al., 2014; Sun et al., 2015; McKenna et al., 2018; Henderson et al., 2018, Siew et al., 2020). This is relevant to blocking as the negative AO is associated with increased blocking throughout the Northern Hemisphere (Thompson and Wallace, 1998; Hassanzadeh and Kuang, 2015). In summer, it is thought that the enhanced thermal contrast between land and ocean under Arctic amplification increases the formation of wave guides that can encourage wave-amplifying resonance between free and forced Rossby waves, in turn promoting high-amplitude, persistent weather patterns such as those associated with atmospheric blocking (Coumou et al., 2018 and references therein).

Observed and Projected Trends in Northern Hemisphere Blocking, the Greenland Ice Sheet, and Poleward Moisture Transport

Documenting observational support of the theoretical linkages between Arctic amplification and blocking outlined above is an active area of research. While there is no current consensus about

observed trends in overall Northern Hemisphere blocking (Woollings et al., 2018), regional trends have been documented despite differences among both blocking metrics and datasets (Barnes et al., 2014).

An analysis of Local Wave Activity has suggested increases in such activity correspond to increases in blocking (Martineau et al., 2017), where cyclonic events are most influential for the development of high-latitude blocks (e.g., Woollings et al., 2018). Martineau et al. (2017) show an increase in local wave amplitudes (i.e., waviness) over East Asia, noting, however, trends in teleconnections such as El Nino/Southern Oscillation (ENSO), the Arctic Oscillation (AO)/North Atlantic Oscillation (NAO), and Pacific-North American teleconnections (PNA) may explain this connection (e.g., Cohen et al., 2012; Kosaka and Xie 2013). In particular, the negative phase of the AO/NAO is associated with both an increased frequency and higher latitude of blocking highs throughout the Northern Hemisphere (Thompson and Wallace, 1998; Hassanzadeh and Kuang, 2015).

Belleflamme et al. (2015) and Ballinger et al. (2014) show that increased anticyclonic activity over the Beaufort Sea and Greenland regions from 1980–2014 may have both contributed to and been the result of Arctic sea ice loss. In particular, the period of 2007–2012 experienced significant anticyclonic circulation anomalies in these regions, which cannot be attributed to either natural climate variability or anthropogenic climate change (Belleflamme et al., 2015; Ballinger et al., 2014; and references therein). In their review paper, Woollings et al. (2018) indicate historical increases in JJA blocking, depending on the metric used, particularly over Greenland and the North Atlantic as well as the Bering Sea during the 1958–2012 period.

GCMs included in the Coupled Model Intercomparison Project phase 3 (CMIP3) and phase 5 (CMIP5) intercomparisons have suggested an overall decrease in blocking frequency in response to climate change in the Northern Hemisphere (e.g., Barnes et al., 2012; Dunn-Sigouin and Son, 2013; Matsueda and Endo, 2017). Most CMIP5 models qualitatively simulate the blocking climatology locations, but underestimate blocking frequency under the RCP8.5 scenario (Dunn-Sigouin and Son, 2013). However, the trends appear to vary both regionally and seasonally. Kennedy et al. (2016) show a decrease in blocking over Eurasia, which is consistent with findings from other studies (e.g., Masato et al., 2013a; Hanna et al., 2018a); Woollings et al., 2018. Under the RCP8.5 scenario, there will likely be a decrease in blocking frequency in both the North Atlantic and North Pacific in fall and winter (Dunn-Sigouin and Son, 2013). Dunn-Sigouin and Son (2013) also show an increase in Ural blocking in future scenarios, although this result is not robust, as described in Woollings et al. (2018). Interestingly, they suggest an increase in European blocking. Additionally, the spatial extent of blocking events is expected to increase, where this increase is greatest for summer blocking (Nabizadeh et al., 2019).

More recently, there has been significant improvement in blocking representation from CMIP5 to CMIP6, though the extent of this improvement still remains dependent on individual models, selected blocking metrics, regions, and seasons (e.g., Davini and D'Andrea, 2020; Schiemann et al., 2020; Simpson et al., 2020). For example, Simpson et al. (2020), Supplementary Information report that overall CMIP6 models appear to better represent the observed spatial climatology compared to CMIP5 although systematic biases in the mean climate state maybe the cause of readily apparent underestimation of wintertime European blocks, and under-(over-)estimation of summer Ural (Eastern Russia) blocking frequency. Similarly, Davini and D'Andrea (2020) confirm the improved overall representation compared to CMIP3. Current CMIP6 projections suggest an overall decrease in blocking more generally in winter and summer, with possible increases in the (summer) Ural and (winter) western North American blocking (Davini and D'Andrea, 2020). Schiemann et al. (2020) report that the regional CMIP6 blocking bias magnitude is sensitive to the blocking metric used.

Given the impact on GrIS SMB, there is a clear motivation to understand long-term variability in Greenland blocking frequency. On an interannual basis, blocking frequency over Greenland has been shown to be strongly related to the North Atlantic Oscillation (NAO). The frequency of blocking highs over Greenland is greater when the NAO is in its negative phase, i.e., when the difference between its two pressure centers, the Azores and Iceland, is minimized (Hanna et al., 2014; Hanna et al., 2015; Hanna et al., 2018a; Hofer et al., 2017). As such, both the NAO and Greenland blocking have been linked to GrIS melt variability, with the latter explaining more of the variance in surface melt (Mote, 1998a; Hanna et al., 2013; McLeod and Mote, 2016).

A growing body of work has highlighted an increase in summer Greenland blocking over the past 2 decades, particularly as measured by the GBI (e.g., Hanna et al., 2016; Hanna et al., 2018a; Hanna et al., 2018b; McLeod and Mote, 2016; Barrett et al., 2020; Wachowicz et al., 2021). Wachowicz et al. (2021) confirmed this summer increase using a 5-years running mean of blocking frequency as measured using both geopotential-height-reversal-based and potential-vorticity-based blocking indices. As one might expect given relationship outlined above, this increase in blocking frequency has coincided with a period of a more negative NAO conditions (Fettweis et al., 2013; van Angelen et al., 2014; Bevis et al., 2019), all of which has occurred against a backdrop of dramatic sea ice and snow cover loss (Derksen and Brown, 2012; Cohen et al., 2014; Pithan and Mauritsen, 2014; Stroeve and Notz, 2018). The coincident nature of these events has spurred interest in the possibility that the change in circulation may be a feature of arctic amplification.

Several studies have invoked either declining sea ice or snow cover as a potential explanation for anomalous anticyclonic conditions over Greenland. A collection of modeling and observational studies has demonstrated anomalous anticyclonic conditions over Greenland in years of low sea ice extent (Screen, 2013; Wu et al., 2013; Petrie et al., 2015; Liu et al., 2016), suggesting the additional heat flux from the ice-free ocean may act to enforce the ridge aloft. Supporting this theory, Wu et al. (2013) tied the summer circulation response to sea ice in the seas west of Greenland by tracking a stationary wave that originates at the surface in spring then persists into summer.

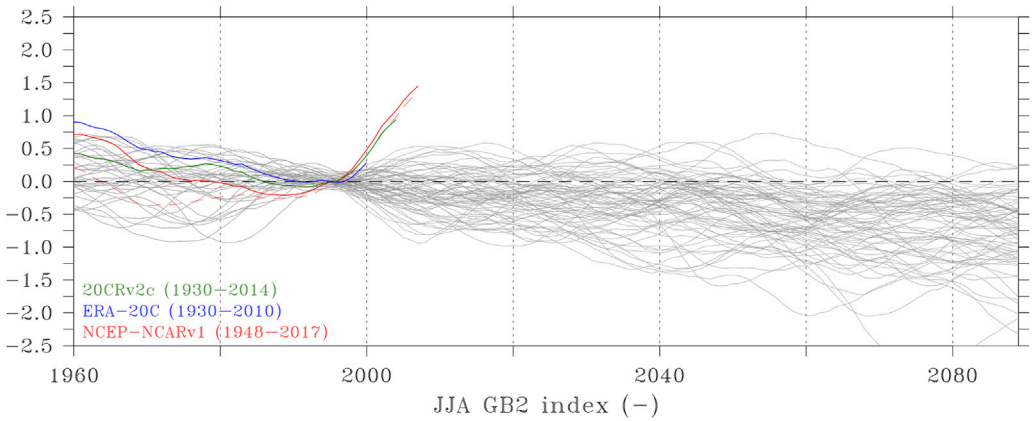

FIGURE 4 | Time series of June, July and August Greenland Blocking Index 1 (dashed red line) and Greenland Blocking Index 2 (solid red line) indices over 1950–2,100 as simulated by NCEP/NCAR Reanalysis 1 (red line), by 20CRv2c reanalysis (green line), and by ERA-20C reanalysis in blue as well as by all the CMIP5 models (gray lines) for which both RCP4.5 and RCP8.5 scenarios are available. For the CMIP5-based time series, the historical scenario is used over 1900–2005 and both RCP4.5 and RCP8.5 afterward. A 20-years running mean has been applied to smooth the time series, and values have been normalized (average = 0 and standard deviation = 1) using 1986–2005 as the reference period, from Hanna et al. (2018a).

Alternatively, Overland et al. (2012) pointed to the observed decline in Northern Hemisphere snow cover extent as a potential explanation for a recent shift in Arctic circulation that features positive pressure anomalies spanning the Arctic coastline of North America, including all of Greenland. Later work demonstrated a possible physical mechanism for this theory where low spring Eurasian snow cover extent increases the poleward propagation of Rossby waves which acts to decelerate the polar jet and encourage a negative AO (Matsumura et al., 2014)—conditions that are associated with increased blocking frequency (Thompson and Wallace, 1998; Hanna et al., 2014; Hanna et al., 2015; Hanna et al., 2018b; Hassanzadeh and Kuang, 2015).

Collectively, GCMs from CMIP3 through CMIP6 have consistently projected a decline in North Atlantic blocking in both winter and summer under future climate scenarios (Davini and D'Andrea, 2020; Masato et al., 2013b; Hanna et al., 2018a). However, GCMs generally fail to adequately represent blocking frequency and duration (Vial and Osborn, 2012; Woollings et al., 2018) and, critically, historical GCM simulations fail to capture the recent positive trend in summertime Greenland blocking, undermining confidence in projections of future blocking in this region (Davini and D'Andrea, 2020; Hanna et al., 2018a) (**Figure 4**). This underrepresentation carries significant implications, as accurate representation of regional circulation over Greenland is essential for GrIS SMB projections. Indeed, underestimation of GrIS SMB loss is a primary contributor to the negative bias in GCM projections of sea-level rise to date (Slater et al., 2020). Furthermore, a recent idealized modeling analysis found that a continuation of the recent increase in Greenland blocking would cause SMB losses to be more than twice than what is currently estimated from GCM projections (Delhasse et al., 2018).

An increasing trend in episodes of warm and moist air intrusion into the Arctic has been observed. Several episodes of extreme winter warmth have extended latitudinally to the North Pole in recent years (Park D. S. R. et al., 2015; Cullather et al., 2016; Moore, 2016; Lee H. J. et al., 2017; Graham et al., 2017a; Binder et al., 2017; Kim et al., 2017; Kohnemann et al., 2017), and southerly winds contributed to the appearance of anomalous polynya north of Greenland during February–March and August–September 2018 (Moore et al., 2018; Ludwig et al., 2019; Lei et al., 2020). These extreme warm events are often coupled to Ural and Scandinavian blocking patterns (Luo et al., 2017; Rinke et al., 2017; Luo et al., 2019), and their frequent recurrence in recent winters may be linked to the increased incursion of warm, salty Atlantic Water—known as "Atlantification"—in the Atlantic sector of the Arctic Ocean (Alexeev et al., 2017; Polyakov et al., 2017; Polyakov et al., 2020a; Polyakov et al., 2020b; Barton et al., 2018; Tsubouchi et al., 2021). Dramatic sea ice decline and ocean warming have also been observed in the Pacific sector of the Arctic during recent years, alongside persistent atmospheric blocking and southerly moisture intrusions (Lee S. et al., 2017; Overland et al., 2018; Ballinger et al., 2019; Tachibana et al., 2019; Polyakov et al., 2020a; Huntington et al., 2020; Kodaira et al., 2020; Thoman et al., 2020).

Model simulations of future climate states indicate that poleward moisture transport into the Arctic will increase in the future, while dry static energy transport will decrease due to a decreased temperature gradient between the Arctic and lower latitudes (Hwang et al., 2011; Yoshimori et al., 2014b; Yoshimori et al., 2017; Graversen and Burtu, 2016; Feldl et al., 2017; Feldl et al., 2020; Graversen and Langen, 2019). In general, increased poleward water vapor flux can be expected to contribute to amplified Arctic warming through the greenhouse effect of water vapor and clouds as well as latent heat release from condensation. However, recent studies reviewed in *Arctic Circulation Features: Blocking, Moisture Transport, and Coupling With the Cryosphere* suggest that the warming

impact of increasing moisture flux will not be spatially and temporally uniform, and will depend on the vertical structure of water vapor transport as well as its interaction with the atmospheric circulation. Further, changes in water vapor transport from outside the Arctic will likely interact in complex ways with changing within-Arctic hydroclimatological conditions resulting from sea ice loss and ocean warming. The influence of declining sea ice on cyclones, moisture transport, and blocking, and in turn the feedbacks of these atmospheric processes into sea ice and oceanic conditions, should be studied further. For example, Kim and Kim (2017) hypothesized that the increasing open water fraction from sea ice decline will reduce the ocean-atmosphere temperature gradient and suppress turbulent heat flux into the atmosphere, which will serve to slow Arctic warming and enhance the role of atmospheric heat and moisture transport from lower latitudes in Arctic climate.

Future Trends in Tropical-To-Arctic Teleconnections

High-latitude atmospheric circulation is strongly influenced by lower-latitude processes, including those from the tropical and subtropical Pacific, through the poleward propagation of Rossby wave trains (e.g., Ding et al., 2014; Feng et al., 2017; Jiménez-Esteve and Domeisen, 2018). In order to understand the potential future evolution of the high-latitude circulation and its association with Arctic amplification, it is necessary to understand the future evolution of those lower-latitude processes. Some studies suggest that recent Arctic amplification could be at least partially attributed to enhanced warm-air advection and moisture transport by Rossby waves associated with an increase in the frequency of MJO activity over the western Pacific and Maritime Continent (Lee et al., 2011; Yoo et al., 2011; Yoo et al., 2012; Seo et al., 2016; Jiang et al., 2020). However, there are more studies that examine changes in the MJO (both historical and future) than changes in MJO-driven teleconnections to the high latitudes. Here, we review aspects of both changes to the MJO and its teleconnections.

The MJO is strongly influenced by the atmospheric mean state in the tropics (Maloney and Hartmann, 2001; Inness and Slingo, 2003; Zhang and Dong, 2004; Maloney and Xie, 2013). Thus, changes in tropical sea-surface temperatures, wind shear, moisture availability, and stability driven by anthropogenic global warming all have the potential to influence the MJO, and by association, Arctic amplification. Some studies suggest that the amplitude of the MJO may intensify and its variance increase with increasing warming (Takahashi et al., 2011; Liu et al., 2013; Schubert et al., 2013; Subramanian et al., 2014; Arnold et al., 2015; Wolding et al., 2017; Haertel, 2018; Rushley et al., 2019). Others suggest the MJO may become spatially more expansive in the zonal direction, with greater surface convergence, enhanced deep convection, faster eastward propagation, and more heating (Caballero and Huber, 2010; Arnold et al., 2013; Liu, 2013; Liu et al., 2013; Chang et al., 2015; Song and Seo, 2016; Adames et al., 2017; Cui and Li 2019). While most studies suggest a more intense MJO over the 21st century, some suggest that an increase in tropical static stability may weaken the MJO's generation of Rossby waves (Bui and Maloney, 2018; Bui and Maloney, 2019a) by weakening the wind response. This weakening would have important implications for Arctic amplification, since the divergent flow anomalies produced by the MJO's anomalous heating are the source for Rossby wave generation into the extratropics (Sardeshmukh and Hoskins, 1988; Wolding et al., 2017; Maloney et al., 2019). Some modeling results suggest that teleconnected impacts in the Arctic may be weaker per unit of MJO precipitation anomaly over the next several decades (Jiang et al., 2020). This is further complicated because the MJO-Arctic link depends strongly on complex, nonlinear changes in extratropical static stability, storm track, North Pacific jet stream, and other aspects of the general circulation that all impact the receivership state of the Arctic to MJO teleconnections (Kang and Tziperman, 2018; Bui and Maloney, 2019b; Jiang et al., 2020).

Given all this, many questions remain unanswered regarding the role of tropical teleconnections and their impact on Arctic amplification. The extent to which MJO can influence atmospheric blocking is relatively understudied; however, preliminary work suggests that not only does MJO affect blocking frequency in particular at higher latitudes (Henderson et al., 2016), the relationship is also influenced by ENSO phase (Henderson et al., 2018). Future implications of this tropical-to-Arctic Amplification linkage are further complicated as studies disagree on projections of increased MJO precipitation under warmer climates (e.g., Schubert et al., 2013; Rushley et al., 2019). Moreover, few studies have examined either MJO teleconnections, in general, or MJO-Arctic linkages in warmer climates (e.g., Maloney et al., 2019; Jiang et al., 2020). More research is needed to fully understand the complex, multi-layered and non-linear processes that connect tropical and extratropical atmospheric circulation, its interaction with atmospheric blocking and moisture transport, and subsequent impacts on and amplification of changing Arctic atmospheric and surface variables.

Summary and Discussion

Arctic amplification is a fundamental feature of past, present, and modeled future climate. However, the causes of this amplification within Earth's climate system are not fully understood. To date, warming in the Arctic has been most pronounced in autumn and winter seasons, with this trend predicted to continue based on model projections of future climate. The intra-Arctic feedbacks by which this is taking place are numerous and interconnected, while extra-Arctic processes, in particular changes to large-scale atmospheric circulation and moisture transport, are entangled with these internal feedbacks in complex ways.

A question we pose is whether external forcing from the tropics is appropriately considered in a discussion of Arctic amplification. If one defines Arctic amplification in a manner in which the Arctic specifies both the region in which the enhanced warming is observed and also all feedbacks involving amplification occur, then consideration of tropical forcing would fall outside the discussion. However, if we broaden the discussion to include mechanisms that import

sensible and latent heat into the Arctic and thereby enhance local longwave forcing, in addition to mechanisms that modulate Arctic atmospheric circulation, triggering within-Arctic feedbacks (e.g., ice-albedo, lapse rate), then inclusion of forcing from lower latitudes becomes critical. We therefore have reviewed forcings acting within and external to the Arctic that lead to enhanced warming and cryospheric impacts in this region.

We have anchored our discussion of Arctic atmospheric circulation features on atmospheric blocking and moisture transport, as these phenomena have been widely studied and are interrelated mechanisms by which lower-latitude processes can couple with high-latitude Arctic climate. Blocking can broadly be defined as a quasi-stationary anomalous anticyclonic circulation pattern which disrupts the eastward propagation of cyclones and other systems, analogous to traffic congestion within the atmosphere (Nakamura and Huang, 2018). Poleward moisture transport into the Arctic is primarily accomplished by short-lived intrusion events associated with cyclones, which preferentially occur in certain regions and seasons as detailed in *Arctic Moisture Transport Pathways and Climatology*. Blocking and moisture transport are closely related, as poleward moisture transport is favored along the upstream flank of a blocking anticyclone, and latent heat release within the moisture plume often helps maintain or strengthen the block. These phenomena have important regional and global climate implications due to their influence on Greenland Ice Sheet surface mass balance and Arctic sea ice variability (*Greenland Blocking: Impacts on Ice Sheet Surface Mass Balance and Relationships With Moisture Transport* and *Arctic Moisture Intrusions: Impacts on Sea Ice and Relationships With Blocking*). Greenland blocking and episodes of extreme moisture transport into the Atlantic and Pacific sectors of the Arctic have shown increasing trends in recent years, highlighting the importance of further research to clarify the complex interrelationship between cyclone-driven moisture intrusions, blocking, and sea and land ice in a rapidly changing Arctic, along with the contribution of these phenomena to overall Arctic amplification.

With the nature of these Arctic moisture intrusions being associated with short-lived, intense events linked to cyclones (Sorteberg and Walsh, 2008; Dufour et al., 2016; Rinke et al., 2017; Villamil-Otero et al., 2018; Fearon et al., 2020) and Rossby wave breaking (Liu and Barnes, 2015), we have also reviewed the role of tropical subseasonal atmospheric variability in forcing extratropical and polar atmospheric circulation (*Tropical-High Latitude Subseasonal Teleconnections*). The MJO has been found to be an effective source of Rossby wave generation to the extratropics (Hoskins and Karoly, 1981; Sardeshmukh and Hoskins, 1988; Bladé and Hartmann 1995; Jin and Hoskins, 1995; Hendon and Salby, 1996), with poleward-propagating Rossby waves excited by MJO-related tropical convection being linked to polar amplification of surface air temperature (Lin and Brunet, 2009; Lee et al., 2011; Yao et al., 2011; Yoo et al., 2011; Yoo et al., 2012; Zhou et al., 2012; Rodney et al., 2013; Johnson et al., 2014; Yoo et al., 2014; Lin, 2015; Oliver, 2015), precipitation (Bond and Vecchi, 2003; Jeong et al., 2008; Lin et al., 2010; Becker et al., 2011; He et al., 2011; Baxter et al., 2014; Jones and Carvalho 2014), sea-level pressure, snow depth (Barrett et al., 2015; Henderson et al., 2017), and sea ice (Henderson et al., 2014).

Although our focus in this review is on subseasonal extra-Arctic forcing originating in the tropical Pacific and Indian Oceans, we also note that a number of studies have shown that Atlantic Ocean variability can influence Northern Hemisphere high latitude climate on interannual to multidecadal time scales (e.g., Kwon and Joyce, 2013; Hahn et al., 2018; Kwon et al., 2018; Kwon et al., 2020; Joyce et al., 2019; Athanasiadis et al., 2020). Future studies should examine the relative importance and characteristic time scales of these Indo-Pacific and Atlantic influences on Arctic climate in a coherent framework.

When considering future Arctic climate, a great deal of uncertainty exists due to rapid, and in some cases unprecedented, changes that have already occurred in recent decades. Here, we have focused on within- and extra-Arctic process drivers, specifically high-latitude atmospheric blocking, poleward moisture transport, and tropical-high latitude subseasonal teleconnections, and the role they have on the Arctic atmosphere, surface variables and amplification of changes in this region. Remaining questions arise from 1) the theoretical linkages between Arctic amplification and blocking, 2) the future evolution of poleward moist and dry static energy transport, and 3) future change in tropical subseasonal variability. Observed blocking trends are dependent on the metrics used to quantify such events and there are inconsistencies in current climate models' abilities to fully capture blocking. Poleward moisture transport is projected to increase in a warming climate, but the vertical structure of moisture transport will likely determine the magnitude of its contribution to Arctic surface warming (*Arctic Moisture Intrusions: Impacts on Sea Ice and Relationships With Blocking*), and decreasing dry static energy transport due to sea ice loss may limit increases in total atmospheric heat transport to the Arctic (Audette et al., 2021). Similarly, divergent consensus on future trends of tropical subseasonal variability under a warmer climate makes projections of MJO-Arctic linkages under such climates challenging, and warrants more research to understand this complex and highly non-linear connection between the tropics and Arctic amplification.

AUTHOR CONTRIBUTIONS

GH outlined the study scope, which was then further developed by all authors. Additionally, she co-led *Intraseasonal Influences on Extratropical Rossby Waves*, *Subseasonal Influence on Mid-to-High Latitude Circulation and Surface Variables*, and *Future Trends in Tropical-To-Arctic Teleconnections* with BB, and led *Summary and Discussion*. Additionally, Barrett produced the **Figure 3** schematic. KM outlined *Arctic Circulation Features: Blocking, Moisture Transport, and Coupling With the Cryosphere* with LW and JP, and led the writing of *Arctic Moisture Transport Pathways and Climatology*, *Arctic Moisture Intrusions: Impacts on Sea Ice and Relationships With Blocking* and *Observed and Projected*

Trends in Northern Hemisphere Blocking, the Greenland Ice Sheet, and Poleward Moisture Transport. LW and JP led the writing on *Blocking Definition, Identification, and Northern Hemisphere Climatology*, *Greenland Blocking: Impacts on Ice Sheet Surface Mass Balance and Relationships With Moisture Transport* and *Arctic Amplification & Northern Hemisphere Blocking*. TM helped frame the paper, and contributed to *Summary and Discussion*.

FUNDING

Funding for this research was provided by the Strategic Environmental Research and Development Program (SERDP), grant award number RC18-1658, and partially by the National Science Foundation Office of Polar Programs (OPP), award number 1821915.

REFERENCES

Adames, Á. F., Kim, D., Sobel, A. H., Del Genio, A., and Wu, J. (2017). Changes in the Structure and Propagation of the M JO with Increasing C O 2. *J. Adv. Model. Earth Syst.* 9 (2), 1251–1268. doi:10.1002/2017ms000913

Akers, P. D., Kopec, B. G., Mattingly, K. S., Klein, E. S., Causey, D., and Welker, J. M. (2020). Baffin Bay Sea Ice Extent and Synoptic Moisture Transport Drive Water Vapor Isotope (δ18O, δD, D-Excess) Variability in Coastal Northwest Greenland. *Atmos. Chem. Phys.* 20 (22), 13929–13955. doi:10.5194/acp-2020-340

Alexeev, V. A., and Jackson, C. H. (2013). Polar Amplification: Is Atmospheric Heat Transport Important?. *Clim. Dyn.* 41, 533–547. doi:10.1007/s00382-012-1601-z

Alexeev, V. A., Walsh, J. E., Ivanov, V. V., Semenov, V. A., and Smirnov, A. V. (2017). Warming in the Nordic Seas, North Atlantic Storms and Thinning Arctic Sea Ice. *Environ. Res. Lett.* 12, 084011. doi:10.1088/1748-9326/aa7a1d

Ali, S. M., and Pithan, F. (2020). Following Moist Intrusions into the Arctic Using SHEBA Observations in a Lagrangian Perspective. *Q. J. R. Meteorol. Soc.* 146, 3522–3533. doi:10.1002/qj.3859

American Meteorological Society (2020). *Blocking. Glossary of Meteorology*. US: Weatherwise. . Available at: http://glossary.ametsoc.org/wiki/blocking.

Arnold, N. P., Branson, M., Kuang, Z., Randall, D. A., and Tziperman, E. (2015). MJO Intensification with Warming in the Superparameterized CESM. *J. Clim.* 28, 2706–2724. doi:10.1175/JCLI-D-14-00494.1

Arnold, N. P., Kuang, Z., and Tziperman, E. (2013). Enhanced MJO-like Variability at High SST. *J. Clim.* 26, 988–1001. doi:10.1175/jcli-d-12-00272.1

Aschwanden, A., Fahnestock, M. A., Truffer, M., Brinkerhoff, D. J., Hock, R., Khroulev, C., et al. (2019). Contribution of the Greenland Ice Sheet to Sea Level over the Next Millennium. *Sci. Adv.* 5, eaav9396. doi:10.1126/sciadv.aav9396

Athanasiadis, P. J., Yeager, S., Kwon, Y.-O., Bellucci, A., Smith, D. W., and Tibaldi, S. (2020). Decadal Predictability of North Atlantic Blocking and the NAO. *Npj Clim. Atmos. Sci.* 3, 20. doi:10.1038/s41612-020-0120-6

Audette, A., Fajber, R. A., Kushner, P. J., Wu, Y., Peings, Y., Magnusdottir, G., et al. (2021). Opposite Responses of the Dry and Moist Eddy Heat Transport into the Arctic in the PAMIP Experiments. *Geophys. Res. Lett.* 48 (9), e2020GL089990. doi:10.1029/2020GL089990

Baggett, C., Lee, S., and Feldstein, S. (2016). An Investigation of the Presence of Atmospheric Rivers over the North Pacific during Planetary-Scale Wave Life Cycles and Their Role in Arctic Warming. *J. Atmos. Sci.* 73, 4329–4347. doi:10.1175/JAS-D-16-0033.1

Baggett, C., and Lee, S. (2019). Summertime Midlatitude Weather and Climate Extremes Induced by Moisture Intrusions to the West of Greenland. *Q. J. R. Meteorol. Soc.* 145, 3148–3160. doi:10.1002/qj.3610

Ballinger, T. J., Hanna, E., Hall, R. J., Cropper, T. E., Miller, J., Ribergaard, M. H., et al. (2018). Anomalous Blocking over Greenland Preceded the 2013 Extreme Early Melt of Local Sea Ice. *Ann. Glaciol.* 59, 181–190. doi:10.1017/aog.2017.30

Ballinger, T. J., Lee, C. C., Sheridan, S. C., Crawford, A. D., Overland, J. E., and Wang, M. (2019). Subseasonal Atmospheric Regimes and Ocean Background Forcing of Pacific Arctic Sea Ice Melt Onset. *Clim. Dyn.* 52, 5657–5672. doi:10.1007/s00382-018-4467-x

Ballinger, T. J., Sheridan, S. C., and Hanna, E. (2014). Resolving the Beaufort Sea High Using Synoptic Climatological Methods. *Int. J. Climatol.* 34, 3312–3319. doi:10.1002/joc.3907

Barnes, E. A., Dunn-Sigouin, E., Masato, G., and Woollings, T. (2014). Exploring Recent Trends in Northern Hemisphere Blocking. *Geophys. Res. Lett.* 41, 638–644. doi:10.1002/2013GL058745

Barnes, E. A., Samarasinghe, S. M., Ebert-Uphoff, I., and Furtado, J. C. (2019). Tropospheric and Stratospheric Causal Pathways between the MJO and NAO. *J. Geophys. Res. Atmos.* 124, 9356–9371. doi:10.1029/2019JD031024

Barnes, E. A., Slingo, J., and Woollings, T. (2012). A Methodology for the Comparison of Blocking Climatologies across Indices, Models and Climate Scenarios. *Clim. Dyn.* 38, 2467–2481. doi:10.1007/s00382-011-1243-6

Barrett, B. S. (2019). Connections between the Madden-Julian Oscillation and Surface Temperatures in winter 2018 over Eastern North America. *Atmos. Sci. Lett.* 20, e869. doi:10.1002/asl.869

Barrett, B. S., Henderson, G. R., McDonnell, E., Henry, M., and Mote, T. (2020). Extreme Greenland Blocking and High-latitude Moisture Transport. *Atmos. Sci. Lett.* 21, e1002. doi:10.1002/asl.1002

Barrett, B. S., Henderson, G. R., and Werling, J. S. (2015). The Influence of the MJO on the Intraseasonal Variability of Northern Hemisphere Spring Snow Depth. *J. Clim.* 28, 7250–7262. doi:10.1175/JCLI-D-15-0092.1

Barrett, B. S., and Leslie, L. M. (2009). Links between Tropical Cyclone Activity and Madden-Julian Oscillation Phase in the North Atlantic and Northeast Pacific Basins. *Monthly Weather Rev.* 137, 727–744. doi:10.1175/2008MWR2602.1

Barriopedro, D., García-Herrera, R., and Trigo, R. M. (2010). Application of Blocking Diagnosis Methods to General Circulation Models. Part I: A Novel Detection Scheme. *Clim. Dyn.* 35, 1373–1391. doi:10.1007/s00382-010-0767-5

Barton, B. I., Lenn, Y.-D., and Lique, C. (2018). Observed Atlantification of the Barents Sea Causes the Polar Front to Limit the Expansion of Winter Sea Ice. *J. Phys. Oceanogr.* 48, 1849–1866. doi:10.1175/JPO-D-18-0003.1

Baxter, S., Weaver, S., Gottschalck, J., and Xue, Y. (2014). Pentad Evolution of Wintertime Impacts of the Madden-Julian Oscillation over the Contiguous United States. *J. Clim.* 27, 7356–7367. doi:10.1175/JCLI-D-14-00105.1

Becker, E. J., Berbery, E. H., and Higgins, R. W. (2011). Modulation of Cold-Season U.S. Daily Precipitation by the Madden-Julian Oscillation. *J. Clim.* 24, 5157–5166. doi:10.1175/2011JCLI4018.1

Belleflamme, A., Fettweis, X., and Erpicum, M. (2015). Recent Summer Arctic Atmospheric Circulation Anomalies in a Historical Perspective. *The Cryosphere* 9, 53–64. doi:10.5194/tc-9-53-2015

Bennartz, R., Shupe, M. D., Turner, D. D., Walden, V. P., Steffen, K., Cox, C. J., et al. (2013). July 2012 Greenland Melt Extent Enhanced by Low-Level Liquid Clouds. *Nature* 496, 83–86. doi:10.1038/nature12002

Bevis, M., Harig, C., Khan, S. A., Brown, A., Simons, F. J., Willis, M., et al. (2019). Accelerating Changes in Ice Mass within Greenland, and the Ice Sheet's Sensitivity to Atmospheric Forcing. *Proc. Natl. Acad. Sci. USA* 116, 1934–1939. doi:10.1073/pnas.1806562116

Binder, H., Boettcher, M., Grams, C. M., Joos, H., Pfahl, S., and Wernli, H. (2017). Exceptional Air Mass Transport and Dynamical Drivers of an Extreme Wintertime Arctic Warm Event. *Geophys. Res. Lett.* 44 (23), 12028–12036. doi:10.1002/2017GL075841

Bintanja, R., and van der Linden, E. C. (2013). The Changing Seasonal Climate in the Arctic. *Sci. Rep.* 3, 1556. doi:10.1038/srep01556

Blackmon, M. L., Lee, Y.-H., Wallace, J. M., and Hsu, H. H. (1984). Time Variation of 500 Mb Height Fluctuations with Long, Intermediate and Short Time Scales as Deduced from Lag-Correlation Statistics. *J. Atmos. Sci.* 41, 981–991. doi:10.1175/1520-0469(1984)041<0981:tvomhf>2.0.co;2

Bladé, I., and Hartmann, D. L. (1995). The Linear and Nonlinear Extratropical Response of the Atmosphere to Tropical Intraseasonal Heating. *J. Atmos. Sci.* 52, 4448–4471. doi:10.1175/1520-0469(1995)052<4448:tlaner>2.0.co;2

Boeke, R. C., Taylor, P. C., and Sejas, S. A. (2021). On the Nature of the Arctic's Positive Lapse-Rate Feedback. *Geophys. Res. Lett.* 48, e2020GL091109. doi:10.1029/2020GL091109

Boisvert, L. N., Wu, D. L., and Shie, C.-L. (2015). Increasing Evaporation Amounts Seen in the Arctic between 2003 and 2013 from AIRS Data. *J. Geophys. Res. Atmos.* 120, 6865–6881. doi:10.1002/2015JD023258

Bond, N. A., and Vecchi, G. A. (2003). The Influence of the Madden-Julian Oscillation on Precipitation in Oregon and Washington*. *Wea. Forecast.* 18, 600–613. doi:10.1175/1520-0434(2003)018<0600:tiotmo>2.0.co;2

Box, J. E., Fettweis, X., Stroeve, J. C., Tedesco, M., Hall, D. K., and Steffen, K. (2012). Greenland Ice Sheet Albedo Feedback: Thermodynamics and Atmospheric Drivers. *The Cryosphere* 6, 821–839. doi:10.5194/tc-6-821-2012

Branstator, G. (2014). Long-Lived Response of the Midlatitude Circulation and Storm Tracks to Pulses of Tropical Heating. *J. Clim.* 27, 8809–8826. doi:10.1175/jcli-d-14-00312.1

Brunner, L., Schaller, N., Anstey, J., Sillmann, J., and Steiner, A. K. (2018). Dependence of Present and Future European Temperature Extremes on the Location of Atmospheric Blocking. *Geophys. Res. Lett.* 45, 6311–6320. doi:10.1029/2018GL077837

Budyko, M. I. (1969). The Effect of Solar Radiation Variations on the Climate of the Earth. *The effect solar Radiat. variations Clim. Earth* 21, 611–619. doi:10.1111/j.2153-3490.1969.tb00466.x

Bui, H. X., and Maloney, E. D. (2018). Changes in Madden-Julian Oscillation Precipitation and Wind Variance under Global Warming. *Geophys. Res. Lett.* 45 (14), 7148–7155. doi:10.1029/2018gl078504

Bui, H. X., and Maloney, E. D. (2019b). Mechanisms for Global Warming Impacts on Madden-Julian Oscillation Precipitation Amplitude. *J. Clim.* 32 (20), 6961–6975. doi:10.1175/jcli-d-19-0051.1

Bui, H. X., and Maloney, E. D. (2019a). Transient Response of MJO Precipitation and Circulation to Greenhouse Gas Forcing. *Geophys. Res. Lett.* 46 (22), 13546–13555. doi:10.1029/2019gl085328

Caballero, R., and Huber, M. (2010). Spontaneous Transition to Superrotation in Warm Climates Simulated by CAM3. *Geophys. Res. Lett.* 37, L11701. doi:10.1029/2010GL043468

Cao, Y., Liang, S., Chen, X., He, T., Wang, D., and Cheng, X. (2017). Enhanced Wintertime Greenhouse Effect Reinforcing Arctic Amplification and Initial Sea-Ice Melting. *Sci. Rep.* 7, 8462. doi:10.1038/s41598-017-08545-2

Cassou, C. (2008). Intraseasonal Interaction between the Madden-Julian Oscillation and the North Atlantic Oscillation. *Nature* 455, 523–527. doi:10.1038/nature07286

Cess, R. D., Potter, G. L., Zhang, M. H., Blanchet, J. P., Chalita, S., Colman, R., et al. (1991). Interpretation of Snow-Climate Feedback as Produced by 17 General Circulation Models. *Science* 253, 888–892. doi:10.1126/science.253.5022.888

Chang, C. W. J., Tseng, W. L., Hsu, H. H., Keenlyside, N., and Tsuang, B. J. (2015). The Madden-Julian Oscillation in a Warmer World. *Geophys. Res. Lett.* 42 (14), 6034–6042. doi:10.1002/2015gl065095

Charney, J. G., Shukla, J., and Mo, K. C. (1981). Comparison of a Barotropic Blocking Theory with Observation. *J. Atmos. Sci.* 38, 762–779. doi:10.1175/1520-0469(1981)038<0762:coabbt>2.0.co;2

Chen, T. C., and Murakami, M. (1988). The 30-50 Day Variation of Convective Activity over the Western Pacific Ocean with Emphasis on the Northwestern Region. *Mon. Wea. Rev.* 116 (4), 892–906. doi:10.1175/1520-0493(1988)116<0892:tdvoca>2.0.co;2

Choi, Y. S., Kim, B. M., Hur, S. K., Kim, S. J., Kim, J. H., and Ho, C. H. (2014). Connecting Early Summer Cloud-Controlled Sunlight and Late Summer Sea Ice in the Arctic. *J. Geophys. Res. Atmos.* 119 (19), 11087–11099. doi:10.1002/2014JD022013

Christidis, N., and Stott, P. A. (2015). Changes in the Geopotential Height at 500 hPa under the Influence of External Climatic Forcings. *Geophys. Res. Lett.* 42, 798–810. doi:10.1002/2015GL066669

Cohen, J. L., Furtado, J. C., Barlow, M. A., Alexeev, V. A., and Cherry, J. E. (2012). Arctic Warming, Increasing Snow Cover and Widespread Boreal winter Cooling. *Environ. Res. Lett.* 7 (1), 014007. doi:10.1088/1748-9326/7/1/014007

Cohen, J., Screen, J. A., Furtado, J. C., Barlow, M., Whittleston, D., Coumou, D., et al. (2014). Recent Arctic Amplification and Extreme Mid-latitude Weather. *Nat. Geosci* 7, 627–637. doi:10.1038/ngeo2234

Cohen, J., Zhang, X., Francis, J., Jung, T., Kwok, R., Overland, J., et al. (2020). Divergent Consensuses on Arctic Amplification Influence on Midlatitude Severe winter Weather. *Nat. Clim. Chang.* 10, 20–29. doi:10.1038/s41558-019-0662-y

Cohen, L., Hudson, S. R., Walden, V. P., Graham, R. M., and Granskog, M. A. (2017). Meteorological Conditions in a Thinner Arctic Sea Ice Regime from winter to Summer during the Norwegian Young Sea Ice Expedition (N-ICE2015). *J. Geophys. Res. Atmos.* 122, 7235–7259. doi:10.1002/2016JD026034

Cohen, J., Barlow, M., Kushner, P. J., and Saito, K. (2007). Stratosphere–Troposphere Coupling and Links with Eurasian Land Surface Variability. *J. Climate* 20, 5335–5343. doi:10.1175/2007JCLI1725.1

Coumou, D., Di Capua, G., Vavrus, S., Wang, L., and Wang, S. (2018). The Influence of Arctic Amplification on Mid-latitude Summer Circulation. *Nat. Commun.* 9, 2959. doi:10.1038/s41467-018-05256-8

Cox, C. J., Uttal, T., Long, C. N., Shupe, M. D., Stone, R. S., and Starkweather, S. (2016). The Role of Springtime Arctic Clouds in Determining Autumn Sea Ice Extent. *J. Clim.* 29, 6581–6596. doi:10.1175/JCLI-D-16-0136.1

Cox, C. J., Walden, V. P., Rowe, P. M., and Shupe, M. D. (2015). Humidity Trends Imply Increased Sensitivity to Clouds in a Warming Arctic. *Nat. Commun.* 6, 10117. doi:10.1038/ncomms10117

Crook, J. A., Forster, P. M., and Stuber, N. (2011). Spatial Patterns of Modeled Climate Feedback and Contributions to Temperature Response and Polar Amplification. *Amplification* 24, 3575–3592. doi:10.1175/2011JCLI3863.1

Cui, J., and Li, T. (2019). Changes of MJO Propagation Characteristics under Global Warming. *Clim. Dyn.* 53 (9), 5311–5327. doi:10.1007/s00382-019-04864-4

Cullather, R. I., Andrews, L. C., Croteau, M. J., Digirolamo, N. E., Hall, D. K., Lim, Y. K., et al. (2020). Anomalous Circulation in July 2019 Resulting in Mass Loss on the Greenland Ice Sheet. *Geophys. Res. Lett.* 47, e2020GL087263. doi:10.1029/2020GL087263

Cullather, R. I., Lim, Y.-K., Boisvert, L. N., Brucker, L., Lee, J. N., and Nowicki, S. M. J. (2016). Analysis of the Warmest Arctic winter, 2015-2016. *Geophys. Res. Lett.* 43, 10808–10816. doi:10.1002/2016GL071228

Cullather, R. I., and Nowicki, S. M. J. (2018). Greenland Ice Sheet Surface Melt and its Relation to Daily Atmospheric Conditions. *J. Clim.* 31, 1897–1919. doi:10.1175/jcli-d-17-0447.1

Cvijanovic, I., and Caldeira, K. (2015). Atmospheric Impacts of Sea Ice Decline in CO2 Induced Global Warming. *Clim. Dyn.* 44, 1173–1186. doi:10.1007/s00382-015-2489-1

Dai, A., Luo, D., Song, M., and Liu, J. (2019). Arctic Amplification Is Caused by Sea-Ice Loss under Increasing CO2. *Nat. Commun.* 10, 121. doi:10.1038/s41467-018-07954-9

Davini, P., and D'Andrea, F. (2020). From CMIP3 to CMIP6: Northern Hemisphere Atmospheric Blocking Simulation in Present and Future Climate. *J. Clim.* 33, 10021–10038. doi:10.1175/JCLI-D-19-0862.110.1175/JCLI-D-12-00032.1

Delhasse, A., Fettweis, X., Kittel, C., Amory, C., and Agosta, C. (2018). Brief Communication: Impact of the Recent Atmospheric Circulation Change in Summer on the Future Surface Mass Balance of the Greenland Ice Sheet. *The Cryosphere* 12, 3409–3418. doi:10.5194/tc-12-3409-2018

Derksen, C., and Brown, R. (2012). Spring Snow Cover Extent Reductions in the 2008-2012 Period Exceeding Climate Model Projections. *Geophys. Res. Lett.* 39, L19504. doi:10.1029/2012GL053387

Deser, C., Tomas, R. A., and Sun, L. (2015). The Role of Ocean-Atmosphere Coupling in the Zonal-Mean Atmospheric Response to Arctic Sea Ice Loss. *J. Clim.* 28, 2168–2186. doi:10.1175/JCLI-D-14-00325.1

Ding, Q., Schweiger, A., L'Heureux, M., Battisti, D. S., Po-Chedley, S., Johnson, N. C., et al. (2017). Influence of High-Latitude Atmospheric Circulation Changes on Summertime Arctic Sea Ice. *Nat. Clim. Change* 7, 289–295. doi:10.1038/nclimate3241

Ding, Q., Schweiger, A., L'Heureux, M., Steig, E. J., Battisti, D. S., Johnson, N. C., et al. (2019). Fingerprints of Internal Drivers of Arctic Sea Ice Loss in Observations and Model Simulations. *Nat. Geosci* 12, 28–33. doi:10.1038/s41561-018-0256-8

Ding, Q., Wallace, J. M., Battisti, D. S., Steig, E. J., Gallant, A. J. E., Kim, H. J., et al. (2014). Tropical Forcing of the Recent Rapid Arctic Warming in Northeastern Canada and Greenland. *Nature* 509, 209–212. doi:10.1038/nature13260

Dole, R. M., and Gordon, N. D. (1983). Persistent Anomalies of the Extratropical Northern Hemisphere Wintertime Circulation: Geographical Distribution and Regional Persistence Characteristics. *Mon. Wea. Rev.* 111 (8), 1567–1586. doi:10.1175/1520-0493(1983)111<1567:paoten>2.0.co;2

Doyle, J. G., Lesins, G., Thackray, C. P., Perro, C., Nott, G. J., Duck, T. J., et al. (2011). Water Vapor Intrusions into the High Arctic during winter. *Geophys. Res. Lett.* 38, L12806. doi:10.1029/2011gl047493

Dufour, A., Zolina, O., and Gulev, S. K. (2016). Atmospheric Moisture Transport to the Arctic: Assessment of Reanalyses and Analysis of Transport Components. *J. Clim.* 29, 5061–5081. doi:10.1175/JCLI-D-15-0559.1

Dunn-Sigouin, E., and Son, S.-W. (2013). Northern Hemisphere Blocking Frequency and Duration in the CMIP5 Models. *J. Geophys. Res. Atmos.* 118, 1179–1188. doi:10.1002/jgrd.50143

Duynkerke, P., and Vandenbroeke, M. (1994). Surface Energy Balance and Katabatic Flow over Glacier and Tundra during GIMEX-91. *Glob. Planet. Change* 9, 17–28. doi:10.1016/0921-8181(94)90004-3

Else, B. G. T., Papakyriakou, T. N., Raddatz, R., Galley, R. J., Mundy, C. J., Barber, D. G., et al. (2014). Surface Energy Budget of Landfast Sea Ice during the Transitions from winter to Snowmelt and Melt Pond Onset: The Importance of Net Longwave Radiation and Cyclone Forcings. *J. Geophys. Res. Oceans* 119, 3679–3693. doi:10.1002/2013JC009672

Fang, Z. F. (2004). "Statistical Relationship between the Northern Hemisphere Sea Ice and Atmospheric Circulation during Wintertime," in *Observation, Theory and Modeling of Atmospheric Variability World Scientific Series on Asia-Pacific Weather and Climate*. Editors Z. Xun, C. Ming, Z. Shuntai, Z. Yuejian, J. Fei-Fei, and Z. Xiaolei (Singapore: World Scientific Publishing Co), 131–141. doi:10.1142/9789812791139_0006

Fausto, R. S., As, D., Box, J. E., Colgan, W., Langen, P. L., and Mottram, R. H. (2016a). The Implication of Nonradiative Energy Fluxes Dominating Greenland Ice Sheet Exceptional Ablation Area Surface Melt in 2012. *Geophys. Res. Lett.* 43, 2649–2658. doi:10.1002/2016GL067720

Fausto, R. S., van As, D., Box, J. E., Colgan, W., and Langen, P. L. (2016b). Quantifying the Surface Energy Fluxes in South Greenland during the 2012 High Melt Episodes Using *In-Situ* Observations. *Front. Earth Sci.* 4, 82. doi:10.3389/feart.2016.00082

Fearon, M. G., Doyle, J. D., Ryglicki, D. R., Finocchio, P. M., and Sprenger, M. (2021). The Role of Cyclones in Moisture Transport into the Arctic. *Geophys. Res. Lett.* 48, e2020GL090353. doi:10.1029/2020GL090353

Feldl, N., Anderson, B. T., and Bordoni, S. (2017). Atmospheric Eddies Mediate Lapse Rate Feedback and Arctic Amplification. *J. Clim.* 30, 9213–9224. doi:10.1175/JCLI-D-16-0706.1

Feldl, N., Po-Chedley, S., Singh, H. K. A., Hay, S., and Kushner, P. J. (2020). Sea Ice and Atmospheric Circulation Shape the High-Latitude Lapse Rate Feedback. *Npj Clim. Atmos. Sci.* 3, 41. doi:10.1038/s41612-020-00146-7

Feng, J., Chen, W., and Li, Y. (2017). Asymmetry of the winter Extra-tropical Teleconnections in the Northern Hemisphere Associated with Two Types of ENSO. *Clim. Dyn.* 48, 2135–2151. doi:10.1007/s00382-016-3196-2

Feng, P. N., and Lin, H. (2019). Modulation of the MJO-Related Teleconnections by the QBO. *J. Geophys. Res. Atmos.* 124, 12022–12033. doi:10.1029/2019JD030878

Fettweis, X., Hanna, E., Lang, C., Belleflamme, A., Erpicum, M., and Gallée, H. (2013). Brief Communication "Important Role of the Mid-tropospheric Atmospheric Circulation in the Recent Surface Melt Increase over the Greenland Ice Sheet". *The Cryosphere* 7, 241–248. doi:10.5194/tc-7-241-2013

Fettweis, X., Tedesco, M., Broeke, M., and Ettema, J. (2011). *Melting Trends over the Greenland Ice Sheet (1958–2009) from Spaceborne Microwave Data and Regional Climate Models*. EU: Publications and Research. Available at: https://academicworks.cuny.edu/cc_pubs/673.

Flatau, M., and Kim, Y. J. (2013). Interaction Between the MJO and Polar Circulations. *J. Climate* 26 (11), 3562–3574. doi:10.1175/JCLI-D-11-00508.1

Francis, J. A., and Vavrus, S. J. (2015). Evidence for a Wavier Jet Stream in Response to Rapid Arctic Warming. *Environ. Res. Lett.* 10, 014005. doi:10.1088/1748-9326/10/1/014005

Francis, J. A., and Vavrus, S. J. (2012). Evidence Linking Arctic Amplification to Extreme Weather in Mid-latitudes. *Geophys. Res. Lett.* 39, L19804. doi:10.1029/2012GL051000

Franzke, C., Feldstein, S. B., and Lee, S. (2011). Synoptic Analysis of the Pacific-North American Teleconnection Pattern. *Q.J.R. Meteorol. Soc.* 137, 329–346. doi:10.1002/qj.768

Franzke, C. L. E., Jelic, D., Lee, S., and Feldstein, S. B. (2019). Systematic Decomposition of the MJO and its Northern Hemispheric Extratropical Response into Rossby and Inertio-gravity Components. *Q.J.R. Meteorol. Soc.* 145, 1147–1164. doi:10.1002/qj.3484

Gadgil, S., and Srinivasan, J. (1990). Low Frequency Variation of Tropical Convergence Zones. *Meteorl. Atmos. Phys.* 44 (1–4), 119–132. doi:10.1007/BF01026814

Gallagher, M. R., Shupe, M. D., and Miller, N. B. (2018). Impact of Atmospheric Circulation on Temperature, Clouds, and Radiation at Summit Station, Greenland, with Self-Organizing Maps. *J. Clim.* 31, 8895–8915. doi:10.1175/JCLI-D-17-0893.1

Geb, M. (1966). Synoptic-statistical Investigations into the Initiation of Blocking Action over the North Atlantic and Europe. *Meteorologishe Abhandlungen* 69, 89.

Gong, T., Feldstein, S., and Lee, S. (2017). The Role of Downward Infrared Radiation in the Recent Arctic Winter Warming Trend. *J. Clim.* 30, 4937–4949. doi:10.1175/JCLI-D-16-0180.1

Goosse, H., Kay, J. E., Armour, K. C., Bodas-Salcedo, A., Chepfer, H., Docquier, D., et al. (2018). Quantifying Climate Feedbacks in Polar Regions. *Nat. Commun.* 9, 1919. doi:10.1038/s41467-018-04173-0

Goss, M., Feldstein, S. B., and Lee, S. (2016). Stationary Wave Interference and its Relation to Tropical Convection and Arctic Warming. *J. Clim.* 29, 1369–1389. doi:10.1175/JCLI-D-15-0267.1

Goss, M., and Feldstein, S. B. (2015). The Impact of the Initial Flow on the Extratropical Response to Madden-Julian Oscillation Convective Heating. *Monthly Weather Rev.* 143 (4), 1104–1121. doi:10.1175/MWR-D-14-00141.1

Graham, R. M., Cohen, L., Petty, A. A., Boisvert, L. N., Rinke, A., Hudson, S. R., et al. (2017a). Increasing Frequency and Duration of Arctic winter Warming Events. *Geophys. Res. Lett.* 44, 6974–6983. doi:10.1002/2017GL073395

Graham, R. M., Itkin, P., Meyer, A., Sundfjord, A., Spreen, G., Smedsrud, L. H., et al. (2019). Winter Storms Accelerate the Demise of Sea Ice in the Atlantic Sector of the Arctic Ocean. *Sci. Rep.* 9, 9222. doi:10.1038/s41598-019-45574-5

Graham, R. M., Rinke, A., Cohen, L., Hudson, S. R., Walden, V. P., Granskog, M. A., et al. (2017b). A Comparison of the Two Arctic Atmospheric winter States Observed during N-ICE2015 and SHEBA. *J. Geophys. Res. Atmos.* 122, 5716–5737. doi:10.1002/2016JD025475

Grams, C. M., and Archambault, H. M. (2016). The Key Role of Diabatic Outflow in Amplifying the Midlatitude Flow: A Representative Case Study of Weather Systems Surrounding Western North Pacific Extratropical Transition. *Mon. Wea. Rev.* 144, 3847–3869. doi:10.1175/MWR-D-15-0419.1

Graversen, R. G., and Burtu, M. (2016). Arctic Amplification Enhanced by Latent Energy Transport of Atmospheric Planetary Waves. *Q.J.R. Meteorol. Soc.* 142, 2046–2054. doi:10.1002/qj.2802

Graversen, R. G., and Langen, P. L. (2019). On the Role of the Atmospheric Energy Transport in 2 × CO2-Induced Polar Amplification in CESM1. *J. Clim.* 32, 3941–3956. doi:10.1175/JCLI-D-18-0546.1

Graversen, R. G., Mauritsen, T., Drijfhout, S., Tjernström, M., and Mårtensson, S. (2011). Warm Winds from the Pacific Caused Extensive Arctic Sea-Ice Melt in Summer 2007. *Clim. Dyn.* 36, 2103–2112. doi:10.1007/s00382-010-0809-z

Graversen, R. G., and Wang, M. (2009). Polar Amplification in a Coupled Climate Model with Locked Albedo. *Clim. Dyn.* 33, 629–643. doi:10.1007/s00382-009-0535-6

Haertel, P. (2018). Sensitivity of the Madden Julian Oscillation to Ocean Warming in a Lagrangian Atmospheric Model. *Climate* 6, 45. doi:10.3390/cli6020045

Hahn, L. C., Armour, K. C., Battisti, D. S., Donohoe, A., Pauling, A. G., and Bitz, C. M. (2020). Antarctic Elevation Drives Hemispheric Asymmetry in Polar Lapse Rate Climatology and Feedback. *Geophys. Res. Lett.* 47, e2020GL088965. doi:10.1029/2020GL088965

Hahn, L., Ummenhofer, C. C., and Kwon, Y.-O. (2018). North Atlantic Natural Variability Modulates Emergence of Widespread Greenland Melt in a Warming Climate. *Geophys. Res. Lett.* 45, 9171–9178. doi:10.1029/2018GL079682

Häkkinen, S., Hall, D. K., Shuman, C. A., Worthen, D. L., and DiGirolamo, N. E. (2014). Greenland Ice Sheet Melt from MODIS and Associated Atmospheric Variability. *Geophys. Res. Lett.* 41, 1600–1607. doi:10.1002/2013GL059185

Hamill, T. M., and Kiladis, G. N. (2014). Skill of the MJO and Northern Hemisphere Blocking in GEFS Medium-Range Reforecasts. *Monthly Weather Rev.* 142 (2), 868–885. doi:10.1175/MWR-D-13-00199.1

Hanna, E., Cropper, T. E., Hall, R. J., and Cappelen, J. (2016). Greenland Blocking Index 1851-2015: a Regional Climate Change Signal. *Int. J. Climatol.* 36, 4847–4861. doi:10.1002/joc.4673

Hanna, E., Cropper, T. E., Jones, P. D., Scaife, A. A., and Allan, R. (2015). Recent Seasonal Asymmetric Changes in the NAO (A Marked Summer Decline and Increased winter Variability) and Associated Changes in the AO and Greenland Blocking Index. *Int. J. Climatol.* 35, 2540–2554. doi:10.1002/joc.4157

Hanna, E., Fettweis, X., and Hall, R. J. (2018a). Brief Communication: Recent Changes in Summer Greenland Blocking Captured by None of the CMIP5 Models. *The Cryosphere* 12, 3287–3292. doi:10.5194/tc-12-3287-2018

Hanna, E., Fettweis, X., Mernild, S. H., Cappelen, J., Ribergaard, M. H., Shuman, C. A., et al. (2014). Atmospheric and Oceanic Climate Forcing of the Exceptional Greenland Ice Sheet Surface Melt in Summer 2012. *Int. J. Climatol.* 34, 1022–1037. doi:10.1002/joc.3743

Hanna, E., Hall, R. J., Cropper, T. E., Ballinger, T. J., Wake, L., Mote, T., et al. (2018b). Greenland Blocking index Daily Series 1851-2015: Analysis of Changes in Extremes and Links with North Atlantic and UK Climate Variability and Change. *Int. J. Climatol* 38, 3546–3564. doi:10.1002/joc.5516

Hanna, E., Jones, J. M., Cappelen, J., Mernild, S. H., Wood, L., Steffen, K., et al. (2013). The Influence of North Atlantic Atmospheric and Oceanic Forcing Effects on 1900-2010 Greenland Summer Climate and Ice Melt/runoff. *Int. J. Climatol.* 33, 862–880. doi:10.1002/joc.3475

Hao, M., Lin, Y., Luo, Y., Nath, R., and Zhao, Z. (2021). The Impact of Atmospheric Moisture Transport on winter Arctic Warming: Radiation versus Latent Heat Release. *Int. J. Climatol* 41, 3982–3993. doi:10.1002/joc.7054

Hao, M., Luo, Y., Lin, Y., Zhao, Z., Wang, L., and Huang, J. (2019). Contribution of Atmospheric Moisture Transport to winter Arctic Warming. *Int. J. Climatol* 39, 2697–2710. doi:10.1002/joc.5982

Hartmann, D. L., and Michelsen, M. L. (1989). Intraseasonal Periodicities in Indian Rainfall. *J. Atmos. Sci.* 46 (18), 2838–2862. doi:10.1175/1520-0469(1989)046<2838:IPIIR>2.0.CO;2

Hassanzadeh, P., and Kuang, Z. (2015). Blocking Variability: Arctic Amplification versus Arctic Oscillation. *Geophys. Res. Lett.* 42, 8586–8595. doi:10.1002/2015GL065923

He, J., Lin, H., and Wu, Z. (2011). Another Look at Influences of the Madden-Julian Oscillation on the Wintertime East Asian Weather. *J. Geophys. Res.* 116, D03109. doi:10.1029/2010JD014787

Hegyi, B. M., and Deng, Y. (2017). Dynamical and Thermodynamical Impacts of High- and Low-Frequency Atmospheric Eddies on the Initial Melt of Arctic Sea Ice. *J. Clim.* 30, 865–883. doi:10.1175/JCLI-D-15-0366.1

Hegyi, B. M., and Taylor, P. C. (2018). The Unprecedented 2016-2017 Arctic Sea Ice Growth Season: The Crucial Role of Atmospheric Rivers and Longwave Fluxes. *Geophys. Res. Lett.* 45, 5204–5212. doi:10.1029/2017GL076717

Henderson, G. R., Barrett, B. S., and M. Lafleur, D. (2014). Arctic Sea Ice and the Madden-Julian Oscillation (MJO). *Clim. Dyn.* 43, 2185–2196. doi:10.1007/s00382-013-2043-y

Henderson, G. R., Barrett, B. S., and South, K. (2017). Eurasian October Snow Water Equivalent: Using Self-organizing Maps to Characterize Variability and Identify Relationships to the MJO. *Int. J. Climatol.* 37, 596–606. doi:10.1002/joc.4725

Henderson, G. R., Peings, Y., Furtado, J. C., and Kushner, P. J. (2018). Snow-atmosphere Coupling in the Northern Hemisphere. *Nat. Clim Change* 8, 954–963. doi:10.1038/s41558-018-0295-6

Henderson, S. A., Maloney, E. D., and Barnes, E. A. (2016). The Influence of the Madden-Julian Oscillation on Northern Hemisphere Winter Blocking. *J. Clim.* 29, 4597–4616. doi:10.1175/JCLI-D-15-0502.1

Henderson, S. A., and Maloney, E. D. (2018). The Impact of the Madden-Julian Oscillation on High-Latitude Winter Blocking during El Niño-Southern Oscillation Events. *J. Clim.* 31, 5293–5318. doi:10.1175/JCLI-D-17-0721.1

Hendon, H. H., and Salby, M. L. (1996). Planetary-scale Circulations Forced by Intraseasonal Variations of Observed Convection. *J. Atmos. Sci.* 53, 1751–1758. doi:10.1175/1520-0469(1996)053<1751:pscfbi>2.0.co;2

Hendon, H. H., and Salby, M. L. (1994). The Life Cycle of the Madden-Julian Oscillation. *J. Atmos. Sci.* 51, 1751–1758. doi:10.1175/1520-0469(1994)051<2225:tlcotm>2.0.co;2

Hermann, M., Papritz, L., and Wernli, H. (2020). A Lagrangian Analysis of the Dynamical and Thermodynamic Drivers of Greenland Melt Events during 1979–2017. *Weather Clim. Dyn. Discuss.* 1, 497–518. doi:10.5194/wcd-1-497-2020

Higgins, R. W., and Mo, K. C. (1997). Persistent North Pacific Circulation Anomalies and the Tropical Intraseasonal Oscillation. *J. Clim.* 10, 223–244. doi:10.1175/1520-0442(1997)010<0223:pnpcaa>2.0.co;2

Higgins, R. W., Schemm, J.-K. E., Shi, W., and Leetmaa, A. (2000). Extreme Precipitation Events in the Western United States Related to Tropical Forcing. *J. Clim.* 13, 793–820. doi:10.1175/1520-0442(2000)013<0793:epeitw>2.0.co;2

Hofer, S., Tedstone, A. J., Fettweis, X., and Bamber, J. L. (2017). Decreasing Cloud Cover Drives the Recent Mass Loss on the Greenland Ice Sheet. *Sci. Adv.* 3, e1700584. doi:10.1126/sciadv.1700584

Hong, J.-Y., Kim, B.-M., Baek, E.-H., Kim, J.-H., Zhang, X., and Kim, S.-J. (2020). A Critical Role of Extreme Atlantic Windstorms in Arctic Warming. *Asia-pacific J. Atmos. Sci.* 56, 17–28. doi:10.1007/s13143-019-00123-y

Horton, D. E., Johnson, N. C., Singh, D., Swain, D. L., Rajaratnam, B., and Diffenbaugh, N. S. (2015). Contribution of Changes in Atmospheric Circulation Patterns to Extreme Temperature Trends. *Nature* 522, 465–469. doi:10.1038/nature14550

Hoskins, B. (1997). A Potential Vorticity View of Synoptic Development. *Meteorol. App.* 4, 325–334. doi:10.1017/S1350482797000716

Hoskins, B. J., and Karoly, D. J. (1981). The Steady Linear Response of a Spherical Atmosphere to thermal and Orographic Forcing. *J. Atmos. Sci.* 38 (6), 1179–1196. doi:10.1175/1520-0469(1981)038<1179:TSLROA>2.0.CO;2

Hoskins, B. J., McIntyre, M. E., and Robertson, A. W. (1985). On the Use and Significance of Isentropic Potential Vorticity Maps. *Quar- terly J. R. Meteorol. Soc.* 111, 877–946. doi:10.1002/qj.49711147002

Hu, W., Liu, P., Zhang, Q., and He, B. (2019). Dominant Patterns of winter-time Intraseasonal Surface Air Temperature over the CONUS in Response to MJO Convections. *Clim. Dyn.* 53, 3917–3936. doi:10.1007/s00382-019-04760-x

Huang, Y., Dong, X., Bailey, D. A., Holland, M. M., Xi, B., DuVivier, A. K., et al. (2019). Thicker Clouds and Accelerated Arctic Sea Ice Decline: The Atmosphere-Sea Ice Interactions in Spring. *Geophys. Res. Lett.* 46, 6980–6989. doi:10.1029/2019GL082791

Huntington, H. P., Danielson, S. L., Wiese, F. K., Baker, M., Boveng, P., Citta, J. J., et al. (2020). Evidence Suggests Potential Transformation of the Pacific Arctic Ecosystem Is Underway. *Nat. Clim. Chang.* 10, 342–348. doi:10.1038/s41558-020-0695-2

Hurrell, J. W., Kushnir, Y., Ottersen, G., and Visbeck, M. (2003). An Overview of the North Atlantic Oscillation. The North Atlantic Oscillation: Climate Significance and Environmental Impact. Editors J. W. Hurrell, Y. Kushnir, G. Ottersen, and M. Visbeck, *Geophysical Monograph Series*, Washington, DC: American Geophysical Union, 134, 1–36, 279.

Hurrell, J. W., Kushner, Y., and Visbeck, M. (2001). CLIMATE: The North Atlantic Oscillation. *Science* 291, 603–605. doi:10.1126/science.1058761

Hwang, Y.-T., Frierson, D. M. W., and Kay, J. E. (2011). Coupling between Arctic Feedbacks and Changes in Poleward Energy Transport. *Geophys. Res. Lett.* 38, L17704. doi:10.1029/2011gl048546

Inness, P. M., and Slingo, J. M. (2003). Simulation of the Madden-Julian Oscillation in a Coupled General Circulation Model. Part I: Comparison with Observations and an Atmosphere-Only GCM. *J. Clim.* 16 (3), 345–364. doi:10.1175/1520-0442(2003)016<0345:sotmjo>2.0.co;2

Izeboud, M., Lhermitte, S., Van Tricht, K., Lenaerts, J. T. M., Van Lipzig, N. P. M., and Wever, N. (2020). The Spatiotemporal Variability of Cloud Radiative Effects on the Greenland Ice Sheet Surface Mass Balance. *Geophys. Res. Lett.* 47, e2020GL087315. doi:10.1029/2020GL087315

Jeong, J.-H., Kim, B.-M., Ho, C.-H., and Noh, Y.-H. (2008). Systematic Variation in Wintertime Precipitation in East Asia by MJO-Induced Extratropical Vertical Motion. *J. Clim.* 21, 788–801. doi:10.1175/2007JCLI1801.1

Jiang, X., Adames, Á. F., Kim, D., Maloney, E. D., Lin, H., Kim, H., et al. (2020). Fifty Years of Research on the Madden-Julian Oscillation: Recent Progress, Challenges, and Perspectives. *J. Geophys. Res. Atmospheres* 125 (17), e2019JD030911. doi:10.1029/2019jd030911

Jiménez-Esteve, B., and Domeisen, D. I. V. (2018). The Tropospheric Pathway of the ENSO-North Atlantic Teleconnection. *J. Clim.* 31, 4563–4584. doi:10.1175/JCLI-D-17-0716.1

Jin, F., and Hoskins, B. J. (1995). The Direct Response to Tropical Heating in a Baroclinic Atmosphere. *J. Atmos. Sci.* 52(3), 307–319. doi:10.1175/1520-0469(1995)052<0307:TDRTTH>2.0.CO;2

Johansson, E., Devasthale, A., Tjernström, M., Ekman, A. M. L., and L'Ecuyer, T. (2017). Response of the Lower Troposphere to Moisture Intrusions into the Arctic. *Geophys. Res. Lett.* 44, 2527–2536. doi:10.1002/2017GL072687

Johnson, N. C., Collins, D. C. S. B. F., Feldstein, S. B., L'Heureux, M. L., and Riddle, E. E. (2014). Skillful Wintertime North American Temperature Forecasts Out to 4 Weeks Based on the State of ENSO and the MJO*. *Wea. Forecast.* 29, 23–38. doi:10.1175/WAF-D-13-00102.1

Johnson, N. C., and Feldstein, S. B. (2010). The Continuum of North Pacific Sea Level Pressure Patterns: Intraseasonal, Interannual, and Interdecadal Variability. *J. Clim.* 23, 851–867. doi:10.1175/2009jcli3099.1

Jones, C., and Carvalho, L. M. V. (2014). Sensitivity to Madden-Julian Oscillation Variations on Heavy Precipitation over the Contiguous United States. *Atmos. Res.* 147-148, 10–26. doi:10.1016/j.atmosres.2014.05.002

Jones, C., Waliser, D. E., Lau, K. M., and Stern, W. (2004). The Madden–Julian Oscillation and its Impact on Northern Hemisphere Weather Predictability. *Monthly Weather Rev.* 132 (6), 1462–1471. doi:10.1175/1520-0493(2004)132<1462:TMOAII>2.0.CO;2

Joyce, T. M., Kwon, Y., Seo, H., and Ummenhofer, C. C. (2019). Meridional Gulf Stream Shifts Can Influence Wintertime Variability in the North Atlantic Storm Track and Greenland Blocking. *Geophys. Res. Lett.* 46, 1702–1708. doi:10.1029/2018GL08108

Jun, S. Y., Ho, C. H., Jeong, J. H., Choi, Y. S., and Kim, B. M. (2016). Recent Changes in winter Arctic Clouds and Their Relationships with Sea Ice and Atmospheric Conditions. *Tellus A: Dynamic Meteorol. Oceanography* 68, 29130. doi:10.3402/tellusa.v68.29130

Kang, W., and Tziperman, E. (2018). The MJO-SSW Teleconnection: Interaction between MJO-forced Waves and the Midlatitude Jet. *Geophys. Res. Lett.* 45 (9), 4400–4409. doi:10.1029/2018GL077937

Kapsch, M. L., Graversen, R. G., Economou, T., and Tjernström, M. (2014). The Importance of spring Atmospheric Conditions for Predictions of the Arctic Summer Sea Ice Extent. *Geophys. Res. Lett.* 41, 5288–5296. doi:10.1002/2014GL060826

Kapsch, M. L., Graversen, R. G., Tjernström, M., and Bintanja, R. (2016). The Effect of Downwelling Longwave and Shortwave Radiation on Arctic Summer Sea Ice. *Radiat. Arctic Summer Sea Ice* 29, 1143–1159. doi:10.1175/JCLI-D-15-0238.1

Kapsch, M. L., Graversen, R. G., and Tjernström, M. (2013). Springtime Atmospheric Energy Transport and the Control of Arctic Summer Sea-Ice Extent. *Nat. Clim Change* 3, 744–748. doi:10.1038/nclimate1884

Kapsch, M. L., Skific, N., Graversen, R. G., Tjernström, M., and Francis, J. A. (2019). Summers with Low Arctic Sea Ice Linked to Persistence of spring Atmospheric Circulation Patterns. *Clim. Dyn.* 52, 2497–2512. doi:10.1007/s00382-018-4279-z

Kay, J. E., L'Ecuyer, T., Chepfer, H., Loeb, N., Morrison, A., and Cesana, G. (2016). Recent Advances in Arctic Cloud and Climate Research. *Curr. Clim. Change Rep.* 2, 159–169. doi:10.1007/s40641-016-0051-9

Kayser, M., Maturilli, M., Graham, R. M., Hudson, S. R., Rinke, A., Cohen, L., et al. (2017). Vertical Thermodynamic Structure of the Troposphere during the Norwegian Young Sea ICE Expedition (N-Ice2015). *J. Geophys. Res. Atmos.* 122, 10855–10872. doi:10.1002/2016JD026089

Kennedy, D., Parker, T., Woollings, T., Harvey, B., and Shaffrey, L. (2016). The Response of High-Impact Blocking Weather Systems to Climate Change. *Geophys. Res. Lett.* 43, 7250–7258. doi:10.1002/2016GL069725

Kiladis, G. N., and Weickmann, K. M. (1992). Circulation Anomalies Associated with Tropical Convection during Northern winter. *Mon. Wea. Rev.* 120, 1900–1923. doi:10.1175/1520-0493(1992)120<1900:caawtc>2.0.co;2

Kim, B. M., Hong, J. Y., Jun, S. Y., Zhang, X., Kwon, H., Kim, S. J., et al. (2017). Major Cause of Unprecedented Arctic Warming in January 2016: Critical Role of an Atlantic Windstorm. *Sci. Rep.* 7, 40051. doi:10.1038/srep40051

Kim, B. M., Lim, G. H., and Kim, K. Y. (2006). A New Look at the Midlatitude-MJO Teleconnection in the Northern Hemisphere winter. *Q. J. R. Meteorol. Soc.* 132, 485–503. doi:10.1256/qj.04.87

Kim, B. M., Son, S. W., Min, S. K., Jeong, J. H., Kim, S. J., Zhang, X., et al. (2014). Weakening of the Stratospheric Polar Vortex by Arctic Sea-Ice Loss. *Nat. Commun.* 5, 4646. doi:10.1038/ncomms5646

Kim, H. M., and Kim, B. M. (2017). Relative Contributions of Atmospheric Energy Transport and Sea Ice Loss to the Recent Warm Arctic Winter. *J. Clim.* 30, 7441–7450. doi:10.1175/JCLI-D-17-0157.1

Klotzbach, P. J., Oliver, E. C. J., Leeper, R. D., and Schreck, C. J., III (2016). The Relationship between the Madden-Julian Oscillation (MJO) and Southeastern New England Snowfall. *Monthly Weather Rev.* 144 (4), 1355–1362. doi:10.1175/MWR-D-15-0434.1

Knutson, T. R., and Weickmann, K. M. (1987). 30-60 Day Atmospheric Oscillations: Composite Life Cycles of Convection and Circulation Anomalies. *Mon. Wea. Rev.* 115, 1407–1436. doi:10.1175/1520-0493(1987)115<1407:daoclc>2.0.co;2

Kodaira, T., Waseda, T., Nose, T., and Inoue, J. (2020). Record High Pacific Arctic Seawater Temperatures and Delayed Sea Ice advance in Response to Episodic Atmospheric Blocking. *Sci. Rep.* 10, 20830. doi:10.1038/s41598-020-77488-y

Kohnemann, S. H. E., Heinemann, G., Bromwich, D. H., and Gutjahr, O. (2017). Extreme Warming in the Kara Sea and Barents Sea during the Winter Period 2000-16. *J. Clim.* 30, 8913–8927. doi:10.1175/JCLI-D-16-0693.1

Komatsu, K. K., Alexeev, V. A., Repina, I. A., and Tachibana, Y. (2018). Poleward Upgliding Siberian Atmospheric Rivers over Sea Ice Heat up Arctic Upper Air. *Sci. Rep.* 8, 2872. doi:10.1038/s41598-018-21159-6

Kosaka, Y., and Xie, S. P. (2013). Recent Global-Warming Hiatus Tied to Equatorial Pacific Surface Cooling. *Nature* 501 (7467), 403–407. doi:10.1038/nature12534

Krishnamurti, T. N., and Subrahmanyam, D. (1982). The 30–50 Day Mode at 850 Mb during MONEX. *J. Atmos. Sci.* 39 (9), 2088–2095. doi:10.1175/1520-0469(1982)039<2088:TDMAMD>2.0.CO;2

Kwon, Y. O., Camacho, A., Martinez, C., and Seo, H. (2018). North Atlantic winter Eddy-Driven Jet and Atmospheric Blocking Variability in the Community Earth System Model Version 1 Large Ensemble Simulations. *Clim. Dyn.* 51, 3275–3289. doi:10.1007/s00382-018-4078-6

Kwon, Y. O., and Joyce, T. M. (2013). Northern Hemisphere Winter Atmospheric Transient Eddy Heat Fluxes and the Gulf Stream and Kuroshio-Oyashio Extension Variability. *J. Clim.* 26, 9839–9859. doi:10.1175/JCLI-D-12-00647.1

Kwon, Y. O., Seo, H., Ummenhofer, C. C., and Joyce, T. M. (2020). Impact of Multidecadal Variability in Atlantic SST on Winter Atmospheric Blocking. *Blocking* 33, 867–892. doi:10.1175/JCLI-D-19-0324.1

L'Heureux, M. L., and Higgins, R. W. (2008). Boreal winter Links between the Madden-Julian Oscillation and the Arctic Oscillation. *J. Clim.* 21, 3040–3050.doi:10.1175/2007JCLI1955.1

Lafleur, D. M., Barrett, B. S., and Henderson, G. R. (2015). Some Climatological Aspects of the Madden-Julian Oscillation (MJO). *J. Clim.* 28, 6039–6053. doi:10.1175/JCLI-D-14-00744.1

Laliberté, F., and Kushner, P. J. (2014). Midlatitude Moisture Contribution to Recent Arctic Tropospheric Summertime Variability*. *J. Clim.* 27, 5693–5707. doi:10.1175/JCLI-D-13-00721.1

Lang, A., Yang, S., and Kaas, E. (2017). Sea Ice Thickness and Recent Arctic Warming. *Geophys. Res. Lett.* 44, 409–418. doi:10.1002/2016GL071274

Lau, K. M., and Chan, P. H. (1986). Aspects of the 40–50 Day Oscillation during the Northern Summer as Inferred from Outgoing Longwave Radiation. *Monthly Weather Rev.* 114 (7), 1354–1367. doi:10.1175/1520-0493(1986)114<1354:AOTDOD>2.0.CO;2

Leathers, D. J., Yarnal, B., and Palecki, M. A. (1991). The Pacific/North American Teleconnection Pattern and United States Climate. Part I: Regional Temperature and Precipitation Associations. *J. Clim.* 4, 517–528. doi:10.1175/1520-0442(1991)004<0517:tpatpa>2.0.co;2

Lee, H. J., Kwon, M. O., Yeh, S. W., Kwon, Y.-O., Park, W., Park, J. H., et al. (2017). Impact of Poleward Moisture Transport from the North Pacific on the Acceleration of Sea Ice Loss in the Arctic since 2002. *J. Clim.* 30, 6757–6769. doi:10.1175/JCLI-D-16-0461.1

Lee, S., Gong, T., Feldstein, S. B., Screen, J. A., and Simmonds, I. (2017). Revisiting the Cause of the 1989-2009 Arctic Surface Warming Using the Surface Energy Budget: Downward Infrared Radiation Dominates the Surface Fluxes. *Geophys. Res. Lett.* 44, 10654–10661. doi:10.1002/2017GL075375

Lee, S., Gong, T., Johnson, N., Feldstein, S. B., and Pollard, D. (2011). On the Possible Link between Tropical Convection and the Northern Hemisphere Arctic Surface Air Temperature Change between 1958 and 2001. *J. Clim.* 24 (16), 4350–4367. doi:10.1175/2011jcli4003.1

Lei, R., Gui, D., Yuan, Z., Pang, X., Tao, D., and Zhai, M. (2020). Characterization of the Unprecedented Polynya Events north of Greenland in 2017/2018 Using

Remote Sensing and Reanalysis Data. *Acta Oceanol. Sin.* 39, 5–17. doi:10.1007/s13131-020-1643-8

Lejenas, H., and Øakland, H. (1983). Characteristics of Northern Hemisphere Blocking as Determined from Long Time Series of Observational Data. *Tellus* 35, 350–362. doi:10.1111/j.1600.0870.1983.tb00210.x

Lenaerts, J. T. M., Medley, B., Broeke, M. R., and Wouters, B. (2019). Observing and Modeling Ice Sheet Surface Mass Balance. *Rev. Geophys.* 57, 376–420. doi:10.1029/2018RG000622

Lin, H., Brunet, G., and Derome, J. (2009). An Observed Connection between the North Atlantic Oscillation and the Madden-Julian Oscillation. *J. Clim.* 22 (2), 364–380. doi:10.1175/2008JCLI2515.1

Lin, H., and Brunet, G. (2018). Extratropical Response to the MJO: Nonlinearity and Sensitivity to the Initial State. *J. Atmos. Sci.* 75 (1), 219–234. doi:10.1175/JAS-D-17-0189.1

Lin, H., Brunet, G., and Mo, R. (2010). Impact of the Madden-Julian Oscillation on Wintertime Precipitation in Canada. *Mon. Wea. Rev.* 138, 3822–3839. doi:10.1175/2010MWR3363.1

Lin, H., and Brunet, G. (2009). The Influence of the Madden-Julian Oscillation on Canadian Wintertime Surface Air Temperature. *Mon. Wea. Rev.* 137, 2250–2262. doi:10.1175/2009MWR2831.1

Lin, H. (2015). Subseasonal Variability of North American Wintertime Surface Air Temperature. *Clim. Dyn.* 45, 1137–1155. doi:10.1007/s00382-014-2363-6

Liu, C., and Barnes, E. A. (2015). Extreme Moisture Transport into the Arctic Linked to Rossby Wave Breaking. *J. Geophys. Res. Atmos.* 120, 3774–3788. doi:10.1002/2014JD022796

Liu, P. (2013). Changes in a Modeled MJO with Idealized Global Warming. *Clim. Dyn.* 40 (3–4), 761–773. doi:10.1007/s00382-012-1323-2

Liu, P., Li, T., Wang, B., Zhang, M., Luo, J.-j., Masumoto, Y., et al. (2013). MJO Change with A1B Global Warming Estimated by the 40-km ECHAM5. *Clim. Dyn.* 41 (3–4), 1009–1023. doi:10.1007/s00382-012-1532-8

Liu, P., Zhang, Q., Zhang, C., Zhu, Y., Khairoutdinov, M., Kim, H., et al. (2016). A Revised Real-Time Multivariate MJO Index. *Monthly Weather Rev.* 144 (2), 627–642. doi:10.1175/MWR-D-15-0237.1

Long, X., and Robinson, W. A. (2017). Dynamical Heating of the Arctic Atmosphere during the Springtime Transition. *J. Clim.* 30, 9539–9553. doi:10.1175/JCLI-D-17-0333.1

Lu, J., and Cai, M. (2009). Seasonality of Polar Surface Warming Amplification in Climate Simulations. *Geophys. Res. Lett.* 36, L16704. doi:10.1029/2009GL040133

Ludwig, V., Spreen, G., Haas, C., Istomina, L., Kauker, F., and Murashkin, D. (2019). The 2018 North Greenland Polynya Observed by a Newly Introduced Merged Optical and Passive Microwave Sea-Ice Concentration Dataset. *The Cryosphere* 13, 2051–2073. doi:10.5194/tc-13-2051-2019

Lukens, K. E., Feldstein, S. B., Yoo, C., and Lee, S. (2017). The Dynamics of the Extratropical Response to Madden-Julian Oscillation Convection. *Q.J.R. Meteorol. Soc.* 143, 1095–1106. doi:10.1002/qj.2993

Luo, B., Luo, D., Wu, L., Zhong, L., and Simmonds, I. (2017). Atmospheric Circulation Patterns Which Promote winter Arctic Sea Ice Decline. *Environ. Res. Lett.* 12, 054017. doi:10.1088/1748-9326/aa69d0

Luo, D., Chen, X., Overland, J., Simmonds, I., Wu, Y., and Zhang, P. (2019). Weakened Potential Vorticity Barrier Linked to Recent Winter Arctic Sea Ice Loss and Midlatitude Cold Extremes. *J. Clim.* 32, 4235–4261. doi:10.1175/JCLI-D-18-0449.1

Lupo, A. R. (2020). *Atmospheric Blocking Events: A Review*. New York: Annals of the New York Academy of Sciences. doi:10.1111/nyas.14557

Lupo, A. R., Jensen, A. D., Mokhov, I. I., Alexander, V. T., Timothy, E., et al. (2019). Changes in Global Blocking Character during the Most Recent Decades. *Atmosphere* 1–19. doi:10.3390/atmos10020092

Madden, R. A., and Julian, P. R. (1972). Description of Global-Scale Circulation Cells in the Tropics with a 40-50 Day Period. *J. Atmos. Sci.* 29, 1109–1123. doi:10.1175/1520-0469(1972)029<1109:dogscc>2.0.co;2

Madden, R. A., and Julian, P. R. (1971). Detection of a 40-50 Day Oscillation in the Zonal Wind in the Tropical Pacific. *J. Atmos. Sci.* 28, 702–708. doi:10.1175/1520-0469(1971)028<0702:doadoi>2.0.co;2

Madden, R. A., and Julian, P. R. (1994). Observations of the 40-50-Day Tropical Oscillation-A Review. *Mon. Wea. Rev.* 122, 814–837. doi:10.1175/1520-0493(1994)122<0814:ootdto>2.0.co;2

Maloney, E. D., Adames, Á. F., and Bui, H. X. (2019). Madden-Julian Oscillation Changes under Anthropogenic Warming. *Nat. Clim Change* 9 (1), 26–33. doi:10.1038/s41558-018-0331-6

Maloney, E. D., and Hartmann, D. L. (2001). The Madden-Julian Oscillation, Barotropic Dynamics, and North Pacific Tropical Cyclone Formation. Part I: Observations. *J. Atmos. Sci.* 58 (17), 2545–2558. doi:10.1175/1520-0469(2001)058<2545:tmjobd>2.0.co;2

Maloney, E. D., and Xie, S. P. (2013). Sensitivity of Tropical Intraseasonal Variability to the Pattern of Climate Warming. *J. Adv. Model. Earth Syst.* 5, 32–47. doi:10.1029/2012MS000171

Manabe, S., and Wetherald, R. T. (1975). The Effects of Doubling the CO2Concentration on the Climate of a General Circulation Model. *J. Atmos. Sci.* 32, 3–15. doi:10.1175/1520-0469(1975)032<0003:teodtc>2.0.co;2

Marshall, A. G., Hudson, D., Wheeler, M. C., Hendon, H. H., and Alves, O. (2011). Assessing the Simulation and Prediction of Rainfall Associated with the MJO in the POAMA Seasonal Forecast System. *Clim. Dyn.* 37, 2129–2141. doi:10.1007/s00382-010-0948-2

Martineau, P., Chen, G., and Burrows, D. A. (2017). Wave Events: Climatology, Trends, and Relationship to Northern Hemisphere winter Blocking and Weather Extremes. *J. Clim.* 30, 5675–5697. doi:10.1175/jcli-d-16-0692.1

Masato, G., Hoskins, B. J., and Woollings, T. J. (2012). Wave-breaking Characteristics of Midlatitude Blocking. *Q.J.R. Meteorol. Soc.* 138, 1285–1296. doi:10.1002/qj.990

Masato, G., Hoskins, B. J., and Woollings, T. (2013a). Wave-Breaking Characteristics of Northern Hemisphere Winter Blocking: A Two-Dimensional Approach. *J. Clim.* 26, 4535–4549. doi:10.1175/JCLI-D-12-00240.1

Masato, G., Hoskins, B. J., and Woollings, T. (2013b). Winter and Summer Northern Hemisphere Blocking in CMIP5 Models. *J. Clim.* 26, 7044–7059. doi:10.1175/JCLI-D-12-00466.1

Matsueda, M., and Endo, H. (2017). The Robustness of Future Changes in Northern Hemisphere Blocking: a Large Ensemble Projection with Multiple Sea Surface Temperature Patterns. *Geophys. Res. Lett.* 44, 5158–5166. doi:10.1002/2017gl073336

Matsueda, S., and Takaya, Y. (2015). The Global Influence of the Madden-Julian Oscillation on Extreme Temperature Events*. *J. Clim.* 28, 4141–4151. doi:10.1175/jcli-d-14-00625.1

Matsumura, S., and Yamazaki, K. (2012). Eurasian Subarctic Summer Climate in Response to Anomalous Snow Cover. *J. Clim.* 25, 1305–1317. doi:10.1175/2011JCLI4116.1

Matsumura, S., Zhang, X., and Yamazaki, K. (2014). Summer Arctic Atmospheric Circulation Response to spring Eurasian Snow Cover and its Possible Linkage to Accelerated Sea Ice Decrease. *J. Clim.* 27, 6551–6558. doi:10.1175/JCLI-D-13-00549.1

Matthews, A. J., Hoskins, B. J., and Masutani, M. (2004). The Global Response to Tropical Heating in the Madden-Julian Oscillation during the Northern winter. *Q. J. R. Meteorol. Soc.* 130, 1991–2011. doi:10.1256/qj.02.123

Matthews, A. J., and Kiladis, G. N. (1999). The Tropical-Extratropical Interaction between High-Frequency Transients and the Madden-Julian Oscillation. *Mon. Wea. Rev.* 127, 661–677. doi:10.1175/1520-0493(1999)127<0661:tteibh>2.0.co;2

Mattingly, K. S., Mote, T. L., and Fettweis, X. (2018). Atmospheric River Impacts on Greenland Ice Sheet Surface Mass Balance. *J. Geophys. Res. Atmos.* 123, 8538–8560. doi:10.1029/2018JD028714

Mattingly, K. S., Mote, T. L., Fettweis, X., van As, D., Van Tricht, K., Lhermitte, S., et al. (2020). Strong Summer Atmospheric Rivers Trigger Greenland Ice Sheet Melt through Spatially Varying Surface Energy Balance and Cloud Regimes. *J. Clim.* 33, 6809–6832. doi:10.1175/JCLI-D-19-0835.1

McKenna, C. M., Bracegirdle, T. J., Shuckburgh, E. F., Haynes, P. H., and Joshi, M. M. (2018). Arctic Sea Ice Loss in Different Regions Leads to Contrasting Northern Hemisphere Impacts. *Geophys. Res. Lett.* 45, 945–954. doi:10.1002/2017GL076433

McLeod, J. T., Ballinger, T. J., and Mote, T. L. (2018). Assessing the Climatic and Environmental Impacts of Mid-tropospheric Anticyclones over Alaska. *J. Climatol* 38, 351–364. doi:10.1002/joc.5180

McLeod, J. T., and Mote, T. L. (2016). Linking Interannual Variability in Extreme Greenland Blocking Episodes to the Recent Increase in Summer Melting across the Greenland Ice Sheet. *Int. J. Climatol.* 36, 1484–1499. doi:10.1002/joc.4440

Merkouriadi, I., Cheng, B., Graham, R. M., Rösel, A., and Granskog, M. A. (2017). Critical Role of Snow on Sea Ice Growth in the Atlantic Sector of the Arctic Ocean. *Geophys. Res. Lett.* 44, 10479–10485. doi:10.1002/2017GL075494

Merkouriadi, I., Cheng, B., Hudson, S. R., and Granskog, M. A. (2020). Effect of Frequent winter Warming Events (Storms) and Snow on Sea-Ice Growth - a Case from the Atlantic Sector of the Arctic Ocean during the N-Ice2015 Campaign. *Ann. Glaciol.* 61, 164–170. doi:10.1017/aog.2020.25

Messori, G., Woods, C., and Caballero, R. (2018). On the Drivers of Wintertime Temperature Extremes in the High Arctic. *J. Clim.* 31, 1597–1618. doi:10.1175/JCLI-D-17-0386.1

Mewes, D., and Jacobi, C. (2019). Heat Transport Pathways into the Arctic and Their Connections to Surface Air Temperatures. *Atmos. Chem. Phys.* 19, 3927–3937. doi:10.5194/acp-19-3927-2019

Mewes, D., and Jacobi, C. (2020). Horizontal Temperature Fluxes in the Arctic in CMIP5 Model Results Analyzed with Self-Organizing Maps. *Atmosphere* 11, 251. doi:10.3390/atmos11030251

Middlemas, E. A., Kay, J. E., Medeiros, B. M., and Maroon, E. A. (2020). Quantifying the Influence of Cloud Radiative Feedbacks on Arctic Surface Warming Using Cloud Locking in an Earth System Model. *Geophys. Res. Lett.* 47, e2020GL089207. doi:10.1029/2020GL089207

Moore, G. W. K., Schweiger, A., Zhang, J., and Steele, M. (2018). What Caused the Remarkable February 2018 North Greenland Polynya?. *Geophys. Res. Lett.* 45, 13342–13350. doi:10.1029/2018GL080902

Moore, G. W. K. (2016). The December 2015 North Pole Warming Event and the Increasing Occurrence of Such Events. *Sci. Rep.* 6, 39084. doi:10.1038/srep39084

Moore, R. W., Martius, O., and Spengler, T. (2010). The Modulation of the Subtropical and Extratropical Atmosphere in the Pacific Basin in Response to the Madden–Julian Oscillation. *Monthly Weather Rev.* 138 (7), 2761–2779. doi:10.1175/2010MWR3194.1

Mori, M., and Watanabe, M. (2008). The Growth and Triggering Mechanisms of the PNA: A MJO-PNA Coherence. *J. Meteorol. Soc. Jpn.* 86, 213–236. doi:10.2151/jmsj.86.213

Mortin, J., Svensson, G., Graversen, R. G., Kapsch, M. L., Stroeve, J. C., and Boisvert, L. N. (2016). Melt Onset over Arctic Sea Ice Controlled by Atmospheric Moisture Transport. *Geophys. Res. Lett.* 43, 6636–6642. doi:10.1002/2016GL069330

Mote, T. L. (1998a). Mid-tropospheric Circulation and Surface Melt on theGreenland Ice Sheet. Part I: Atmospheric Teleconnections. *Int. J. Climatol.* 18, 111–129. doi:10.1002/(sici)1097-0088(199802)18:2<111::aid-joc227>3.0.co;2-x

Mote, T. L. (1998b). Mid-tropospheric Circulation and Surface Melt on the Greenland Ice Sheet. Part II: Synoptic Climatology. *Int. J. Climatol.* 18, 131–145. doi:10.1002/(sici)1097-0088(199802)18:2<131::aid-joc228>3.0.co;2-s

Mouginot, J., Rignot, E., Bjørk, A. A., van den Broeke, M., Millan, R., Morlighem, M., et al. (2019). Forty-six Years of Greenland Ice Sheet Mass Balance from 1972 to 2018. *Proc. Natl. Acad. Sci. USA* 116, 9239–9244. doi:10.1073/pnas.1904242116

Mundhenk, B. D., Barnes, E. A., and Maloney, E. D. (2016). All-season Climatology and Variability of Atmospheric River Frequencies over the North Pacific. *J. Clim.* 29, 4885–4903. doi:10.1175/JCLI-D-15-0655.1

Murakami, T. (1980). Empirical Orthogonal Function Analysis of Satellite-observed Outgoing Longwave Radiation during Summer. *Monthly Weather Rev.* 108 (2), 205–222. doi:10.1175/1520-0493(1980)108<0205:EOFAOS>2.0.CO;2

Murakami, T., and Nakazawa, T. (1985). Tropical 45 Day Oscillations during the 1979 Northern Hemisphere Summer. *J. Atmos. Sci.* 42 (11), 1107–1122. doi:10.1175/1520-0469(1985)042<1107:TDODTN>2.0.CO;2

Naakka, T., Nygård, T., Vihma, T., Sedlar, J., and Graversen, R. (2019). Atmospheric Moisture Transport between Mid-latitudes and the Arctic: Regional, Seasonal and Vertical Distributions. *Int. J. Climatol* 39, 2862–2879. doi:10.1002/joc.5988

Nabizadeh, E., Hassanzadeh, P., Yang, D., and Barnes, E. A. (2019). Size of the Atmospheric Blocking Events: Scaling Law and Response to Climate Change. *Geophys. Res. Lett.* 46, 13488–13499. doi:10.1029/2019gl084863

Nakamura, N., and Huang, C. S. Y. (2018). Atmospheric Blocking as a Traffic Jam in the Jet Stream. *Science* 361, 42–47. doi:10.1126/science.aat0721

Nash, D., Waliser, D., Guan, B., Ye, H., and Ralph, F. M. (2018). The Role of Atmospheric Rivers in Extratropical and Polar Hydroclimate. *J. Geophys. Res. Atmos.* 123, 6804–6821. doi:10.1029/2017JD028130

Neff, W., Compo, G. P., Martin Ralph, F., and Shupe, M. D. (2014). Continental Heat Anomalies and the Extreme Melting of the Greenland Ice Surface in 2012 and 1889. *J. Geophys. Res. Atmos.* 119, 6520–6536. doi:10.1002/2014JD021470

Nghiem, S. V., Hall, D. K., Mote, T. L., Tedesco, M., Albert, M. R., Keegan, K., et al. (2012). The Extreme Melt across the Greenland Ice Sheet in 2012. *Geophys. Res. Lett.* 39, 2012GL053611. doi:10.1029/2012GL053611

Noël, B., van de Berg, W. J., Lhermitte, S., and van den Broeke, M. R. (2019). Rapid Ablation Zone Expansion Amplifies north Greenland Mass Loss. *Sci. Adv.* 5, eaaw0123. doi:10.1126/sciadv.aaw0123

Nygård, T., Naakka, T., and Vihma, T. (2020). Horizontal Moisture Transport Dominates the Regional Moistening Patterns in the Arctic. *J. Clim.* 33, 6793–6807. doi:10.1175/JCLI-D-19-0891.1

Ogi, M., and Wallace, J. M. (2012). The Role of Summer Surface Wind Anomalies in the Summer Arctic Sea Ice Extent in 2010 and 2011. *Geophys. Res. Lett.* 39, L09704. doi:10.1029/2012gl051330

Oliver, E. C. J. (2015). Multidecadal Variations in the Modulation of Alaska Wintertime Air Temperature by the Madden-Julian Oscillation. *Theor. Appl. Climatol.* 121, 1–11. doi:10.1007/s00704-014-1215-y

Oltmanns, M., Straneo, F., and Tedesco, M. (2019). Increased Greenland Melt Triggered by Large-Scale, Year-Round Cyclonic Moisture Intrusions. *The Cryosphere* 13, 815–825. doi:10.5194/tc-13-815-2019

Overland, J. E., Francis, J. A., Hanna, E., and Wang, M. (2012). The Recent Shift in Early Summer Arctic Atmospheric Circulation. *Geophys. Res. Lett.* 39, L19804. doi:10.1029/2012GL053268

Overland, J. E., Turet, P., and Oort, A. H. (1996). Regional Variations of Moist Static Energy Flux into the Arctic. *J. Clim.* 9, 54–65. doi:10.1175/1520-0442(1996)009<0054:rvomse>2.0.co;2

Overland, J. E., Wang, M., and Ballinger, T. J. (2018). Recent Increased Warming of the Alaskan marine Arctic Due to Midlatitude Linkages. *Adv. Atmos. Sci.* 35, 75–84. doi:10.1007/s00376-017-7026-1

Papritz, L. (2020). Arctic Lower-Tropospheric Warm and Cold Extremes: Horizontal and Vertical Transport, Diabatic Processes, and Linkage to Synoptic Circulation Features. *J. Clim.* 33, 993–1016. doi:10.1175/JCLI-D-19-0638.1

Papritz, L., and Dunn-Sigouin, E. (2020). What Configuration of the Atmospheric Circulation Drives Extreme Net and Total Moisture Transport into the Arctic. *Geophys. Res. Lett.* 47, 14. doi:10.1029/2020GL089769

Park, D. S. R., Lee, S., and Feldstein, S. B. (2015). Attribution of the Recent Winter Sea Ice Decline over the Atlantic Sector of the Arctic Ocean*. *J. Clim.* 28, 4027–4033. doi:10.1175/JCLI-D-15-0042.1

Park, H. S., Lee, S., Kosaka, Y., Son, S. W., and Kim, S. W. (2015a). The Impact of Arctic Winter Infrared Radiation on Early Summer Sea Ice. *J. Clim.* 28, 6281–6296. doi:10.1175/JCLI-D-14-00773.1

Park, H. S., Lee, S., Son, S. W., Feldstein, S. B., and Kosaka, Y. (2015b). The Impact of Poleward Moisture and Sensible Heat Flux on Arctic Winter Sea Ice Variability*. *J. Clim.* 28, 5030–5040. doi:10.1175/JCLI-D-15-0074.1

Park, K., Kang, S. M., Kim, D., Stuecker, M. F., and Jin, F. F. (2018). Contrasting Local and Remote Impacts of Surface Heating on Polar Warming and Amplification. *J. Clim.* 31, 3155–3166. doi:10.1175/JCLI-D-17-0600.1

Pelly, J. L., and Hoskins, B. J. (2003). A New Perspective on Blocking. *J. Atmos. Sci.* 60, 743–755. doi:10.1175/1520-0469(2003)060<0743:anpob>2.0.co;2

Persson, P. O. G. (2012). Onset and End of the Summer Melt Season over Sea Ice: thermal Structure and Surface Energy Perspective from SHEBA. *Clim. Dyn.* 39, 1349–1371. doi:10.1007/s00382-011-1196-9

Persson, P. O. G., Shupe, M. D., Perovich, D., and Solomon, A. (2017). Linking Atmospheric Synoptic Transport, Cloud Phase, Surface Energy Fluxes, and Sea-Ice Growth: Observations of Midwinter SHEBA Conditions. *Clim. Dyn.* 49, 1341–1364. doi:10.1007/s00382-016-3383-1

Petrie, R. E., Shaffrey, L. C., and Sutton, R. T. (2015). Atmospheric Response in Summer Linked to Recent Arctic Sea Ice Loss. *Q.J.R. Meteorol. Soc.* 141, 2070–2076. doi:10.1002/qj.2502

Pfahl, S., Schwierz, C., Croci-Maspoli, M., Grams, C. M., and Wernli, H. (2015). Importance of Latent Heat Release in Ascending Air Streams for Atmospheric Blocking. *Nat. Geosci* 8, 610–614. doi:10.1038/ngeo2487

Pithan, F., and Mauritsen, T. (2014). Arctic Amplification Dominated by Temperature Feedbacks in Contemporary Climate Models. *Nat. Geosci* 7, 181–184. doi:10.1038/ngeo2071

Polyakov, I. V., Alkire, M. B., Bluhm, B. A., Brown, K. A., Carmack, E. C., Chierici, M., et al. (2020a). Borealization of the Arctic Ocean in Response to Anomalous Advection from Sub-arctic Seas. *Front. Mar. Sci.* 7, 491. doi:10.3389/fmars.2020.00491

Polyakov, I. V., Pnyushkov, A. V., Alkire, M. B., Ashik, I. M., Baumann, T. M., Carmack, E. C., et al. (2017). Greater Role for Atlantic Inflows on Sea-Ice Loss in the Eurasian Basin of the Arctic Ocean. *Science* 356, 285–291. doi:10.1126/science.aai8204

Polyakov, I. V., Rippeth, T. P., Fer, I., Alkire, M. B., Baumann, T. M., Carmack, E. C., et al. (2020b). Weakening of Cold Halocline Layer Exposes Sea Ice to Oceanic Heat in the Eastern Arctic Ocean. *Ocean* 33, 8107–8123. doi:10.1175/JCLI-D-19-0976.1

Previdi, M., Janoski, T. P., Chiodo, G., Smith, K. L., and Polvani, L. M. (2020). Arctic Amplification: A Rapid Response to Radiative Forcing. *Geophys. Res. Lett.* 47, e2020GL089933. doi:10.1029/2020GL089933

Rex, D. F. (1950). Blocking Action in the Middle Troposphere and its Effect upon Regional Climate. *Tellus* 2, 196–211. doi:10.1111/j.2153-3490.1950.tb00331.x10.3402/tellusa.v2i3.8546

Riddle, E. E., Stoner, M. B., Johnson, N. C., L'Heureux, M. L., Collins, D. C., and Feldstein, S. B. (2013). The Impact of the MJO on Clusters of Wintertime Circulation Anomalies over the North American Region. *Clim. Dyn.* 40, 1749–1766. doi:10.1007/s00382-012-1493-y

Rinke, A., Knudsen, E. M., Mewes, D., Dorn, W., Handorf, D., Dethloff, K., et al. (2019a). Arctic Summer Sea Ice Melt and Related Atmospheric Conditions in Coupled Regional Climate Model Simulations and Observations. *J. Geophys. Res. Atmos.* 124, 6027–6039. doi:10.1029/2018JD030207

Rinke, A., Maturilli, M., Graham, R. M., Matthes, H., Handorf, D., Cohen, L., et al. (2017). Extreme Cyclone Events in the Arctic: Wintertime Variability and Trends. *Environ. Res. Lett.* 12, 094006. doi:10.1088/1748-9326/aa7def

Rinke, A., Segger, B., Crewell, S., Maturilli, M., Naakka, T., Nygård, T., et al. (2019b). Trends of Vertically Integrated Water Vapor over the Arctic during 1979-2016: Consistent Moistening All over?. *J. Clim.* 32, 6097–6116. doi:10.1175/JCLI-D-19-0092.1

Rodney, M., Lin, H., and Derome, J. (2013). Subseasonal Prediction of Wintertime North American Surface Air Temperature during Strong MJO Events. *Monthly Weather Rev.* 141 (8), 2897–2909. doi:10.1175/MWR-D-12-00221.1

Roundy, P. E., MacRitchie, K., Asuma, J., and Melino, T. (2010). Modulation of the Global Atmospheric Circulation by Combined Activity in the Madden-Julian Oscillation and the El Niño-Southern Oscillation during Boreal Winter. *J. Clim.* 23 (15), 4045–4059. doi:10.1175/2010JCLI3446.1

Roundy, P. E. (2012). "Tropical-extratropical Interactions," in *Intraseasonal Variability of the Atmosphere–Ocean Climate System*. Editors W. K. M. Lau and D. E. Waliser. 2nd ed. (Berlin: Heidelberg), 497–512.

Roundy, P. E. (2021). "The Association between the Phase Speed of the Madden-Julian Oscillation and Atmospheric Circulation," in *The Multiscale Global Monsoon System*. 4th ed. Editors C. P. Chang, K. J. Ha, R. H. Johnson, G. N. C. Lau, and B. Wang (Singapore: World Scientific Publishing Co), 301–314. doi:10.1142/9789811216602_0024

Rushley, S. S., Kim, D., and Adames, Á. F. (2019). Changes in the MJO under Greenhouse Gas-Induced Warming in CMIP5 Models. *J. Clim.* 32, 803–821. doi:10.1175/jcli-d-18-0437.1

Sánchez, C., Methven, J., Gray, S., and Cullen, M. (2020). Linking Rapid Forecast Error Growth to Diabatic Processes. *Q. J. R. Meteorol. Soc.* 146, 3548–3569. doi:10.1002/qj.3861

Sardeshmukh, P. D., and Hoskins, B. J. (1988). The Generation of Global Rotational Flow by Steady Idealized Tropical Divergence. *J. Atmos. Sci.* 45, 1228–1251. doi:10.1175/1520-0469(1988)045<1228:tgogrf>2.0.co;2

Schaller, N., Sillmann, J., Anstey, J., Fischer, E. M., Grams, C. M., and Russo, S. (2018). Influence of Blocking on Northern European and Western Russian Heatwaves in Large Climate Model Ensembles. *Environ. Res. Lett.* 13, 054015. doi:10.1088/1748-9326/aaba55

Schiemann, R., Athanasiadis, P., Barriopedro, D., Doblas-Reyes, F., Lohmann, K., Roberts, M. J., et al. (2020). Northern Hemisphere Blocking Simulation in Current Climate Models: Evaluating Progress from the Climate Model Intercomparison Project Phase 5 to 6 and Sensitivity to Resolution. *Weather Clim. Dynam.* 1, 277–292. doi:10.5194/wcd-1-277-2020

Schreck, C. J., III, Cordeira, J. M., and Margolin, D. (2013). Which MJO Events Affect North American Temperatures?. *Mon Weather Rev.* 141, 3840–3850. doi:10.1175/mwr-d-13-00118.1

Schubert, J. J., Stevens, B., and Crueger, T. (2013). Madden-Julian Oscillation as Simulated by the MPI Earth System Model: Over the Last and into the Next Millennium. *J. Adv. Model. Earth Syst.* 5, 71–84. doi:10.1029/2012MS000180

Schwendike, J., Berry, G. J., Fodor, K., and Reeder, M. J. (2021). On the Relationship between the Madden-Julian Oscillation and the Hadley and Walker Circulations. *Geophys. Res. Atmos.* 126, e2019JD032117. doi:10.1029/2019JD032117

Schwendike, J., Govekar, P., Reeder, M. J., Wardle, R., Berry, G. J., and Jakob, C. (2014). Local Partitioning of the Overturning Circulation in the Tropics and the Connection to the Hadley and Walker Circulations. *J. Geophys. Res. Atmos.* 119, 1322–1339. doi:10.1002/2013JD020742

Screen, J. A. (2013). Influence of Arctic Sea Ice on European Summer Precipitation. *Environ. Res. Lett.* 8, 044015. doi:10.1088/1748-9326/8/4/044015

Screen, J. A., and Simmonds, I. (2010). Increasing Fall-winter Energy Loss from the Arctic Ocean and its Role in Arctic Temperature Amplification. *Geophys. Res. Lett.* 37, L16707. doi:10.1029/2010gl044136

Sedlar, J. (2018). Spring Arctic Atmospheric Preconditioning: Do Not Rule Out Shortwave Radiation Just yet. *J. Clim.* 31, 4225–4240. doi:10.1175/JCLI-D-17-0710.1

Seo, K. H., Lee, H. J., and Frierson, D. M. W. (2016). Unraveling the Teleconnection Mechanisms that Induce Wintertime Temperature Anomalies over the Northern Hemisphere Continents in Response to the MJO. *J. Atmos. Sci.* 73, 3557–3571. doi:10.1175/JAS-D-16-0036.1

Seo, K. H., and Son, S. W. (2012). The Global Atmospheric Circulation Response to Tropical Diabatic Heating Associated with the Madden-Julian Oscillation during Northern Winter. *J. Atmos. Sci.* 69 (1), 79–96. doi:10.1175/2011JAS3686.1

Seo, K., and Lee, H. (2017). Mechanisms for a PNA-like Teleconnection Pattern in Response to the MJO. *J. Atmos. Sci.* 74 (6), 1767–1781. doi:10.1175/JAS-D-16-0343.1

Serreze, M. C., Barrett, A. P., Stroeve, J. C., Kindig, D. N., and Holland, M. M. (2009). The Emergence of Surface-Based Arctic Amplification. *The Cryosphere* 9, 11–19. doi:10.5194/tc-3-11-2009

Serreze, M. C., and Barry, R. G. (2011). Processes and Impacts of Arctic Amplification: A Research Synthesis. *Glob. Planet. Change* 77, 85–96. doi:10.1016/j.gloplacha.2011.03.004

Serreze, M. C., and Francis, J. A. (2006). The Arctic Amplification Debate. *Climatic Change* 76, 241–264. doi:10.1007/s10584-005-9017-y

Siew, P. Y. F., Li, C., Sobolowski, S. P., and King, M. P. (2020). Intermittency of Arctic-Mid-Latitude Teleconnections: Stratospheric Pathway between Autumn Sea Ice and the winter North Atlantic Oscillation. *Weather Clim. Dynam.* 1, 261–275. doi:10.5194/wcd-1-261-2020

Simpson, I. R., Bacmeister, J., Neale, R. B., Hannay, C., Gettelman, A., Garcia, R. R., et al. (2020). An Evaluation of the Large-Scale Atmospheric Circulation and its Variability in CESM2 and Other CMIP Models. *J. Geophys. Res. Atmos.* 125, e2020JD032835. doi:10.1029/2020JD032835

Slater, T., Hogg, A. E., and Mottram, R. (2020). Ice-sheet Losses Track High-End Sea-Level Rise Projections. *Nat. Clim. Chang.* 10, 879–881. doi:10.1038/s41558-020-0893-y

Södergren, A. H., McDonald, A. J., and Bodeker, G. E. (2018). An Energy Balance Model Exploration of the Impacts of Interactions between Surface Albedo, Cloud Cover and Water Vapor on Polar Amplification. *Clim. Dyn.* 51, 1639–1658. doi:10.1007/s00382-017-3974-5

Song, E.-J., and Seo, K.-H. (2016). Past- and Present-Day Madden-Julian Oscillation in CNRM-CM5. *Geophys. Res. Lett.* 43, 4042–4048. doi:10.1002/2016GL068771

Sorteberg, A., and Walsh, J. E. (2008). Seasonal Cyclone Variability at 70°N and its Impact on Moisture Transport into the Arctic. *Tellus A* 60, 570–586. doi:10.1111/j.1600-0870.2007.00314.x10.1111/j.1600-0870.2008.00314.x

Stan, C., Straus, D. M., Frederiksen, J. S., Lin, H., Maloney, E. D., and Schumacher, C. (2017). Review of Tropical-Extratropical Teleconnections on Intraseasonal Time Scales. *Rev. Geophys.* 55, 902–937. doi:10.1002/2016RG000538

Steinfeld, D., Boettcher, M., Forbes, R., and Pfahl, S. (2020). The Sensitivity of Atmospheric Blocking to Upstream Latent Heating - Numerical Experiments. *Weather Clim. Dynam.* 1 (2), 405–426. doi:10.5194/wcd-1-405-2020

Steinfeld, D., and Pfahl, S. (2019). The Role of Latent Heating in Atmospheric Blocking Dynamics: a Global Climatology. *Clim. Dyn.* 53, 6159–6180. doi:10.1007/s00382-019-04919-6

Stramler, K., Del Genio, A. D., and Rossow, W. B. (2011). Synoptically Driven Arctic Winter States. *J. Clim.* 24, 1747–1762. doi:10.1175/2010JCLI3817.1

Stroeve, J., and Notz, D. (2018). Changing State of Arctic Sea Ice across All Seasons. *Environ. Res. Lett.* 13, 103001. doi:10.1088/1748-9326/aade56

Stuecker, M. F., Bitz, C. M., Armour, K. C., Proistosescu, C., Kang, S. M., Xie, S.-P., et al. (2018). Polar Amplification Dominated by Local Forcing and Feedbacks. *Nat. Clim. Change* 8, 1076–1081. doi:10.1038/s41558-018-0339-y

Subramanian, A., Jochum, M., Miller, A. J., Neale, R., Seo, H., Waliser, D., et al. (2014). The MJO and Global Warming: A Study in CCSM4. *Clim. Dyn.* 42 (7–8), 2019–2031. doi:10.1007/s00382-013-1846-1

Sun, L., Deser, C., and Tomas, R. A. (2015). Mechanisms of Stratospheric and Tropospheric Circulation Response to Projected Arctic Sea Ice Loss*. *J. Clim.* 28, 7824–7845. doi:10.1175/JCLI-D-15-0169.1

Tachibana, Y., Komatsu, K. K., Alexeev, V. A., Cai, L., and Ando, Y. (2019). Warm Hole in Pacific Arctic Sea Ice Cover Forced Mid-latitude Northern Hemisphere Cooling during winter 2017-18. *Sci. Rep.* 9, 5567. doi:10.1038/s41598-019-41682-4

Takahashi, C., Sato, N., Seiki, A., Yoneyama, K., and Shirooka, R. (2011). Projected Future Change of MJO and its Extratropical Teleconnection in East Asia during the Northern winter Simulated in IPCC AR4 Models. *SOLA* 7, 201–204. doi:10.2151/sola.2011-051

Taylor, P. C., Cai, M., Hu, A., Meehl, J., Washington, W., and Zhang, G. J. (2013). A Decomposition of Feedback Contributions to Polar Warming Amplification. *J. Clim.* 26, 7023–7043. doi:10.1175/JCLI-D-12-00696.1

Taylor, P., Hegyi, B., Boeke, R., and Boisvert, L. (2018). On the Increasing Importance of Air-Sea Exchanges in a Thawing Arctic: A Review. *Atmosphere* 9, 41. doi:10.3390/atmos9020041

Tedesco, M., Fettweis, X., Mote, T., Wahr, J., Alexander, P., Box, J. E., et al. (2013). Evidence and Analysis of 2012 Greenland Records from Spaceborne Observations, a Regional Climate Model and Reanalysis Data. *The Cryosphere* 7, 615–630. doi:10.7916/D8J38SGV.10.5194/tc-7-615-2013

Tedesco, M., and Fettweis, X. (2020). Unprecedented Atmospheric Conditions (1948-2019) Drive the 2019 Exceptional Melting Season over the Greenland Ice Sheet. *The Cryosphere* 14, 1209–1223. doi:10.5194/tc-14-1209-2020

Tedesco, M., Fettweis, X., van den Broeke, M. R., van de Wal, R. S. W., Smeets, C. J. P. P., van de Berg, W. J., et al. (2011). The Role of Albedo and Accumulation in the 2010 Melting Record in Greenland. *Environ. Res. Lett.* 6, 014005. doi:10.1088/1748-9326/6/1/014005

Tedesco, M., Mote, T., Fettweis, X., Hanna, E., Jeyaratnam, J., Booth, J. F., et al. (2016). Arctic Cut-Off High Drives the Poleward Shift of a New Greenland Melting Record. *Nat. Commun.* 7, 11723. doi:10.1038/ncomms11723

Thoman, R. L., Bhatt, U. S., Bieniek, P. A., Brettschneider, B. R., Brubaker, M., Danielson, S. L., et al. (2020). The Record Low Bering Sea Ice Extent in 2018: Context, Impacts, and an Assessment of the Role of Anthropogenic Climate Change. *Bull. Am. Meteorol. Soc.* 101, S53–S58. doi:10.1175/BAMS-D-19-0175.1

Thompson, D. W. J., and Wallace, J. M. (1998). The Arctic Oscillation Signature in the Wintertime Geopotential Height and Temperature fields. *Geophys. Res. Lett.* 25, 1297–1300. doi:10.1029/98GL00950

Tibaldi, S., and Molteni, F. (1990). On the Operational Predictability of Blocking. *Tellus A* 42, 343–365. doi:10.1034/j.1600-0870.1990.t01-2-00003.x

Tilinina, N., Gulev, S. K., and Bromwich, D. H. (2014). New View of Arctic Cyclone Activity from the Arctic System Reanalysis. *Geophys. Res. Lett.* 41, 1766–1772. doi:10.1002/2013GL058924

Tjernström, M., Shupe, M. D., Brooks, I. M., Achtert, P., Prytherch, J., and Sedlar, J. (2019). Arctic Summer Airmass Transformation, Surface Inversions, and the Surface Energy Budget. *J. Clim.* 32, 769–789. doi:10.1175/JCLI-D-18-0216.1

Tjernström, M., Shupe, M. D., Brooks, I. M., Persson, P. O. G., Prytherch, J., Salisbury, D. J., et al. (2015). Warm-air Advection, Air Mass Transformation and Fog Causes Rapid Ice Melt. *Geophys. Res. Lett.* 42, 5594–5602. doi:10.1002/2015GL064373

Treidl, R. A., Birch, E. C., and Sajecki, P. (1981). Blocking Action in the Northern Hemisphere: A Climatological Study. *Atmosphere-Ocean* 19 (1), 1–23. doi:10.1080/07055900.1981.9649096

Trenberth, K. E., and Solomon, A. (1994). The Global Heat Balance: Heat Transports in the Atmosphere and Ocean. Clim. Dynam. 10 (3), 107–134. 10.1007/BF00210625

Tseng, K. C., Barnes, E. A., and Maloney, E. D. (2018). Prediction of the Midlatitude Response to Strong Madden-Julian Oscillation Events on S2S Time Scales. *Geophys. Res. Lett.* 45, 463–470. doi:10.1002/2017GL075734

Tseng, K., Maloney, E., and Barnes, E. A. (2020). The Consistency of MJO Teleconnection Patterns on Interannual Time Scales. *J. Clim.* 33 (9), 3471–3486. doi:10.1175/JCLI-D-19-0510.1

Tsubouchi, T., Våge, K., Hansen, B., Larsen, K. M. H., Østerhus, S., Johnson, C., et al. (2021). Increased Ocean Heat Transport into the Nordic Seas and Arctic Ocean over the Period 1993-2016. *Nat. Clim. Chang.* 11, 21–26. doi:10.1038/s41558-020-00941-3

Tyrlis, E., Bader, J., Manzini, E., and Matei, D. (2021). Reconciling Different Methods of High-latitude Blocking Detection. *Q. J. R. Meteorol. Soc.* 147, 1070–1096. doi:10.1002/qj.3960

Tyrlis, E., and Hoskins, B. J. (2008). Aspects of a Northern Hemisphere Atmospheric Blocking Climatology. *J. Atmos. Sci.* 65, 1638–1652. doi:10.1175/2007JAS2337.1

van Angelen, J. H., van den Broeke, M. R., Wouters, B., and Lenaerts, J. T. M. (2014). Contemporary (1960-2012) Evolution of the Climate and Surface Mass Balance of the Greenland Ice Sheet. *Surv. Geophys.* 35, 1155–1174. doi:10.1007/s10712-013-9261-z

van den Broeke, M. R., and Gallée, H. (1996). Observation and Simulation of Barrier Winds at the Western Margin of the Greenland Ice Sheet. *Q.J R. Met. Soc.* 122, 1365–1383. doi:10.1002/qj.49712253407

Van Tricht, K., Lhermitte, S., Lenaerts, J. T. M., Gorodetskaya, I. V., L'Ecuyer, T. S., Noël, B., et al. (2016). Clouds Enhance Greenland Ice Sheet Meltwater Runoff. *Nat. Commun.* 7, 10266. doi:10.1038/ncomms10266

Vavrus, S. J., Wang, F., Martin, J. E., Francis, J. A., Peings, Y., and Cattiaux, J. (2017). Changes in North American Atmospheric Circulation and Extreme Weather: Influence of Arctic Amplification and Northern Hemisphere Snow Cover. *J. Clim.* 30, 4317–4333. doi:10.1175/JCLI-D-16-0762.1

Vázquez, M., Algarra, I., Eiras-Barca, J., Ramos, A. M., Nieto, R., and Gimeno, L. (2018). Atmospheric Rivers over the Arctic: Lagrangian Characterisation of Their Moisture Sources. *Water* 11, 41. doi:10.3390/w11010041

Vázquez, M., Nieto, R., Drumond, A., and Gimeno, L. (2016). Moisture Transport into the Arctic: Source-Receptor Relationships and the Roles of Atmospheric Circulation and Evaporation. *J. Geophys. Res. Atmos.* 121, 13493–13509. doi:10.1002/2016JD025400

Vecchi, G. A., and Bond, N. A. (2004). The Madden-Julian Oscillation (MJO) and Northern High Latitude Wintertime Surface Air Temperatures. *Geophys. Res. Lett.* 31, L04104. doi:10.1029/2003GL018645

Vial, J., and Osborn, T. J. (2012). Assessment of Atmosphere-Ocean General Circulation Model Simulations of winter Northern Hemisphere Atmospheric Blocking. *Clim. Dyn.* 39, 95–112. doi:10.1007/s00382-011-1177-z

Villamil-Otero, G. A., Zhang, J., He, J., and Zhang, X. (2018). Role of Extratropical Cyclones in the Recently Observed Increase in Poleward Moisture Transport into the Arctic Ocean. *Adv. Atmos. Sci.* 35, 85–94. doi:10.1007/s00376-017-7116-0

Wachowicz, L. J., Preece, J. R., Mote, T. L., Barrett, B. S., and Henderson, G. R. (2021). Historical Trends of Seasonal Greenland Blocking under Different Blocking Metrics. *Int. J. Climatol* 41, E3263–E3278. doi:10.1002/joc.6923

Wang, B., Lee, S.-S., Waliser, D. E., Zhang, C., Sobel, A., Maloney, E., et al. (2018). Dynamics-oriented Diagnostics for the Madden-Julian Oscillation. *J. Clim.* 31 (8), 3117–3135. doi:10.1175/JCLI-D-17-0332.1

Wang, J., Kim, H., Kim, D., Henderson, S. A., Stan, C., and Maloney, E. D. (2020a). MJO Teleconnections over the PNA Region in Climate Models. Part I: Performance- and Process-Based Skill Metrics. *J. Clim.* 33 (3), 1051–1067. doi:10.1175/JCLI-D-19-0253.1

Wang, J., Kim, H., Kim, D., Henderson, S. A., Stan, C., and Maloney, E. D. (2020b). MJO Teleconnections over the PNA Region in Climate Models. Part II: Impacts of the MJO and Basic State. *J. Clim.* 33 (12), 5081–5101. doi:10.1175/JCLI-D-19-0865.1

Wang, W., Zender, C. S., As, D., and Miller, N. B. (2019). Spatial Distribution of Melt Season Cloud Radiative Effects over Greenland: Evaluating Satellite Observations, Reanalyses, and Model Simulations against *In Situ* Measurements. *J. Geophys. Res. Atmos.* 124, 57–71. doi:10.1029/2018JD028919

Wang, W., Zender, C. S., and As, D. (2018). Temporal Characteristics of Cloud Radiative Effects on the Greenland Ice Sheet: Discoveries from Multiyear Automatic Weather Station Measurements. *J. Geophys. Res. Atmos.* 123, 11348–11361. doi:10.1029/2018JD028540

Ward, J. L., Flanner, M. G., and Dunn-Sigouin, E. (2020). Impacts of Greenland Block Location on Clouds and Surface Energy Fluxes over the Greenland Ice Sheet. *J. Geophys. Res. Atmos.* 125, e2020JD033172. doi:10.1029/2020JD033172

Wernli, H., and Papritz, L. (2018). Role of Polar Anticyclones and Mid-latitude Cyclones for Arctic Summertime Sea-Ice Melting. *Nat. Geosci* 11, 108–113. doi:10.1038/s41561-017-0041-0

Wolding, B. O., Maloney, E. D., Henderson, S., and Branson, M. (2017). Climate Change and the M Adden- J Ulian O Scillation: A Vertically Resolved Weak Temperature Gradient Analysis. *J. Adv. Model. Earth Syst.* 9, 307–331. doi:10.1002/2016MS000843

Woods, C., Caballero, R., and Svensson, G. (2013). Large-scale Circulation Associated with Moisture Intrusions into the Arctic during winter. *Geophys. Res. Lett.* 40, 4717–4721. doi:10.1002/grl.50912

Woods, C., Caballero, R., and Svensson, G. (2017). Representation of Arctic Moist Intrusions in CMIP5 Models and Implications for Winter Climate Biases. *J. Clim.* 30, 4083–4102. doi:10.1175/JCLI-D-16-0710.1

Woods, C., and Caballero, R. (2016). The Role of Moist Intrusions in Winter Arctic Warming and Sea Ice Decline. *J. Clim.* 29, 4473–4485. doi:10.1175/JCLI-D-15-0773.1

Woollings, T., Barriopedro, D., Methven, J., Son, S.-W., Martius, O., Harvey, B., et al. (2018). Blocking and its Response to Climate Change. *Curr. Clim. Change Rep.* 4, 287–300. doi:10.1007/s40641-018-0108-z

Wu, B., Zhang, R., D'Arrigo, R., and Su, J. (2013). On the Relationship between Winter Sea Ice and Summer Atmospheric Circulation over Eurasia. *J. Clim.* 26, 5523–5536. doi:10.1175/JCLI-D-12-00524.1

Xu, D., Du, L., Ma, J., and Shi, H. (2020). Pathways of Meridional Atmospheric Moisture Transport in the central Arctic. *Acta Oceanol. Sin.* 39, 55–64. doi:10.1007/s13131-020-1598-9

Yadav, P., and Straus, D. M. (2017). Circulation Response to Fast and Slow MJO Episodes. *Monthly Weather Rev.* 145 (5), 1577–1596. doi:10.1175/MWR-D-16-0352.1

Yamanouchi, T. (2019). Arctic Warming by Cloud Radiation Enhanced by Moist Air Intrusion Observed at Ny-Ålesund, Svalbard. *Polar Sci.* 21, 110–116. doi:10.1016/j.polar.2018.10.009

Yang, W., and Magnusdottir, G. (2017). Springtime Extreme Moisture Transport into the Arctic and its Impact on Sea Ice Concentration. *J. Geophys. Res. Atmos.* 122, 5316–5329. doi:10.1002/2016JD026324

Yang, X.-Y., Fyfe, J. C., and Flato, G. M. (2010). The Role of Poleward Energy Transport in Arctic Temperature Evolution. *Geophys. Res. Lett.* 37, L14803. doi:10.1029/2010gl043934

Yao, W., Lin, H., and Derome, J. (2011). Submonthly Forecasting of winter Surface Air Temperature in North America Based on Organized Tropical Convection. *Atmos. Ocean* 49, 51–60. doi:10.1080/07055900.2011.556882

Yasunari, T. (1979). Cloudiness Fluctuations Associated with the Northern Summer Monsoon. *J. Meteorol. Soc. Jpn.* 57 (3), 16. doi:10.2151/jmsj1965.57.3_227

Yoo, C., Feldstein, S. B., and Lee, S. (2014). The Prominence of a Tropical Convective Signal in the Wintertime Arctic Temperature. *Atmos. Sci. Lett.* 15, 7–12. doi:10.1002/asl2.455

Yoo, C., Feldstein, S., and Lee, S. (2011). The Impact of the Madden-Julian Oscillation Trend on the Arctic Amplification of Surface Air Temperature during the 1979-2008 Boreal winter. *Geophys. Res. Lett.* 38, a–n. doi:10.1029/2011GL049881

Yoo, C., Lee, S., and Feldstein, S. B. (2012). Mechanisms of Arctic Surface Air Temperature Change in Response to the Madden-Julian Oscillation. *J. Clim.* 25, 5777–5790. doi:10.1175/JCLI-D-11-00566.1

Yoo, C., and Son, S. W. (2016). Modulation of the Boreal Wintertime Madden-Julian Oscillation by the Stratospheric Quasi-biennial Oscillation. *Geophys. Res. Lett.* 43, 1392–1398. doi:10.1002/2016GL067762

Yoshimori, M., Abe-Ouchi, A., and Laîné, A. (2017). The Role of Atmospheric Heat Transport and Regional Feedbacks in the Arctic Warming at Equilibrium. *Clim. Dyn.* 49, 3457–3472. doi:10.1007/s00382-017-3523-2

Yoshimori, M., Abe-Ouchi, A., Watanabe, M., Oka, A., and Ogura, T. (2014a). Robust Seasonality of Arctic Warming Processes in Two Different Versions of the MIROC GCM. *J. Clim.* 27, 6358–6375. doi:10.1175/JCLI-D-14-00086.1

Yoshimori, M., Watanabe, M., Abe-Ouchi, A., Shiogama, H., and Ogura, T. (2014b). Relative Contribution of Feedback Processes to Arctic Amplification of Temperature Change in MIROC GCM. *Clim. Dyn.* 42, 1613–1630. doi:10.1007/s00382-013-1875-9

You, C., Tjernström, M., and Devasthale, A. (2020). Warm-Air Advection over Melting Sea-Ice: A Lagrangian Case Study. *Boundary-layer Meteorol.* 179, 99–116. doi:10.1007/s10546-020-00590-1

Zhang, C. (2005). Madden–Julian Oscillation. *Rev. Geophys.* 43, RG2003. doi:10.1029/2004RG000158

Zhang, C., and Dong, M. (2004). Seasonality in the Madden-Julian Oscillation. *J. Clim.* 17 (16), 3169–3180. doi:10.1175/1520-0442(2004)017<3169:sitmo>2.0.co;2

Zhang, G., and Wang, Z. (2018). North Atlantic Extratropical Rossby Wave Breaking during the Warm Season: Wave Life Cycle and Role of Diabatic Heating. *Mon. Wea. Rev.* 146, 695–712. doi:10.1175/MWR-D-17-0204.1

Zhang, X., He, J., Zhang, J., Polyakov, I., Gerdes, R., Inoue, J., et al. (2013). Enhanced Poleward Moisture Transport and Amplified Northern High-Latitude Wetting Trend. *Nat. Clim Change* 3, 47–51. doi:10.1038/nclimate1631

Zheng, C., Chang, E. K. M., Kim, H., Zhang, M., and Wang, W. (2019). Subseasonal to Seasonal Prediction of Wintertime Northern Hemisphere Extratropical Cyclone Activity by S2S and NMME Models. *J. Geophys. Res. Atmos.* 124, 12057–12077. doi:10.1029/2019JD031252

Zheng, C., and Chang, E. K. M. (2019). The Role of MJO Propagation, Lifetime, and Intensity on Modulating the Temporal Evolution of the MJO Extratropical Response. *J. Geophys. Res. Atmos.* 124, 5352–5378. doi:10.1029/2019JD030258

Zheng, C., Kar-Man Chang, E., Kim, H.-M., Zhang, M., and Wang, W. (2018). Impacts of the Madden-Julian Oscillation on Storm-Track Activity, Surface Air Temperature, and Precipitation over North America. *J. Clim.* 31 (15), 6113–6134. doi:10.1175/JCLI-D-17-0534.1

Zheng, C., and Chang, E. K. M (2020). The Role of Extratropical Background Flow in Modulating the MJO Extratropical Response. *J. Clim.* 33 (11), 4513–4536. doi:10.1175/JCLI-D-19-0708.1

Zhou, S., L'Heureux, M., Weaver, S., and Kumar, A. (2012). A Composite Study of the MJO Influence on the Surface Air Temperature and Precipitation over the continental United States. *Clim. Dyn.* 38, 1459–1471. doi:10.1007/s00382-011-1001-9

Conflict of Interest: The authors declare that the research was conducted in the absence of any commercial or financial relationships that could be construed as a potential conflict of interest.

frontiers in Earth Science

ORIGINAL RESEARCH
published: 04 August 2021
doi: 10.3389/feart.2021.693779

The Nonlinear Radiative Feedback Effects in the Arctic Warming

Yi Huang, Han Huang and Aliia Shakirova*

Department of Atmospheric and Oceanic Sciences, McGill University, Montreal, QC, Canada

The analysis of radiative feedbacks requires the separation and quantification of the radiative contributions of different feedback variables, such as atmospheric temperature, water vapor, surface albedo, cloud, etc. It has been a challenge to include the nonlinear radiative effects of these variables in the feedback analysis. For instance, the kernel method that is widely used in the literature assumes linearity and completely neglects the nonlinear effects. Nonlinear effects may arise from the nonlinear dependency of radiation on each of the feedback variables, especially when the change in them is of large magnitude such as in the case of the Arctic climate change. Nonlinear effects may also arise from the coupling between different feedback variables, which often occurs as feedback variables including temperature, humidity and cloud tend to vary in a coherent manner. In this paper, we use brute-force radiation model calculations to quantify both univariate and multivariate nonlinear feedback effects and provide a qualitative explanation of their causes based on simple analytical models. We identify these prominent nonlinear effects in the CO_2-driven Arctic climate change: 1) the univariate nonlinear effect in the surface albedo feedback, which results from a nonlinear dependency of planetary albedo on the surface albedo, which causes the linear kernel method to overestimate the univariate surface albedo feedback; 2) the coupling effect between surface albedo and cloud, which offsets the univariate surface albedo feedback; 3) the coupling effect between atmospheric temperature and cloud, which offsets the very strong univariate temperature feedback. These results illustrate the hidden biases in the linear feedback analysis methods and highlight the need for nonlinear methods in feedback quantification.

Keywords: arctic, surface albedo feedback, cloud feedback, feedback coupling, radiative feedback, climate sensitivity, global warming

OPEN ACCESS

Edited by:
Patrick Charles Taylor, National Aeronautics and Space Administration (NASA), United States

Reviewed by:
Beate G. Liepert, Seattle University, United States
Zhen-Qiang Zhou, Fudan University, China

****Correspondence:***
Yi Huang
yi.huang@mcgill.ca

Specialty section:
This article was submitted to Atmospheric Science, a section of the journal Frontiers in Earth Science

Received: *12 April 2021*
Accepted: *16 July 2021*
Published: *04 August 2021*

Citation:
Huang Y, Huang H and Shakirova A (2021) The Nonlinear Radiative Feedback Effects in the Arctic Warming. Front. Earth Sci. 9:693779. doi: 10.3389/feart.2021.693779

INTRODUCTION

Radiative forcing and feedbacks strongly influence the Arctic climate. The warming in the Arctic has occurred in a faster pace than the global average, due to greenhouse gas forcing and amplifying feedbacks (Stocker et al., 2013). It requires accurate quantification of the radiative effects of associated feedback variables (surface albedo, atmospheric temperature, water vapor, cloud, etc.,) in order to ascertain their contributions to the climate change of interest. For instance, based on the energy budget balance with regard to the Top-of-Atmosphere (TOA), surface or atmospheric budget and assuming the warming induced thermal radiation (Planck effect) balances the radiation changes caused by feedbacks, one can infer how much global or regional warming, e.g., the Arctic warming amplification, can be attributed to individual feedbacks (Held and Soden 2000; Lu and Cai 2009; Pithan and Mauritsen 2014).

Often assumed in feedback analysis is linear additivity of the radiative effects of different feedback variables. For instance, the widely adopted kernel method (Soden and Held 2006) measures the radiation change caused by a feedback variable (X) by multiplying a pre-calculated radiative kernel ($\frac{\partial R}{\partial X}$) with the climate response (dX). Due to its simple concept and computational efficiency, a large number of studies have been conducted using this method (e.g., Soden and Held 2006; Zelinka et al., 2012; Vial et al., 2013; Zhang and Huang, 2014) and pre-computed kernels based on different atmospheric datasets, including climate models, reanalyses and satellite data (e.g., Soden et al., 2008; Yue et al., 2016; Huang et al., 2017).

The nonlinear effects, however, are often too large to ignore. When individual feedback terms are independently measured, such as the non-cloud feedbacks in the clear-sky case in the kernel method, the ignored nonlinear effects may lead to a non-closure of the radiation budget, i.e., the sum of the individual terms cannot reproduce the overall radiation change (e.g., Huang 2013; Vial et al., 2013). In the Arctic, where climate perturbations are of large magnitudes, e.g., in the case of sea ice melt, the non-closure issue is especially noticeable (e.g., Shell et al., 2008; Block and Mauritsen 2013; Zhu et al., 2019). Besides the large perturbations in surface albedo, the Arctic is also noted for its strong and unique lapse rate (e.g., Pithan and Mauritsen 2014) and cloud (e.g., Kato et al., 2006) feedbacks. It should be noted that although some methods exhibit a seemingly good radiation closure, the nonlinear effects are not treated but hidden in the feedback term(s) measured as a residual, e.g., the cloud feedback term in the typical kernel method, including the adjusted cloud radiative forcing (aCRF) technique (Shell et al., 2008; Soden et al., 2008).

Although the existence of the nonlinear effects has been recognized (e.g., Zhang et al., 1994; Colman et al., 1997), their impacts were seldom isolated and quantified. Some recent works have specifically addressed the nonlinearity issue in the radiative feedback analysis. Zhu et al. (2019) for the first time used a neural network model (a nonlinear diagnostic method without linearity assumption) to assess the radiative feedbacks and identified a few strong nonlinear effects, including a strong cloud-water vapor coupling effect in the tropical climate variations and a strong nonlinear dependence of radiation flux on the surface albedo. Using Partial-Radiative-Perturbation (PRP) experiments and brute-force radiation model-based computations, Huang and Huang (2021) verified the cloud-water vapor coupling effect and offered an analytic estimation of this effect on the longwave radiation. Shakirova and Huang (2021) advanced the neural network model of Zhu et al. and demonstrated its advantages particularly for quantifying the albedo feedback.

In this paper, we aim to give an overview of the nonlinear radiative feedback effects in Arctic climate change. Based on a heuristic climate change scenario of broad interest: the abrupt quadrupling of atmospheric CO_2 ($4xCO_2$), we investigate how the nonlinear radiative effects arise from the univariate and multivariate variations of the feedback variables, such as atmospheric and surface temperature (t), water vapor (q), surface albedo (a) and cloud (c), and measure how the nonlinear effects compare to the linear effects in terms of magnitude and pattern. We note that in this paper we are not concerned with how the changes in these variables are resulted, which if nonlinearly related to the surface warming may also cause nonlinearity in climate feedbacks, but focus on how their changes, as projected by the GCM, lead to nonlinear changes in the TOA longwave (LW) and shortwave (SW) radiation energy fluxes. In the following sections, we will define, demonstrate and discuss the various feedback effects of interest in order.

METHOD: FEEDBACK DEFINITIONS

Here, we define a *radiative feedback* as the (partial) radiation change, in the units of W m^{-2}, due to one or multiple feedback variables. This should be distinguished from a *feedback parameter*, which is normalized by surface temperature change and is in the units of W m^{-2} K^{-1}.

Consider the radiation field of interest, e.g., the TOA or surface radiation flux, as a function of the feedback variables: $R = R(x, y, z)$, where the letters (x, y, z) are generic notations of the feedback variables. The total radiation change in a given climate change scenario can thus be expressed by a Taylor series as

$$\begin{aligned}\Delta R_{(x,y,z)} &= R(x_2, y_2, z_2) - R(x_1, y_1, z_1)\\ &= \frac{\partial R}{\partial x}\Delta x + \frac{\partial R}{\partial y}\Delta y + \frac{\partial R}{\partial z}\Delta z \quad \text{(univariate linear effects)}\\ &+ \frac{1}{2}\Big[\frac{\partial^2 R}{\partial x^2}(\Delta x)^2 + \frac{\partial^2 R}{\partial y^2}(\Delta y)^2 + \frac{\partial^2 R}{\partial z^2}(\Delta z)^2 \quad \text{(univariate nonlinear effects)}\\ &+ 2\frac{\partial^2 R}{\partial x \partial y}\Delta x\Delta y + 2\frac{\partial^2 R}{\partial y \partial z}\Delta y\Delta z + 2\frac{\partial^2 R}{\partial x \partial z}\Delta x\Delta z\Big] \quad \text{(multivariate nonlinear effects)}\\ &+ O(\Delta^3)\end{aligned} \tag{1}$$

where the subscripts 1 and 2 denote two different climate states, e.g., those before and after quadrupling CO_2 (noted as $1xCO_2$ and $4xCO_2$, respectively from now on); such terms as $\Delta x = x_2 - x_1$ denote the *climate responses*. The terms on the righthand side of **Eq. (1)** illustrate three types of radiative effects that we aim to elucidate here:

1) The univariate linear effects, such as $\frac{\partial R}{\partial x}\Delta x$, which we denote as ΔR_x;
2) The univariate nonlinear effects, such as $\frac{1}{2}\frac{\partial^2 R}{\partial x^2}(\Delta x)^2$, which we denote as ΔR_{xx};
3) The multivariate nonlinear effects, such as $\frac{\partial^2 R}{\partial x \partial y}\Delta x\Delta y$, which we denote as ΔR_{xy}.

To avoid confusion, we denote a univariate feedback, i.e., the overall radiation change due to a single variable, as $\Delta R_{(x)}$, which consists of both univariate linear (ΔR_x) and univariate nonlinear (ΔR_{xx}) effects:

$$\begin{aligned}\Delta R_{(x)} &= R(x_2, y_1, \ldots) - R(x_1, y_1, \ldots)\\ &= \frac{\partial R}{\partial x}\Delta x + \frac{1}{2}\frac{\partial^2 R}{\partial x^2}(\Delta x)^2 + O(\Delta^3)\\ &= \Delta R_x + \Delta R_{xx}\end{aligned} \tag{2}$$

Equation (2) is written following the PRP concept (Wetherald and Manabe 1988) and measures the univariate feedbacks by simply evaluating the radiation flux twice: first with an unperturbed profile, $R(x_1, y_1, ...)$, and then perturbing x only, $R(x_2, y_1, ...)$. Note that other unperturbed independent variables than y are omitted in these expressions. If not otherwise stated, unspecified independent variables all take the unperturbed values when the radiation fluxes are evaluated in the following. The evaluation of the radiation fluxes can be done using a physical model, i.e., a radiative transfer model (RTM) (Huang and Huang 2021), or a statistical model, e.g., a neural network model that emulate the radiation fluxes (Zhu et al., 2019).

Similarly, a bivariate feedback can be expressed as:

$$\begin{aligned}\Delta R_{(x,y)} &= R(x_2, y_2) - R(x_1, y_1)\\ &= \frac{\partial R}{\partial x}\Delta x + \frac{\partial R}{\partial y}\Delta y + \frac{1}{2}\frac{\partial^2 R}{\partial x^2}(\Delta x)^2 + \frac{1}{2}\frac{\partial^2 R}{\partial y^2}(\Delta y)^2 + \frac{\partial^2 R}{\partial x \partial y}\Delta x \Delta y + O(\Delta^3)\\ &= \Delta R_x + \Delta R_y + \Delta R_{xx} + \Delta R_{yy} + \Delta R_{xy}\end{aligned} \tag{3}$$

From **Eq. 2** and **Eq. 3**, the bivariate coupling effect ΔR_{xy} can be obtained as

$$\begin{aligned}\Delta R_{xy} &= \Delta R_{(x,y)} - \Delta R_{(x)} - \Delta R_{(y)}\\ &= R(x_2, y_2) - R(x_2, y_1) - R(x_1, y_2) + R(x_1, y_1)\end{aligned} \tag{4}$$

Based on the above equations and following Huang and Huang (2021), we evaluate the radiation fluxes and isolate the respective feedback effects (ΔR_x, ΔR_{xx}, ΔR_{xy}, *etc.*), using the Rapid Radiative Transfer Model (RRTM, Mlawer et al., 1997). Using this RTM, the TOA and surface radiation fluxes are computed offline from instantaneous atmospheric profiles generated by the Community Earth System Model, CESM1.2, in a quadrupling CO_2 experiment (Wang and Huang, 2020). More details of the flux computation can be found in Huang and Huang (2021); we note that the radiative transfer computations, including the PRP computations, are based on instantaneous (3-hourly, as opposed to monthly mean) profiles at the original horizontal resolutions ($1.9^\circ \times 2.5^\circ$) of the CESM and then averaged monthly or annually in all the results presented in the following section.

Note that we use a one-sided PRP, starting with the unperturbed climate and then prescribing the change(s) in the variables of interest, to define feedbacks, i.e., how much radiation change is caused by the change of the feedback variable(s) of concern. Some studies opt to use two-sided perturbations (e.g., Colman and McAvaney 1997). In contrast to **Eq. (2)**, one may evaluate the feedback of x as

$$\begin{aligned}\delta R_{(x)} &= \frac{1}{2}R\left[(x_2, y_1) - R(x_1, y_1) + R(x_2, y_2) - R(x_1, y_2)\right]\\ &\approx \frac{1}{2}\left[\left.\frac{\partial R}{\partial x}\right|_{y1}\Delta x + \left.\frac{\partial R}{\partial x}\right|_{y2}\Delta x\right] \approx \frac{1}{2}\left[\left.\frac{\partial R}{\partial x}\right|_{y1}\Delta x + \left(\left.\frac{\partial R}{\partial x}\right|_{y1}\right.\right.\\ &\left.\left. + \frac{\partial}{\partial y}\left(\left.\frac{\partial R}{\partial x}\right)\right|_{y1}\Delta y\right)\Delta x\right.\\ &= \frac{\partial R}{\partial x} + \frac{1}{2}\frac{\partial^2 R}{\partial x \partial y}\Delta x \Delta y\end{aligned} \tag{5}$$

which, as shown in the above expansion, effectively includes nonlinear coupling effects such as $\frac{1}{2}\frac{\partial^2 R}{\partial x \partial y}\Delta x \Delta y$ in $\delta R_{(x)}$. When individual feedbacks are evaluated this way, their sum can better reproduce the overall radiation change, i.e., achieving a better radiation closure. However, it should be noted these "individual" feedbacks $\delta R_{(x)}$ differ from the univariate feedbacks $\Delta R_{(x)}$ as $\delta R_{(x)}$ contains coupling effects. To disclose these coupling effects, we adopt the one-sided formulations as exemplified by **Eq. 2**, **Eq. 3**, and **Eq. 4**

RESULTS

In this paper, we use the climate change in an abrupt $4xCO_2$ experiment of CESM (Wang and Huang, 2020) to provide a context for examining the linear and nonlinear radiative feedbacks. As illustrated in **Figure 1** for a few selected variables, this scenario represents strong perturbations in the Arctic climate, including reduction in surface albedo due to sea ice melt, surface warming and atmospheric moistening. The feedback quantifications presented in the following are based on the two months exemplified in **Figure 1** if not otherwise noted.

Univariate Linear Effects

The univariate linear effect ΔR_x can be measured, following its definition, by multiplying the radiative linear sensitivity kernel $K_x = \frac{\partial R}{\partial x}$ with the climate response Δx: $R_x = K_x \Delta x$. This is the core idea of the kernel method (Soden et al., 2008). The kernels are usually pre-computed, again, following the PRP idea, by prescribing small perturbations to the individual variables, e.g., 1-K in atmospheric and surface temperatures, several percent change in water vapor concentration, or 0.01 increment of surface albedo (e.g., Shell et al., 2008):

$$K_x = \frac{\Delta R_0}{\Delta x_0} = \frac{R(x_1 + \Delta x_0, y_1) - R(x_1, y_1)}{\Delta x_0} \tag{6}$$

so that the kernel method is in essence to scale up the radiation change due to an infinitesimal (small) perturbation, R_0, to estimate the radiation change due to a finite (large) perturbation:

$$\Delta R_x = K_x \Delta x = \Delta R_0 \frac{\Delta x}{\Delta x_0} \tag{7}$$

It is worth noting that when defining and applying the kernels, it is advisable to choose a scaling scheme appropriate to the radiation dependency on the feedback variable. For instance, in the case of such greenhouse gases as carbon dioxide and water vapor, their radiative effects are logarithmically dependent on their concentrations (e.g., Bani Shahabadi and Huang., 2014), so that it is common to define the water vapor kernel with respect to the change in the logarithm of the specific humidity, i.e., $K_q = \frac{\Delta R_0}{\Delta(ln(q))_0}$, or, in an approximate form, using the fractional change in q in the denominator, i.e., $K_q = \frac{\Delta R_0}{(\Delta q/q)_0}$. As shown by **Figure 2**, using the logarithmic scaling scheme, the radiation change caused by water vapor perturbations, even when the perturbations are of large magnitudes (about 200% increase of TCWV), can be well approximated according to **Eq. (7)**.

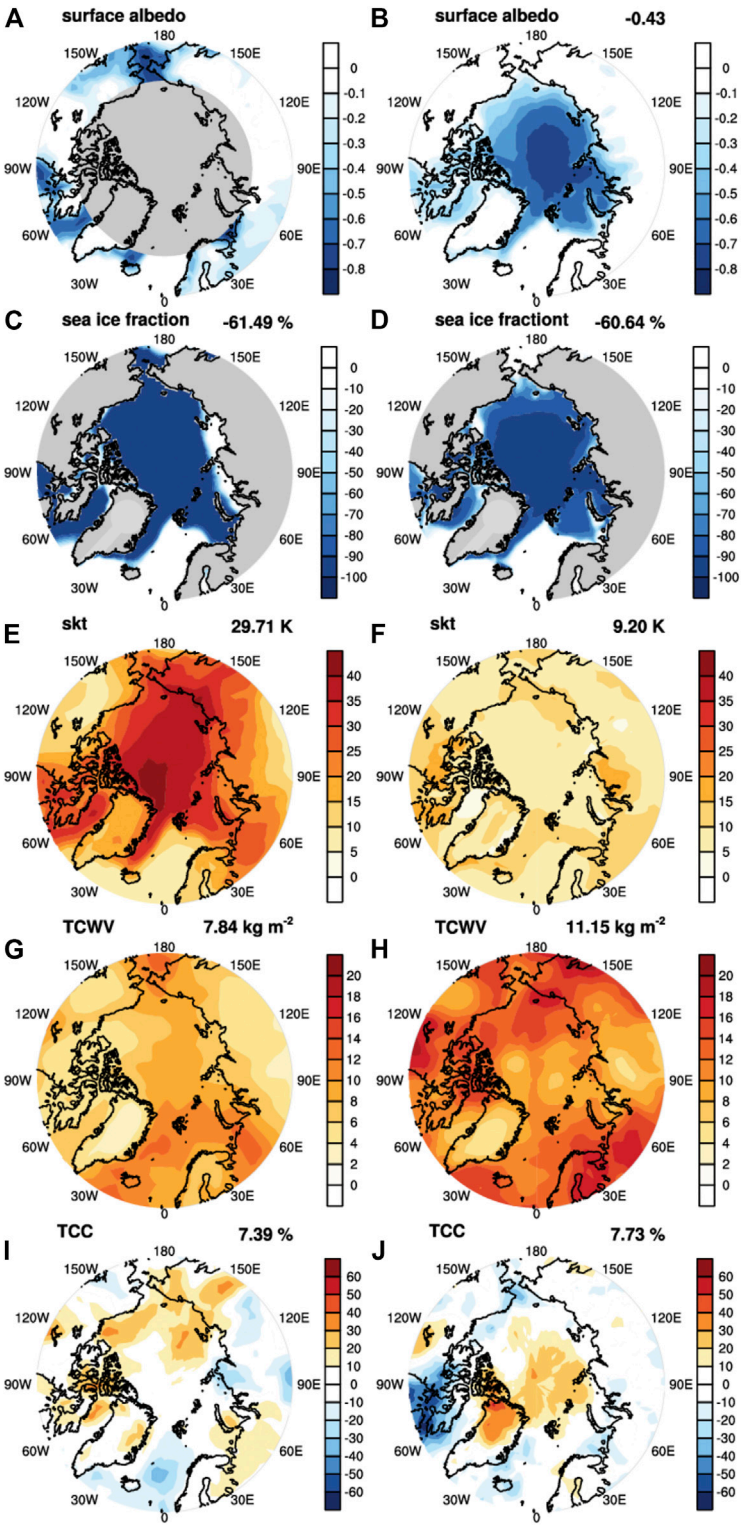

FIGURE 1 | Changes in climate variables in the 4xCO_2 experiment, exemplified by two months a January **(left column)** and a June **(right column)**. **(A,B)** Suface albedo; **(C,D)** sea ice fraction; **(E,F)** surface skin temperature; **(G,H)** column-integrated water vapor; **(I,J)** total cloud fraction. The numbers on the upper right corner of each panel are the Arctic mean values, averaged over the latitude range of 70–90°N. Shaded in grey are regions with no data, for instance, due to no solar insolation to infer surface albedo in **(A)**.

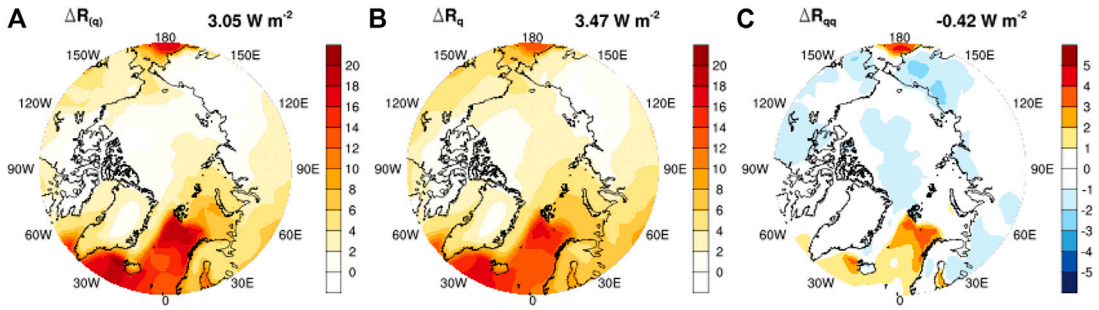

FIGURE 2 | Clear-sky univariate water vapor LW feedback. **(A)** RTM-computed (truth) overall univariate feedback, $\Delta R_{(q)}$; **(B)** kernel-estimated univriate linear feedback, ΔR_q, based on logarithmic scaling; **(C)** the residual **(A–B)**, i.e., the univariate nonlinear feedback, ΔR_{qq}. Shown here is the clear-sky TOA LW radiation flux change due to the water vapor change in January in the 4xCO_2 experiment (as illustrated in **Figure 1E**). The kernel used in **(B)** is computed from the GCM instantaneous atmospheric profiles of the same month and is not subject to the bias discussed in **Eq. 8**.

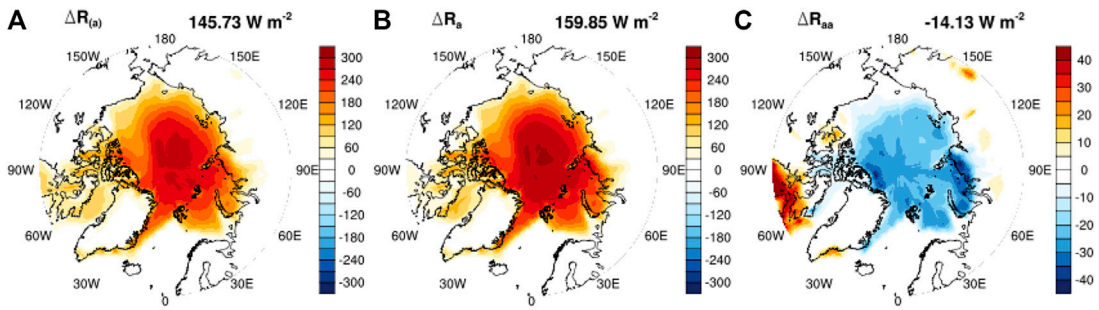

FIGURE 3 | All-sky univariate surface albedo SW feedback. **(A)** RTM-computed (truth), $\Delta qR_{(a)}$; **(B)** kernel-estimated univariate linear feedback, ΔR_a; and **(C)** the residual **(A–B)**, i.e., the univariate nonlinear term ΔR_{aa}. Shown here is the all-sky TOA SW radiation flux change due to the surface albedo change in June in the 4xCO_2 experiment (as illustrated in **Figure 1B**).

The validations against RTM-computed truth in **Figures 2**, **3** show that the non-cloud univariate radiative feedbacks $\Delta R_{(x)}$, even in the case of large climate perturbations, can be reasonably approximated by the linear term ΔR_x. This is the basis of the kernel method (Soden et al., 2008). Nevertheless, the biases, i.e., the univariate nonlinear effects ΔR_{xx} may amount to non-negligible extent: in the case of the univariate water vapor feedback and the surface albedo feedback, the biases can amount to more than 10% in terms of Arctic mean (averaged over 70–90°N).

It should be cautioned that the kernel itself has a dependency on the atmospheric conditions (x, y, z, . . .) and such dependency should be recognized when interpreting the kernel-diagnosed feedbacks. The kernels appropriate to evaluating the linear feedbacks in **Eq. 1**, **Eq. 2**, and **Eq. 3**, and used to compute ΔR_q in **Figure 2** and ΔR_a in **Figure 3**, are computed from the GCM atmopsheric profiles in the unperturbed (1xCO2) climate, i.e., $K_x = \frac{\partial R}{\partial x}\Big|_{x_1,y_1,z_1}$, where (x_1, y_1, z_1) denotes the 1xCO_2 climate. If computed from different atmospheric states, the kernel values may quantitatively differ (e.g., see the kernel comparisons in Huang et al., 2017; Smith et al., 2020 and others). If a kernel computed from a different atmospheric state (x_1', y_1', z_1') is used to measure the linear feedback, a bias is resulted:

$$\begin{aligned}\Delta R_x' &= \frac{\partial R}{\partial x}\Big|_{x_1',y_1',z_1'}\Delta x \\ &\approx \left(\frac{\partial R}{\partial x}\Big|_{x_1,y_1,z_1} + \frac{\partial^2 R}{\partial x^2}\Big|_{x_1,y_1,z_1} dx' + \frac{\partial^2 R}{\partial x \partial y}\Big|_{x_1,y_1,z_1} dy' + \frac{\partial^2 R}{\partial x \partial z}\Big|_{x_1,y_1,z_1} dz'\right)\Delta x \\ &= \Delta R_x + bias\end{aligned} \tag{8}$$

Equation (8) shows that the *bias* can be considered one type of nonlinear effect in that it, like the nonlinear effects analyzed below, results from the nonlinear dependency of the radiation on the feedback variables (e.g., $\frac{\partial^2 R}{\partial x \partial y}$). For the simplicity of the expressions, we omit the notation $(...)|_{x_1,y_1,z_1}$ in the following, where the conditioned states can be inferred from the context.

The magnitude of the feedback bias caused by kernel bias is proportional to the discrepancies in the atmospheric states (dx', dy', and dz' in **Eq. (8)**), which may introduce noticeable quantitative differences in the kernels. For example, one may see from Fig. S3 of Huang et al. (2017), as well as the discussions of Sanderson and Shell (2012), the temperature kernel discrepancies due to the ubiquitous discrepancies in the cloud distribution in different atmospheric datasets used for kernel computation. Here, as a sanity check, we recalculate

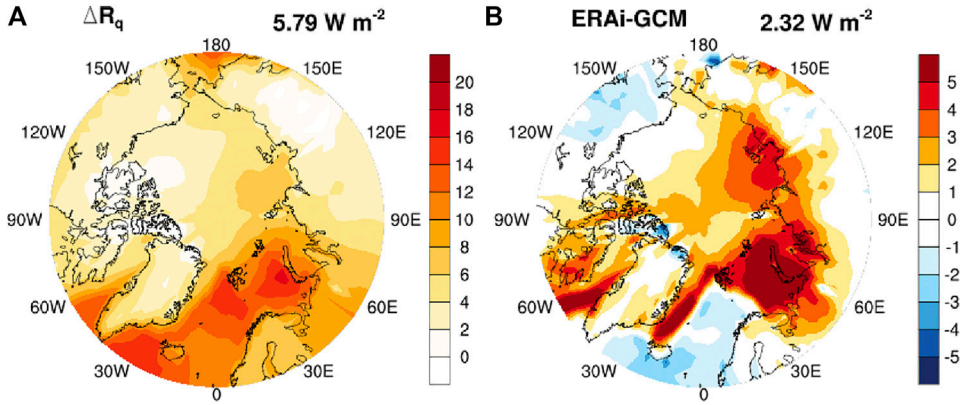

FIGURE 4 | Clear-sky water vapor feedback bias due to kernel bias. **(A)** Like **Figure 2B**, but using the kernels computed from different atmospheric profiles (Huang et al., 2017); **(B)** Bias compared to **Figure 2B**.

the Arctic mean clear-sky water vapor feedback shown in **Figure 2** using the clear-sky kernels of Huang et al. (2017) and obtain an Arctic mean ΔR_q of 5.79 W m^{-2} (**Figure 4**). This, compared to the RTM-computed truth value of 3.05 W m^{-2}, representes a 90% bias and is much larger than the bias when the correct (GCM 1xCO_2 climate based) kernels are used (3.47 W m^{-2}, as shown by **Figure 2B**). The results indicates that, contradictory to common belief, there may be large biases, especially in regional (e.g., Arctic) feedbacks, resulting from kernel biases.

Lastly, we note that cloud feedback is difficult, if not impossible, to be approximated by linear kernels. This is because cloud variations involve multiple radiative properties, including cloud fraction, droplet concentration and size distribution, etc., each of which may experience large, discrete perturbations and strongly affect the radiative sensitivity to each other. The cloud radiative effects measured in the cloud property histogram method (Zelinka et al., 2012) illustrate how the radiative sensitivity to cloud varies strongly with the cloud properties. Among other issues, a notable challenge is the vertical masking effect: for instance, the increase of upper-level clouds greatly reduces the sensitivity of the TOA fluxes to the lower-level clouds.

In summary, the non-cloud univariate feedbacks in general can be approximated well by the kernel method, although one should be mindful about the biases introduced by kernel discrepancies. One most noticeable univariate nonlinear effect in the Arctic is the surface albedo feedback. We further analyze this and other nonlinear effects in the following subsections.

Univariate Nonlinear Effects

Because radiative transfer is a complex nonlinear process (e.g., see Goody and Yung 1989), atmospheric radiation fluxes generally have a nonlinear dependency on the feedback variables and thus the univariate nonlinear effects generally exist.

Temperature

With regard to the univariate temperature feedback, a well-recognized cause of the nonlinearity is the Planck function, although this nonlinearity is weak at the terrestrial temperatures. Based on the Stefan-Boltzmann Law,

$$R = \sigma t^4 \tag{9}$$

Given the constant $\sigma = 5.67 \times 10^{-8}$ W m^{-2} K^{-4}, one may find that the nonlinear effect $\frac{\partial^2 R}{\partial t^2}$ is only about 1% of the linear effect $\frac{\partial R}{\partial t}$, for a 1-K perturbation around the equivalent blackbody temperature of Earth (t = 255K). Another cause of the nonlinearity is the dependence of the gas absorptivity on the temperature, which also has a minor impact (Huang et al., 2007). This explains why the temperature feedback in the case of large perturbations can still be very well approximated by the linear kernels (not shown).

Water Vapor

The univariate water vapor feedback is generally well estimated when the logarithmic scaling scheme is used, although **Figure 2C** shows that the bias (i.e., the univariate nonlinear effect, ΔR_{qq}) can be non-negligible. A notable reason that causes the feedback to deviate from the logarithmic behavior is the unsaturated atmospheric absorption in the mid-infrared window around 10 μm wavelength. Here, the surface emission strongly contributes to the OLR and thus the water vapor feedback cannot be interpreted simply as the elevation of the atmospheric emission level, which gives rise to the logarithmic dependence (Bani Shahabadi and Huang., 2014). **Figure 5** suggests that the water vapor feedback estimation may be improved if different scaling schemes are used for different spectral bands: logarithmic in the absorption bands (where atmospheric optical depth is large) and linear in the window bands (where optical depth is small):

$$\Delta R_{(q)} = K_q^{log} \Delta \left(ln\left(q\right)\right) + K_q^{lin} \Delta q \tag{10}$$

where the logarithmic kernel K_q^{log} accounts for the logarithmic response of the radiation flux in the absorption bands to water

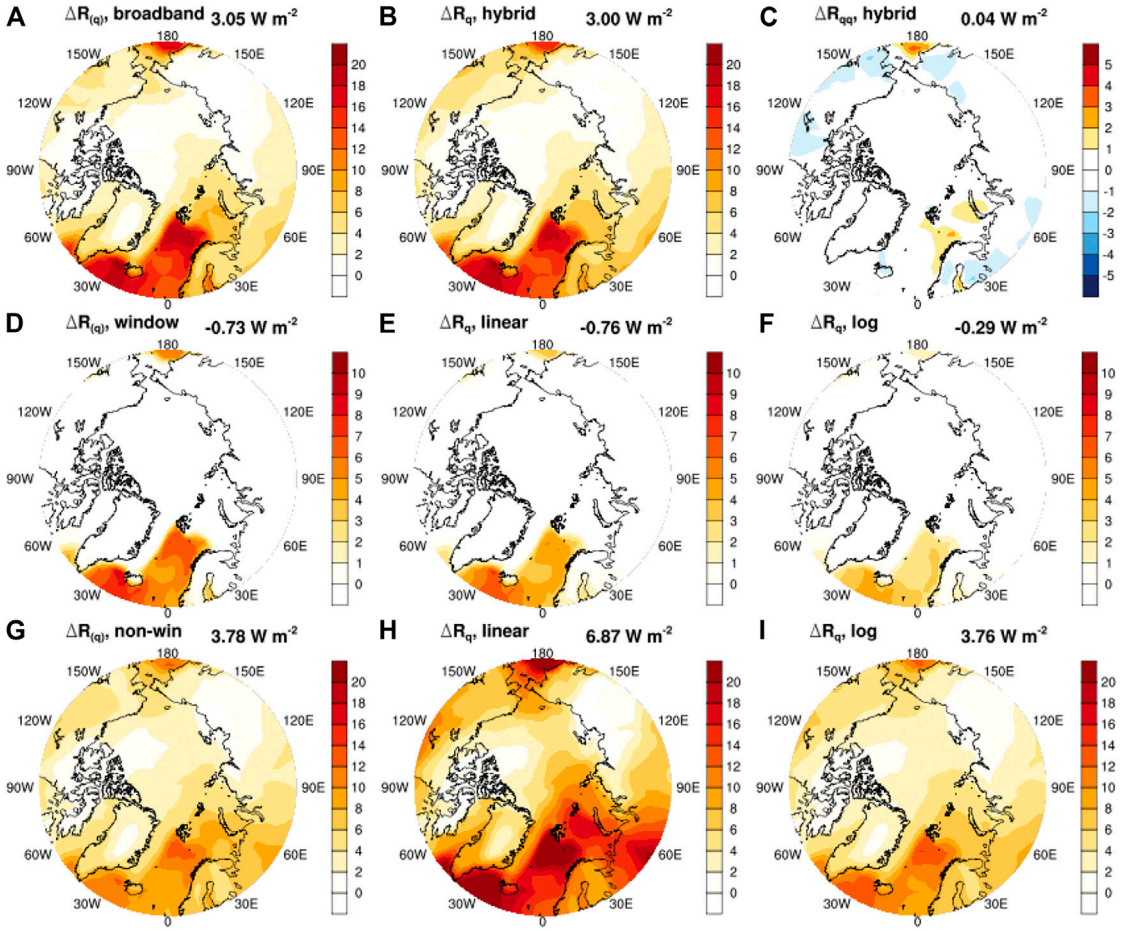

FIGURE 5 | Spectral breakdown of the clear-sky univariate water vapor feedback. **(A)** RTM-computed (truth) broadband univariate feedback, $\Delta R_{(q)}$; **(B)** kernel-diagnosed broadband feedback, ΔR_q, using the hybrid scaling (**Eq. 10**); **(C)** residual, ΔR_{qq}. **(D–F)** Window band (700–1,180 cm^{-1}) feedback, computed by RTM and estimated by linear and logarithmic scaling. **(G–I)** Like **(D–F)**, but for the non-window (absorption) bands.

vapor perturbation and the linear kernel K_q^{lin} accounts for the linear response in the window band. Further research is required to develop and validate a global hybrid kernel set.

Surface Albedo

The univariate surface albedo feedback shows especially strong nonlinear dependence on the surface albedo a (**Figure 6**). This is because the multiple scattering of radiation between the surface and atmosphere renders a nonlinear dependency of planetary albedo on surface albedo. Following Stephens et al. (2015), the planetary albedo a_p can be expressed as

$$a_p = r + \frac{a\tau^2}{1 - ra} \tag{11}$$

Here r and τ denote atmospheric reflectance and transmittance respectively; they are related as $\tau + r + \varepsilon = 1$, where ε denotes atmospheric absorptivity. This relation means that a_p and thus the net shortwave radiation flux at TOA has a nonlinear dependency on a:

$$\frac{\partial a_p}{\partial a} = \frac{\tau^2}{(1 - ra)^2} \tag{12}$$

That the radiative sensitivity to surface albedo continuously varies with the albedo value makes it difficult for any linear methods such as the kernel method to accurately measure the albedo feedback. It is interesting to notice from **Eq. (12)** that the radiative sensitivity decreases with a. This means that if the surface albedo kernel is computed with relatively larger albedo values under the unperturbed climate ($1xCO_2$), it will overestimate the univariate albedo feedback in a warming scenario ($4xCO_2$). This is clearly seen from **Figure 6**. If the kernel method is used to estimate the feedback when sea ice completely melts, the intercepts on y-axis indicate the overestimate can be serveral dozens of W m^{-2}. This overestimation issue was also noted in the previous studies (e.g., Block and Mauristen 2013; Zhu et al., 2019). It is also interesting to notice that although the analytical model qualitatively captures the change of radiative sensitivity to albedo, it does not accurately predict it. The neural network method proposed by Zhu et al. (2019) and Shakirova and Huang (2021) may be better suited for

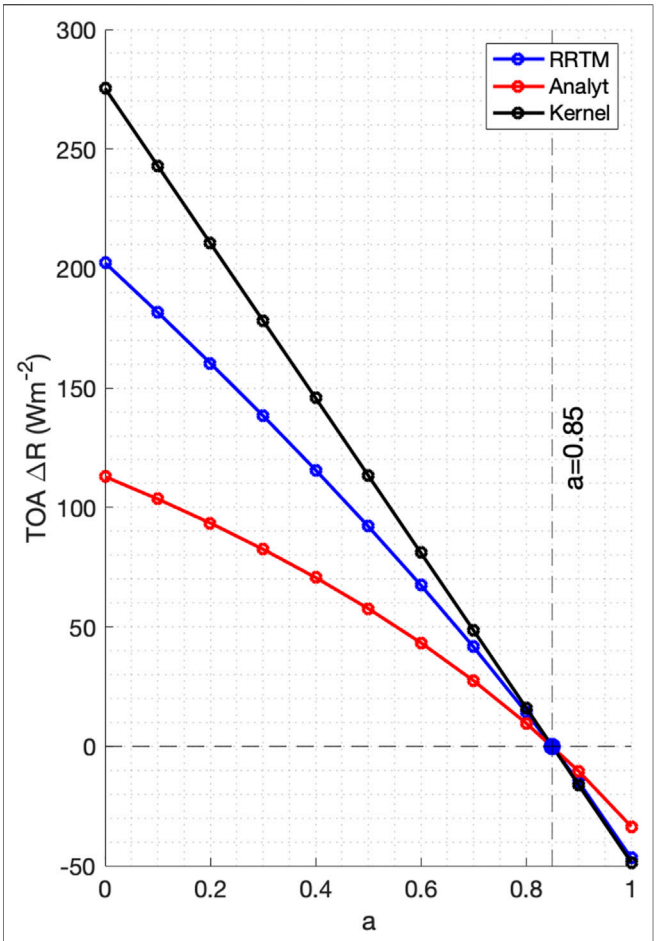

FIGURE 6 | All-sky univariate surface albedo SW feedback corresponding to different albedo values. By perturbing the surface albedo to values from 0 to 1, the TOA SW feedback is computed by three different methods: RRTM-computed truth, kernel-estimation and the single-layer analytical model (**Eq. 11**). The results are computed based on one arbitrarily chosen grid box at (78°W, 82°N), where the intial surface albedo is 0.85.

the albedo feedback quantification and deserves further development and more extensive validations.

Multivariate Nonlinear Effects

Besides the univariate nonlinear effects, **Eq. (1)** indicates that multivariate nonlinear effects, represented by such terms as $\frac{\partial^2 R}{\partial x \partial y}\Delta x \Delta y$, may also strongly contribute to the radiative flux variations. Such terms are often referred to as the *coupling* effects because they result from concerted variations of the involved variables; otherwise, if their covariance were small, the average of this term over time or region would be negligible. In reality, this necessary condition is usually met because the variations of the feedback variables of concern tend to be strongly correlated. For instance, temperature warming and sea ice melt may expose more open water, which in turn leads to more evaporation, atmospheric humidity and cloudiness.

Due to large computational expenses of the brute-force RTM-based feedback calculation, we base our discussions on two representative months in the $4xCO_2$ experiment: January (winter) for the longwave feedbacks and June (summer) for the shortwave feedbacks, because the two types of feedbacks are the most prominent in the two respective seasons. **Figures 7**,**8** show the radiative feedbacks corresponding to the changes in the feedback variables illustrated in **Figure 1**. **Table 1** summarizes their Arctic mean values. These results disclose two strongest multivariate feedback effects in the Arctic: the coupling effect between temperature and cloud, ΔR_{tc}, in the longwave and the coupling effect between albedo and cloud, ΔR_{ac}, in the shortwave.

In the longwave, we find that the multivariate (bivariate) feedback is dominated by the coupling effect between temperature and cloud, ΔR_{tc}. The pattern of this coupling effect resembles, but strongly offsets, the univariate temperature feedback, $\Delta R_{(t)}$, which is the dominant feedback that controls the overall LW feedback in the Arctic. This coupling effect can be explained by a simple analytical model. Consider a single-layer atmosphere, with temperature t_a and emissivity (absorptivity) ε, and assume the surface to be a blackbody with temperature t_s:

$$OLR = (1-\varepsilon)\sigma t_s^4 + \varepsilon\,\sigma t_a^4 \tag{13}$$

Hence, the coupling effect ΔOLR_{tc} is found to be

$$\Delta OLR_{tc} = 4\sigma\left(t_a^3\Delta t_a - t_s^3\Delta t_s\right)\frac{d\varepsilon}{dc}\Delta c \tag{14}$$

Because the warming in the Arctic is capped in near-surface layers, $\Delta t_a << \Delta t_s$. This leads to reduction in OLR, offseting the increase of OLR by temperature warming. The coupling effect between temperature and water vapor can be understood in the same way. Becaue water vapor affects OLR also by affecting the atmospheric emissivity; the coupling effect ΔOLR_{tq} is thus also affected by the factor $(t_a^3\Delta t_a - t_s^3\Delta t_s)$ in **Eq. (14)**. Although this nonlinear effect arises from the nonuniform vertical structure of temperatuure warming and thus share the physical cause of the temperature lapse rate feedback, this nonlinear effect should be distinguished from the lapse rate feedback, which is part of the univariate temperature feedback, ΔR_t. Note that the sign of ΔR_{tc} and ΔR_{cq} is positive in **Figure 7** because the fluxes are defined to be downward positive.

In the shortwave, the dominant multivariate effect is found to be the albedo-cloud coupling, which offsets the univariate albedo feedback. From the simple model described above (**Eq. 11** and **Eq. 12**, this can be understood as cloud-caused reduction in the atmospheric transmittance and thus reduction in the radiative senstivity to surface albedo.

It is interesting to note that the patterns of some coupling feedback effects are correlated with the change patterns of the associated feedback variables. For example, the LW cloud-temperature coupling effect is correlated with surface temperature change, with a correlation coefficient of 0.86; the LW cloud-water vapor coupling effect is correlated with total water vapor (TCWV) at 0.62; the SW albedo-cloud coupling effect is correlated with the surface albedo change at 0.89. Such

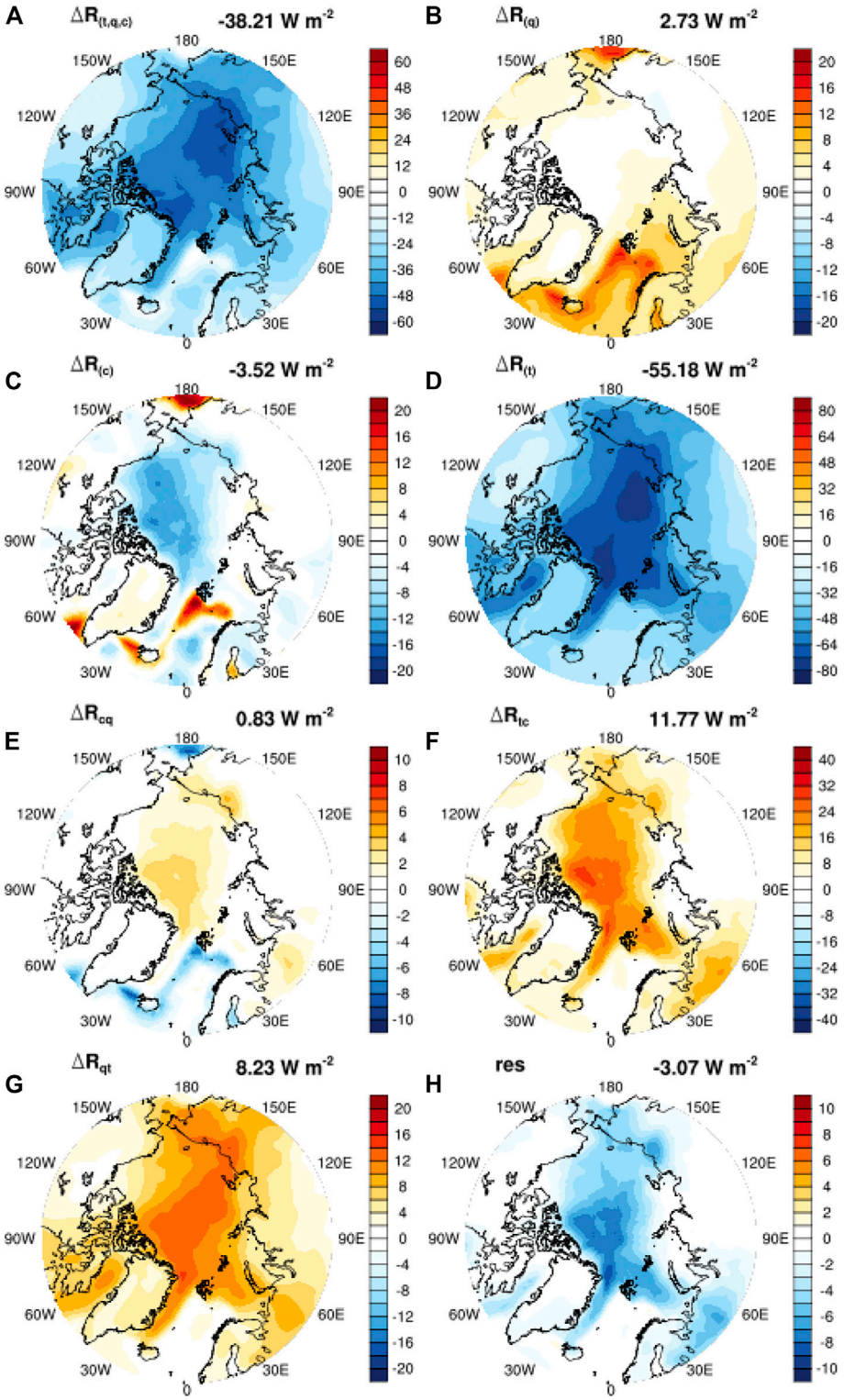

FIGURE 7 | All-sky LW feedback effects in January. Units: W m^{-2}. Shown here are the total and component all-sky feedbacks in the 4xCO_2 experiment evaluated according to **Eq. 2**, **Eq. 3**, and **Eq. 4** by using an RTM. *t*: atmospheric and surface temperatures; *q*: atmospheric water vapor; *c*: cloud; *a*: surface albedo; res: residual. The Arctic mean values are noted on the top right corner of each panel.

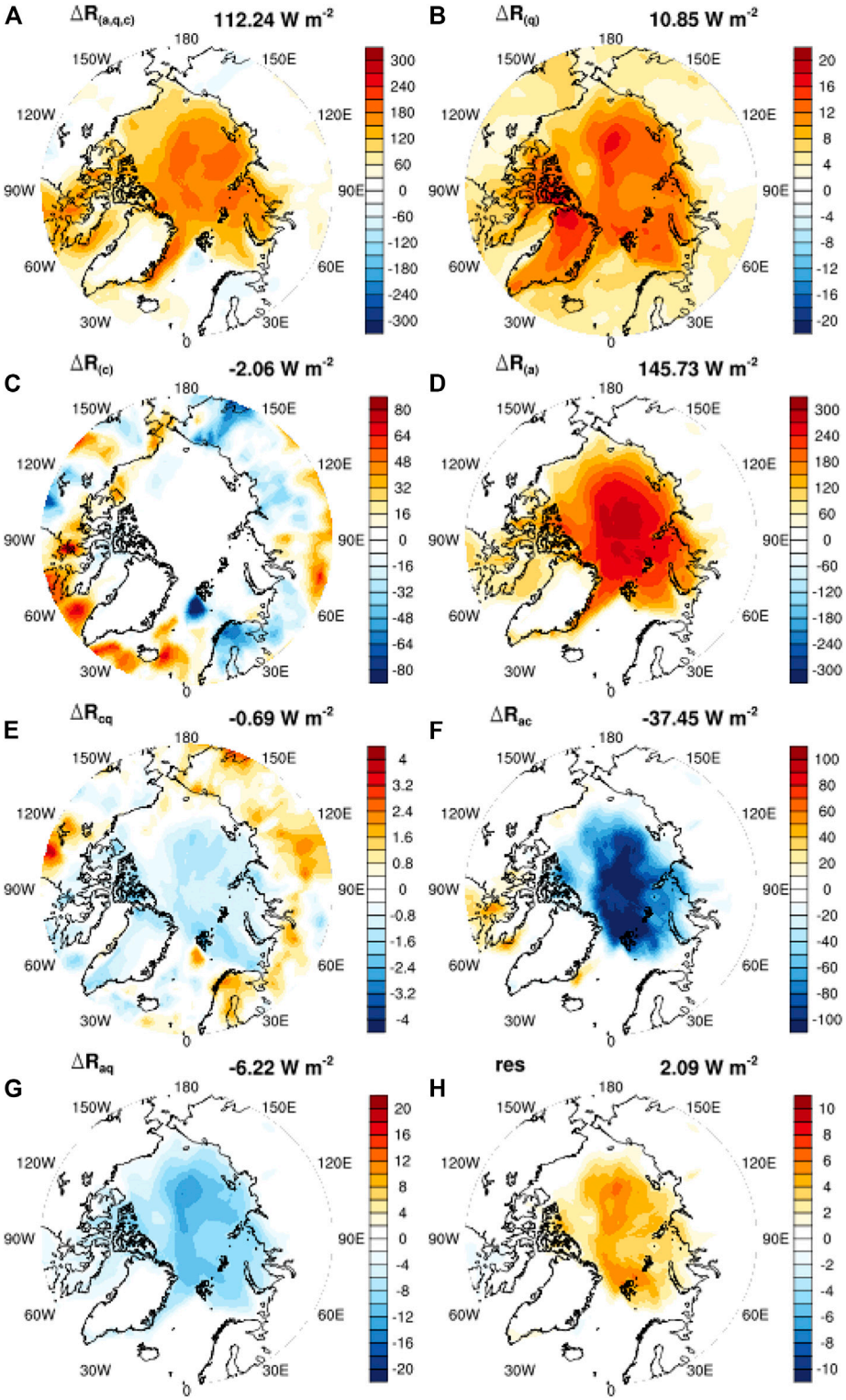

FIGURE 8 | Like **Figure 7**, but for the all-sky SW feedback effects in June. Units: W m^{-2}.

relation suggests that it may be possible to estimate these nonlinear effects using analytical or statistical models. Huang and Huang (2021) used such an model to explain the cloud-water vapor coupling effect and found it to be the dominant multivariate longwave feedback effect in the tropics. Although this coupling effect is not as strong

TABLE 1 | Arctic mean all-sky feedbacks in the 4xCO2 experiment for the two selected months. Units: W m-2. Area-weighted averages are taken for the region 70–90°N. Two sets of radiative kernels have been used to measure the univariate linear feedbacks: Ker1 is computed from the GCM instantaneous profiles in this work and thus is of no kernel bias; Ker2 is the kernel computed by Huang et al. (2017) from the ERA-interim reanalysis profiles, which leads to biases in diagnosed univariate feedback as explained by **Eq. 8**.

LW (jan	$\Delta R_{(t,q,c)}$	$\Delta R_{(t)}$	$\Delta R_{(q)}$	$\Delta R_{(c)}$	ΔR_{cq}	R_{tc}	ΔR_{qt}	**res**	ΔT_S (K)	
									Global mean	**Arctic mean**
RTM	−38.21	−55.18	2.73	−3.52	0.83	11.77	8.23	−3.07	7.95	29.71
—	—	ΔR_t	ΔR_q	ΔR_c^*	—	—	—	—		
Ker1	—	−48.98	3.08	7.68	—	—	—	—		
Ker2	—	−44.53	5.35	0.97	—	—	—	—		
SW (Jun.)	$\Delta R_{(a,q,c)}$	$\Delta R_{(a)}$	$\Delta R_{(q)}$	$\Delta R_{(c)}$	ΔR_{cq}	ΔR_{ac}	ΔR_{qa}	**res**	ΔT_S (K)	
									Global mean	**Arctic mean**
RTM	112.24	145.73	10.05	−2.06	−0.69	−37.45	−6.22	2.09	6.97	9.20
—	—	ΔR_a	ΔR_q	ΔR_c^*	—	—	—	—		
Ker1	—	159.85	12.26	−59.88	—	—	—	—		
Ker2	—	117.04	8.14	12.95	—	—	—	—		

compared to the temperature-related coupling effects in the Arctic, we find that adopting the same estimation method of Huang and Huang, 2021, Eq. 19 and using a parameter value appropriate to the Arctic ($A = 0.04\ kg^{-1}\ m^2$), we can very well predict the cloud-water vapor coupling effect (spatial correlation = 0.99, RMSE = 0.41 W m^{-2}). Future works are warranted to identify methods for explaining and predicting the other coupling effects.

Lastly, for comparison, we include in **Table 1** the respective feedbacks analyzed from the kernel method, i.e., the univariate linear effects for non-cloud feedbacks and the cloud feedback (ΔR_c^*) obtained as a residual of total radiation change decomposition. Besides the biases in the univariate feedbacks as noted above, it is worth noting that the kernel-based estimations may also greatly bias the cloud feedback, mainly due to its negligence of the coupling effects.

CONCLUSIONS AND DISCUSSIONS

In this paper, we present an overview of the nonlinear effects in both longwave and shortwave radiative feedbacks in the CO_2-driven Arctic warming. Based on brute-force radiation model calculations we disclose the most prominent nonlinear feedback effects and based on simple analytical models we offer explanations of their physcial causes. Although the presentation and discussion are focused on the Arctic feedbacks, the diagnostic framework (**Eq. 1**) and the theoretical explanations are applicable to global feedback analyses.

We identify these important nonlinear feedback effects:

1) The univariate nonlinear effect in the surface albedo feedback in the shortwave. This nonlinearity can be understood from a simple analytical model [**Eq. (11)**] that accounts for the coupling, due to multiple-scattering, between the surface and atmosphere (clouds). This coupling makes the radiative sensitivity to surface albedo decrease with the surface albedo value (**Figure 6**). Because of this effect, it generally leads to an overestimate of the surface albedo feedback when albedo kernels computed from the current climate are used to quantify the albedo feedback in a warming climate (**Figure 3**; **Table 1**).

2) The bivariate surface albedo-cloud coupling effect in the shortwave. This effect is attributable to the masking effect of cloud increase that damps the radiative sensitivity to surface albedo. This effect is the most prominent in the summer when solar insolation is strong, as illustrated by **Figure 8** for the month of June.

3) The multivariate temperature-cloud feedback in the longwave. This effect is attributable to the fact that the Arctic warming is much stronger at and near the surface than in the upper air, which leads to a damping effect on the temperature feedback. This nonlinear effect should be distinguished from the temperature lapse rate feedback and is found to be the strongest in the winter as illustrated by **Figure 7** for the month of January.

4) Although the univariate water vapor feedback largely scales logarithmically with water vapor changes, it is found that the relation deviates from the logarithmic scaling, especially in the window band. This is due to the unsaturated atmospheric absorption in this band and suggests that a hybrid scaling method as proposed by **Eq. (10)** may improve the accuracy of the kernel-diagnosed water vapor feedback (compare **Figure 2C** and **Figure 5C**).

It should be noted that the large nonlinear effects discovered here is not limited to the $4xCO_2$ experiment. As shown by Huang and Huang (2021) for the longwave feedbacks and Shakirova and Huang (2021) for the shortwave feedbacks, similar, strong nonlinear effects exist even also interannual climate variations. It is noted that the nonlinear effects may quantitatively differ in different forcing experiments, thus requiring them to be assessed more comprehensively in future work.

The strong nonlinear effects as disclosed here call into question the accuracy of linear methods currently used in the feedback analysis. Nonlinear methods are needed to improve the accuracy of feedback quantificaiton when RTM-based PRP experiments are not feasible due to its forbidding computational demands. Especially in need are replacement of the linear kernels for the surface albedo feedback and cloud feedback quantification. Although a handful of

studies have touched this topic, for instance, using quadratic fitting (Colman et al., 1997), histogram (Zelinka et al., 2012) and neural network (Zhu et al., 2019) methods, this challenging problem demands devoted research programs to further develop, test and mature the candidate methods.

DATA AVAILABILITY STATEMENT

The datasets presented in this study can be found in online repositories. The names of the repository/repositories and accession number(s) can be found below: The CESM codes can be downloaded from National Center for Atmospheric Research (NCAR) website (http://www.cesm.ucar.edu/models/cesm1.2/). The RRTM code can be downloaded at http://rtweb.aer.com/rrtm_frame.html.

AUTHOR CONTRIBUTIONS

YH designed the research and wrote the paper. HH conducted the longwave feedback analysis and AS conducted the shortwave feedback analysis.

ACKNOWLEDGMENTS

We thank Tim Merlis, Ivy Tan, Patrick Taylor and two reviewers, whose comments helped improve this paper. We acknowledge grants from the Natural Sciences and Engineering Research Council of Canada (RGPIN-2019-04511) and from the Fonds de recherche du Québec—Nature et technologies (2021-PR-283823).

REFERENCES

Bani Shahabadi, M., and Huang, Y. (2014). Logarithmic Radiative Effect of Water Vapor and Spectral Kernels. *J. Geophys. Res. Atmos.* 119 (10), 6000–6008. doi:10.1002/2014jd021623

Block, K., and Mauritsen, T. (2013). Forcing and Feedback in the MPI-ESM-LR Coupled Model under Abruptly Quadrupled CO2. *J. Adv. Model. Earth Syst.* 5 (4), 676–691. doi:10.1002/jame.20041

Colman, R. A., Power, S. B., and McAvaney, B. J. (1997). Non-linear Climate Feedback Analysis in an Atmospheric General Circulation Model. *Clim. Dyn.* 13 (10), 717–731. doi:10.1007/s003820050193

Colman, R., and McAvaney, B. J. (1997). A Study of General Circulation Model Climate Feedbacks Determined from Perturbed SST Experiments. *J. Geophys. Res.* 102, 19 383–419. doi:10.1029/97jd00206

Huang, H., and Huang, Y. (2021). Nonlinear Coupling between Longwave Radiative Climate Feedbacks. *J. Geophys. Res.*

Huang, Y. (2013). On the Longwave Climate Feedbacks. *J. Clim.* 26 (19), 7603–7610. doi:10.1175/jcli-d-13-00025.1

Huang, Y., Ramaswamy, V., and Soden, B. (2007). An Investigation of the Sensitivity of the clear-sky Outgoing Longwave Radiation to Atmospheric Temperature and Water Vapor. *J. Geophys. Res. Atmospheres* 112 (D5). doi:10.1029/2005jd006906

Huang, Y., Xia, Y., and Tan, X. (2017). On the Pattern of CO2 Radiative Forcing and Poleward Energy Transport. *J. Geophys. Res. Atmos.* 122 (10), 578–593. doi:10.1002/2017jd027221

Mlawer, E. J., Taubman, S. J., Brown, P. D., Iacono, M. J., and Clough, S. A. (1997). Radiative Transfer for Inhomogeneous Atmospheres: RRTM, a Validated Correlated-K Model for the Longwave. *J. Geophys. Res.* 102 (D14), 16663–16682. doi:10.1029/97jd00237

Sanderson, B. M., and Shell, K. M. (2012). Model-Specific Radiative Kernels for Calculating Cloud and Noncloud Climate Feedbacks. *J. Clim.* 25 (21), 7607–7624. doi:10.1175/jcli-d-11-00726.1

Shakirova, A., and Huang, Y. (2021). An Neural Network Model for Shortwave Radiative Feedback Estimation. *J. Geophys. Res. Atmosphere* under revision for.

Shell, K. M., Kiehl, J. T., and Shields, C. A. (2008). Using the Radiative Kernel Technique to Calculate Climate Feedbacks in NCAR's Community Atmospheric Model. *J. Clim.* 21 (10), 2269–2282. doi:10.1175/2007jcli2044.1

Smith, C. J., Kramer, R. J., and Sima, A. (2020). The HadGEM3-GA7.1 Radiative Kernel: the Importance of a Well-Resolved Stratosphere. *Earth Syst. Sci. Data Discuss* 12, 2057–2068. doi:10.5194/essd-2019-254

Soden, B. J., and Held, I. M. (2006). An Assessment of Climate Feedbacks in Coupled Ocean-Atmosphere Models. *J. Clim.* 19 (14), 3354–3360. doi:10.1175/jcli3799.1

Soden, B. J., Held, I. M., Colman, R., Shell, K. M., Kiehl, J. T., and Shields, C. A. (2008). Quantifying Climate Feedbacks Using Radiative Kernels. *J. Clim.* 21 (14), 3504–3520. doi:10.1175/2007jcli2110.1

Vial, J., Dufresne, J.-L., and Bony, S. (2013). On the Interpretation of Inter-model Spread in CMIP5 Climate Sensitivity Estimates. *Clim. Dyn.* 41 (11-12), 3339–3362. doi:10.1007/s00382-013-1725-9

Wang, Y., and Huang, Y. (2020). The Surface Warming Attributable to Stratospheric Water Vapor in CO2-caused Global Warming. *J. Geophys. Res. Atmospheres* 125, e2020JD032752. doi:10.1029/2020JD032752

Wetherald, R. T., and Manabe, S. (1988). Cloud Feedback Processes in a General Circulation Model. *J. Atmos. Sci.* 45 (8), 1397–1416. doi:10.1175/1520-0469(1988)045<1397:cfpiag>2.0.co;2

Yue, Q., Kahn, B. H., Fetzer, E. J., Schreier, M., Wong, S., Chen, X., et al. (2016). Observation-Based Longwave Cloud Radiative Kernels Derived from the A-Train. *J. Clim.* 29, 2023–2040. doi:10.1175/JCLI-D-15-0257.1

Zelinka, M. D., Klein, S. A., and Hartmann, D. L. (2012). Computing and Partitioning Cloud Feedbacks Using Cloud Property Histograms. Part I: Cloud Radiative Kernels. *J. Clim.* 25 (11), 3715–3735. doi:10.1175/jcli-d-11-00248.1

Zhang, M. H., Hack, J. J., Kiehl, J. T., and Cess, R. D. (1994). Diagnostic Study of Climate Feedback Processes in Atmospheric General Circulation Models. *J. Geophys. Res.* 99 (D3), 5525–5537. doi:10.1029/93jd03523

Zhang, M., and Huang, Y. (2014). Radiative Forcing of Quadrupling CO2. *J. Clim.* 27 (7), 2496–2508. doi:10.1175/jcli-d-13-00535.1

Zhu, T., Huang, Y., and Wei, H. (2019). Estimating Climate Feedbacks Using a Neural Network. *J. Geophys. Res. Atmos.* 124 (6), 3246–3258. doi:10.1029/2018jd029223

Conflict of Interest: The authors declare that the research was conducted in the absence of any commercial or financial relationships that could be construed as a potential conflict of interest.

Publisher's Note: All claims expressed in this article are solely those of the authors and do not necessarily represent those of their affiliated organizations, or those of the publisher, the editors and the reviewers. Any product that may be evaluated in this article, or claim that may be made by its manufacturer, is not guaranteed or endorsed by the publisher.

frontiers in Earth Science

ORIGINAL RESEARCH
published: 20 August 2021
doi: 10.3389/feart.2021.710036

Contributions to Polar Amplification in CMIP5 and CMIP6 Models

L. C. Hahn[1]*, *K. C. Armour*[1,2], *M. D. Zelinka*[3], *C. M. Bitz*[1] and *A. Donohoe*[4]

[1]Department of Atmospheric Sciences, University of Washington, Seattle, WA, United States, [2]School of Oceanography, University of Washington, Seattle, WA, United States, [3]Lawrence Livermore National Laboratory, Livermore, CA, United States, [4]Polar Science Center, Applied Physics Lab, University of Washington, Seattle, WA, United States

As a step towards understanding the fundamental drivers of polar climate change, we evaluate contributions to polar warming and its seasonal and hemispheric asymmetries in Coupled Model Intercomparison Project phase 6 (CMIP6) as compared with CMIP5. CMIP6 models broadly capture the observed pattern of surface- and winter-dominated Arctic warming that has outpaced both tropical and Antarctic warming in recent decades. For both CMIP5 and CMIP6, CO_2 quadrupling experiments reveal that the lapse-rate and surface albedo feedbacks contribute most to stronger warming in the Arctic than the tropics or Antarctic. The relative strength of the polar surface albedo feedback in comparison to the lapse-rate feedback is sensitive to the choice of radiative kernel, and the albedo feedback contributes most to intermodel spread in polar warming at both poles. By separately calculating moist and dry atmospheric heat transport, we show that increased poleward moisture transport is another important driver of Arctic amplification and the largest contributor to projected Antarctic warming. Seasonal ocean heat storage and winter-amplified temperature feedbacks contribute most to the winter peak in warming in the Arctic and a weaker winter peak in the Antarctic. In comparison with CMIP5, stronger polar warming in CMIP6 results from a larger surface albedo feedback at both poles, combined with less-negative cloud feedbacks in the Arctic and increased poleward moisture transport in the Antarctic. However, normalizing by the global-mean surface warming yields a similar degree of Arctic amplification and only slightly increased Antarctic amplification in CMIP6 compared to CMIP5.

Keywords: CMIP6, CMIP5, polar amplification, climate feedbacks, Arctic, Antarctic

OPEN ACCESS

Edited by:
Patrick Charles Taylor, National Aeronautics and Space Administration (NASA), United States

Reviewed by:
James Overland, National Oceanic and Atmospheric Administration (NOAA), United States
Felix Pithan, Alfred Wegener Institute, Germany

***Correspondence:**
L. C. Hahn
lchahn@uw.edu

Specialty section:
This article was submitted to Interdisciplinary Climate Studies, a section of the journal Frontiers in Earth Science

Received: *15 May 2021*
Accepted: *09 August 2021*
Published: *20 August 2021*

Citation:
Hahn LC, Armour KC, Zelinka MD, Bitz CM and Donohoe A (2021) Contributions to Polar Amplification in CMIP5 and CMIP6 Models. Front. Earth Sci. 9:710036. doi: 10.3389/feart.2021.710036

INTRODUCTION

Observations (Serreze et al., 2009; Screen and Simmonds, 2010a) and climate model projections (Manabe and Stouffer, 1980; Holland and Bitz, 2003) consistently exhibit a pattern of enhanced surface warming in the Arctic compared to the rest of the globe. This so-called Arctic amplification peaks during winter and is at its minimum during summer (Manabe and Stouffer, 1980; Holland and Bitz, 2003; Screen and Simmonds, 2010b; Deser et al., 2010). There is also a strong warming asymmetry between the poles: Antarctic amplification has yet to be observed and is projected to be much weaker than Arctic amplification (Marshall et al., 2015; Smith et al., 2019). Multiple processes contribute to polar amplification, making it a robust feature of the long-term climate response to forcing while at the same time making polar warming inherently more uncertain than global-mean warming (e.g., Holland and Bitz, 2003; Roe et al., 2015; Bonan et al., 2018; Stuecker et al., 2018). Further investigation into the causes of polar

warming and its seasonal and hemispheric asymmetry is thus needed to develop reliable projections of future polar change.

Studies examining a suite of climate models in the Coupled Model Intercomparison Project phase 5 (CMIP5; Block et al., 2020; Goosse et al., 2018; Pithan and Mauritsen, 2014) have quantified key contributors to the magnitude and intermodel spread of polar amplification, motivating the direction of further research with a refined focus. These studies suggest that the largest contributor to Arctic-amplified warming is the lapse-rate feedback, which is more positive in the Arctic than elsewhere. Unlike in the tropics, where deep convection causes surface warming to be amplified with height, in polar regions, a stable lower troposphere inhibits vertical mixing and contributes to stronger warming near the surface than aloft (Cronin and Jansen, 2015; Payne et al., 2015; Hahn et al., 2020). This surface-trapped warming leads to a positive lapse-rate feedback by producing less longwave emission to space than a vertically uniform heating of the atmospheric column.

While the positive surface albedo feedback associated with sea-ice loss plays a key role in polar warming (e.g., Hall, 2004; Dai et al., 2019), Pithan and Mauritsen (2014) suggest that its contribution to Arctic amplification is secondary to that of the lapse-rate feedback. However, the strength of the lapse-rate feedback itself is highly dependent on the degree of surface warming and sea-ice loss (Graversen et al., 2014; Feldl et al., 2017; Feldl et al., 2020; Boeke et al., 2021). The albedo feedback additionally contributes most to intermodel spread in polar warming among CMIP5 models, followed by the lapse-rate feedback (Pithan and Mauritsen, 2014).

Another substantial contribution to Arctic amplification is made by the Planck feedback (Pithan and Mauritsen, 2014). Following the Stefan-Boltzmann law, a given surface warming at initially colder temperatures produces a weaker increase in emitted longwave radiation, causing a less-negative Planck feedback in the Arctic than the tropics. Finally, poleward atmospheric heat transport (AHT) into the Arctic increases only a small amount under climate warming within CMIP5 models, suggesting that AHT makes only a small contribution to Arctic amplification (Pithan and Mauritsen, 2014; Goosse et al., 2018). However, many studies highlight increased latent heat transport into the Arctic as a primary driver of polar warming and note that the small change in total AHT reflects compensating changes in latent and dry heat transports (e.g., Alexeev et al., 2005; Armour et al., 2019). Other processes such as water-vapor and cloud feedbacks, Arctic surface heat fluxes (i.e., ocean heat uptake), and the meridional structure of CO_2 forcing contribute more to tropical than polar warming (Pithan and Mauritsen, 2014; Goosse et al., 2018).

Assessments of polar warming in CMIP5 highlight key drivers not only of Arctic amplification, but also of seasonal and hemispheric asymmetry in polar warming. Summer ocean heat storage and its release to the atmosphere in winter contributes most to the winter peak in Arctic warming, and drives substantial intermodel spread in Arctic amplification (Pithan and Mauritsen, 2014; Boeke and Taylor, 2018). As a result of enhanced vertical stability in winter, the winter-peaking lapse-rate feedback makes an additional contribution to the winter maximum in Arctic warming (Pithan and Mauritsen, 2014). The lapse-rate feedback is also the largest contributor to greater warming in the Arctic than Antarctic in CMIP5 models (Goosse et al., 2018) due to the elevation of the Antarctic ice sheet and resulting shallower and weaker base-state Antarctic inversions (Salzmann, 2017; Hahn et al., 2020). Goosse et al. (2018) also confirm a large role for Southern Ocean heat uptake (Marshall et al., 2015; Armour et al., 2016) and a more-negative cloud feedback in weakening transient Antarctic warming compared to the Arctic.

The Coupled Model Intercomparison Project phase 6 (CMIP6) offers an opportunity to reexamine the processes contributing to polar amplification in a new model ensemble and evaluate the evolution of relevant processes between model generations. The higher effective climate sensitivity in CMIP6 than CMIP5, on average, has been traced to less-negative extratropical cloud feedbacks within many CMIP6 models (Zelinka et al., 2020), suggesting that extratropical cloud feedbacks may also contribute more to polar warming in CMIP6. To explore how cloud and other feedbacks contribute to polar amplification in CMIP6 models, we apply a 'warming contribution' analysis (Pithan and Mauritsen, 2014; Goosse et al., 2018) to CMIP6 and compare with the same analysis applied to CMIP5. We evaluate the drivers of Arctic amplification, weaker Antarctic amplification, and seasonal asymmetry in polar warming, considering also the spread in warming contributed by model differences. We note that Cai et al. (2021) have previously examined Arctic and Antarctic warming contributions in CMIP6, but here we expand this analysis from 15 to 42 CMIP6 models (**Supplementary Table S1**), add a comparison to CMIP5, consider climate feedback sensitivity to the choice of radiative kernel, and consider more closely the role of AHT in driving polar amplification by partitioning its changes into moist and dry components. We also apply the warming contribution analysis to Atmospheric Model Intercomparison Project phase 6 (AMIP6) models to estimate contributions to historical modelled warming in comparison to warming projected by fully-coupled CMIP6 models. By quantifying key contributors to polar warming and its asymmetries in CMIP6, we hope to assess previously established mechanisms of Arctic amplification as well as identify open questions in support of future polar research.

HISTORICAL POLAR AMPLIFICATION IN OBSERVATIONS AND MODELS

Before quantifying contributions to projected surface warming in CMIP6, we compare historical near-surface and atmospheric temperature trends over 1979–2014 from fully-coupled CMIP6 models with reanalysis data and observations (**Figures 1**, **2**). We use the European Centre for Medium-Range Weather Forecasts Interim Re-Analysis (ERA-Interim; Dee et al., 2011) which, in an evaluation of seven reanalyses over the Arctic, has been found to perform best in simulating observations of near-surface air temperature, surface radiative fluxes, precipitation, and wind speed (Lindsay et al., 2014). Limitations of this and other reanalyses in the Arctic include a positive near-surface

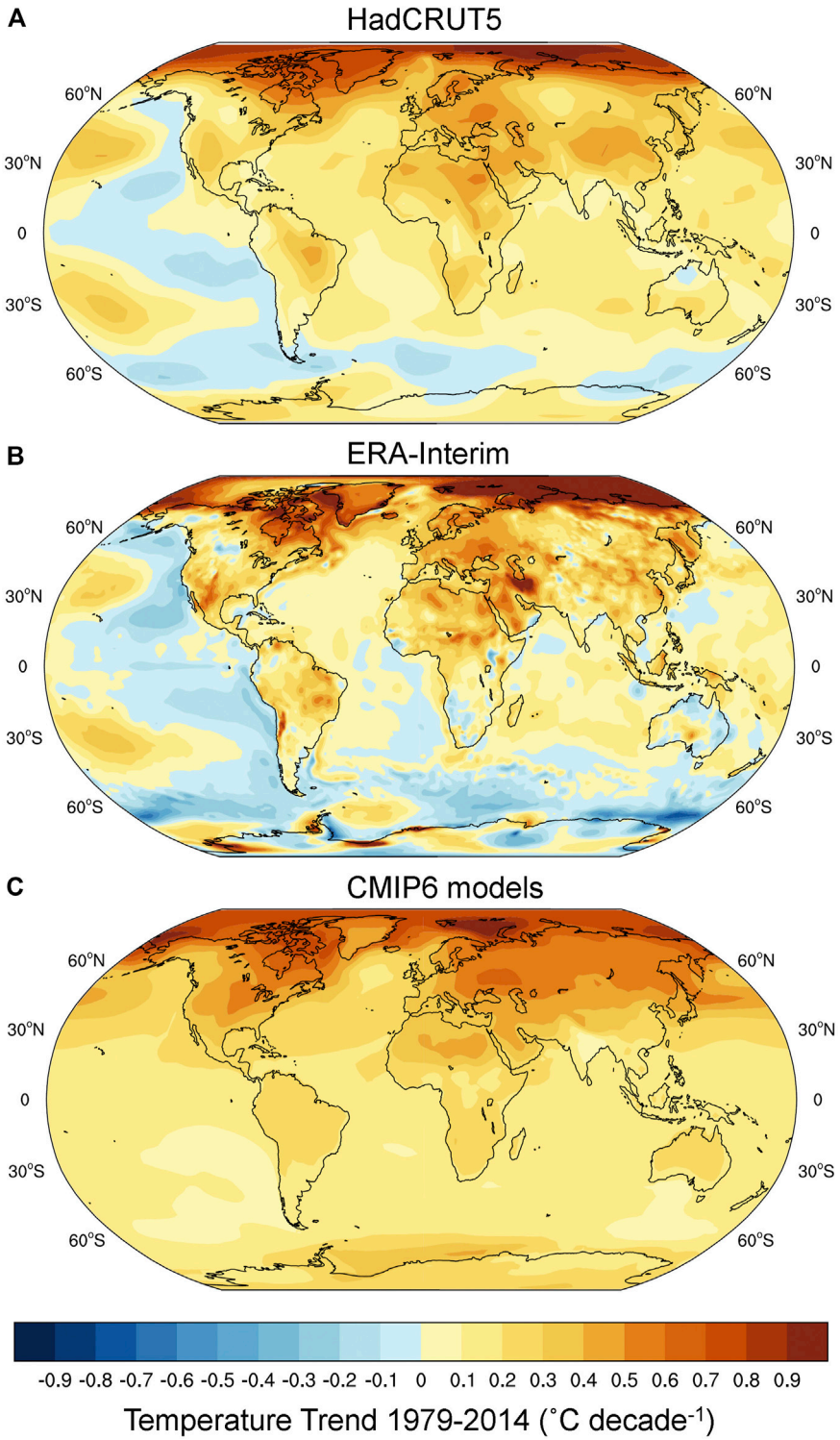

FIGURE 1 | Annual-mean near-surface temperature trends (°C decade^{-1}) for 1979–2014 from **(A)** HadCRUT5 observations, **(B)** the ERA-Interim reanalysis, and **(C)** the historical CMIP6 multimodel mean.

temperature bias over sea ice in winter, with a slightly smaller bias for ERA-Interim than its successor, ERA5 (Graham et al., 2019; Wang et al., 2019). Although ERA-Interim also overestimates the lowest observed near-surface temperatures over Antarctica, it correlates relatively well with Antarctic observations of near-surface temperatures (Gossart et al., 2019) and their trends

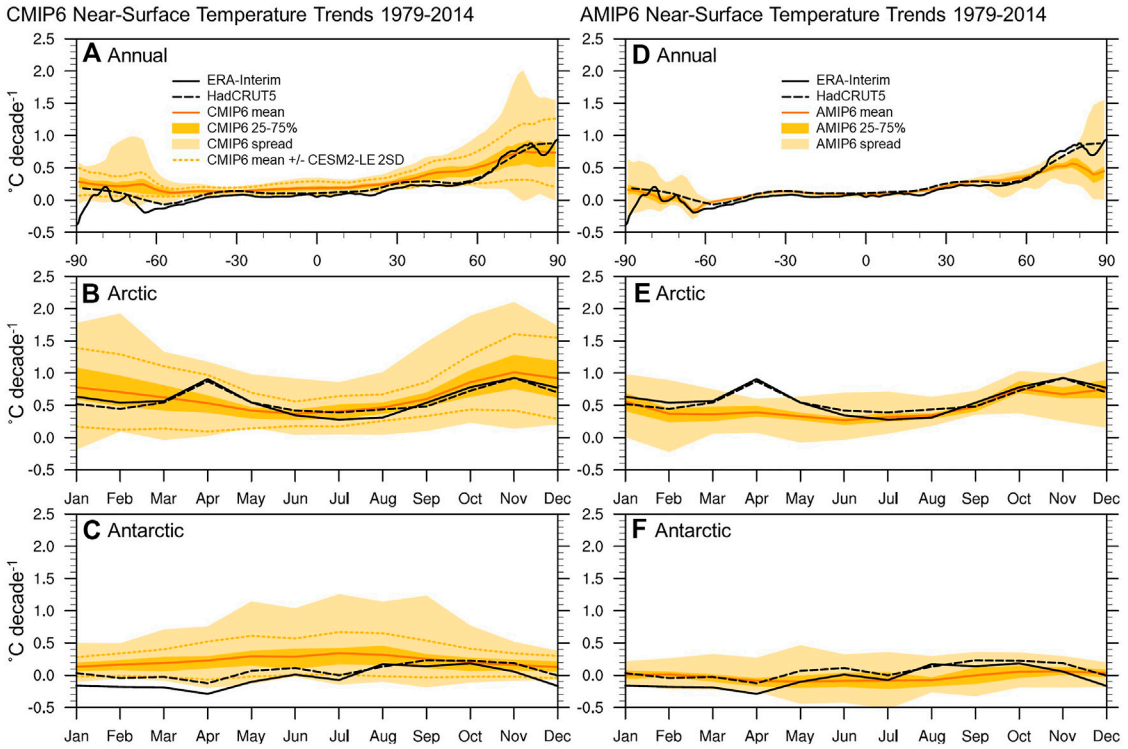

FIGURE 2 | Near-surface temperature trends (°C decade^{-1}) for 1979–2014 for **(A,D)** the annual- and zonal-mean, **(B,E)** the Arctic seasonal cycle, and **(C,F)** the Antarctic seasonal cycle in the ERA-Interim reanalysis (solid black line), HadCRUT5 observations (dashed black line), and the historical CMIP6 **(A–C)** and AMIP6 **(D–F)** multimodel means (solid orange line). The dark orange shading shows the 25th to 75th percentiles, and the light orange shading shows the full intermodel spread. The dashed orange lines **(A–C)** show the CMIP6 mean ± 2 standard deviations across ensemble members in the CESM2-LE.

(Wang et al., 2016). We also show historical near-surface temperature trends for HadCRUT5, an observational dataset which combines CRUTEM5 near-surface air temperature over land with HadSST4 sea-surface temperatures, with statistical infilling where observations are unavailable (Morice et al., 2021). Throughout this study, we define the Arctic as 60 to 90°N and the Antarctic as 60 to 90°S, and define polar amplification as the near-surface warming poleward of 60° in a given hemisphere divided by global-mean near-surface warming.

The ensemble mean of fully-coupled CMIP6 models (hereafter called the CMIP6 mean) for historical simulations reproduces the observed pattern of amplified Arctic warming and weaker warming in the Antarctic, but exceeds the observed warming at all latitudes except in the Arctic (**Figures 1**, **2A**). As a result, the CMIP6 mean produces too little Arctic amplification and too much Antarctic amplification over this historical period: the degree of Arctic and Antarctic amplification in the CMIP6 mean is 2.6 and 0.9, respectively, compared to 3.5 and 0.4 in HadCRUT5 observations. **Figure 2** also shows the CMIP6 mean near-surface temperature trend with ± 2 standard deviations of trends calculated across the first 90 ensemble members of the Community Earth System Model version 2 Large Ensemble (CESM2-LE) as a reference for the range of internal variability within a single climate model in CMIP6. The CESM2-LE uses identical time-varying external forcing for its ensemble members, but begins each with a combination of different oceanic and atmospheric initial conditions (Rodgers et al., 2021). With the exception of the Southern Hemisphere mid-latitudes, zonal-mean warming trends in HadCRUT5 fall within the range of CMIP6 intermodel spread and the range of internal variability for CESM2-LE, suggesting that CMIP6 models may be largely consistent with observations when internal variability is taken into account.

CMIP6 models capture the seasonality of near-surface warming in the Arctic, with a peak in warming during early winter (**Figure 2B**). While the CMIP6 multimodel mean excludes a second peak in warming in April found in observations and reanalyses (Screen et al., 2012), this April maximum falls within the intermodel spread for CMIP6 and the ensemble spread for CESM2-LE, suggesting that it may be explained by internal variability. Model underestimation of observed reductions in spring snow cover extent over land may also contribute to a low bias in modeled Arctic springtime warming (Screen et al., 2012; Brutel-Vuilmet et al., 2013). In the Antarctic, CMIP6 models on average simulate year-round warming with a winter maximum (**Figure 2C**) whereas the observations and reanalysis show near-zero warming or slight cooling. Both the intermodel spread and spread due to internal variability in historical near-surface warming are largest in polar regions and during winter.

In addition to considering historical trends from fully coupled models in CMIP6, we show historical near-surface and atmospheric temperature trends from models in the

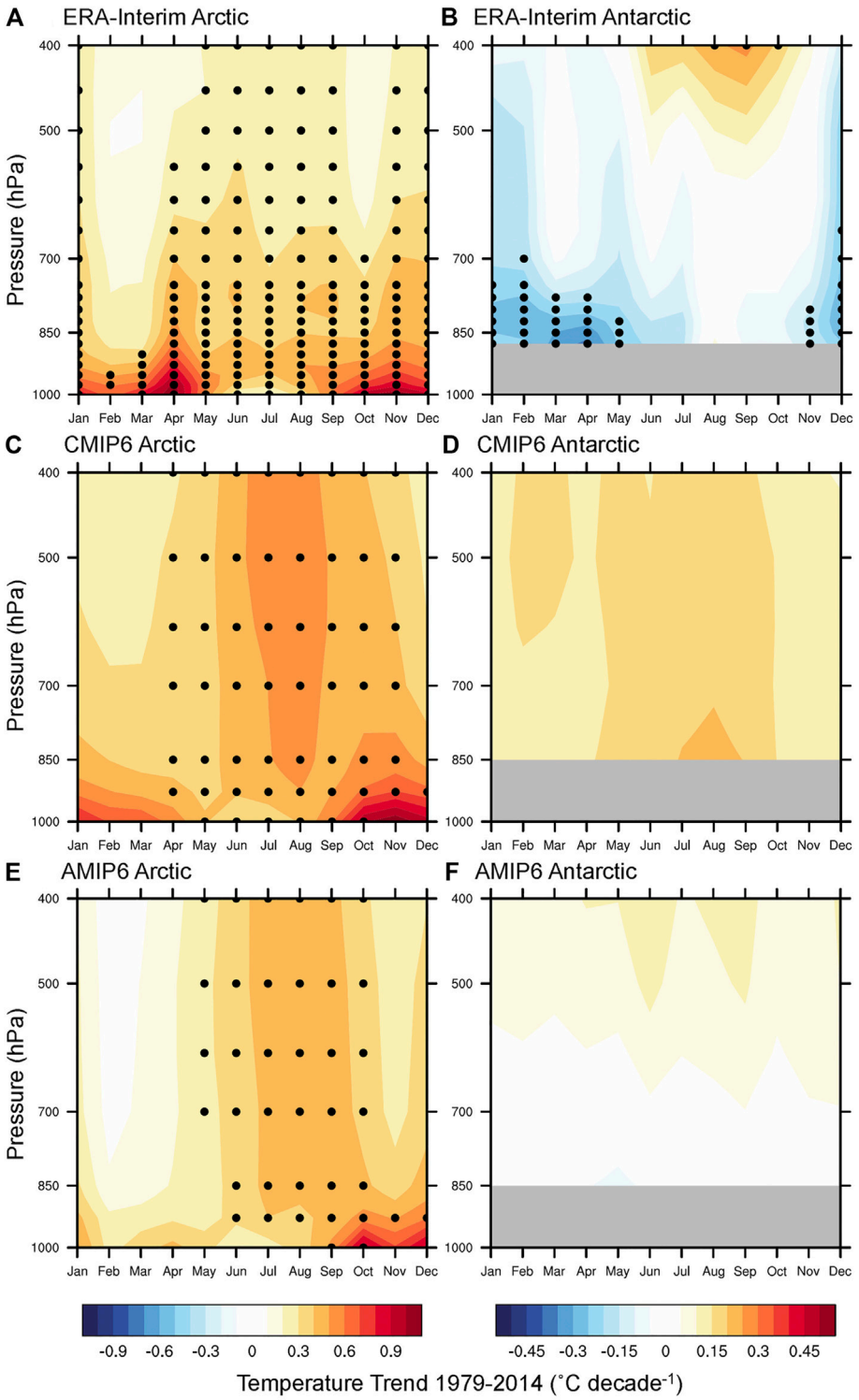

FIGURE 3 | Atmospheric temperature trends (°C decade^{-1}) for 1979–2014 for **(A,C,E)** the Arctic and **(B,D,F)** the Antarctic in the ERA-Interim reanalysis **(A,B)**, and historical CMIP6 **(C,D)** and AMIP6 **(E,F)** multimodel mean trends. Black dots in **(A,B)** show statistically significant trends at the 95% level based on a two-tailed Student's t-test, and black dots in **(C,D)** and **(E,F)** show where 75% of models meet these criteria for significant trends. For the reanalysis and models, temperature data is first masked at pressures greater than the surface pressure, and trends are only shown where more than 50% of area-averaged grid points are non-missing.

Atmospheric Model Intercomparison Project phase 6 (AMIP6; **Supplementary Table S1**). These models prescribe time-varying monthly sea-surface temperatures and sea-ice concentrations based on observations, while still including atmosphere-land coupling, along with time-varying historical forcing agents (Eyring et al., 2016). The ensemble mean of AMIP6 models aligns more closely than the CMIP6 mean with observed near-surface atmospheric temperature trends in the tropics and Antarctic (**Figures 2D–F**). Despite having prescribed observational sea-surface temperature and sea-ice concentration changes, the AMIP6 mean underestimates observed Arctic warming over both land and sea-ice surfaces. This may result from differences between models and observations in sea-ice thickness and the near-surface air temperature response to sea-ice loss. Underestimated Arctic amplification in both the CMIP6 and AMIP6 means is also shown in **Supplementary Figure S1**, with historical temperature trends normalized by global-mean near-surface warming.

Consistent with previous modelling and observational studies, the vertical and seasonal pattern of Arctic warming for both ERA-Interim and CMIP6 is amplified near the surface during winter and is more vertically-uniform during summer (**Figures 3A,C**). For both summer and winter, mid-tropospheric warming trends are stronger for CMIP6 than ERA-Interim, which may reflect stronger increased poleward AHT due to overestimated mid-latitude surface warming (Fajber et al., 2018; Feldl et al., 2020; Kosaka and Xie, 2013). Consistent with this hypothesis, AMIP6 models, which simulate mid-latitude near-surface temperature trends closer to observations, show weaker warming aloft than CMIP6 (**Figure 3E**). AMIP6 models still demonstrate stronger mid-tropospheric summer warming than ERA-Interim, which may be related to AHT differences contributed by surface temperatures over land, or to enhanced atmospheric shortwave absorption by water vapor in these models (Donohoe and Battisti, 2013).

In contrast to CMIP6 models, which propagate Arctic winter surface warming further aloft than the ERA-Interim reanalysis, CMIP3 and CMIP5 models simulate excessively surface-trapped Arctic warming as a result of overestimating mean-state inversion strength (Medeiros et al., 2011; Pithan et al., 2014; Screen et al., 2012). This overestimated stability in earlier models has been attributed to a low bias in the supercooled liquid fraction of mixed-phase clouds, which allows for too much surface radiative cooling (Pithan et al., 2014). While CMIP6 models also tend to overestimate winter surface inversion strength in the Arctic (**Supplementary Figure S2**), increased supercooled liquid fraction in some CMIP6 models may have reduced these biases in inversion strength and surface-trapped warming compared to earlier models. A weaker ice-to-liquid transition in CMIP6 models with more mean-state supercooled liquid may also lead to a smaller increase in downward longwave radiation under warming, additionally causing weaker surface-trapped warming in CMIP6 (Tan and Storelvmo., 2019).

In both models and observations, Antarctic temperature trends are much weaker than those in the Arctic (**Figures 3B,D,F**; note the reduced colorbar range for the Antarctic). CMIP6 models demonstrate a small surface-amplified warming during winter, while ERA-Interim shows surface-amplified cooling particularly for December-May, as observed in near-surface temperature trends. In summary, although differences exist between observed and modeled Antarctic temperature trends, CMIP6 models generally agree with observations in producing winter- and surface-amplified warming in the Arctic, with much weaker trends in the Antarctic. Next we investigate the drivers of this Arctic-amplified warming and its hemispheric and seasonal asymmetry in CMIP5 and CMIP6 models.

CONTRIBUTIONS TO POLAR WARMING IN CMIP5 AND CMIP6 MODELS

Warming Contribution Methodology

Following previous studies (Lu and Cai, 2009; Crook and Forster 2011; Feldl and Roe 2013; Taylor et al., 2013; Pithan and Mauritsen, 2014; Goosse et al., 2018), we calculate contributions to projected polar warming based on an energy budget analysis. To do so, we use CMIP5 and CMIP6 output from pre-industrial control (piControl) and abrupt CO_2 quadrupling (abrupt4xCO2) experiments, in which CO_2 concentrations are quadrupled from piControl conditions and then held fixed for 150 years. As in Zelinka et al. (2020) and Caldwell et al. (2014), we apply a 21-year running average to piControl experiments to account for model drift before computing anomalies between abrupt4xCO2 and piControl during corresponding time periods (i.e., after branching to abrupt4xCO2, year-100 in piControl is compared to year-100 in abrupt4xCO2). With the assumption of similar model drift in the abrupt4xCO2 and piControl experiments, this approach isolates anomalies due to CO_2 forcing rather than model drift. We calculate the effective radiative forcing (ERF) as the *y*-intercept of the regression between top-of-atmosphere (TOA) radiation anomalies at each grid point against the global-mean near-surface temperature anomalies for the first 20 years after CO_2 quadrupling (Gregory et al., 2004). Smith et al. (2020) demonstrate that this 20-year regression yields ERF values which closely match methods using fixed sea-surface temperatures (Hansen et al., 2005) under CO_2 quadrupling in CMIP6 models, while regression over the full 150-year abrupt4xCO2 period instead underestimates ERF as a result of time-varying feedbacks in models (Andrews et al., 2015; Dong et al., 2020).

To calculate temperature anomalies, climate feedbacks, and heat transport anomalies under CO_2 quadrupling, we use monthly climate variable anomalies averaged over 31 years centered on year-100 of the abrupt4xCO2 experiments. We calculate climate feedbacks using the radiative kernel method (Shell et al., 2008; Soden et al., 2008), in which relevant climate variable anomalies are multiplied by monthly- and spatially-resolved radiative kernels, which quantify the change in radiative flux per unit change in a given climate variable. Vertically integrating this product throughout the troposphere gives the contribution of each feedback to TOA radiation anomalies. Temperature feedbacks are separated into the effect

of surface temperature changes propagated throughout the troposphere (the Planck feedback) and the effect of departures from this vertically uniform temperature change (the lapse-rate feedback). Cloud feedbacks are calculated using the change in cloud radiative forcing (ΔCRF), equal to the change in all-sky minus clear-sky TOA radiation, minus a cloud masking term. This cloud masking term is defined as the effect of noncloud variables (temperature, water vapor, and surface albedo) on ΔCRF, calculated using all-sky and clear-sky radiative kernels. While our method is consistent with Goosse et al. (2018), one caveat of using year-100 feedback energetic contributions divided by year-100 temperature anomalies as opposed to linear regression of these fields (as in Zelinka et al. (2020)) is that the resulting feedbacks include both the true temperature-mediated feedbacks and rapid adjustments that occur immediately upon quadrupling CO_2. Resulting differences from the regression method used in Zelinka et al. (2020) for cloud feedbacks are discussed at the end of the section *Warming Contributions in CMIP5 and CMIP6*.

We primarily show feedbacks calculated using the Huang et al. (2017) kernels, which are based on ERA-Interim reanalysis data and give the smallest residual terms between the modelled TOA radiation anomalies and the sum of feedback and forcing radiative contributions (Zelinka et al., 2020). However, we additionally consider sensitivity to kernel choice, including kernels from Soden et al. (2008) (based on GFDL AM2), Shell et al. (2008) (based on NCAR CAM3), Block and Mauritsen (2013) (based on MPI ECHAM6), Pendergrass et al. (2018) (based on NCAR CAM5), and Smith et al. (2018) (based on HadGEM2). For comparison with the kernel-derived surface albedo feedback, we also compute the surface albedo feedback using the approximate partial radiative perturbation (APRP) method (Taylor et al., 2007).

As in Pithan and Mauritsen (2014), we calculate the annual AHT convergence as the difference between surface and net TOA fluxes. We further partition this into a moist component using the difference between precipitation and evaporation multiplied by the latent heat of vaporization (with the latent heat of fusion for solid precipitation neglected), and a dry component calculated as the residual between total and moist AHT convergence. To calculate the seasonal cycle of AHT convergence, we additionally subtract atmospheric energy and moisture storage terms following Donohoe et al. (2020a). Anomalous surface heat fluxes (referred to here as ocean heat uptake) implicitly include both ocean heat transport and ocean heat storage, on both seasonal and annual timescales.

We use a local energy budget (**Eq. 1** below) to convert these energetic contributions of climate feedbacks and heat transport anomalies surrounding year-100 of the abrupt4xCO2 experiments into contributions to near-surface warming (ΔT) in the tropics, Arctic, and Antarctic, as in previous studies (Lu and Cai, 2009; Crook and Forster, 2011; Feldl and Roe, 2013; Taylor et al., 2013; Pithan and Mauritsen, 2014; Goosse et al., 2018). **Equation 1** includes the ERF, energetic contributions of climate feedbacks ($\lambda_i \Delta T$) and the Planck response ($\lambda_p \Delta T$), anomalies in AHT convergence (ΔAHT) and ocean heat uptake (ΔO), and a residual term (ΔR_{res}), all in units of Wm^{-2}:

$$ERF + \left(\lambda_p + \sum_i \lambda_i\right)\Delta T + \Delta AHT + \Delta O + \Delta R_{res} = 0 \quad (1)$$

In addition to computing annual-mean warming contributions, we calculate contributions during winter (December-January-February for the Arctic and June-July-August for the Antarctic) and summer (June-July-August for the Arctic and December-January-February for the Antarctic) seasons. For each region and season, warming contributions are defined by dividing each term in **Eq. 1** by the global- and annual-mean Planck feedback ($\overline{\lambda_p}$) in $Wm^{-2}\ K^{-1}$:

$$\Delta T = -\frac{ERF}{\overline{\lambda_p}} - \frac{\lambda_p' \Delta T}{\overline{\lambda_p}} - \frac{\sum_i \lambda_i \Delta T}{\overline{\lambda_p}} - \frac{\Delta AHT}{\overline{\lambda_p}} - \frac{\Delta O}{\overline{\lambda_p}} - \frac{\Delta R_{res}}{\overline{\lambda_p}} \quad (2)$$

where $\lambda_p' = \lambda_p - \overline{\lambda_p}$ is the difference between the regional, seasonal Planck feedback, λ_p, and its annual- and global-mean value, $\overline{\lambda_p}$.

Warming Contributions in CMIP5 and CMIP6

Near-surface temperature anomalies centered around year-100 of the abrupt4xCO2 simulations in CMIP5 and CMIP6 are shown in **Figure 4A**. Consistent with observed and modelled historical temperature trends (**Figures 1**, **2**), both CMIP5 and CMIP6 models project transient warming under CO_2 quadrupling that is amplified in the Arctic compared to the tropics, with weaker Antarctic amplification. CMIP6 models exhibit large intermodel spread in the Arctic, with an interquartile range of up to 8°C in Arctic warming compared to about 4°C in the Antarctic and 2°C in the tropics. In the multimodel mean, Arctic warming has increased from 10.1°C in CMIP5 to 11.5°C in CMIP6, while Antarctic warming has increased from 5.1°C in CMIP5 to 6.4°C in CMIP6. This increase in polar warming is greater than the increase in tropical warming from 4.3°C in CMIP5 to 4.8°C in CMIP6. However, normalizing by the global-mean surface warming in each model (**Figure 4B**) demonstrates a similar degree of Arctic amplification and only slightly increased Antarctic amplification in CMIP6 compared to CMIP5.

To investigate the drivers of polar amplification and hemispheric asymmetry in CMIP6 as compared to CMIP5, we calculate contributions to polar warming from feedbacks, AHT changes, and ocean heat uptake following **Eq. 2**. We use the Huang et al. (2017) kernels for climate feedbacks in **Figures 4C,D**, and investigate the sensitivity to kernel choice in **Figure 5**. Consistent with Pithan and Mauritsen (2014) and Goosse et al. (2018), key contributors to Arctic amplification in both CMIP5 and CMIP6 are the lapse-rate, albedo, and Planck feedbacks (**Figure 4C**). In contrast to the secondary role of the albedo feedback found in Pithan and Mauritsen (2014) using the Block and Mauritsen (2013) radiative kernels, use of the Huang et al. (2017) kernels yields lapse-rate and albedo feedbacks of almost equal importance for polar amplification in CMIP5, and equivalent importance in CMIP6. Partitioning AHT into moist and dry components illustrates that while reduced dry AHT opposes Arctic amplification, increased moist AHT is a large contributor to Arctic amplification.

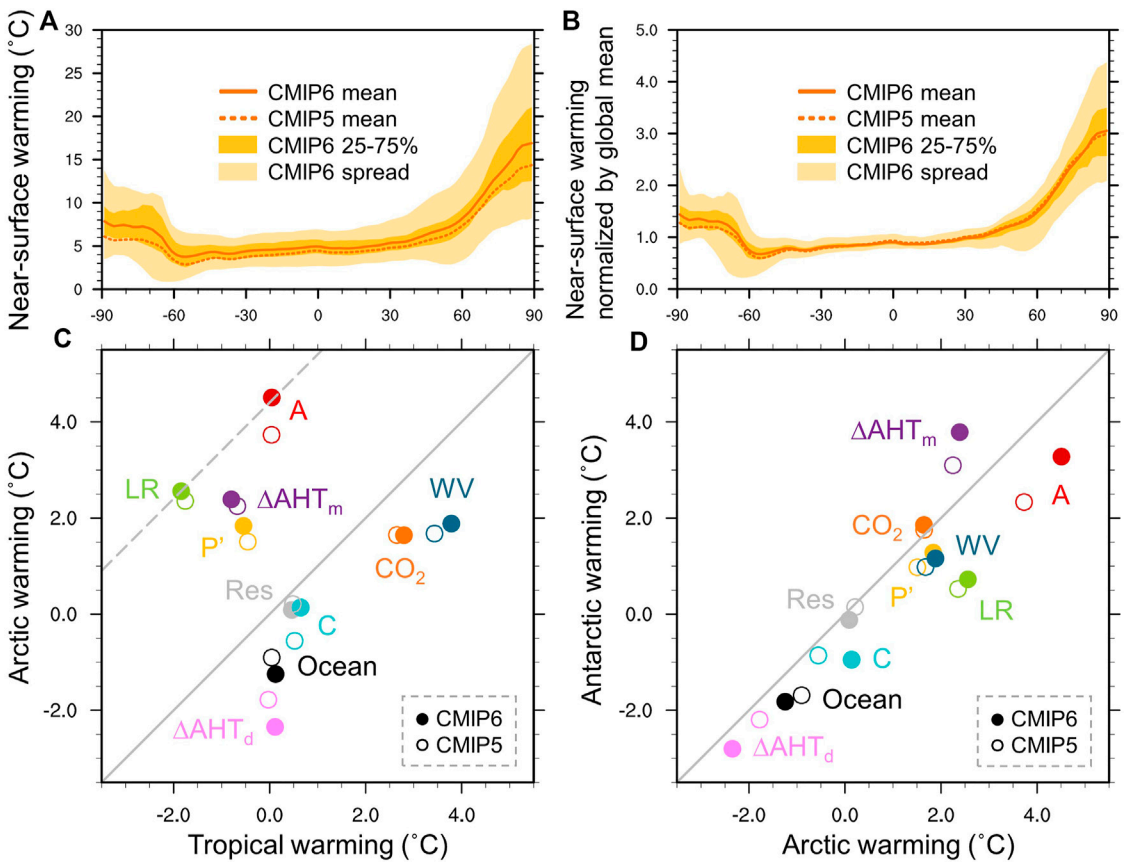

FIGURE 4 | (A) Annual- and zonal-mean near-surface warming (°C) averaged over 31 years centered on year-100 after CO_2 quadrupling for the CMIP6 (solid orange line) and CMIP5 (dashed orange line) multimodel means. The dark orange shading shows the 25th to 75th percentiles, and the light orange shading shows the full intermodel spread for CMIP6. **(B)** As in **(A)**, but with zonal-mean near-surface warming normalized by global-mean near-surface warming within each model. **(C,D)** Contributions of each feedback and atmospheric forcing to warming (°C) centered around year-100 of abrupt CO_2 quadrupling in CMIP6 (filled circles) and CMIP5 (hollow circles) for **(C)** the tropics relative to the Arctic and **(D)** the Arctic relative to the Antarctic. Warming contributions are shown for the lapse-rate (LR), surface albedo (A), water-vapor (WV), and cloud (C) feedbacks, the variation in the Planck response from its global-mean value (P'), effective radiative forcing (CO_2), change in moist and dry AHT convergence (ΔAHT_m; ΔAHT_d) and ocean heat uptake (Ocean), and residual term (Res). Dashed grey line shows a 1-to-1 slope through the lapse-rate feedback warming contribution.

Stronger Arctic warming in CMIP6 than CMIP5 is mainly contributed by more-positive albedo and less-negative cloud feedbacks. Less-negative Arctic cloud feedbacks in CMIP6 result from less-negative shortwave low cloud amount and scattering feedbacks, likely due to updated treatment of supercooled liquid fraction in mixed phase clouds (Zelinka et al., 2020). The lapse-rate feedback, Planck response, and moist AHT changes also contribute to stronger Arctic warming in CMIP6, while increased ocean heat uptake and equatorward dry AHT more strongly oppose Arctic warming in CMIP6. Normalizing Arctic warming contributions by the global-mean warming yields contributions which sum to the total Arctic amplification in CMIP5 and CMIP6 (**Supplementary Figure S3A**, vertical axis): less-negative cloud and more-positive albedo feedbacks support greater Arctic amplification in CMIP6, while most other contributions support weaker Arctic amplification in CMIP6 due to normalizing by the larger global-mean warming in CMIP6 than CMIP5. This results in a similar degree of Arctic amplification in CMIP5 and CMIP6 (**Figure 4B**).

Consistent with Goosse et al. (2018), the largest contributor to stronger warming in the Arctic than Antarctic is the lapse-rate feedback for both CMIP5 and CMIP6 (**Figure 4D**). In fact, all factors except for CO_2 forcing and moist AHT changes support greater warming in the Arctic than Antarctic, with an additionally large contribution from the albedo feedback in CMIP5 and CMIP6. This feedback asymmetry between the poles is supported by the elevation of the Antarctic ice sheet (Salzmann, 2017), which primarily weakens the Antarctic lapse-rate feedback through reducing the average strength of mean-state inversions (Hahn et al., 2020). We note that the Planck feedback (in W m^{-2} K^{-1}) is slightly less negative in the Antarctic than Arctic, likely due to colder and drier initial conditions, but that the Planck warming contribution is larger in the Arctic due to a larger Arctic ΔT resulting in a larger contribution $\lambda_p^{'}\Delta T$ in **Eq. 2**. This illustrates one limitation of the warming contribution framework: a warming contribution from one feedback is influenced by all other feedbacks through their influence on ΔT.

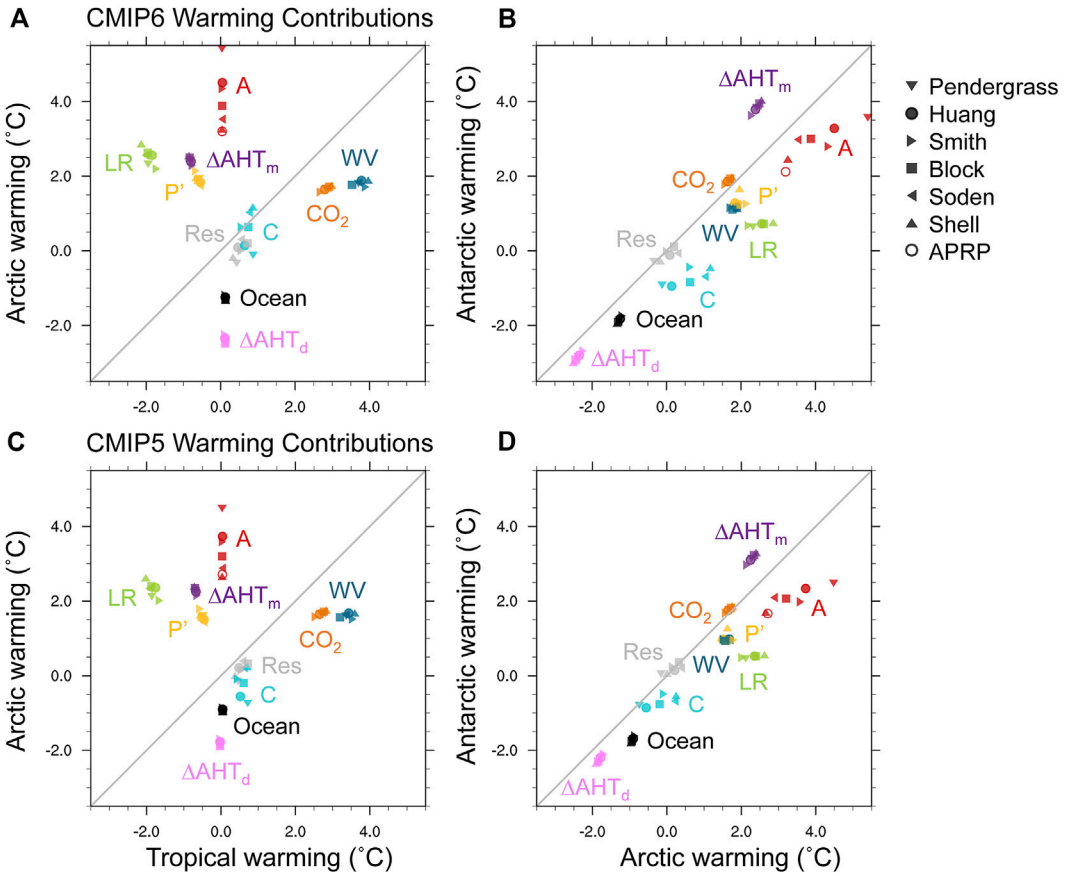

FIGURE 5 | Sensitivity of warming contributions (˚C) to radiative kernels in **(A,B)** CMIP6 and **(C,D)** CMIP5 centered around year-100 of abrupt CO_2 quadrupling for **(A,C)** the tropics relative to the Arctic and **(B,D)** the Arctic relative to the Antarctic. Warming contributions are shown for the lapse-rate (LR), surface albedo (A), water-vapor (WV), and cloud (C) feedbacks, the variation in the Planck response from its global-mean value (P'), effective radiative forcing (CO_2), change in moist and dry AHT convergence (ΔAHT_m; ΔAHT_d) and ocean heat uptake (Ocean), and residual term (Res). The warming contribution for the albedo feedback is additionally calculated using the APRP method.

Moist AHT is the largest contributor to Antarctic warming in both CMIP5 and CMIP6. Combined with initially colder Antarctic temperatures and Clausius-Clapeyron nonlinearity, weaker warming in the Antarctic under CO_2 quadrupling produces a weaker moisture increase compared to the Arctic. As a result, the equator-to-Antarctic latent heat gradient increases more than the equator-to-Arctic gradient, contributing to a stronger increase in moist AHT to the Antarctic (**Supplementary Figure S4**). Moist AHT changes are also sensitive to climate feedbacks which alter the equator-to-pole moist static energy gradient, particularly shortwave cloud feedbacks (Hwang and Frierson, 2010; Zelinka and Hartmann, 2012; Shaw and Voigt, 2016; Chen et al., 2021). More-negative shortwave cloud feedbacks in the Antarctic may therefore also contribute to larger increased moist AHT to the Antarctic than Arctic by enhancing the equator-to-pole moist static energy gradient in the Southern Hemisphere.

Most warming contributions change similarly for the Arctic and Antarctic from CMIP5 to CMIP6 (i.e., on a one-to-one slope in **Figure 4D**), including the lapse-rate, water-vapor, Planck, and albedo feedbacks, as well as ocean heat uptake and dry AHT. The two warming contributions that change differently for the Arctic and Antarctic from CMIP5 to CMIP6 are the cloud and moist AHT contributions. While the cloud contribution primarily increases in the Arctic, the moist AHT contribution primarily increases in the Antarctic. Stronger Arctic than Antarctic changes in cloud feedbacks result from shortwave cloud feedback changes (**Supplementary Figure S5**), and this polar difference appears to be amplified by the use of year-100 feedbacks rather than the 150-year regression method of Zelinka et al. (2020). Still, the year-100 feedbacks are generally consistent with the 150-year regression method in demonstrating less-negative polar cloud feedbacks in CMIP6 compared to CMIP5 (**Supplementary Figure S5**).

Dependence on Choice of Kernel and Feedback Definition

While most feedbacks are relatively insensitive to the choice of radiative kernel, polar surface albedo and cloud feedbacks particularly for the Arctic show substantial kernel sensitivity in both CMIP5 and CMIP6 (**Figure 5**). This is consistent with evidence that the radiative sensitivity to albedo changes (the albedo radiative kernel) varies by a factor of two across climate

models in the Arctic and Southern Ocean due to intermodel differences in mean-state cloudiness (Donohoe et al., 2020b). Kernel sensitivity in the albedo feedback also contributes to kernel sensitivity in the cloud feedback, which is calculated using radiative kernels to compute and subtract the cloud masking effect of noncloud variables, including surface albedo, from the total ΔCRF. The APRP method gives an albedo feedback near the bottom of the range in kernel-derived albedo feedbacks. This may result from using the average of a forward- and backward-radiative substitution in the APRP method, whereas the kernels rely solely on a forward calculation. The surface albedo feedback derived from the APRP method versus radiative kernels are thus conceptually different quantities, as the APRP method allows cloud changes to impact the surface albedo feedback while the kernel method does not.

Of the model-derived surface albedo kernels, the Smith et al. (2018) kernels come closest to simulating the radiative sensitivity to albedo changes derived from satellite observations in the Arctic (Donohoe et al., 2020b). The Smith et al. (2018) kernels also produce an Arctic albedo feedback similar to the Huang et al. (2017) observationally-derived kernels (**Figure 5A**). This suggests that the observed mean state is consistent with a stronger Arctic albedo feedback than previously found, on par with the lapse rate feedback in its contribution to Arctic amplification.

An important result of kernel sensitivity in the albedo feedback is that the relative importance of the albedo versus lapse-rate feedback depends on the choice of kernel. However, for all kernels the lapse-rate and albedo feedbacks remain key contributors to Arctic amplification and hemispheric asymmetry in polar warming. Additionally, because the albedo and cloud feedbacks have compensating sensitivity to kernel choice, the total polar feedback remains relatively insensitive to kernel choice, as evidenced by the small kernel sensitivity in the residual term.

In addition to the traditional feedback framework applied here, alternative feedback definitions can be used, including a framework which quantifies the effect of warming and moistening at constant relative humidity (RH) separately from the effect of RH changes (Held and Shell, 2012). We compare the traditional feedback framework with the fixed-RH method, where the lapse-rate and Planck feedbacks are calculated at constant RH, an RH feedback is calculated, and all other feedbacks are identical to the traditional feedbacks (**Supplementary Figure S6**). Consistent with Held and Shell (2012), the magnitude of the fixed-RH Planck, fixed-RH lapse-rate, and RH feedbacks is reduced compared to the traditional Planck, lapse-rate, and water-vapor feedbacks. Although the other feedbacks are unchanged, division by a weaker global Planck feedback contributes to larger fixed-RH warming contributions for these feedbacks. Applied to the tropics, the fixed-RH framework gives a less-negative lapse-rate feedback than in the traditional framework: while amplified warming aloft promotes a large, negative lapse-rate feedback, amplified moistening aloft to maintain constant relative humidity offsets this negative feedback. In the Arctic, the fixed-RH framework produces a less-positive lapse-rate feedback: while weaker warming aloft compared to the surface supports a large, positive lapse-rate feedback, weaker moistening aloft to maintain constant relative humidity reduces the magnitude of the positive fixed-RH lapse-rate feedback. As a result, the relative contribution of the lapse-rate feedback to Arctic amplification is weakened in the fixed-RH framework, with stronger contributions from the albedo feedback and poleward moisture transport. While feedback definition choice can impact the relative roles of contributions to Arctic warming, we note that moist AHT and the albedo and lapse-rate feedbacks remain important contributors to Arctic amplification for both the traditional and fixed-RH frameworks.

Intermodel Spread

Following Pithan and Mauritsen (2014), we also investigate what factors contribute to substantial intermodel spread in polar warming by analyzing intermodel spread in CMIP6 warming contributions in both the Arctic and Antarctic (**Figure 6**). The albedo feedback is the single largest contributor to increased intermodel spread in both Arctic and Antarctic warming. While the dry AHT term itself exhibits substantial intermodel spread, it contributes more cooling to models with stronger polar warming and thus reduces intermodel spread in polar warming, as shown in Hwang et al. (2011). In contrast, changes in moist AHT generally increase with total polar warming and contribute to intermodel spread. Relationships between total polar warming and each warming contribution are similar for CMIP6 and CMIP5 (**Supplementary Figure S7**) with the exception of ocean heat uptake changes. In CMIP5, the ocean term becomes more negative (greater ocean heat uptake) in models with greater Arctic warming, while in CMIP6, models with weaker ocean heat uptake simulate greater Arctic warming. In the Antarctic, CMIP5 models with weaker ocean heat uptake simulate greater warming, while there is no correlation between ocean heat uptake and Antarctic warming across different models in CMIP6.

Intermodel spread in polar warming is contributed not only by individual warming contributions, but also by their covariances; to quantify both, we show covariance matrices of the contributions to Arctic and Antarctic warming in **Figure 7**, following Caldwell et al. (2014). Each term has been normalized by the total warming variance ($10.2\,K^2$ in the Arctic; $4.9\,K^2$ in the Antarctic) to illustrate fractional contributions to warming variance in each region. To avoid showing redundant information in these symmetric matrices, covariance terms below the diagonal are omitted and those above the diagonal are multiplied by two. Consistent with **Figure 6**, the main diagonal in **Figure 7** shows large variances contributed by the albedo feedback and dry AHT at both poles. However, strong negative covariance between these two terms leads to a large damping of intermodel spread. Negative covariances between dry AHT and almost every other warming contribution suggest that dry AHT responds to polar warming, with stronger polar warming weakening the equator-to-pole temperature gradient and reducing dry AHT to polar regions. In contrast, large positive covariance between the albedo and lapse-rate feedbacks magnifies the intermodel spread in polar warming. In the Antarctic, variance in moist AHT and its covariance with the albedo

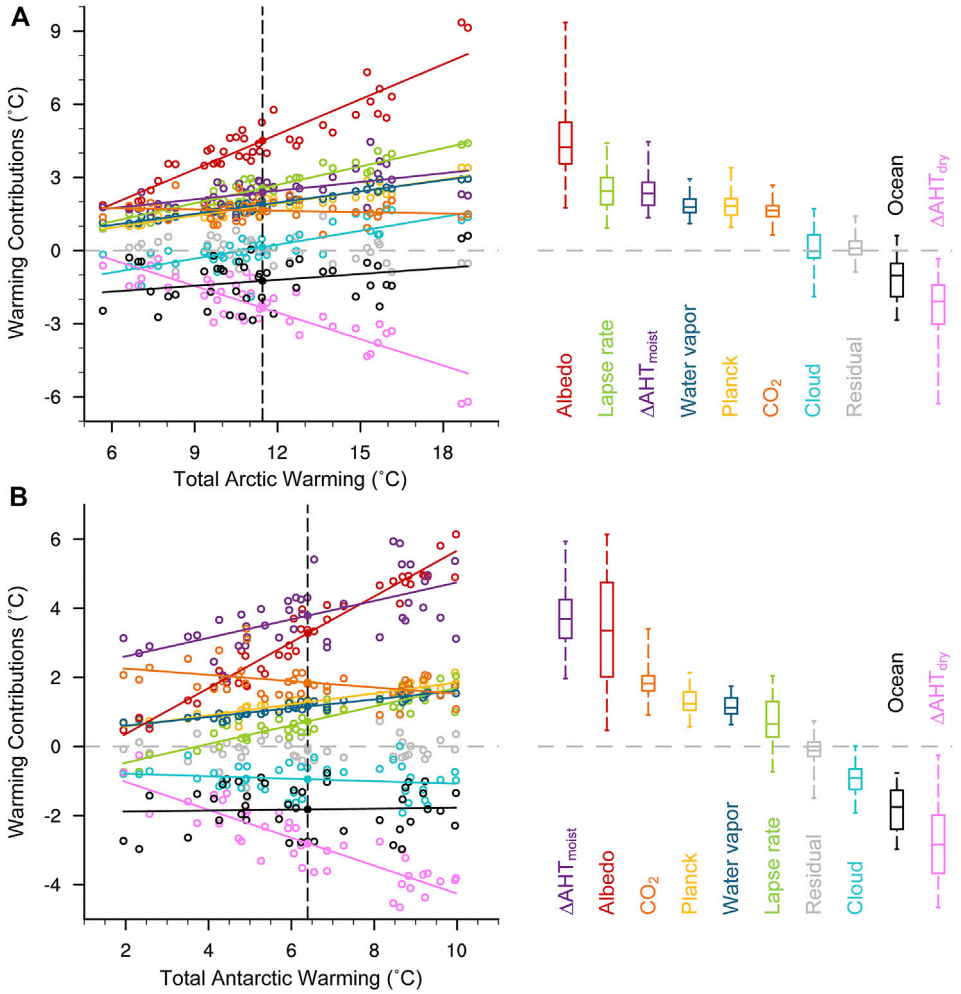

FIGURE 6 | Intermodel spread of warming contributions versus total warming (˚C) in individual models for **(A)** the Arctic and **(B)** the Antarctic in CMIP6. Solid lines show linear regressions of feedback contributions against total warming at each pole. Filled circles on the black dashed line show the CMIP6 multimodel mean. In the right-hand panel, boxes indicate the median and 25th and 75th percentiles, and whiskers show the full intermodel spread of polar warming contributions.

feedback also contribute strongly to total warming variance. Although the total warming variance is smaller in the Antarctic than the Arctic, the albedo feedback constitutes a larger fraction of the total variance in Antarctic warming. These results support previous suggestions that constraining the albedo feedback may reduce intermodel spread in polar warming contributed both directly by this feedback and by covariances with other feedbacks (e.g., Feldl et al., 2020; Boeke et al., 2021).

Seasonality in Polar Warming Contributions

Lastly, we consider what drives seasonality in warming for the Arctic and Antarctic. As seen in historical CMIP6 trends, polar warming under CO_2 quadrupling peaks during winter (**Figures 8A,B**). Compared to the Antarctic, stronger seasonality in Arctic warming largely stems from stronger winter warming, while summer warming is more similar between the poles. Contributions to Arctic seasonality in warming in CMIP6 are consistent with CMIP5 results (**Supplementary Figure S8** and Pithan and Mauritsen, 2014): while the albedo and water-vapor feedbacks support stronger summer warming, summer ocean heat storage and its release to the atmosphere in winter contributes to stronger winter warming. In addition, the lapse-rate and Planck feedbacks contribute to winter-amplified Arctic warming. While similar factors contribute to Antarctic seasonality in warming, weaker winter warming in the Antarctic compared to the Arctic results from weaker temperature feedbacks and seasonal ocean heat storage.

Comparison With Historical Warming Contributions in AMIP6

Applying the above methodology to historical AMIP6 simulations allows us to evaluate polar warming contributions within models that use the observed patterns of sea-surface temperatures and sea-ice concentrations as boundary

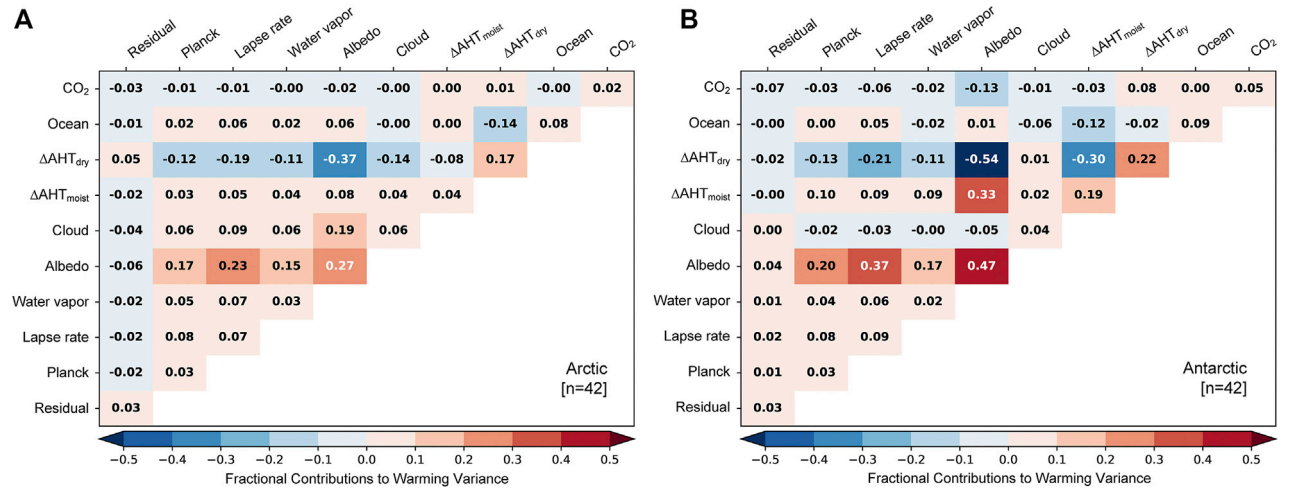

FIGURE 7 | Fractional contributions of each warming contribution term to intermodel variance in **(A)** Arctic and **(B)** Antarctic warming in CMIP6.

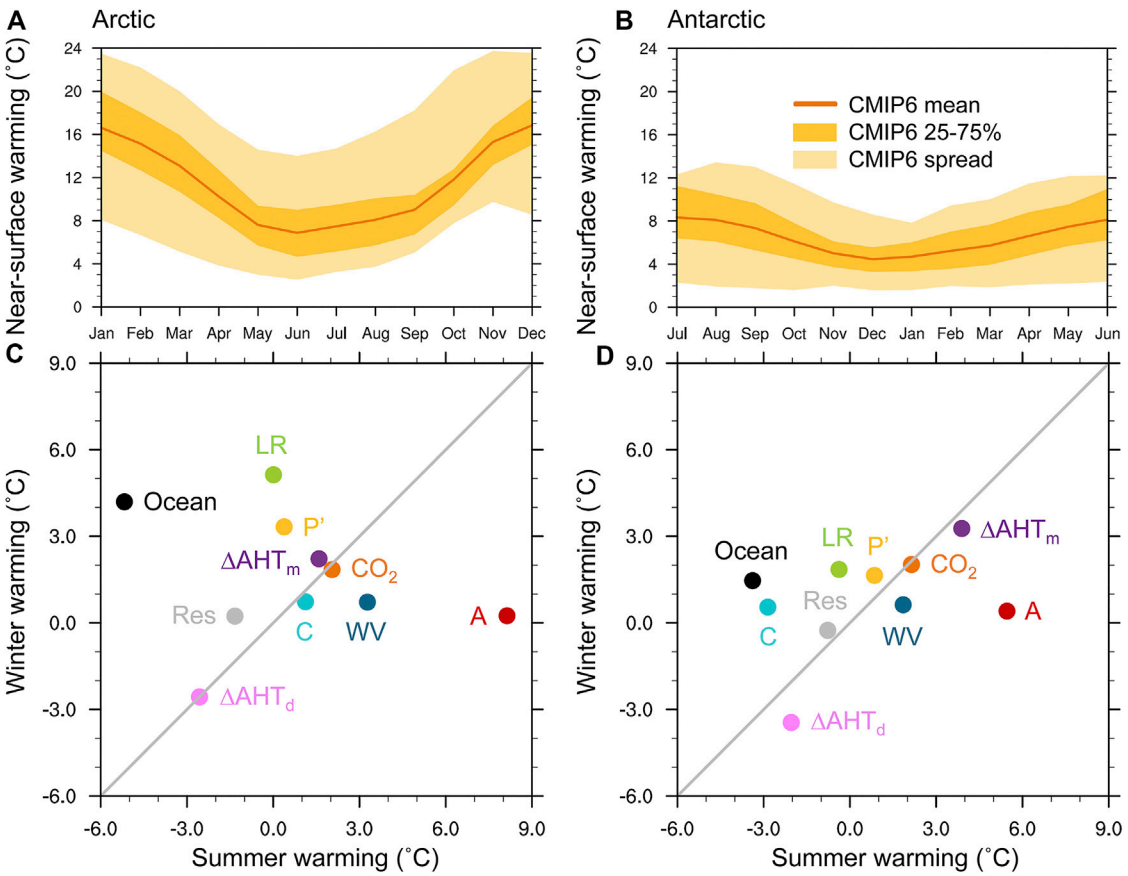

FIGURE 8 | Monthly near-surface warming (°C) centered around year-100 of abrupt CO_2 quadrupling for the CMIP6 multimodel mean (orange line), the 25th to 75th percentile (dark orange shading), and the full intermodel spread (light orange shading) in **(A)** the Arctic and **(B)** the Antarctic. **(C,D)** Contributions to winter and summer warming (°C) centered around year-100 of abrupt CO_2 quadrupling in CMIP6 for **(C)** the Arctic and **(D)** the Antarctic. Warming contributions are shown for the lapse-rate (LR), surface albedo (A), water-vapor (WV), and cloud (C) feedbacks, the variation in the Planck response from its global-mean value (P'), effective radiative forcing (CO_2), change in moist and dry AHT convergence (ΔAHT_m; ΔAHT_d) and ocean heat uptake (Ocean), and residual term (Res).

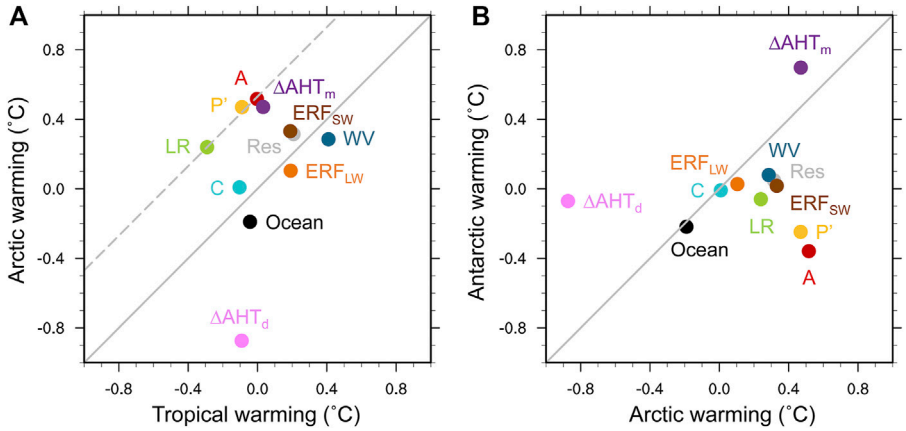

FIGURE 9 | Contributions to warming (°C) for 1979–2014 in AMIP6 models for **(A)** the tropics relative to the Arctic and **(B)** the Arctic relative to the Antarctic. Warming contributions are shown for the lapse-rate (LR), surface albedo (A), water-vapor (WV), and cloud (C) feedbacks, the variation in the Planck response from its global-mean value (P'), longwave and shortwave effective radiative forcing (ERF_{LW}; ERF_{SW}), change in moist and dry AHT convergence (ΔAHT_m; ΔAHT_d) and ocean heat uptake (Ocean), and residual term (Res). Dashed grey line shows a 1-to-1 slope through the lapse-rate feedback warming contribution.

conditions, which may produce some differences from the fully-coupled CMIP6 results under CO_2 quadrupling shown above. To calculate feedbacks in AMIP6, we compute monthly anomalies in climate variables with respect to the 1979–2014 climatology, and regress radiative contributions of feedbacks against near-surface air temperature anomalies for this period. We then calculate warming contributions again using **Eq. 2**, where Δ now indicates the trend in each variable from 1979 to 2014, multiplied by the period of 36 years.

Unlike the idealized CO_2 quadrupling experiments, AMIP simulations have time-evolving effective radiative forcing (ERF) that must be accounted for. Previous studies have derived the historical ERF in AMIP6 models using experiments from the Radiative Forcing Model Intercomparison Project (RFMIP, Pincus et al., 2016) with time-varying forcing applied on top of constant pre-industrial sea-surface temperature and sea-ice concentrations (e.g.,Zhang et al., 2020). However, these RFMIP experiments are only available for 7 CMIP6 models. To increase our model sample size, we estimate ERF using kernels in each model as follows. Because clear-sky TOA radiation anomalies are equal to the sum of clear-sky feedback energetic contributions, the clear-sky ERF, and a residual term arising from errors in the kernel approach, we estimate the clear-sky ERF as the difference between TOA radiation anomalies and the sum of kernel-derived clear-sky feedback energetic contributions. The neglect of kernel residual terms is justified by the fact that 1) kernel-derived and RFMIP-derived estimates of clear-sky ERF are in excellent agreement and 2) kernel residuals are very close to zero in amip-piForcing experiments from the Cloud Feedback Model Intercomparison Project (CFMIP, Webb et al., 2017) in which forcings are held constant at pre-industrial levels while sea-surface temperature and sea-ice concentration fields are prescribed to follow time-varying observations (not shown). Following standard practice, we then estimate the all-sky ERF by dividing clear-sky ERF by 1.16 (Soden et al., 2008). This method allows us to include 38 AMIP6 models in this analysis (**Supplementary Table S1**).

As in CMIP6 CO_2-quadrupling experiments, historical AMIP6 experiments show strong contributions to Arctic amplification from increased moist AHT and the lapse-rate, Planck, and albedo feedbacks, while the water-vapor feedback, Arctic ocean heat uptake, longwave forcing, and changes in dry AHT oppose Arctic amplification (**Figure 9A**). Despite differences in the vertical structure of warming between CMIP6 and AMIP6 models, their lapse-rate contributions to Arctic amplification appear relatively similar and consistently on par with respective surface albedo contributions. As suggested by Boeke et al. (2021), this may indicate the strong dependence of the lapse-rate feedback on the surface albedo feedback and surface temperature changes, more so than the vertical structure of warming. Differences in warming contributions between AMIP6 and CMIP6 include a relatively larger Planck contribution to Arctic amplification in AMIP6 and an Arctic-amplified SW ERF contribution in AMIP6. This positive SW forcing may be driven by reduced European sulfate emissions since 1980, which disproportionately warmed the Arctic compared to the rest of the globe (Acosta Navarro et al., 2016).

In both AMIP6 and CMIP6, the lapse rate, water vapor, Planck, and albedo feedbacks contribute to weaker warming in the Antarctic than Arctic, while increased poleward moisture transport contributes more strongly to Antarctic warming (**Figure 9B**). In contrast to CMIP6 projections, negative Antarctic warming contributions in AMIP6 for the albedo feedback and Planck feedback deviation from its global-mean value reflect historical cooling and sea-ice expansion over the Southern Ocean. As a result, the albedo feedback contributes most to stronger Arctic than Antarctic warming in AMIP6, while the lapse-rate feedback makes the largest contribution to this hemispheric asymmetry in CMIP6 projections. Weaker historical than projected Antarctic warming also weakens the equatorward dry AHT opposing Antarctic warming in AMIP6. These differences between AMIP6 and CMIP6 illustrate the strong

dependence of Antarctic feedbacks on changes in Southern Ocean sea-surface temperature and sea ice.

Even with identical prescribed sea-surface temperature and sea-ice concentration changes for all models in AMIP6, there is still considerable intermodel spread in polar warming contributions (**Supplementary Figure S9**). Consistent with Crook and Forster (2011), intermodel spread in polar ocean heat uptake outweighs intermodel spread in most polar feedbacks for this modelled historical period, while intermodel spread in the albedo feedback plays a relatively larger role under CO_2 quadrupling.

DISCUSSION

Analysis of polar warming in CMIP6 reveals key contributors to polar amplification and their changes from CMIP5. While CMIP6 models overestimate historical Antarctic warming, they generally capture the observed pattern of strong Arctic amplification and weaker Antarctic warming. As in reanalysis data, Arctic warming in CMIP6 models is both surface- and winter-amplified, although CMIP6 shows stronger mid-tropospheric warming than the ERA-Interim reanalysis and previous climate models.

Our quantification of contributions to polar warming in CMIP6 is largely consistent with previous results for CMIP5 (e.g., Pithan and Mauritsen, 2014; Goosse et al., 2018). As in CMIP5, abrupt CO_2 quadrupling experiments in CMIP6 demonstrate that the lapse-rate and albedo feedbacks are the largest contributors to both Arctic amplification and weaker warming in the Antarctic than Arctic. The albedo feedback also contributes most to intermodel spread in polar warming, while the lapse-rate feedback and seasonal ocean heat storage contribute most to seasonal asymmetry in warming at both poles.

Novel results in comparison to existing literature include our assessment of the sensitivity of polar warming contributions to the choice of radiative kernel. While most feedbacks are relatively insensitive to kernel choice, the Arctic albedo warming contribution in CMIP6 varies by almost a factor of two for different kernels. This yields an Arctic albedo warming contribution in CMIP6 of equal or greater importance than the lapse-rate feedback for half of the kernels considered, while the other half suggest that the lapse-rate feedback contributes more to polar amplification. However, the kernels most consistent with observations produce a stronger Arctic albedo feedback than previously found, on par with the lapse-rate feedback in its contribution to Arctic amplification. We also add a partitioning of AHT changes into moist and dry components, which demonstrates that increased moist AHT contributes to stronger Arctic amplification, and is the largest contributor to warming in the Antarctic. We find that increased polar warming in CMIP6 versus CMIP5 is explained by a stronger albedo feedback at both poles, combined with a less-negative cloud feedback in the Arctic and a larger increase in moist AHT to the Antarctic. Lastly, similar factors contribute to historical Arctic amplification in AMIP6 models compared to CMIP6 CO_2-quadrupling experiments, although the albedo feedback plays a larger role in weakening Antarctic warming in AMIP6 compared to CMIP6.

A limitation of using warming contribution methods to diagnose the mechanisms of polar amplification is that it implicitly includes interactions between feedbacks, making mechanistic interpretation difficult. For example, the strength of the lapse-rate feedback may be impacted by the amount of surface warming contributed by the albedo feedback (Graversen et al., 2014; Feldl et al., 2017) and mixed-phase cloud changes (Tan and Storelvmo, 2019), but the warming contribution method diagnoses the contributions of surface albedo, cloud, and lapse-rate changes separately. Others have argued that a strong winter lapse-rate feedback additionally requires seasonal ocean heat storage and sea-ice insulation loss in order to increase surface turbulent heat fluxes and upward longwave radiation, promoting warming in the lower-troposphere (Dai et al., 2019; Feldl et al., 2020; Chung et al., 2021). As demonstrated by these studies, experiments isolating specific mechanisms in climate models are needed to fully address the interconnected feedbacks promoting polar amplification.

While this study applies a TOA feedback framework, analysis from a surface perspective (e.g., Lu and Cai, 2009; Taylor et al., 2013; Pithan and Mauritsen, 2014; Boeke and Taylor, 2018) can provide additional insight on warming mechanisms in polar regions, where the surface and tropospheric responses to forcing are decoupled. Surface albedo and temperature feedbacks remain important contributors to Arctic amplification from a surface perspective in CMIP5 models, while the water vapor feedback and ocean heat uptake continue to oppose Arctic amplification (Pithan and Mauritsen, 2014). One key difference between surface and TOA frameworks in CMIP5 is that cloud feedbacks oppose Arctic amplification from a TOA perspective but slightly promote Arctic amplification from a surface perspective: changes in low-level clouds increase longwave radiation to the surface but have little impact on TOA longwave radiation, yielding a negative TOA cloud feedback due to shortwave radiative effects (Pithan and Mauritsen, 2014). Further analysis from a surface perspective may also be useful for understanding physical drivers of the surface-trapped warming that supports the positive Arctic lapse-rate feedback (Boeke et al., 2021).

Our analysis both confirms and updates previous results in consideration of CMIP6, while also highlighting several open questions about the mechanisms driving polar amplification, such as: 1) What controls the vertical profile of Arctic warming in CMIP6 models? Compared to reanalyses, stronger mid-tropospheric warming in CMIP6 models may be driven by shortwave atmospheric absorption (Donohoe and Battisti, 2013) or by overestimated midlatitude surface temperatures and poleward AHT (Laliberté and Kushner, 2013; Fajber et al., 2018; Feldl et al., 2020). Weaker surface-trapped warming in the lower troposphere may also be influenced by updated mixed-phase clouds and surface inversions in CMIP6 (Tan and Storelvmo, 2019). 2) Which kernels or other methods should be used to calculate the albedo feedback? Our kernel sensitivity analysis demonstrates the importance of evaluating and standardizing radiative kernels or alternative methods used to compare albedo and cloud feedbacks across models and studies. 3) Why does increased moist AHT contribute more to Antarctic

than Arctic warming? While this may be explained by Clausius-Clapeyron nonlinearity and more-negative Antarctic cloud feedbacks, other possible mechanisms include any process (e.g., ocean heat uptake, water vapor feedback) that leads to a stronger equator-to-pole moist static energy gradient in the Southern Hemisphere than Northern Hemisphere under CO_2 quadrupling. Further investigation of these polar warming asymmetries may highlight key processes for constraining both Arctic and Antarctic amplification.

DATA AVAILABILITY STATEMENT

Publicly available datasets were analyzed in this study. This data can be found here: All CMIP and AMIP data analyzed for this study can be found in the Earth System Grid Federation (ESGF) repository at https://esgf-node.llnl.gov/projects/esgf-llnl/. ERA-Interim data was provided by the ECMWF Data Archive at https://apps.ecmwf.int/datasets/data/interim-full-moda/levtype=pl/. The HadCRUT5 Analysis is available from the University of East Anglia Climatic Research Unit at https://crudata.uea.ac.uk/cru/data/temperature/.

AUTHOR CONTRIBUTIONS

All authors contributed to the study design. MZ calculated the climate feedbacks and AMIP forcing, and LH computed the warming contributions and remaining analysis. LH wrote the original draft, and all authors contributed to the final manuscript.

FUNDING

LH was supported by the National Science Foundation (NSF) Graduate Research Fellowship Grant DGE-1762114 and the ARCS Foundation Fellowship. KA was supported by National Science Foundation Grants AGS-1752796 and OCE-1850900 and an Alfred P. Sloan Research Fellowship. MZ was supported by the Regional and Global Model Analysis Program of the Office of Science at the U.S. Department of Energy. CB was supported by NOAA MAPP NA18OAR4310274. AD was supported by the NSF Antarctic Program Grant PLR-1643436 and NOAA MAPP Grant eGC1#A127135.

ACKNOWLEDGMENTS

We acknowledge computing resources (doi:10.5065/D6RX99HX) provided by NCAR's Computational and Information Systems Laboratory (2019), sponsored by the National Science Foundation. The work of MZ was performed under the auspices of the U.S. Department of Energy by Lawrence Livermore National Laboratory under Contract DE-AC52-07NA27344.

SUPPLEMENTARY MATERIAL

The Supplementary Material for this article can be found online at: https://www.frontiersin.org/articles/10.3389/feart.2021.710036/full#supplementary-material

REFERENCES

Acosta Navarro, J. C., Varma, V., Riipinen, I., Seland, Ø., Kirkevåg, A., Struthers, H., et al. (2016). Amplification of Arctic Warming by Past Air Pollution Reductions in Europe. *Nat. Geosci* 9, 277–281. doi:10.1038/ngeo2673

Alexeev, V. A., Langen, P. L., and Bates, J. R. (2005). Polar Amplification of Surface Warming on an Aquaplanet in "Ghost Forcing" Experiments without Sea Ice Feedbacks. *Clim. Dyn.* 24, 655–666. doi:10.1007/s00382-005-0018-3

Andrews, T., Gregory, J. M., and Webb, M. J. (2015). The Dependence of Radiative Forcing and Feedback on Evolving Patterns of Surface Temperature Change in Climate Models. *J. Clim.* 28 (4), 1630–1648. doi:10.1175/jcli-d-14-00545.1

Armour, K. C., Marshall, J., Scott, J. R., Donohoe, A., and Newsom, E. R. (2016). Southern Ocean Warming Delayed by Circumpolar Upwelling and Equatorward Transport. *Nat. Geosci* 9 (7), 549–554. doi:10.1038/ngeo2731

Armour, K. C., Siler, N., Donohoe, A., and Roe, G. H. (2019). Meridional Atmospheric Heat Transport Constrained by Energetics and Mediated by Large-Scale Diffusion. *J. Clim.* 32 (12), 3655–3680. doi:10.1175/JCLI-D-18-0563.1

Block, K., and Mauritsen, T. (2013). Forcing and Feedback in the MPI-ESM-LR Coupled Model under Abruptly Quadrupled CO2. *J. Adv. Model. Earth Syst.* 5, 676–691. doi:10.1002/jame.20041

Block, K., Schneider, F. A., Mülmenstädt, J., Salzmann, M., and Quaas, J. (2020). Climate Models Disagree on the Sign of Total Radiative Feedback in the Arctic. *Tellus A: Dynamic Meteorology and Oceanography* 72 (1), 1–14. doi:10.1080/16000870.2019.1696139

Boeke, R. C., and Taylor, P. C. (2018). Seasonal Energy Exchange in Sea Ice Retreat Regions Contributes to Differences in Projected Arctic Warming. *Nat. Commun.* 9, 5017. doi:10.1038/s41467-018-07061-9

Boeke, R. C., Taylor, P. C., and Sejas, S. A. (2021). On the Nature of the Arctic's Positive Lapse-Rate Feedback. *Geophys. Res. Lett.* 48, e2020GL091109. doi:10.1029/2020GL091109

Bonan, D. B., Armour, K. C., Roe, G. H., Siler, N., and Feldl, N. (2018). Sources of Uncertainty in the Meridional Pattern of Climate Change. *Geophys. Res. Lett.* 45, 9131–9140. doi:10.1029/2018GL079429

Brutel-Vuilmet, C., Ménégoz, M., and Krinner, G. (2013). An Analysis of Present and Future Seasonal Northern Hemisphere Land Snow Cover Simulated by CMIP5 Coupled Climate Models. *The Cryosphere* 7, 67–80. doi:10.5194/tc-7-67-2013

Cai, S., Hsu, P.-C., and Liu, F. (2021). Changes in Polar Amplification in Response to Increasing Warming in CMIP6. *Atmos. Oceanic Sci. Lett.* 14, 100043–102834. doi:10.1016/j.aosl.2021.100043

Caldwell, P. M., Bretherton, C. S., Zelinka, M. D., Klein, S. A., Santer, B. D., and Sanderson, B. M. (2014). Statistical Significance of Climate Sensitivity Predictors Obtained by Data Mining. *Geophys. Res. Lett.* 41, 1803–1808. doi:10.1002/2014GL059205

Chen, Y.-J., Hwang, Y.-T., and Ceppi, P. (2021). The Impacts of Cloud-Radiative Changes on Poleward Atmospheric and Oceanic Energy Transport in a Warmer Climate. *J. Clim.*, 1–63. published online ahead of print 2021. doi:10.1175/JCLI-D-20-0949.1

Chung, E. S., Ha, K. J., Timmermann, A., Stuecker, M. F., Bodai, T., and Lee, S. K. (2021). Cold-Season Arctic Amplification Driven by Arctic Ocean-Mediated Seasonal Energy Transfer. *Earth's Future* 9, e2020EF001898. doi:10.1029/2020EF001898

Computational and Information Systems Laboratory (2019). *Cheyenne: HPE/SGI ICE XA System*. Boulder, CO: University Community Computing)National Center for Atmospheric Research. doi:10.5065/D6RX99HX

Cronin, T. W., and Jansen, M. F. (2016). Analytic Radiative-advective Equilibrium as a Model for High-latitude Climate. *Geophys. Res. Lett.* 43, 449–457. doi:10.1002/2015GL067172

Crook, J. A., and Forster, P. M. (2011). A Balance between Radiative Forcing and Climate Feedback in the Modeled 20th century Temperature Response. *J. Geophys. Res.* 116, D17108. doi:10.1029/2011JD015924

Dai, A., Luo, D., Song, M., and Liu, J. (2019). Arctic Amplification Is Caused by Sea-Ice Loss under Increasing CO2. *Nat. Commun.* 10, 121. doi:10.1038/s41467-018-07954-9

Dee, D. P., Uppala, S. M., Simmons, A. J., Berrisford, P., Poli, P., Kobayashi, S., et al. (2011). The ERA-Interim Reanalysis: Configuration and Performance of the Data Assimilation System. *Q.J.R. Meteorol. Soc.* 137, 553–597. doi:10.1002/qj.828

Deser, C., Tomas, R., Alexander, M., and Lawrence, D. (2010). The Seasonal Atmospheric Response to Projected Arctic Sea Ice Loss in the Late Twenty-First Century. *J. Clim.* 23 (2), 333–351. doi:10.1175/2009JCLI3053.1

Dong, Y., Armour, K. C., Zelinka, M. D., Proistosescu, C., Battisti, D. S., Zhou, C., et al. (2020). Intermodel Spread in the Pattern Effect and its Contribution to Climate Sensitivity in CMIP5 and CMIP6 Models. *J. Clim.* 33 (18), 7755–7775. doi:10.1175/JCLI-D-19-1011.1

Donohoe, A., Armour, K. C., Roe, G. H., Battisti, D. S., and Hahn, L. (2020a). The Partitioning of Meridional Heat Transport from the Last Glacial Maximum to CO2 Quadrupling in Coupled Climate Models. *J. Clim.* 33 (10), 4141–4165. doi:10.1175/JCLI-D-19-0797.1

Donohoe, A., and Battisti, D. S. (2013). The Seasonal Cycle of Atmospheric Heating and Temperature. *J. Clim.* 26, 4962–4980. doi:10.1175/JCLI-D-12-00713.1

Donohoe, A., Blanchard-Wrigglesworth, E., Schweiger, A., and Rasch, P. J. (2020b). The Effect of Atmospheric Transmissivity on Model and Observational Estimates of the Sea Ice Albedo Feedback. *J. Clim.* 33 (13), 5743–5765. doi:10.1175/JCLI-D-19-0674.1

Eyring, V., Bony, S., Meehl, G. A., Senior, C. A., Stevens, B., Stouffer, R. J., et al. (2016). Overview of the Coupled Model Intercomparison Project Phase 6 (CMIP6) Experimental Design and Organization. *Geosci. Model. Dev.* 9, 1937–1958. doi:10.5194/gmd-9-1937-2016

Fajber, R., Kushner, P. J., and Laliberté, F. (2018). Influence of Midlatitude Surface Thermal Anomalies on the Polar Midtroposphere in an Idealized Moist Model. *J. Atmos. Sci.* 75 (4), 1089–1104. doi:10.1175/JAS-D-17-0283.1

Feldl, N., Bordoni, S., and Merlis, T. M. (2017). Coupled High-Latitude Climate Feedbacks and Their Impact on Atmospheric Heat Transport. *J. Clim.* 30, 189–201. doi:10.1175/JCLI-D-16-0324.1

Feldl, N., Po-Chedley, S., Singh, H. K. A., Hay, S., and Kushner, P. J. (2020). Sea Ice and Atmospheric Circulation Shape the High-Latitude Lapse Rate Feedback. *Npj Clim. Atmos. Sci.* 3 (41). doi:10.1038/s41612-020-00146-7

Feldl, N., and Roe, G. H. (2013). Four Perspectives on Climate Feedbacks. *Geophys. Res. Lett.* 40, 4007–4011. doi:10.1002/grl.50711

Goosse, H., Kay, J. E., Armour, K. C., Bodas-Salcedo, A., Chepfer, H., Docquier, D., et al. (2018). Quantifying Climate Feedbacks in Polar Regions. *Nat. Commun.* 9, 1919. doi:10.1038/s41467-018-04173-0

Gossart, A., Helsen, S., Lenaerts, J. T. M., Broucke, S. V., van Lipzig, N. P. M., and Souverijns, N. (2019). An Evaluation of Surface Climatology in State-Of-The-Art Reanalyses over the Antarctic Ice Sheet. *J. Clim.* 32 (20), 6899–6915. doi:10.1175/JCLI-D-19-0030.1

Graham, R. M., Cohen, L., Ritzhaupt, N., Segger, B., Graversen, R. G., Rinke, A., et al. (2019). Evaluation of Six Atmospheric Reanalyses over Arctic Sea Ice from Winter to Early Summer. *J. Clim.* 32 (14), 4121–4143. doi:10.1175/JCLI-D-18-0643.1

Graversen, R. G., Langen, P. L., and Mauritsen, T. (2014). Polar Amplification in CCSM4: Contributions from the Lapse Rate and Surface Albedo Feedbacks. *J. Clim.* 27, 4433–4450. doi:10.1175/JCLI-D-13-00551.1

Gregory, J. M., Ingram, W. J., Palmer, M. A., Jones, G. S., Stott, P. A., Thorpe, R. B., et al. (2004). A New Method for Diagnosing Radiative Forcing and Climate Sensitivity. *Geophys. Res. Lett.* 31, L03205. doi:10.1029/2003GL018747

Hahn, L. C., Armour, K. C., Battisti, D. S., Donohoe, A., Pauling, A. G., and Bitz, C. M. (2020). Antarctic Elevation Drives Hemispheric Asymmetry in Polar Lapse Rate Climatology and Feedback. *Geophys. Res. Lett.* 47, e2020GL088965. doi:10.1029/2020GL088965

Hall, A. (2004). The Role of Surface Albedo Feedback in Climate. *J. Clim.* 17 (7), 1550–1568. doi:10.1175/1520-0442(2004)017%3C1550:TROSAF%3E2.0.CO;2

Hansen, J., Sato, M., Ruedy, R., Nazarenko, L., Lacis, A., Schmidt, G. A., et al. (2005). Efficacy of Climate Forcings. *J. Geophys. Res.* 110, d18104. doi:10.1029/2005JD005776

Held, I. M., and Shell, K. M. (2012). Using Relative Humidity as a State Variable in Climate Feedback Analysis. *J. Clim.* 25 (8), 2578–2582. doi:10.1175/JCLI-D-11-00721.1

Holland, M. M., and Bitz, C. M. (2003). Polar Amplification of Climate Change in Coupled Models. *Clim. Dyn.* 21, 221–232. doi:10.1007/s00382-003-0332-6

Huang, Y., Xia, Y., and Tan, X. (2017). On the Pattern of CO2 Radiative Forcing and Poleward Energy Transport. *J. Geophys. Res. Atmos.* 122, 10578–10593. doi:10.1002/2017JD027221

Hwang, Y.-T., and Frierson, D. M. W. (2010). Increasing Atmospheric Poleward Energy Transport with Global Warming. *Geophys. Res. Lett.* 37, L24807. doi:10.1029/2010GL045440

Hwang, Y.-T., Frierson, D. M. W., and Kay, J. E. (2011). Coupling between Arctic Feedbacks and Changes in Poleward Energy Transport. *Geophys. Res. Lett.* 38, L17704. doi:10.1029/2011GL048546

Kosaka, Y., and Xie, S.-P. (2013). Recent Global-Warming Hiatus Tied to Equatorial Pacific Surface Cooling. *Nature* 501, 403–407. doi:10.1038/nature12534

Laliberté, F., and Kushner, P. J. (2013). Isentropic Constraints by Midlatitude Surface Warming on the Arctic Midtroposphere. *Geophys. Res. Lett.* 40, 606–611. doi:10.1029/2012GL054306

Lindsay, R., Wensnahan, M., Schweiger, A., and Zhang, J. (2014). Evaluation of Seven Different Atmospheric Reanalysis Products in the Arctic*. *J. Clim.* 27, 2588–2606. doi:10.1175/JCLI-D-13-00014.1

Lu, J., and Cai, M. (2009). A New Framework for Isolating Individual Feedback Processes in Coupled General Circulation Climate Models. Part I: Formulation. *Clim. Dyn.* 32, 873–885. doi:10.1007/s00382-008-0425-3

Manabe, S., and Stouffer, R. J. (1980). Sensitivity of a Global Climate Model to an Increase of CO2concentration in the Atmosphere. *J. Geophys. Res.* 85 (C10), 5529–5554. doi:10.1029/JC085iC10p05529

Marshall, J., Scott, J. R., Armour, K. C., Campin, J.-M., Kelley, M., and Romanou, A. (2015). The Ocean's Role in the Transient Response of Climate to Abrupt Greenhouse Gas Forcing. *Clim. Dyn.* 44, 2287–2299. doi:10.1007/s00382-014-2308-0

Medeiros, B., Deser, C., Tomas, R. A., and Kay, J. E. (2011). Arctic Inversion Strength in Climate Models. *J. Clim.* 24, 4733–4740. doi:10.1175/2011JCLI3968.1

Morice, C. P., Kennedy, J. J., Rayner, N. A., Winn, J. P., Hogan, E., Killick, R. E., et al. (2021). An Updated Assessment of Near-Surface Temperature Change from 1850: The HadCRUT5 Data Set. *Geophys. Res. Atmos.* 126, e2019JD032361. doi:10.1029/2019JD032361

Payne, A. E., Jansen, M. F., and Cronin, T. W. (2015). Conceptual Model Analysis of the Influence of Temperature Feedbacks on Polar Amplification. *Geophys. Res. Lett.* 42, 9561–9570. doi:10.1002/2015GL065889

Pendergrass, A. G., Conley, A., and Vitt, F. M. (2018). Surface and Top-Of-Atmosphere Radiative Feedback Kernels for CESM-CAM5. *Earth Syst. Sci. Data* 10 (1), 317–324. doi:10.5194/essd-10-317-2018

Pithan, F., and Mauritsen, T. (2014). Arctic Amplification Dominated by Temperature Feedbacks in Contemporary Climate Models. *Nat. Geosci* 7, 181–184. doi:10.1038/ngeo2071

Pithan, F., Medeiros, B., and Mauritsen, T. (2014). Mixed-phase Clouds Cause Climate Model Biases in Arctic Wintertime Temperature Inversions. *Clim. Dyn.* 43, 289–303. doi:10.1007/s00382-013-1964-9

Pincus, R., Forster, P. M., and Stevens, B. (2016). The Radiative Forcing Model Intercomparison Project (RFMIP): experimental protocol for CMIP6. *Geosci. Model Dev.* 9, 3447–3460. doi:10.5194/gmd-9-3447-2016

Rodgers, K., Lee, S.-S., Rosenbloom, N., Timmermann, A., Danabasoglu, G., Deser, C., et al. (2021). Ubiquity of Human-Induced Changes in Climate Variability. *Submitted Earth Syst. Dyn.*. doi:10.31223/X5GP79

Roe, G. H., Feldl, N., Armour, K. C., Hwang, Y.-T., and Frierson, D. M. W. (2015). The Remote Impacts of Climate Feedbacks on Regional Climate Predictability. *Nat. Geosci* 8, 135–139. doi:10.1038/ngeo2346

Salzmann, M. (2017). The Polar Amplification Asymmetry: Role of Antarctic Surface Height. *Earth Syst. Dynam.* 8, 323–336. doi:10.5194/esd-8-323-2017

Screen, J. A., Deser, C., and Simmonds, I. (2012). Local and Remote Controls on Observed Arctic Warming. *Geophys. Res. Lett.* 39, L10709. doi:10.1029/2012GL051598

Screen, J. A., and Simmonds, I. (2010b). Increasing Fall-winter Energy Loss from the Arctic Ocean and its Role in Arctic Temperature Amplification. *Geophys. Res. Lett.* 37, L16707. doi:10.1029/2010GL044136

Screen, J. A., and Simmonds, I. (2010a). The central Role of Diminishing Sea Ice in Recent Arctic Temperature Amplification. *Nature* 464, 1334–1337. doi:10.1038/nature09051

Serreze, M. C., Barrett, A. P., Stroeve, J. C., Kindig, D. N., and Holland, M. M. (2009). The Emergence of Surface-Based Arctic Amplification. *The Cryosphere* 3, 11–19. doi:10.5194/tc-3-11-2009

Shaw, T. A., and Voigt, A. (2016). What Can Moist Thermodynamics Tell Us about Circulation Shifts in Response to Uniform Warming?. *Geophys. Res. Lett.* 43, 4566–4575. doi:10.1002/2016GL068712

Shell, K. M., Kiehl, J. T., and Shields, C. A. (2008). Using the Radiative Kernel Technique to Calculate Climate Feedbacks in NCAR's Community Atmospheric Model. *J. Clim.* 21, 2269–2282. doi:10.1175/2007JCLI2044.1

Smith, C. J., Kramer, R. J., Myhre, G., Alterskjær, K., Collins, W., Sima, A., et al. (2020). Effective Radiative Forcing and Adjustments in CMIP6 Models. *Atmos. Chem. Phys.* 20, 9591–9618. doi:10.5194/acp-20-9591-2020

Smith, C. J., Kramer, R. J., Myhre, G., Forster, P. M., Soden, B. J., Andrews, T., et al. (2018). Understanding Rapid Adjustments to Diverse Forcing Agents. *Geophys. Res. Lett.* 45, 12023–12031. doi:10.1029/2018GL079826

Smith, D. M., Screen, J. A., Deser, C., Cohen, J., Fyfe, J. C., García-Serrano, J., et al. (2019). The Polar Amplification Model Intercomparison Project (PAMIP) Contribution to CMIP6: Investigating the Causes and Consequences of Polar Amplification. *Geosci. Model. Dev.* 12, 1139–1164. doi:10.5194/gmd-12-1139-2019

Soden, B. J., Held, I. M., Colman, R., Shell, K. M., Kiehl, J. T., and Shields, C. A. (2008). Quantifying Climate Feedbacks Using Radiative Kernels. *J. Clim.* 21, 3504–3520. doi:10.1175/2007JCLI2110.1

Stuecker, M. F., Bitz, C. M., Armour, K. C., Proistosescu, C., Kang, S. M., Xie, S.-P., et al. (2018). Polar Amplification Dominated by Local Forcing and Feedbacks. *Nat. Clim Change* 8, 1076–1081. doi:10.1038/s41558-018-0339-y

Tan, I., and Storelvmo, T. (2019). Evidence of Strong Contributions from Mixed-Phase Clouds to Arctic Climate Change. *Geophys. Res. Lett.* 46, 2894–2902. doi:10.1029/2018GL081871

Taylor, K. E., Crucifix, M., Braconnot, P., Hewitt, C. D., Doutriaux, C., Broccoli, A. J., et al. (2007). Estimating Shortwave Radiative Forcing and Response in Climate Models. *J. Clim.* 20 (11), 2530–2543. doi:10.1175/JCLI4143.1

Taylor, P. C., Cai, M., Hu, A., Meehl, J., Washington, W., and Zhang, G. J. (2013). A Decomposition of Feedback Contributions to Polar Warming Amplification. *J. Clim.* 26 (18), 7023–7043. doi:10.1175/JCLI-D-12-00696.1

Wang, C., Graham, R. M., Wang, K., Gerland, S., and Granskog, M. A. (2019). Comparison of ERA5 and ERA-Interim Near-Surface Air Temperature, Snowfall and Precipitation over Arctic Sea Ice: Effects on Sea Ice Thermodynamics and Evolution. *The Cryosphere* 13, 1661–1679. doi:10.5194/tc-13-1661-2019

Wang, Y., Zhou, D., Bunde, A., and Havlin, S. (2016). Testing Reanalysis Data Sets in Antarctica: Trends, Persistence Properties, and Trend Significance. *J. Geophys. Res. Atmos.* 121, 839–12855. doi:10.1002/2016JD024864

Webb, M. J., Andrews, T., Bodas-Salcedo, A., Bony, S., Bretherton, C. S., Chadwick, R., et al. (2017). The Cloud Feedback Model Intercomparison Project (CFMIP) Contribution to CMIP6. *Geosci. Model. Dev.* 10, 359–384. doi:10.5194/gmd-10-359-2017

Zelinka, M. D., and Hartmann, D. L. (2012). Climate Feedbacks and Their Implications for Poleward Energy Flux Changes in a Warming Climate. *J. Clim.* 25 (2), 608–624. doi:10.1175/JCLI-D-11-00096.1

Zelinka, M. D., Myers, T. A., McCoy, D. T., Po-Chedley, S., Caldwell, P. M., Ceppi, P., et al. (2020). Causes of Higher Climate Sensitivity in CMIP6 Models. *Geophys. Res. Lett.* 47, e2019GL085782. doi:10.1029/2019GL085782

Zhang, R., Wang, H., Fu, Q., and Rasch, P. J. (2020). Assessing Global and Local Radiative Feedbacks Based on AGCM Simulations for 1980–2014/2017. *Geophys. Res. Lett.* 47, e2020GL088063. doi:10.1029/2020GL088063

Conflict of Interest: The authors declare that the research was conducted in the absence of any commercial or financial relationships that could be construed as a potential conflict of interest.

Publisher's Note: All claims expressed in this article are solely those of the authors and do not necessarily represent those of their affiliated organizations, or those of the publisher, the editors and the reviewers. Any product that may be evaluated in this article, or claim that may be made by its manufacturer, is not guaranteed or endorsed by the publisher.

frontiers in Earth Science

ORIGINAL RESEARCH
published: 01 September 2021
doi: 10.3389/feart.2021.719024

The Emergence and Transient Nature of Arctic Amplification in Coupled Climate Models

Marika M. Holland and Laura Landrum*

Climate and Global Dynamics Laboratory, National Center for Atmospheric Research, Boulder, CO, United States

Under rising atmospheric greenhouse gas concentrations, the Arctic exhibits amplified warming relative to the globe. This Arctic amplification is a defining feature of global warming. However, the Arctic is also home to large internal variability, which can make the detection of a forced climate response difficult. Here we use results from seven model large ensembles, which have different rates of Arctic warming and sea ice loss, to assess the time of emergence of anthropogenically-forced Arctic amplification. We find that this time of emergence occurs at the turn of the century in all models, ranging across the models by a decade from 1994–2005. We also assess transient changes in this amplified signal across the 21st century and beyond. Over the 21st century, the projections indicate that the maximum Arctic warming will transition from fall to winter due to sea ice reductions that extend further into the fall. Additionally, the magnitude of the annual amplification signal declines over the 21st century associated in part with a weakening albedo feedback strength. In a simulation that extends to the 23rd century, we find that as sea ice cover is completely lost, there is little further reduction in the surface albedo and Arctic amplification saturates at a level that is reduced from its 21st century value.

Keywords: arctic amplification, climate change, sea ice, climate modelling, time of emergence (TOE)

OPEN ACCESS

Edited by:
Patrick Charles Taylor, National Aeronautics and Space Administration, United States

Reviewed by:
Chad Thackeray, University of California, Los Angeles, United States
Dirk Notz, University of Hamburg, Germany

****Correspondence:***
Marika M. Holland
mholland@ucar.edu

Specialty section:
This article was submitted to Interdisciplinary Climate Studies, a section of the journal Frontiers in Earth Science

Received: *01 June 2021*
Accepted: *17 August 2021*
Published: *01 September 2021*

Citation:
Holland MM and Landrum L (2021) The Emergence and Transient Nature of Arctic Amplification in Coupled Climate Models. Front. Earth Sci. 9:719024. doi: 10.3389/feart.2021.719024

INTRODUCTION

Surface-based Arctic amplification is a well-known phenomenon in which the Arctic surface temperature warms more than the global average when the climate is subject to increased atmospheric greenhouse gas concentrations (or other similar external forcing). Climate models consistently simulate surface-based Arctic amplification in climate change projections (e.g., Manabe and Stouffer, 1980; Holland and Bitz, 2003) and it is also apparent in observations of the warming climate (e.g., Serreze et al., 2009; Screen and Simmonds, 2010). However, there are large uncertainties in projected Arctic warming across models primarily as a consequence of differences in model structure (e.g., Cai et al., 2021).

Numerous factors contribute to the amplified warming in the Arctic, including both radiative and non-radiative feedbacks (e.g., Goosse et al., 2018). These feedbacks are often a consequence of unique conditions in the Arctic, such as the presence of snow and ice, the relatively cold temperatures, and the prevalance of a stably stratified atmosphere. The feedbacks influencing Arctic amplification can also be interrelated. For example, both the surface-albedo feedback and the positive Arctic lapse rate feedback are strongly influenced by the loss of sea ice (e.g., Boeke et al., 2020; Feldl et al., 2020). Evidence from coupled climate models suggests that feedbacks local to the Arctic are the dominant drivers of amplification (e.g., Stuecker et al., 2018) although interactions with lower latitudes through changing atmospheric and oceanic heat transport for example can play some role (e.g., Mahlstein and

TABLE 1 | Information on the SMILE simulations used in this study and their Arctic amplification. Properties are shown for annual ensemble mean values. Values in parenthesis indicate the standard deviation across ensemble members.

Model	Number of members	ToE	70–90N Warming at ToE (°C)	Amplification factor at ToE	21st century amplification factor change	References
CanESM2	50	1997	1.3 (0.3)	2.4 (0.4)	−0.1	Kirchmeier-Young et al. (2017)
CESM1-CAM5	40	1994	1.0 (0.3)	3.3 (0.7)	−0.5	Kay et al. (2015)
CSIRO-Mk3-6-0	30	2005	1.3 (0.3)	2.7 (0.4)	−0.7	Jeffrey et al. (2013)
GFDL-CM3	20	1999	1.7 (0.5)	3.5 (0.9)	−0.7	Sun et al. (2018)
GFDL-ESM2M	30	2004	1.7 (0.4)	2.6 (0.5)	−0.3	Rodgers et al. (2015)
MPI-ESM	100	2002	1.6 (0.3)	2.8 (0.5)	−0.3	Maher et al. (2019)
EC-EARTH	16	1998	1.5 (0.4)	3.0 (0.5)	−0.3	Hazeleger et al. (2010)

Knutti, 2011). There are considerable discrepancies across models in the magnitude and relative importance of various feedbacks which contributes to uncertainty in Arctic warming (e.g., Pithan and Mauritsen, 2014; Bonan et al., 2018; Hu et al., 2020).

The amplified warming signature has a seasonal and spatial dependence. Even early climate models exhibited that amplified surface warming in the Arctic would primarily occur in fall and winter with much smaller warming in summer months (Manabe and Stouffer, 1980). This is due to a surface heat gain in summer associated primarily with reduced albedos and increased solar heating that warms the ocean and melts sea ice but has a small effect on air temperatures. This heat is then released to the atmosphere during fall and winter, causing a large amplification at that time. More recent studies (e.g., Deser et al., 2010; Dai et al., 2019) confirm that the seasonality of Arctic warming is associated with sea ice loss and seasonal variations in the oceanic storage and release of energy. Further work (Boeke and Taylor, 2018) suggests that the efficiency with which this localized seasonal heat exchange is dispersed across the Arctic are important for explaining inter-model spread in Arctic warming.

Much of this past work has considered Arctic warming and/or amplification at a certain point in time or for a certain increase in CO_2 concentrations. Here we focus on the transient nature of surface-based Arctic amplification in 20th-21st century climate projections. We address several questions: 1.) When does Arctic amplification emerge from the background noise of the climate system? 2.) How does the Arctic amplification evolve over the 21st century? 3.) How is this evolution related to sea ice conditions? and 4.) How robust are these properties across climate models? We address these questions using the multi-model large ensemble (Deser et al., 2020) which includes seven climate models that have performed a large ensemble of simulations subject to historical and future forcing. The use of large ensemble simulations allows us to address questions of emergence of the anthropogenic signal.

DATA AND METHODS

We use models from the multi-model large ensemble (MMLE; Deser et al., 2020) to assess the time of emergence and transient nature of Arctic amplification. The MMLE includes data from seven single model initial-condition large ensembles (SMILEs) (**Table 1**). Differences in the ensemble members within a SMILE arise from internal variability as simulated by a particular model. Differences across the SMILEs provide a measure of model structural uncertainty. Thus, we are able to assess the influence of both factors, albeit with relatively few models.

The SMILE simulations are run using CMIP5 historical forcing to 2005 and the RCP8.5 forcing scenario from 2006–2100 (Meinshausen et al., 2011). The minimum number of simulations from an individual model is 16 and the latest start year for the integrations is 1950. Because of this, we assess conditions over the 1950–2100 period for all of the SMILEs to enable intercomparison. Previous work has assessed the uncertainty in projected sea ice (Bonan et al., 2021) and the emergence of some metrics of Arctic climate conditions (Landrum and Holland, 2020) within these simulations. As noted by Bonan et al. (2021), these simulations are generally representative of the CMIP5 inter-model spread in Arctic sea ice and have considerably different representations of Arctic climate conditions. To further assess transient changes in amplification, we also analyze a single CESM1-CAM5 simulation that has been extended to 2300 (Meehl et al., 2013). This simulation is forced with an extension to the RCP8.5 scenario in which the CO_2 level stabilizes in the mid-2200s. It reaches year-round ice-free conditions in the Arctic in the later part of the 22nd century.

As a metric of Arctic amplification, for each ensemble member, we define an amplification factor as the ratio of the running decadal mean 70–90N surface air temperature change relative to the running decadal mean global surface air temperature change. The change is computed relative to the 1950–1969 mean for each ensemble member within a SMILE (i.e., for a particular model) and for the CESM1-CAM5 extension simulation. We choose a 20-years base period here to reduce the effects of any potential decadal memory that is present for the simulations that are initialized in 1950 with a small initial perturbation error. 10-year running mean changes are used to allow us to assess how Arctic amplification evolves over time given the rapid decadal scale changes present in the Arctic.

To determine an Arctic amplification Time of Emergence (ToE), we quantify the time at which the decadal Arctic warming is larger than that of the global warming. In particular, for each SMILE model, we assess the year at which the decadal average centered on that year of the 70–90N surface

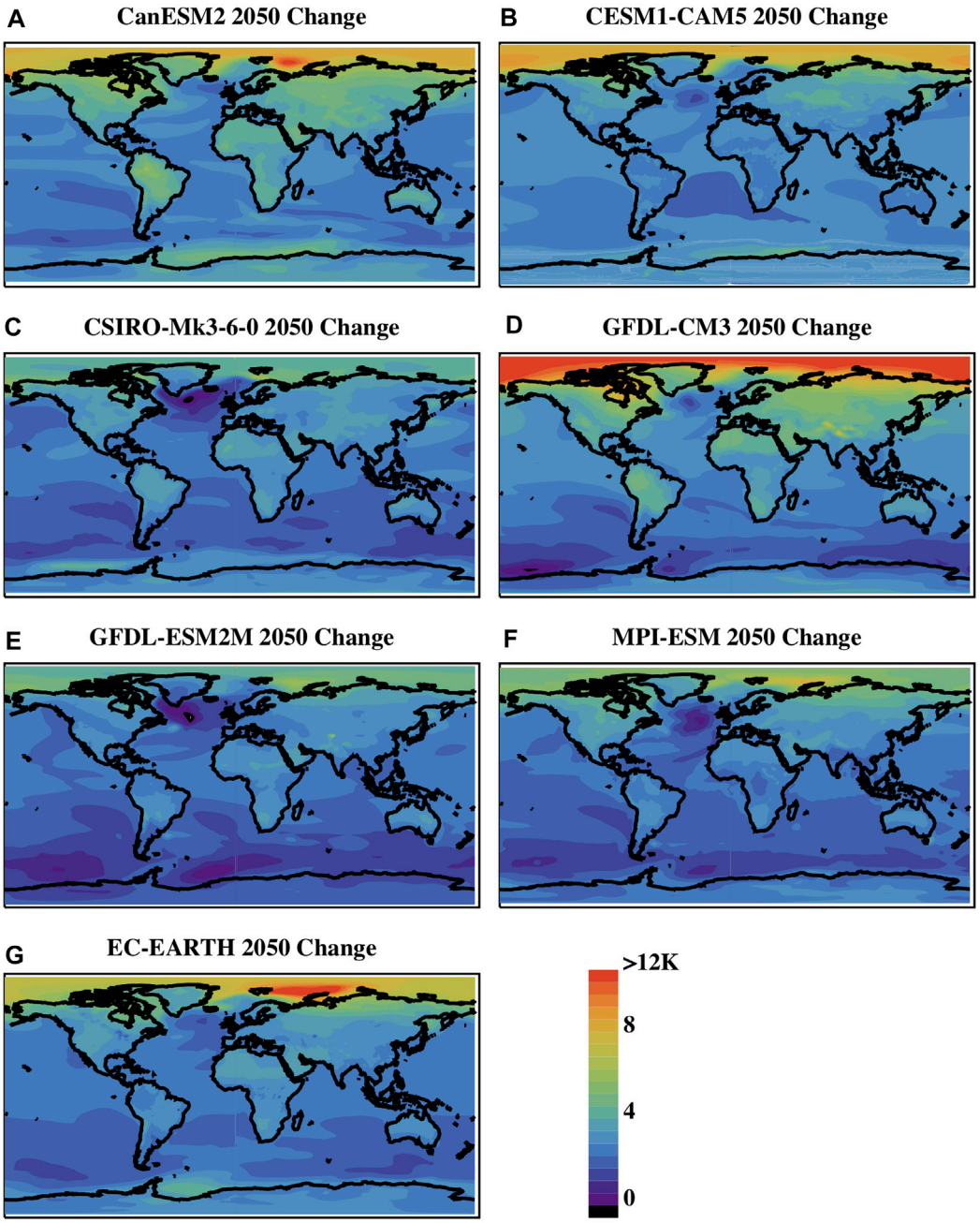

FIGURE 1 | The annual ensemble mean surface air temperature change for the 2050s relative to the reference period for different SMILEs including **(A)** CanESM2, **(B)** CESM1-CAM5, **(C)** CSIRO-Mk-3-6-0, **(D)** GFDL-CM3, **(E)** GFDL-ESM2M, **(F)** MPI-ESM, and **(G)** EC-EARTH.

air temperature change in all individual ensemble members is larger than the maximum ensemble member global mean decadal temperature change. This metric provides an estimate of when the anthropogenic signal of amplified Arctic warming emerges from the internal climate noise. By considering that the ensemble envelope of Arctic warming is outside the envelope of global change, it accounts for internal variability in both the Arctic and global temperature change. Note that this metric is sensitive to the choice of averaging length (which is chosen here to be decadal) and the choice that the Arctic warming is outside the range of global warming (instead of greater than a standard deviation metric or greater than the warming of an individual ensemble member for example). However, the choices made here are reasonable given the rapid change underway in the Arctic, the

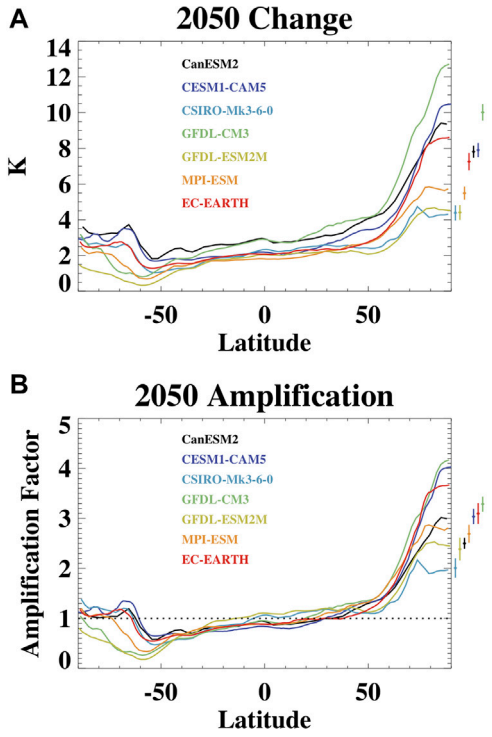

FIGURE 2 | (A) The zonal mean change in surface air temperature for the 2050s relative to the reference period and **(B)** The amplification factor of that warming, defined as the zonal temperature change relative to the global mean change. The diamonds shown to the left indicate the ensemble mean 70–90N values for each model with the whiskers indicating one standard deviation.

internal variability in both Arctic and global warming, and the fact that the real system only has a single climate realization. It also provides a reasonable means to compare across models.

We also compare the transient Arctic warming and amplification signal to various metrics of sea ice. For this analysis, we process the ice data following Landrum and Holland (2020) to obtain time series of Northern Hemisphere monthly ice area. The sea ice data was not available from the EC-EARTH model and so that model is excluded from any analysis involving sea ice.

We also assess the changing surface albedo feedback from the individual ensemble members of the various models using the radiative kernel method (e.g., Shell et al., 2008; Soden et al., 2008). This quantifies the surface albedo feedback as:

$$\lambda_\alpha = \frac{\partial R}{\partial \alpha}\frac{d\alpha}{dT}$$

Where R is the net top of atmosphere (TOA) radiative flux, α is the surface albedo, and T is the global mean surface air temperature. We use a monthly and spatially resolved radiative kernel that quantifies the sensitivity of the TOA flux to surface albedo change ($\frac{\partial R}{\partial \alpha}$) from CESM1-CAM5 (Pendergrass et al., 2018). While radiative kernels do differ somewhat depending on the climate model from which they are computed, Soden et al. (2008) found that the quantification of feedbacks using the radiative kernel method is generally robust to the particular kernel that is used and so we use only a single kernel in our analysis. For each model that had shortwave flux data available, this kernel is then interpolated to the appropriate model grid and multiplied by the monthly and spatially resolved decadal change in surface albedo relative to the decadal global temperature change. The surface albedo is computed from the monthly averaged surface upward solar flux divided by the surface downward surface flux. We then compute a decadal timeseries of regional averages of the feedback values and also assess the spatial structure of the feedback change from maps of the feedback values. The solar flux data were not available for the MPI-ESM and EC-EARTH models and so those models are excluded from the albedo feedback analysis.

RESULTS

Conditions in 2050

To illustrate the general properties of Arctic temperature change, Arctic amplification and the differences across the models, we assess ensemble mean changes for 2050–2059 relative to the 1950–1969 base period. The decadal ensemble mean surface air temperature change at 2050 relative to 1950 is shown in **Figure 1**. All the models exhibit amplified warming in the Arctic. However, the magnitude of warming, both globally and regionally, and the location of maximum warming differ across the models. In some models (GFDL-CM3, CESM1-CAM5), the maximum warming is centered over the Arctic Ocean; whereas in others (CanESM2, GFDL-ESM2M, MPI-ESM, EC-EARTH) the maximum warming occurs in the Barents Sea. The maximum zonal mean temperature change (**Figure 2A**) also differs considerably across the models with a maximum high latitude warming of just over 4°C in GFDL-ESM2M and CSIRO-Mk3-6–0 and over 12°C in GFDL-CM3. Models with larger Arctic warming typically also have a larger amplification factor (**Figure 2B**) although there are some discrepancies which are related to the differences in global warming across the models. Across the models, the maximum zonal mean Arctic warming ranges from about 2 to 4 times the global average warming at 2050.

The 2050 temperature change and temperature amplification have a distinct seasonal structure (**Figure 3**). All models exhibit reduced Arctic amplification during the summer months from June through August, which occurs as the surface ocean gains heat and there is limited coupling with the atmosphere. Indeed, for these months, several models simulate less warming in the Arctic than for the globe as a whole and so have an amplification factor less than one during these months (**Figure 3H**). Amplified Arctic warming is generally most apparent during the fall months as heat gained by the surface during summer is fluxed back to the atmosphere. The maximum amplification factor in 2050 typically occurs in November although this timing does vary somewhat across the models. The warming extends into the winter and an

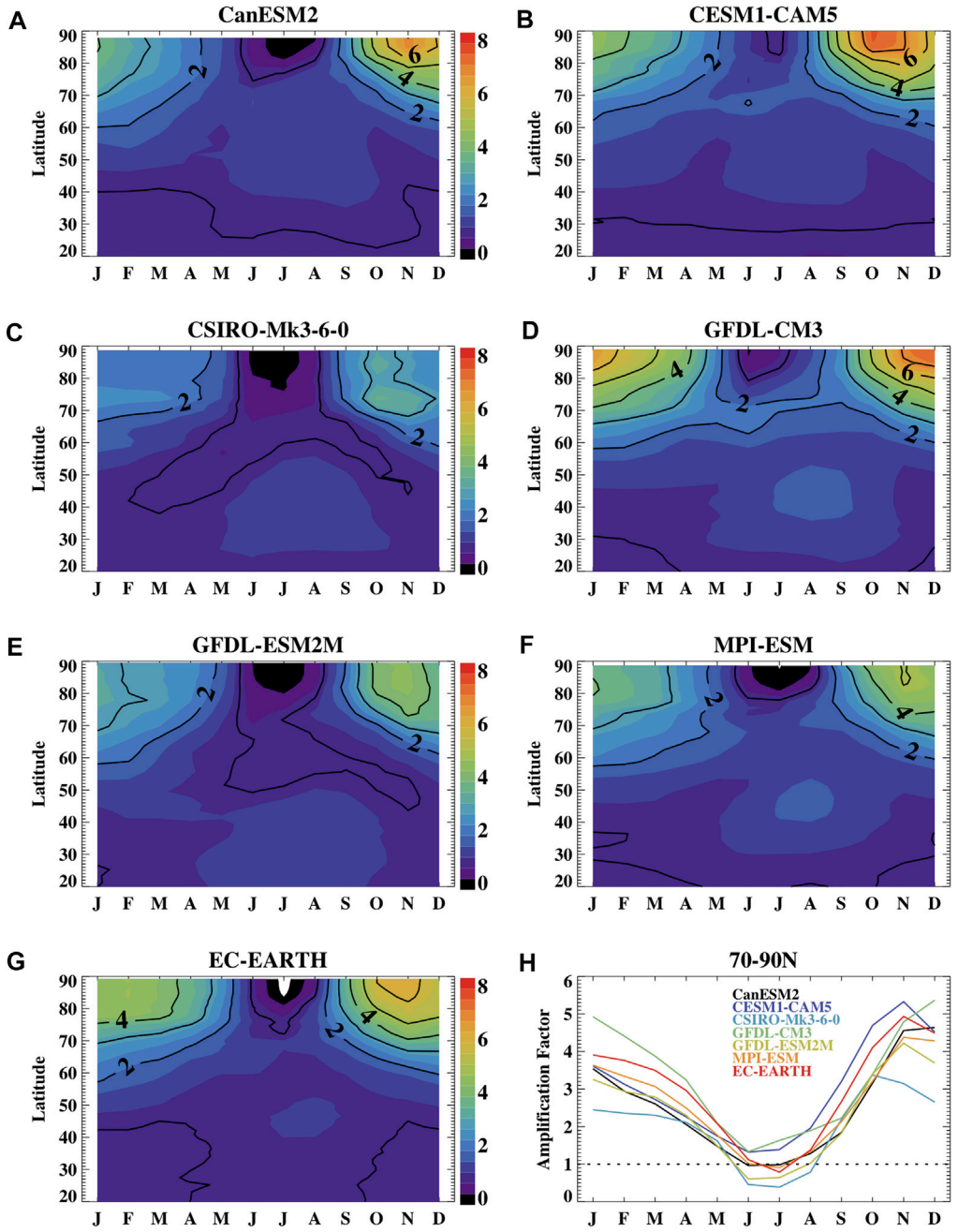

FIGURE 3 | The zonal monthly ensemble mean amplification factor at 2050 as a function of month and latitude for the different models including **(A)** CanESM2, **(B)** CESM1-CAM5, **(C)** CSIRO-Mk-3-6-0, **(D)** GFDL-CM3, **(E)** GFDL-ESM2M, **(F)** MPI-ESM, and **(G)** EC-EARTH and (final panel) the 70–90N Amplification factor at 2050 as a function of month. The lined contour interval is one. The dotted line on the final panel shows a value of one for reference.

amplified Arctic warming (amplification factor greater than one) occurs for all but the summer (JJA) months in all models. These properties of the seasonality of the surface-based amplified warming agree with results from previous modeling studies (e.g., Manabe and Stouffer, 1980; Holland and Bitz, 2003; Deser et al., 2010; Dai et al., 2019) and are consistent with observed Arctic amplification (e.g., Serreze et al., 2009).

Emergence of Surface Amplified Arctic Warming

Many of these features of Arctic amplification have been documented in previous work. Large internal climate variability has also been noted for the Arctic. Because of this, the signal-to-noise ratio of surface air temperature change is small in the Arctic relative to other parts of the

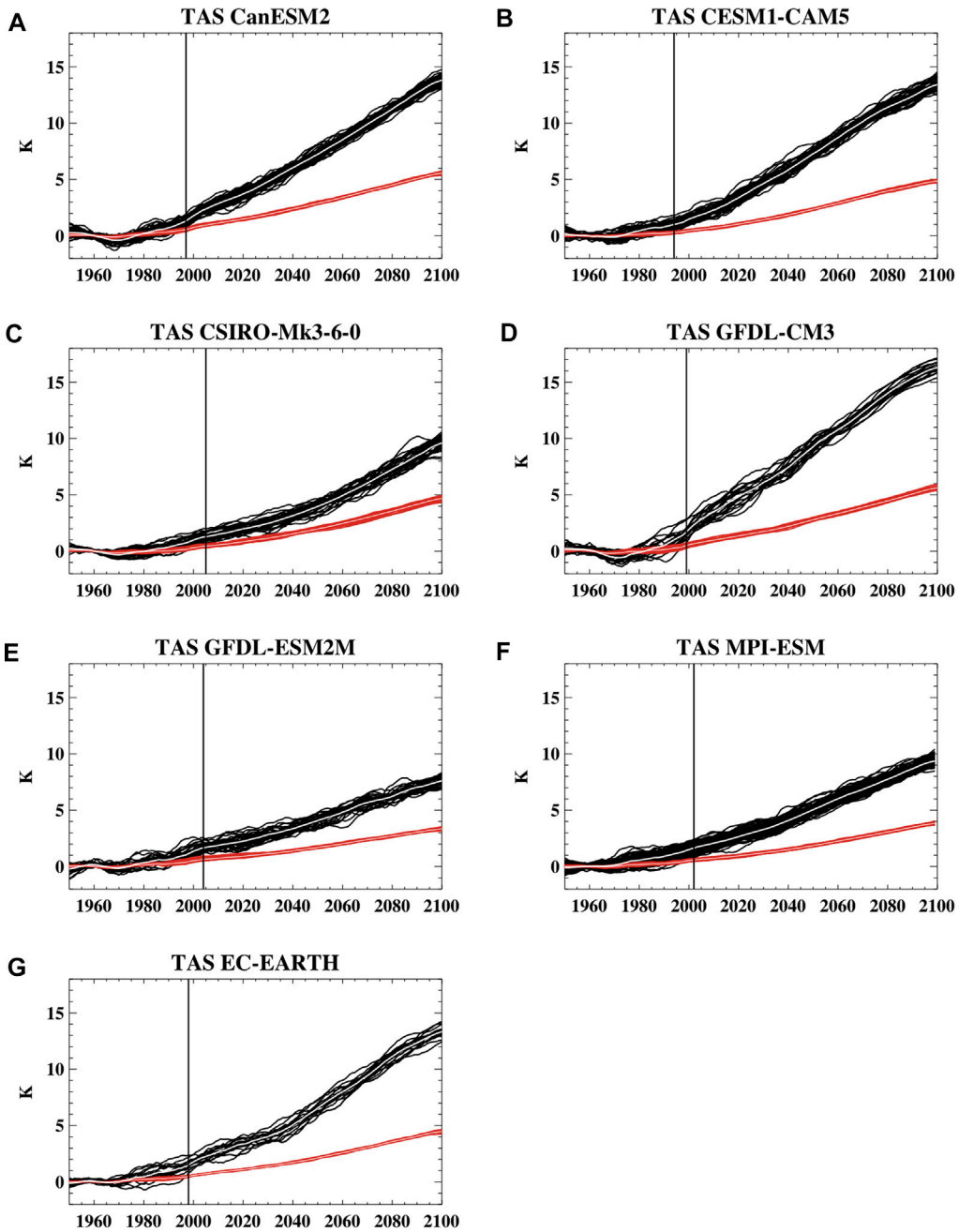

FIGURE 4 | Timeseries of decadal running mean surface air temperature change relative to the reference period for the 70–90N average in black and the globe average in red for the different models including **(A)** CanESM2, **(B)** CESM1-CAM5, **(C)** CSIRO-Mk-3-6-0, **(D)** GFDL-CM3, **(E)** GFDL-ESM2M, **(F)** MPI-ESM, and **(G)** EC-EARTH. The ToE of an amplified Arctic warming signal is indicated by the vertical line.

globe that have a modest change in temperature but also modest internal variability noise (e.g., Hawkins et al., 2020). Previous work indicates that an Arctic surface air temperature signal emerges from the noise in the first half of the 21st century, although it differs by season and by the metric used for emergence (Hawkins and Sutton, 2012). However, there is limited information on when the signal of amplified Arctic warming emerges from the background climate noise. Here we build on this previous work by assessing the emergence of Arctic amplification.

Figure 4 shows the timeseries of running decadal annual mean surface air temperature change for the 70–90N region and the globe. Based on our definition, the time of emergence of Arctic amplification occurs when the range of Arctic warming across the

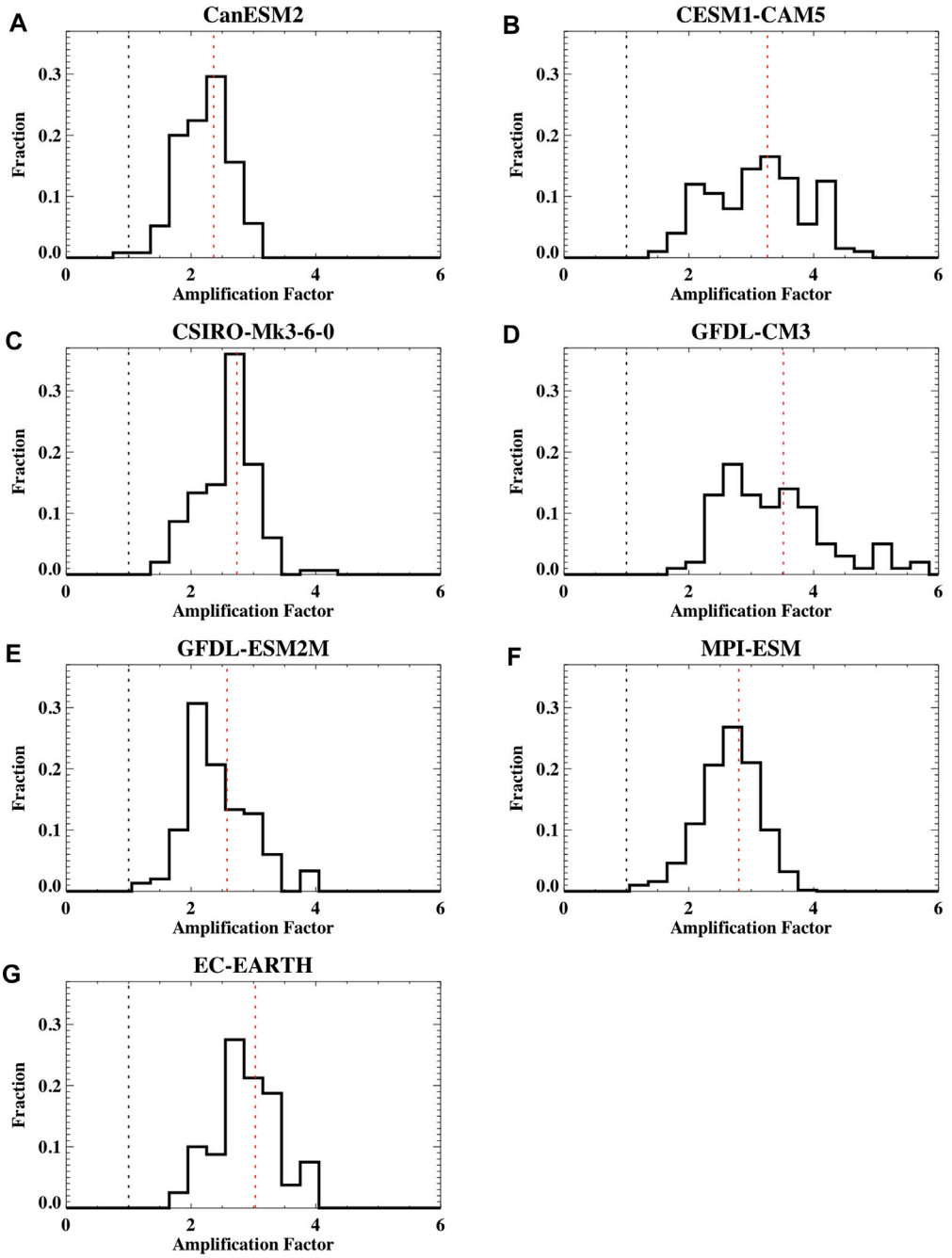

FIGURE 5 | The histogram of the annual mean Arctic amplification factor at the ToE across the different ensemble members for each SMILE including **(A)** CanESM2, **(B)** CESM1-CAM5, **(C)** CSIRO-Mk-3-6-0, **(D)** GFDL-CM3, **(E)** GFDL-ESM2M, **(F)** MPI-ESM, and **(G)** EC-EARTH. A value of one (no amplification) is shown for reference in the black dotted line. The average amplification factor at the ToE is shown in the red dotted line.

ensemble members is outside the envelope of the global mean warming. This timing differs across the models by approximately a decade, with the earliest emergence in 1994 in CESM1-CAM5 and the latest in 2005 in CSIRO-Mk3-6–0. The timing for the annual mean emergence is similar to that of a fall amplification emergence (not shown) because the annual mean warming is dominated by warming in the fall. At the ToE, the magnitude of the ensemble mean Arctic warming ranges from 1.0 to 1.7°C across the models and the 70–90N amplification factor varies from 2.4 to 3.5 (**Table 1**). From GISTEMP observations (GISTEMP Team, 2021), the observed 70–90N amplification factor for the 2000–2009 decadal

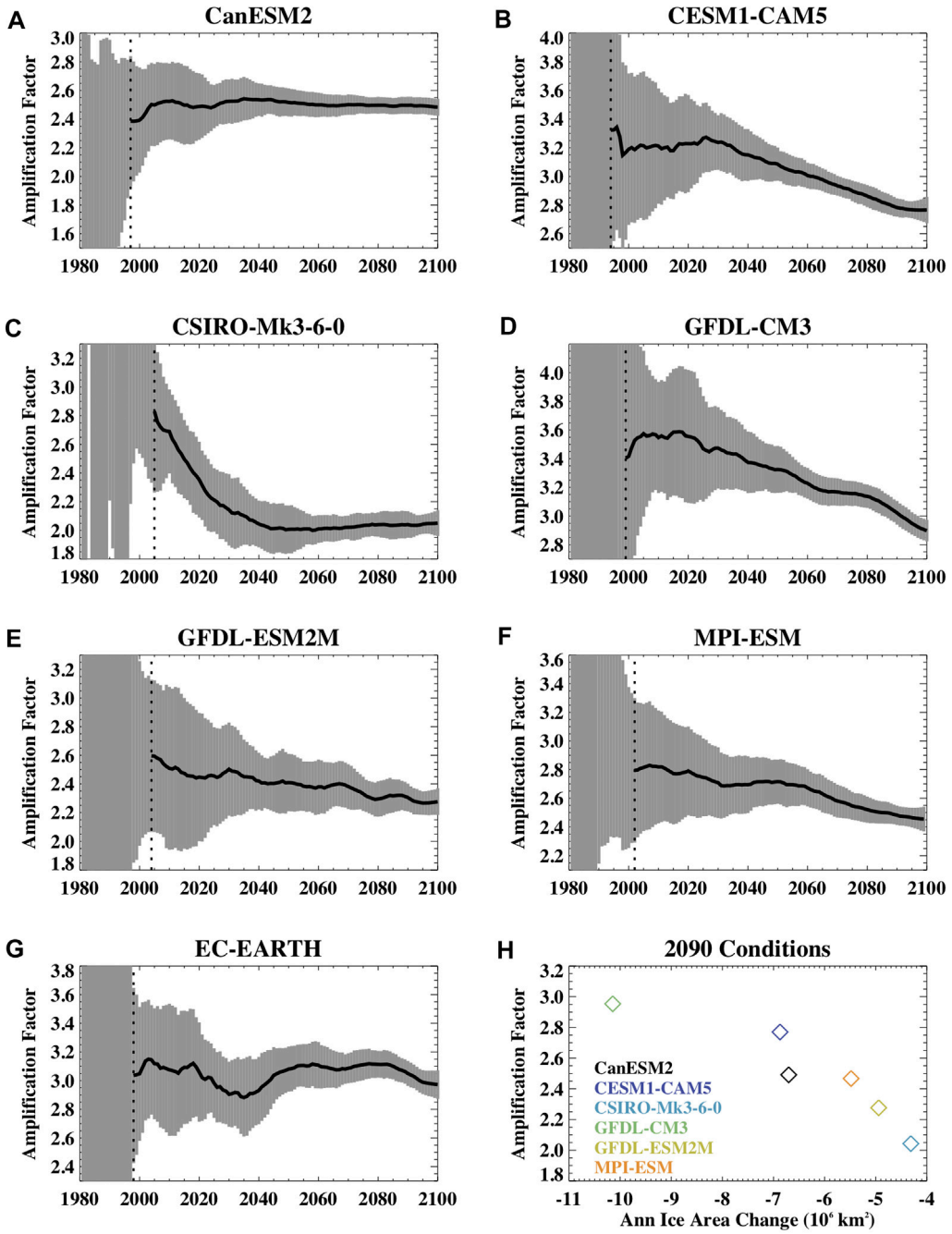

FIGURE 6 | The 1980–2100 timeseries of the Arctic amplification factor for different SMILES computed from annual mean temperature including for **(A)** CanESM2, **(B)** CESM1-CAM5, **(C)** CSIRO-Mk-3-6-0, **(D)** GFDL-CM3, **(E)** GFDL-ESM2M, **(F)** MPI-ESM, and **(G)** EC-EARTH. The black line shows the ensemble mean amplification factor and the grey shading shows the standard deviation across the ensemble members. The dashed vertical line is the time of emergence. Note that the *y*-axis values are different across the different panels to better illustrate the changes within a model over time but all panels have the same *y*-axis range of 1.5. Panel **(H)** shows the average 2090s Amplification Factor as a function of the annual sea ice area loss across the models (except for EC-EARTH for which no sea ice data was available).

average relative to the 1950–1969 base period is about 2.2 and it increases to 2.9 for the 2010–2019 average period, indicating large decadal variability in this property from the observations. The simulated values at ToE are generally consistent with the observations given the internal variability uncertainty. The GFDL based models, GFDL-CM3 and GFDL-ESM2M, are an interesting case study given that they are from the same model lineage and are quite close within the climate model "family tree" (Knutti et al., 2013), but differ considerably in their ToE amplification factor with a value of 3.5 in GFDL-CM3 and 2.6 in GFDL-ESM2M. These models also differ in their equilibrium climate sensitivity

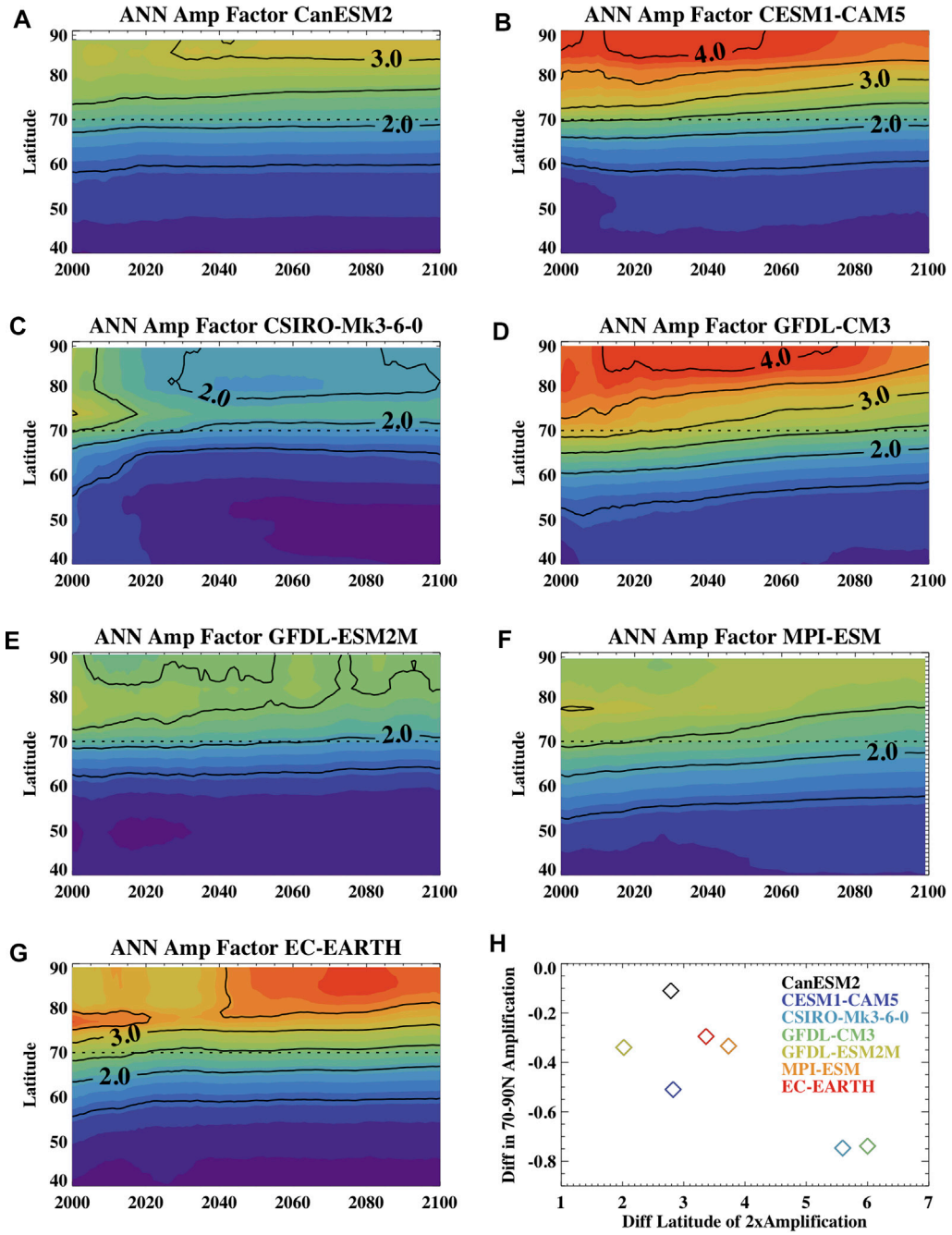

FIGURE 7 | The ensemble mean annual mean amplification factor for the different SMILES over the 21st century as a function of year and latitude for **(A)** CanESM2, **(B)** CESM1-CAM5, **(C)** CSIRO-Mk-3-6-0, **(D)** GFDL-CM3, **(E)** GFDL-ESM2M, **(F)** MPI-ESM, and **(G)** EC-EARTH. The lined contour interval is 0.5. Panel **(H)** shows the 21st century change in the latitude at which doubled amplification occurs relative to the change in the 70–90N amplification factor for the ensemble means from different SMILES. The 21st century change is computed as the ensemble mean values in 2099 minus that in 2000.

which is likely due to different atmospheric moist physics (Winton et al., 2013). Our results suggest that these (and possibly other) aspects of model uncertainty between GFDL-CM3 and GFDL-ESM2M also influence the magnitude of Arctic amplification.

Notably, even at the time of emergence, there is a large variation in the amplification factor across ensemble members that is often larger than the across-model spread in the ensemble mean amplification (**Table 1**). This indicates large uncertainty in this metric due to internal climate

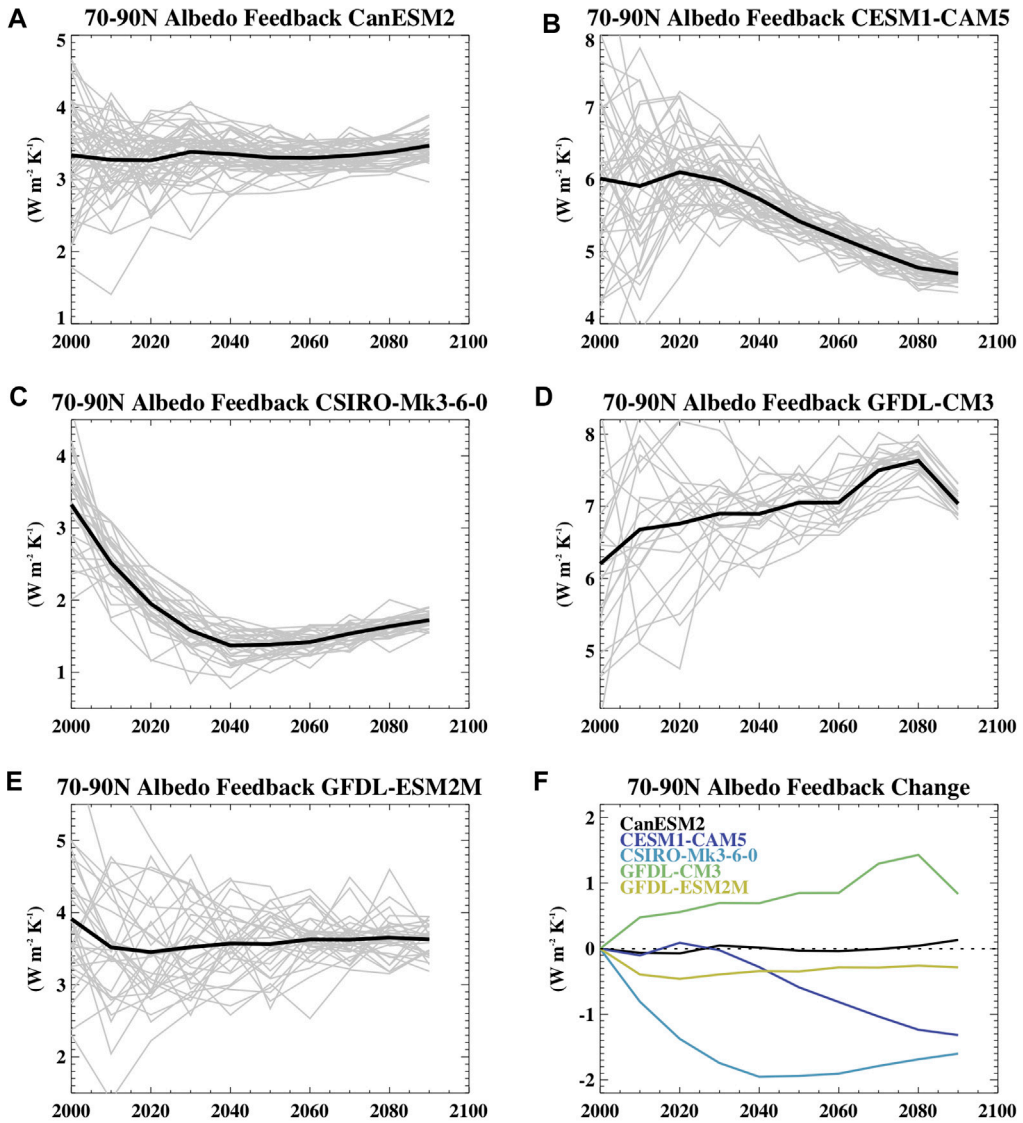

FIGURE 8 | The 70–90N annual decadal mean surface albedo feedback in models that had shortwave terms available including for **(A)** CanESM2, **(B)** CESM1-CAM5, **(C)** CSIRO-Mk-3-6-0, **(D)** GFDL-CM3, and **(E)** GFDL-ESM2M. The final panel **(F)** shows the change in the ensemble mean albedo feedback over the 21st century computed as the ensemble mean values for the 2090–2099 average minus the 2000–2009 average to allow comparison across the models. For panels **(A–E)**, individual ensemble members are shown in grey and the ensemble mean in black.

variability (**Figure 5**). The spread in amplification is primarily related to across-member spread in the decadal Arctic temperature change. This is consistent with previous work which has indicated large internal-variability uncertainty in decadal Arctic temperature variations (Hodson et al., 2013). The spread in the amplification factor across ensemble members within a SMILE at the time of emergence is correlated to the Northern Hemisphere annual mean sea ice area. Members with higher Arctic warming and consequently higher amplification typically exhibit lower sea ice. The correlation between the ensemble member values of ToE annual average ice area and their ToE amplification is similar for the different models at about R = −0.5, except in the two GFDL models where the relationship between ice area and amplification is weaker at R = −0.2 (for GFDL-CM3) and R = −0.3 (for GFDL-ESM2M).

Evolution of Arctic Amplification Over the 21st Century

Projected change in the amplification of annual mean Arctic warming over the 21st century is shown in **Figure 6**. The uncertainty associated with internal variability, as quantified by

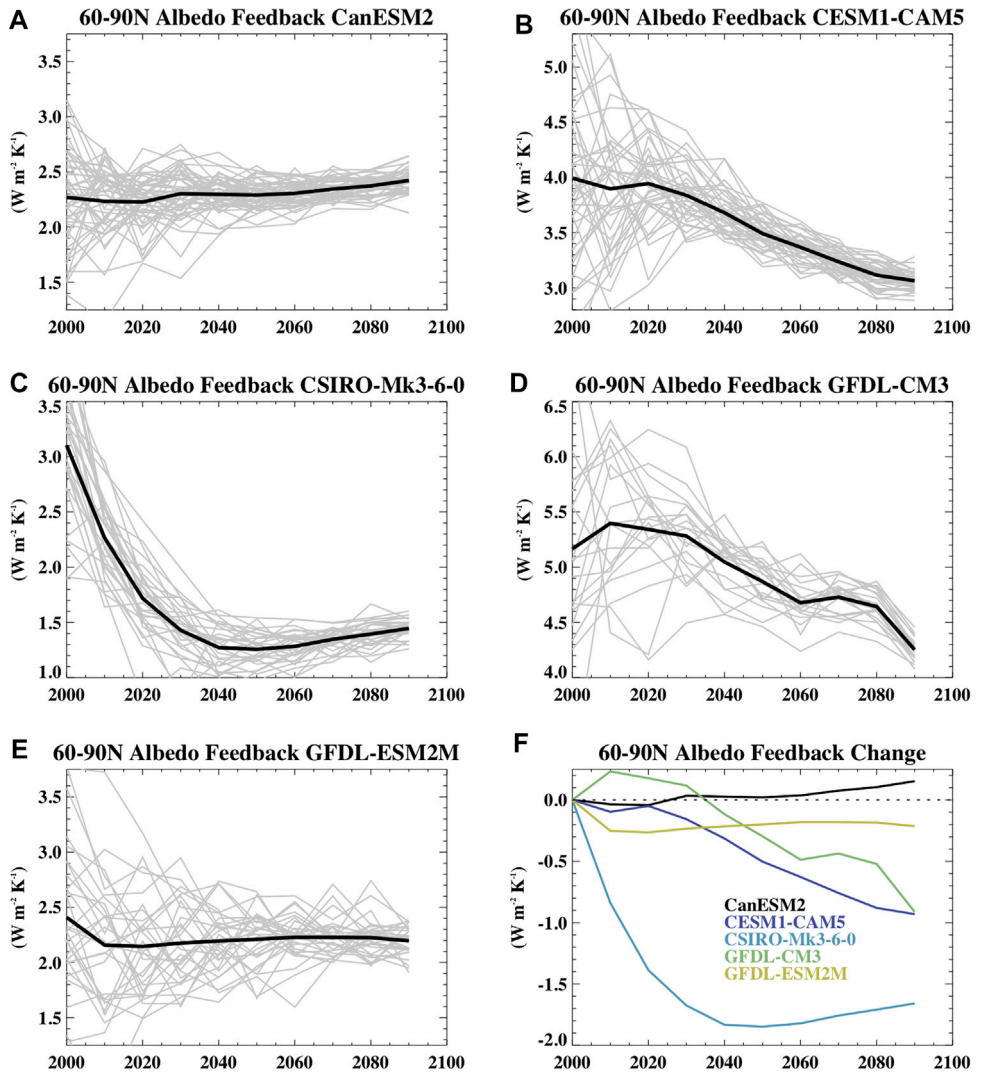

FIGURE 9 | Same as **Figure 8** but for the 60–90N average.

the spread across ensemble members, declines over the 21st century. This arises because the change in temperature since the mid-20th century for both the Arctic and the globe become large relative to the internal variability uncertainty in that change. It is an indication that as time progresses the ensemble members have a similar Arctic temperature change relative to the global change. Note that this does not necessarily represent a change in the internal variability of Arctic or global temperatures over the 21st century. Indeed, the within-model spread in the annual mean Arctic air temperature changes little over time and in most models, the spread in global temperatures also exhibits little change (not shown).

The annual ensemble mean amplification factor declines over the 21st century in the models (**Table 1**). This is largely related to a reduced amplification in the southern portion of the Arctic domain as is evident by the time series of the zonal mean amplification factor (**Figure 7**) when considering the values near 70N. We expect that this is associated with the location of sea ice loss which will contribute to a warming of the overlying atmosphere and which transitions northward over time. In some models, such as CanESM2 and EC-Earth, the change in 70N temperatures is relatively small and compensated in part by an increased warming amplification near the pole, leading to only a small reduction in the 70–90N amplification. Other models such as CESM1-CAM5 and GFDL-CM3, have a 21st century reduction in the amplification across the entire Arctic domain.

Sea ice both responds to and affects Arctic surface warming. At the end of the 21st century, models with larger annual mean amplification (and typically larger Arctic warming) have larger annual mean sea ice loss (**Figure 6H**). Interestingly, there is no consistent relationship between the 21st century amplification and historical ice conditions, including 1950s sea ice area and volume (not shown). Within an individual model, the amplification factor declines over the 21st century with increasing ice loss. In response to global warming and as a consequence of snow and ice loss, the Arctic surface albedo declines over the 21st century. The magnitude of this decline

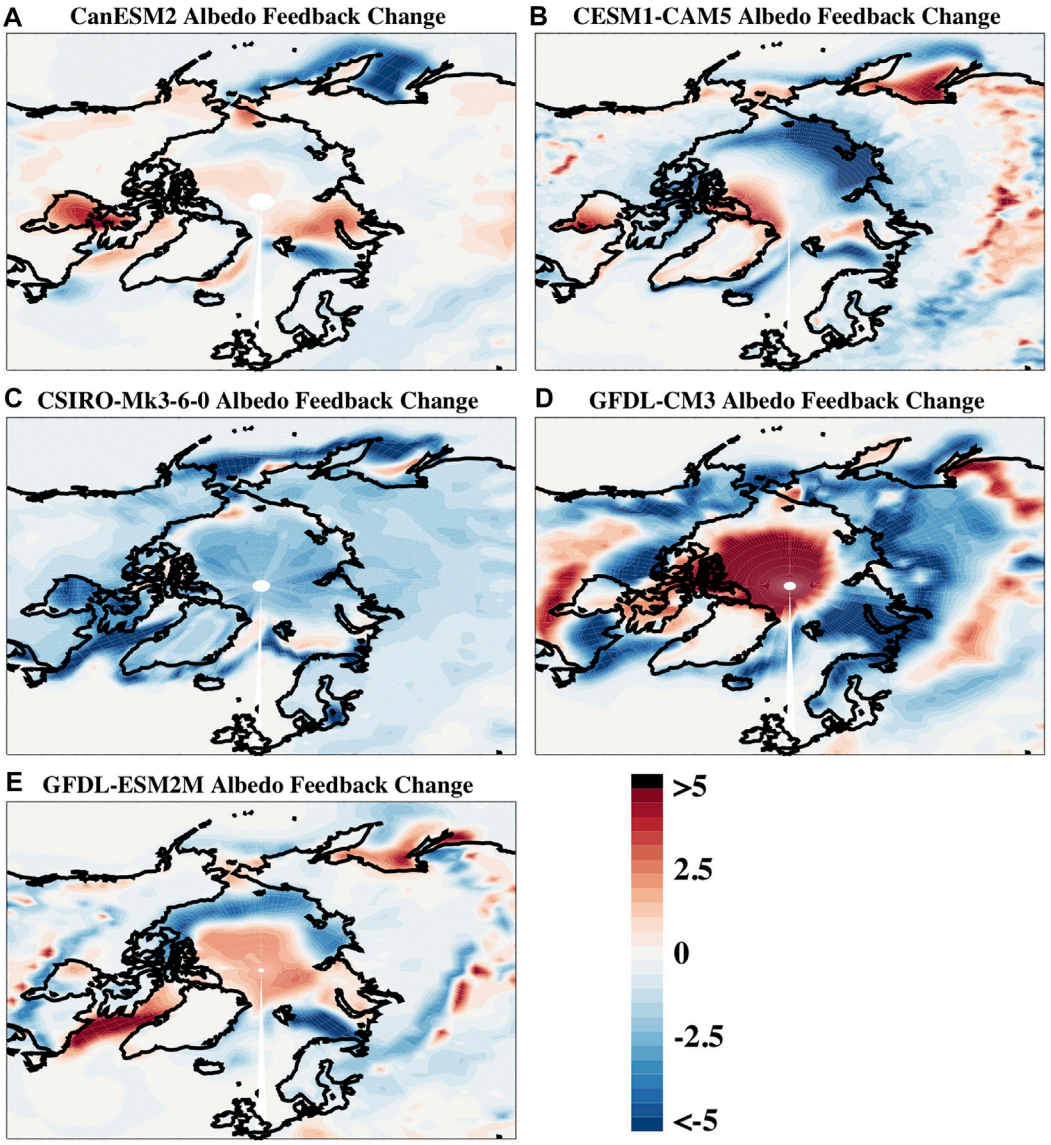

FIGURE 10 | The changes in the ensemble mean surface albedo feedback for the 2090–2099 decadal average minus the 2000–2009 decadal average for the different models including **(A)** CanESM2, **(B)** CESM-CAM5, **(C)** CSIRO-Mk-3-6-0, **(D)** GFDL-CM3, and **(E)** GFDL-ESM2M. Values are shown in W m^{-2} K^{-1}.

is influenced by the amount of ice and snow loss, the simulated albedo of those surfaces which can differ considerably across models (e.g., Holland and Landrum, 2015), and the interaction of those changing albedos with the large annual cycle in solar radiation. It is possible that with continued warming, the albedo changes can saturate (for example, with complete sea ice loss in a particular month), and since the global temperature will continue to increase, the albedo feedback can weaken and thus contribute to a declining amplification. To assess this, we have computed the annual albedo feedback from decadal averages over the 21st century relative to the 1950–1969 base period for the models with available fields. **Figure 8** shows the timeseries of feedback strength for the 70–90N region. For this region, three of the five models (CESM1-CAM5, CSIRO-Mk3-6-0, GFDL-ESM2M) show a declining feedback strength, CanESM2 has little change, and GFDL-CM3 shows an increase in strength. However, if we assess conditions for 60–90N (**Figure 9**), we find that all models have a declining feedback strength, except for CanESM2, which has little change. On the global scale, all models simulate a weakened albedo feedback by the end of the 21st century (not shown).

To better understand these disparate results, we assess the regional structure of the changing albedo feedback (**Figure 10**). This indicates that, in all models, there are ocean regions of reduced feedback strength, suggesting an albedo saturation. These are likely associated with regional sea ice loss that has largely maxed out in these areas for the sunlit time of year. In most models (except CSIRO-Mk3-6-0), there are also sizable

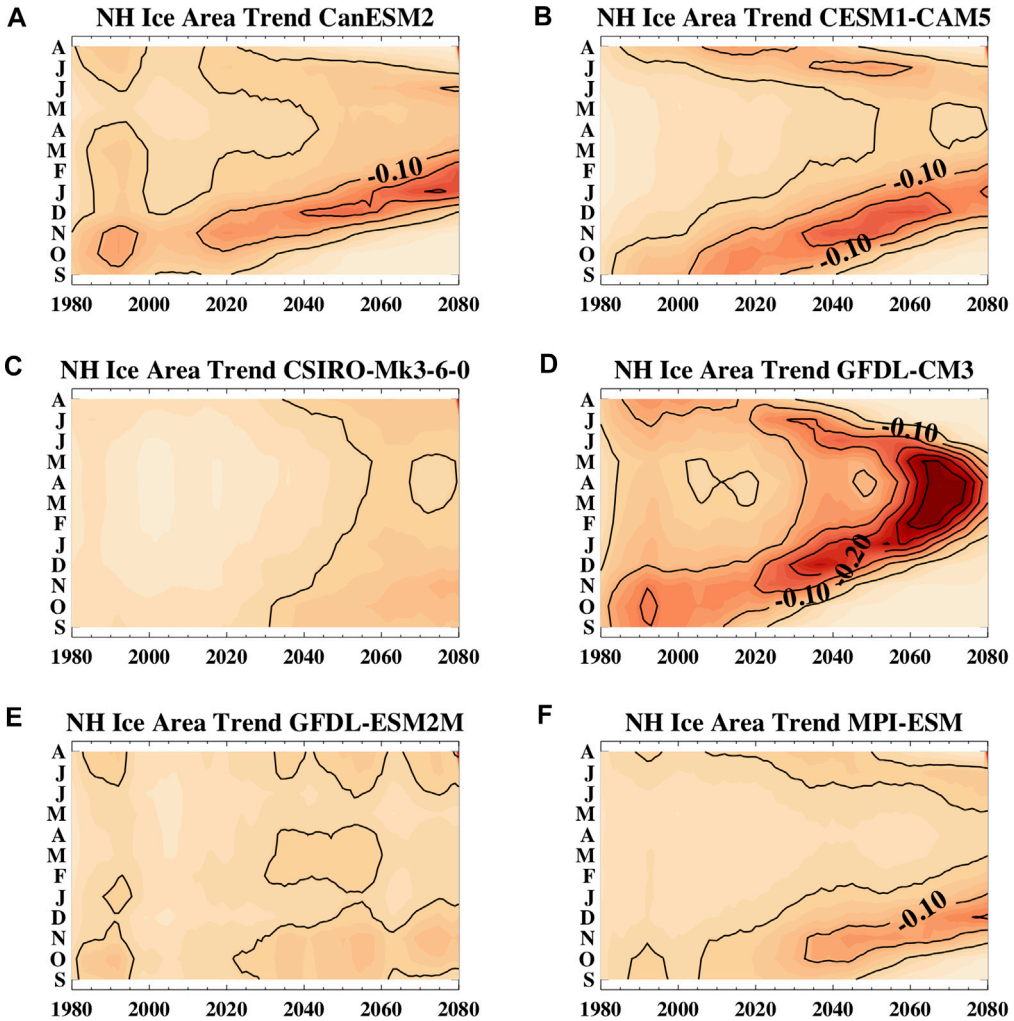

FIGURE 11 | The 20-years running trend of Northern Hemisphere ensemble mean sea ice area for the different models as a function of month and year for **(A)** CanESM2, **(B)** CESM1-CAM5, **(C)** CSIRO-Mk-3-6-0, **(D)** GFDL-CM3, **(E)** GFDL-ESM2M, and **(F)** MPI-ESM. The lined contour interval is 0.05 million km^2 per year. Note that as in **Figure 12**, the *y*-axis runs from September on bottom through August on top. Sea ice data was not available for EC-Earth and so that model is not shown.

ocean regions of increasing feedback strength often in the central Arctic where ice is still being lost during the spring and summer months. Interestingly, reductions in the Arctic ocean feedback strength in CSIRO-MK3-6-0 happen despite low sea ice loss (shown and discussed below in reference to **Figure 11**), suggesting a possible role for the snow on sea ice. Changing terrestrial snow also appears to be important in some models, leading to a weakened feedback indicative of an albedo saturation effect over land. This is most notable in GFDL-CM3 where the weakened feedback in high latitude terrestrial regions compensates for the strengthened feedback over the Arctic ocean and explains the discrepancy for the 60–90N versus 70–90N average feedback strength change in that model. Overall, the reduced high latitude feedback strength in most of the models will tend to reduce Arctic amplification but there is obviously considerable complexity in the interplay of regional changes in the ice and snow and the solar insolation annual cycle. Note that our results appear in conflict with Schneider et al. (2018) who found an increase in the global surface albedo feedback in the 21st century. However, there are differences in our analysis that we expect are responsible. Most notable are the use of large ensembles in this study and an analysis that computes decadal changes relative to the same base period of 1950–1969. In contrast, Schneider et al. (2018) computed the albedo feedback using temperature and albedo changes over 23 years periods at the beginning and end of the 21st century (rather than decadal mean changes from the 1950–1969 base period), used single simulations from multiple models, and focused on global rather than Arctic surface albedo feedbacks.

With further and finally complete ice and snow loss in the sunlit season, we would expect that further reductions in the surface albedo would be negligible and that the albedo feedback

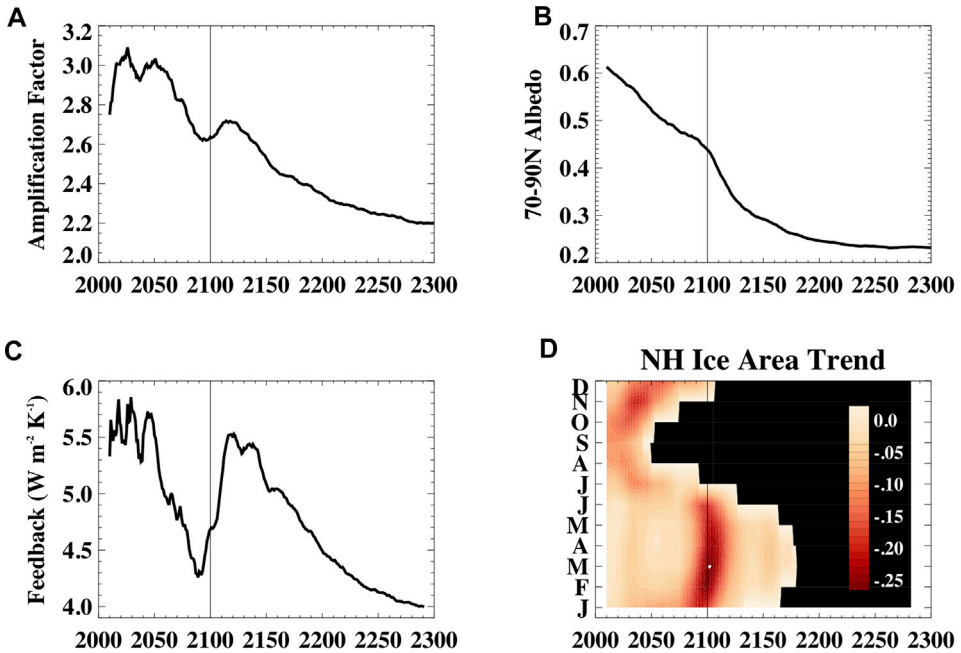

FIGURE 12 | Results from CESM-CAM5 runs that are extended to 2300 using the RCP8.5 scenario including, **(A)** the annual mean Arctic amplification factor, **(B)** the annual mean 70–90N effective albedo, **(C)** the 70–90N surface albedo feedback, and **(D)** the running decadal trend in monthly sea ice area. Values in panel (a), (b), and (c) use 10-years running means. The annual mean effective albedo is computed as the annual surface upward solar radiation divided by the annual mean surface downward radiation and represents the fraction of solar radiation reflected from the surface on an annual basis. In panel (d), black regions indicate when the ice area is lower than one million km^2 and trends are shown in units of million km^2 per year.

would saturate across the northern high latitudes. This state is not yet reached in the SMILE climate simulations considered here. However, CESM-CAM5 runs extended to 2300 simulate complete Arctic ice loss (Meehl et al., 2013), and show that further Arctic albedo changes are minimal after about 2150 (**Figure 12B**), the albedo feedback weakens after 2150 (**Figure 12C**), and Arctic amplification declines from 2000–2300 (**Figure 12A**). Interestingly, this decline is not linear and the albedo feedback actually strengthens in the early part of the 22nd century (**Figure 12C**). There are indications that this is associated with the evolving seasonality of sea ice loss (**Figure 12D**). In these simulations, sea ice in July-September shows large declines in the 21st century and reaches an area less than one million km^2 by 2100. However, an acceleration of May and June ice loss occurs around 2100 (**Figure 12D**). Because May and June are a time of high solar insolation, there is a consequent acceleration in the annual albedo reduction (**Figure 12B**). This contributes to a brief reversal in the declining albedo feedback and Arctic amplification. Thus, to understand the evolving amplification of Arctic warming, we must consider variations in the rate of ice and snow loss over both time and season. Notably, the strengths of other Arctic feedbacks are also likely to change in the warming climate and affect the transient amplification signal across the models. For example, the lapse rate feedback is also tightly tied to sea ice loss (e.g., Boeke et al., 2020; Feldl et al., 2020) suggesting that its strength will also be impacted by the changing rate of seasonal ice loss.

Consistent with changes in seasonality of ice loss, the seasonality of Arctic warming also changes over the 21st century (**Figure 13**). Most models simulate that the maximum warming trends are initially largest in fall (October-November) but shift to winter (or even spring in the case of GFDL-CM3) over the 21st century. As noted, the changing seasonality of warming and how it differs across the models is related to their simulated ice loss rates (**Figure 11**). In the late 20th-early 21st centuries, the highest ice loss rates are in September and the surface heat gained over the melt season is then fluxed to the atmosphere resulting in maximum warming rates a month or so later. However, as ice-free conditions are reached in September, the maximum sea ice loss rates shift to later in the fall and winter. This indicates a longer melt season, a shift in when the surface loses its accumulated summer heat, and a later freeze up. In models with lower ice loss rates, such as CSIRO-Mk3.6 and GFDL-ESM2M, there is only a minimal seasonal shift in atmospheric warming in the 21st century.

CONCLUSION

Arctic amplification is a hallmark of the climate response to changing external forcing. It arises from multiple positive feedbacks that are related to the unique climate conditions of the Arctic (e.g., Pithan and Mauritsen, 2014). Among the most important of these are the surface albedo feedback, associated

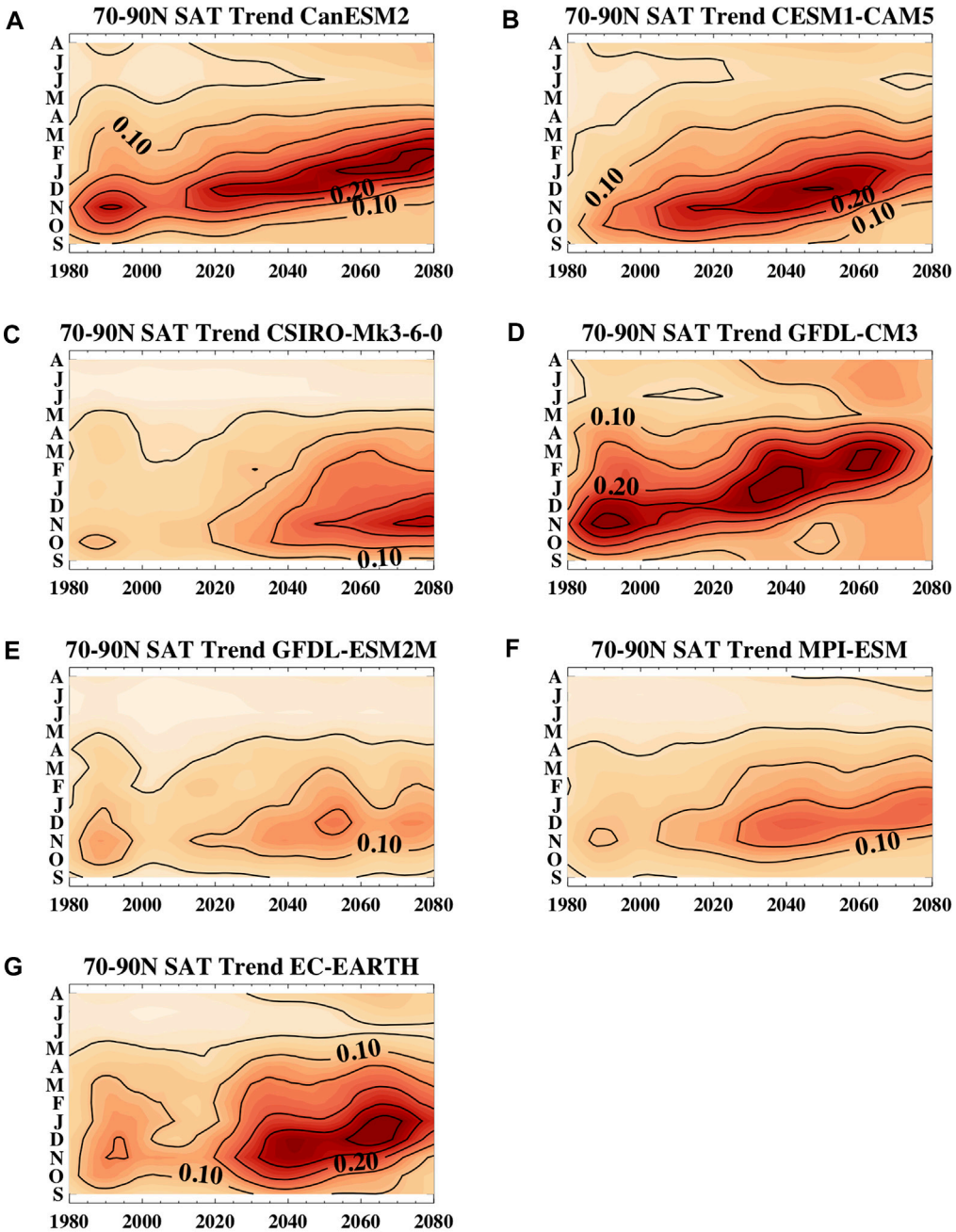

FIGURE 13 | The running 20-years trend in the 70–90N ensemble mean surface air temperature as a function of month over the 21st century in the different SMILES including **(A)** CanESM2, **(B)** CESM1-CAM5, **(C)** CSIRO-Mk-3-6-0, **(D)** GFDL-CM3, **(E)** GFDL-ESM2M, **(F)** MPI-ESM, and **(G)** EC-EARTH. The lined contour interval is 0.05°C per year. Note that the *y*-axis runs from September on bottom through August on top to better highlight the changing seasonality of warming in the models.

with the loss of high-albedo surfaces, and the positive lapse rate feedback, associated with variations in the vertical structure of temperature changes (e.g., Goosse et al., 2018). Both these feedbacks are strongly related to sea ice loss (e.g., Boeke et al., 2020; Feldl et al., 2020) and are both driven by and reinforce surface-based amplified warming in the Arctic. Notably, the positive Arctic feedbacks also lead to large internal variability in the region. Because these feedbacks are dependent on the climate state within the Arctic, it follows that their strength may vary with conditions such as the sea ice area and albedo.

Here we have considered the emergence and transient nature of amplified warming in the Arctic. We have used simulations from the multi-model large ensemble (Deser et al., 2020) which includes seven climate models that have performed initial-condition large ensembles that include the

period from 1950–2100. The availability of large ensembles allows us to diagnose when amplified Arctic warming in response to rising greenhouse gases emerges from the internal variability of the climate system. Assessing this across multiple models provides information on the influence of model structural uncertainty on the characteristics of Arctic amplification.

We find that amplified Arctic warming emerges between 1994 and 2005 across all of the large ensembles and so the detection and timing of an anthropogenic signal in the amplified Arctic warming differs by about a decade across the models. The emergence of other characteristics of Arctic climate from these simulations is discussed in Landrum and Holland (2020). While an anthropogenically-driven Arctic amplification emerges near the transition of the 20th-21st centuries, the magnitude of that amplification remains quite uncertain at that time due to the influence of internal variability. It also varies considerably across the models, with the ensemble mean amplification factor ranging from 2.4 in CanESM2 to 3.5 in GFDL-CM3.

Over the course of the 21st century, the uncertainty in amplification magnitude that is associated with internal variability declines. However, the range in the amplification factor across the models remains similar, varying in 2,100 from a factor of 2.0 in CSIRO-Mk3-6-0 to 3.0 in EC-EARTH. This indicates that structural model uncertainty in the amplification magnitude remains high. In all models, the amplification factor declines over the 21st century, although in some (CanESM2 and EC-EARTH), the change is small. Analysis suggests that the 21st century reduction in Arctic amplification is associated in part with a declining surface albedo feedback strength. This is consistent with a possible "albedo saturation" effect in which the globe keeps warming as greenhouse gas concentrations rise, but ongoing reductions in surface albedo become limited due to complete sea ice or terrestrial snow loss during the sunlit season. However, in considering spatial maps of the 21st century albedo feedback change, we find that while this mechanism appears present in some high latitude locations in all the models with available data in the 21st centuries, other regions simulate a strengthening feedback as further ice (and snow) loss occur. Thus, for the 21st century, there are considerable complexities in the changing Arctic surface albedo feedback that are associated with spatial variations in the sea ice and terrestrial snow loss and the seasonality of that loss.

To assess how these factors play out with continued warming, we have also considered a CESM1-CAM5 simulation that has been extended to 2300 using RCP8.5 extension forcing (Meehl et al., 2013). This model reaches complete loss of the Arctic sea ice by the end of the 22nd century. We find that with total Arctic sea ice loss, the albedo reductions max out. This results in a saturation of the albedo feedback and further reductions in the amplification factor in the 22nd and 23rd centuries. However, reversals in the declining amplification occur in the early 22nd century when there is accelerated ice loss in May and June; a time of year with high solar insolation. This results in a temporary increase in the albedo feedback strength and Arctic amplification before complete ice loss occurs.

The characteristics of the transient nature of the amplification factor highlight the importance of seasonality in ice loss and albedo changes. Previous work (e.g., Manabe and Stouffer, 1980) has shown that amplified Arctic warming is a seasonal phenomenon and is highest in fall. We find that the seasonality of this signal transitions in the 21st century. In particular, the maximum rate of surface air temperature change transitions from the fall months in the early 21st century to winter or even spring by 2100. This transition and how it varies across the models is related to the seasonal timing of sea ice loss and the consequences that this has for the seasonality of increased air-sea heat exchange.

Taken together, our results show that while Arctic amplification is a defining characteristic of global warming, its magnitude and seasonality are likely to change with the changing climate. This has implications for comparisons across models and suggests that differences in models for a particular time period should consider that the amplification signal within a model may not be static over time. It also has implications for using paleoclimate records to constrain the magnitude of amplification in a future climate (e.g., Miller et al., 2010) given that the strength of feedbacks and consequent amplification are dependent on the particular features of a given climate state.

DATA AVAILABILITY STATEMENT

Publicly available datasets were analyzed in this study. This data can be found here: https://www.cesm.ucar.edu/projects/community-projects/MMLEA/

AUTHOR CONTRIBUTIONS

MH conceived of the study, performed much of the analysis, and wrote the article. LL contributed analysis of the sea ice data and to the writing of the article.

FUNDING

MH and LL acknowledge funding from the National Science Foundation under award OPP-1724748. MH's contributions were also supported by the National Center for Atmospheric Research (NCAR), which is a major facility sponsored by the NSF under Cooperative Agreement 1852977.

ACKNOWLEDGMENTS

We acknowledge the US CLIVAR Working Group on Large Ensembles for organizing the Multi-model Large Ensemble project and making simulations available. We also acknowledge computing resources (doi:10.5065/D6RX99HX) provided by the Climate Simulation Laboratory at NCAR's

Computational and Information Systems Laboratory, sponsored by the National Science Foundation and other agencies. We thank all of the modelling groups listed in **Table 1** for making their Large Ensemble simulations available. We thank Dirk Notz and an reviewer for helpful comments that led to improvements in the manuscript.

REFERENCES

Boeke, R. C., and Taylor, P. C. (2018). Seasonal Energy Exchange in Sea Ice Retreat Regions Contributes to Differences in Projected Arctic Warming. *Nat. Commun.* 9, 5017. doi:10.1038/s41467-018-07061-9

Boeke, R. C., Taylor, P. C., and Sejas, S. A. (2021). On the Nature of the Arctic's Positive Lapse-Rate Feedback. *Geophys. Res. Lett.* 48, e2020GL091109. doi:10.1029/2020GL091109

Bonan, D. B., Armour, K. C., Roe, G. H., Siler, N., and Feldl, N. (2018). Sources of Uncertainty in the Meridional Pattern of Climate Change. *Geophys. Res. Lett.* 45 (17), 9131–9140. doi:10.1029/2018GL079429

Bonan, D. B., Lehner, F., and Holland, M. M. (2021). Partitioning Uncertainty in Projections of Arctic Sea Ice. *Environ. Res. Lett.* 16 (4), 044002. doi:10.1088/1748-9326/ABE0EC

Cai, Z., You, Q., Wu, F., Chen, H. W., Chen, D., and Cohen, J. (2021). Arctic Warming Revealed by Multiple CMIP6 Models: Evaluation of Historical Simulations and Quantification of Future Projection Uncertainties. *J. Clim.* 1, 1–52. doi:10.1175/JCLI-D-20-0791.1

Dai, A., Luo, D., Song, M., and Liu, J. (2019). Arctic Amplification Is Caused by Sea-Ice Loss under Increasing CO2. *Nat. Commun.* 10, 121. doi:10.1038/s41467-018-07954-9

Deser, C., Lehner, F., Rodgers, K. B., Ault, T., Delworth, T. L., DiNezio, P. N., et al. (2020). Insights from Earth System Model Initial-Condition Large Ensembles and Future Prospects. *Nat. Clim. Chang.* 10, 277–286. doi:10.1038/s41558-020-0731-2

Deser, C., Tomas, R., Alexander, M., and Lawrence, D. (2010). The Seasonal Atmospheric Response to Projected Arctic Sea Ice Loss in the Late Twenty-First Century. *J. Clim.* 23, 333–351. doi:10.1175/2009JCLI3053.1

Feldl, N., Po-Chedley, S., Singh, H. K. A., Hay, S., and Kushner, P. J. (2020). Sea Ice and Atmospheric Circulation Shape the High-Latitude Lapse Rate Feedback. *Npj Clim. Atmos. Sci.* 3, 41. doi:10.1038/s41612-020-00146-7

GISTEMP Team (2021). *GISS Surface Temperature Analysis (GISTEMP), Version 4*. New York, NY: NASA Goddard Institute for Space Studies. Available at: https://data.giss.nasa.gov/gistemp (Accessed 01 01, 2021).

Goosse, H., Kay, J. E., Armour, K. C., Bodas-Salcedo, A., Chepfer, H., Docquier, D., et al. (2018). Quantifying Climate Feedbacks in Polar Regions. *Nat. Commun.* 9, 1919–2013. doi:10.1038/s41467-018-04173-0

Hawkins, E., Frame, D., Harrington, L., Joshi, M., King, A., Rojas, M., et al. (2020). Observed Emergence of the Climate Change Signal: From the Familiar to the Unknown. *Geophys. Res. Lett.* 47, e2019GL086259. doi:10.1029/2019GL086259

Hawkins, E., and Sutton, R. (2012). Time of Emergence of Climate Signals. *Geophys. Res. Lett.* 39, L01702. doi:10.1029/2011GL050087

Hazeleger, W., Severijns, C., Semmler, T., Ştefănescu, S., Yang, S., Wang, X., et al. (2010). EC-earth. *Bull. Amer. Meteorol. Soc.* 91, 1357–1364. doi:10.1175/2010bams2877.1

Hodson, D. L. R., Keeley, S. P. E., West, A., Ridley, J., Hawkins, E., and Hewitt, H. T. (2013). Identifying Uncertainties in Arctic Climate Change Projections. *Clim. Dyn.* 40, 2849–2865. doi:10.1007/s00382-012-1512-z

Holland, M. M., and Bitz, C. M. (2003). Polar Amplification of Climate Change in Coupled Models. *Clim. Dyn.* 21, 221–232. doi:10.1007/s00382-003-0332-6

Holland, M. M., and Landrum, L. (2015). Factors Affecting Projected Arctic Surface Shortwave Heating and Albedo Change in Coupled Climate Models. *Phil. Trans. R. Soc. A.* 373, 20140162. doi:10.1098/rsta.2014.0162

Hu, X., Fan, H., Cai, M., Sejas, S. A., Taylor, P., and Yang, S. (2020). A Less Cloudy Picture of the Inter-model Spread in Future Global Warming Projections. *Nat. Commun.* 11, 4472. doi:10.1038/s41467-020-18227-9

Jeffrey, S., Rotstayn, L., Collier, M., Dravitzki, S., Hamalainen, C., Moeseneder, C., et al. (2013). Australia's CMIP5 Submission Using the CSIRO-Mk3.6 Model. *Aust. Meteorol. Oceanographic* 63, 1–14. doi:10.22499/2.6301.001

Kay, J. E., Deser, C., Phillips, A., Mai, A., Hannay, C., Strand, G., et al. (2015). The Community Earth System Model (CESM) Large Ensemble Project: a Community Resource for Studying Climate Change in the Presence of Internal Climate Variability. *Bull. Am. Meteorol. Soc.* 96, 1333–1349. doi:10.1175/bams-d-13-00255.1

Kirchmeier-Young, M. C., Zwiers, F. W., and Gillett, N. P. (2017). Attribution of Extreme Events in Arctic Sea Ice Extent. *J. Clim.* 30, 553–571. doi:10.1175/jcli-d-16-0412.1

Knutti, R., Masson, D., and Gettelman, A. (2013). Climate Model Genealogy: Generation CMIP5 and How We Got There. *Geophys. Res. Lett.* 40, 1194–1199. doi:10.1002/grl.50256

Landrum, L., and Holland, M. M. (2020). Extremes Become Routine in an Emerging New Arctic. *Nat. Clim. Chang.* 10, 1108–1115. doi:10.1038/s41558-020-0892-z

Maher, N., Milinski, S., Suarez-Gutierrez, L., Botzet, M., Dobrynin, M., Kornblueh, L., et al. (2019). The Max Planck Institute Grand Ensemble: Enabling the Exploration of Climate System Variability. *J. Adv. Model. Earth Syst.* 11, 2050–2069. doi:10.1029/2019ms001639

Mahlstein, I., and Knutti, R. (2011). Ocean Heat Transport as a Cause for Model Uncertainty in Projected Arctic Warming. *J. Clim.* 24, 1451–1460. doi:10.1175/2010JCLI3713.1

Manabe, S., and Stouffer, R. J. (1980). Sensitivity of a Global Climate Model to an Increase of CO2concentration in the Atmosphere. *J. Geophys. Res.* 85, 5529–5554. doi:10.1029/jc085ic10p05529

Meehl, G. A., Washington, W. M., Arblaster, J. M., Hu, A., Teng, H., Kay, J. E., et al. (2013). Climate Change Projections in CESM1(CAM5) Compared to CCSM4. *J. Clim.* 26 (17), 6287–6308. doi:10.1175/jcli-d-12-00572.1

Meinshausen, M., Smith, S. J., Calvin, K., Daniel, J. S., Kainuma, M. L. T., Lamarque, J.-F., et al. (2011). The RCP Greenhouse Gas Concentrations and Their Extensions from 1765 to 2300. *Climatic Change* 109, 213–241. doi:10.1007/s10584-011-0156-z

Miller, G. H., Alley, R. B., Brigham-Grette, J., Fitzpatrick, J. J., Polyak, L., Serreze, M. C., et al. (2010). Arctic Amplification: Can the Past Constrain the Future? *Quat. Sci. Rev.* 29 (15–16), 1779–1790. doi:10.1016/j.quascirev.2010.02.008

Pendergrass, A. G., Conley, A., and Vitt, F. M. (2018). Surface and Top-Of-Atmosphere Radiative Feedback Kernels for CESM-CAM5. *Earth Syst. Sci. Data* 10, 317–324. doi:10.5194/essd-10-317-2018

Pithan, F., and Mauritsen, T. (2014). Arctic Amplification Dominated by Temperature Feedbacks in Contemporary Climate Models. *Nat. Geosci* 7, 181–184. doi:10.1038/ngeo2071

Rodgers, K. B., Lin, J., and Frölicher, T. L. (2015). Emergence of Multiple Ocean Ecosystem Drivers in a Large Ensemble Suite with an Earth System Model. *Biogeosciences* 12, 3301–3320. doi:10.5194/bg-12-3301-2015

Schneider, A., Flanner, M., and Perket, J. (2018). Multidecadal Variability in Surface Albedo Feedback across CMIP5 Models. *Geophys. Res. Lett.* 45, 1972–1980. doi:10.1002/2017GL076293

Screen, J. A., and Simmonds, I. (2010). The central Role of Diminishing Sea Ice in Recent Arctic Temperature Amplification. *Nature* 464, 1334–1337. doi:10.1038/nature09051

Serreze, M. C., Barrett, A. P., Stroeve, J. C., Kindig, D. N., and Holland, M. M. (2009). The Emergence of Surface-Based Arctic Amplification. *The Cryosphere* 3, 11–19. doi:10.5194/tc-3-11-2009

Shell, K. M., Kiehl, J. T., and Shields, C. A. (2008). Using the Radiative Kernel Technique to Calculate Climate Feedbacks in NCAR's Community Atmospheric Model. *J. Clim.* 21, 2269–2282. doi:10.1175/2007JCLI2044.1

Soden, B. J., Held, I. M., Colman, R., Shell, K. M., Kiehl, J. T., and Shields, C. A. (2008). Quantifying Climate Feedbacks using Radiative Kernels. *J. Clim.* 21, 3504–3520. doi:10.1175/2007JCLI2110.1

Stuecker, M. F., Bitz, C. M., Armour, K. C., Proistosescu, C., Kang, S. M., Xie, S.-P., et al. (2018). Polar Amplification Dominated by Local Forcing and Feedbacks. *Nat. Clim. Change* 8, 1076–1081. doi:10.1038/s41558-018-0339-y

Sun, L., Alexander, M., and Deser, C. (2018). Evolution of the Global Coupled Climate Response to Arctic Sea Ice Loss during 1990-2090 and its Contribution to Climate Change. *J. Clim.* 31, 7823–7843. doi:10.1175/jcli-d-18-0134.1

Winton, M., Adcroft, A., Griffies, S. M., Hallberg, R. W., Horowitz, L. W., and Stouffer, R. J. (2013). Influence of Ocean and Atmosphere Components on

Simulated Climate Sensitivities. *J. Clim.* 26, 231–245. doi:10.1175/JCLI-D-12-00121.1

Conflict of Interest: The authors declare that the research was conducted in the absence of any commercial or financial relationships that could be construed as a potential conflict of interest.

Publisher's Note: All claims expressed in this article are solely those of the authors and do not necessarily represent those of their affiliated organizations, or those of the publisher, the editors and the reviewers. Any product that may be evaluated in this article, or claim that may be made by its manufacturer, is not guaranteed or endorsed by the publisher.

frontiers in Earth Science

ORIGINAL RESEARCH
published: 20 September 2021
doi: 10.3389/feart.2021.738497

Summer Cyclones and Their Association With Short-Term Sea Ice Variability in the Pacific Sector of the Arctic

Peter M. Finocchio and James D. Doyle*

Naval Research Laboratory, Monterey, CA, United States

We investigate the effects of summer cyclones on sea ice within the Pacific sector of the Arctic by analyzing the surface energy flux and wind forcing from a large sample of cyclones. Consistent with recent studies, we find that cyclones earlier in the melt season tend to be associated with less 1–5 day sea ice loss than what occurs in the absence of cyclones. In contrast, cyclones later in the melt season slightly accelerate the 1-day sea ice loss. The reduced ice loss following cyclones in June is primarily due to increased cloud cover reducing the net shortwave flux at the surface. Clouds associated with cyclones in July and August also reduce the net shortwave flux at the surface, but only over high-concentration sea ice. Southerly winds associated with August cyclones increase both the negative local sea ice advection and the surface heat flux, particularly for the low concentration sea ice that is prevalent in August. Sea ice advection and surface heat flux are the only two factors we examined that can explain the enhanced ice loss on cyclone days in August. We also examined two cyclone cases that impacted sea ice in the East Siberian Sea in June 2012 and August 2016, and found for both cyclones that the sensible heat flux is the largest positive anomalous forcing and the shortwave radiative flux is the largest negative anomalous forcing. Similar to the large sample of cyclones, the shortwave flux has a stronger relationship to local changes in SIC in June than in August. Part of the reason for this is that the cloud shortwave radiative forcing during the August cyclone is 26% weaker than during the June cyclone. In an area averaged sense, the anomalous surface energy and wind forcing of both cyclone cases is similar in magnitude, yet the August cyclone is followed by a greater reduction in both sea ice area and mean sea ice concentration than the June cyclone. This result emphasizes how the underlying sea ice characteristics largely determine cyclone impacts on sea ice on short time scales.

Keywords: sea ice, marginal ice zone, melt season, arctic, cyclone

OPEN ACCESS

Edited by:
Ivy Tan,
McGill University, Canada

Reviewed by:
Tomoko Koyama,
Japan Aerospace Exploration Agency (JAXA), Japan
Youichi Kamae,
University of Tsukuba, Japan

****Correspondence:***
Peter M. Finocchio
peter.finocchio@nrlmry.navy.mil

Specialty section:
This article was submitted to Atmospheric Science, a section of the journal Frontiers in Earth Science

Received: *08 July 2021*
Accepted: *02 September 2021*
Published: *20 September 2021*

Citation:
Finocchio PM and Doyle JD (2021) Summer Cyclones and Their Association With Short-Term Sea Ice Variability in the Pacific Sector of the Arctic. Front. Earth Sci. 9:738497. doi: 10.3389/feart.2021.738497

INTRODUCTION

Arctic summer sea ice cover is decreasing at such a rate that ice-free summers are projected to occur by the middle of this century (Stroeve et al., 2012; Overland and Wang 2013). This remarkable loss of sea ice is a result of the significant warming of the Arctic atmosphere and ocean that has taken place in recent decades. Whether transient Arctic cyclones during the summer months have contributed to the accelerating loss of sea ice remains unclear. There has been no significant increase in Arctic-wide

cyclone frequency or intensity that would suggest stronger or more frequent cyclones during the summer are responsible for accelerating summer ice loss (Screen et al., 2011; Koyama et al., 2017; Semenov et al., 2019). However, cyclones are likely having a larger effect on sea ice cover as young and thin sea ice becomes more widespread in the Arctic (Rampal et al., 2009; Maslanik et al., 2011; Spreen et al., 2011; Lindsay and Schweiger 2015; Itkin et al., 2017). Despite uncertainty in whether cyclones are a significant source of seasonal or interannual variability in pan-Arctic sea ice cover (Rae et al., 2017), numerous studies have demonstrated that cyclones are indeed a source of local and short term variability in sea ice cover and concentration (Zhang et al., 2013; Stern et al., 2020; Lukovich et al., 2021), and these short-term changes in sea ice are critical for navigability within the Arctic region. This study examines how the surface winds and atmospheric energy flux from recent Arctic summer cyclones affects sea ice concentration on synoptic weather time scales of 1–10 days.

The strong surface winds associated with summer cyclones affect sea ice in several ways. Wind-induced drift is a key source of short term sea ice variability—particularly where the sea ice cover is thinner, farther from the coastline, and primarily composed of floes (Thorndike and Colony 1982; Hakkinen et al., 2008; Spreen et al., 2011; Vihma et al., 2012). Whether the wind-induced advection of sea ice increases or decreases sea ice concentration at a given location, however, depends on the direction of the surface winds relative to the local gradient in ice concentration. Cyclonic surface winds enhance sea ice divergence, which locally reduces sea ice concentration in the vicinity of a cyclone (Maslanik and Barry 1989; Kriegsmann and Brümmer, 2014; Lukovich et al., 2021). In addition, strong surface winds later in the summer are increasingly capable of mixing relatively warm sub-surface sea water upward toward the surface, which causes substantial melting along the ocean-facing side of sea ice (Steele et al., 2010; Zhang et al., 2013; Stern et al., 2020).

Cyclones also contribute to the short-term variability in sea ice concentration by changing the local energy balance on the atmosphere-facing side of sea ice. Clouds associated with cyclones reflect solar radiation that would otherwise melt the top surface of sea ice and/or heat the open water areas around sea ice (Finocchio et al., 2020; Schreiber and Serreze 2020). Finocchio et al. (2020) found this cloud shading effect was particularly strong in the Arctic marginal ice zone (MIZ) in June, when shortwave radiation reaches its annual maximum and when clouds have a strong cooling effect at the surface (Kay and L'Ecuyer 2013). Schreiber and Serreze (2020) showed that the cloud shading effect of cyclones temporarily decelerates the seasonal reduction in sea ice concentration near the ice edge during summer. Although cloud cover also increases the downward longwave flux at the surface, which can have important implications for sea ice change in the winter and spring months (Shupe and Intrieri 2004; Persson 2012), Finocchio et al. (2020) found that the average reduction in shortwave radiation due to early summer cyclones more than compensates for the increased longwave radiation from clouds in their sample of cyclone cases, resulting in a net decrease in the atmospheric energy flux at the surface due to cyclones. Although Arctic cyclones tend to decelerate the seasonal loss of sea ice early in the melt season, the strong sensible and latent heat fluxes within the warm sector of cyclones later in the melt season can locally accelerate sea ice loss. For example, Stern et al. (2020) showed that the sensible heat flux in the warm sector of an exceptionally strong cyclone in August 2012 (frequently referred to as the "Great Arctic Cyclone") contributed to anomalous surface energy forcing that locally accelerated ice loss in the Beaufort Sea.

Cyclone impacts on sea ice vary from case to case not only because of variability in the cyclones themselves, but also because of differences in the underlying sea ice cover. Lukovich et al. (2021) compared the impacts of similarly intense Arctic cyclones in August 2012 and August 2016 on the sea ice. They found that the August 2012 cyclone had a more destructive effect on sea ice primarily because it affected thinner, lower-concentration sea ice than the August 2016 cyclone. The apparent dependency of cyclone impacts on the characteristics of the underlying sea ice motivates a new approach to analyzing the relationship between cyclones and sea ice loss that involves stratifying cyclone impacts based on the underlying sea ice concentration.

Similar to Finocchio et al. (2020), this study adopts a statistical approach to analyzing the effects of Arctic cyclones on sea ice within the marginal ice zone. We focus here on the Pacific sector of the Arctic, which experiences high interannual variability in summer sea ice cover and frequent summer cyclones. Within this region, we stratify the effects of cyclones on sea ice by the sea ice concentration in order to gain a more detailed understanding of the relationship between cyclone impacts and short-term sea ice changes. A description of the methods and data used for this study appears in Methods and Data. The Results section describes the results of the statistical analysis of cyclones located within the Pacific sector of the Arctic from June-August in the years 1999–2018, as well as a comparison of two Arctic cyclones that occurred at the beginning and the end of the melt season. The Discussion and Conclusions section contains a discussion of the results and some concluding remarks.

METHODS AND DATA

The primary data used for this study includes sea ice concentration and atmospheric fields from the European Centre for Medium Range Weather Forecasts (ECMWF) ERA-5 Reanalysis (Hersbach et al., 2020). All ERA-5 fields are available on a common 0.25-degree (~31 km) grid and the atmospheric fields are updated hourly, though we only use 6-hourly data in this study. Sea ice concentration (SIC) in ERA-5 is updated once daily at 00Z based on the real-time European Organisation for the Exploitation of Meteorological Satellites (EUMETSAT) Satellite Application Facility on Ocean and Sea Ice (OSI-SAF) product (Eastwood et al., 2014; Hirahara et al., 2016). The OSI-SAF product is generated from an algorithm that estimates SIC using corrected brightness temperature observations from passive microwave satellites.

The geographic focus of this study is on the marginal seas in the Pacific sector of the Arctic, defined here as the region from 70

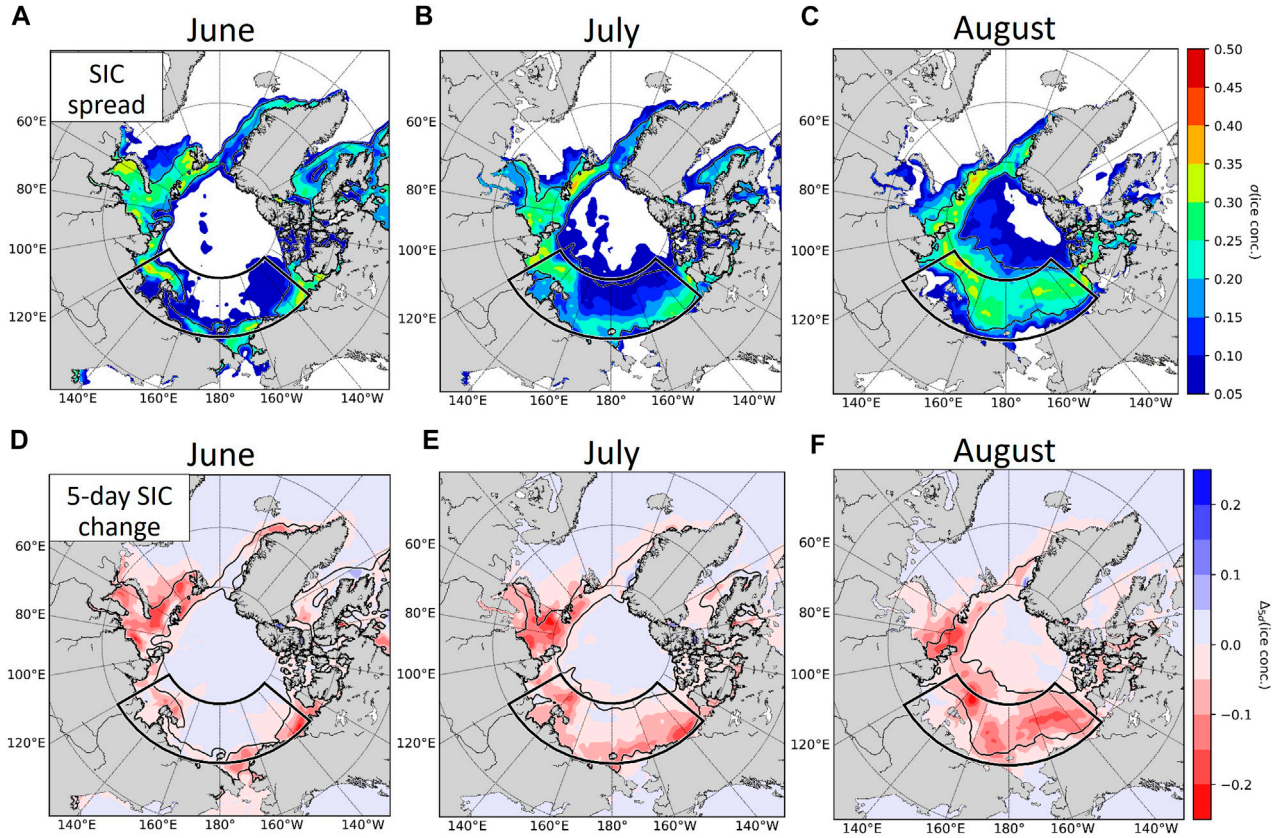

FIGURE 1 | Standard deviation of sea ice concentration (SIC) over all days in June **(A)**, July **(B)**, and August **(C)**, and the monthly averaged 5-day change in SIC in June **(D)**, July **(E)**, and August **(F)**. The ECB region is outlined with a thick black line in each panel. The black contours are the 15 and 80% sea ice concentration contours outlining the marginal ice zone.

to 80N and from 120E to 130W. Because this region encompasses the East Siberian, Chukchi, and Beaufort Seas, we henceforth refer to it as the ECB region. We focus on this region for multiple reasons. First, the sea ice within the ECB region is frequently impacted by cyclones during the summer months that develop within a low-level baroclinic zone along the northern coast of Siberia (Crawford and Serreze 2016). In addition, this region features high interannual variability in SIC (**Figures 1A–C**) and large average 5-day losses of SIC (**Figures 1D–F**) during the summer months. Part of the reason for the large reductions in SIC within this region is that it encompasses a large portion of the summertime MIZ, defined by sea ice concentrations between 15 and 80% (Strong et al., 2017). The MIZ primarily consists of young, thin, and broken sea ice that is more apt to drift in response to surface winds and ocean currents than the more consolidated pack ice. Finally, from a seasonal perspective, the sea ice cover within the ECB region is often what differentiates years with anomalously low and high pan-Arctic sea ice cover.

Although the melt season typically begins in May and ends in September (Persson 2012), we restrict our analysis to the core months of the melt season (June, July, and August) in which each day is climatologically associated with sea ice loss and a sizeable fraction of the study area is covered by the MIZ. We also only consider cyclone cases that occurred during the recent period of 1999–2018 in order to capture the effects of cyclones on the younger and thinner sea ice that has come to characterize the "New Arctic" regime (Landrum and Holland 2020).

We use a database of Arctic cyclone tracks generated from the cyclone tracking algorithm of Sprenger et al. (2017) in order to identify Arctic cyclones that occur within the ECB region during the study period. This algorithm identifies local minima in ERA-5 sea level pressure and tracks the positions of these local minima through time using the method of Wernli and Schwierz (2006, their Section 2D), but using hourly ERA-5 fields rather than 6-hourly ERA-interim data. For this study, we only consider cyclones that achieve a minimum sea level pressure ≤995 hPa and which are tracked continuously for at least 48 h. We define cyclone days as days in which a valid cyclone is located within 300 km of the latitude-longitude box outlining the ECB region defined above. This buffer distance around the ECB region is based on the average cyclone radius from Kriegsmann and Brümmer (2014), and is included to account for cyclone cases whose impacts are felt within the ECB region while the cyclone is located outside of the region. The left panels of **Figure 2** show the 00Z positions of the valid cyclone cases and the SIC averaged over the cyclone days in each month. Consistent with Crawford and

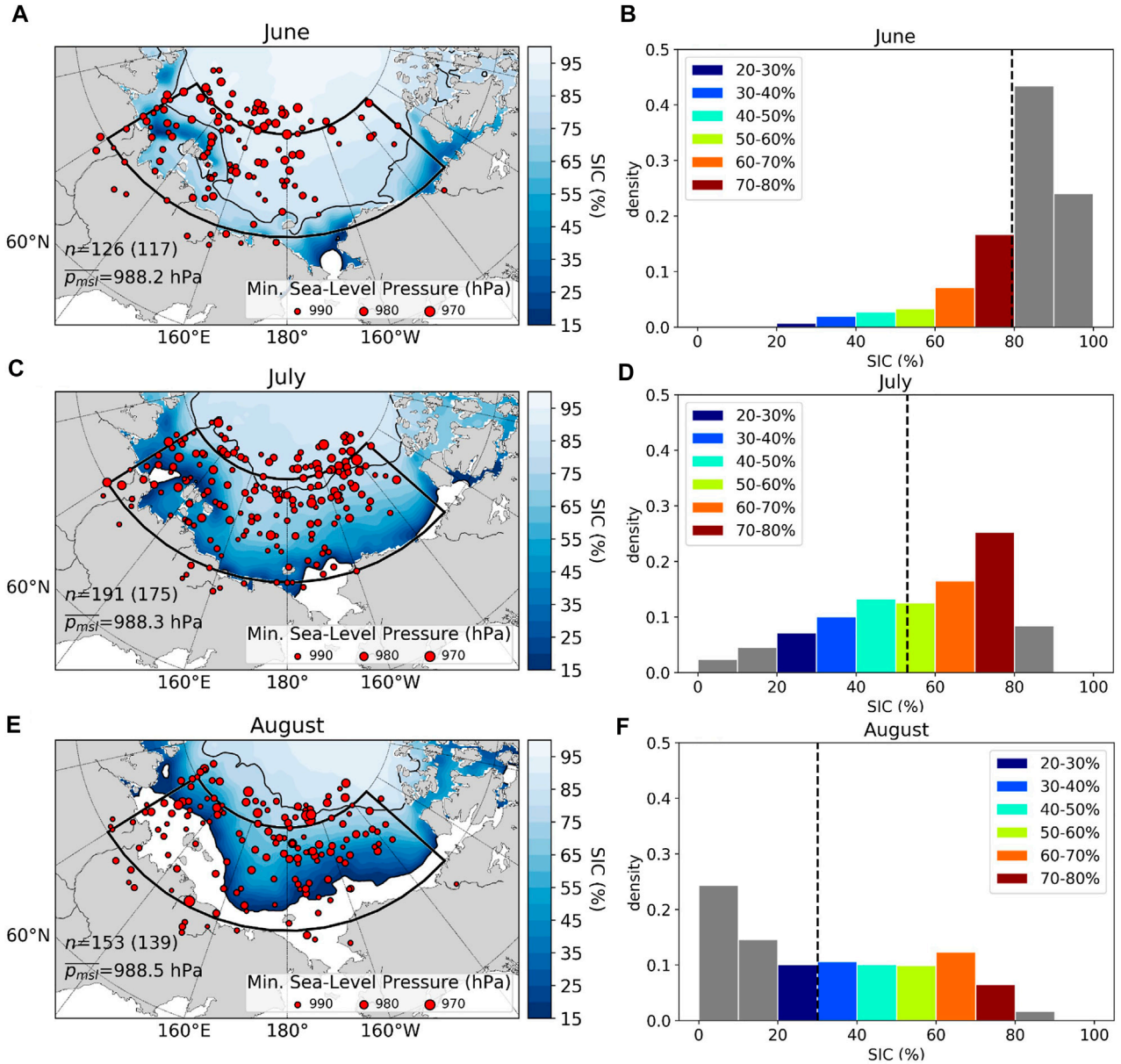

FIGURE 2 | (A,C,E) Cyclone cases (red dots) and the average SIC on cyclone days in each month (shading). The black contour is the 80% SIC contour denoting the poleward extent of the marginal ice zone, and the black box outlines the ECB region. The size of the dots corresponds to the cyclone minimum sea level pressure (see legend). The values printed in the lower left are the number of cyclone cases (n) and the number of unique cyclones in parentheses (as multiple cases can correspond to a single cyclone), and the average minimum sea level pressure of all cyclone cases in each month (p_{msl}); **(B,D,F)** probability density of monthly averaged SIC within the outlined ECB region. Bars are colored according to the SIC bins, with grey bars denoting SIC<20% or SIC>80%. The vertical dashed line denotes the mean SIC within the ECB region in each month.

Serreze (2016), there are more valid cyclone cases in July and August compared to June. Cyclones in June primarily occur in the western half of the region, while cyclones in July and August are more evenly distributed throughout the region.

The cyclone impacts on sea ice that can be estimated from the uncoupled ERA-5 include SIC advection by the surface winds and the surface energy flux from the atmosphere. Sea ice advection is part of the dynamic contribution of the atmosphere to local changes in SIC. We compute sea ice advection using the 10-m wind vector and the local gradient in SIC at each grid point, and assume that sea ice drifts at 2% of the surface wind speed (Spreen et al., 2011). The net surface energy flux from the atmosphere is the direct thermodynamic contribution that influences melting on top of the sea ice. We believe ERA-5 is the first reanalysis product that is suitable for this analysis because it has been shown to have smaller biases in surface winds and atmospheric surface energy fluxes in the Arctic than previous reanalysis products (Graham et al., 2019). However, ERA-5 does not contain

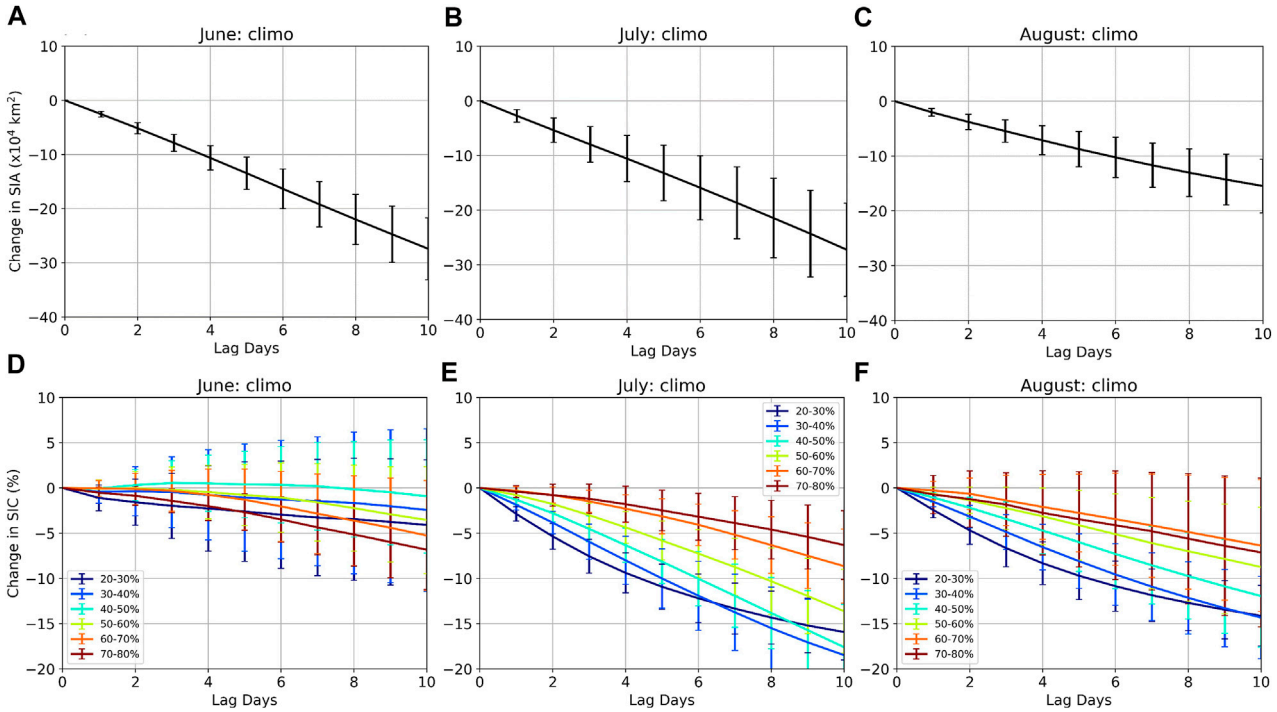

FIGURE 3 | Average change in total sea ice area (SIA) within the ECB region **(A–C)** and the average change in SIC at each grid point in the ECB region and within each 10%-wide bin **(D–F)** from 1–10 days after a given day in each month. The error bars extend ± 1 standard deviation from the average SIA or SIC change at each lag day.

sufficient information about the upper ocean for a detailed analysis of the indirect thermodynamic contributions of the atmosphere to sea ice loss, which involve upper ocean heating due to vertical mixing that results in lateral and basal ice melt (Steele et al., 2010; Zhang et al., 2013).

The right panels in **Figure 2** show the distribution of the monthly average SIC within the ECB region. June features predominately high-concentration sea ice with an average concentration of ~80%, while August features predominately low-concentration sea ice with an average concentration of ~30%. This distributional shift in SIC over the course of the melt season has important implications for the amount of sea ice loss that can be expected to occur in response to a cyclone. The net shortwave radiative flux at the surface, for example, varies strongly with SIC due to differences in the average surface albedo. Consequently, the cloud shading effect of cyclones is expected to be greater in regions of low-concentration sea ice where more shortwave radiation is absorbed rather than reflected at the surface (Perovich 2018). Furthermore, low concentration sea ice has weaker internal forces than high concentration sea ice, which allows such sea ice to drift more easily in response to the surface wind forcing (Spreen et al., 2011). Therefore, the advective effects of surface winds on sea ice will also tend to be larger in areas with low SIC. In order to account for these ice concentration dependencies in the ensuing analysis, we compute sea ice advection and atmospheric energy flux at the surface separately for grid points categorized by their SIC into six 10%-wide bins ranging from 20 to 80% ice concentration.

RESULTS

Climatology of Short-Term Sea Ice Changes During Summer

We begin by examining the climatological change in SIC and total sea ice area (SIA) during the summer months within the ECB region. We compute SIA by taking the sum across the ECB region of the product of SIC and the area of each grid point. **Figure 3** shows the average change in SIA (A-C) and SIC (D-F) from 1–10 days after all days in each month in the 20-year study period of 1999–2018. Error bars represent ± 1 standard deviation of the change in SIA or SIC at each lag day. As expected during the melt season, both SIA and SIC decreases on average from 1–10 days after a given day in June, July, and August. The 10-day reductions in SIA are largest in June and July (**Figures 3A,B**), and the 10-day reductions in local SIC are largest for low-concentration sea ice in July (**Figure 3E**). Specifically, grid points with SIC between 20 and 40% in July experience more than 15% SIC reduction after 10 days on average, indicating almost a complete loss of sea ice at these grid points (**Figure 3E**). The rate of SIC loss in the 20–40% SIC bins starts to level off after about 5 days in both July and August due to the limited amount of possible SIC loss that can occur within these bins (e.g., the SIC loss for a grid point with 20% SIC cannot exceed 20%). The remainder of this analysis focuses on the 1–5 day changes in sea ice in order to exclude the longer lag times when the rate of SIC loss begins to level off in the low SIC bins.

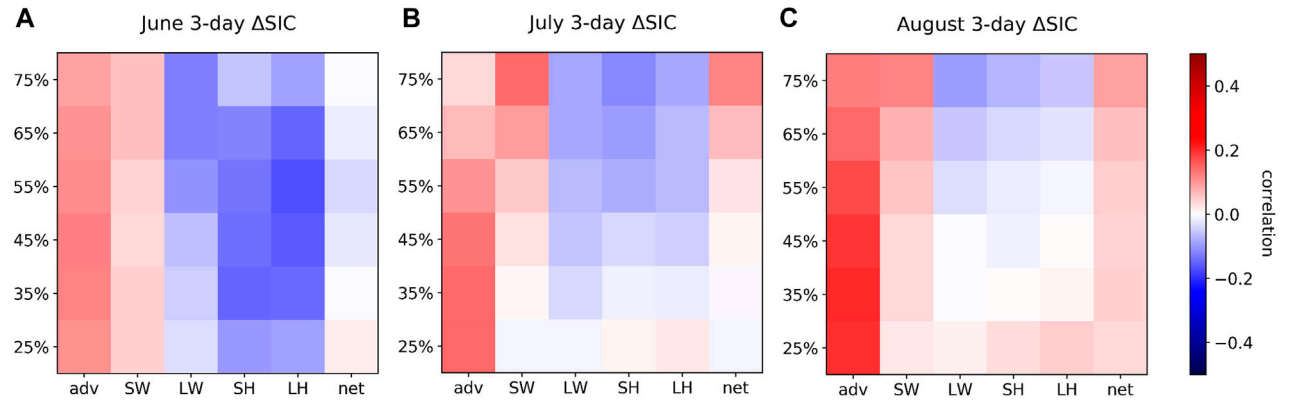

FIGURE 4 | Pearson correlation coefficients in June **(A)**, July **(B)**, and August **(C)** between the 3-day change in sea ice concentration (ΔSIC) and the negative SIC advective tendency ("adv"), the net shortwave flux at the surface ("SW"), the net longwave flux at the surface ("LW"), the sensible surface heat flux ("SH"), the latent surface heat flux ("LH"), and the total surface energy flux from the atmosphere ("net"). Correlations are computed separately for grid points in each 10%-wide SIC bin, labeled along the left side of each panel according to the mid-point SIC value in each bin.

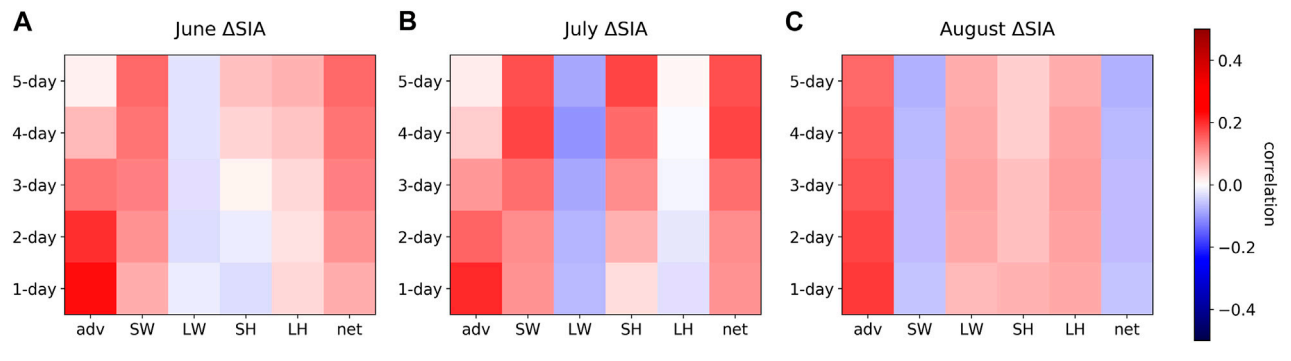

FIGURE 5 | Pearson correlation coefficients in June **(A)**, July **(B)**, and August **(C)** between the 1–5 day change in total sea ice area (ΔSIA) within the ECB region and each forcing term shown in **Figure 4**. The *y*-axis on each panel indicates the lag time over which SIA is computed.

In order to get a statistical sense for the extent to which each dynamic and thermodynamic forcing is associated with climatological SIC loss in each month, **Figure 4** shows the correlation between 3-day SIC loss in each bin and the SIC advective tendency by the 10-m wind ("adv"), the net shortwave ("SW") flux at the surface, the net longwave ("LW") flux at the surface, the surface sensible heat flux ("SH"), the surface latent heat flux ("LH"), and the sum of all four surface fluxes ("net"). Red (blue) colors in **Figure 4** indicate that a forcing term is statistically associated with more (less) local SIC loss (we multiply the advective tendency by −1 in order for this to be the case). In June, stronger SIC advection and, to a lesser extent, SW flux is associated with enhanced local SIC loss, while stronger LW, SH, and LH fluxes are associated with less SIC loss in June. This is likely due to a strong anticorrelation between the SW flux and each of the LW, SH, and LH fluxes (not shown), and does not actually mean that stronger LW, SH, or LH fluxes cause SIC to increase at a location. In July and August, SIC advection has the strongest relationship to local SIC loss, with larger positive correlations at lower ice concentrations. The relationship between SIC loss and each of the different atmospheric energy fluxes in July and August is similar to June for high concentration sea ice. However, for SIC between 20 and 40%, stronger LW, SH, and LH fluxes start to be weakly associated with more SIC loss later in the melt season. Nevertheless, the net atmospheric energy flux explains no more than about 2% of the variance in local SIC changes throughout the melt season. Among the forcing terms considered here, the wind-induced SIC advection has the strongest and most consistent relationship to local SIC loss during the summer months.

If we instead compute correlations between the loss of total SIA within the ECB region and area-averages of each forcing term (**Figure 5**), we find somewhat different statistical relationships than for local SIC loss. In June and July, SIC advection has a moderate correlation with 1-day SIA loss and a much weaker correlation with 5-day SIA loss. By August, SIC advection has a stronger correlation to 4–5 day SIA loss than in June and July. This statistical signal of a near-instantaneous response of sea ice cover to wind-induced advection of sea ice early in the melt season, followed by a more lagged response later in the melt

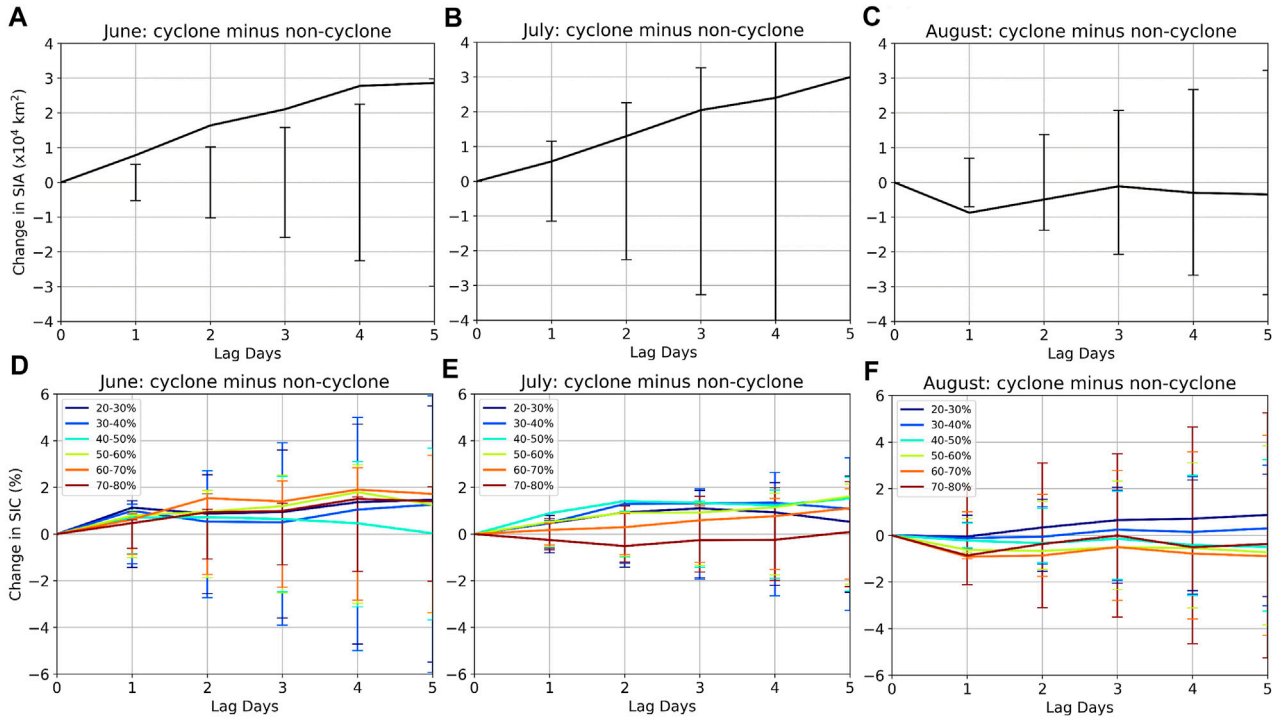

FIGURE 6 | (A–C) Difference in the 1–5 day change in SIA in the ECB region between cyclone and non-cyclone days in each month. Error bars are the same as in **Figures 3A–C**, and indicate ± 1-standard deviation in SIA change at each lag time in each month. **(D–F)** Difference in the 1–5 day change in SIC at each grid point in the ECB region between cyclone and non-cyclone days. Each line indicates difference for grid points with SIC in each 10%-wide SIC bin. Error bars are the same as in **Figures 3D–F**, and indicate ± 1-standard deviation in local SIC change at each lag time in each month. Differences are considered significant if they are outside of the error bars.

season is consistent with the findings of Finocchio et al. (2020). Similar to the SIC correlations shown in **Figure 4**, increased SW flux is associated with more SIA loss in June and July. Because the SW flux is the largest component of the surface atmospheric energy balance during the summer months, correlations between SIA loss and the net flux closely reflect those for the SW flux in all 3 months. In June and July, the magnitude of the correlation between the SW flux and SIA loss increases at longer lag times, indicating that SIA exhibits a lagged response to anomalous surface energy forcing from the atmosphere. This is in contrast to the near-instantaneous response of SIA to the surface wind forcing (i.e., advection), suggesting that surface energy forcing affects sea ice on longer time scales than surface wind forcing during June and July. By August, both the SW flux and the net flux are anti-correlated with SIA loss at all lag times. This negative correlation between SW flux and SIA loss in August suggests that the SW flux is no longer the key component of the surface atmospheric energy budget for understanding short-term SIA changes later in the melt season.

Physically speaking, an increase in any of the surface energy forcing terms should result in enhanced ice loss because an increase in the energy flux from the atmosphere into the sea ice will increase surface melt. Similarly, stronger negative sea ice advection should locally decrease SIC. Therefore, any instances of negative correlations in **Figures 4**, **5** are most likely due to covariances between the forcing terms and do not reflect a causal link to sea ice loss, while positive correlations are more likely to indicate the factors that actually cause ice loss. By this reasoning, the advective tendency and the SW forcing are the most likely forcing terms to cause SIA loss in June and July, while the advective tendency and the combination of LW, SH, and LH fluxes are the most likely forcing terms to cause SIA loss in August. Advection and SW flux (for high concentration sea ice) appear to be the only two terms that consistently have a potential causal link to local SIC loss (**Figure 4**).

Statistical Analysis of Summer Cyclone Effects on Sea Ice

The statistical relationships between each forcing term and both local (**Figure 4**) and regional (**Figure 5**) changes in sea ice provide context for understanding how cyclones affect sea ice, as cyclones locally change the surface energy balance in sea ice-covered areas and induce anomalous wind forcing on sea ice. **Figure 6** shows the differences in the average 1–5 day change in SIA (A-C) and SIC (D-F) between cyclone and non-cyclone days in each month during the study period, where non-cyclone days are simply the days in which there is no valid cyclone case inside or within 300 km of the ECB region boundary. The presence of a cyclone is associated with an average of about 3×10^4 km^2 less SIA loss over a 5-day period in June and July compared to days without cyclones. In August, however, the presence of a cyclone is

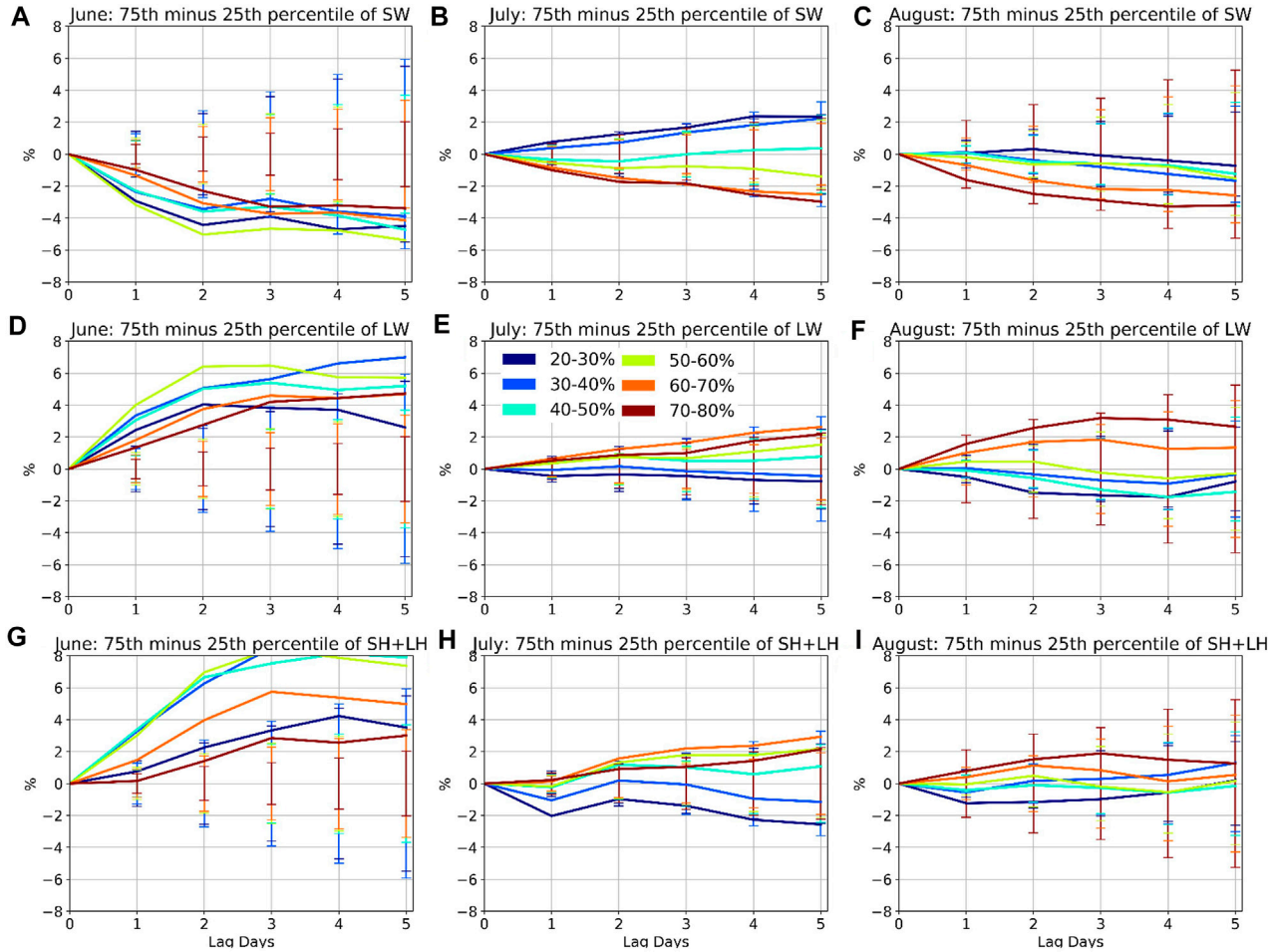

FIGURE 7 | Differences in each month in the 1–5 day change in SIC concentration averaged over grid points in the upper versus lower quartiles of the SW flux **(A–C)**, LW flux **(D–F)**, and surface heat flux **(H–J)**. As in **Figures 3**, **6**, line colors indicate the different 10%-wide SIC bins. Error bars are the ± 1 standard deviation of each flux term for grid points with SIC in each bin computed over all days in each month for the 20-year study period.

associated with about $1 \times 10^4\,km^2$ more 1-day SIA loss, on average. The smaller amount of SIA lost from 1–5 day after cyclones in June is greater than the climatological variability in SIA changes (represented by the error bars in **Figure 6A** extending ± 1 standard deviation from the mean values). Similarly, the increased 1-day SIA loss in August that is associated with cyclones is also outside of the range of climatological variability in SIA changes in August.

The presence of a cyclone in June and July is also associated with less local SIC loss, while cyclones in August are associated with slightly more local SIC loss (**Figures 6D–F**). Cyclones decelerate SIC loss by about 1% in the 20–30% SIC bin in June, and by slightly more than 1% in the 20–50% SIC bins in July. Cyclones in July and August, however, are also associated with an accelerated SIC loss by about 1% for higher concentration sea ice (**Figures 4D–F**). The differences in local SIC changes between cyclone and non-cyclone days are rarely outside the range of climatological variation of SIC changes in each month, indicating that cyclones have a less significant effect on 1–5 day changes in local SIC than they do on the 1–5 day changes in the region-wide SIA.

The key takeaways from **Figure 6** are that 1) cyclone days in June and July have less local and region-wide ice loss compared to days without cyclones, 2) cyclone days in August have slightly more local and region-wide ice loss compared to days without cyclones, and 3) the greater ice loss following August cyclones only persists for about 1 day after the cyclone day. The remainder of this section focuses on the cyclone days in order to understand the cyclone-related surface forcings that are responsible for the reduced 1–5 day ice loss in June and July and the accelerated 1-day ice loss in August.

Figure 7 shows differences in the average 1–5 day change in SIC between grid points in the upper and lower quartiles of each component of the surface atmospheric energy flux on cyclone days. In June, grid points in the upper SW flux quartile experience significantly more 1–5 day SIC loss than grid points in the lower SW flux quartile, regardless of the initial SIC (**Figure 7A**). In contrast, grid points in the upper quartiles of both LW flux (**Figure 7D**) and the surface heat flux (**Figure 7G**) experience significantly *less* SIC loss than grid points in the lower quartiles of each flux. This unintuitive relationship in which larger surface

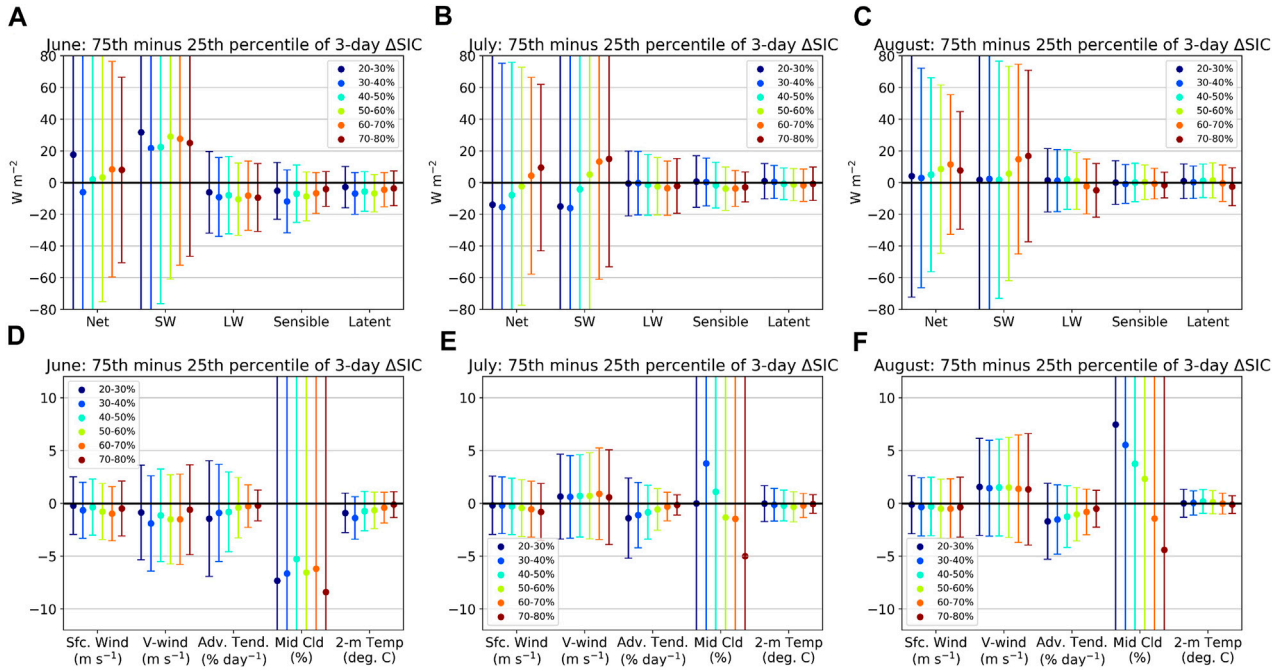

FIGURE 8 | Differences in each term in the surface energy budget **(A–C)** and in the surface wind, advective tendency, mid-level cloud, and 2-m temperature **(D–F)** between grid points in the upper and lower quartiles of 3-day SIC loss. Differences are computed separately for grid points within each 10%-wide SIC bin. Error bars indicate ± 1 standard deviation in each term computed over all days in each month for the 20-year study period.

heat fluxes and LW fluxes are associated with decreased SIC loss suggests that these fluxes do not drive the local changes in SIC, but co-vary with other surface forcings that do. For example, the cloud radiative forcing at the surface is negative in the shortwave and positive in the longwave. Because the negative SW anomalies due to clouds in June tend to be larger in magnitude than the positive LW anomalies (e.g., Finocchio et al., 2020), cloudy grid points frequently end up having less ice loss despite having positive LW flux anomalies.

In July and August, the difference in SIC change between the upper and lower quartiles of SW flux depends on the SIC; strong SW fluxes are associated with less 1–5 day SIC loss for initially low-concentration sea ice, and more SIC loss for initially high-concentration sea ice (**Figures 7B,C**). This suggests that as the melt season progresses, stronger SW fluxes continue to be an important factor in accelerating the local SIC loss for initially high ice concentrations, while other factors begin to play a greater role in accelerating local SIC loss at lower ice concentrations. One of those factors is the surface heat flux. Low ice concentration (SIC<40%) grid points in the upper quartile of surface heat flux in July and August experience 1–2% more 1-day SIC loss on average than grid points in the lower quartile of surface heat flux (**Figures 7H,I**). The surface heat flux is a function of both the surface wind speed and the surface temperature and moisture disequilibrium. We find that the 2-m air temperature differentiates grid points in the upper versus lower quartiles of the surface heat flux better than the 10-m wind speed; grid points with ice concentration <40% that are in the upper heat flux quartile in July and August are consistently 2°C warmer, on average, than grid points in the lower heat flux quartile, while the average 10-m wind speed of grid points in each quartile differs by less than 1 m s^{-1}. This indicates that the warm air masses that Arctic cyclones transport poleward into the Arctic (e.g., Fearon et al., 2020) are capable of accelerating the short-term loss of low-concentration sea ice later in the melt season by locally increasing the surface heat flux over sea ice.

Figures 8A–C shows the differences in each term in the surface energy budget between grid points in the upper versus lower-quartiles of 3-day SIC change on cyclone days, where the upper quartile here represents the largest local SIC loss. We note that in all 3 months, differences in each flux are never larger than the climatological variability of each term (indicated by error bars extending ± 1 standard deviation from the mean values), which indicates that factors other than the local surface energy flux from the atmosphere also contribute to local SIC variability during the summer. Nevertheless, these differences are still useful for understanding the relative contributions of each atmospheric flux to local SIC loss. In June, the net flux is ~19 W m^{-2} larger on average for grid points in the upper quartile of SIC loss in the 20–30% SIC bins. This larger net flux is due to a larger SW flux that is only partially offset by a smaller LW and sensible heat flux. For the grid points with SIC between 30 and 60%, however, the larger SW fluxes are completely offset by reduced LW and surface heat fluxes. In July and August, differences in the average LW and surface heat fluxes between grid points in the upper and lower quartiles of SIC loss are generally less than 5 W m^{-2}, and differences in the net flux are due primarily to differences in the SW flux. Low-concentration sea ice grid points that experience the

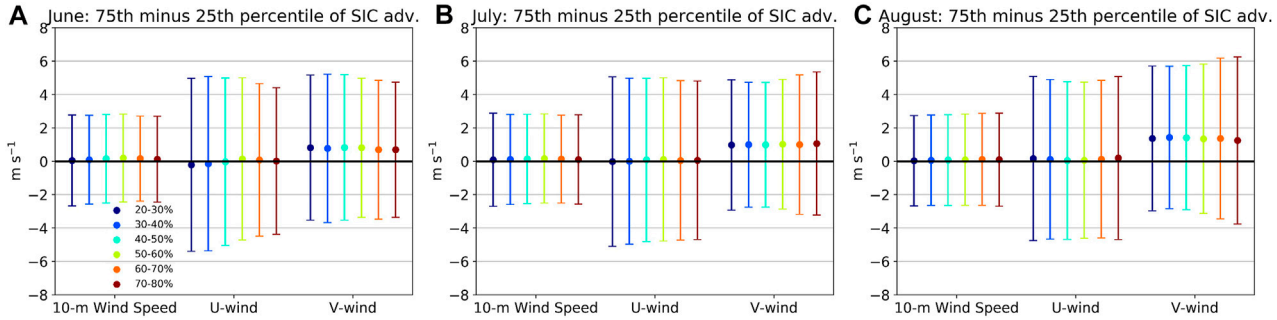

FIGURE 9 | Differences in the 10-m wind speed and the u- and v-wind components between grid points in the **upper** and **lower** quartiles of SIC advective tendency in each SIC bin. Error bars indicate ± 1 standard deviation in each term computed over all days in each month for the 20-year study period.

most SIC loss have net and SW fluxes that are 10–15 W m^{-2} smaller than grid points that experience the least SIC loss. For higher concentration sea ice in July and August, however, the largest SIC loss is associated with 10–15 W m^{-2} larger SW fluxes. This is consistent with **Figures 7B,C**, which showed that larger SW fluxes in July and August are only associated with enhanced sea ice loss for high concentration sea ice.

Figures 8D–F shows differences in the 10-m wind speed, the 10-m meridional wind, the mid-level (800–450 hPa) cloud fraction, and the 2-m air temperature between grid points in the upper versus lower quartiles of SIC loss on cyclone days. We only consider mid-level clouds because of their relatively large SW radiative forcing and because their variability is more closely tied to cyclones than the fog and low-level stratiform clouds that are prevalent in the Arctic during summer (Eastman and Warren 2010). Similar to the surface fluxes, differences in each of the variables shown in **Figures 8D–F** are never larger than the climatological variability, but are still useful for understanding the relative contributions of each variable to anomalous local SIC loss. In June, surface winds tend to be slightly weaker and less southerly on average at grid points with the most SIC loss. The SIC advection by the 10-m wind is more negative by about 1.5% per day for low concentration sea ice. Furthermore, the 2-m temperature is cooler by up to 1.5 C and the mid-level cloud fraction is 5–8% lower at grid points with the most SIC loss, which is consistent with a larger SW flux (**Figure 8A**). Together, these results suggest that the largest 3-day reductions in local SIC during June tend to occur where conditions are calmer, clearer, and cooler. By July and August, the surface wind speed and surface temperature are strikingly similar between grid points with the largest and smallest 3-day SIC loss, but the meridional wind component tends to be more southerly for the largest SIC loss. The differences in the mid-level cloud fraction have more of a dependence on the SIC than in June. For high-concentration sea ice, large local SIC loss is associated with reduced mid-level cloud fraction (**Figures 8E,F**) and increased SW flux (**Figures 8B,C**), as in June. However, the largest local reductions in low-concentration sea ice in July and August are associated with a larger cloud fraction and smaller SW fluxes. This combined with the increased southerly wind and more negative SIC advection by about 2% per day on average for low-concentration sea ice in July and August suggests that cloudy, southerly flow regimes increasingly accompany large local SIC loss events in the Arctic as summer progresses.

Certain surface wind regimes may promote the strong, negative SIC advection that is frequently associated with large reductions in low-concentration sea ice. To further explore this, we compute differences in the total wind speed and each component of the local wind vector between cases in the upper versus lower quartiles of SIC advection (**Figure 9**). In all 3 months, grid points that experience strong SIC advective tendencies have an average total and zonal wind speed that is similar to grid points that experience weak SIC advection. However, the average meridional wind speed is up to 1.5 m s^{-1} larger (i.e., more southerly) at grid points with the largest negative SIC advection. The more southerly wind component associated with strong negative SIC advection also becomes more apparent as the melt season progresses. Thus, the meridional wind component is what determines how much negative SIC advection occurs within the ECB region—particularly later in the melt season when low concentration sea ice is prevalent. The preference for large negative SIC advection under southerly wind conditions likely relates to the primarily northward-directed SIC gradient within this region of the Arctic (**Figure 2**).

Comparison of an Early and a Late Season Cyclone

A key result from the previous section is that the surface forcings that differentiate large from small local and regional ice loss events vary over the course of the melt season and depend to some extent on the initial ice concentration. In this section, we further explore the seasonal dependence of cyclone impacts on sea ice by comparing two cyclone cases that impacted the same region of the Arctic early and late in the melt season. As in the previous section, the analysis of cyclone impacts focuses on the surface wind and energy forcing.

The two selected cyclones occurred in June 2012 and August 2016. Both cyclones reached a similar maximum intensity and affected sea ice in the East Siberian Sea. The June 2012 cyclone emerged from Siberia on 19 June and intensified as it moved toward the northeast, reaching a maximum intensity of 970 hPa

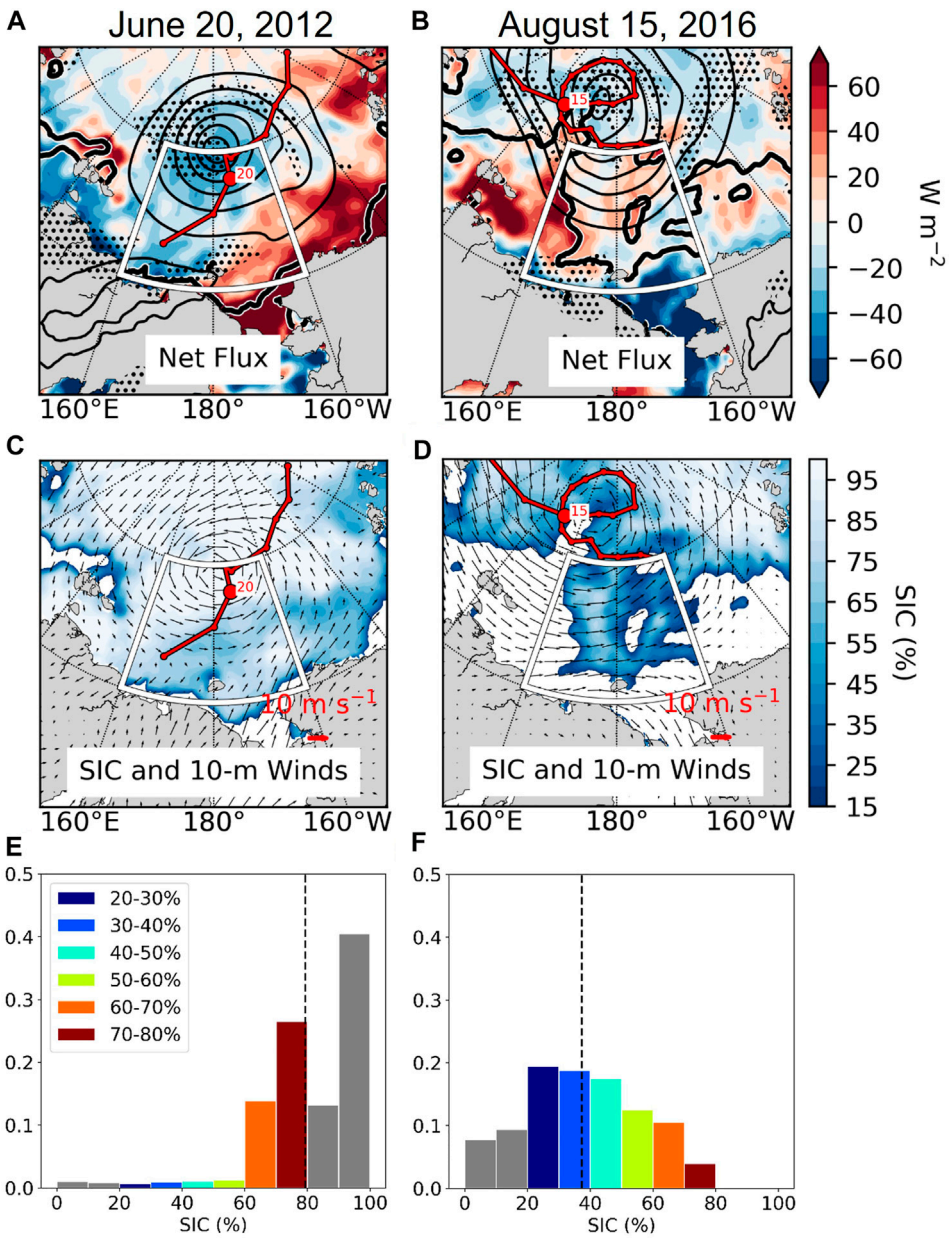

FIGURE 10 | (A,B) Cyclone tracks (red line, 00Z cyclone position labeled by day of month), daily averaged net surface energy flux anomalies (shading), mid-level cloud fraction >70% (black stippling), and sea level pressure at 12Z (black contour) on June 20, 2012 **(A)**, and August 15, 2016 **(B)**. The thick black line is the 15% SIC contour indicating the sea ice edge. Sea level pressure contours are drawn every 5 hPa less than 1,000 hPa. **(C,D)** Sea ice concentration (shading), cyclone track (red line) and daily averaged surface wind vectors on June 20, 2012 **(C)**, and August 15, 2016 **(D)**. **(E,F)** Probability density of SIC within the white outlined region in **A-D** on each date colored according to SIC bins as in **Figure 2**. The vertical dashed line in **10E,F** denotes the average SIC within the outlined region.

at 12Z on 20 June. The August 2016 cyclone was located further north and translated eastward from the Laptev Sea, reaching a maximum intensity of 968 hPa at around 12Z on 15 August and maintaining that intensity for several hours as it made a loop into the central Arctic. **Figures 10A,B** show the cyclone tracks and the sea level pressure contours at 12Z on the day when the cyclones were near their peak intensity. The color shading denotes the net surface energy flux anomalies relative to the 1999–2018 average. Both cyclones have areas where the net flux over sea ice is more than 20 W m^{-2} higher than the 20-year average. In both cases, the positive net flux anomalies are primarily associated with positive anomalies in the net longwave, sensible, and latent heat fluxes, while the negative net flux anomalies are associated with negative anomalies in the net SW flux (not shown). The middle panels (10C,D) show SIC and daily averaged 10-m wind vectors, and reveal that positive surface flux anomalies tend to coincide with where the surface winds are directed off of the Eurasian continent. The bottom panels (10E,F) show the distributions of SIC within

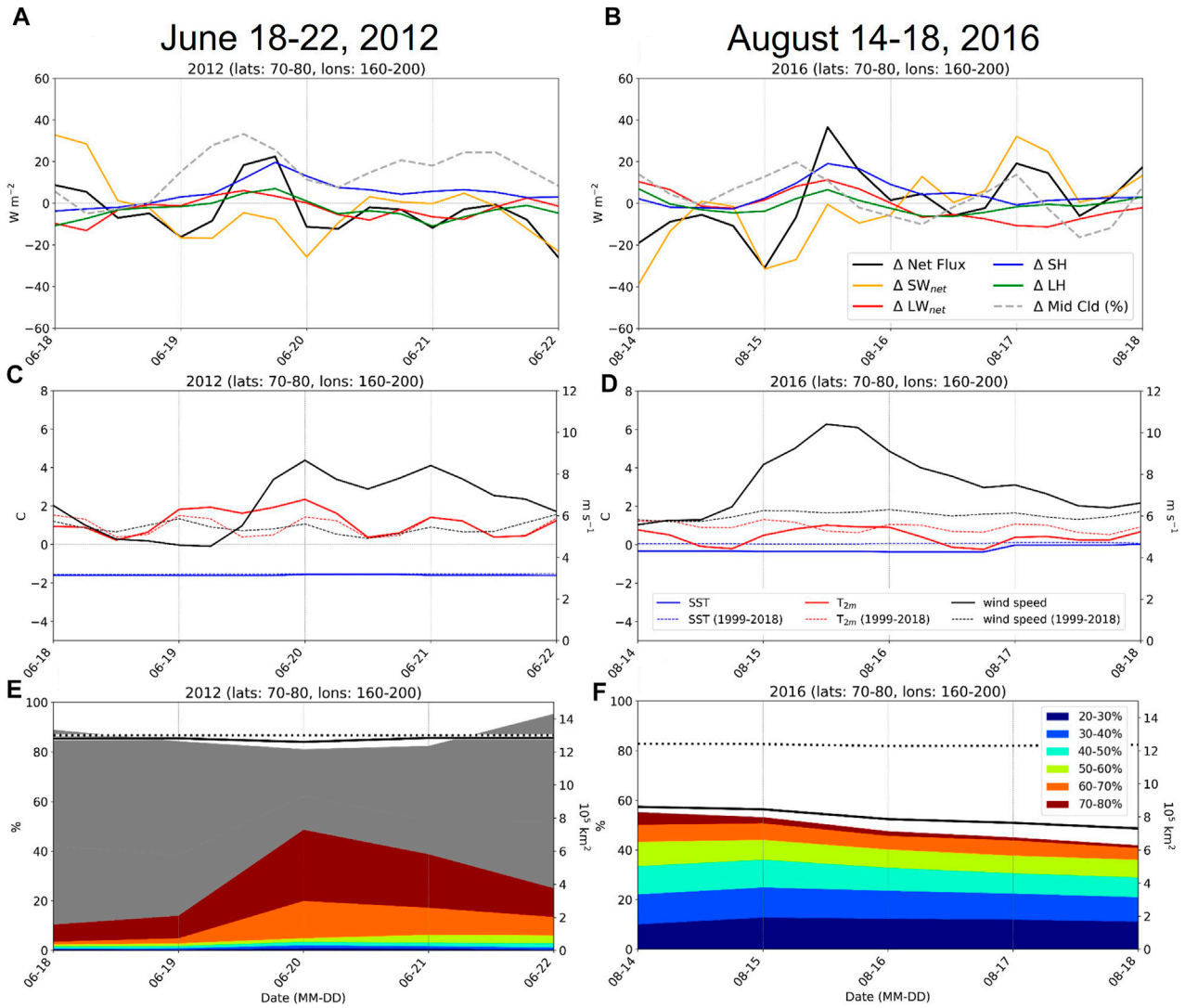

FIGURE 11 | (A,B) Time series of the area-weighted average of anomalies in each term in the surface energy budget (W m^{-2}) and the mid-level cloud fraction (%) from 18–22 June 2012 **(A)** and 14–18 August 2016 **(B)**. Averages are taken within the region outlined in white in **Figures 10A–D**, and anomalies are computed with the respect to the 20-year average of each quantity in this region. **(C,D)** As in 11**A,B,** but for the average SST and 2-m air temperature (left *y*-axis), and 10-m wind speed (right *y*-axis) for June 2012 **(C)** and August 2016 **(D)**. Solid lines denote averages computed in the year in which the cyclone occurred and dotted lines denote the 20-year averages. **(E,F)** The total fraction of grid points that are in each SIC bin during the same period in June 2012 **(E)**, and August 2016 **(F)**. Color-filled areas indicate the fraction of the region covered by grid points with SIC between 20 and 80%. Gray (white) regions indicate the fraction of area covered by SIC>80% (SIC<20%). The solid black line is the total sea ice area and the dotted black line is the 20-year average sea ice area in the region (right *y*-axis).

the boxes outlined in **Figures 10A–D**. The June cyclone primarily affected sea ice with concentrations >60%, much of which was adjacent to the Siberian coast. Consequently, internal ice forces were likely to be considerably stronger in this case than in August, greatly reducing the wind-induced drift of sea ice. In contrast, the August 2016 cyclone affected lower-concentration sea ice that was further from the Eurasian coastline. This made the sea ice more susceptible to drifting in response to the surface winds of the cyclone.

Figures 11A,B show times series of the area-weighted average within the outlined regions in **Figure 10** of the surface energy flux and the mid-level cloud fraction anomalies (relative to the 20-year average) for each cyclone. Quantities are only averaged over grid points covered by sea ice or open water (i.e., land points are excluded). **Figures 11C,D** show time series of the maximum 10-m wind speed, 2-m temperature, and SST averaged in the same region as in **Figures 11A,B**. During both cyclones, the largest positive anomaly in the net surface energy flux occurs about 6 h after the largest positive anomaly in mid-level cloud fraction. During the June cyclone, surface flux anomalies reach a local maximum about 12 h before the peak 10-m wind speeds occur, while the peak wind speed and surface flux anomalies roughly coincide during the August cyclone. In both cyclones, the sensible heat flux is the largest positive anomalous energy forcing, which is

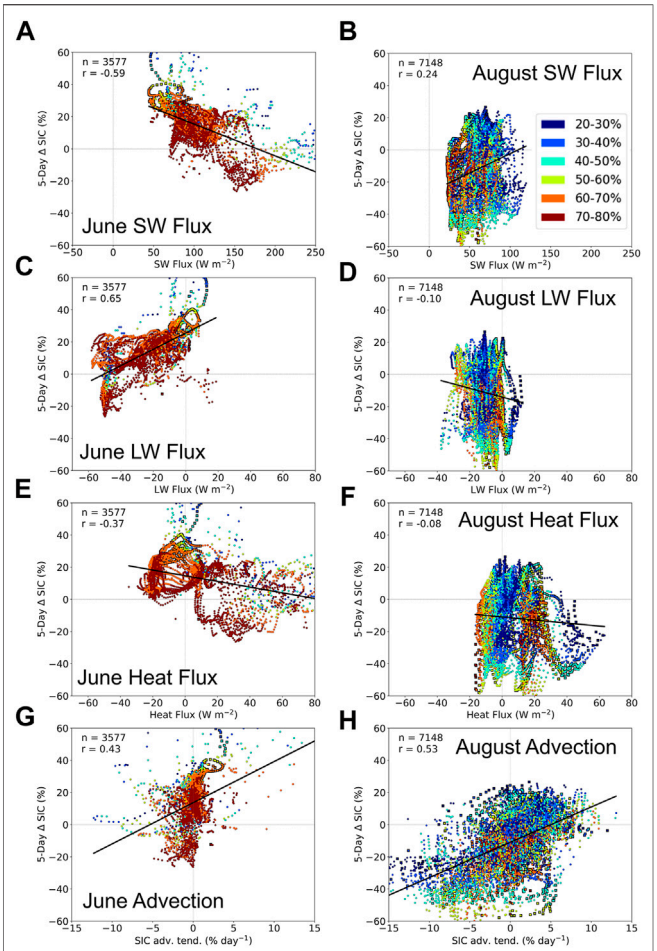

FIGURE 12 | Scatter plots of 5-day change in SIC at each grid point and the net SW flux **(A,B)**, the net LW flux **(C,D)**, the surface sensible + latent heat flux **(E,F)**, and the SIC advective tendency **(G,H)** on 19–20 June 2012 **(left column)** and on 15–16 August 2016 **(right column)**. Grid points are colored according to the SIC bin. Only grid points with SIC between 20 and 80% are plotted. Grid points that are in the **upper** decile of total cloud fraction are outlined in black. The black line is the linear fit through the data. The number of grid points (*n*) and the linear correlation (*r*) is printed in the **upper left** corner of each plot. Note the different *x*-axis ranges in each row. All correlations are significant at the 98% confidence level.

likely due to the combination of strong surface winds and above average 2-m temperature. The largest negative anomalies in the net SW flux associated with the cloud cover from each cyclone case occur at local noon (~00Z) on 20 June and 15 August, respectively. Despite clouds reducing the downward SW flux by a larger amount in June, the magnitude of the negative anomalies in the net SW flux is similar during the June and August cyclones, which is likely because the area-averaged surface albedo in June (0.55 on 20 June) is so much larger than in August (0.18 on 15 August).

Figures 11E,F show times series of the SIC distributions. In August, the initial SIC distribution has a much higher frequency of low-concentration sea ice compared to in June. Furthermore, the sea ice area in August 2016 (thick black line in **Figure 11F**) was already 30–50% lower than the 20-year average ice area

TABLE 1 | Average values of each surface energy flux and SIC advective tendency over different sets of grid points shown in **Figures 12A,C,E,G** during the June 2012 cyclone: All grid points ("All"), only grid points with 5-day SIC loss ("Ice Loss"), grid points in the upper decile of total cloud fraction ("Cloudy") and grid points in the lower decile of total cloud fraction ("Clear").

June 2012	SW (W m^{-2})	LW (W m^{-2})	Heat (W m^{-2})	Net (W m^{-2})	SIC Adv. (% day^{-1})
All	111	−24	8	95	−0.2
Ice Loss	157	−40	34	150	−1.1
Cloudy	73	−5	−3	65	0.5
Clear	178	−48	31	161	−1.6

TABLE 2 | As in **Table 1**, but for the grid points shown in **Figures 12B,D,F,H** during the August 2016 cyclone.

August 2016	SW (W m^{-2})	LW (W m^{-2})	Heat (W m^{-2})	Net (W m^{-2})	SIC Adv. (% day^{-1})
All	63	−10	4	57	−0.2
Ice Loss	60	−10	4	54	−1.3
Cloudy	52	−5	9	56	0.5
Clear	82	−22	-4	56	0.4

within this sub-region (dotted black line). As a result, both the reductions in sea ice area and the shift toward lower concentration sea ice associated with the August 2016 cyclone are more apparent than for the June 2012 cyclone. The June 2012 cyclone also induces a distributional shift toward lower concentration sea ice, but has almost no effect on the total sea ice area (**Figure 11E**). Moreover, the distributional shift in SIC during the June cyclone is only temporary, as the SIC distribution begins to resemble the pre-cyclone distribution 2 days after the passage of the cyclone. These differences in the apparent sea ice impacts of two cyclones that have similar intensity and similar effects on the surface energy balance emphasize the importance of the initial sea ice state for anticipating how cyclones will affect sea ice on short time scales (Lukovich et al., 2021).

Figure 12 shows scatter plots of the 5-day change in SIC versus the various surface forcing terms computed from ERA-5 within the boxed region outlined in **Figures 10A,B**, and for grid points with SIC between 20 and 80%. The surface energy fluxes in **Figures 12A–F** and the winds used to compute the advective tendencies in **Figures 12G,H** are averages of ERA-5 fields at four 6-hourly time steps in each day. In order to increase the sample size, the scatter plots include data from 2 days for each cyclone case during which there were positive net surface flux anomalies in **Figures 11A,B** (19 and 20 June for the 2012 cyclone, and 15 and 16 August for the 2016 cyclone). Points in **Figure 12** that correspond to grid points in the upper decile of total cloud fraction are outlined in black.

The relationship between the SW flux and changes in SIC varies considerably between the June and August cyclones. For the June cyclone, the relationship between local SIC change and SW flux (**Figure 12A**) is negative (r = -0.59), indicating that stronger SW flux is associated with enhanced local SIC loss. The sign of the relationship is consistent with climatology

(**Figure 4A**), but the magnitude is much larger. In contrast, the relationship between local SIC change and SW flux for the August cyclone is weakly positive (r = 0.24, **Figure 12B**). **Tables 1** and **2** list the average values of each flux over all the grid points shown in **Figure 12** ("All"), grid points with 5-day SIC loss ("Ice Loss"), and grid points in either the lower decile of total cloud fraction ("Clear") or the upper decile ("Cloudy"). Only a small fraction of the grid points in June experience SIC loss, but among those, the average SW flux is 41% larger than the average SW flux over all grid points in **Figure 12A** (**Table 1**). In contrast, the SW flux among the much larger number of grid points that experience SIC loss in August (60 W m^{-2}) is similar to the overall average (63 W m^{-2}), suggesting that the SW flux plays less of a role in local SIC changes in August. The smaller role of the SW flux in modulating sea ice variability in August may relate to a weaker cloud SW radiative forcing during the August cyclone. We estimate the cloud SW radiative forcing by comparing the downward component of the SW flux between the clear and cloudy grid points for each cyclone case. In June, the average downward SW flux is 371 W m^{-2} for clear grid points and 135 W m^{-2} for cloudy grid points, so clouds reduce the downward SW flux at the surface by 64%. During the August cyclone, clouds only reduce the downward SW flux by 38% relative to clear skies. Thus, the cloud SW radiative forcing is 26% smaller for the August cyclone than for the June cyclone. Because the average surface albedo is similar for clear and cloudy grid points in June and August, the reduced cloud SW radiative forcing in August means that clouds associated with the August cyclone have a significantly smaller impact on how much SW radiation is absorbed at the surface than clouds associated with the June cyclone.

In terms of the LW flux, we find a strong positive relationship between SIC change and LW flux in June (**Figure 12C**) and a weak negative relationship in August (**Figure 12D**). The positive relationship in June, in which stronger (or less upward) LW fluxes are associated with less SIC loss, is consistent with the climatology in this region (**Figure 4A** and **Figure 5A**) and, as discussed earlier, is likely a result of strong covariances between the LW and SW flux. The average LW flux in clear conditions is more negative than in cloudy conditions by 43 W m^{-2} in June (**Table 1**), which on its own would favor less ice loss, but the 105 W m^{-2} increase in SW flux in clear conditions compared to cloudy conditions more than compensates for the reduced LW flux. In August, the averages of both the SW and LW fluxes over ice loss grid points are similar to the respective averages over all grid points. In addition, the net radiative flux (SW + LW) in cloudy conditions is only about 13 W m^{-2} larger than in clear conditions in August (**Table 2**), providing further support for the idea that clouds associated with the June cyclone are much more likely to affect sea ice by changing the surface energy balance than clouds associated with the August cyclone.

Although the surface sensible and latent heat fluxes contribute substantially to the positive surface energy flux anomalies associated with the cyclones (**Figures 11A,B**), the surface heat flux on its own has only a weak relationship to local SIC loss in both the June and August cyclones (**Figures 12E,F**). This is because the magnitude of the heat flux is generally much smaller than that of the net radiative flux (**Table 1** and **Table 2**). Nevertheless, the average heat flux for ice loss grid points in June is 26 W m^{-2} larger than the average over all grid points, indicating a supporting role of stronger heat fluxes in local SIC loss. The average heat flux is larger at clear grid points for the June cyclone (**Table 1**), and at cloudy grid points for the August cyclone (**Table 2**). However, the increased heat flux in cloudy conditions during the August cyclone does not appear to be the main cause of local SIC loss within the region of interest, as the average heat flux for ice loss grid points during the August cyclone is the same as the average over all grid points (**Table 2**).

Figures 12G,H show the relationship between 5-day SIC change and the SIC advective tendency from the 10-m winds. For both the June and August cyclones, the sign of the relationship is positive and significant at the 98% confidence level. In addition, higher concentration sea ice tends to be associated with the weakest advective tendencies, while lower concentration sea ice is associated with stronger advective tendencies. Because the June cyclone primarily impacts higher concentration sea ice, the positive relationship between SIC advection and the local change in SIC is somewhat weaker than that for the August cyclone (r = 0.43 in June vs 0.53 in August). This is consistent with **Figure 4**, which shows that the magnitude of the correlation between SIC loss and the negative SIC advection is largest for low concentration sea ice in August. Nevertheless, the average advective tendency over ice loss grid points for both of the cyclone cases is more negative than the average over all grid points by about 1% per day (**Tables 1** and **2**). Unlike the surface energy fluxes, whose contributions to local SIC loss vary considerably between the June and August cyclones, sea ice advection has a consistent relationship to the local changes in SIC for both cyclone cases.

DISCUSSION AND CONCLUSION

This study quantifies the effect of cyclone winds and surface energy forcing on sea ice within the Pacific sector of the Arctic during the melt season months of June, July, and August. We consider the climatology of sea ice change during these months, as well as the statistics of cyclone effects on sea ice for a large sample of cyclone cases and for two individual cyclone cases that impacted sea ice in the East Siberian Sea near the beginning and end of the melt season.

From the statistical analysis of the large set of summer cyclones, we find that cyclone days in June and July have less local SIC loss and less region-wide SIA loss compared to days without cyclones. In contrast, cyclone days in August tend to be followed by slightly more SIC and SIA loss than non-cyclone days, although the relative enhancement of ice loss only persists for about 1 day. Although this analysis is limited to the Pacific sector of the Arctic, these results are broadly consistent with the localized effects of cyclones on sea ice cover throughout the Arctic marginal ice zone (Finocchio et al., 2020; Schreiber and Serreze 2020).

The SW flux has the largest influence of all terms in the surface energy budget on both local and regional ice loss during the summer. In June and July, larger SW fluxes are associated with more short-term ice loss than smaller SW fluxes. Consequently, the

largest reductions in local SIC in June tend to occur when skies are clear, indicating that the cloud radiative forcing is a key mechanism by which cyclones affect sea ice on short time scales early in the melt season. Calm and slightly cooler conditions in June also tend to be associated with larger local SIC loss, possibly because such conditions frequently accompany the clear skies that result in stronger SW fluxes at the surface. Later in the melt season, this correspondence between stronger SW fluxes and accelerated ice loss is only apparent for initially higher concentration sea ice. By August, cloudier conditions with more southerly surface winds are associated with slightly more local SIC loss. This suggests that the increased surface heat fluxes and enhanced sea ice advection in the warm sector of August cyclones enable these late-summer cyclones to be statistically associated with slightly enhanced local sea ice loss.

The advective tendency of SIC due to the 10-m wind is one of the most consistent predictors of both local and regional ice loss for the large sample of cyclones in the ECB region. We find the strongest relationship between advection and sea ice loss for low concentration sea ice in August. This supports previous studies arguing that the reduced mechanical strength of lower concentration sea ice makes it more susceptible to wind-induced drift and deformation (Hakkinen et al., 2008; Rampal et al., 2009; Spreen et al., 2011). The magnitude of the SIC advection within the ECB region is primarily controlled by the meridional component of the wind, with southerly winds favoring stronger negative sea ice advection. It is worth noting, however, that wind-driven advection only affects sea ice cover at a particular location, but does not affect the total sea ice volume across the Arctic.

We also analyzed two cyclones that reached a similar maximum intensity and affected a similar area in the East Siberian Sea, but at different times during the melt season. The early season cyclone that occurred in June 2012 primarily affected high concentration sea ice that extended from the central Arctic to the Siberian coast, while the late season cyclone that occurred in August 2016 affected an area of lower concentration sea ice located farther from the coast. In both cyclones, positive anomalies in the net surface energy flux are primarily a result of positive sensible heat flux anomalies, while negative anomalies in the net surface energy flux are due to negative SW flux anomalies. The magnitude and duration of positive anomalies in the net surface energy flux and surface wind speed are comparable between the two cyclones, yet the changes in the underlying sea ice distributions that followed the two cyclone cases are quite different. The August 2016 cyclone was followed by a reduction in sea ice area and a shift toward lower concentration sea ice (**Figure 11F**). Meanwhile, there was only a temporary shift toward lower SIC and no change in sea ice area (**Figure 11E**) following the June 2012 cyclone. This temporary shift to lower SIC may be an artifact of melt ponds being misclassified as open ocean (e.g., Meier et al., 2015), and this requires further investigation. Nonetheless, these apparent differences in the sea ice impacts of the two cyclones, despite their similar surface wind and energy forcing anomalies on sea ice, underscore the importance of the initial sea ice state and coupled upper ocean processes for determining the extent to which a cyclone impacts sea ice on short time scales (Lukovich et al., 2021).

A more detailed analysis of the surface energy balance and sea ice advection confirms many of the findings from the large set of cyclones regarding the evolving nature of how each forcing contributes to local sea ice changes during the melt season. For instance, SIC loss has a close relationship to the SW flux at each grid point during the June cyclone, and a relatively weaker relationship to SW flux during the August cyclone. The sign of the relationship between SIC loss and the LW flux is the opposite of that between SIC loss and the SW flux, which is not surprising given the strong anti-correlation between SW and LW fluxes. The different magnitudes of each radiative flux in June versus August ultimately determine which flux is most influential in the net. In June, the SW fluxes are so strong and the modulation of SW fluxes by clouds so large that variability in the SW flux is the most influential term in the surface energy budget in terms of local sea ice loss. Specifically, the decreased SW flux at the surface due to clouds reflecting sunlight far outweighs the increased LW flux at the surface due to clouds in June, such that clouds in June appear to behave more like an umbrella than a blanket (Perovich 2018). By August however, clouds behave like neither an umbrella nor a blanket in the net because the amount by which clouds decrease the SW flux at the surface, on average, is comparable to the amount by which they increase LW flux at the surface. As a result, the difference between clear and cloudy conditions is more likely to determine how much local SIC loss occurs during the June cyclone than during the August cyclone.

Although we generally find that larger surface heat fluxes are associated with enhanced ice loss in both the large sample of cyclones and for the two cyclone cases, this relationship is weaker than what was expected based on previous studies. Zhang et al. (2013) and Stern et al. (2020), for example, found that the anomalous sensible heat flux was the primary cause of the enhanced surface ice melt that occurred during the Great Arctic Cyclone of August 2012. The August 2016 cyclone analyzed in this study is comparable in many ways to the Great Arctic Cyclone, except that it was located further north and, perhaps as a result, was not associated with as much warm air advection from the Eurasian continent over sea ice. Based on our analysis in this study, the surface heat flux during the August 2016 cyclone was too small to explain the enhanced local SIC loss that followed. Instead, the SIC advection due to the surface wind forcing has a stronger statistical relationship to the local SIC loss following the August 2016 cyclone. This difference from the Great Arctic Cyclone in August 2012 highlights how the cyclone location relative to both land and the sea ice edge, and the underlying characteristics of the sea ice critically determine how a given cyclone will affect sea ice. Whether processes such as upper-ocean mixing, which was found to be a key cause of ice loss during the Great Arctic Cyclone, also contribute to the sea ice loss following the August 2016 cyclone requires further investigation. Fully coupled simulations of a diverse sample of Arctic summer cyclones spanning multiple decades would provide a richer understanding of the many ways in which cyclones affect sea ice, and could offer important clues as to how decadal variability and the rapidly evolving Arctic environment affect cyclone impacts on sea ice.

DATA AVAILABILITY STATEMENT

The ERA-5 datasets analyzed for this study can be found on the Copernicus Climate Change Service Climate Data Store (https://cds.climate.copernicus.eu/).

AUTHOR CONTRIBUTIONS

PF performed the analysis and wrote the manuscript. JD helped conceive the idea for this manuscript and contributed substantially to the analysis and interpretation of the results.

FUNDING

This research was supported by the Office of Naval Research Arctic Cyclones Departmental Research Initiative (Program Element 0601153N).

ACKNOWLEDGMENTS

We would like to thank the reviewers for their helpful feedback on an earlier version of this manuscript, Dave Ryglicki and Matt Fearon for preparing the ERA-5 data, and Michael Sprenger at ETH-Zurich for generating the cyclone tracks from the ERA-5 data.

REFERENCES

Crawford, A. D., and Serreze, M. C. (2016). Does the Summer Arctic Frontal Zone Influence Arctic Ocean Cyclone Activity? *J. Clim.* 29 (13), 4977–4993. doi:10.1175/JCLI-D-15-0755.1

Eastman, R., and Warren, S. G. (2010). Interannual Variations of Arctic Cloud Types in Relation to Sea Ice. *J. Clim.* 23 (15), 4216–4232. doi:10.1175/2010JCLI3492.1

Eastwood, S., Lavergne, T., and Tonboe, R. (2014). *Algorithm Theoretical Basis Document for the OSI SAF Global Reprocessed Sea Ice Concentration Product OSI-409*. The EUMETSAT Network of Satellite Appl. Fac.

Fearon, M. G., Doyle, J. D., Ryglicki, D. R., Finocchio, P. M., and Sprenger, M. (2021). The Role of Cyclones in Moisture Transport Into the Arctic. *Geophys. Res. Lett.* 48, e2020GL090353. doi:10.1029/2020gl090353

Finocchio, P. M., Doyle, J. D., Stern, D. P., and Fearon, M. G. (2020). Short-Term Impacts of Arctic Summer Cyclones on Sea Ice Extent in the Marginal Ice Zone. *Geophys. Res. Lett.* 47, e2020GL088338. doi:10.1029/2020gl088338

Graham, R. M., Cohen, L., Ritzhaupt, N., Segger, B., Graversen, R. G., Rinke, A., et al. (2019). Evaluation of Six Atmospheric Reanalyses Over Arctic Sea Ice From Winter to Early Summer. *J. Clim.* 32 (14), 4121–4143. doi:10.1175/JCLI-D-18-0643.1

Hakkinen, S., Proshutinsky, A., and Ashik, I. (2008). Sea Ice Drift in the Arctic Since the 1950s. *Geophys. Res. Lett.* 35 (19), 1–5. doi:10.1029/2008GL034791

Hersbach, H., Bell, B., Berrisford, P., Hirahara, S., Horányi, A., Muñoz-Sabater, J., et al. (2020). The ERA5 Global Reanalysis. *Q.J.R. Meteorol. Soc.* 146 (730), 1999–2049. doi:10.1002/qj.3803

Hirahara, S., Balmaseda, M. A., Boisseson, E. De., and Hersbach, H. (2016). Sea Surface Temperature and Sea Ice Concentration for ERA5. ERA Report Series. Available at: http://old.ecmwf.int/publications/.

Itkin, P., Spreen, G., Cheng, B., Doble, M., Girard-Ardhuin, F., Haapala, J., et al. (2017). Thin Ice and Storms: Sea Ice Deformation From Buoy Arrays Deployed During N-Ice2015. *J. Geophys. Res. Oceans.* 122 (6), 4661–4674. doi:10.1002/2016JC012403

Kay, J. E., and L'Ecuyer, T. (2013). Observational Constraints on Arctic Ocean Clouds and Radiative Fluxes During the Early 21st Century. *J. Geophys. Res. Atmos.* 118 (13), 7219–7236. doi:10.1002/jgrd.50489

Koyama, T., Stroeve, J., Cassano, J., and Crawford, A. (2017). Sea Ice Loss and Arctic Cyclone Activity From 1979 to 2014. *J. Clim.* 30 (12), 4735–4754. doi:10.1175/JCLI-D-16-0542.1

Kriegsmann, A., and Brümmer, B. (2014). Cyclone Impact on Sea Ice in the Central Arctic Ocean: A Statistical Study. *The Cryosphere.* 8 (1), 303–317. doi:10.5194/tc-8-303-2014

Landrum, L., and Holland, M. M. (2020). Extremes Become Routine in an Emerging New Arctic. *Nat. Clim. Chang.* 10, 1108–1115. doi:10.1038/s41558-020-0892-z

Lindsay, R., and Schweiger, A. (2015). Arctic Sea Ice Thickness Loss Determined Using Subsurface, Aircraft, and Satellite Observations. *The Cryosphere.* 9 (1), 269–283. doi:10.5194/tc-9-269-2015

Lukovich, J. V., Stroeve, J., Crawford, A., Hamilton, L., Tsamados, M., Heorton, H., et al. (2021). Summer Extreme Cyclone Impacts on Arctic Sea Ice. *J. Clim.* 34 (12), 1–54. doi:10.1175/jcli-d-19-0925.1

Maslanik, J. A., and Barry, R. G. (1989). Short-Term Interactions Between Atmospheric Synoptic Conditions and Sea-Ice Behaviour in the Arctic. *A. Glaciology.* 12 (January), 113–117. doi:10.3189/s0260305500007059

Maslanik, J., Stroeve, J., Fowler, C., and Emery, W. (2011). Distribution and Trends in Arctic Sea Ice Age Through Spring 2011. *Geophys. Res. Lett.* 38 (13), a–n. doi:10.1029/2011GL047735

Meier, W. N., Fetterer, F., Stewart, J. S., and Helfrich, S. (2015). How Do Sea-Ice Concentrations From Operational Data Compare With Passive Microwave Estimates? Implications for Improved Model Evaluations and Forecasting. *Ann. Glaciol.* 56 (69), 332–340. doi:10.3189/2015aog69a694

Overland, J. E., and Wang, M. (2013). When Will the Summer Arctic Be Nearly Sea Ice Free? *Geophys. Res. Lett.* 40 (10), 2097–2101. doi:10.1002/grl.50316

Perovich, D. K. (2018). Sunlight, Clouds, Sea Ice, Albedo, and the Radiative Budget: The Umbrella versus the Blanket. *The Cryosphere.* 12 (6), 2159–2165. doi:10.5194/tc-12-2159-2018

Persson, P. O. G. (2012). Onset and End of the Summer Melt Season over Sea Ice: Thermal Structure and Surface Energy Perspective From SHEBA. *Clim. Dyn.* 39 (6), 1349–1371. doi:10.1007/s00382-011-1196-9

Rae, J. G. L., Todd, A. D., Blockley, E. W., and Ridley, J. K. (2017). How Much Should We Believe Correlations Between Arctic Cyclones and Sea Ice Extent? *The Cryosphere.* 11, 3023–3034. doi:10.5194/tc-11-3023-2017

Rampal, P., Weiss, J., and Marsan, D. (2009). Positive Trend in the Mean Speed and Deformation Rate of Arctic Sea Ice, 1979-2007. *J. Geophys. Res.* 114 (5), 1–14. doi:10.1029/2008JC005066

Schreiber, E. A. P., and Serreze, M. C. (2020). Impacts of Synoptic-Scale Cyclones on Arctic Sea-Ice Concentration: a Systematic Analysis. *Ann. Glaciology.* 61 (82), 1–15. doi:10.1017/aog.2020.23

Screen, J. A., Simmonds, I., and Keay, K. (2011). Dramatic Interannual Changes of Perennial Arctic Sea Ice Linked to Abnormal Summer Storm Activity. *J. Geophys. Res.* 116 (15), 1–10. doi:10.1029/2011JD015847

Semenov, A., Zhang, X., Rinke, A., Dorn, W., and Dethloff, K. (2019). Arctic Intense Summer Storms and Their Impacts on Sea Ice-A Regional Climate Modeling Study. *Atmosphere.* 10 (4), 218. doi:10.3390/atmos10040218

Shupe, M. D., and Intrieri, J. M. (2004). Cloud Radiative Forcing of the Arctic Surface: The Influence of Cloud Properties, Surface Albedo, and Solar Zenith Angle. *J. Clim.* 17 (3), 616–628. doi:10.1175/1520-0442(2004)017<0616:CRFOTA>2.0.CO;2

Spreen, G., Kwok, R., and Menemenlis, D. (2011). Trends in Arctic Sea Ice Drift and Role of Wind Forcing: 1992-2009. *Geophys. Res. Lett.* 38 (19), a–n. doi:10.1029/2011GL048970

Sprenger, M., Fragkoulidis, G., Binder, H., Croci-Maspoli, M., Graf, P., Grams, C. M., et al. (2017). Global Climatologies of Eulerian and Lagrangian Flow Features Based on ERA-Interim. *Bull. Am. Meteorol. Soc.* 98 (8), 1739–1748. doi:10.1175/BAMS-D-15-00299.1

Steele, M., Zhang, J., and Ermold, W. (2010). Mechanisms of Summertime Upper Arctic Ocean Warming and the Effect on Sea Ice Melt. *J. Geophys. Res.* 115 (11), 1–12. doi:10.1029/2009JC005849

Stern, D. P., Doyle, J. D., Barton, N. P., Finocchio, P. M., Komaromi, W. A., and Metzger, E. J. (2020). The Impact of an Intense Cyclone on Short-Term Sea Ice Loss in a Fully Coupled Atmosphere-Ocean-Ice Model. *Geophys. Res. Lett.* 47, 1–10. doi:10.1029/2019gl085580

Stroeve, J. C., Serreze, M. C., Holland, M. M., Kay, J. E., Malanik, J., and Barrett, A. P. (2012). The Arctic's Rapidly Shrinking Sea Ice Cover: a Research Synthesis. *Climatic Change.* 110 (3–4), 1005–1027. doi:10.1007/s10584-011-0101-1

Strong, C., Foster, D., Cherkaev, E., Eisenman, I., and Golden, K. M. (2017). On the Definition of Marginal Ice Zone Width. *J. Atmos. Oceanic Technology.* 34 (7), 1565–1584. doi:10.1175/JTECH-D-16-0171.1

Thorndike, A. S., and Colony, R. (1982). Sea Ice Motion in Response to Geostrophic Winds. *J. Geophys. Res.* 87 (C8), 5845. doi:10.1029/jc087ic08p05845

Vihma, T., Tisler, P., and Uotila, P. (2012). Atmospheric Forcing on the Drift of Arctic Sea Ice in 1989-2009. *Geophys. Res. Lett.* 39 (2), a–n. doi:10.1029/2011GL050118

Wernli, H., and Schwierz, C. (2006). Surface Cyclones in the ERA-40 Dataset (1958-2001). Part I: Novel Identification Method and Global Climatology. *J. Atmos. Sci.* 63, 2486. doi:10.1175/jas3766.1

Zhang, J., Lindsay, R., Schweiger, A., and Steele, M. (2013). The Impact of an Intense Summer Cyclone on 2012 Arctic Sea Ice Retreat. *Geophys. Res. Lett.* 40 (4), 720–726. doi:10.1002/grl.50190

Conflict of Interest: The authors declare that the research was conducted in the absence of any commercial or financial relationships that could be construed as a potential conflict of interest.

frontiers in Earth Science

ORIGINAL RESEARCH
published: 20 October 2021
doi: 10.3389/feart.2021.725816

Understanding the Differences Between TOA and Surface Energy Budget Attributions of Surface Warming

Sergio A. Sejas[1], Xiaoming Hu[2,3,4], Ming Cai[5] and Hanjie Fan[6]*

[1]Science Systems and Applications Inc., Hampton, VA, United States, [2]School of Atmospheric Sciences, Sun Yat-sen University, Zhuhai, China, [3]Southern Marine Science and Engineering Guangdong Laboratory, Zhuhai, China, [4]Guangdong Province Key Laboratory for Climate Change and Natural Disaster Studies, Zhuhai, China, [5]Department of Earth, Ocean and Atmospheric Sciences, Florida State University, Tallahassee, FL, United States, [6]State Key Laboratory of Tropical Oceanography, South China Sea Institute of Oceanology, Chinese Academy of Sciences, Guangzhou, China

Energy budget decompositions have widely been used to evaluate individual process contributions to surface warming. Conventionally, the top-of-atmosphere (TOA) energy budget has been used to carry out such attribution, while other studies use the surface energy budget instead. However, the two perspectives do not provide the same interpretation of process contributions to surface warming, particularly when executing a spatial analysis. These differences cloud our understanding and inhibit our ability to shrink the inter-model spread. Changes to the TOA energy budget are equivalent to the sum of the changes in the atmospheric and surface energy budgets. Therefore, we show that the major discrepancies between the surface and TOA perspectives are due to non-negligible changes in the atmospheric energy budget that differ from their counterparts at the surface. The TOA lapse-rate feedback is the manifestation of multiple processes that produce a vertically non-uniform warming response such that it accounts for the asymmetry between the changes in the atmospheric and surface energy budgets. Using the climate feedback-response analysis method, we are able to decompose the lapse-rate feedback into contributions by individual processes. Combining the process contributions that are hidden within the lapse-rate feedback with their respective direct impacts on the TOA energy budget allows for a very consistent picture of process contributions to surface warming and its inter-model spread as that given by the surface energy budget approach.

Keywords: lapse-rate feedback, climate feedbacks, surface warming, feedback decomposition, inter-model spread, air temperature feedback, TOA energy budget, surface energy budget

OPEN ACCESS

Edited by:
Jing-Jia Luo,
Nanjing University of Information Science and Technology, China

Reviewed by:
Beate G. Liepert,
Seattle University, United States
Michael Previdi,
Lamont Doherty Earth Observatory (LDEO), United States

****Correspondence:***
Sergio A. Sejas
sergio.sejas@nasa.gov

Specialty section:
This article was submitted to Atmospheric Science, a section of the journal Frontiers in Earth Science

Received: *15 June 2021*
Accepted: *28 September 2021*
Published: *20 October 2021*

Citation:
Sejas SA, Hu X, Cai M and Fan H (2021) Understanding the Differences Between TOA and Surface Energy Budget Attributions of Surface Warming. Front. Earth Sci. 9:725816. doi: 10.3389/feart.2021.725816

INTRODUCTION

The Intergovernmental Panel on Climate Change (IPCC) Assessment Report (AR) five states that the warming of the climate system is unequivocal [IPCC, 2013]. There is a clear globally averaged combined land and ocean surface warming of ~0.85 K with a 90% confidence interval of 0.65–1.06 K, calculated by a linear trend over the period 1880–2012 (Hartmann et al., 2013). Over the same time period there has also been a pronounced increase in well-mixed greenhouse gases, particularly carbon

dioxide (CO_2), due to human activities (Hartmann et al., 2013). This anthropogenic increase in CO_2 is the primary driver of the surface warming, which is corroborated by simple climate models and complex coupled global climate models demonstrating that increasing the CO_2 concentration leads to a warming of the surface (Manabe and Wetherald 1975; Robock 1983; Washington and Meehl 1984; Schlesinger and Mitchell 1987; Manabe et al., 1991).

Increased CO_2 triggers not only an increase of surface temperature but influences many other climate variables through the complex interactions of the climate system. These perturbed climate variables, including surface and air temperatures, atmospheric water vapor, clouds, ice coverage, feedback on each other leading to the observed or simulated response of the climate system to an increase of CO_2. A particular emphasis has been placed in the climate literature on understanding the surface warming response to an increase of CO_2, and thus understanding how the different climate feedbacks triggered by the CO_2 increase contribute to the surface temperature response. With this purpose in mind, many climate feedback analysis methods have been developed to attribute and understand the contributions of individual climate feedbacks to surface warming (Wetherald and Manabe 1988; Cess et al., 1996; Aires and Rossow 2003; Gregory et al., 2004; Soden et al., 2008; Lu and Cai 2009a; Lahellec and Dufresne 2013). The advantages and disadvantages of these methods have been previously discussed (Aires and Rossow 2003; Soden et al., 2004; Stephens 2005; Bony et al., 2006; Bates 2007; Cai and Lu 2009; Klocke et al., 2013; Lahellec and Dufresne 2013, 2014).

The most commonly applied methods use a top-of-atmosphere (TOA) energy budget analysis to attribute the different climate feedback effects on surface temperature. The TOA serves as a natural reference point as it determines the total energy budget of Earth's climate system. An advantage of using a TOA point-of-view is that radiative processes dominate the TOA energy budget. In a global-mean analysis, at equilibrium, all that has to be analyzed is the insolation, outgoing solar radiation, and outgoing longwave (LW) radiation (OLR), while oceanic and atmospheric heat transport must also be taken into account in a spatial analysis. Due to the extensive spatial coverage and reliability of recent satellite measurements of outgoing solar and LW radiation compared to surface measurements of radiative fluxes, latent and sensible heat fluxes, and dynamic transport, the TOA perspective is the favored method when performing observation-to-model feedback comparisons (e.g., Thorsen et al., 2018; Kramer et al., 2021). The TOA energy budget is thought to be a proper tool to evaluate surface temperature change, as moist convection in the Tropics leads to a vertical temperature profile that follows the moist lapse rate; this makes tropical atmospheric warming proportional to the surface warming (Hansen et al., 1997; Sobel et al., 2001; Goosse et al., 2018). Since moist convection only connects the surface to the troposphere, stratospheric adjustment is typically carried out, such that the radiative equilibrium response in the stratosphere is included in the radiative forcing at the TOA, or alternatively the analysis is carried out at the tropopause instead of the TOA (Hansen et al., 1997). Strong static stability at high latitudes, however, suppresses deep convection decoupling the surface from most of the troposphere. Thus, the applicability of using the conventional TOA feedback analysis to evaluate surface temperature change at high latitudes has been brought into question (Pithan and Mauritsen 2014; Payne et al., 2015; Goosse et al., 2018). The simplicity of the TOA perspective is also a limitation, as studies indicate the TOA lapse-rate feedback is a reflection of multiple processes (including non-radiative and non-local processes) that establish the non-uniform vertical warming pattern (Cai and Lu 2009; Cronin and Jansen 2016; Feldl et al., 2020; Boeke and Sejas, 2021). To avoid some of the limitations in the conventional TOA feedback analysis, recent studies have used the surface energy budget to analyze climate feedback effects on surface temperature (Andrews et al., 2009; Lu and Cai 2009b; Pithan and Mauritsen 2014; Laîné et al., 2016; Sejas and Cai 2016; Boeke and Taylor 2018), as surface temperature change is directly connected to surface energy flux changes. However, the simplicity, utility, and long-standing tradition of the TOA perspective have made it the preferred way to evaluate climate feedback contributions to surface warming.

Regardless of perspective, we contend that the forcing and feedback analysis should provide, at minimum, the same qualitative conclusions for the CO_2 forcing and all the different radiative feedback contributions to the surface warming. After all, we do not want differing perspectives to provide contrasting views on which radiative feedbacks contribute most to global warming, polar warming amplification (PWA), or whether a specific radiative feedback amplifies or reduces the surface warming. Otherwise, it would be difficult to gain a true understanding of the warming response and spatial pattern, and thus difficult to comprehend the causes of the inter-model warming spread in model projections. If differences exist it is important to understand their physical cause and evaluate whether these differences are model dependent or robust features of climate models.

Unfortunately, previous studies show that the magnitude and spatial structure of TOA radiative feedbacks do differ from their surface counterparts, particularly LW feedbacks (Previdi and Liepert 2012; Pithan and Mauritsen 2014; Colman 2015). The differences are mainly due to the large atmospheric optical depth in the LW that causes TOA LW feedbacks to be predominantly impacted by upper tropospheric changes, while surface LW feedbacks are impacted by lower tropospheric changes.

Ideally, we should be able to unify the two perspectives to provide a consistent picture of process contributions to surface warming and its latitudinal pattern. The goal of this study is thus to analyze and explain the differences between the results given by the TOA and surface energy budget decompositions by evaluating the impact of the atmospheric energy budget. Then, on the basis of the understanding gained, we seek to reconcile the results provided by the two perspectives.

FEEDBACK ANALYSIS

TOA Perspective

Feedback analysis methods, such as the partial radiative perturbation (PRP; Wetherald and Manabe 1988) and radiative kernel techniques (Soden et al., 2008) have used a

TOA perspective to analyze forcing and feedback contributions to surface warming. The TOA feedback analysis makes use of the perturbation of the TOA energy budget triggered by some external forcing,

$$\Delta\frac{\partial E_{TOA}}{\partial t} = \Delta S_{TOA} - \Delta R_{TOA} + \Delta Dyn\_trans, \tag{1}$$

where the term on the left is the change in the heat uptake below the TOA for a given grid point. ΔS_{TOA} is the change in net incoming solar or shortwave (SW) radiative flux, ΔR_{TOA} is the change in net outgoing longwave (LW) radiative flux, and ΔDyn_trans is the change in net heat transport into the column below the TOA by the atmosphere and ocean dynamics. The radiative perturbation is then assumed small enough to linearize,

$$\Delta\left(S_{TOA} - R_{TOA}\right) = \begin{bmatrix} \Delta\left(S^{ext}_{TOA} - R^{ext}_{TOA}\right) + \Delta\left(S^{wv}_{TOA} - R^{wv}_{TOA}\right) + \Delta\left(S^{cld}_{TOA} - R^{cld}_{TOA}\right) \\ +\Delta S^{alb}_{TOA} - \sum_{j=1}^{M}\frac{\partial R_{TOA}}{\partial T_j}\Delta T_j - \frac{\partial R_{TOA}}{\partial T_s}\Delta T_s \end{bmatrix}, \tag{2}$$

where the change in radiative flux has been decomposed into changes in radiative flux caused by the external forcing (*ext*), water vapor changes (*wv*), cloud changes (*cld*), surface albedo changes (*alb*), atmospheric temperature changes over *M* atmospheric layers, and surface temperature changes. Substituting **(2)** into **(1)** and rearranging the equation gives

$$\frac{\partial R_{TOA}}{\partial T_s}\Delta T_s = \begin{bmatrix} \Delta\left(S^{ext}_{TOA} - R^{ext}_{TOA}\right) + \Delta\left(S^{wv}_{TOA} - R^{wv}_{TOA}\right) + \Delta\left(S^{cld}_{TOA} - R^{cld}_{TOA}\right) \\ +\Delta S^{alb}_{TOA} - \sum_{j=1}^{M}\frac{\partial R_{TOA}}{\partial T_j}\Delta T_j + \Delta Dyn\_trans - \Delta\frac{\partial E_{TOA}}{\partial t} \end{bmatrix}. \tag{3}$$

In the conventional TOA feedback analysis, it is also common for the atmospheric temperature change to be decomposed into an atmospheric temperature response equal to the surface temperature change plus the deviation from vertical uniformity,

$$-\sum_{j=1}^{M}\frac{\partial R_{TOA}}{\partial T_j}\Delta T_j = \left(-\sum_{j=1}^{M}\frac{\partial R_{TOA}}{\partial T_j}\right)\Delta T_s - \sum_{j=1}^{M}\frac{\partial R_{TOA}}{\partial T_j}\left(\Delta T_j - \Delta T_s\right). \tag{4}$$

After substituting **(4)** into **(3)** and rearranging, **(3)** becomes

$$\sum_{j=1}^{M+1}\frac{\partial R_{TOA}}{\partial T_j}\Delta T_s = \begin{bmatrix} \Delta\left(S^{ext}_{TOA} - R^{ext}_{TOA}\right) + \Delta\left(S^{wv}_{TOA} - R^{wv}_{TOA}\right) + \Delta\left(S^{cld}_{TOA} - R^{cld}_{TOA}\right) + \\ \Delta S^{alb}_{TOA} - \sum_{j=1}^{M}\frac{\partial R_{TOA}}{\partial T_j}\left(\Delta T_j - \Delta T_s\right) + \Delta Dyn\_trans - \Delta\frac{\partial E_{TOA}}{\partial t} \end{bmatrix}, \tag{5}$$

where 'M+1' corresponds to the surface layer 's', and $-\sum_{j=1}^{M}\frac{\partial R_{TOA}}{\partial T_j}\left(\Delta T_j - \Delta T_s\right)$ is known as the lapse-rate feedback. It follows from **(5)** that if the external forcing causes an increase in net energy flux into the climate system (positive value) the climate will warm. Thus, if any of the changes triggered by the external forcing causes the net energy flux into the climate system to further increase (positive value), the warming will be amplified, and that process is said to be a positive feedback. On the other hand, if the physical process enhances the energy loss to space the warming will be suppressed and the process is said to be a negative feedback. Considering equilibrium conditions, the heat uptake term disappears in **(3)** and **(5)**. The non-radiative heat transport term will vanish in **(3)** and **(5)** by taking a global-mean.

Surface Perspective

While much less common in the climate literature, feedback analysis methods have also employed a surface perspective to analyze the contributions of forcing and feedbacks to the surface warming (Andrews et al., 2009; Lu and Cai 2009b; Pithan and Mauritsen 2014; Laîné et al., 2016; Sejas and Cai 2016; Boeke and Taylor 2018; Hu et al., 2018). The surface perspective entails the use of the surface energy budget perturbed by the external forcing and feedbacks,

$$\Delta\left(\frac{\partial E_s}{\partial t}\right) = \Delta S_s - \Delta R_s + \Delta Q_s^{non\_rad}, \tag{6}$$

where the terms are similar to **(1)**, except everything is restricted to the surface layer. Following a linearization similar to that in **(2)** and after some rearrangement, **(6)** becomes

$$\frac{\partial R_s}{\partial T_s}\Delta T_s = \begin{bmatrix} \Delta\left(S^{ext}_s - R^{ext}_s\right) + \Delta\left(S^{wv}_s - R^{wv}_s\right) + \Delta\left(S^{cld}_s - R^{cld}_s\right) + \Delta S^{alb}_s \\ -\sum_{j=1}^{M}\frac{\partial R_{TOA}}{\partial T_j}\Delta T_j - \Delta Q_s^{non\_rad} - \Delta\left(\frac{\partial E_s}{\partial t}\right) \end{bmatrix}. \tag{7}$$

Equation 7 states that the change in surface thermal emission is equal to the sum of the net radiative flux change due to the external forcing (*ext*), water vapor changes (*wv*), cloud changes (*cld*), surface albedo changes (*alb*), and atmospheric temperature changes plus the surface energy flux change due to non-radiative processes (such as surface latent and sensible heat fluxes, and ocean heat transport) minus the change in surface heat uptake. Therefore, if the external forcing causes an increase in net energy flux into the surface layer, **(7)** implies the surface will warm. If a feedback also increases the net energy flux into the surface layer (positive value) it will amplify the surface warming (i.e., positive feedback), but if it decreases the net energy flux into the surface layer (negative value) it will counter the surface warming (i.e., negative feedback). Unlike the conventional TOA feedback analysis, climate studies using the surface perspective do not decompose the atmospheric temperature change into that equal to the surface temperature response plus the deviation from vertical uniformity. Furthermore, notice that while the heat uptake term would disappear for equilibrium conditions, the non-radiative term in the surface perspective would not vanish in the global-mean.

Atmosphere's Energy Budget

The TOA energy budget is equal to the vertical sum of the surface and atmospheric energy budgets. Therefore, the atmospheric energy budget can be used to understand the differences between the surface and TOA energy budgets. The perturbation of the atmospheric energy budget by an external forcing is given by,

$$\Delta\left(\frac{\partial E_i}{\partial t}\right) = \Delta S_i - \Delta R_i + \Delta Q_i^{non-rad}, \quad (8)$$

which is similar to **(6)**, except each term is evaluated at the *i*-th atmospheric layer. The total atmospheric energy budget is the sum of all *M* atmospheric layers. Summing the *M* atmospheric layers and linearizing the radiative terms similar to **(2)**, which is denoted by subscript "atm", provides the total atmospheric energy budget,

$$\Delta\left(\frac{\partial E_{atm}}{\partial t}\right) \approx \begin{bmatrix} \Delta\left(S_{atm}^{ext} - R_{atm}^{ext}\right) + \Delta\left(S_{atm}^{wv} - R_{atm}^{wv}\right) + \Delta\left(S_{atm}^{cld} - R_{atm}^{cld}\right) \\ +\Delta S_{atm}^{alb} - \sum_{j=1}^{M}\frac{\partial R_{atm}}{\partial T_j}\Delta T_j - \frac{\partial R_{atm}}{\partial T_s}\Delta T_s + \Delta Q_{atm}^{non\_rad} \end{bmatrix}. \quad (9)$$

The sum of corresponding terms in **(7)** and **(9)** are equal to their corresponding terms in **(3)**.

Climate Feedback-Response Analysis Method

The 3-dimensional partial temperature changes due to external forcing and climate feedbacks can be obtained by using the climate feedback-response analysis method (CFRAM; Lu and Cai 2009a; Cai and Lu 2009). At a given grid point, the CFRAM considers the energy budget of its atmosphere-surface column to evaluate the local temperature change needed to balance the local energy flux perturbation:

$$\Delta\vec{T} = \left(\frac{\partial\vec{R}}{\partial\vec{T}}\right)^{-1}\left[\Delta\left(\vec{S}^{ext} - \vec{R}^{ext}\right) + \Delta\left(\vec{S}^{wv} - \vec{R}^{wv}\right) + \Delta\left(\vec{S}^{cld} - \vec{R}^{cld}\right) + \Delta\vec{S}^{alb} + \Delta\vec{Q}^{non\_rad}\right], \quad (10)$$

where the vector symbol denotes the vertical profile of a variable from the surface layer j = (M+1) to the top layer of the atmosphere j = 1 with $\vec{T}$ standing for temperature, $\vec{S}$ for the vertical convergence of shortwave radiative fluxes, $\vec{R}$ for the vertical divergence of longwave radiative fluxes, and $\vec{Q}$ for the (horizontal or vertical) convergence of non-radiative energy fluxes. In **(10)**, $\left(\frac{\partial\vec{R}}{\partial\vec{T}}\right)$ is the Planck feedback matrix whose jth column represents the vertical profile of (linearized) thermal radiative cooling perturbation due to 1 K warming in the jth layer alone. The CFRAM allows us to calculate the vertical profile of partial temperature changes due to changes in process *x* (e.g., water vapor, clouds, dynamics, etc. . .):

$$\Delta\vec{T}^{(x)} = \left(\frac{\partial\vec{R}}{\partial\vec{T}}\right)^{-1}\Delta\vec{F}^{(x)}, \quad (11)$$

where $\Delta\vec{F}^{(x)}$ is the vertical energy flux perturbation profile due to changes in process *x*. We can leverage the CFRAM results to decompose the lapse-rate feedback in the TOA perspective and the atmospheric temperature feedback in the surface perspective into individual contributions by radiative and non-radiative processes, respectively:

$$-\sum_{j=1}^{M}\frac{\partial R_{TOA}}{\partial T_j}\left(\Delta T_j - \Delta T_s\right) = -\sum_x\left[\sum_{j=1}^{M}\frac{\partial R_{TOA}}{\partial T_j}\left(\Delta T_j^x - \Delta T_s^x\right)\right] \quad (12)$$

$$-\sum_{j=1}^{M}\frac{\partial R_s}{\partial T_j}\Delta T_j = -\sum_x\sum_{j=1}^{M}\frac{\partial R_s}{\partial T_j}\Delta T_j^x. \quad (13)$$

The direct contribution of individual processes to the TOA energy budget (i.e., from **Eq. 5**) can be combined with their lapse-rate feedback contributions to produce the total TOA energy flux perturbation due to process *x*,

$$\Delta Fnet_{TOA}^x = \Delta F_{TOA}^x - \sum_{j=1}^{M}\frac{\partial R_{TOA}}{\partial T_j}\left(\Delta T_j^x - \Delta T_s^x\right). \quad (14)$$

Similarly, the direct contribution of individual processes to the surface energy budget (i.e., from **Eq. 7**) can be combined with their air temperature feedback contributions to produce the total surface energy flux perturbation due to process *x*,

$$\Delta Fnet_{sfc}^x = \Delta F_{sfc}^x - \sum_{j=1}^{M}\frac{\partial R_{sfc}}{\partial T_j}\Delta T_j^x. \quad (15)$$

DATA AND ANALYSIS PROCEDURES

CMIP5 Simulations

All data used in this study are derived from the monthly mean outputs of the Historical and RCP8.5 model simulations produced by the Coupled Model Intercomparison Project Version 5 (CMIP5), which are archived and freely accessible at http://data.ceda.ac.uk/badc/cmip5/data/cmip5/ and https://esgf-node.llnl.gov/search/cmip5/. **Table 1** lists the 25 models' simulations considered in this study, whereas **Supplementary Table S1** lists the seven models whose CMIP5 simulations are archived in the CMIP5 websites but are not used in this study because of the lack of either cloud fields or the information necessary to process cloud fields. Only a single ensemble member (r1i1p1) is used for each model. The historical and future climate states are evaluated as the 50-year means of the 1951–2000 period in the historical simulations and the 2051–2100 period in the RCP8.5 simulations. The surface temperature difference between the future and historical climate states of each model corresponds to the global warming projection of that model. The specific output fields of the historical and RCP8.5 simulations used in the analysis include cloud area fraction (cl), mass fraction of cloud ice (cli), mass fraction of cloud water (clw), specific humidity (hus), air temperature (ta), mole fraction of O3 (tro3), surface air pressure (ps), near-surface specific humidity (huss), surface temperature (ts), surface downwelling shortwave radiation (rsds), surface upwelling shortwave radiation (rsus), TOA incident shortwave radiation (rsdt), surface upward sensible heat flux (hfss), and surface upward latent heat flux (hfls). Well-mixed greenhouse gas concentrations (e.g., CO_2, CH_4, and N_2O) are obtained from the RCP forcing database freely accessible at https://tntcat.iiasa.ac.at/RcpDb/. The first six

TABLE 1 | A list of the CMIP5 models analyzed in this study.

	Model acronym	Institution
1	bcc-csm1-1	Beijing Climate Center
2	BNU-ESM	College of Global Change and Earth System Science, Beijing Normal University
3	CanESM2	Canadian Centre for Climate Modelling and Analysis
4	CCSM4	National Center for Atmospheric Research
5	CESM1-BGC	NSF/DOE, National Center for Atmospheric Research
6	CESM1-CAM5	
7	CMCC-CESM	Centro Euro-Mediterraneo per I Cambiamenti Climatici
8	CMCC-CM	
9	CMCC-CMS	
10	CSIRO-Mk3.6.0	CSIRO in collaboration with Queensland Climate Change Centre of Excellence
11	FGOALS-g2	Institute of Atmospheric Physics, Chinese Academy of Sciences, and Tsinghua University
12	GFDL-CM3	NOAA-Geophysical Fluid Dynamics Laboratory
13	GFDL-ESM2G	
14	GFDL-ESM2M	
15	GISS-E2-H	NASA-Goddard Institute for Space Studies
16	GISS-E2-R	
17	IPSL-CM5A-LR	Institute Pierre-Simon Laplace
18	IPSL-CM5A-MR	
19	IPSL-CM5B-LR	
20	MIROC5	The University of Tokyo, National Institute for Environmental Studies, and Japan Agency for Marine-Earth Science and Technology
21	MPI-ESM-LR	Max Planck Institute for Meteorology
22	MPI-ESM-MR	
23	MRI-CGCM3	Meteorological Research Institute
24	NorESM1-M	Norwegian Climate Centre
25	NorESM1-ME	

variables are multi-level and interpolated into 17-level P coordinate (1,000, 925, 850, 700, 600, 500, 400, 300, 250, 200, 150, 100, 70, 50, 30, 20, and 10 hPa) before conducting the analysis. The results for of all 25 models have been interpolated onto a common grid with a $1^{\circ} \times 1^{\circ}$ horizontal resolution.

Analysis Procedures

To obtain and isolate the radiative effects of the forcing and feedbacks on the TOA, atmospheric, and surface energy budgets the Fu-Liou radiative transfer mode (RTM; Fu and Liou 1992, 1993) is used for all offline radiative flux calculations at each longitude-latitude grid point of the model using the 50-year monthly mean outputs from the CMIP5 historical and RCP8.5 climate simulations. The radiative flux change at the TOA, atmosphere, and surface due to a specific process (e.g. water vapor change) is calculated by taking the perturbed 50-year monthly mean field of the process in question from the RCP8.5 simulations, with all other variables being held to their 50-year monthly mean fields from the historical simulations, and using these fields as input in our offline radiative flux calculations; then the historical radiative flux is subtracted from the perturbed offline radiative flux giving the radiative flux change due to that process alone, consistent with the PRP approach. As an extension of the PRP approach, similar to the radiative kernel technique, the partial derivatives in the above equations are obtained with the offline radiative transfer model by individually perturbing the temperature in each layer '*j*' by 1 K and calculating the perturbed radiative flux at the TOA, atmosphere, and surface due to the 1 K increase of that specific layer alone; then as before the unperturbed radiative flux is subtracted from the perturbed offline radiative flux giving the approximate value of the partial derivative. The monthly-mean calculations are then annually averaged, from which the analysis follows.

The use of time-mean fields and a different RTM (i.e., the Fu-Liou RTM) than that native to the CMIP5 models to calculate the offline radiative fluxes introduces an error that is distinct from the linearization error. Previous studies indicate that the use of time-mean cloud fields accounts for most of this error (Sejas et al., 2014; Song et al., 2014a). Song et al. (2014a) found that accounting for the diurnal cycle using hourly data greatly reduced the error introduced by time-mean cloud fields. **Supplementary Figure S1** shows there are non-negligible differences between the net radiative flux changes outputted by the CMIP5 models (left column in **Supplementary Figure S1**) and that calculated with the Fu-Liou RTM using time-mean fields (middle column in **Supplementary Figure S1**). The linearization error, however, is small, as the linearized version of the net radiative flux changes (right column in **Supplementary Figure S1**) is quite similar to the non-linearized version given by the Fu-Liou RTM (middle column in **Supplementary Figure S1**).

The non-radiative terms (e.g., thermodynamics, convection, large-scale dynamics, etc. . .) are not decomposed in this study, primarily because the energy flux changes due to non-radiative processes are generally not part of the standard CMIP5 data output. In addition, the CMIP5 present and future climate states are not in equilibrium indicating the ocean heat storage is non-negligible. Therefore, we calculate the combined net energy flux

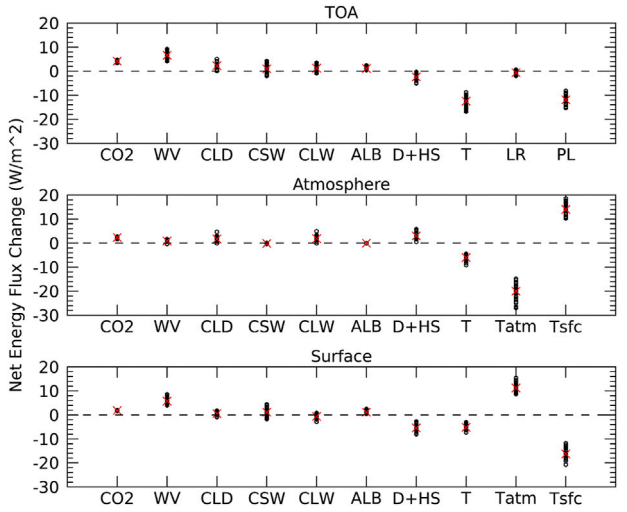

FIGURE 1 | The global-mean net energy flux changes (W^*m^{-2}) between the CMIP5 RCP8.5 and historical simulations at the TOA, atmosphere, and surface due to changes in CO_2, water vapor (WV), clouds (CLD), the shortwave (CSW) and longwave (CLW) cloud components, surface albedo (ALB), dynamics plus heat storage (D + HS), and temperature (T). Temperature feedback (T) is further divided into lapse-rate (LR) and Planck (PL) feedbacks at the TOA, and atmospheric (Tatm) and surface (Tsfc) temperature feedbacks in the atmosphere and surface. Note that the sum of the surface and atmosphere contributions equals their respective TOA contributions, except for the last two terms on the right. Black circles indicate individual CMIP5 model results, while red crosses show the CMIP5 ensemble mean.

changes of the non-radiative terms and heat storage as a residual, taking advantage of the energy budget **Eqs 1**, **6**, **8**:

$$\begin{aligned}
\Delta Dyn_{trans} - \Delta\frac{\partial E_{TOA}}{\partial t} &= -(\Delta S_{TOA} - \Delta R_{TOA}) \\
\Delta Q_{atm}^{non-rad} - \Delta\left(\frac{\partial E_{atm}}{\partial t}\right) &= -(\Delta S_{atm} - \Delta R_{atm}) \\
\Delta Q_{s}^{non-rad} - \Delta\left(\frac{\partial E_{s}}{\partial t}\right) &= -(\Delta S_{s} - \Delta R_{s})
\end{aligned} \tag{16}$$

As indicated by **(16)**, the TOA, atmospheric, and surface net energy flux changes of the non-radiative plus heat storage term are given by the negative sign of the corresponding net radiative energy flux changes.

RESULTS

Energy Flux Changes

Global-Mean

Figure 1 shows the net global-mean energy flux changes at the TOA, atmosphere, and surface due to individual processes. Though, the CMIP5 RCP8.5 simulations are not forced solely by CO_2, the contributions of other well-mixed greenhouse gases (e.g., methane), solar forcing, and aerosol forcing are negligible relative to CO_2 forcing and therefore not shown. The CO_2 forcing in the atmosphere and the surface are positive and approximately equal, meaning the TOA forcing is about twice as large as the surface forcing. The energy flux changes due to water vapor and surface albedo are positive, have similar spreads, and have very small differences between their TOA and surface contributions, as their atmospheric contribution is near-zero. The TOA energy flux change due to non-radiative processes plus heat storage, which is non-zero for a non-equilibrium state, has the same sign as the corresponding surface contribution but with a smaller magnitude due to the partial offset by the positive contribution in the atmosphere. The (net) temperature contributions at the surface and atmosphere are also very similar but negative; the temperature contribution at the TOA is thus substantially more negative and with a greater inter-model spread.

The cloud contribution at the surface can be positive or negative depending on the model, producing a slightly positive ensemble mean value (~0.6 W^*m^{-2}). For nearly all models the TOA cloud contribution is positive and resembles the atmospheric cloud contribution more than the surface, which has a smaller spread. The difference between the TOA and surface cloud contribution is due to the LW cloud component, as the SW component is nearly the same for the TOA and surface. Overall, though, the surface and TOA global-mean results provide a very similar qualitative understanding of process contributions to surface warming.

Zonal-Mean

Unlike the global-mean, more noticeable differences are observed between the TOA and surface perspectives in the zonal-mean. The CO_2 TOA forcing is largest in the tropics and decreases towards the poles, while the surface CO_2 forcing is smallest in the tropics and increases poleward (**Figure 2A**). The difference is explained by the atmospheric CO_2 forcing, which is positive and larger than the CO_2 surface forcing in the tropics and decreases towards the poles even becoming negative in the Southern Hemisphere polar region. The TOA CO_2 forcing is thus more indicative of the atmospheric than surface forcing. Additionally, the CO_2 forcing has a larger inter-model spread at the TOA than surface. On the other hand, the water vapor TOA energy flux change is more indicative of the surface than atmospheric water vapor energy flux change (**Figure 2B**). This is a consequence of the atmospheric water vapor net energy flux change being smaller in magnitude than the surface. The negative atmospheric water vapor energy flux change in polar regions does cause the TOA water vapor energy flux change to decrease more from the tropics to poles than at the surface. The albedo TOA energy flux change is nearly the same as that at the surface (**Figure 2C**). This is because the albedo atmospheric energy flux changes, though slightly negative, are relatively very small. Both perspectives show a large inter-model spread for water vapor and surface albedo feedbacks, particularly in the tropics for the former and in polar regions for the latter. The TOA energy flux change pattern due to (atmospheric and surface) temperature changes is similar to that at the surface (**Figure 2D**) but is much more negative in the tropics and midlatitudes due to the large negative contribution by the atmospheric component there. The

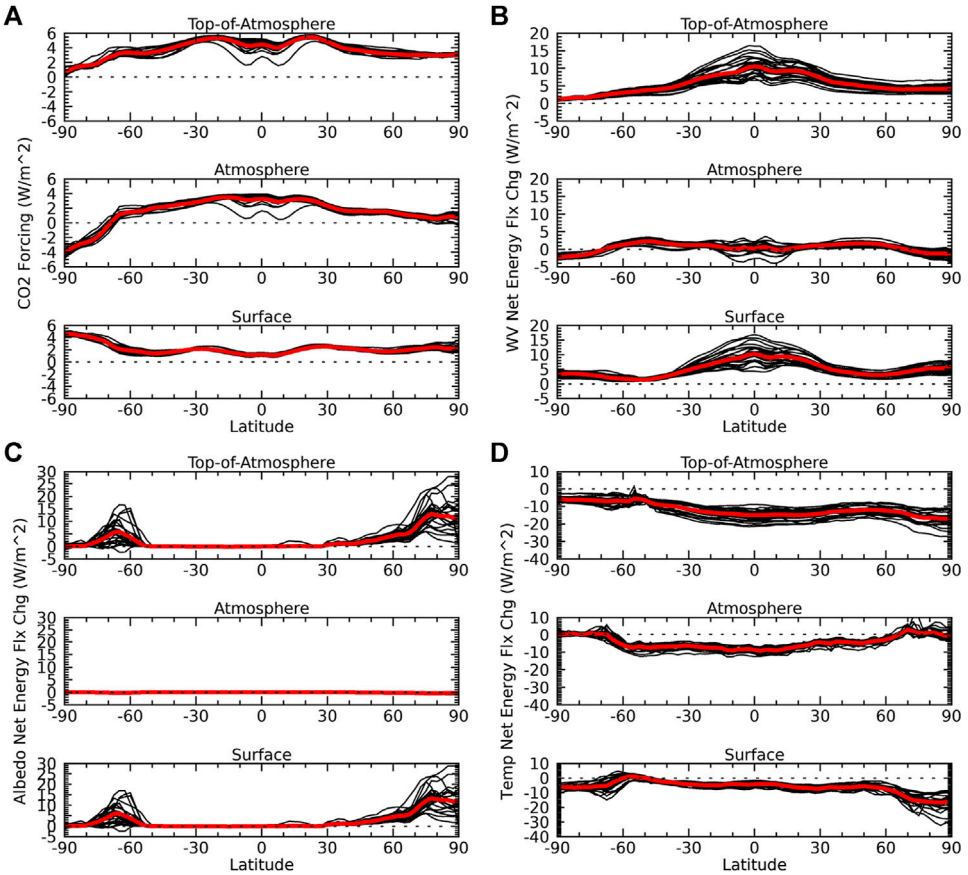

FIGURE 2 | The zonal-mean net energy flux change (W^*m^{-2}) at the TOA, atmosphere, and surface due exclusively to changes in **(A)** CO_2, **(B)** water vapor, **(C)** surface albedo, **(D)** and temperature. The sum of the surface and atmosphere contributions equals their respective TOA contributions. Individual CMIP5 models (black lines); CMIP5 ensemble mean (red lines).

inter-model spread is much greater at the TOA than surface, except in polar regions.

The energy flux changes due to non-radiative processes and heat storage tend to be negative at the surface but positive in the atmosphere (**Figure 3A**). This offset leads to a TOA contribution that has a similar pattern to the surface contribution but with a much weaker amplitude. Additionally, the non-radiative TOA energy flux change is positive in the Southern Hemisphere polar region in opposition to the sign of the surface contribution. Both perspectives show a large inter-model spread for this term, though the spread at the TOA is larger, particularly in the Arctic. The meridional pattern and magnitude of the TOA cloud energy flux changes, on the other hand, is more indicative of the atmospheric than surface component, except in the Arctic where the negative atmospheric contribution is canceled by the positive surface contribution (**Figure 3B**). This is because the SW and LW cloud contributions at the surface offset each other except in the Arctic, where the large positive LW cloud contribution dominates the relatively small negative SW cloud contribution (**Figures 3C,D**). The atmospheric cloud contribution is dominated by its LW component, as its SW contribution is very small, indicating that the atmospheric LW cloud contribution is mainly responsible for the TOA cloud energy flux changes, excluding the Arctic. The inter-model spread of the cloud feedback is larger at the TOA than surface, mainly due to its LW component. The SW cloud component, however, has a larger spread than its LW component for both perspectives.

Reconciliation

Thus far the net energy flux changes due to the lapse-rate feedback have not been discussed. The lapse-rate feedback represents the impacts of the deviation from a uniform atmospheric-surface temperature change (equal to the surface temperature change). As indicated by previous studies, the lapse-rate feedback is a manifestation of multiple processes that produce the non-uniform warming response (Cai and Lu 2009; Cronin and Jansen 2016; Feldl et al., 2020; Henry and Merlis 2020; Boeke and Sejas, 2021). As shown in **Figures 1–3**, the energy flux changes due to radiative and non-radiative processes are not uniform in nature. Therefore, radiative and non-radiative processes naturally produce a non-uniform temperature

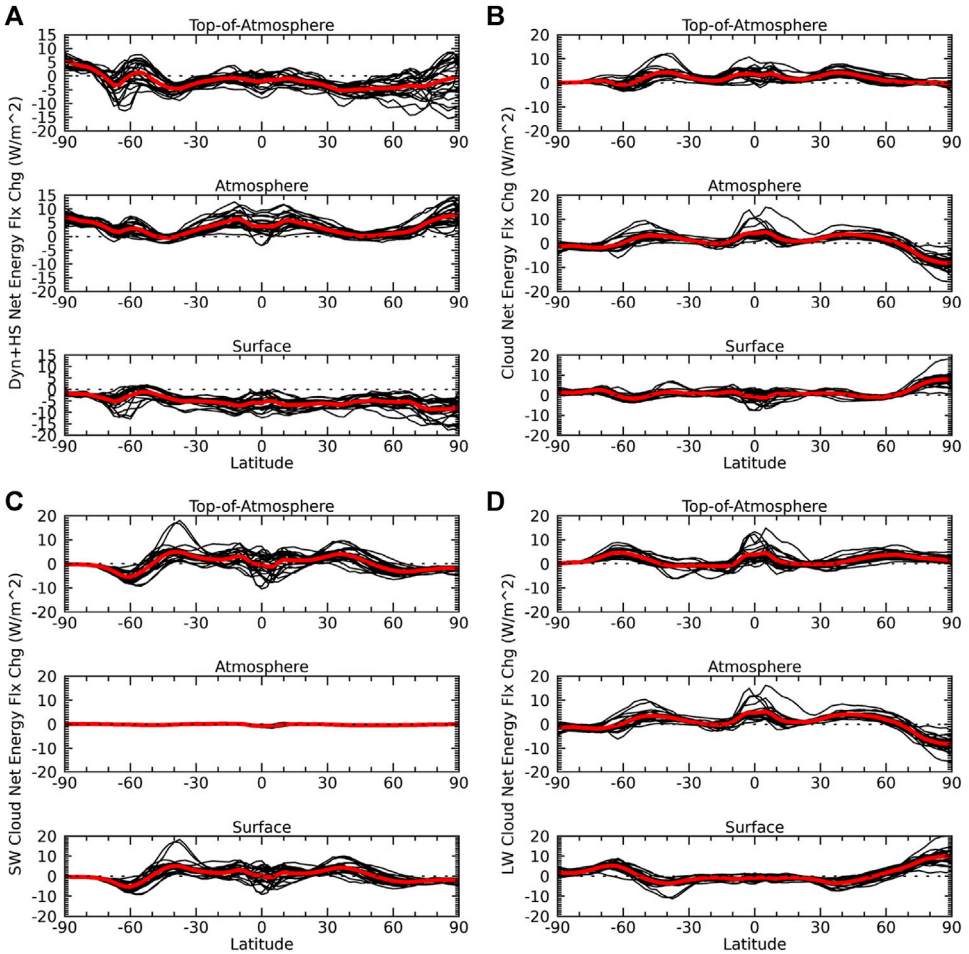

FIGURE 3 | Same as **Figure 2** but due to changes in **(A)** dynamics plus heat storage, **(B)** clouds, and the **(C)** shortwave and **(D)** longwave cloud components.

response. The impact of this non-uniform response on the TOA energy budget is precisely what is taken into account with the lapse-rate feedback. If we could quantify the contribution of individual processes to the lapse-rate feedback and combine it with their corresponding direct impacts on the TOA energy budget, we could obtain the net contribution of radiative and non-radiative processes to the TOA energy flux perturbations.

The CFRAM provides a 3-dimensional picture of radiative and non-radiative process contributions to the surface and atmospheric temperature change. Therefore, we leverage the CFRAM to quantify the contributions of radiative and non-radiative processes to the lapse-rate feedback (**Eq. 12**) and add it to their corresponding direct energy flux change **Eq. 14**. As originally shown by Sejas and Cai (2016), we can also quantify the contributions of radiative and non-radiative processes to the atmospheric temperature feedback in the surface perspective **Eq. 13**. Similarly, these can be combined with the corresponding direct impacts of radiative and non-radiative processes on the surface energy budget **Eq. 15**. Taking into account the impact of radiative and non-radiative processes on the lapse-rate and atmospheric temperature feedbacks should provide a more consistent picture of process contributions to surface warming, as given by the TOA and surface perspectives.

Global-Mean

Process contributions to the global-mean lapse-rate feedback are shown in **Figure 4** (top-left). Non-radiative processes plus ocean heat storage are shown to be the cause of the negative lapse-rate feedback, as greater moist convection enhances upper tropospheric warming and ocean heat storage suppresses surface warming. It is also the source of greatest uncertainty for the lapse-rate feedback. We also find that water vapor feedback is the greatest reducer of the negative lapse-rate feedback (i.e., positive lapse-rate contribution), consistent with the well-known compensation between the two (Cess 1975; Zhang et al., 1994; Soden and Held 2006; Held and Shell 2012; Pendergrass and Hartmann 2014). Adding the decomposed lapse-rate feedback contributions to their corresponding direct TOA contributions (**Figure 1**), we find carbon dioxide, water vapor, and albedo contributions increase at the TOA, while the non-radiative plus heat storage contribution substantially decreases (**Figure 4**, top-right). The TOA cloud contribution

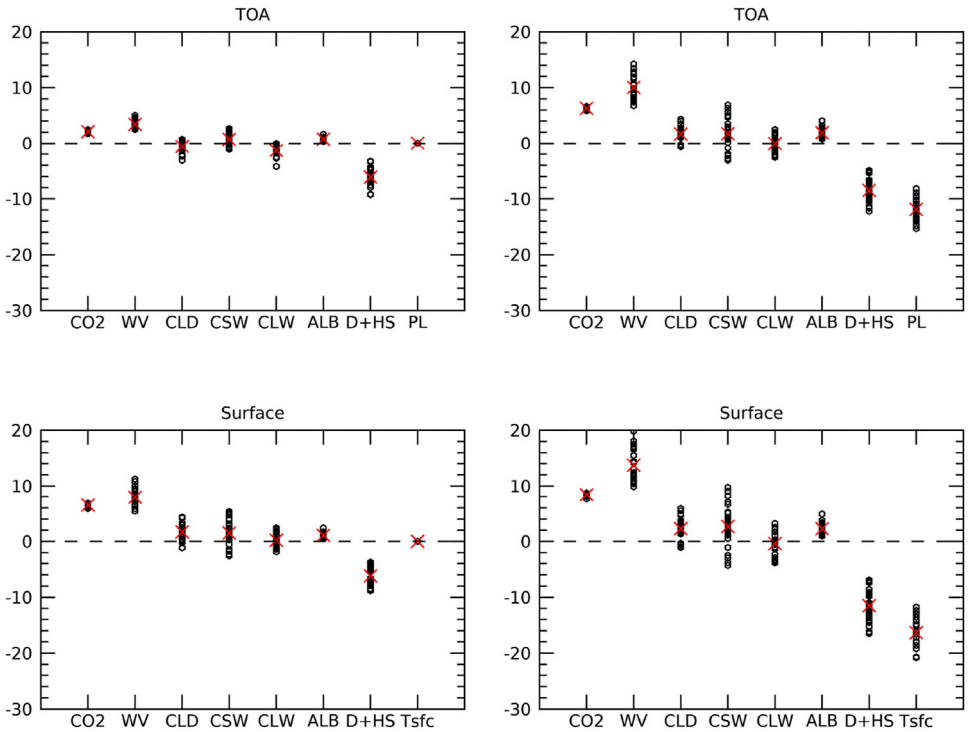

FIGURE 4 | The global-mean decomposition of the net energy flux change (W*m^{-2}) due to the lapse-rate feedback at the TOA **(upper-left)** and due to the atmospheric temperature feedback at the surface **(bottom-left)**. The sum of the left column with the corresponding direct impacts of CO_2 (CO2), water vapor (WV), clouds (CLD), SW clouds (CSW), LW clouds (CLW), surface albedo (ALB), dynamics plus heat storage (D + HS), Planck (PL), and surface temperature (Tsfc) given in **Figure 1** provides the total contribution of these processes at the TOA **(upper-right)** and surface **(bottom-right)**, respectively. Black circles indicate individual CMIP5 model results, while red crosses show the CMIP5 ensemble mean.

experiences a very small change as the slight SW increase is offset by the slight LW decrease. Overall, the inter-model spread of all terms increases, particularly the water vapor and non-radiative plus heat storage terms.

The warming of the atmosphere enhances the downward LW emission to the surface and thus represents a positive feedback (**Figure 1**). The decomposition of the atmospheric temperature feedback indicates that the water vapor feedback is the largest contributor to the positive atmospheric temperature feedback with the non-radiative plus heat storage term serving as the largest suppressor (**Figure 4**, bottom-left); the reverse of the lapse-rate feedback decomposition. Adding the decomposed atmospheric temperature feedback contribution to their corresponding direct surface contributions (**Figure 4**, bottom-right) increases the magnitude of all process contributions to the surface energy budget. The surface cloud contribution increases mainly as a result of the SW component increasing. The inter-model spread substantially increases for all terms as well, even more than at the TOA.

As shown in **Figure 4** (right-panel), including the lapse-rate and atmospheric temperature contributions in the TOA and surface radiative and non-radiative net energy flux changes, respectively, does provide a much more consistent picture between the two perspectives. Both perspectives indicate water vapor feedback is the largest contributor to surface warming, though with large inter-model spread, followed by the CO_2 forcing. Negative energy flux changes due to non-radiative processes plus heat storage are the strongest suppressors of the surface warming and also exhibit large inter-model spread. The largest decrease in net energy flux at the TOA and surface, though, is due to the Planck feedback and surface temperature change, respectively, as these depict the increase in LW emission due to surface warming. Since these two factors are manifestations of the surface warming response itself and its inter-model spread, they do not amplify or suppress the surface warming but instead show how the climate system seeks to balance the positive energy flux perturbations by increasing LW emission through surface warming.

Zonal-Mean

The consistency between the TOA and surface individual process contributions in the zonal-mean is also greatly improved when taking into account their lapse-rate and atmospheric temperature feedback contributions (**Figures 5**–**8**). The contributions of the CO_2 forcing to the lapse-rate and atmospheric temperature feedbacks (**Figure 5A**) are positive like its direct contributions (**Figure 2A**), but the meridional patterns are reversed. Their addition (**Figure 2A** plus **Figure 5A**) leads to a more positive CO_2 forcing for both perspectives, flattens the meridional gradient at the TOA, and flips the sign of the meridional gradient at the

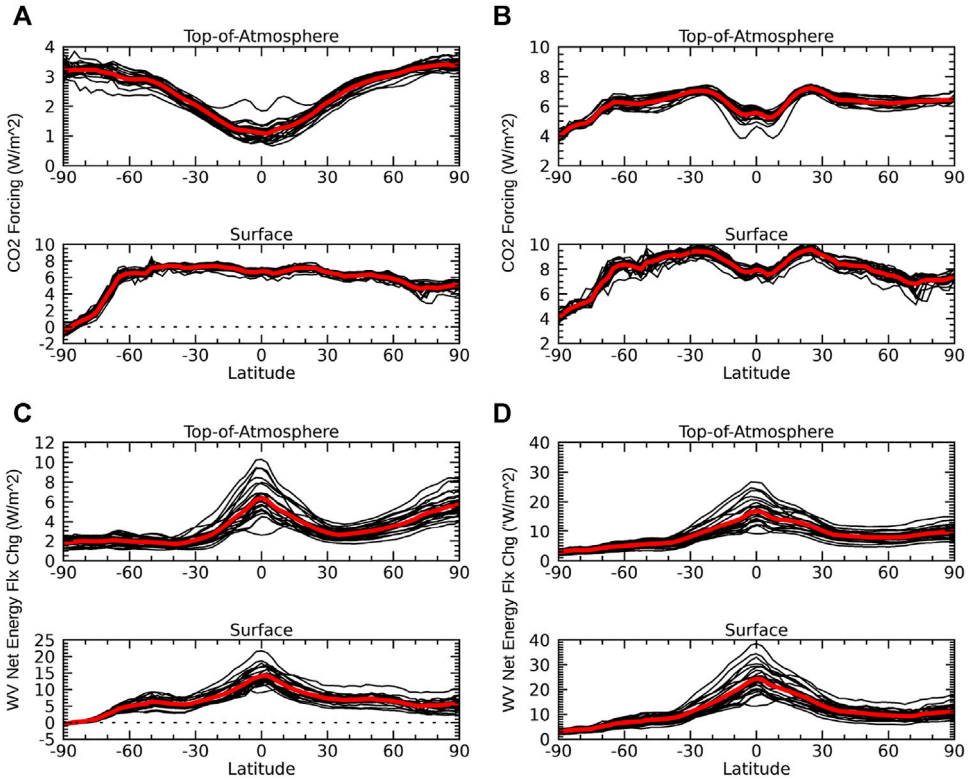

FIGURE 5 | The contributions of the **(A)** CO_2 forcing and **(C)** water vapor feedback to the net energy flux change ($W*m^{-2}$) associated with the lapse-rate and atmospheric temperature feedbacks at the TOA and surface, respectively. The sum of **(A)** and **(C)** with their direct effects (**Figures 2A,B**, respectively) gives the total energy flux change ($W*m^{-2}$) due to the (b) CO_2 forcing and (d) water vapor feedback at the TOA and surface. Individual CMIP5 models (black lines); CMIP5 ensemble mean (red lines).

surface (**Figure 5B**). On the other hand, the contributions of water vapor feedback to the lapse-rate and atmospheric temperature feedbacks (**Figure 5C**) are more similar to their direct contributions (**Figure 2B**). The water vapor feedback contribution to the lapse-rate feedback, however, displays a meridional gradient that decreases from the tropics to mid-latitudes but then increases in the Arctic. Water vapor feedback is thus an important contributor to the positive lapse-rate feedback in the Arctic, consistent with previous studies (Song et al., 2014b; Henry and Merlis, 2020). The total water vapor feedback contribution (**Figure 5D**), though, does decrease from the tropics to poles, but with a greater magnitude and inter-model spread, particularly at the surface. Both perspectives indicate water vapor feedback is the largest positive feedback in the tropics.

The contributions of surface albedo feedback to the lapse-rate and atmospheric temperature feedbacks (**Figure 6A**) are very similar to their respective direct contributions (**Figure 2C**). In line with past studies, we find the surface albedo feedback is the largest contributor to the positive lapse-rate (Graversen et al., 2014; Song et al., 2014b; Feldl et al., 2020) and atmospheric temperature feedbacks (Sejas and Cai 2016) in polar regions, particularly the Arctic. Like its direct contributions, the total surface albedo feedback continues to display no difference between the two perspectives (**Figure 6B**). However, the inclusion of the lapse-rate and atmospheric temperature contributions does increase the magnitude and inter-model spread of the surface albedo feedback in polar regions (**Figures 6B vs. 2C**), where both perspectives indicate the surface albedo feedback is the largest positive feedback.

The contribution of the non-radiative plus heat storage term to the lapse-rate feedback (**Figure 6C**) shows that it is responsible for the negative lapse-rate feedback in the tropics, consistent with the connection between moist convection and the lapse-rate feedback outlined in previous studies (Hansen et al., 1997; Sobel et al., 2001; Cronin and Jansen 2016), and suppresses the positive lapse-rate feedback in polar regions due to ocean heat storage. At the surface, the contribution of the non-radiative plus heat storage term to the atmospheric temperature feedback is largely negative except in the Antarctic; in the Arctic the inter-model uncertainty is very large with differing sign among models (**Figure 6C**). The total non-radiative plus heat storage contribution tends to be negative with a similar meridional pattern relative to its direct contributions at both the TOA and surface (**Figures 6D** ve. **3A**), but the negative contribution and inter-model spreads are much larger. We also find the surface contribution is now positive in the Antarctic matching the TOA perspective.

The SW cloud feedback contributions to the lapse-rate and atmospheric temperature feedbacks matches its direct

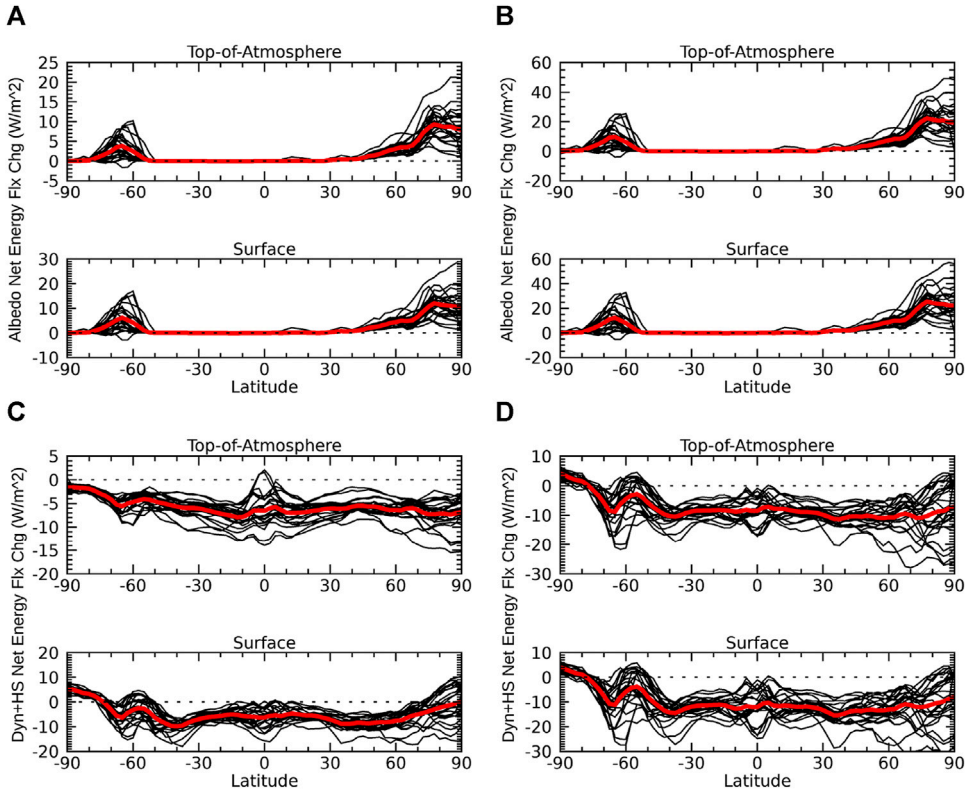

FIGURE 6 | Same as **Figure 5** but due to changes in surface albedo and dynamics plus heat storage.

contributions (**Figure 7A**); its addition just amplifies the magnitude and inter-model spread of the direct contributions (**Figure 7B**). On the other hand, the LW cloud feedback contributions to the lapse-rate and atmospheric temperature feedbacks do not match its direct contributions (**Figure 7C**). The LW cloud feedback contributes to both the negative and positive lapse-rate feedback in the tropics and polar regions, respectively. At the surface, the LW cloud feedback tends to contribute positively to the atmospheric temperature feedback, though there is large inter-model uncertainty. The total LW cloud feedback displays less inter-model spread at the TOA, but more inter-model spread at the surface (**Figures 7D** vs. **3D**). Though there is substantial offsetting between the LW and SW cloud feedbacks in the ensemble mean, the SW cloud feedback tends to dominate everywhere, except in the Arctic; thus, leading to a slight increase in the magnitude and inter-model spread of the net cloud feedback relative to its direct contributions (**Figures 8B** vs **3B**).

DISCUSSION

In this study we compared the surface and TOA energy budget decompositions used to attribute surface warming to individual process contributions. We show that the differences between the two methodologies are explained by non-negligible changes to the atmospheric energy budget. In the global-mean, the impact of the atmospheric energy flux perturbations due to individual processes is smaller or of the same sign as the corresponding surface energy flux perturbations such that the TOA and surface perspectives provide a similar qualitative understanding. However, when expanding to a zonal-mean analysis, differences in pattern and even sign become apparent. This is due to individual processes, such as the CO_2 forcing, clouds, dynamics and ocean heat storage, modifying the atmospheric and surface energy budgets very differently. Energy perturbations at the TOA due to individual processes and their inter-model spreads are thus a manifestation of the combined inter-model uncertainty and impacts of these processes on the atmospheric and surface energy budgets. When the magnitude of the atmospheric energy flux perturbation due to a specific process is large and pattern different than the energy flux perturbation it causes at the surface, the TOA and surface energy budget perturbations due to that process will differ greatly.

The asymmetry between the atmospheric and surface energy flux perturbations is precisely what is taken into account with the lapse-rate feedback. When we decompose the lapse-rate feedback at the TOA and the atmospheric temperature feedback at the surface into contributions by individual processes and add it to their corresponding direct effects a much more consistent picture between the two perspectives is achieved. Though differences in magnitude persist, the modified decomposition provides the same qualitative understanding of the inter-model spread, spatial pattern, and sign of the individual process contributions for both perspectives. Moreover, the relative

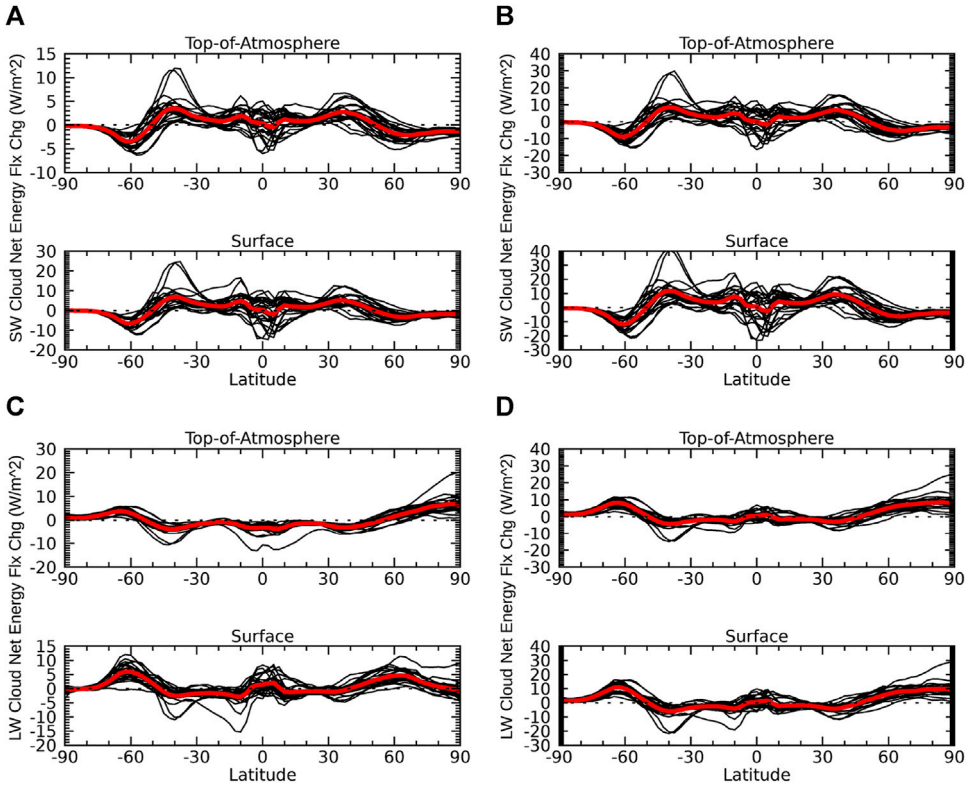

FIGURE 7 | Same as **Figure 5** but due to the shortwave and longwave cloud feedbacks.

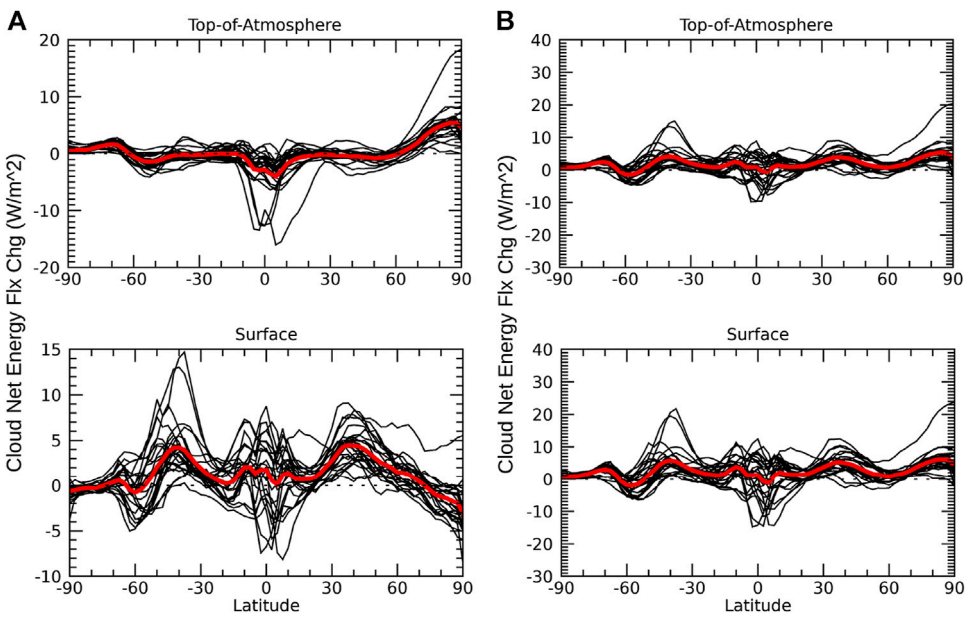

FIGURE 8 | Same as **Figure 5** but due to the net cloud feedback.

importance of individual contributions to surface warming are in agreement.

With the modified approach, both perspectives indicate water vapor feedback is the largest contributor in the tropics, while surface albedo feedback is the greatest contributor in polar regions. Dynamics and ocean heat storage are the main suppressors of surface warming, except over Antarctica. Both perspectives show there is large inter-model uncertainty in the contributions of water vapor, clouds, albedo, and dynamics plus ocean heat storage. How these uncertainties amplify or offset each other and thus contribute to the inter-model warming spread is beyond the scope of this paper. However, the large inter-model spread in the dynamics plus ocean heat storage term does present a possible source of uncertainty hidden within the lapse-rate feedback that is often overlooked.

We note that our TOA energy budget decomposition uses the instantaneous instead of the stratospheric-adjusted radiative forcing. Since the stratosphere cools, its main impact is the reduction (increase) in magnitude of the negative (positive) lapse-rate feedback in the tropics (Arctic). This is mainly compensated by the global decrease in the CO_2 forcing (i.e., instantaneous vs stratospheric-adjusted radiative forcing), since CO_2 forcing is the predominant cause of stratospheric cooling (Fels et al., 1980). The total CO_2 forcing (i.e., including its contribution to the lapse-rate feedback) takes this compensation into account such that the total CO_2 forcing effectively includes stratospheric adjustment.

The non-negligible error, due to the use of time-mean fields in our offline radiative calculations, will impact some of the details in our analysis (**Supplementary Figure S1**). The error, however, is unlikely to change our main conclusions as indicated by previous studies (Sejas et al., 2014; Song et al., 2014a). More importantly, the ability to reconcile the TOA and surface process contributions to surface warming through decompositions of the lapse-rate and atmospheric temperature feedbacks is not dependent on the offline error.

The reconciliation of the TOA and surface perspectives relies on a decomposition made solely possible by the 3-dimensional CFRAM analysis. The need to carry out a 3-dimensional CFRAM analysis, however, detracts from the simplicity provided by the TOA methodology. Therefore, if using a TOA approach, it is important to understand that the differences in interpretation are due to process contributions hidden within the lapse-rate feedback. Alternatively, one could solely use the CFRAM to study radiative and non-radiative process contributions to surface and atmospheric warming and the inter-model warming spread (Cai and Tung 2012; Taylor et al., 2013; Sejas et al., 2014; Song et al., 2014a; Yoshimori et al., 2014; Hu et al., 2020).

DATA AVAILABILITY STATEMENT

Publicly available datasets were analyzed in this study. This data can be found here: http://data.ceda.ac.uk/badc/cmip5/data/cmip5/ and https://esgf-node.llnl.gov/search/cmip5/. The RCP forcing database is freely accessible at https://tntcat.iiasa.ac.at/RcpDb/.

AUTHOR CONTRIBUTIONS

SS conceived the idea for this study, analyzed the data, and was the lead writer. MC, XH, and HF helped with the writing of the manuscript. XH and HF downloaded the CMIP5 data and carried out the CFRAM analysis. All authors discussed the results and provided input throughout the study.

FUNDING

This study was supported by the National Natural Science Foundation of China (Grants 41690123, 41690120, and 41805050), the Natural Science Foundation of Guangdong Province of China (Grant 2018A0303130268), and the National Science Foundation (AGS-2012479).

SUPPLEMENTARY MATERIAL

The Supplementary Material for this article can be found online at: https://www.frontiersin.org/articles/10.3389/feart.2021.725816/full#supplementary-material

REFERENCES

Aires, F., and Rossow, W. B. (2003). Inferring Instantaneous, Multivariate and Nonlinear Sensitivities for the Analysis of Feedback Processes in a Dynamical System: Lorenz Model Case-Study. *Q. J. R. Meteorol. Soc.* 129, 239–275. doi:10.1256/qj.01.174

Andrews, T., Forster, P. M., and Gregory, J. M. (2009). A Surface Energy Perspective on Climate Change. *J. Clim.* 22, 2557–2570. doi:10.1175/2008JCLI2759.1

Bates, J. R. (2007). Some Considerations of the Concept of Climate Feedback. *Q.J.R. Meteorol. Soc.* 133, 545–560. doi:10.1002/qj.62

Boeke, R. C., and Taylor, P. C. (2018). Seasonal Energy Exchange in Sea Ice Retreat Regions Contributes to Differences in Projected Arctic Warming. *Nat. Commun.* 9, 5017. doi:10.1038/s41467-018-07061-9

Boeke, R. C., Taylor, P. C., and Sejas, S. A. (2021). On the Nature of the Arctic's Positive Lapse-Rate Feedback. *Geophys. Res. Lett.* 48, e2020GL091109. doi:10.1029/2020GL091109

Bony, S., Colman, R., Kattsov, V. M., Allan, R. P., Bretherton, C. S., Dufresne, J.-L., et al. (2006). How Well Do We Understand and Evaluate Climate Change Feedback Processes? *J. Clim.* 19, 3445–3482. doi:10.1175/jcli3819.1

Cai, M., and Lu, J. (2009). A New Framework for Isolating Individual Feedback Processes in Coupled General Circulation Climate Models. Part II: Method Demonstrations and Comparisons. *Clim. Dyn.* 32, 887–900. doi:10.1007/s00382-008-0424-4

Cai, M., and Tung, K.-K. (2012). Robustness of Dynamical Feedbacks from Radiative Forcing: 2% Solar versus 2 × CO_2 Experiments in an Idealized GCM. *J. Atmos. Sci.* 69, 2256–2271. doi:10.1175/JAS-D-11-0117.1

Cess, R. D. (1975). Global Climate Change: an Investigation of Atmospheric Feedback Mechanisms. *Tellus* 27, 193–198. doi:10.3402/tellusa.v27i3.9901

Cess, R. D., Zhang, M. H., Ingram, W. J., Potter, G. L., Alekseev, V., Barker, H. W., et al. (1996). Cloud Feedback in Atmospheric General Circulation Models: An Update. *J. Geophys. Res.* 101, 12791–12794. doi:10.1029/96JD00822

Colman, R. A. (2015). Climate Radiative Feedbacks and Adjustments at the Earth's Surface. *J. Geophys. Res. Atmos.* 120, 3173–3182. doi:10.1002/2014JD022896

Cronin, T. W., and Jansen, M. F. (2016). Analytic Radiative-advective Equilibrium as a Model for High-latitude Climate. *Geophys. Res. Lett.* 43, 449–457. doi:10.1002/2015GL067172

Feldl, N., Anderson, B. T., and Bordoni, S. (2017). Atmospheric Eddies Mediate Lapse Rate Feedback and Arctic Amplification. *J. Clim.* 30, 9213–9224. doi:10.1175/JCLI-D-16-0706.1

Feldl, N., Po-Chedley, S., Singh, H. K. A., Hay, S., and Kushner, P. J. (2020). Sea Ice and Atmospheric Circulation Shape the High-Latitude Lapse Rate Feedback. *Npj Clim. Atmos. Sci.* 3, 1–9. doi:10.1038/s41612-020-00146-7

Fels, S. B., Mahlman, J. D., Schwarzkopf, M. D., and Sinclair, R. W. (1980). Stratospheric Sensitivity to Perturbations in Ozone and Carbon Dioxide: Radiative and Dynamical Response. *J. Atmos. Sci.* 37, 2265–2297. doi:10.1175/1520-0469(1980)037<2265:sstpio>2.0.co;2

Fu, Q., and Liou, K. N. (1992). On the Correlated k -Distribution Method for Radiative Transfer in Nonhomogeneous Atmospheres. *J. Atmospheric Sci.* 49, 2139–2156.

Fu, Q., and Liou, K. N. (1993). Parameterization of the Radiative Properties of Cirrus Clouds. *J. Atmospheric Sci.* 50, 2008–2025. doi:10.1175/JCLI-D-16-0706.1

Goosse, H., Kay, J. E., Armour, K. C., Bodas-Salcedo, A., Chepfer, H., Docquier, D., et al. (2018). Quantifying Climate Feedbacks in Polar Regions. *Nat. Commun.* 9, 1919. doi:10.1038/s41467-018-04173-0

Graversen, R. G., Langen, P. L., and Mauritsen, T. (2014). Polar Amplification in CCSM4: Contributions from the Lapse Rate and Surface Albedo Feedbacks. *J. Clim.* 27, 4433–4450. doi:10.1175/JCLI-D-13-00551.1

Gregory, J. M., Ingram, W. J., Palmer, M. A., Jones, G. S., Stott, P. A., Thorpe, R. B., et al. (2004). A New Method for Diagnosing Radiative Forcing and Climate Sensitivity. *Geophys. Res. Lett.* 31, L03205. doi:10.1029/2003GL018747

Hansen, J., Sato, M., and Ruedy, R. (1997). Radiative Forcing and Climate Response. *J. Geophys. Res.* 102, 6831–6864. doi:10.1029/96JD03436

Hartmann, D. L., Klein Tank, A. M. G., and Rusticucci, M. (2013). "Observations: Atmosphere and Surface," in Climate Change 2013: The Physical Science Basis. Contribution of Working Group I to the Fifth Assessment Report of the IPCC (Cambridge, UK, and New York, NY, USA: Cambridge University Press).

Held, I. M., and Shell, K. M. (2012). Using Relative Humidity as a State Variable in Climate Feedback Analysis. *J. Clim.* 25, 2578–2582. doi:10.1175/JCLI-D-11-00721.1

Henry, M., and Merlis, T. M. (2020). Forcing Dependence of Atmospheric Lapse Rate Changes Dominates Residual Polar Warming in Solar Radiation Management Climate Scenarios. *Geophys. Res. Lett.* 47, e2020GL087929. doi:10.1029/2020GL087929

Hu, X., Cai, M., Yang, S., and Sejas, S. A. (2018). Air Temperature Feedback and its Contribution to Global Warming. *Sci. China Earth Sci.* 61, 1491–1509. doi:10.1007/s11430-017-9226-6

Hu, X., Fan, H., Cai, M., Sejas, S. A., Taylor, P., and Yang, S. (2020). A Less Cloudy Picture of the Inter-model Spread in Future Global Warming Projections. *Nat. Commun.* 11, 4472. doi:10.1038/s41467-020-18227-9

IPCC (2013). Climate Change 2013: The Physical Science Basis. Contribution of Working Group I to the Fifth Assessment Report of the IPCC [Stocker, T. F., D. Qin, G.-K. Plattner, M. Tignor, S. K. Allen, J. Boschung, A. Nauels, Y. Xia, V. Bex and P. M. Midgley (eds.)], Cambridge, UK, and New York, NY: Cambridge University Press, 1535.

Klocke, D., Quaas, J., and Stevens, B. (2013). Assessment of Different Metrics for Physical Climate Feedbacks. *Clim. Dyn.* 41, 1173–1185. doi:10.1007/s00382-013-1757-1

Kramer, R. J., He, H., Soden, B. J., Oreopoulos, L., Myhre, G., Forster, P. M., et al. (2021). Observational Evidence of Increasing Global Radiative Forcing. *Geophys. Res. Lett.* 48, e2020GL091585. doi:10.1029/2020GL091585

Lahellec, A., and Dufresne, J.-L. (2013). A Formal Analysis of the Feedback Concept in Climate Models. Part I: Exclusive and Inclusive Feedback Analyses*. *J. Atmos. Sci.* 70, 3940–3958. doi:10.1175/JAS-D-12-0218.1

Lahellec, A., and Dufresne, J.-L. (2014). A Formal Analysis of the Feedback Concept in Climate Models. Part II: Tangent Linear Systems in GCMs. *J. Atmos. Sci.* 71, 3350–3375. doi:10.1175/JAS-D-13-0334.1

Laîné, A., Yoshimori, M., and Abe-Ouchi, A. (2016). Surface Arctic Amplification Factors in CMIP5 Models: Land and Oceanic Surfaces and Seasonality. *J. Clim.* 29, 3297–3316. doi:10.1175/JCLI-D-15-0497.1

Lu, J., and Cai, M. (2009a). A New Framework for Isolating Individual Feedback Processes in Coupled General Circulation Climate Models. Part I: Formulation. *Clim. Dyn.* 32, 873–885. doi:10.1007/s00382-008-0425-3

Lu, J., and Cai, M. (2009b). Seasonality of Polar Surface Warming Amplification in Climate Simulations. *Geophys. Res. Lett.* 36, L16704. doi:10.1029/2009GL040133

Manabe, S., Stouffer, R. J., Spelman, M. J., and Bryan, K. (1991). Transient Responses of a Coupled Ocean-Atmosphere Model to Gradual Changes of Atmospheric CO2. Part I. Annual Mean Response. *J. Clim.* 4, 785–818. doi:10.1175/1520-0442(1991)004<0785:TROACO>2.0.CO;2

Manabe, S., and Wetherald, R. T. (1975). The Effects of Doubling the CO2Concentration on the Climate of a General Circulation Model. *J. Atmos. Sci.* 32, 3–15. doi:10.1175/1520-0469(1975)032<0003:TEODTC>2.0.CO;2

Payne, A. E., Jansen, M. F., and Cronin, T. W. (2015). Conceptual Model Analysis of the Influence of Temperature Feedbacks on Polar Amplification. *Geophys. Res. Lett.* 42, 9561–9570. doi:10.1002/2015GL065889

Pendergrass, A. G., and Hartmann, D. L. (2014). The Atmospheric Energy Constraint on Global-Mean Precipitation Change. *J. Clim.* 27, 757–768. doi:10.1175/JCLI-D-13-00163.1

Pithan, F., and Mauritsen, T. (2014). Arctic Amplification Dominated by Temperature Feedbacks in Contemporary Climate Models. *Nat. Geosci* 7, 181–184. doi:10.1038/ngeo2071

Previdi, M., and Liepert, B. G. (2012). The Vertical Distribution of Climate Forcings and Feedbacks from the Surface to Top of Atmosphere. *Clim. Dyn.* 39, 941–951. doi:10.1007/s00382-011-1233-8

Robock, A. (1983). Ice and Snow Feedbacks and the Latitudinal and Seasonal Distribution of Climate Sensitivity. *J. Atmos. Sci.* 40, 986–997. doi:10.1175/1520-0469(1983)040<0986:iasfat>2.0.co;2

Schlesinger, M. E., and Mitchell, J. F. B. (1987). Climate Model Simulations of the Equilibrium Climatic Response to Increased Carbon Dioxide. *Rev. Geophys.* 25, 760–798. doi:10.1029/RG025i004p00760

Sejas, S. A., Cai, M., Hu, A., Meehl, G. A., Washington, W., and Taylor, P. C. (2014). Individual Feedback Contributions to the Seasonality of Surface Warming. *J. Clim.* 27, 5653–5669. doi:10.1175/JCLI-D-13-00658.1

Sejas, S. A., and Cai, M. (2016). Isolating the Temperature Feedback Loop and its Effects on Surface Temperature. *J. Atmos. Sci.* 73, 3287–3303. doi:10.1175/JAS-D-15-0287.1

Sobel, A. H., Nilsson, J., and Polvani, L. M. (2001). The Weak Temperature Gradient Approximation and Balanced Tropical Moisture Waves*. *J. Atmos. Sci.* 58, 3650–3665. doi:10.1175/1520-0469(2001)058<3650:TWTGAA>2.0.CO;2

Soden, B. J., Broccoli, A. J., and Hemler, R. S. (2004). On the Use of Cloud Forcing to Estimate Cloud Feedback. *J. Clim.* 17, 3661–3665. doi:10.1175/1520-0442(2004)017<3661:OTUOCF>2.0.CO;2

Soden, B. J., and Held, I. M. (2006). An Assessment of Climate Feedbacks in Coupled Ocean-Atmosphere Models. *J. Clim.* 19, 3354–3360. doi:10.1175/jcli3799.1

Soden, B. J., Held, I. M., Colman, R., Shell, K. M., Kiehl, J. T., and Shields, C. A. (2008). Quantifying Climate Feedbacks Using Radiative Kernels. *J. Clim.* 21, 3504–3520. doi:10.1175/2007JCLI2110.1

Song, X., Zhang, G. J., and Cai, M. (2014a). Characterizing the Climate Feedback Pattern in the NCAR CCSM3-SOM Using Hourly Data. *J. Clim.* 27, 2912–2930. doi:10.1175/JCLI-D-13-00567.1

Song, X., Zhang, G. J., and Cai, M. (2014b). Quantifying contributions of climate feedbacks to tropospheric warming in the NCAR CCSM3.0. *Clim. Dyn.* 42, 901–917. doi:10.1007/s00382-013-1805-x

Stephens, G. L. (2005). Cloud Feedbacks in the Climate System: A Critical Review. *J. Clim.* 18, 237–273. doi:10.1175/jcli-3243.1

Taylor, P. C., Cai, M., Hu, A., Meehl, J., Washington, W., and Zhang, G. J. (2013). A Decomposition of Feedback Contributions to Polar Warming Amplification. *J. Clim.* 26, 7023–7043. doi:10.1175/JCLI-D-12-00696.1

Thorsen, T. J., Kato, S., Loeb, N. G., and Rose, F. G. (2018). Observation-Based Decomposition of Radiative Perturbations and Radiative Kernels. *J. Clim.* 31, 10039–10058. doi:10.1175/JCLI-D-18-0045.1

Washington, W. M., and Meehl, G. A. (1984). Seasonal Cycle experiment on the Climate Sensitivity Due to a Doubling of CO2with an Atmospheric General Circulation Model Coupled to a Simple Mixed-Layer Ocean Model. *J. Geophys. Res.* 89, 9475–9503. doi:10.1029/JD089iD06p09475

Wetherald, R. T., and Manabe, S. (1988). Cloud Feedback Processes in a General Circulation Model. *J. Atmos. Sci.* 45, 1397–1416. doi:10.1175/1520-0469(1988)045<1397:cfpiag>2.0.co;2

Yoshimori, M., Watanabe, M., Abe-Ouchi, A., Shiogama, H., and Ogura, T. (2014). Relative Contribution of Feedback Processes to Arctic Amplification of

Temperature Change in MIROC GCM. *Clim. Dyn.* 42, 1613–1630. doi:10.1007/s00382-013-1875-9

Zhang, M. H., Hack, J. J., Kiehl, J. T., and Cess, R. D. (1994). Diagnostic Study of Climate Feedback Processes in Atmospheric General Circulation Models. *J. Geophys. Res.* 99, 5525–5537. doi:10.1029/93JD03523

Conflict of Interest: SS is employed by the company Science Systems and Applications Inc.

The remaining authors declare that the research was conducted in the absence of any commercial or financial relationships that could be construed as a potential conflict of interest.

Publisher's Note: All claims expressed in this article are solely those of the authors and do not necessarily represent those of their affiliated organizations, or those of the publisher, the editors and the reviewers. Any product that may be evaluated in this article, or claim that may be made by its manufacturer, is not guaranteed or endorsed by the publisher.

frontiers in Earth Science

ORIGINAL RESEARCH
published: 02 December 2021
doi: 10.3389/feart.2021.769844

A Cloudier Picture of Ice-Albedo Feedback in CMIP6 Models

Anne Sledd[1]* *and Tristan S. L'Ecuyer*[1,2]

[1]Department of Atmospheric and Oceanic Sciences, University of Wisconsin-Madison, Madison, WI, United States, [2]Cooperative Institute for Meteorological Satellite Studies, Madison, WI, United States

Increased solar absorption is an important driver of Arctic Amplification, the interconnected set of processes and feedbacks by which Arctic temperatures respond more rapidly than global temperatures to climate forcing. The amount of sunlight absorbed in the Arctic is strongly modulated by seasonal ice and snow cover. Sea ice declines and shorter periods of seasonal snow cover in recent decades have increased solar absorption, amplifying local warming relative to the planet as a whole. However, this Arctic albedo feedback would be substantially larger in the absence of the ubiquitous cloud cover that exists throughout the region. Clouds have been observed to mask the effects of reduced surface albedo and slow the emergence of secular trends in net solar absorption. Applying analogous metrics to several models from the 6th Climate Model Intercomparison Project (CMIP6), we find that ambiguity in the influence of clouds on predicted Arctic solar absorption trends has increased relative to the previous generation of climate models despite better agreement with the observed albedo sensitivity to sea ice variations. Arctic albedo responses to sea ice loss are stronger in CMIP6 than in CMIP5 in all summer months. This agrees better with observations, but models still slightly underestimate albedo sensitivity to sea ice changes relative to observations. Never-the-less, nearly all CMIP6 models predict that the Arctic is now absorbing more solar radiation than at the start of the century, consistent with recent observations. In fact, many CMIP6 models simulate trends that are too strong relative to internal variability, and spread in predicted Arctic albedo changes has increased since CMIP5. This increased uncertainty can be traced to increased ambiguity in how clouds influence natural and forced variations in Arctic solar absorption. While nearly all CMIP5 models agreed with observations that clouds delay the emergence of forced trends, about half of CMIP6 models suggest that clouds accelerate their emergence from natural variability. Isolating atmospheric contributions to total Arctic reflection suggests that this diverging behavior may be linked to stronger Arctic cloud feedbacks in the latest generation of climate models.

Keywords: arctic, climate change, solar absorption, clouds, sea ice, albedo

OPEN ACCESS

Edited by:
Patrick Charles Taylor, National Aeronautics and Space Administration (NASA), United States

Reviewed by:
Aku Riihelä, Finnish Meteorological Institute, Finland
Yiyi Huang, University of Arizona, United States

***Correspondence:**
Anne Sledd
sledd@wisc.edu

Specialty section:
This article was submitted to Atmospheric Science, a section of the journal Frontiers in Earth Science

Received: *02 September 2021*
Accepted: *25 October 2021*
Published: *02 December 2021*

Citation:
Sledd A and L'Ecuyer TS (2021) A Cloudier Picture of Ice-Albedo Feedback in CMIP6 Models. Front. Earth Sci. 9:769844. doi: 10.3389/feart.2021.769844

1 INTRODUCTION

Recent analyses of the nearly 20-year Clouds Earth Radiation and Energy System Energy Balance and Filled (CERES-EBAF) record of top of atmosphere (TOA) outgoing shortwave radiation (OSR) reveal that the Arctic is absorbing more sunlight now than at the start of this century, even when inter-annual variability is explicitly considered (Sledd and L'Ecuyer, 2021a). This result, coupled with

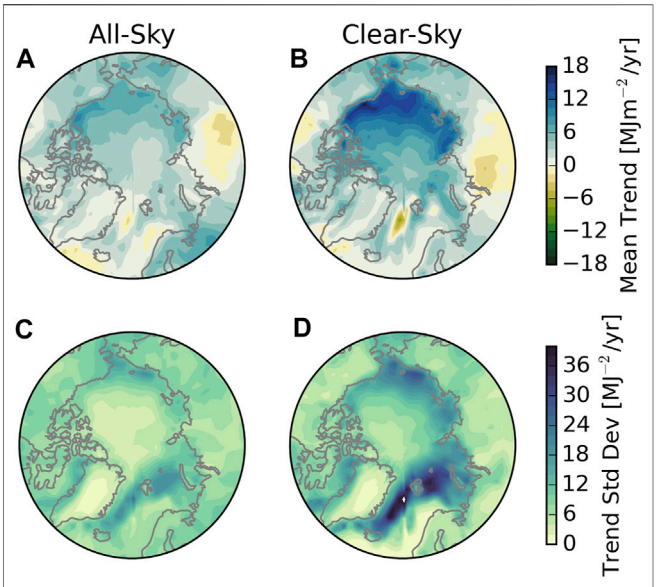

FIGURE 1 | CMIP6 mean ensemble accumulated SW (SW_{acc}) trends **(A,B)** and ensemble standard deviations **(C,D)** for all-sky **(A,C)** and clear-sky **(B,D)** conditions. SW_{acc} is the total net SW energy absorbed over the melt season (**Eq. 6**). SW fluxes are interpolated onto the same 2.5°x2.5° grid as CERES in ArORIS. The models included are listed in **Table 2**. Results from individual models are shown in the **Supplementary Material**.

the finding that clouds have delayed the emergence of this trend by about 5 years, indicates that the satellite record is now sufficiently long to provide a useful benchmark for assessing predicted increases in Arctic absorbed shortwave radiation due to sea ice loss, a major contributor to accelerated rates of Arctic warming relative to globe.

As the Arctic warms, reduced areas of bright snow and ice covers expose darker land and ocean surfaces that absorb more solar radiation in the sunlit summer months. This extra energy input induces additional Arctic warming that melts more ice creating an ice-albedo feedback (Budyko, 1969; Sellers, 1969; Serreze et al., 2009; Screen and Simmonds, 2010b). The impact of surface albedo changes on the net Arctic energy balance is strongly modulated by the atmosphere, though. Cloud cover, in particular, plays a large role modulating the surface energy budget, warming the surface by trapping longwave radiation and cooling the surface by reflecting SW radiation. The latter effect of clouds also obscures changes in the surface albedo that would otherwise be viewed from space (Sedlar et al., 2011; Wu et al., 2020). Sledd and L'Ecuyer (2019) showed that this "cloud masking" effect reduces the sensitivity of the Arctic-mean all-sky albedo to changes in sea ice area (SIA) by a factor of two relative to clear-skies.

Thus, while declines in sea ice and their associated impacts on surface albedo could be detected in observations some time ago (Stroeve et al., 2012; Letterly et al., 2018; Stroeve and Notz, 2018), secular trends in net solar absorption at the TOA have only recently emerged in the satellite record (Sledd and L'Ecuyer, 2021a). This stems in part from the need for direct measurements of TOA fluxes across polar regions that only became available with the launch of the CERES instruments aboard the Terra and Aqua satellites in early 2000 (Loeb et al., 2018). Using these new observations, Kato et al. (2006) quickly identified trends in Arctic shortwave (SW) irradiances, but their statistical significance was low owing to the short 4 year data record available at the time. Subsequent analyses by Hartmann and Ceppi (2014) using 13 years of CERES data indicated robustly negative trends in SW reflection over the high northern latitudes but increased interannual variability in subsequent years obscured this signal until very recently.

Increasing Arctic solar absorption is also evident in reanalyses (Perovich et al., 2007) and climate models (Choi et al., 2020; Hahn et al., 2021). **Figure 1** shows recent trends in Arctic absorbed solar radiation in the ensemble of 6th Climate Model Intercomparison Project (CMIP6) models listed in **Table 1**. Despite the short period covered (2000–2014 is chosen to overlap the observational record), the model ensemble shows that many ocean regions are absorbing more SW radiation than at the start of the century. Also evident in **Figure 1** is the fact that clear-sky trends are frequently larger than those in all-sky conditions, consistent with the notion that clouds mask the impact of surface albedo changes on TOA or planetary albedo.

While these trends qualitatively reflect basic physical principles, **Figures 1C,D** reveal that the standard deviation across models is often larger than the ensemble mean trend. Thus, while the ensemble agrees with recent observational evidence that most regions of the Arctic are absorbing more solar radiation than they were at the start of the century, individual models exhibit a wide range of behaviors over this relatively short analysis period (**Supplementary Figures S1, S2**). This is consistent with many recent studies that caution against using individual model realizations to assess trends on such short timescales due to internal variability. It has been well-documented that any single model realization represents just one of many possible climate trajectories that would all be consistent with model physics (Deser et al., 2012; Kay et al., 2015; Deser et al., 2020).

While this internal variability precludes direct comparison against observations which, themselves, correspond to one particular Arctic climate trajectory from the physically plausible states (evidenced by inter-annual variability), it is encouraging to note that the observations (denoted by CERES) fall within the range of states captured by the CMIP6 ensemble (Notz and Community, 2020). However, while there is value in confirming that the Arctic is absorbing more solar radiation than it was just two decades ago, these comparisons don't address the causes of these increases or establish the combination of factors responsible for the rate of change. Establishing and modeling the coupled influences of sea ice and clouds on absorbed SW radiation and how they evolve as the Arctic warms, is essential for predicting future Arctic climate.

Many previous studies have evaluated the representation of sea ice and snow cover in CMIP6 models using satellite observations (Davy and Outten, 2020; Notz and Community, 2020; Shu et al., 2020). Yet, to quantify and ultimately predict ice-albedo feedbacks and their influence on the Arctic climate, it is equally important to establish how well models simulate the

TABLE 1 | Output is used from the following models from phase six of the Coupled Model Intercomparison Project.

Model	Institute
ACCESS-CM2	Commonwealth Scientific and Industrial Research Organisation
ACCESS-ESM1-5	Commonwealth Scientific and Industrial Research Organisation
BCC-CSM2-MR	Beijing Climate Center
CESM2	National Center for Atmospheric Research
CESM2-WACCM	National Center for Atmospheric Research
CanESM5	Canadian Centre of Climate Modelling and Analysis
EC-Earth3	EC-Earth Consortium
EC-Earth3-Veg	EC-Earth Consortium
GFDL-ESM4	NOAA Geophysical Fluid Dynamics Laboratory
INM-CM4-8	Institute for Numerical Mathematics
INM-CM5-0	Institute for Numerical Mathematics
IPSL-CM6A-LR	Institut Pierre-Simon Laplace
MIROC6	Japan Agency for Marine-Earth Science and Technology
MPI-ESM1-2-LR	Max Planck Institute for Meteorology
MPI-ESM1-2-HR	Max Planck Institute for Meteorology
MRI-ESM2-0	Meteorological Research Institute
NESM3	Nanjing University of Information Science and Technology
NorESM2-LM	Norwegian Climate Center

impact of changes in these bright surfaces on Arctic energy flows. Fewer studies make this important connection directly using both models and observations. This paper applies new metrics that explicitly connect sea ice changes to their influence on Arctic albedo to assess the evolution of Arctic solar absorption in the latest generation of climate models in the context of observed changes. We seek to establish how tightly CMIP6 models constrain the Arctic albedo response to changing sea ice concentration, quantify differences in their representation of the role of clouds in modulating this relationship and the emergence of trends in Arctic solar absorption, and determine how these have changed since CMIP5. For a thorough assessment of other drivers of Arctic Amplification, the reader is directed to Cai et al. (2021) or Hahn et al. (2021).

2 MATERIALS AND METHODS

To answer these questions, observations are extracted from the Arctic Observations and Reanalysis Integrated System (ArORIS). ArORIS is a collection of satellite observations, ground measurements, and atmospheric reanalyses that supports Arctic climate research (Christensen et al., 2016) by collocating and interpolating all included datasets to a uniform monthly, 2.5^ox2.5^o grid. We use TOA all-sky and total-region clear-sky shortwave (SW) fluxes from CERES-EBAF that leverage *in situ* ocean heat content observations to adjust TOA fluxes within their ranges of uncertainty for consistency (Loeb et al., 2018). Total-region clear-sky fluxes are calculated with an adjustment factor based on the difference between clear-sky fluxes for cloud-free regions compared to fluxes from a radiative transfer calculation with a cloud-free atmospheric column (Loeb et al., 2020). This method of calculating total-region clear-sky fluxes is intended to allow direct comparison between observational and model generated clear-sky fluxes. TOA net SW flux uncertainty is 3 (6) Wm^{-2} for March 2000-June 2002 and 2.5 Wm^{-2} after for all-sky (clear-sky) conditions (Loeb et al., 2018). At the surface, uncertainty for all-sky upwelling (downwelling) SW flux is 6 (5) Wm^{-2} (Kato et al., 2018).

Sea ice concentration (SIC) is obtained from the NSIDC Equal-Area Scalable Earth grid (EASE) weekly product, estimated with brightness temperatures from the Nimbus-7 Scanning Multichannel Microwave Radiometer (SMMR), the Defense Meteorological Satellite Program (DMSP) F8, F11, and F13 Special Sensor Microwave/Imagers (SSM/Is), and the DMSP F17 Special Sensor Microwave Imager/Sounder (SSMIS) (Brodzik and Armstrong, 2013). SIC is used to calculate sea ice area (SIA) by multiplying SIC in a grid box by its area and summing over all area north of the Arctic circle (66.56 N). SIC has an uncertainty of 15% during the melt season.

Observed relationships between surface and TOA albedo and SIA as well as trends in Arctic solar absorption are compared to similar metrics derived from the models participating in CMIP5 and 6 (Taylor et al. (2012); Eyring et al. (2016)). The specific models included in this study are listed in **Tables 1** and **2**. We use the historical forcing up to 2005 (2014) in CMIP5 (CMIP6), and the "business as usual" future scenario (SSP585 for CMIP6, RCP8.5 for CMIP5) through 2100. In all cases, monthly output from the first ensemble member (r1i1p1f1 in CMIP6, r1i1p1 in CMIP5) of each model is adopted, and we maintain the native model resolution prior to averaging or summing variables.

2.1 Albedo Partitioning

To correctly simulate the disposition of sunlight incident at the Arctic TOA and predict its evolution in a warming Arctic, models must correctly represent albedo changes due to both changing sea ice cover as well as the modulating effects of the intervening cloud cover. To isolate these effects, we adopt the framework of Donohoe and Battisti (2011) to separate the atmospheric and surface contributions to the planetary, or TOA, albedo. This simplified framework considers each grid cell to have a single layer atmosphere over a reflective surface. The atmosphere is assumed to be isotropic and can absorb and reflect SW radiation.

TABLE 2 | Output is used from the following models from phase five of the Coupled Model Intercomparison Project.

Model	Institute
ACCESS1.0	Commonwealth Scientic and Industrial Research Organisation
ACCESS1.3	Commonwealth Scientic and Industrial Research Organisation
CESM1-CAM5	National Center for Atmospheric Research
CNRM-CM5	Centre National de Recherches Meteorologiques
CanESM2	Canadian Centre of Climate Modelling and Analysis
GISS-E2-H	Goddard Institute for Space Studies
GISS-E2-H-CC	Goddard Institute for Space Studies
GISS-E2-R-CC	Goddard Institute for Space Studies
HadGEM2-CC	Met Office Hadley Centre
INM-CM4	Institute for Numerical Mathematics
MIROC-ESM	Japan Agency for Marine-Earth Science and Technology
MIROC-ESM-CHEM	Japan Agency for Marine-Earth Science and Technology
MIROC5	Japan Agency for Marine-Earth Science and Technology
MPI-ESM-LR	Max Planck Institute for Meteorology
MPI-ESM-MR	Max Planck Institute for Meteorology
MRI-CGCM3	Meteorological Research Institute
MRI-ESM1	Meteorological Research Institute
NorESM1-ME	Norwegian Climate Center

TABLE 3 | Monthly TOA and surface (SFC) albedo sensitivities to sea ice area in June through September.

	Jun	Jul	Aug	Sep
		TOA Albedo-SIA sensitivity [$(10^6\ km^2)^{-1}$]		
CMIP5 (1900–2005)	0.0154 (0.0073)	0.0099 (0.006)	0.0069 (0.0037)	0.0074 (0.0037)
CMIP6 (1900–2005)	0.0155 (0.0053)	0.0122 (0.0039)	0.0087 (0.0023)	0.0089 (0.0026)
CMIP6 (2000–2014)	0.0184 (0.0097)	0.0095 (0.0073)	0.0058 (0.0061)	0.0047 (0.0041)
CERES (2000–2014)	0.0348 (0.0135)	0.0188 (0.0091)	0.0115 (0.0039)	0.0136 (0.0029)
		SFC Albedo-SIA Sensitivity [$(10^6\ km^2)^{-1}$]		
CMIP5 (1900–2005)	0.0367 (0.0139)	0.0272 (0.0117)	0.0255 (0.0082)	0.0313 (0.0068)
CMIP6 (1900–2005)	0.0417 (0.0093)	0.0342 (0.0091)	0.0306 (0.0059)	0.0354 (0.0049)
CMIP6 (2000–2014)	0.0468 (0.0141)	0.0304 (0.0076)	0.0259 (0.0039)	0.0321 (0.0052)
CERES (2000–2014)	0.0727 (0.0024)	0.0405 (0.0118)	0.0443 (0.0055)	0.04189 (0.0041)

Ensemble means are listed for CMIP5 and CMIP6 with standard deviations given in parentheses. Monthly sensitivities from CERES-EBAF are also shown for comparison, with the standard error from regressing the albedo versus sea ice given in parentheses.

The surface and TOA albedos (α_{SFC}, α_{TOA}) can be calculated from upwelling ($SW^{\uparrow}$) and downwelling ($SW^{\downarrow}$) fluxes at each interface:

$$\alpha = \frac{SW^{\uparrow}}{SW^{\downarrow}}. \tag{1}$$

The TOA albedo can be further decomposed into a sum of two parts, one from the atmosphere:

$$\alpha_{TOA,ATM} = \frac{SW^{\downarrow}_{SFC} \times SW^{\uparrow}_{SFC} - SW^{\downarrow}_{TOA} \times SW^{\uparrow}_{TOA}}{(SW^{\uparrow}_{SFC})^2 - (SW^{\downarrow}_{TOA})^2} = R \tag{2}$$

and one from the surface:

$$\alpha_{TOA,SFC} = \alpha_{SFC}\frac{(1 - R - A)^2}{1 - R \times \alpha_{SFC}}, \tag{3}$$

where A is the atmospheric absorption

$$A = \frac{SW^{\downarrow}_{TOA} - SW^{\uparrow}_{TOA} - SW^{\downarrow}_{SFC} + SW^{\uparrow}_{SFC}}{SW^{\uparrow}_{SFC} + SW^{\downarrow}_{TOA}}. \tag{4}$$

The atmospheric contribution ($\alpha_{TOA,ATM}$) to the TOA albedo is equal to the direct reflectance by the atmosphere (R), and the surface contribution ($\alpha_{TOA,SFC}$) is the SW radiation reflected by the surface that passes through the atmosphere and exits at the TOA. Interested readers are directed to Donohoe and Battisti (2011) for a more detailed derivation. Together, $\alpha_{TOA,ATM}$ and $\alpha_{TOA,SFC}$ provide additional insights into model performance than α_{TOA} alone since the former is more directly related to clouds while the latter depends on both surface conditions and the intervening atmospheric conditions.

For albedo partitioning in observations, the uncertainty is propagated for each term assuming the errors are independent. For the TOA and surface albedos, fractional errors are calculated for up- and downwelling SW fluxes using annual uncertainties and averages (Kato et al., 2018; Loeb et al., 2018). These fractional uncertainties are added in quadrature to give 0.01 (0.12) for the TOA (surface) albedo. They are multiplied by the monthly values for each albedo. For each of the TOA albedo contributions, the absolute uncertainty, $\Delta\alpha$, is calculated using

TABLE 4 | Mean TTE in years for all-sky and clear-sky SW_{acc} trends from CMIP6 models.

Model	All-sky	Clear-sky
ACCESS-CM2	13 (3)	13 (3)
ACCESS-ESM1-5	12 (3)	11 (2)
BCC-CSM2-MR	22 (6)	10 (3)
CESM2	11 (3)	16 (3)
CESM2-WACCM	7 (2)	11 (3)
CanESM5	8 (2)	9 (2)
EC-Earth3	13 (4)	13 (4)
EC-Earth3-Veg	13 (3)	12 (3)
GFDL-ESM4	14 (3)	11 (3)
INM-CM4-8	19 (6)	13 (4)
INM-CM5-0	17 (4)	19 (3)
IPSL-CM6A-LR	8 (3)	10 (3)
MIROC6	7 (2)	8 (2)
MPI-ESM1-2-HR	16 (4)	19 (4)
MPI-ESM1-2-LR	20 (6)	12 (3)
MRI-ESM2-0	14 (4)	11 (3)
NESM3	13 (3)	9 (2)
NorESM2-LM	17 (4)	17 (3)
Ensemble Mean	14 (4)	13 (3)

$$\Delta\alpha = \sqrt{\sum_i \left(\frac{\partial\alpha}{\partial SW_i} * \Delta SW_i\right)^2}, \tag{5}$$

where SW_i refers to the four all-sky SW fluxes used in **Eqs 2**, **3**. The partial derivatives are evaluated using annual average values, and the absolute uncertainty is divided by the annual average albedo contribution. The resulting fractional uncertainties are 0.05 for the atmospheric contribution and 0.07 for the surface contribution.

2.2 Accumulated Shortwave

Ultimately, our ability to simulate the ice-albedo feedback and predict changes in Arctic climate depends on how well we can model the amount of solar radiation absorbed in the Arctic and the associated feedbacks. To provide a stationary time-series suitable for assessing the emergence of solar absorption trends, we adopt the accumulated net SW radiation absorbed in the Arctic climate system over the melt season, defined as:

$$SW_{acc} = \sum_{m=3}^{9} \sum_{i,j} (SW^{\downarrow}_{TOA} - SW^{\uparrow}_{TOA})_{i,j} \times A_{i,j} \times t_m, \tag{6}$$

where $A_{i,j}$ is the area of grid box i, j and t_m is the seconds in each month m. SW_{acc} is computed separately using all-sky and clear-sky SW fluxes integrated over the area north of the Arctic circle to assess both the total SW energy absorbed into the Arctic over the year and quantify the influence of clouds.

Quantifying changes in SW_{acc} provides an important measure of the Arctic climate response to increased greenhouse gas concentrations. Systematic increases in annual SW_{acc} (relative to an initial equilibrium where incoming solar radiation balances thermal emission and heat transport from lower latitudes) supplies energy for melting additional sea ice and snow or warming the Arctic ocean. As a result, the strength of SW_{acc} trends are closely linked to both Arctic and global temperature changes. Climate models that produce detectable trends in SW accumulation sooner have been shown to exhibit the largest global temperature responses under multiple shared societal pathways (Sledd and L'Ecuyer, 2021b).

TABLE 5 | Mean TTE in years for all-sky and clear-sky SW_{acc} trends from CMIP5 models.

Model	All-sky	Clear-sky
ACCESS1.0	12 (4)	12 (3)
ACCESS1.3	14 (4)	21 (3)
CESM1-CAM5	15 (3)	14 (3)
CNRM-CM5	16 (4)	10 (3)
CanESM2	19 (5)	16 (3)
GISS-E2-H	27 (8)	15 (4)
GISS-E2-R-CC	63 (17)	25 (5)
HadGEM2-CC	13 (3)	12 (2)
INM-CM4	18 (4)	17 (3)
MIROC-ESM	8 (3)	8 (2)
MIROC-ESM-CHEM	8 (3)	8 (2)
MIROC5	12 (2)	12 (2)
MPI-ESM-LR	12 (4)	12 (3)
MPI-ESM-MR	21 (5)	13 (3)
MRI-CGCM3	26 (6)	16 (4)
MRI-ESM1	28 (6)	20 (3)
NorESM1-ME	20 (3)	17 (3)
Ensemble Mean	20 (12)	15 (5)

In this study, to bridge the timescales between monthly albedo partitioning and seasonal SW_{acc}, we further calculate the total SW energy reflected over the melt season by the atmosphere:

$$SW_{ref_{atm}} = \sum_{m=3}^{9} \sum_{i,j} \alpha_{TOA,ATM_{i,j}} SW^{\downarrow}_{TOA} \times A_{i,j} \times t_m \tag{7}$$

and the surface:

$$SW_{ref_{sfc}} = \sum_{m=3}^{9} \sum_{i,j} \alpha_{TOA,SFC_{i,j}} SW^{\downarrow}_{TOA} \times A_{i,j} \times t_m. \tag{8}$$

2.3 Time to Emergence

Beyond the response of SW_{acc} to warming from increasing greenhouse gas concentrations, there is also considerable natural variability owing to year-to-year variations in cloud cover and sea ice extent. To compare the statistical significance of forced responses between models and evaluate them against the recent observational record, we adopt criteria from Weatherhead et al. (1998) that assesses the time required for trends in SW_{acc} to exceed its natural variability. A measured trend ($\hat{\omega}$) must be twice as great as its standard deviation to be considered statistically significant with 95% confidence, or $|\hat{\omega}/\sigma_{\hat{\omega}}| > 2$, where the standard deviation of the trend, $\sigma_{\hat{\omega}}$, is given by:

$$\sigma_{\hat{\omega}} \approx \sigma_N \left[\frac{12dt}{T^3} \frac{(1+\phi)}{(1-\phi)}\right]^{1/2}. \tag{9}$$

In **Eq. 9**, T is the length of the time series, dt is the time interval ($dt = 1$ for annual observations), σ_N is the standard deviation, and ϕ is the 1-lag autocorrelation. The number of years needed to

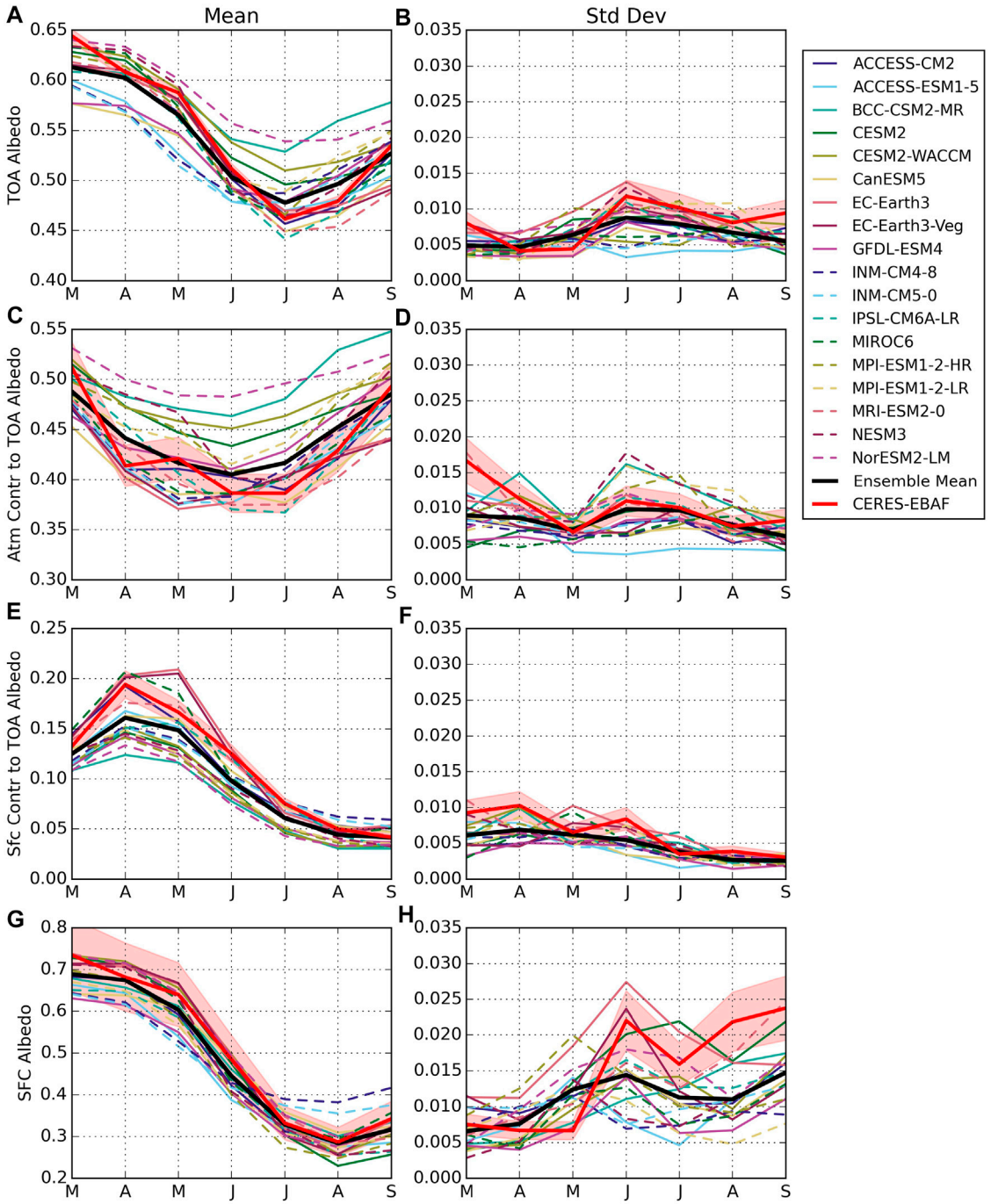

FIGURE 2 | Monthly means **(left column)** and standard deviations **(right column)** of TOA and surface albedos and TOA albedo partitions in CMIP6 during the melt season, March through September. Values are calculated from historical forcing years 1900–2014 and averaged over the area north of the Arctic Circle. Ensemble means are shown in black, and observations from CERES-EBAF are shown in red. Light red shading represents uncertainty in CERES-EBAF, found by calculating annual fractional errors for each component and multiplying by the monthly values.

measure a statistically significant trend is termed the time to emergence (TTE). This method assumes the detrended anomalies can be modeled as a first order autoregressive (AR(1)) process, although Phojanamongkolkij et al. (2014) showed it can also be used for AR(0) processes. Over the CERES record, autocorrelations in SW_{acc} are not significant for any number of lags due to the high uncertainty in correlations from so few years of observations. Furthermore, SW_{acc} appears as white or red noise in CMIP6 models tested over the historical period (Sledd and L'Ecuyer, 2021b).

While the TTE can be calculated for a single time series, internal variability can result in a range of TTE even for the same magnitudes of trend, variance, and autocorrelation (Sledd and L'Ecuyer, 2021b). We therefore follow Chepfer et al. (2018) and use synthetic time series of SW_{acc} to calculate a mean TTE from observations and models. A synthetic time series is created by adding a linear trend to random noise based on the statistical properties (variance and 1-lag autocorrelation) of the original time series. The synthetic time series is extended out for 150 years, which is long enough for trends to emerge in observations and all models. The mean TTE is found from a synthetic ensemble of 300 synthetic time series from each data source. Creating synthetic ensembles, as opposed to using large ensembles from GCMs, allows us to evaluate more models, as well as to compare observations with the same method. Further details concerning the application of these methods can be found in Sledd and L'Ecuyer (2021b).

3 RESULTS AND DISCUSSION

3.1 Mean State Arctic Albedo

The planetary or TOA albedo governs how much solar energy is absorbed in a region after reflection by the surface and atmosphere. The CMIP6 models examined here broadly agree on the seasonal cycles of Arctic mean TOA albedo and the relative magnitudes of its surface and atmospheric contributions (**Figure 2**). In fact, the ensemble mean TOA albedo (black) tracks CERES-EBAF (red) very closely over the entire melt season with the exception of March when models predict a slightly less reflective Arctic than observed. Despite this agreement in the ensemble mean, there is significant spread between models, upwards of 0.1 difference in July and August. Thus models with the highest albedos reflect 10% more incoming solar radiation than the models with the lowest albedos, which translates to differences of more than 40 Wm^{-2} in solar energy input to the region in these summer months. This far exceeds year-to-year variations in TOA albedo that are generally less than 0.01 in both the observations and individual models in all months except June (**Figure 2B**).

Similar conclusions can be drawn for surface albedo. The ensemble mean quite closely follows the CERES observations throughout the melt season, but models exhibit a spread of 0.1 in spring that increases to more than 0.16 in September. However, despite similar model spreads in SFC and TOA albedos, SFC albedo differences are not responsible for the observed range in modeled Arctic TOA albedo. Both the models and CERES observations agree that the surface contributes less than a third of the TOA albedo in the Arctic, and this contribution falls to a narrow range around 10% in late summer. Consistent with previous studies, e.g. (Qu and Hall, 2005; Sledd and L'Ecuyer, 2019), the atmosphere contributes at least twice as much as the surface to the TOA albedo at all times of year. As a result, model spread in the atmospheric contribution dominates the range of TOA albedos as evidenced by the ordering of individual models within the ensemble in **Figures 2A,C**.

This spread in model representations of present day Arctic albedo has implications for achieving consensus in predicting future changes in Arctic absorption. **Figure 3B** shows that all CMIP6 models predict that the Arctic will be darker (in other words the Arctic will absorb more solar radiation) by the end of the 21st century, consistent with the ice-albedo feedback. The largest decreases occur in early summer due to lower surface contributions (not shown). These changes occur when incident solar radiation is strong and present-day sea ice extents are relatively large, but the magnitude of these changes, and, by extension, the strength of the ice-albedo feedback, vary by a nearly a factor of 6 between models.

To understand the source of this wide range of predictions, **Figure 3** also shows the changes in atmospheric and surface contributions to TOA albedo by the end of the century. Note that here the surface and atmosphere contributions are expressed as percents of the TOA albedo as opposed to absolute values in **Figure 2** to focus on relative changes. **Figure 3C** shows that, on average, the atmosphere accounts for 67% of the TOA albedo in late spring and as much as 93% of the TOA albedo by the end of summer based on CERES observations. Many CMIP6 models actually predict even stronger atmospheric contributions than observations. In some models, such as NESM3 and BCC-CSM3-MR, the surface never accounts for more than 20% of the TOA albedo. This may indicate that their atmospheres are too cloudy, their sea ice is too dark or too little, or some combination of these factors. In addition, it is possible model atmospheres absorb too much SW radiation, i.e. their atmospheres are too moist.

CMIP6 models also exhibit a wide range of behaviors that far exceed interannual variations in the CERES observations (less than 3% based on **Figure 2D**). This is especially true in spring when the models span a range of approximately 15%. Models converge in late summer when the atmosphere contributes most of the TOA albedo. To put the magnitude of this model spread into perspective, **Figures 3D,F** show how the contributions from the atmosphere and surface change over the 21st century. The surface contribution declines as the Arctic loses sea ice and snow cover and the atmospheric absorption slightly increases (not shown) with a moister Arctic (Nygård et al., 2020). In other words, all models predict that the atmosphere contributes a larger percentage of the TOA albedo at the end of the century. Yet some models predict increases of less than 5% throughout the year while others suggest that increases peak at 15% in May and June. These differences may be connected to the present day mean state in the models since models with larger surface contributions today (e.g. EC-Earth3, solid rose line) tend to predict the largest changes with increased greenhouse gas concentrations. However, given the important role that the atmosphere plays in defining the net radiation absorbed at TOA, differences in the distribution of water vapor and clouds and, especially, how they may change in the future, likely contribute to the spread in model predictions as well, e.g. Alkama et al. (2020). Once again, models converge in late summer since the surface contributes so little in the present day that there is little room for further decline.

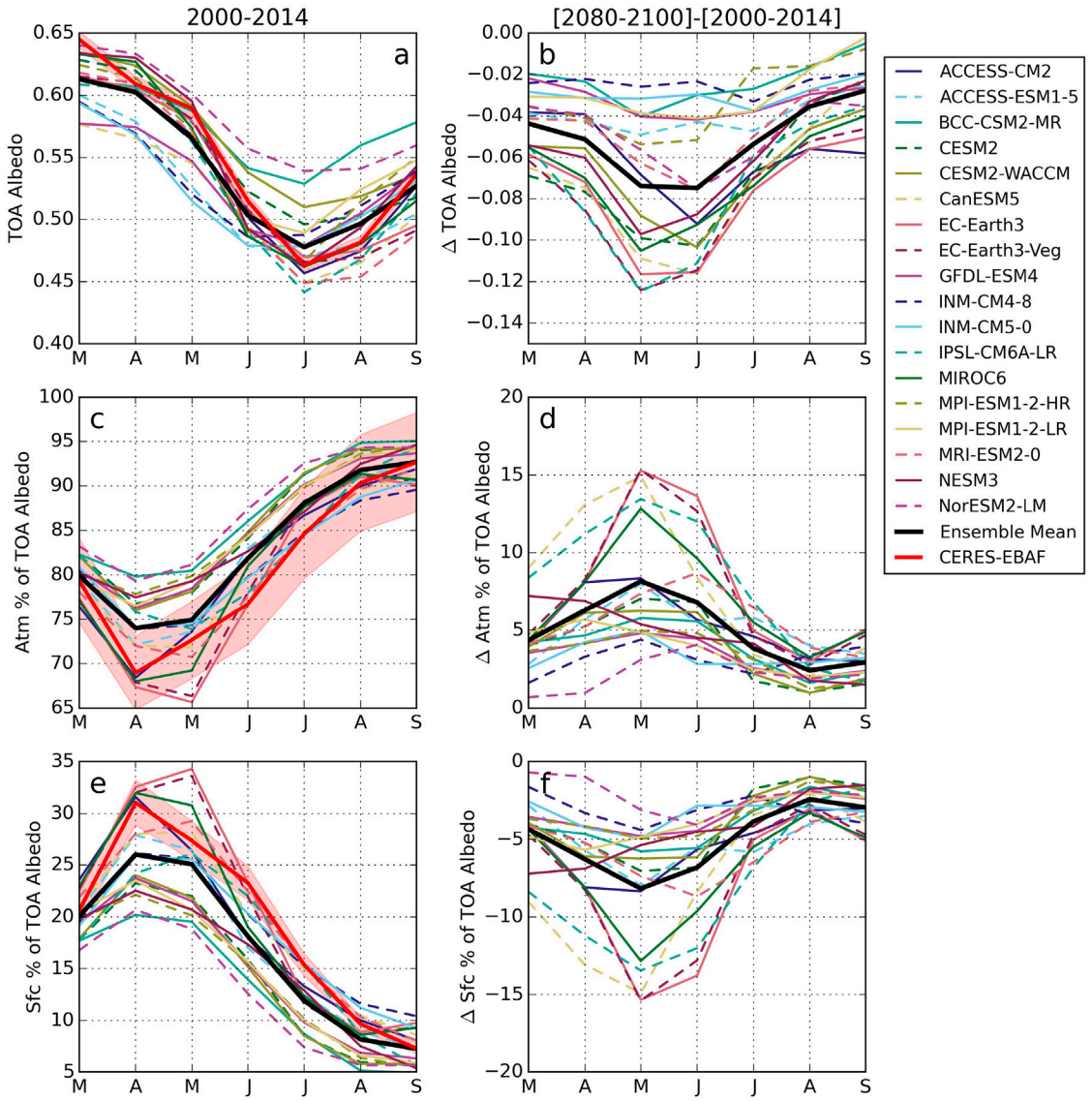

FIGURE 3 | Mean TOA albedo **(A)** and fraction of the TOA albedo contributed by the atmosphere **(C)** and surface **(E)** over 2000–2014 in CMIP6 and observations (CERES-EBAF), March through September. Differences between historical and end of century (2080–2100) fractional TOA contributions are shown in **(B**,**D**,**F)**, calculated with SSP585. Ensemble means are shown in black. Light red shading represents uncertainty in CERES-EBAF, found by calculating annual fractional errors for each component and multiplying by the monthly values.

3.2 The Radiative Impact of Sea Ice Changes

While the atmosphere always contributes more than the surface to TOA albedo, **Figure 2** shows that surface albedo plays a significant role in determining the shape of the annual cycle of Arctic albedo. Higher albedos associated with widespread sea ice in spring lead to the highest TOA albedos across the Arctic, and melting sea ice in mid-summer coincides with the lowest TOA albedos. Only in late summer, when sea ice reaches a minimum, do we observe an apparent decoupling of TOA and SFC albedo where the Arctic becomes more reflective as a whole in August and September despite having its darkest surface. This demonstrates very clearly that the Arctic albedo is sensitive to sea ice cover but that this sensitivity is modulated by the cloudy atmosphere. As a result, the amplitude of the annual cycle of observed SFC albedo in **Figure 2**, defined as the difference between the maximum and minimum value over the months examined, is about 2.5 times larger than that at the TOA.

However, this ratio of surface to TOA annual cycle amplitudes is far from constant across CMIP6 models. The amplitude of the annual cycle of SFC albedo in EC-EARTH3 (solid rose line in **Figure 2**), for example, is 2.7 times larger than at the TOA, similar to observations. On the other hand, the amplitude of the SFC albedo annual cycle in BCC-CSM2-MR (solid light green line in **Figure 2**) is 4.2 times larger than that at the TOA. This is

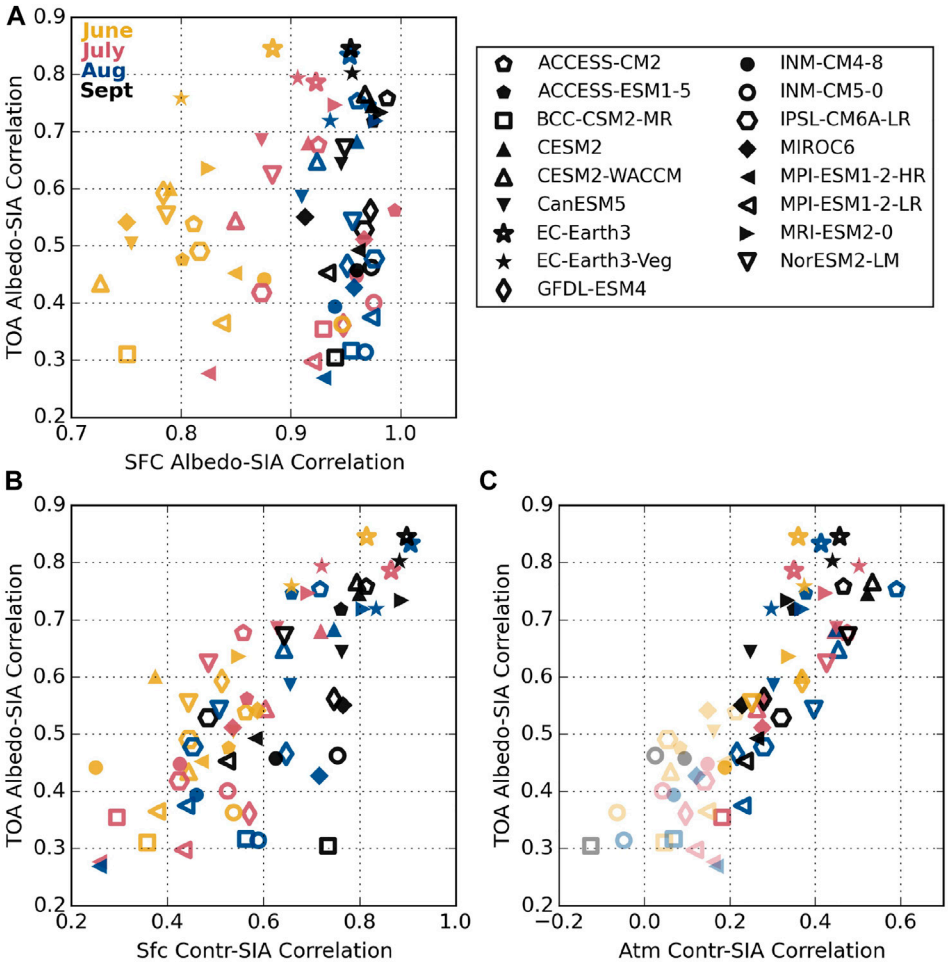

FIGURE 4 | Correlations between albedos and SIA as they relate to each other during summer months. Correlation coefficients are calculated over the historical period, 1900–2014, using detrended anomalies. Correlation coefficients that are considered statistically significant using a *t*-test with 95% significance level and effective sample sizes that take into autocorrelation have opaque markers; statistically insignificant correlations are semi-transparent.

consistent with the fact that the Beijing Climate Center model exhibits larger than average atmospheric contributions to TOA albedo, suggesting that its clouds are more effective at masking surface albedo changes.

These inter-model differences in the extent to which surface albedo changes are realized at the TOA indicate that Arctic solar absorption responds differently to the annual cycle of sea ice extent across the CMIP6 models. To test whether these distinct responses extend to inter-annual variations in sea ice extent, **Figure 4A** summarizes how TOA and SFC albedos correlate to SIA. There is broad consensus across CMIP6 that the surface albedo is highly correlated with SIA over the historical period from 1900–2014. In June (yellow markers) correlations are all greater than 0.7, and in August and September (blue and black) correlations are above 0.9 for all models. This agreement makes physical sense as reduced areas of brighter sea ice reveal more dark open ocean.

This close agreement between models breaks down when considering TOA albedo, though. Correlations between the TOA albedo and SIA plotted on the y-axis in **Figure 4A** range from less than 0.3 to more than 0.8 in all 4 months. This spread means that, in some models the TOA albedo is strongly linked to the surface and sea ice (e.g. EC-Earth3, EC-Earth3-Veg, MRI-ESM2-0), while in other models the response is relatively weak (e.g. BCC-CSM2-MR, MPI-ESM1-2-HR, MPI-ESM1-2-LR), i.e. what happens at the surface stays at the surface.

Figures 4B,C show that, like the annual cycle, the extent to which changes in TOA albedo are correlated with longer-term sea ice declines is related to the atmospheric influence. Like TOA albedo, correlations between both surface and atmospheric contributions to TOA albedo and SIA vary widely across the CMIP6 models. Correlations between surface contribution and SIA range from about 0.2 to 0.9 while atmospheric contribution correlations range from −0.1 to 0.6, although correlations with magnitudes below approximately 0.2 are not statistically significant at the 95% confidence level (represented as semi-transparent markers in **Figure 4C**, determined using an effective sample size that takes into account autocorrelation present in

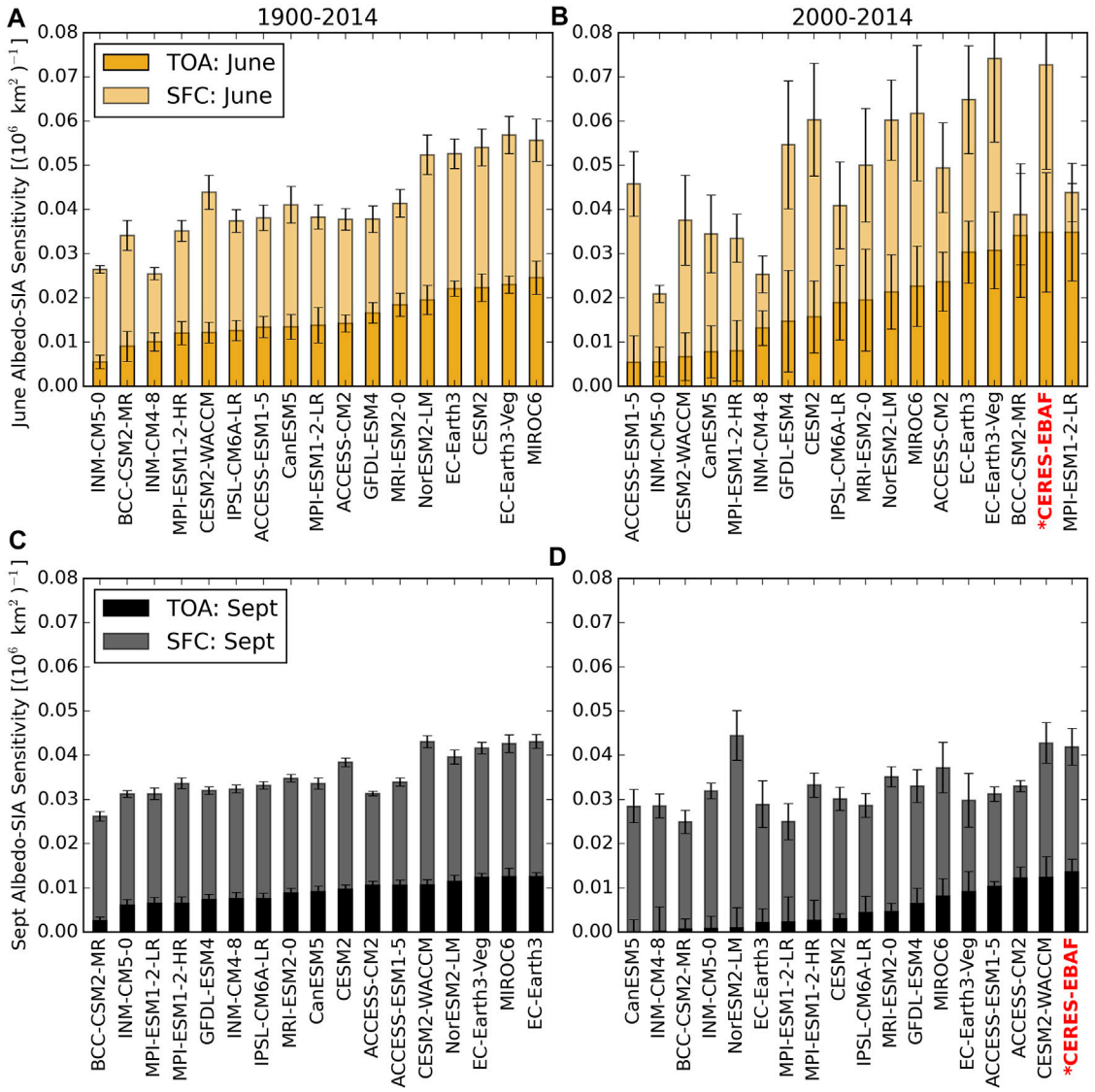

FIGURE 5 | Sensitivity of TOA and surface albedos to sea ice area (SIA) in June **(A,B)** and September **(C,D)**. Sensitivity is found from the regression of each albedo against SIA for a given month across the historical time period, 1900–2014 **(A,C)** and the overlap with the CERES observational record, 2000–2014 **(B,D)**. Models are sorted from lowest **(left)** to highest **(right)** TOA sensitivity to SIA. Error bars represent the standard error of the estimated gradient for each sensitivity.

each time series). While models with the largest correlations between TOA albedo and SIA tend to also exhibit strong correlations between surface contributions and SIA, the SFC contribution is not the main driver, as indicated by the substantial spread below 0.7 in **Figure 4B**. Notice, for example, that in September BCC-CSM2-MR (black hexagon) shows a strong correlation between the surface contribution and SIA (0.7) but that it has one of the lowest TOA albedo-SIA correlations in the ensemble (0.3). A strong correlation between the atmospheric contribution and SIA is required for TOA albedo to be highly correlated with SIA. This reflects the fact that the atmosphere contributes a large percentage of the TOA albedo, so the disparate model behaviors may have significant implications for their responses to systematic declines in sea ice cover associated with Arctic warming.

This is confirmed in **Figure 5** that shows the sensitivity of TOA and surface albedo to a 1 million square kilometer change in sea ice area, found by regressing albedos against SIA for the months of June and September. Results are presented for both the historic period 1900–2014 (left column) and the shorter modern period from 2000–2014 (right column) to allow comparison with CERES-EBAF. The corresponding ensemble means are given in **Table 3**. Using the longer historical time period allows for more robust statistics compared to only the years that overlap with CERES-EBAF, although it does assume that the response of albedos to SIA changes do not deviate too much in the latter time period. As expected, the surface albedo (indicated by the

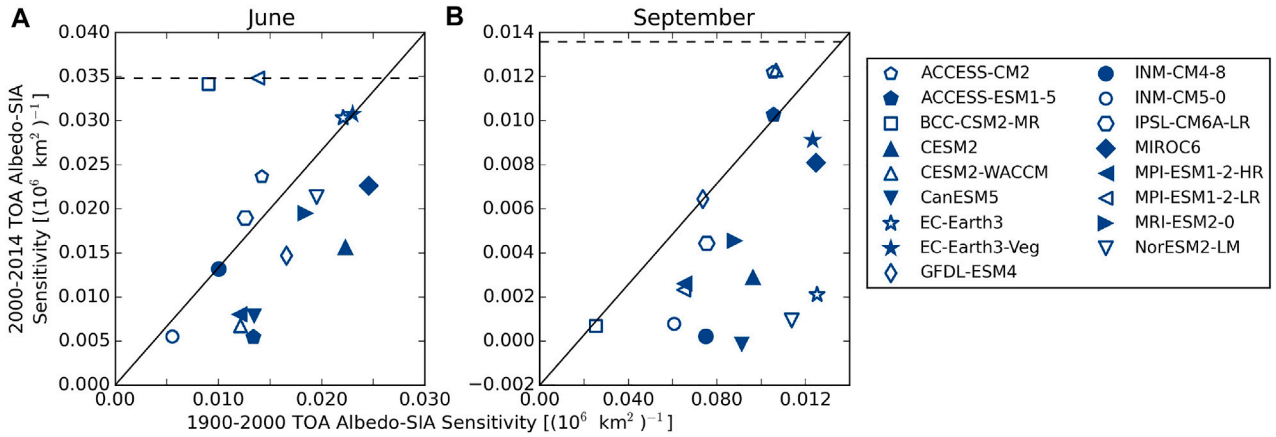

FIGURE 6 | Sensitivity of TOA albedo to SIA in CMIP6 calculated over 1900–2005 compared to 2000–2014 for June **(A)** and September **(B)**. Sensitivity from CERES over 2000–2014 is plotted as the horizontal line for reference.

more transparent shading) is more sensitive to changes in SIA than the TOA albedo in all months, consistent with observations (Sledd and L'Ecuyer, 2019). Surface albedo sensitivities also tend to be better constrained between models, particularly in September when a 10^6 km^{-2} reduction in sea ice area decreases surface albedo by 0.03–0.04 in a majority of models in both epochs. This is consistent with the 0.04 sensitivity derived from CERES-EBAF observations from 2000–2014. Larger inter-model differences in June surface albedo responses, especially in the recent 2000–2014 period, are likely caused by differences in sea ice albedo (Davy and Outten, 2020).

Recall, though, that Arctic energy balance and warming are primarily governed by the TOA albedo that determines how much solar radiation is absorbed in the region. The magnitude of the TOA response to SIA changes is much more variable across CMIP6 models in both June and September in both epochs. For example, MIROC6 is about five times more sensitive to sea ice changes than INM-CM5-0 in June over the historical 1900–2014 period with sensitivities of 2.5 and 0.5 %/10^6 km^2, respectively. Assuming an average incident SW radiation at the TOA of 500 Wm^{-2} (typical of the Arctic in June), a 1 million km^2 loss of sea ice, would result in an average of (Δ SW$_{absorbed}$=$-\Delta\alpha_{TOA}\times$SW $\downarrow$) 12.5 Wm^{-2} more solar absorption in MIROC6 but only 2.5 Wm^{-2} in INM-CM5-0. For context, this difference of 10 Wm^{-2} is more than double the anticipated global mean radiative forcing from doubling current carbon dioxide concentrations (Etminan et al., 2016).

In most models, the TOA albedo is about half as sensitive to SIA in September as in June over the historical period, a direct consequence of the increased atmospheric contributions in fall compared to summer. Furthermore, changes in albedo exert a smaller influence on Arctic absorbed SW radiation in September due to the lower mean incident solar radiation. Never-the-less, September TOA albedo sensitivity to SIA over the last century varies by about a factor of 5 across CMIP6 models bracketed by BCC-CSM2-MR (0.25) and EC-Earth3 (1.25). While the precise ordering of models from lowest to highest TOA albedo sensitivity in **Figure 5** varies somewhat from June to September, models with higher sensitivities in June tend to also have higher sensitivities to SIA in September.

Sensitivities calculated over the modern Arctic (2000–2014), characterized by more seasonal ice coverage, exhibit signatures consistent with this change in base state relative to the last century (**Figures 5B,D**). In most models, the TOA albedo in June is at least as sensitive to sea ice changes in the modern epoch compared to during the longer historical period. This is clearly evident in **Figure 6** where TOA albedo sensitivity to SIA in the modern Arctic is plotted against that in the historical period for all CMIP6 models. While a few models show decreased sensitivity in June (e.g. ACCESS-ESM1-5, CESM2, and CanESM5), other models exhibit much larger increases (e.g. BCC-CSM2-MR and MIP-ESM1-2-LR). The latter models have TOA albedos that are at least three times as sensitive to SIA changes over 2000–2014 as compared to 1900–2000, which may suggest their climates are already changing significantly. A more robust but opposite trend is evident in September where the TOA albedo is less sensitive to SIA across all CMIP6 models in the modern epoch compared to the last century. In extreme cases (e.g. CanESM3, NorESM-2-LM, and EC-Earth3), the TOA albedo in September has almost no sensitivity to changing SIA in today's climate while it varied by more than 1% per 10^6 km^{-1} over the past century. This is a consequence of the diminished September SIA in recent years that has increased the atmospheric contribution to TOA albedo even relative to last century (not shown but analogous to **Figure 3D**).

While the modern period from 2000–2014 has fewer years and, therefore, less robust statistics than the full historical 1900–2014 record, it provides a snapshot of the modern Arctic that overlaps the observational record provided by CERES-EBAF. Furthermore, unlike the trends shown in **Supplementary Figures S1, S2**, the regressions shown in **Figure 5** are less sensitive to internal model variability since they do not depend on the time-evolution of the modeled

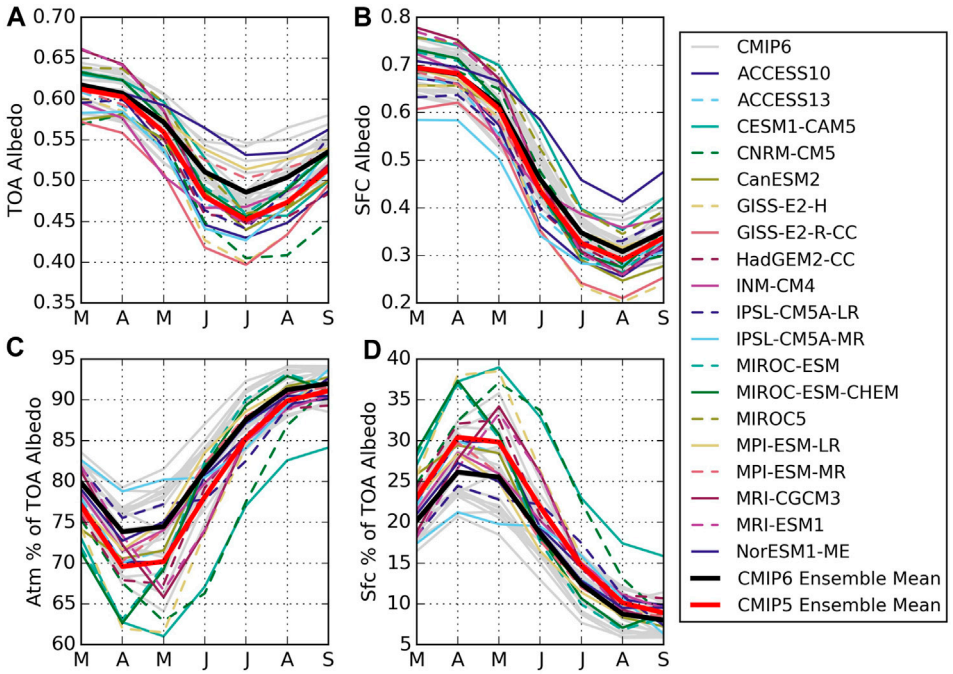

FIGURE 7 | Annual cycles of TOA and surface (SFC) albedos **(A,B)** and percent contributions of the atmosphere **(C)** and surface **(D)** to the TOA albedo from CMIP5 (color lines) and CMIP6 (grey). Averages are calculated over 1986–2005. Ensemble means are shown in black for CMIP6 and red for CMIP5.

climate but rather the statistical relationship between two quantities: TOA albedo and SIA. The computed regressions do not depend on the specific model years that exhibit higher or lower SIA nor the actual magnitude of the SIA changes and are, therefore, less dependent on the specific trajectory of the model. Never-the-less, these relationships do depend on the mean state of the system as noted above, so some additional scatter among models should be expected relative to the longer historical period.

CERES-EBAF observations confirm that the TOA albedo sensitivity to SIA is more than two and a half times larger in June than in September. However, the observed sensitivities are larger than those in almost all of the CMIP6 in both months suggesting that Arctic solar absorption is more sensitive to changes in SIA than models predict. While internal variability likely plays a role in model behavior over this shorter period, it is not clear how it could result in all models underestimating Arctic albedo sensitivity to changes in sea ice cover. It may, instead, point to a more systematic bias in the way clouds covary with sea ice in models compared to observations, but identifying such biases would require more detailed analysis beyond that presented here.

3.3 Comparison with CMIP5

These comparisons against CERES-EBAF reveal some basic characteristics about the representation of absorbed solar radiation in the Arctic. The CMIP6 ensemble captures the observed mean annual cycle of TOA and surface albedo very well and generally simulates the observed partitioning of TOA albedo into its surface and atmospheric contributions. And yet, inter-model spread in TOA albedo, which governs the net energy input into the Arctic, is large owing primarily to substantial disagreement in the contributions from the atmosphere (i.e. clouds). This has significant implications for reconciling predicted increases in Arctic absorbed solar radiation owing to ice-albedo feedbacks over the next century, and CMIP6 models tend to systematically underestimate the sensitivity of TOA albedo to changing sea ice cover.

To put this snapshot of climate model behavior into the broader context of model development, the mean state and sensitivity of Arctic albedo to SIA in CMIP6 are compared against the preceding generation of models, CMIP5, in **Figures 7**, **8**. Since there are only 5 years over overlap between CERES observations and historical forcing from CMIP5, observations are omitted from these comparisons.

Annual cycles of albedos from 1986–2005 are presented in **Figure 7**. Note that this period has slightly larger TOA and surface albedos and marginally higher (lower) surface (atmospheric) contributions in CMIP6 relative to 2000–2014 (**Figure 2**) because sea ice concentrations were somewhat larger at the end of the 20^{th} century. The spread of albedos has narrowed between CMIP5 and CMIP6 and the Arctic is somewhat brighter in the summer months (June-August) in the latest generation of models. Although the ensemble means are very similar, CMIP5 had a notably larger spread in surface albedos over the melt season (e.g. Koenigk et al., 2014), fully encompassing the current CMIP6 ensemble (**Figure 7B**). The reduced spread in CMIP6 surface albedo is consistent with efforts to more closely align Arctic sea ice extents to observations (Shu et al., 2020). The actual spread in sea ice albedo is larger than that

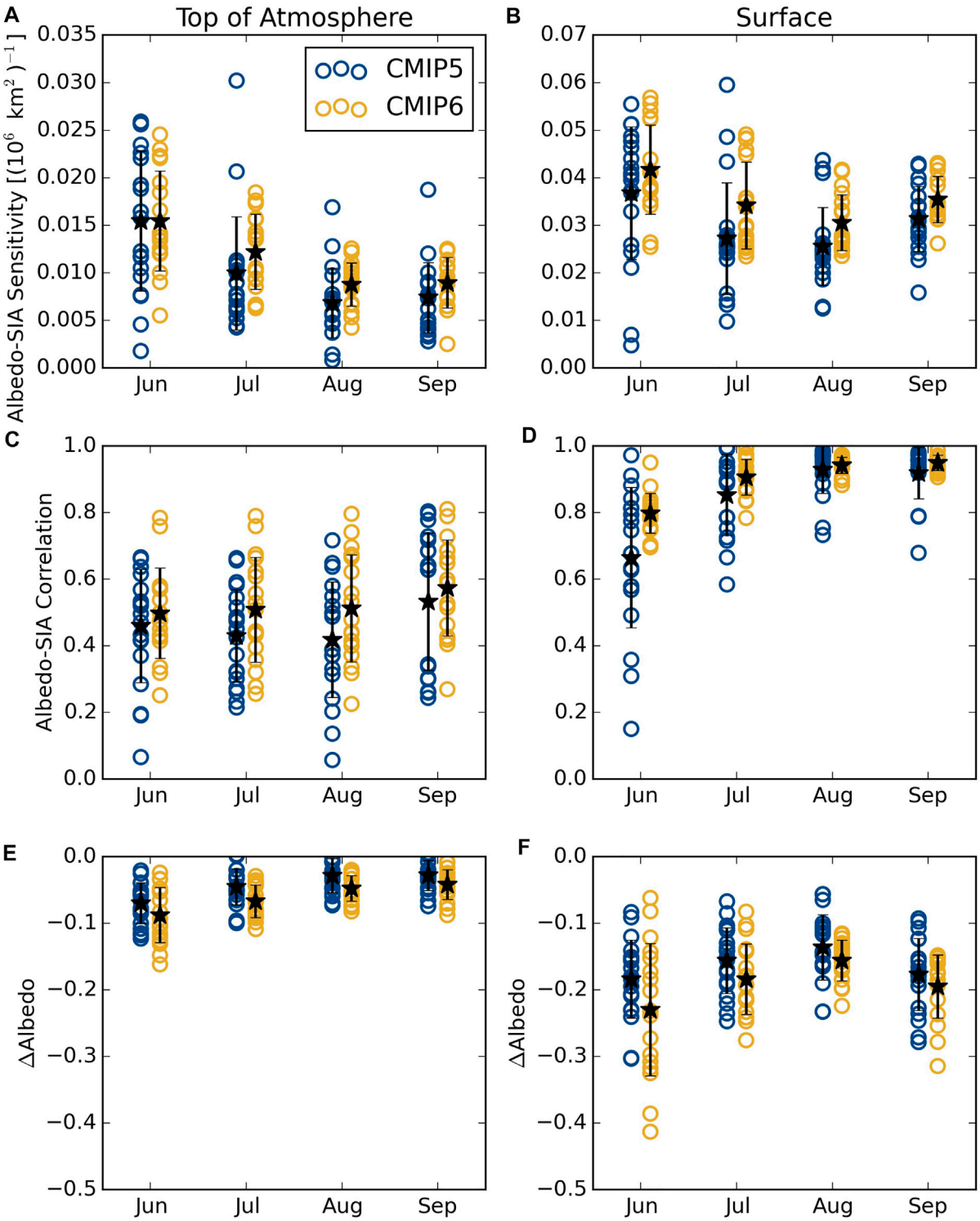

FIGURE 8 | Comparison of albedo-SIA sensitivities **(A,B)** and correlations **(C,D)** at the top of the atmosphere **(A,C)** and surface **(B,D)**. Values are calculated over 1900–2005 from CMIP5 and CMIP6. Changes over the 21st century ([2080–2100] minus [1900–2005]) are also shown for the TOA albedo **(E)** and surface albedo **(F)**. Ensemble means are shown as stars for each month.

shown since averaging over the Arctic includes dark open ocean areas. The lowest average surface albedos are from the GISS models that have documented low sea ice albedos due to excessive melt pond formation (Schmidt et al., 2014). NorESM1-ME has the highest average surface albedos in summer, likely because of its high sea ice albedo (Koenigk et al., 2014).

CMIP5 models also show a larger spread in monthly TOA albedos (15% versus 10%), particularly after May. As in CMIP6, this spread is more closely linked to differences in atmospheric contributions than surface behavior, which follows the diverging representations of Arctic clouds in CMIP5 (Cesana and Chepfer, 2012). For example, although NorESM1-ME shows average summer surface albedos larger than the CMIP6 ensemble, its average TOA albedos during summer are within the CMIP6 spread since its surface contributes relatively little to the TOA albedo and its atmospheric albedo aligns well with the ensemble average, likely due to higher cloud fractions and LWP as compared to observations (Seland et al., 2020).

Overall, CMIP5 models exhibit lower atmospheric contributions to TOA albedo compared to CMIP6, both in terms of raw values (not shown) and percent contributions (**Figure 7C**). This larger atmospheric contribution to TOA albedo in CMIP6 is responsible for the brighter Arctic in the latest generation of models. This is consistent with increased total cloud fractions in CMIP6 compared to CMIP5 and improvements in the representation of super-cooled liquid containing clouds (Wu et al., 2019; McIlhattan et al., 2020). Such changes may stem from an increased focus on improving polar cloud parameterizations by the modeling community in recent years (Seland et al., 2020; Vignesh et al., 2020; Wei et al., 2021). This effort may also have helped to narrow the model spread in atmospheric contributions to TOA albedo between CMIP5 and CMIP6. There is about a 15% range in the percentage of TOA albedo contributed by the atmosphere across CMIP5 models in all months. Conversely, while CMIP6 exhibits similar spreads in spring, their atmospheric contributions agree to within about 5% in September, a sign that simulated late-season sea ice and cloud cover has converged in the latest generation of climate models.

There may be evidence of another significant impact of changes to Arctic cloud parameterizations in the latest generation of climate models evident in **Figure 8** that compares TOA and surface albedo sensitivities to SIA changes in CMIP5 and CMIP6. Here the period 1900–2005 is adopted to ensure overlap between model generations, but omitting the last decade has a minimal impact on the magnitudes of these values in CMIP6. The corresponding mean all-sky and clear-sky TTE are given in **Tables 4** and **5** for CMIP5 and CMIP6, respectively. Although the relative contributions of the atmosphere and surface to the TOA albedo shift between CMIP5 to CMIP6, there is less change in the response of surface and TOA albedos to SIA between CMIP generations. More surprising, however, is that there has been a modest shift toward stronger TOA albedo sensitivity to (and higher correlations with) SIA in CMIP6 even though the surface contributes less to TOA albedo in CMIP6 than in CMIP5. This suggests that the atmospheric albedo itself (i.e. cloud cover) may respond more strongly to sea ice changes in CMIP6 hinting that Arctic cloud feedbacks may be stronger in the current generation of climate models (Zelinka et al., 2020; Sledd and L'Ecuyer, 2021b).

Figure 8 also shows that the spread in SIA sensitivity has improved relative to CMIP5. In fact, the inter-model range of both sensitivities to SIA and correlations with SIA are smaller in the latest generation of climate models. This is consistent with reduced uncertainty in sea ice albedo feedback from CMIP5 to CMIP6 (Zelinka et al., 2020). Never-the-less, CMIP6 albedos continue to exhibit a wide range of sensitivities to SIA that have significant implications for predicted changes in absorbed SW radiation and, ultimately, the evolution of Arctic climate. This is evident in the wide range of predicted decreases in Arctic TOA and surface albedos shown in **Figures 8E,F** that highlight the compounding effects of model differences in both the mean state solar absorption and its sensitivity to sea ice changes. The surprisingly large spread in predicted changes in surface albedo by the end of the century, especially in June, reflects the impacts of large discrepancies in absorbed solar radiation amplified by the myriad of associated feedbacks on SIA at the end of the century (Hahn et al., 2021). CMIP6 models also predict larger increases in overall Arctic solar absorption (lower albedos) by the end of the century than their CMIP5 counterparts, but the spread between individual models has also increased.

3.4 Implications for Solar Absorption Trends

Given the reduced spread in TOA and surface albedo sensitivities to SIA in CMIP6 relative to CMIP5, the increased uncertainty in 21^{st} century predictions is somewhat surprising. This, together with the shift toward greater atmospheric contributions to TOA albedo in CMIP6, suggests that the diverging predictions of future Arctic albedo may stem from differing cloud responses to changing SIA in the latest generation of some models (Hahn et al., 2021).

The increased role of the atmosphere in defining future Arctic albedo has significant implications for the time to emergence of trends in models. Sledd and L'Ecuyer (2021a) recently showed that clouds have delayed the emergence of trends in observed Arctic SW absorption by about 5 years relative to clear-sky conditions by reducing the magnitude of accumulated shortwave radiation (SW_{acc}) trends. A similar analysis applied to CMIP6 models, however, shows a more varied picture possibly related to cloud cover feedbacks that amplify the impacts of surface albedo changes.

Figure 9 examines the connection between the TTE of SW_{acc} trends and SIA responses explicitly and documents an apparent divergence of model behavior from CMIP5 to CMIP6. The y-axis on all plots shows the ratio of the TTE of clear-sky SW_{acc} trends to those in all-sky conditions. For reference, CERES observations since 2000 predict a ratio of 0.8. The choice of September SIA regressions on the x-axis is motivated by the fact that it represents the integrated effects of the melt season. Recall that SW_{acc} represents the net input of SW energy at the TOA into the Arctic system over the melt season, March through September. SIA reaches its minimum in September, the result of energy exchanged throughout the preceding melt season, including SW, so it is not unreasonable for there to be a connection across these different time scales.

While it is challenging to compare observed TTE to those from the different CMIP5 and CMIP6 emissions pathways directly, the clear to all-sky ratio isolates the role of clouds in modifying TTE, a physical characteristic we may expect to be less sensitive to subtle differences in climate trajectories. This is confirmed by the fact

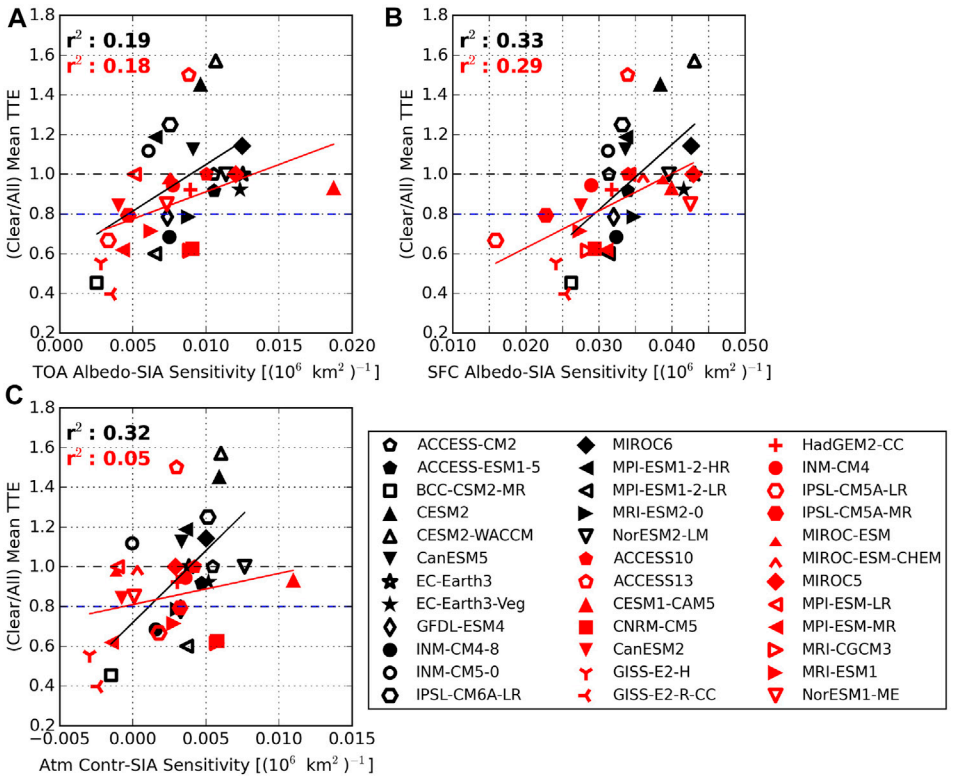

FIGURE 9 | Relationships between the ratio of all-sky to clear-sky SW_{acc} TTE and the sensitivity of **(A)** TOA albedo, **(B)** surface albedo, and **(C)** the atmospheric contribution to September SIA. Results calculated from CMIP6 SSP585 are shown in black or while those from CMIP5 RCP8.5 are in red. Wherever possible, similar symbols have been adopted for models from the same center. TTE ratio from CERES (0.8) is shown as the blue dashed horizontal line for reference.

that the TTE ratio is very consistent between SSP245 and SSP585 (Sledd and L'Ecuyer, 2021b). Two striking results are immediately evident in **Figure 9**: *1*) while all but one of the CMIP5 models agree with observations that clear-sky trends emerge more quickly than all-sky trends (ratios < 1), CMIP6 models are equally divided in whether clouds accelerate or delay the emergence of trends; and *2*) the TTE ratio is correlated with the sensitivity of the atmospheric contribution to SIA in CMIP6 while no such correlation existed in CMIP5 (**Figure 9C**).

These findings are likely related. In CMIP6 models where the atmospheric contribution shows little response to September SIA, the all-sky SW_{acc} trend takes relatively longer to emerge than the clear-sky SW_{acc} trend. These are the models where clouds presumably exhibit little change with SIA and the primary role of constant cloud cover is to mask surface changes, slowing the emergence of trends in solar absorption. CMIP5 models, on the other hand, exhibit no statistically significant relationship between TTE ratio and atmospheric contribution response to SIA, and all but one outlier reproduce the observed cloud delaying of TTE (although some models show ratios very near 1).

While **Figure 9** does not examine cloud feedbacks directly, it suggests that, in some CMIP6 models, increases in atmospheric contributions to TOA albedo in response to sea ice loss may enhance trends in SW_{acc} more than in CMIP5. For example, the Community Earth System Model (CESM) has undergone a significant shift from CESM1 (▲) where clouds slowed the emergence of SW_{acc} trends to CESM2 (▲) where clouds accelerate these trends by nearly 50%. Such a strong shift could be due to changes in cloud parameterizations that can have a dramatic influence on surface radiative balance, e.g. Huang et al. (2021). In **Figure 10**, the integrated solar radiation reflected by the atmosphere over the melt season, $SW_{ref_{atm}}$ (**Eq. 7**), has increased by nearly 30% between CESM1 and CESM2, consistent with McIlhattan et al. (2020) who showed that increased cloud cover and cloud liquid water path in summer led to decreased downwelling SW at the surface in CESM2 as compared to CESM1. The more SW energy the atmosphere reflects compared to the surface, the greater the impact clouds have on the Arctic mean SW_{acc}. This is true across all models in both CMIP generations (**Figure 10B**). In the case of CESM, brighter clouds in CESM2 reduce absorbed SW radiation across the Arctic by 33%, more than double their effect in CESM1 (16%). More generally, the population of CMIP6 models has shifted toward brighter atmospheres that suppress more SW_{acc} relative to clear skies than the population of CMIP5 models.

The standard deviation of $SW_{ref_{atm}}$ influences whether internal variability in cloud reflection increases or decreases SW_{acc} variability across models. This is notable because the relative "noisiness" of all-sky versus clear-sky SW_{acc} is a determining factor in whether clouds increase or decrease SW_{acc} TTE. If clouds increase SW_{acc} variability, they can increase TTE because it takes

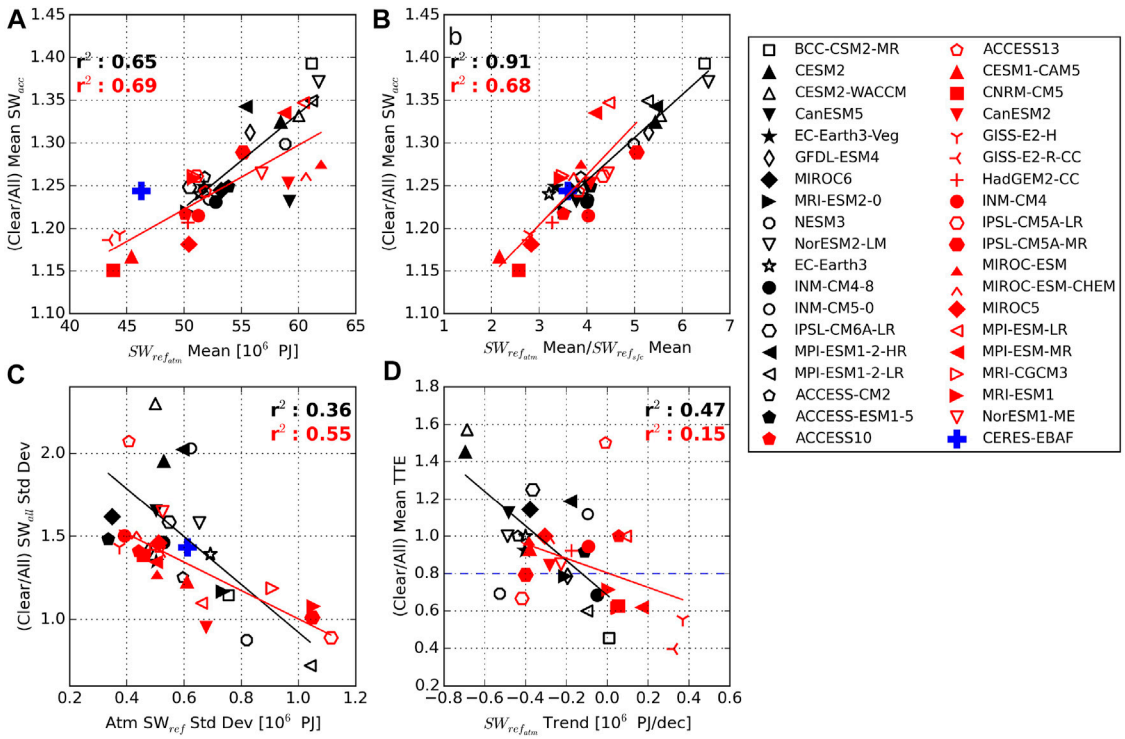

FIGURE 10 | Total SW reflected due to the atmosphere ($SW_{ref_{atm}}$) as it relates to accumulated SW (SW_{acc}) ratios of all-sky to clear-sky for **(A)** means, **(B)** standard deviations, and **(C)** trends and time to emergence (TTE). Means and standard deviations are calculated over 2000–2014, and trends and SW_{acc} TTE are calculated using SSP585 over 2000–2100 for CMIP6 (black) and RCP8.5 for CMIP5 (red). CERES observations are shown for values calculated over 2000–2014. Wherever possible, similar symbols have been adopted for models from the same center.

longer for a trend to emerge from a noisier timeseries, and vice versa. $SW_{ref_{atm}}$ standard deviations vary by almost a factor of three across CMIP6 models in **Figure 10C**. Models with the greatest $SW_{ref_{atm}}$ standard deviations (MPI-ESM1-2-LR and NESM3) are the only models where clouds increase the variability of SW_{acc}. In models where the atmospheric reflectivity is less variable, clouds decrease SW_{acc} variability (ratio > 1) potentially reducing time to emergence relative to clear skies. In CESM2, for example, clouds decrease the standard deviation of SW_{acc} by nearly a factor of two while they had a minimal impact in CESM1. This may explain the shift in CESM from clouds delaying the emergence of SW_{acc} trends in CESM1 (consistent with observations) to accelerating it in CESM2. In observations, clouds only slightly decrease SW_{acc} variability when averaged over the full Arctic, although the regional impact of clouds on SW_{acc} depends on the underlying surface (Sledd and L'Ecuyer, 2021a). Model biases could, therefore, stem directly from their representations of clouds or from covariability with the underlying distribution of sea ice and snow cover.

Since variability in $SW_{ref_{atm}}$ influences the noise in the ratio of clear-sky to all-sky SW_{acc} time-series, one might anticipate that trends in $SW_{ref_{atm}}$ may also influence the ratio of clear-sky to all-sky TTE. If cloud feedbacks are involved in accelerating the TTE of SIA trends, i.e. if cloud cover becomes less reflective as SIA decreases, we would anticipate a negative relationship between TTE ratio and trends in $SW_{ref_{atm}}$. **Figure 10D** suggests that the clear-sky to all-sky TTE ratio is more strongly inversely related to the $SW_{ref_{atm}}$ trend over the 21st century in CMIP6 than CMIP5. Some inverse relationship is expected since **Eq. 2** shows that the atmospheric contribution depends on multiple reflections from the surface. A lower surface albedo will generate less upwelling SW from the surface and consequently reduce SW reflection by the atmosphere to space over the melt season in spite of the fact that the atmospheric contribution to TOA albedo increases. However, the inverse relationship between between TTE ratio and $SW_{ref_{atm}}$ trend is much weaker in CMIP5 models, lending further evidence that cloud feedbacks may be responsible for the increased ambiguity in SW_{acc} trends in CMIP6.

All CMIP6 models agree that the melt-season integrated SW reflected by the atmosphere decreases in the future, but the magnitude of that decline ranges from near zero (BCC-CSM2-MR, □) to about -0.7×10^6 PJ/decade (CESM2-CAM5 and CESM2-WACCM, ▲ and △). Like the shift toward brighter present-day atmospheres, there is a systematic shift toward larger dimming trends in CMIP6 compared to CMIP5. Sledd and L'Ecuyer (2021b) attributed ambiguity in TTE ratios to cloud fraction (CF) trends. These results support that hypothesis by showing that models where clouds enhance TTE of SW_{acc} trends exhibit larger declines in $SW_{ref_{atm}}$. For example, the two versions of CESM2 predict the largest 21st century declines in $SW_{ref_{atm}}$ and have the highest TTE ratios of all CMIP6 models while CESM1 predicted less than half the decline in $SW_{ref_{atm}}$ and a TTE ratio of 0.9. This analysis, however, only provides a broad comparison of

the characteristics of absorbed SW radiation in the CMIP6 models and documents changes relative to CMIP5. Tracing the specific causes of the wide range of atmospheric influences on Arctic absorbed shortwave radiation in CMIP6 models will require comprehensive analysis of cloud fraction, opacity, phase, and other characteristics that is beyond the current scope of this work.

4 CONCLUSION

An accelerated rate of Arctic warming relative to the globe has been a robust feature of observed and modeled anthropogenic climate change for many years (Serreze et al., 2009; Screen and Simmonds, 2010a). While numerous processes and feedbacks are ultimately responsible for the overall Arctic temperature response to anthropogenic forcings (Pithan and Mauritsen, 2014; Goosse et al., 2018; Hahn et al., 2021), this study examines the factors that modulate solar absorption, a direct consequence of ice-albedo feedback that can be probed using modern satellite data records. We use a simple framework to quantify the sensitivity of planetary or TOA albedo to changing sea ice cover and establish the relative roles of the atmosphere (clouds) and surface in defining this response in the last two generations of climate models in the context of satellite-derived solar reflection and sea ice cover estimates. While the framework used is not intended as a predictive model, it provides a means for collapsing the atmospheric influence on planetary albedo into a single number that is entirely defined using fluxes at the TOA and surface boundaries, allowing models and observations to be compared. The growing satellite record is further used to statistically assess the emergence of trends in Arctic absorbed radiation over the summer season, providing a measure of when the radiative impacts of ice-albedo feedbacks have exceeded internal variability.

Multiple parameters characterizing the influence of sea ice changes on Arctic solar absorption suggest that CMIP6 models have converged to a more accurate representation of present day Arctic albedo and its sensitivity to sea ice cover than their predecessors in CMIP5, which had known biases in terms of clouds and SW fluxes (e.g. Karlsson and Svensson (2013); Taylor et al. (2019)). Ensemble mean TOA and surface albedos agree more closely with CERES-EBAF, and inter-model spreads have reduced in the latest generation of climate models. As a whole, CMIP6 models simulate a brighter present-day Arctic than CMIP5 and predict stronger responses to declining sea ice cover in better agreement with observations. However, observed Arctic solar absorption remains more sensitive to changes in SIA in the modern era of seasonal sea ice cover than climate models predict.

The improved representation of present-day Arctic albedo in CMIP6 has not, however, translated into reduced spread in predicted changes. In fact, CMIP6 models exhibit wider variation in predicted declines in both surface and TOA albedos by the end of the century than CMIP5. These differences, that exceed 10% in mid-summer when incoming solar radiation is strongest, can be traced to the wide range of atmospheric contributions to TOA albedo across models. The atmosphere generally contributes more to the TOA albedo in CMIP6 and is predicted to change more dramatically by the end of the 21st century than in CMIP5.

This lack of consensus in atmospheric reflectance among models is also evident in the estimated time to emergence of predicted trends in solar absorption in the modern Arctic. While models generally agree with observations that the cloud-free Arctic is absorbing more solar radiation than at the start of the century, CMIP6 model paint contradictory pictures regarding whether clouds suppress or enhance this trend. All but one of the CMIP5 models analyzed (**Table 2**) agree with observations that clouds have delayed the emergence of trends since the start of the century (Sledd and L'Ecuyer, 2021b). However, the influence of clouds on absorbed SW trends is ambiguous in CMIP6 with nearly half of the models examined (**Table 1**) diverging from observations and suggesting that clouds decrease TTE.

Though specific cloud parameterizations are not explicitly examined here, the increased ambiguity in the role of clouds in modulating ice-albedo feedback appears to be linked to different cloud responses to sea ice changes across models. CMIP6 models exhibit a distinct relationship between how strongly the atmospheric contribution to TOA albedo responds to SIA and how clouds influence the TTE of SW absorption trends that wasn't present in CMIP5. Models with strong atmospheric responses to SIA tend to predict that clouds accelerate the emergence of solar absorption trends while models with weaker atmospheric responses to SIA tend to reproduce the observed cloud delays. The CMIP6 ensemble also predicts stronger seasonally-integrated atmospheric reflectance trends than the CMIP5 ensemble. The models that predict clouds reduce TTE are those that exhibit the largest declines in atmospheric reflectance with time, suggesting that ice-albedo and cloud feedbacks may work in concert to produce the most rapid changes in Arctic albedo.

Thus, while CMIP6 is converging to a better representation of current Arctic TOA and surface albedo, increased sensitivity to sea ice changes in some models amplifies initial state differences and leads to divergent cloud responses between models that were not present in CMIP5. When acting in concert with the numerous other feedbacks that amplify Arctic warming, the resulting range of Arctic absorption may have significant implications for the trajectories of Arctic temperature and sea ice across models. Continued investigation into the interplay of sea ice and clouds and their mutual impact on absorbed solar radiation in both observations and models is warranted.

DATA AVAILABILITY STATEMENT

Publicly available datasets were analyzed in this study. Observational fluxes and sea ice concentration from ArORIS can be found at http://www.cloudsat.cira.colostate.edu/community-products/arctic-observation-and-reanalysisintegrated-system. Model output can be downloaded from https://esgf-node.llnl.gov/projects/esgfllnl.

AUTHOR CONTRIBUTIONS

The authors have contributed equally to this work.

FUNDING

This work was supported by NASA CloudSat/CALIPSO Science Team grant 80NSSC20K0135.

ACKNOWLEDGMENTS

The authors thank the CloudSat Data Processing Center where ArORIS data is available. We acknowledge the World Climate Research Programme, which, through its Working Group on Coupled Modelling, coordinated and promoted CMIP. We thank the climate modeling groups for producing and making available their model output, the Earth System Grid Federation (ESGF) for archiving the data and providing access, and the multiple funding agencies who support CMIP and ESGF. We are also grateful to the anonymous reviewers whose comments helped improve this paper.

SUPPLEMENTARY MATERIAL

The Supplementary Material for this article can be found online at: https://www.frontiersin.org/articles/10.3389/feart.2021.769844/full#supplementary-material

REFERENCES

Alkama, R., Taylor, P. C., Garcia-San Martin, L., Douville, H., Duveiller, G., Forzieri, G., et al. (2020). Clouds Damp the Radiative Impacts of Polar Sea Ice Loss. *The Cryosphere* 14, 2673–2686. doi:10.5194/tc-14-2673-2020

Brodzik, M. J., and Armstrong, R. (2013). Northern Hemisphere EASE-Grid 2.0 Weekly Snow Cover and Sea Ice Extent. Available at: https://doi.org/10.5067/P7O0HGJLYUQU.

Budyko, M. I. (1969). The Effect of Solar Radiation Variations on the Climate of the Earth. *Tellus* 21, 611–619. doi:10.3402/tellusa.v21i5.10109

Cai, S., Hsu, P.-C., and Liu, F. (2021). Changes in Polar Amplification in Response to Increasing Warming in CMIP6. *Atmos. Oceanic Sci. Lett.* 14, 100043. doi:10.1016/j.aosl.2021.100043

Cesana, G., and Chepfer, H. (2012). How Well Do Climate Models Simulate Cloud Vertical Structure? A Comparison between CALIPSO-GOCCP Satellite Observations and CMIP5 Models. *Geophys. Res. Lett.* 39. doi:10.1029/2012gl053153

Chepfer, H., Noël, V., Chiriaco, M., Wielicki, B., Winker, D., Loeb, N., et al. (2018). The Potential of a Multidecade Spaceborne Lidar Record to Constrain Cloud Feedback. *J. Geophys. Res. Atmos.* 123, 5433–5454. doi:10.1002/2017jd027742

Choi, Y. S., Hwang, J., Ok, J., Park, D. S. R., Su, H., Jiang, J. H., et al. (2020). Effect of Arctic Clouds on the Ice-albedo Feedback in Midsummer. *Int. J. Climatol.* 40, 4707–4714. doi:10.1002/joc.6469

Christensen, M. W., Behrangi, A., L'ecuyer, T. S., Wood, N. B., Lebsock, M. D., and Stephens, G. L. (2016). Arctic Observation and Reanalysis Integrated System: A New Data Product for Validation and Climate Study. *Bull. Am. Meteorol. Soc.* 97, 907–916. doi:10.1175/bams-d-14-00273.1

Davy, R., and Outten, S. (2020). The Arctic Surface Climate in CMIP6: Status and Developments Since CMIP5. *J. Clim.* 33, 8047–8068. doi:10.1175/jcli-d-19-0990.1

Deser, C., Lehner, F., Rodgers, K. B., Ault, T., Delworth, T. L., DiNezio, P. N., et al. (2020). Insights from Earth System Model Initial-Condition Large Ensembles and Future Prospects. *Nat. Clim. Chang.* 10, 277–286. doi:10.1038/s41558-020-0731-2

Deser, C., Phillips, A., Bourdette, V., and Teng, H. (2012). Uncertainty in Climate Change Projections: The Role of Internal Variability. *Clim. Dyn.* 38, 527–546. doi:10.1007/s00382-010-0977-x

Donohoe, A., and Battisti, D. S. (2011). Atmospheric and Surface Contributions to Planetary Albedo. *J. Clim.* 24, 4402–4418. doi:10.1175/2011jcli3946.1

Etminan, M., Myhre, G., Highwood, E., and Shine, K. (2016). Radiative Forcing of Carbon Dioxide, Methane, and Nitrous Oxide: A Significant Revision of the Methane Radiative Forcing. *Geophys. Res. Lett.* 43, 12–614. doi:10.1002/2016gl071930

Eyring, V., Bony, S., Meehl, G. A., Senior, C. A., Stevens, B., Stouffer, R. J., et al. (2016). Overview of the Coupled Model Intercomparison Project Phase 6 (CMIP6) Experimental Design and Organization. *Geoscientific Model. Dev. (Online)* 9, 1937–1958. doi:10.5194/gmd-9-1937-2016

Goosse, H., Kay, J. E., Armour, K. C., Bodas-Salcedo, A., Chepfer, H., Docquier, D., et al. (2018). Quantifying Climate Feedbacks in Polar Regions. *Nat. Commun.* 9, 1919. doi:10.1038/s41467-018-04173-0

Hahn, L. C., Armour, K. C., Zelinka, M. D., Bitz, C. M., and Donohoe, A. (2021). Contributions to Polar Amplification in CMIP5 and CMIP6 Models. *Front. Earth Sci.* 9, 710036. doi:10.3389/feart.2021.710036

Hartmann, D. L., and Ceppi, P. (2014). Trends in the CERES Dataset, 2000-13: The Effects of Sea Ice and Jet Shifts and Comparison to Climate Models. *J. Clim.* 27, 2444–2456. doi:10.1175/jcli-d-13-00411.1

Huang, Y., Dong, X., Kay, J. E., Xi, B., and McIlhattan, E. A. (2021). The Climate Response to Increased Cloud Liquid Water Over the Arctic in CESM1: A Sensitivity Study of Wegener-Bergeron-Findeisen Process. *Clim. Dyn.* 56, 3373–3394. doi:10.1007/s00382-021-05648-5

Karlsson, J., and Svensson, G. (2013). Consequences of Poor Representation of Arctic Sea-Ice Albedo and Cloud-Radiation Interactions in the CMIP5 Model Ensemble. *Geophys. Res. Lett.* 40, 4374–4379. doi:10.1002/grl.50768

Kato, S., Loeb, N. G., Minnis, P., Francis, J. A., Charlock, T. P., Rutan, D. A., et al. (2006). Seasonal and Interannual Variations of Top-Of-Atmosphere Irradiance and Cloud Cover Over Polar Regions Derived from the CERES Data Set. *Geophys. Res. Lett.* 33. doi:10.1029/2006gl026685

Kato, S., Rose, F. G., Rutan, D. A., Thorsen, T. J., Loeb, N. G., Doelling, D. R., et al. (2018). Surface Irradiances of Edition 4.0 Clouds and the Earth's Radiant Energy System (CERES) Energy Balanced and Filled (EBAF) Data Product. *J. Clim.* 31, 4501–4527. doi:10.1175/jcli-d-17-0523.1

Kay, J. E., Deser, C., Phillips, A., Mai, A., Hannay, C., Strand, G., et al. (2015). The Community Earth System Model (CESM) Large Ensemble Project: A Community Resource for Studying Climate Change in the Presence of Internal Climate Variability. *Bull. Am. Meteorol. Soc.* 96, 1333–1349. doi:10.1175/bams-d-13-00255.1

Koenigk, T., Devasthale, A., and Karlsson, K.-G. (2014). Summer Arctic Sea Ice Albedo in CMIP5 Models. *Atmos. Chem. Phys.* 14, 1987–1998. doi:10.5194/acp-14-1987-2014

Letterly, A., Key, J., and Liu, Y. (2018). Arctic Climate: Changes in Sea Ice Extent Outweigh Changes in Snow Cover. *The Cryosphere* 12, 3373–3382. doi:10.5194/tc-12-3373-2018

Loeb, N. G., Doelling, D. R., Wang, H., Su, W., Nguyen, C., Corbett, J. G., et al. (2018). Clouds and the Earth's Radiant Energy System (CERES) Energy Balanced and Filled (EBAF) Top-Of-Atmosphere (TOA) Edition-4.0 Data Product. *J. Clim.* 31, 895–918. doi:10.1175/jcli-d-17-0208.1

Loeb, N. G., Rose, F. G., Kato, S., Rutan, D. A., Su, W., Wang, H., et al. (2020). Toward a Consistent Definition Between Satellite and Model Clear-sky Radiative Fluxes. *J. Clim.* 33, 61–75. doi:10.1175/jcli-d-19-0381.1

McIlhattan, E. A., Kay, J. E., and L'Ecuyer, T. S. (2020). Arctic Clouds and Precipitation in the Community Earth System Model Version 2. *J. Geophys. Res. Atmos.* 125, e2020JD032521. doi:10.1029/2020JD032521

Notz, D., and Community, S. (2020). Arctic Sea Ice in CMIP6. *Geophys. Res. Lett.* 47, e2019GL086749. doi:10.1029/2019gl086749

Nygård, T., Naakka, T., and Vihma, T. (2020). Horizontal Moisture Transport Dominates the Regional Moistening Patterns in the Arctic. *J. Clim.* 33, 6793–6807. doi:10.1175/jcli-d-19-0891.1

Perovich, D. K., Light, B., Eicken, H., Jones, K. F., Runciman, K., and Nghiem, S. V. (2007). Increasing Solar Heating of the Arctic Ocean and Adjacent Seas, 1979–2005: Attribution and Role in the Ice-Albedo Feedback. *Geophys. Res. Lett.* 34. doi:10.1029/2007gl031480

Phojanamongkolkij, N., Kato, S., Wielicki, B. A., Taylor, P. C., and Mlynczak, M. G. (2014). A Comparison of Climate Signal Trend Detection Uncertainty Analysis Methods. *J. Clim.* 27, 3363–3376. doi:10.1175/jcli-d-13-00400.1

Pithan, F., and Mauritsen, T. (2014). Arctic Amplification Dominated by Temperature Feedbacks in Contemporary Climate Models. *Nat. Geosci.* 7, 181–184. doi:10.1038/ngeo2071

Qu, X., and Hall, A. (2005). Surface Contribution to Planetary Albedo Variability in Cryosphere Regions. *J. Clim.* 18, 5239–5252. doi:10.1175/jcli3555.1

Schmidt, G. A., Kelley, M., Nazarenko, L., Ruedy, R., Russell, G. L., Aleinov, I., et al. (2014). Configuration and Assessment of the GISS ModelE2 Contributions to the CMIP5 Archive. *J. Adv. Model. Earth Syst.* 6, 141–184.

Screen, J. A., and Simmonds, I. (2010b). Increasing Fall-winter Energy Loss from the Arctic Ocean and its Role in Arctic Temperature Amplification. *Geophys. Res. Lett.* 37. doi:10.1029/2010gl044136

Screen, J. A., and Simmonds, I. (2010a). The central Role of Diminishing Sea Ice in Recent Arctic Temperature Amplification. *Nature* 464, 1334–1337. doi:10.1038/nature09051

Sedlar, J., Tjernström, M., Mauritsen, T., Shupe, M. D., Brooks, I. M., Persson, P. O. G., et al. (2011). A Transitioning Arctic Surface Energy Budget: The Impacts of Solar Zenith Angle, Surface Albedo and Cloud Radiative Forcing. *Clim. Dyn.* 37, 1643–1660. doi:10.1007/s00382-010-0937-5

Seland, Ø., Bentsen, M., Olivié, D., Toniazzo, T., Gjermundsen, A., Graff, L. S., et al. (2020). Overview of the Norwegian Earth System Model (NorESM2) and Key Climate Response of CMIP6 DECK, Historical, and Scenario Simulations. *Geosci. Model. Dev.* 13, 6165–6200. doi:10.5194/gmd-13-6165-2020

Sellers, W. D. (1969). A Global Climatic Model Based on the Energy Balance of the Earth-Atmosphere System. *J. Appl. Meteorol.* 8, 392–400. doi:10.1175/1520-0450(1969)008<0392:agcmbo>2.0.co;2

Serreze, M. C., Barrett, A. P., Stroeve, J. C., Kindig, D. N., and Holland, M. M. (2009). The Emergence of Surface-Based Arctic Amplification. *The Cryosphere* 3, 11–19. doi:10.5194/tc-3-11-2009

Shu, Q., Wang, Q., Song, Z., Qiao, F., Zhao, J., Chu, M., et al. (2020). Assessment of Sea Ice Extent in CMIP6 with Comparison to Observations and CMIP5. *Geophys. Res. Lett.* 47, e2020GL087965. doi:10.1029/2020gl087965

Sledd, A., and L'Ecuyer, T. (2019). How Much Do Clouds Mask the Impacts of Arctic Sea Ice and Snow Cover Variations? Different Perspectives from Observations and Reanalyses. *Atmosphere* 10, 12. doi:10.3390/atmos10010012

Sledd, A., and L'Ecuyer, T. (2021a). Emerging Trends in Arctic Solar Absorption. In review.

Sledd, A., and L'Ecuyer, T. (2021b). Uncertainty in Forced and Natural Arctic Solar Absorption Variations in CMIP6 Models. *J. Clim.* 34, 931–948. doi:10.1175/jcli-d-20-0244.1

Stroeve, J. C., Serreze, M. C., Holland, M. M., Kay, J. E., Malanik, J., and Barrett, A. P. (2012). The Arctic's Rapidly Shrinking Sea Ice Cover: A Research Synthesis. *Climatic Change* 110, 1005–1027. doi:10.1007/s10584-011-0101-1

Stroeve, J., and Notz, D. (2018). Changing State of Arctic Sea Ice Across All Seasons. *Environ. Res. Lett.* 13, 103001. doi:10.1088/1748-9326/aade56

Taylor, K. E., Stouffer, R. J., and Meehl, G. A. (2012). An Overview of CMIP5 and the Experiment Design. *Bull. Am. Meteorol. Soc.* 93, 485–498. doi:10.1175/bams-d-11-00094.1

Taylor, P. C., Boeke, R. C., Li, Y., and Thompson, D. W. J. (2019). Arctic Cloud Annual Cycle Biases in Climate Models. *Atmos. Chem. Phys.* 19, 8759–8782. doi:10.5194/acp-19-8759-2019

Vignesh, P. P., Jiang, J. H., Kishore, P., Su, H., Smay, T., Brighton, N., et al. (2020). Assessment of CMIP6 Cloud Fraction and Comparison with Satellite Observations. *Earth Space Sci.* 7, e2019EA000975. doi:10.1029/2019ea000975

Weatherhead, E. C., Reinsel, G. C., Tiao, G. C., Meng, X.-L., Choi, D., Cheang, W.-K., et al. (1998). Factors Affecting the Detection of Trends: Statistical Considerations and Applications to Environmental Data. *J. Geophys. Res.* 103, 17149–17161. doi:10.1029/98jd00995

Wei, J., Wang, Z., Gu, M., Luo, J.-J., and Wang, Y. (2021). An Evaluation of the Arctic Clouds and Surface Radiative Fluxes in CMIP6 Models. *Acta Oceanol. Sin.* 40, 85–102. doi:10.1007/s13131-021-1705-6

Wu, D. L., Lee, J. N., Kim, K.-M., and Lim, Y.-K. (2020). Interannual Variations of TOA Albedo over the Arctic, Antarctic and Tibetan Plateau in 2000-2019. *Remote Sensing* 12, 1460. doi:10.3390/rs12091460

Wu, T., Lu, Y., Fang, Y., Xin, X., Li, L., Li, W., et al. (2019). The Beijing Climate Center Climate System Model (BCC-CSM): The Main Progress from CMIP5 to CMIP6. *Geosci. Model. Dev.* 12, 1573–1600. doi:10.5194/gmd-12-1573-2019

Zelinka, M. D., Myers, T. A., McCoy, D. T., Po-Chedley, S., Caldwell, P. M., Ceppi, P., et al. (2020). Causes of Higher Climate Sensitivity in CMIP6 Models. *Geophys. Res. Lett.* 47, e2019GL085782. doi:10.1029/2019gl085782

Conflict of Interest: The authors declare that the research was conducted in the absence of any commercial or financial relationships that could be construed as a potential conflict of interest.

Publisher's Note: All claims expressed in this article are solely those of the authors and do not necessarily represent those of their affiliated organizations, or those of the publisher, the editors and the reviewers. Any product that may be evaluated in this article, or claim that may be made by its manufacturer, is not guaranteed or endorsed by the publisher.

frontiers in Earth Science

REVIEW
published: 09 February 2022
doi: 10.3389/feart.2021.758361

Process Drivers, Inter-Model Spread, and the Path Forward: A Review of Amplified Arctic Warming

Patrick C. Taylor[1], Robyn C. Boeke[2], Linette N. Boisvert[3], Nicole Feldl[4], Matthew Henry[5], Yiyi Huang[2], Peter L. Langen[6], Wei Liu[7], Felix Pithan[8], Sergio A. Sejas[2] and Ivy Tan[9]*

[1]NASA Langley Research Center, Hampton, VA, United States, [2]Science Systems and Applications Inc., Hampton, VA, United States, [3]Cryospheric Sciences Lab, NASA Goddard Space Flight Center, Greenbelt, MD, United States, [4]Department of Earth and Planetary Sciences, University of California, Santa Cruz, Santa Cruz, CA, United States, [5]College of Engineering, Mathematics and Physical Sciences, University of Exeter, Exeter, United Kingdom, [6]Department of Environmental Science, IClimate, Aarhus University, Roskilde, Denmark, [7]Department of Earth and Planetary Sciences, University of California Riverside, Riverside, CA, United States, [8]Alfred Wegener Institute Helmholtz Centre for Polar and Marine Research, Bremerhaven, Germany, [9]Department of Atmospheric and Oceanic Sciences, McGill University, Montreal, QC, Canada

Arctic amplification (AA) is a coupled atmosphere-sea ice-ocean process. This understanding has evolved from the early concept of AA, as a consequence of snow-ice line progressions, through more than a century of research that has clarified the relevant processes and driving mechanisms of AA. The predictions made by early modeling studies, namely the fall/winter maximum, bottom-heavy structure, the prominence of surface albedo feedback, and the importance of stable stratification have withstood the scrutiny of multi-decadal observations and more complex models. Yet, the uncertainty in Arctic climate projections is larger than in any other region of the planet, making the assessment of high-impact, near-term regional changes difficult or impossible. Reducing this large spread in Arctic climate projections requires a quantitative process understanding. This manuscript aims to build such an understanding by synthesizing current knowledge of AA and to produce a set of recommendations to guide future research. It briefly reviews the history of AA science, summarizes observed Arctic changes, discusses modeling approaches and feedback diagnostics, and assesses the current understanding of the most relevant feedbacks to AA. These sections culminate in a conceptual model of the fundamental physical mechanisms causing AA and a collection of recommendations to accelerate progress towards reduced uncertainty in Arctic climate projections. Our conceptual model highlights the need to account for local feedback and remote process interactions within the context of the annual cycle to constrain projected AA. We recommend raising the priority of Arctic climate sensitivity research, improving the accuracy of Arctic surface energy budget observations, rethinking climate feedback definitions, coordinating new model experiments and intercomparisons, and further investigating the role of episodic variability in AA.

Keywords: arctic amplification, climate feedback mechanisms, cloud feedback, sea ice albedo feedback, remote mechanisms, sea ice

OPEN ACCESS

Edited by:
Matthew Collins,
University of Exeter, United Kingdom

Reviewed by:
Peng Zhang,
Fudan University, China
John Virgin,
University of Waterloo, Canada

****Correspondence:***
Patrick C. Taylor
patrick.c.taylor@nasa.gov

Specialty section:
This article was submitted to Interdisciplinary Climate Studies, a section of the journal Frontiers in Earth Science

Received: *13 August 2021*
Accepted: *20 December 2021*
Published: *09 February 2022*

Citation:
Taylor PC, Boeke RC, Boisvert LN, Feldl N, Henry M, Huang Y, Langen PL, Liu W, Pithan F, Sejas SA and Tan I (2022) Process Drivers, Inter-Model Spread, and the Path Forward: A Review of Amplified Arctic Warming. Front. Earth Sci. 9:758361. doi: 10.3389/feart.2021.758361

INTRODUCTION

Anthropogenic carbon dioxide (CO_2) emissions and other greenhouse gases are changing Earth's climate. Global mean surface temperature has risen by ≥ 1.0°C relative to the pre-industrial period, making this the warmest period in the history of modern civilization (Wuebbles et al., 2017). As the impacts of warming cascade through the physical climate and natural systems, society grapples with decisions on the countermeasures needed to offset the increased vulnerability in the systems that underpin modern society: food, energy, water, health, security, and economy. Global temperature targets (e.g., Paris Climate Accord) serve as the basis to gauge the required aggressiveness of countermeasures. Global targets, however, fail to consider the uncertainty and high impact of dramatic regional changes, such as in the Arctic where consequential ice sheet melt and untenable global sea level rise cannot be ruled out at 1.5°C of global warming (IPCC 2018; Meredith et al., 2019; IPCC 2021). Global temperature targets leave substantial climate risks unconsidered; using regional indicators as policy targets helps account for the uneven spatial distribution of climate change impacts and risks.

Climate change is spread unevenly across the globe. The Arctic surface has warmed more than twice as fast as the global average surface temperature (**Figure 1**; Lenssen et al., 2019), a phenomenon known as Arctic Amplification (AA). AA is part of the broader polar amplification phenomenon that also applies to the Antarctic. However, amplified Antarctic warming is expected to be weaker and delayed because of the Antarctic continent surface height, smaller albedo and lapse rate feedbacks, and Southern Ocean heat uptake (Salzmann 2017; Hahn et al., 2021). Rapid Arctic surface warming is driving changes in several physical climate characteristics (e.g., sea ice and snow cover) and impacting ecosystems and vegetation distribution (Taylor et al., 2017). The use of climate change indicators from regions with the largest expected changes (e.g. Arctic surface temperature change and sea ice extent and thickness) ensures that high-impact regional climate change outcomes are considered in climate risk assessment.

Accurate long-term observations and trustworthy climate projections are needed to effectively inform regional targets; however, the harsh and complex Arctic environment makes the necessary observations and climate projections challenging to obtain, resulting in substantial uncertainty. A meaningful adoption of Arctic climate indicators as policy targets requires an improved process understanding to reduce uncertainty in AA projections—the topic of this review.

Research over the last 50 years has identified the fundamental characteristics of AA and advanced our understanding. It is widely accepted that AA manifests as a surface-based warming profile (Manabe and Wetherald 1975; hereafter MW75); it is strongest in fall and winter and absent in summer (Manabe and Stouffer 1980; hereafter MS80); it is strongest in regions of sea ice retreat (Washington and Meehl 1984) and that the seasonal energy transfer from summer to fall via ocean heat storage plays a critical role in its seasonality and magnitude (MS80; Washington and Meehl 1986). Moreover, the melting of sea ice and snow represents a fundamental feedback mechanism (e.g., Arrhenius 1896; Budyko 1966).

As our knowledge has deepened, additional considerations have been identified that make it harder to reduce Arctic climate projection uncertainty. Natural variability complicates our ability to quantify the forced Arctic climate change signal and distinguish the processes driving observed AA. While our understanding of interannual variability has advanced, it remains incomplete (e.g., Ding et al., 2017; Wu et al., 2021). Natural variability also represents an irreducible uncertainty in decadal and multi-decadal predictions (Kay et al., 2011; Swart et al., 2015; Swart 2017). In addition, the quantitative assessment of specific process contributions to AA is affected by the metric used to define AA and the feedback diagnostic approach applied (Hind et al., 2016).

Important advances in AA science have occurred in the last decade. The aim of this manuscript is to synthesize this

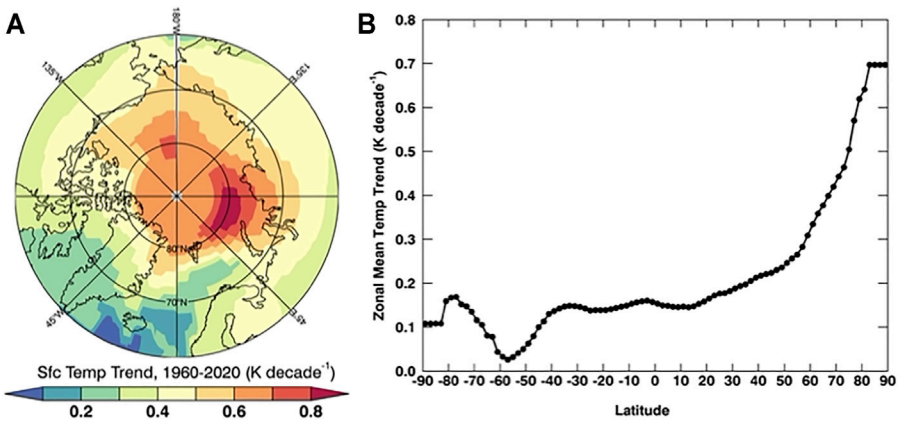

FIGURE 1 | Arctic and zonal mean linear surface temperature trends since 1960. **(A)** The spatial pattern of the surface temperature trend at 2° × 2° resolution and **(B)** the zonal mean surface temperature trend (K decade^{-1}) assessed by applying a ordinary least squares fit linear regression to the GISTEMP time series (Lenssen et al., 2019; GISTEMP Team 2021).

knowledge and guide future research. **Section 2** provides a brief history of AA science, highlighting the most pertinent results and contributing factors. **Section 3** provides an overall context of the observed Arctic changes over the last several decades. **Section 4** provides a discussion of the modeling approaches and feedback diagnostic techniques. **Section 5** describes our current understanding of the processes driving AA. **Section 6** provides a conceptual model of the key physical mechanisms. Lastly, **Section 7** proposes a collection of recommendations to accelerate progress in AA science and reduce uncertainty in Arctic climate projections.

HISTORICAL PERSPECTIVE

The expectation that the polar regions are more sensitive to climate forcing has been around since Arrhenius (1896) wrote on the ebb and flow of glacial periods in a seminal paper on the impact of CO_2 concentrations on temperature. However, the phrase "amplified polar warming" or "polar amplification" did not appear until nearly a century later (Broecker 1975; Schneider 1975). The explanation for polar amplification has evolved from the earliest idea as a consequence of the progression of the snow-ice line (e.g., Arrhenius 1896) to modern ideas of a coupled atmosphere-sea ice-ocean process (e.g., MS80). While impossible to definitively say, it seems likely that the origin of polar amplification within the context of ice ages favored hypotheses pertaining to ice and snow. Computational expediency could also have played a role, as the surface albedo feedback is easily manipulated within energy balance models (EBMs). Be it by intuition or luck, early scientists correctly identified the leading role of the surface albedo feedback. Despite this early success, large gaps remain in our understanding of the Arctic climate system that preclude more accurate predictions. In constructing a roadmap for improving Arctic climate projections, we consider the historical evolution of polar amplification science.

Early studies employed EBMs—models representing the relationship between Earth's surface temperature and the top-of-atmosphere (TOA) energy budget—containing many shortcomings and yet captured the essence of polar amplification. Budyko (1966) and Rakipova (1966) demonstrated the fundamental role of surface albedo and the latitudinal position of the snow-ice line in determining polar surface temperature sensitivity to climate forcing. An impressive accomplishment considering that EBMs were informed by little snow and sea ice data and contained invalid assumptions. The most consequential assumption was the exclusion of vertical and horizontal heat transports.

The influence of vertical and horizontal heat transports on polar climate was considered in EBMs later in the 1960s. Manabe and Wetherald (1967) found that the damping of vertical heat transport by strong stability at high latitudes caused a surface albedo perturbation to have a larger effect on near-surface atmospheric temperature than at higher altitudes. Budyko (1969) and Sellers (1969) represented horizontal poleward heat transport in zonally-averaged EBMs as horizontal diffusion proportional to the meridional temperature gradient. Sellers (1969) concluded that the specific representation of poleward heat transport had the potential to offset polar amplification. This research illustrated the substantial sensitivity of the polar climate to poleward heat transport and the need to fully resolve the large-scale atmospheric circulation.

With this knowledge in hand, MW75 employed a GCM to resolve atmospheric eddies and cemented polar amplification as a prominent feature of the global climate response to increased CO_2. MW75 established the surface-based vertical structure of polar warming, confirmed in modern studies (e.g., Graversen et al., 2008; Serreze et al., 2009), the role of strong atmospheric stability in confining warming near the surface (e.g., Bintanja et al., 2011), and the compensation between increased latent heat (LH) and decreased poleward sensible heat (SH) transport (e.g., Hwang et al., 2011). While including many simplifications (e.g., idealized geography, fixed clouds, temperature-dependent sea ice and snow albedo, and annual mean insolation), much of our current understanding of polar amplification can be traced to the Nobel prize-winning work in MW75.

MS80 extended MW75 by incorporating a mixed-layer ocean and the annual cycle of insolation revealing that polar amplification is strongest in fall and winter and non-existent in summer. The seasonality of polar amplification is partly attributed to the seasonal energy transfer from summer to fall by the ocean (MS80); an explanation also supported by later studies (Washington and Meehl 1984; Wilson and Mitchell 1987). While adding important ocean physics to resolve the annual cycle, MW75 and MS80 did not consider oceanic poleward heat transport.

The eventual inclusion of poleward heat transport by ocean currents revealed a relationship between high latitude control climate and global climate sensitivity. Spelman and Manabe (1984) presented fully-coupled atmosphere-ocean simulations capturing the observed climate state with some realism. The inclusion of poleward ocean heat transport yielded warmer high latitude surface temperatures, a poleward shift of the snow and sea ice margin, a weakened albedo feedback, and a reduced climate sensitivity. The influence of control climate surface temperature and sea ice extent on high latitude climate sensitivity was recognized in other studies in relation to the surface albedo parameterization (Budyko 1969; Washington and Meehl 1986) and recently shown to influence CMIP5 inter-model spread (Hu et al., 2017). Rind et al. (1995) illustrated a dependence of simulated sea ice decline on sea ice thickness. Control climate-climate sensitivity relationships are attractive because of the potential ability to constrain model predictions; however, as noted by Washington and Meehl (1986), control climate-climate sensitivity relationships may only be valid when considering the same model.

Adding more climate models to the fold revealed the importance of interactions between the ocean and sea ice to the polar climate response. Washington and Meehl (1984; 1986; 1989) performed model simulations with increasingly complex representations of the ocean (swamp, slab, and a coupled ocean circulation model) finding a smaller climate sensitivity and less polar amplification than MW75 and MS80. These differences were attributed to different sea ice albedo-temperature

relationships (Washington and Meehl 1984). Additionally, MW75 allowed melt pond formation to change sea ice albedo whereas Washington and Meehl (1984) did not. Washington and Meehl (1989) showed that the regional sea ice distribution was sensitive to the representation of the ocean circulation due to changes in poleward ocean heat transport and deep ocean convection. Further, the way that ocean heat is applied to sea ice (e.g., to the bottom or to the bottom and laterally) also strongly influences sea ice melt (Hansen et al., 1984). These early model intercomparisons demonstrated their value for identifying key uncertainties.

Extracting maximum value from model comparisons requires diagnostic techniques that consistently quantify the causes of model differences (Coakley 1977; Ramanathan 1977; Hansen et al., 1984; Washington and Meehl 1986; Dickinson et al., 1987; Wetherald and Manabe 1988; **Section 4**). Many of these studies focus on the surface albedo feedback, diagnosing it using slightly different methods, and finding large inter-model differences. However, the inter-model differences in the surface albedo feedback were mainly due to methodological differences (Ingram et al., 1989). Methods were also developed to diagnose all TOA radiative feedbacks (Hansen et al., 1984; Wetherald and Manabe 1988). Moreover, Cess and Potter (1988) developed a methodology designed to assess cloud feedback. Feedback diagnostic methods paved the way for broader model intercomparisons and enabled a consistent understanding of why projections differ (see **Section 4**).

Early multi-model intercomparisons identified snow and sea ice albedo feedbacks and their interactions with cloud feedback as a key polar climate uncertainty. The first large-scale, coordinated climate model intercomparison occurred in the late 1980s finding a three-fold difference in global climate sensitivity mainly due to cloud feedback differences (Cess et al., 1989; 1990). Using a similar set of models, Cess et al. (1991) reported substantial snow-albedo feedback differences; interestingly, these differences stemmed not only from the snow-albedo treatment but also from interactions with clouds. Given the demonstrated value of using the large-scale model intercomparisons to indicate uncertainty, model intercomparison projects (MIPs) emerged as a major research theme and continue to be a valuable resource for hypothesis testing, identifying projection uncertainty, and informing climate observation system design (e.g., Wielicki et al., 2013).

In the 1990s, aided by improved computational capabilities, transient climate change simulations became widespread alongside MIPs and advanced our understanding of the interactions between ocean and atmosphere circulation and polar climate. A decade earlier, Bryan et al. (1982) made the first attempt to simulate the transient climate response using a 1% per year CO_2 increase experiment finding different high- and low-latitude transient responses. Subsequent transient experiments show a profound influence of the ocean circulation on the spatial distribution of Arctic warming with slower warming over the ocean and in regions of deep water formation (e.g., northern North Atlantic) and faster warming over land (Washington and Meehl 1989; Manabe et al., 1991; Washington and Meehl 1996; Meehl et al., 2000). Manabe et al. (1992) argued that the land-ocean warming contrast affects the land precipitation and soil moisture response by delaying latent heat transport from ocean to land. Washington and Meehl (1989) found a time-dependence of the high-latitude atmospheric circulation response suggesting that there may not be a single atmospheric circulation pattern that amplifies monotonically with increased forcing. While advancing our knowledge of the transient Arctic climate response, these studies did not change the underlying understanding of the physical drivers of polar amplification.

In the 2000s, the drastic sea ice retreat and warming in the Arctic seems to have spurred a newfound urgency and polar amplification began appearing as a unique research topic, as opposed to an aspect of CO_2-induced climate change. Studies using multi-decadal records of Arctic temperature, snow cover, and sea ice became prominent and enabled the verification of many early predictions of AA including its fall/winter maximum, bottom-heavy structure, and the prominence of surface albedo feedback (e.g., Graversen et al., 2008; Serreze et al., 2009; Pistone et al., 2014). This application of observations is in sharp contrast to the 1980s when the quality and quantity of observations limited their use to control climate tuning. Multi-decadal observations further enabled studies of emergent constraints—relationships between an uncertain aspect of climate projections and an observable quantity (e.g., Hall and Qu 2006; Caldwell et al., 2014; Hall et al., 2019). MIP activities revealed that sea ice extent and thickness, ocean heat transport, and clouds are key sources of inter-model differences in AA (Holland and Bitz 2003) and potential emergent constraints.

Several studies in the early 2000s altered the trajectory of polar amplification research by showing that polar amplification was possible without the surface albedo feedback. First, aquaplanet experiments by Alexeev (2003) illustrated polar amplification in the absence of sea ice. Second, coupled GCM experiments with a suppressed surface albedo feedback showed polar amplification, albeit weaker (Hall 2004). These results appear at odds with earlier studies also suppressing the surface albedo feedback that concluded the sea ice albedo feedback was necessary for polar amplification (e.g., Ingram et al., 1989; Rind et al., 1995). The Ingram et al. (1989) modeling setup prohibited ocean energy transfer across seasons, which may explain the different conclusion; the reason for the difference with Rind et al. (1995) is unclear. Studies argue that poleward heat transport produces polar amplification due to an increased efficiency, as poleward traveling air is warmer and moister than before (Alexeev et al., 2005; Cai 2005; Cai 2006). Differences in insolation and clouds are also possible explanations as they can control the existence of polar amplification (Kim et al., 2018). This debate continues (**Section 5e**) and these studies mark an inflection point in our thinking on the role of atmospheric poleward heat transport in polar amplification.

Since 2010, studies have focused on using observations and coupled models synergistically to understand polar amplification, including a reemergence of idealized model set-ups (e.g., Chung and Räisänen, 2011; Feldl et al., 2017a; Yoshimori et al., 2017; Park et al., 2018; Shaw and Tan, 2018; Stuecker et al., 2018; Previdi et al., 2020; Semmler et al., 2020). New satellite data sets (Winker et al., 2010; Boisvert et al., 2013; Kato et al., 2018; Loeb et al., 2018; Duncan et al., 2020) and more sophisticated meteorological reanalyses have been enabling factors (Screen and Simmonds, 2010; Boisvert and Stroeve

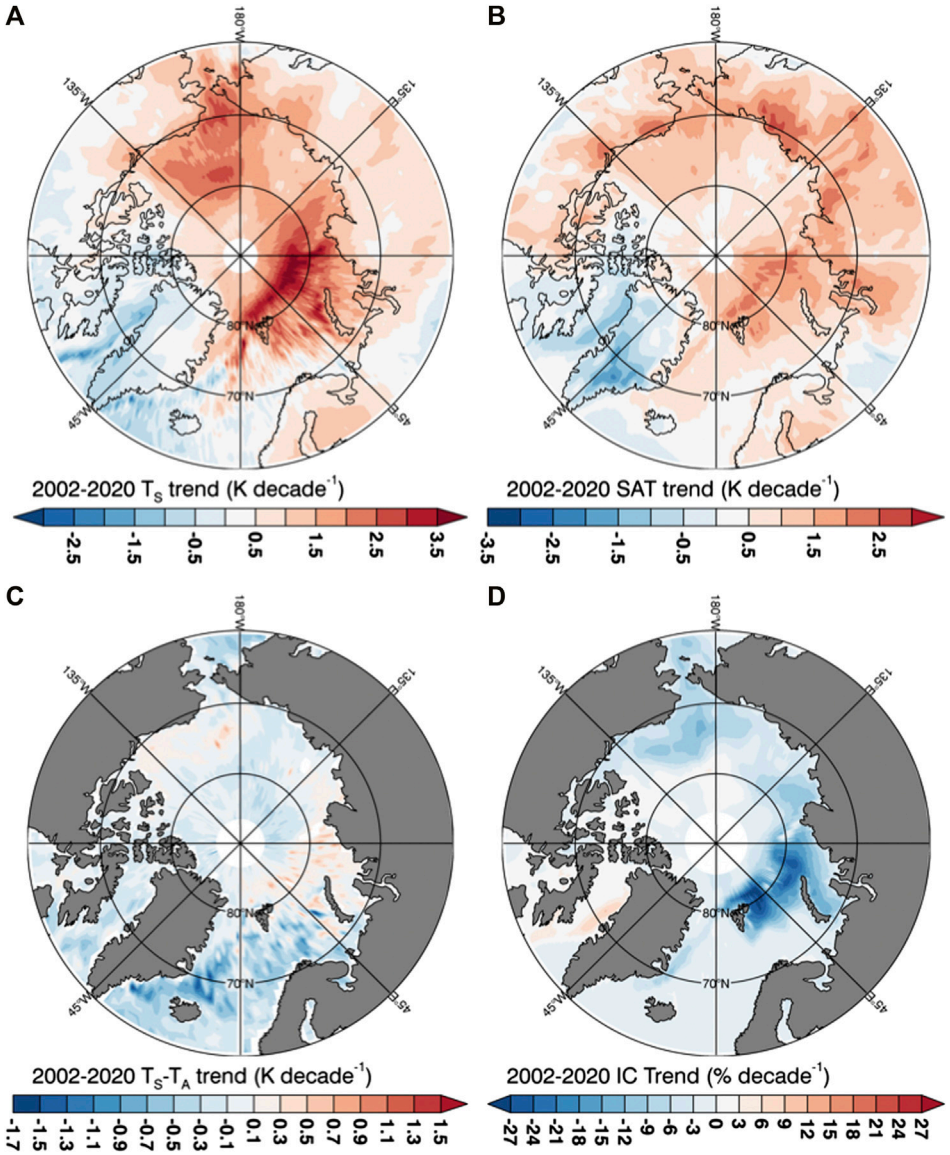

FIGURE 2 | Recent changes in the Arctic surface climate. Linear, annual mean trends from 2002–2020 for **(A)** skin temperature (K decade^{-1}), **(B)** surface air temperature (K decade^{-1}), **(C)** skin and surface air temperature difference (K decade^{-1}), and **(D)** sea ice concentration (% decade^{-1}) from the Atmospheric Infrared Sounder (AIRS; Susskind et al., 2014) and passive microwave sea ice concentration data (Cavalieri et al., 1996).

2015). Key outcomes of recent work include confirming the role of ocean heat storage, seasonal energy transfer, and the surface turbulent flux response on AA and inter-model spread (Screen and Simmonds, 2010; Boeke and Taylor 2018; Kim et al., 2019; Dai et al., 2019). Studies continue to focus on understanding atmosphere, sea ice, and ocean processes with a keen focus on coupling. Idealized model simulations have been combined with observations to understand shorter time scale atmosphere-ocean-sea ice interactions, including links between air-mass transformation and Arctic climate (e.g., atmospheric rivers and cold air outbreaks; Pithan et al., 2018). Additionally, large single-model initial condition ensembles (e.g., Kay et al., 2015) hold incredible value for understanding the impact of internal variability on observed and projected trends. Studies continue to leverage the trove of information available from MIP activities including the first Polar Amplification MIP (PAMIP; Smith et al., 2019). While our understanding of polar amplification has advanced since Arrhenius, substantial uncertainty remains in polar climate projections warranting continued research.

OBSERVATIONAL PERSPECTIVES

Sustained polar observations (satellite, ground-based, and airborne) have enabled the identification of many fundamental characteristics of AA and the verification of early modeling

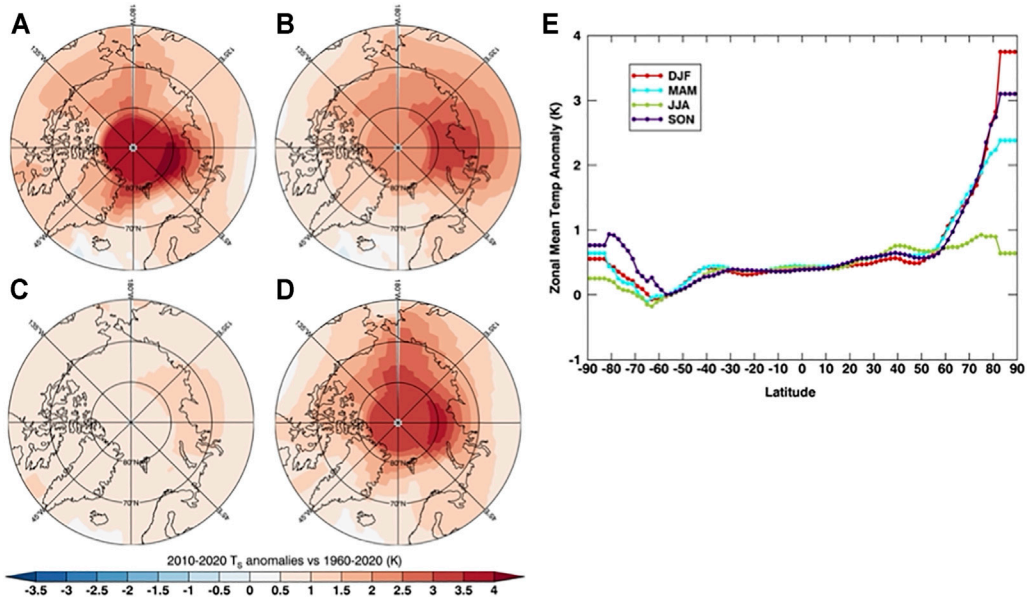

FIGURE 3 | Arctic surface warming seasonality. The spatial pattern of the 2010–2020 surface temperature anomalies (units: K) relative to the 1960–2020 average are shown for **(A)** DJF, **(B)** MAM, **(C)** JJA, and **(D)** SON. Panel **(E)** shows the zonal mean temperature anomalies for each season. All temperature anomalies are computed from GISTEMP (GISTEMP team 2021).

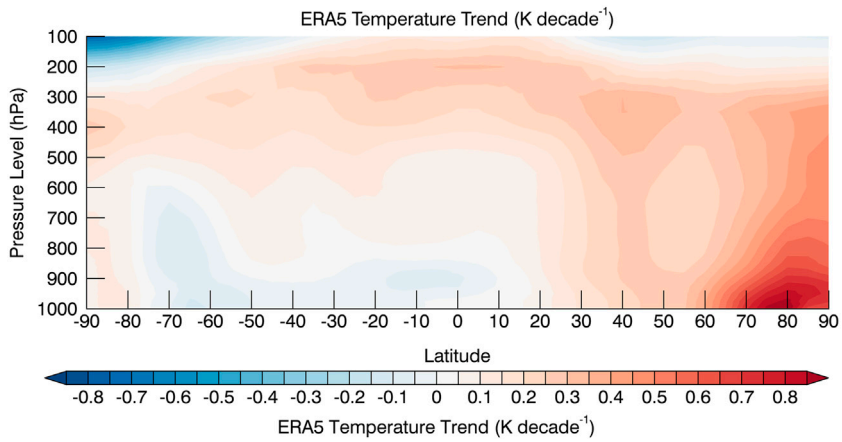

FIGURE 4 | Vertical structure of recent Arctic warming. Annual, zonal mean air temperature linear trends (K decade^{-1}) between for 1979–2020 computed from ERA-5 (Hersbach et al., 2019).

results. Technological advances in polar observation have led to higher quality data records and a broader set of observed variables. Developments in meteorological, oceanic, and sea ice reanalysis have made these a primary source of Arctic climate information and are invaluable to AA science. In addition to multi-decadal records, observational capabilities now provide near-real time monitoring of the Arctic, elevating the episodic nature and interconnectedness of the region to the forefront of Arctic research. Detailed process-oriented observations reveal how sea ice, ocean and atmosphere interact and which processes shape the surface energy budget (SEB; e.g., Uttal et al., 2002; Shupe et al., 2020).

Since 1960, the Arctic has warmed faster than any other region of the planet (**Figure 1**). The zonal average surface temperature trends poleward of 60°N range from ~0.3 to 0.7 K decade^{-1} and are strongest near the pole. Spatially, Arctic surface temperature trends range from ~0.1 to 0.8 K decade^{-1} with the largest warming coinciding with substantial sea ice concentration declines (**Figure 2**). The seasonal contrast in Arctic surface warming is also evident (**Figure 3**) with maximum warming

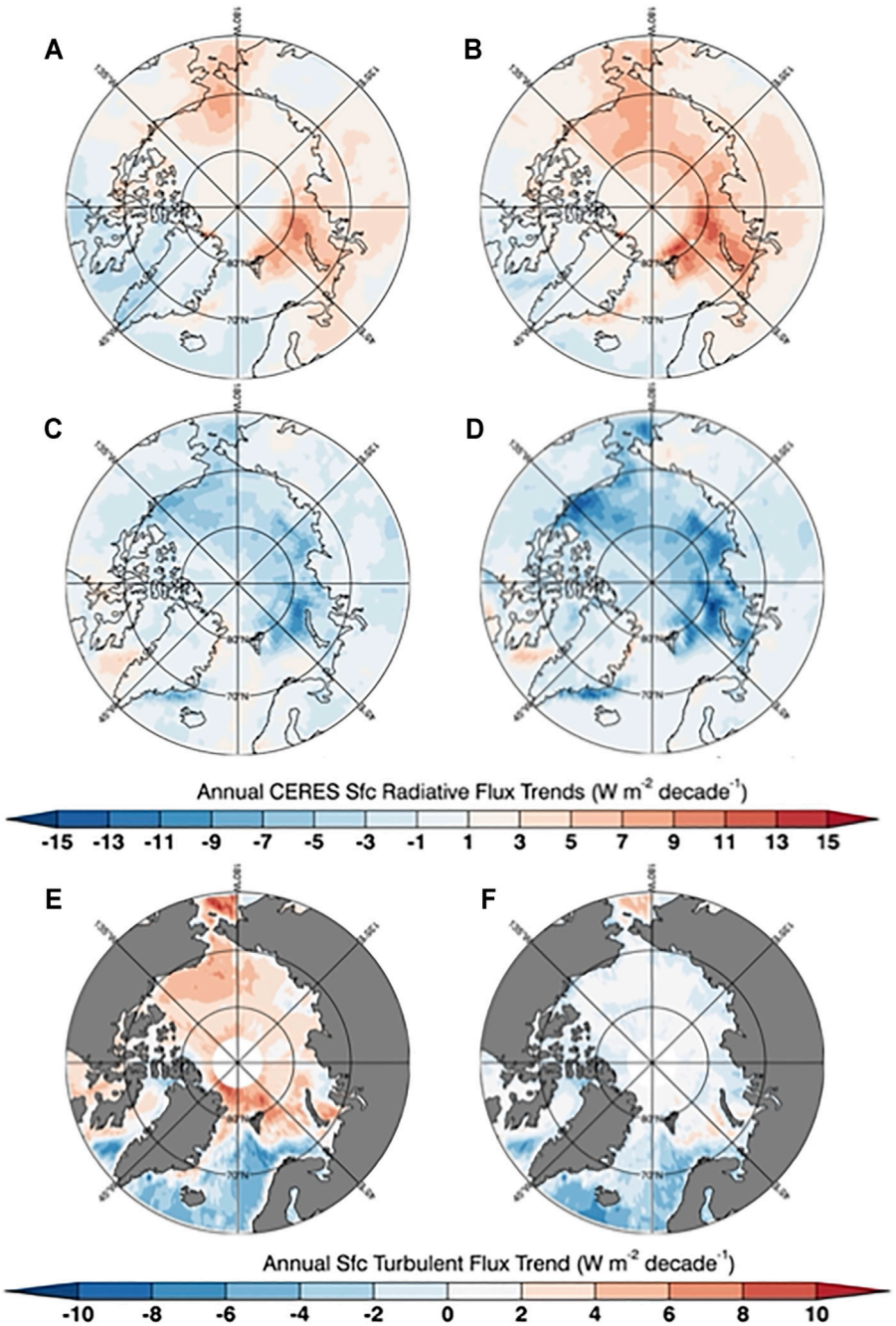

FIGURE 5 | Recent changes in the Arctic surface energy budget. Linear, annual mean trends from 2002–2020 for surface **(A)** downwelling LW radiation, **(B)** upwelling LW radiation, **(C)** downwelling SW radiation, and **(D)** upwelling SW radiation, **(E)** sensible heat, and **(F)** latent heat flux trends (W m^{-2} $decade^{-1}$). Radiation data is taken from CERES (Kato et al., 2018) and SH and LH fluxes are derived from AIRS (Boisvert et al., 2013).

in December-January-February (DJF), minimum warming in June-July-August (JJA), and substantial warming in September-October-November (SON) and March-April-May (MAM). **Figure 3** indicates a spatial variation of the seasonal surface warming pattern that coincides with the seasonality of sea ice loss modulated by atmospheric circulation variability (Ding et al., 2017; Dai et al., 2019; Wu et al., 2021). The characteristic surface-based warming profile is evident in the 1979–2020 ERA5 annual, zonal mean atmospheric temperature trends with surface trends exceeding 0.8 K $decade^{-1}$ decreasing to ~0.4 K $decade^{-1}$ at 300 hPa (**Figure 4**).

Arctic sea ice cover and thickness have declined dramatically since 1979, further evidence that sea ice is a key aspect of observed AA (Screen and Simmonds, 2010; Boeke and Taylor 2018; Dai

et al., 2019). September sea ice extent has declined more rapidly than during any other month, ~–13% decade^{-1} (e.g., Parkinson and DiGirolamo 2016; Taylor et al., 2017). September sea ice volume has declined by >70% since the early 1980s (Schweiger et al., 2011; Kwok 2018). The Arctic sea ice melt season has also lengthened by 5–10 days decade^{-1} over the last four decades (earlier melt onset and later freeze-up) with larger regional changes (Markus et al., 2009; Stroeve et al., 2014; Bliss and Anderson 2018). The thinner and less expansive sea ice cover is also more susceptible to thermodynamic and dynamic forcing (Hibler 1979; Maslanik et al., 2011; Hegyi and Deng 2017; Huang et al., 2019a) promoting earlier and more rapid spring melting (Markus et al., 2009; Maslanik et al., 2011; Stroeve et al., 2014; Bliss and Anderson, 2018), contributing to the observed AA.

The Arctic SEB has responded to the sea ice and temperature trends. Clouds and Earth's Radiant Energy System (CERES) data show strong trends in TOA and surface energy fluxes in the Arctic (Loeb et al., 2018; Kato et al., 2018). Surface albedo has declined by ~0.03–0.04 decade^{-1} over the central Arctic (Duncan et al., 2020) suggesting an additional ~1.2 Wm^{-2} decade^{-1} of shortwave (SW) energy deposited in the Arctic Ocean since 2000 (**Figure 5**). Strong SH and LH flux increases (**Figure 5**) have also occurred, coinciding with sea ice loss (Screen and Simmonds, 2010; Boisvert et al., 2013; Boisvert et al., 2015; Taylor et al., 2018). Importantly, polar TOA and surface radiative (SW and longwave (LW)) and turbulent (SH and LH) energy flux observations contain substantial uncertainties—5–20 Wm^{-2} and 20%, respectively—that stymie studies of climate-relevant processes (Boisvert et al., 2015; Kato et al., 2018; Taylor et al., 2018).

Several key insights are gleaned from the observed Arctic changes. First, the spatially coincident changes in the Arctic surface temperature, sea ice, and SEB demonstrates the importance of atmosphere-sea ice-ocean coupling to observed Arctic changes. Second, observations verify the existence of AA and key characteristics including its seasonal, vertical, and spatial structure. Lastly, the expected SEB changes (e.g., reduced surface albedo and increased SH and LH fluxes) are observed, although observational uncertainty limits progress.

MODELING PERSPECTIVES

A hierarchy of models have been used to advance AA science. This evolution in modeling studies coincided with advances in computational capabilities and trends towards increased complexity beginning with EBMs (Budyko 1966, 1969; Sellers 1969), simplified/idealized atmospheric GCMs (MW75; MS80; Alexeev et al., 2005), atmospheric GCMs (Washington and Meehl 1984), coupled atmospheric-ocean GCMs (Bryan et al., 1982; Spelman and Manabe 1984; Washington and Meehl 1989), and now Earth System Models. The march from idealized to complex progressed piecewise, one new component at a time, providing insight into the influence of various climate system components on Arctic climate.

The less complex, computationally-constrained models of the 1980s identified fundamental features of AA that have withstood observational evidence and the scrutiny of more complex models. These features include the magnitude of AA (~2–3 times global mean warming), seasonality and spatial variation of Arctic warming, bottom-heavy/surface-based profile, increased poleward LH transport, and the acceleration of the hydrologic cycle. Reduced-complexity models captured the fundamental processes influencing the Arctic response to increased CO_2 including the sea ice and snow surface albedo, poleward atmospheric and oceanic heat transports, seasonal energy transfer, atmosphere-sea ice-ocean coupling, and cloud radiative effects. While increasingly complex and more realistic contemporary models provide similar insights into AA (**Figure 6**), their value is from the refined quantitative estimates of process contributions and more reliable projections of future climate. While no one argues for a return to reduced-complexity representations of sea ice, clouds, and the ocean to produce climate projections, reduced-complexity models enable an intuitive understanding of climate processes that is hard to glean from comprehensive models (Held 2005; Jeevanjee et al., 2017; Maher et al., 2019).

Climate community organization around MIP activities has played a key role in AA science by providing inputs for climate projections and uncertainty assessments. Model intercomparison activities have grown from 14 models (Cess et al., 1989) to >40 models in Coupled MIP 5 and 6 (CMIP5 and 6) allowing for robust assessments of inter-model spread. Considering the two most recent CMIPs, the overall spread in the AA factor (defined as the ratio of Arctic-to-global mean surface warming) at the end of the 21st Century for the CMIP5 RCP8.5 (Taylor et al., 2012) and CMIP6 SSP8.5 scenarios (Eyring et al., 2016) has not narrowed significantly (**Figure 7**). However, no CMIP6 model with the available output simulates an AA factor <2. MIPs have also expanded to dedicated projects organized around scientific themes, including Polar Amplification MIP (Smith et al., 2019). Details on advances from model intercomparison studies can be found in **Sections 2** and **5**.

Innovative modeling approaches and experimental designs are being developed to test AA hypotheses, including a revitalization of idealized experiments. Specific results are covered in the feedback diagnostics section and **Section 5**. The complementary use of complex and idealized model experiments is a critical component of advancing AA science.

Arctic Feedback Diagnosis Frameworks

Frameworks quantifying how forcings and feedbacks contribute to AA can be classified into the following: energy budget-based diagnostics, mechanism denial experiments, latitudinally-constrained or otherwise idealized forcing, and sea ice forcing experiments.

Energy budget decompositions have been widely used to diagnose climate feedback contributions to surface warming. Individual feedback contributions are evaluated as climate feedback parameters that quantify the global mean TOA energy flux perturbation per unit of global mean surface warming (Wetherald and Manabe 1988; Soden and Held 2006; Shell et al., 2008; Huang et al., 2017a; Pendergrass et al., 2018). Although this method assumes that feedbacks are linear and additive, neural networks can account for nonlinearity (Zhu et al.,

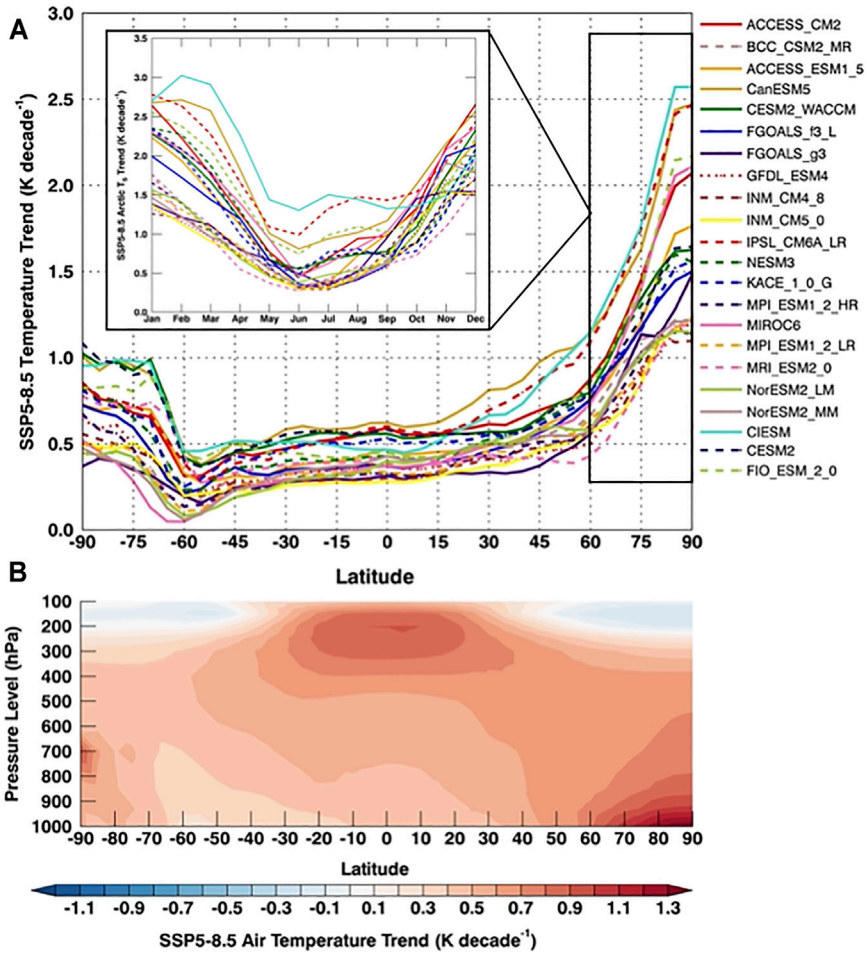

FIGURE 6 | Arctic Amplification in CMIP6. **(A)** Zonal mean temperature trends (K decade^{-1}) for 22 CMIP6 models from the SSP5-8.5 simulation. The inset depicts the seasonal cycle of temperature trends for the Arctic domain (poleward of 60°N). **(B)** The vertical profile of zonal mean temperature trends (K decade^{-1}) for CMIP6 ensemble mean is shown.

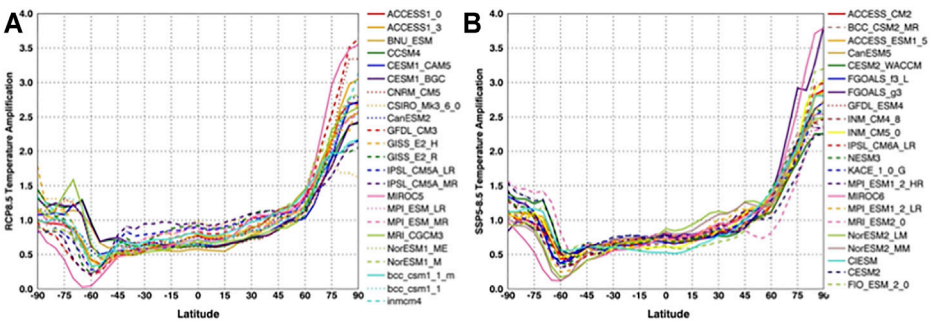

FIGURE 7 | Arctic Amplification and Contemporary Climate Models. Zonal mean Arctic Amplification factor (ratio of zonal average to global mean surface temperature change) for **(A)** CMIP5 RCP8.5 and **(B)** CMIP6 SSP5-8.5. The surface temperature change is computed as the difference between the 2080–2100 and the 2015–2025 periods.

2019; Huang et al., 2021a). The energy budget decomposition method can also quantify the influence of regional feedbacks on the warming pattern alongside the radiative forcing, atmospheric energy transport, and ocean heat uptake (e.g., Crook et al., 2011; Taylor et al., 2011a,b; Feldl and Roe 2013; Armour et al., 2013; Pithan and Mauritsen 2014; Hu et al., 2020).

A complementary approach uses the SEB, which is important in the Arctic where the physical validity of the TOA framework is questioned (Pithan and Mauritsen 2014; Payne et al., 2015; Goosse et al., 2018; Henry et al., 2021). Like TOA, the contributions of individual SEB terms to surface temperature change can be diagnosed (Lu and Cai 2009a; Pithan and Mauritsen 2014; Sejas et al., 2014; Laîné et al., 2016; Sejas and Cai 2016; Boeke and Taylor 2018). A SEB decomposition includes additional non-radiative terms (surface turbulent fluxes and ocean heat storage) that are especially important when considering the surface temperature response seasonality.

An expansion of the SEB approach is the coupled atmosphere surface climate feedback response analysis method (CFRAM)—a vertically-resolved version of the energy budget decomposition method (Lu and Cai 2009b; Cai and Lu 2009; Taylor et al., 2013). CFRAM provides a three-dimensional analysis of feedback contributions to the surface and atmospheric temperature response from radiative and non-radiative processes (convection, condensational heating, surface turbulent fluxes, and horizontal heat transport) (Song et al., 2014; Yoshimori et al., 2014). CFRAM does not include a lapse rate feedback and provides a clearer diagnosis of the process contributions to the vertical warming structure. However, the CFRAM is computationally expensive and computes heat transports as a residual; explicitly calculated heat transport terms are straightforward to include in CFRAM however these terms are not routine model outputs. A disadvantage of all energy budget decompositions is that they do not provide clear insights into how different feedbacks are coupled. For example, the radiative sensitivity to albedo changes varies by a factor of two across climate models in the Arctic and Southern Ocean due to inter-model differences in mean-state cloudiness (Donohoe et al., 2020).

Mechanism denial experiments—model simulations where a physical process is "turned off" or locked—also provide insights into the role of various feedbacks (e.g., Wetherald and Manabe 1988; Ingram et al., 1989; Rind et al., 1995; Hall 2004; Vavrus 2004; Graversen and Wang 2009). These studies analyze differences between climate model simulations with a specific process "turned off" and experiments with the process "turned on," such as sea ice albedo locking (e.g., Graversen et al., 2014), cloud locking (Vavrus 2004; Middlemas et al., 2020), and atmospheric heat transport divergence locking experiments (Graversen and Langen 2019). This approach highlights the coupling between processes that energy budget decomposition approaches cannot (Merlis 2014). The disadvantages of mechanism denial experiments are that they can modify the reference climate, introduce compensating effects, are challenging to apply to comprehensive climate models, and the results are difficult to compare with observations.

Lastly, different modelling protocols have been designed to understand the local and remote mechanisms to AA. Regionally applied greenhouse gas forcing experiments (**Section 5e**) are one such protocol designed to separate these contributions to Arctic warming (Alexeev et al., 2005; Chung and Räisänen 2011; Yoshimori et al., 2017; Shaw and Tan 2018; Stuecker et al., 2018). Another protocol isolates local and remote mechanisms by prescribing local and remote changes in sea surface temperature and sea ice concentration. Using this approach, Screen et al. (2012) attribute near-surface Arctic warming to local feedbacks and upper tropospheric warming to remote processes. Recent years have seen a proliferation of modeling experiments in which the sea ice component of a coupled ocean-atmosphere model is perturbed, including albedo reduction (e.g., Blackport and Kushner 2016; Liu and Fedorov, 2019), LW emissivity manipulation (e.g., Liu et al., 2019); sea-ice ghost forcing (e.g., Deser et al., 2015), ocean heat flux adjustment (Oudar et al., 2017), and sea ice nudging (McCusker et al., 2017; Smith et al., 2017). Although they all produce a consistent atmospheric circulation response (Screen et al., 2018), the various protocols make different and confounding assumptions regarding conservation of energy and melt water.

Each diagnostic method has strengths and weaknesses (**Table 1**) associated with technical aspects and underlying assumptions. These differences confound the ability to clearly assess the process contributions to AA. The community needs to address this issue to advance AA science.

ARCTIC AMPLIFICATION FACTORS AND PROCESSES

Sea Ice Feedbacks

Sea ice and snow cover changes via the positive surface albedo feedback are a principal driver of AA (Arrhenius 1896; Budyko 1969; MW75; Hall 2004). The surface albedo feedback operates when (high albedo) sea ice and snow cover melts and reduces surface albedo by uncovering the (low albedo) ocean and land surfaces underneath. Reducing surface albedo causes greater absorption of solar radiation that warms the surface and drives additional sea ice and snow melt. Studies estimate that the sea ice-snow albedo feedback is responsible for 30–60% of the total CO_2-induced Arctic warming (Dickinson et al., 1987; Hall 2004; Taylor et al., 2013; Boeke and Taylor 2018; Duan et al., 2019) and is the largest local Arctic feedback (Taylor et al., 2013; Yoshimori et al., 2014; Goosse et al., 2018). Multi-centennial climate simulations show that Arctic warming slows after most of the sea ice melts, further highlighting the importance of sea ice (Bintanja and van der Linden 2013; Dai et al., 2019).

The surface albedo feedback has substantially contributed to the observed Arctic warming. Observations of a reduced snowpack (Warren et al., 1999; Brown and Robinson 2011; Webster et al., 2014) and significant declines in sea ice extent, thickness, and age since 1979 indicate a reduced Arctic surface albedo (Nghiem et al., 2007; Maslanik et al., 2011; Parkinson and DiGirolamo, 2016; Kwok, 2018). Additionally, the albedo of multi-year sea ice has decreased (Riihelä et al., 2013). Perovich

TABLE 1 | Summary of feedback diagnostic frameworks. The selected example reference in the right column represents a single study that demonstrates each framework.

Diagnosis framework	Strengths	Weaknesses	Example References
Global/Regional TOA (or surface) energy budget decomposition	• Easy to apply to comprehensive model output and model intercomparisons • Compares all the feedbacks	• Assumes linearity and does not provide insights into how different feedbacks are coupled • Lapse rate feedback conceptually unclear at high latitudes in TOA frameworks	Pithan and Mauritsen (2014)
Coupled Feedback Response Analysis Method (CFRAM)	• 3D analysis of feedback contributions • Resolves process contributions to vertical warming profile	• Does not provide insights into how different feedbacks are coupled • Computationally expensive	Taylor et al. (2013)
Mechanism denial	• Tests how a given process interacts with different feedbacks	• Hard to implement in comprehensive models • Modifies the reference climate state	Graversen and Wang (2009)
Idealized forcing	• Compares roles of local and remote forcings and feedbacks	• Separation between local and remote is sometimes unclear	Stuecker et al. (2018)
Sea ice forcing	• Tests the importance of sea ice for Arctic warming	• Differing assumptions regarding conservation of energy and melt water	Screen et al. (2018)
Neural network	• Captures nonlinear feedbacks either due to large perturbation or coupling effects, e.g. cloud-masking of the albedo and water vapor feedbacks	• The valid value range and accuracy of predicted feedbacks depends on the training dataset	Zhu et al. (2019)

et al. (2007) computed that reduced surface albedo has increased the solar energy deposited into the Arctic Ocean by 89% from 1979–2005. CERES data indicate a -0.025 ± 0.004 decade^{-1} Arctic average albedo decline and a +1.2–1.3 Wm^{-2} decade^{-1} increase in absorbed TOA solar radiation between 2000 and 2018 (Duncan et al., 2020).

The surface albedo feedback has contributed substantially to the inter-model spread in Arctic warming across multiple generations of intercomparisons (Cess et al., 1991; Holland and Bitz, 2003; Hu et al., 2020). This uncertainty results from the complexities of modeling the continuously evolving sea ice and snow coverage, thickness, and optical properties (Zhang et al., 2000; Laxon et al., 2003)—processes for which available data is insufficient. Furthermore, the rapidly evolving factors that govern surface albedo (e.g., snow and sea ice thickness distribution, topography, drift, melt pond and floe size distribution) occur at small scales making parameterization difficult (Holland et al., 2010, 2012; Schweiger et al., 2011; Jahn et al., 2012; Stroeve et al., 2014).

Sea ice and snow also modulate surface turbulent energy fluxes giving rise to the sea ice insulation feedback. This feedback operates when changes in sea ice concentration and snow and ice thickness alter the non-radiative surface fluxes (sea ice conductance and surface turbulent fluxes; Burt et al., 2016). Sea ice loss exposes a larger area of the Arctic Ocean to the atmosphere and allows for a freer exchange of water vapor, aerosol particles, energy, and momentum with the atmosphere. The sea ice insulation feedback is strongest where there are large surface and near surface air temperature differences collocated with reduced sea ice cover (Serreze et al., 2009; Screen and Simmonds 2010a; Screen and Simmonds, 2010b; Serreze and Barry 2011; Boisvert et al., 2015; Boisvert and Stroeve, 2015; Boeke and Taylor 2018; Taylor et al., 2018). In addition, thinner and less snow-covered sea ice promotes greater heat conduction through sea ice (MS80; Rind et al., 1995; Persson et al., 2017). Through these mechanisms, the ice insulation feedback warms and moistens the lower Arctic atmosphere promoting additional warming via an enhanced greenhouse effect (Kim et al., 2016; Boeke and Taylor 2018; Kim et al., 2019; Feldl et al., 2020; Chung et al., 2021).

Sea ice cover influences the Arctic SEB differently during polar day and night and in both cases strongly impacts surface temperature. Less sea ice cover during polar day decreases the surface albedo and increases SW absorption (**Figures 8A,B**). Less sea ice cover also promotes larger ocean waves due to longer fetches that have the potential to mechanically break-up sea ice (Rogers et al., 2016). The greater effective heat capacity of the ocean relative to sea ice suppresses warming caused by the surface energy gain during polar day, leading to ocean heat storage and a delayed sea ice freeze up (Dwyer et al., 2012). During polar night, less sea ice cover corresponds to a warmer surface temperature, weaker static stability, and larger upwards surface turbulent fluxes (**Figures 8C,D**); climatologically cold temperatures over sea ice enable large surface warming when the ice thins and transitions to open ocean (Feldl and Merlis 2021). Atmospheric temperature tends to be warmer in regions with less sea ice in part due to the warming and moistening of the lower atmosphere by increased surface turbulent fluxes, increasing downwelling LW (DLW) radiation (**Figure 8D**). The greater ocean effective heat capacity also changes the relationship between DLW and upwelling LW (ULW); over sea ice surface DLW anomalies do not lead to strong net LW flux imbalances because sea ice temperature quickly warms in response (Persson et al., 2017; Hegyi and Taylor 2018). These differences in the SEB response to a sea ice change during polar day and night are key components of our conceptual model (**Section 6**).

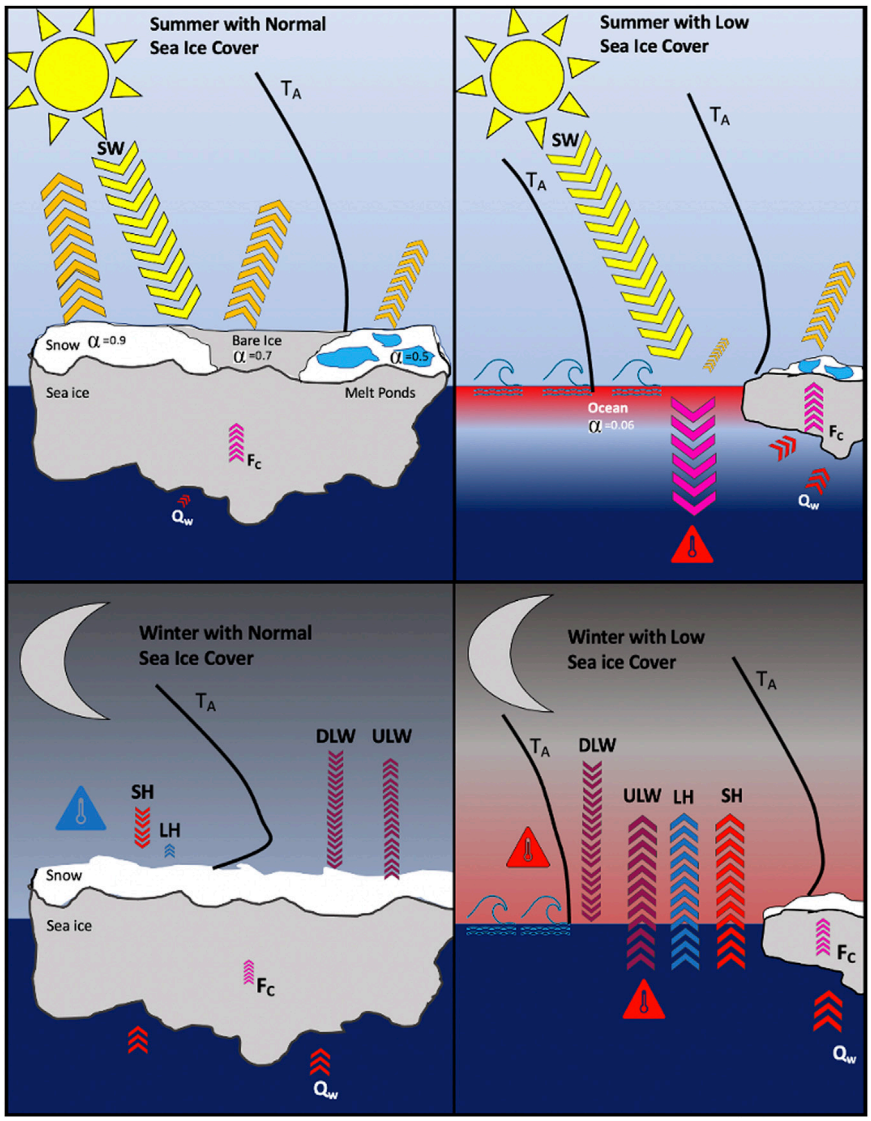

FIGURE 8 | Modulation of surface energy fluxes by sea ice. A schematic illustration of the sea ice albedo and ice insulation feedbacks and associated surface energy budget changes from sea ice loss: shortwave (SW), downwelling longwave (DLW), upwelling LW (ULW), sensible heat (SH), latent heat (LH), conductive heat flux through sea ice (F_C) and oceanic heat flux to sea ice (Q_W). The black line represents the characteristic atmospheric temperature profiles (T_A) over ocean and sea ice during polar **(A,B)** day and **(C,D)** night.

Temperature Feedbacks

Temperature feedbacks are major contributors to AA and contribute substantially to the inter-model differences in CMIP5 (Pithan and Mauritsen 2014). Temperature feedbacks are related to the efficiency of radiative cooling to space and are decomposed into contributions from a vertically-uniform temperature change (the Planck feedback) and the effect of the deviation from a vertically-uniform warming (the lapse rate feedback).

The Planck feedback contribution to AA originates from the nonlinearity of blackbody radiation with temperature, such that at colder temperatures, a larger increase in temperature is required to increase outgoing LW radiation (OLR) by 1 W m^{-2}. The Planck feedback is negative at all latitudes and contributes to AA because it is more negative at low latitudes. However, this nonlinearity effect may be small. Henry and Merlis (2019) replace the nonlinear temperature dependence of blackbody radiation with a linearized version in an idealized moist GCM and find that it does not modify the surface temperature change pattern, as energy transport and lapse rate changes compensate.

The lapse rate feedback contribution to AA originates from the meridional gradient of the feedback sign, negative at low latitudes and positive at high latitudes. In the tropics, convection pins the atmospheric temperature profile to the moist adiabat leading to a larger warming in the upper troposphere than at the surface. This

"top-heavy" vertical warming structure leads to a larger increase in OLR per unit increase in surface temperature—a negative lapse rate feedback. By contrast, the Arctic lapse rate feedback is positive because stable stratification promotes bottom-heavy warming. At high-latitudes, the atmosphere is close to radiative-advective equilibrium causing the lapse rate feedback to depend on the type of perturbation: a change in greenhouse forcing, for example, has a more bottom-heavy temperature response than a change in atmospheric heat transport (Payne et al., 2015; Cronin and Jansen, 2016).

This dependence on perturbation type presents a challenge in determining the relative importance of radiative, surface-based, and advective controls on the lapse rate feedback. In the absence of a surface albedo feedback, Henry et al. (2021) finds that the increase in CO_2 and water vapor alone cause a surface-enhanced warming, consistent with analytic column model results (Cronin and Jansen 2016). Song et al. (2014) argue that the water vapor and albedo feedbacks cause the positive Arctic lapse rate feedback. Mechanism denial experiments reveal that the surface albedo feedback enhances the high-latitude lapse rate feedback (Graversen et al., 2014; Feldl et al., 2017a), or equivalently surface-amplified warming is found in targeted sea ice loss experiments (e.g., Screen et al., 2018). Further, the Arctic lapse rate feedback is strongly correlated across models with summer sea ice loss and cold-season increases in surface turbulent heat fluxes (Feldl et al., 2020; Boeke et al., 2021). Atmospheric energy transport changes tend to reduce the Arctic lapse rate feedback (Feldl et al., 2020) via increases in moist energy transport and decreases in dry energy transport that warm the mid-troposphere and cool the near-surface atmosphere (Henry et al., 2021). Moreover, the decrease in dry transport is strongly controlled by the surface albedo feedback strength (Feldl et al., 2017b; Henry et al., 2021). The high latitude lapse rate feedback results from the sum of these different processes with strong evidence for the importance of surface processes (Cai and Lu 2009; Boeke et al., 2021).

From the surface perspective, the temperature feedback manifests as increased DLW radiation due to atmospheric warming, warming the surface and increasing ULW radiation. The coupling between increased DLW and ULW via the greenhouse effect constitutes a positive feedback loop amplifying surface and atmospheric warming (Sejas and Cai 2016; Zeppetello et al., 2019). Previous studies argue that this feedback accounts for most of the Arctic surface warming (Pithan and Mauritsen 2014; Laîné et al., 2016; Sejas and Cai 2016). Additional studies point to the importance of increased clear-sky DLW on the fall/winter Arctic warming maximum (Lu and Cai 2009a; Boeke and Taylor 2018). Though important to AA, the surface perspective of the temperature feedback does not provide clear insight into the processes that trigger it.

Cloud Feedbacks

Cloud processes modulate the radiative fluxes and thermodynamic structure of the Arctic atmosphere. The TOA Arctic cloud feedback in CMIP5 is generally negative (Zelinka et al., 2012) and is positive from the surface perspective (Taylor et al., 2013; Boeke and Taylor 2018), indicating that cloud feedback both increases TOA reflected SW and increases surface DLW (Taylor et al., 2011b; Taylor et al., 2013; Pithan and Mauritsen 2014). The magnitude and large inter-model spread of the Arctic cloud feedback comes from model discrepancies in the projected changes in cloud fraction, particularly at low-levels, and optical depth (Vavrus 2004, Vavrus et al., 2008, Vavrus et al., 2011; Liu et al., 2012; Morrison et al., 2019; English et al., 2014, Vignesh et al., 2020). Multiple interacting processes, illustrated in **Figure 9**, contribute to inter-model differences in the Arctic cloud feedback: surface-atmosphere coupling, cloud microphysics and precipitation, and interactions with large-scale atmospheric dynamics and thermodynamics (e.g., Curry et al., 1996).

The Arctic optical depth feedback is shaped by changes in cloud thermodynamic phase. In response to warming, cloud ice transitions to water increasing cloud albedo and causing a negative feedback (**Figures 9C,D**; Mitchell et al., 1989; Li and Le Treut 1992). This feedback is sensitive to cloud ice in the control climate, by determining the amount of ice available to transition. The cloud phase feedback magnitude is likely biased negative in most contemporary climate models due to excessive cloud ice and too little supercooled liquid under present-day conditions, yielding unrealistically large increases in mixed-phase cloud optical thickness with warming (Tsushima et al., 2006; Klein et al., 2009; Komurcu et al., 2014; McCoy et al., 2016; Tan et al., 2016). This cloud optical depth feedback bias may have broader implications to AA by enhancing the Arctic lapse rate feedback (Tan and Storelvmo 2019). Recent model experiments revealed that while global cloud feedbacks warm the Arctic, the local feedback contributes negligibly to Arctic warming (Middlemas et al., 2020) suggesting a potential remote influence (**Section 5e**). However, the model exhibits a low mixed-phase supercooled liquid bias and likely an optical depth feedback that is too negative.

The stability of the lower troposphere affects cloud processes and constitutes a cloud feedback mechanism. Arctic cloud fraction and optical thickness tend to increase with reduced lower tropospheric stability (LTS; Barton et al., 2012; Solomon et al., 2014; Taylor et al., 2015; Yu et al., 2019). In response to increased CO_2, LTS is expected to decrease, promoting increased cloud fraction and optical depth with a seasonally varying character (Boeke et al., 2021). CMIP5 models show substantial cloud-induced warming in fall and winter coincident with large reductions in LTS (**Figures 9C,D**; Boeke and Taylor 2018). These reductions in LTS are in part due to the large reductions in sea ice (Pavelsky et al., 2011). Thus, cloud changes induced by the LTS mechanism are coincident with cloud-surface turbulent coupling (Kay and Gettelman 2009; Shupe et al., 2013; Solomon et al., 2014; Taylor et al., 2015; Yu et al., 2019).

Cloud-surface coupling represents an important mechanism through which sea ice influences cloud feedback. Sea ice loss tends to increase cloud fraction and optical depth through increased surface evaporation (Curry et al., 1996; Taylor et al., 2015; Abe et al., 2015; Huang et al., 2017b; Morrison et al., 2019; Huang et al., 2021b). However, the sensitivity of clouds to sea ice loss depends on the cloud-

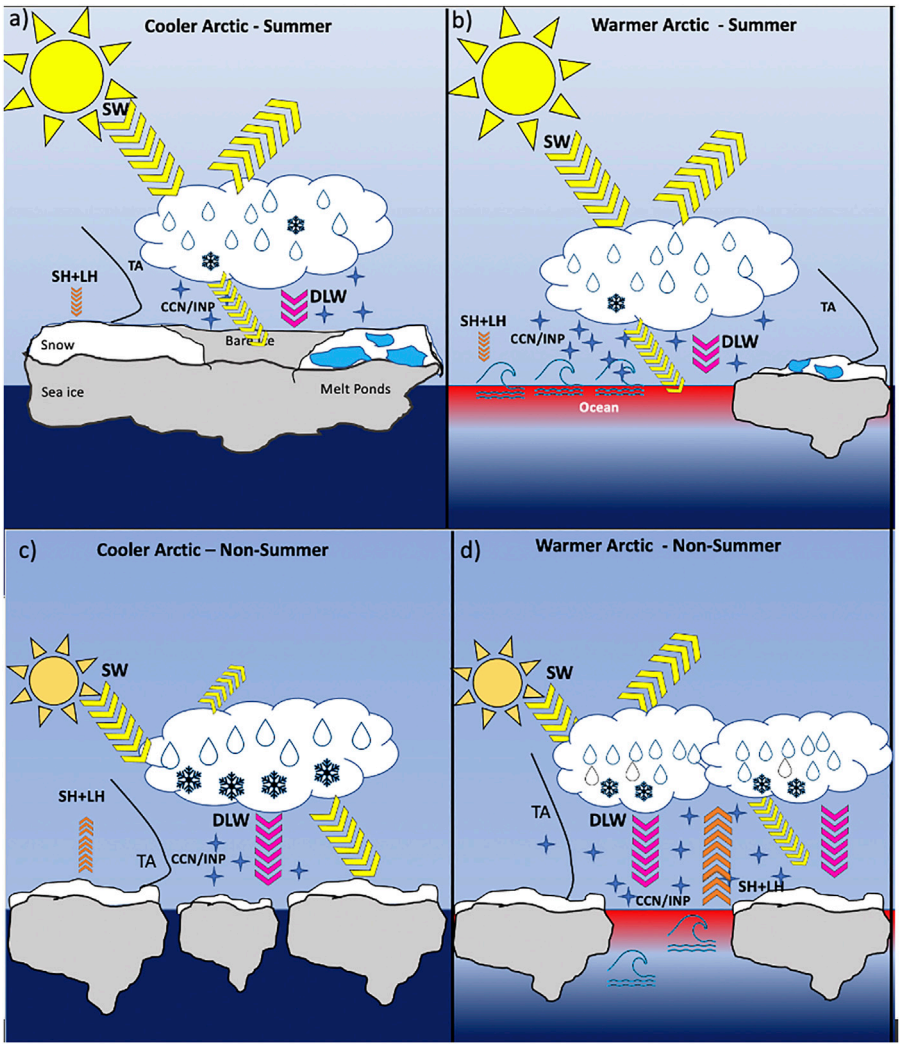

FIGURE 9 | Dominant Arctic cloud responses to warming during summer and non-summer months. Summer cloud fraction and optical depth changes between a **(A)** cooler to a **(B)** warmer Arctic are small due weak surface-cloud coupling and a weak cloud-phase feedback. Cloud masking (not depicted) damps the TOA radiative budget response to reduced surface albedo by blocking sunlight from reaching the newly uncovered, underlying, and darker ocean. Non-summer (mainly spring and fall) cloud fraction and optical depth between a **(C)** cooler and a **(D)** warmer Arctic generally increase as a result of stronger surface-atmospheric coupling and enhanced latent and sensible heat fluxes (orange arrows), a positive cloud phase feedback (warmer temperature replace ice crystals with liquid droplets), and reduced lower tropospheric stability (black line represents the characteristic atmospheric temperature profiles, T_A). In summer and non-summer months, newly exposed sea ice exposes the atmosphere to new local sources of marine aerosols that can increase CCN and INP with an uncertain influence on cloud microphysical properties. Note that depicted sea ice conditions are illustrative.

surface coupling state and the air-surface temperature gradient. This condition-dependent behavior is responsible for the seasonality of the cloud response to sea ice loss (**Figures 9A,B**); observational studies find that more liquid clouds result from reduced sea ice in all seasons except summer (Kay and Gettelman 2009; Boisvert et al., 2015; Taylor et al., 2015; Morrison et al., 2018; Huang et al., 2019a; Huang et al., 2019b). Weak air-surface temperature gradients and decoupled cloud layers are typical in Arctic summer conditions (Shupe et al., 2013). Recent research suggests that LH and SH flux increases may elicit different cloud responses (Li et al., 2020). The evidence suggests that the cloud-sea ice feedback promotes surface warming in non-summer months.

Cloud masking influences AA by modifying the strength of other feedbacks. Cloud masking is defined as the difference in the cloud feedback determined using the cloud radiative effect and that using the partial radiative perturbation approach. The cloud masking effect operates by altering the TOA radiative perturbation from a feedback relative to clear-sky and is sensitive to present-day cloud properties. Most pertinent for the Arctic, cloud masking damps the magnitude of the surface albedo feedback by reducing the TOA radiative perturbation from a surface albedo change (Soden et al., 2004). Several

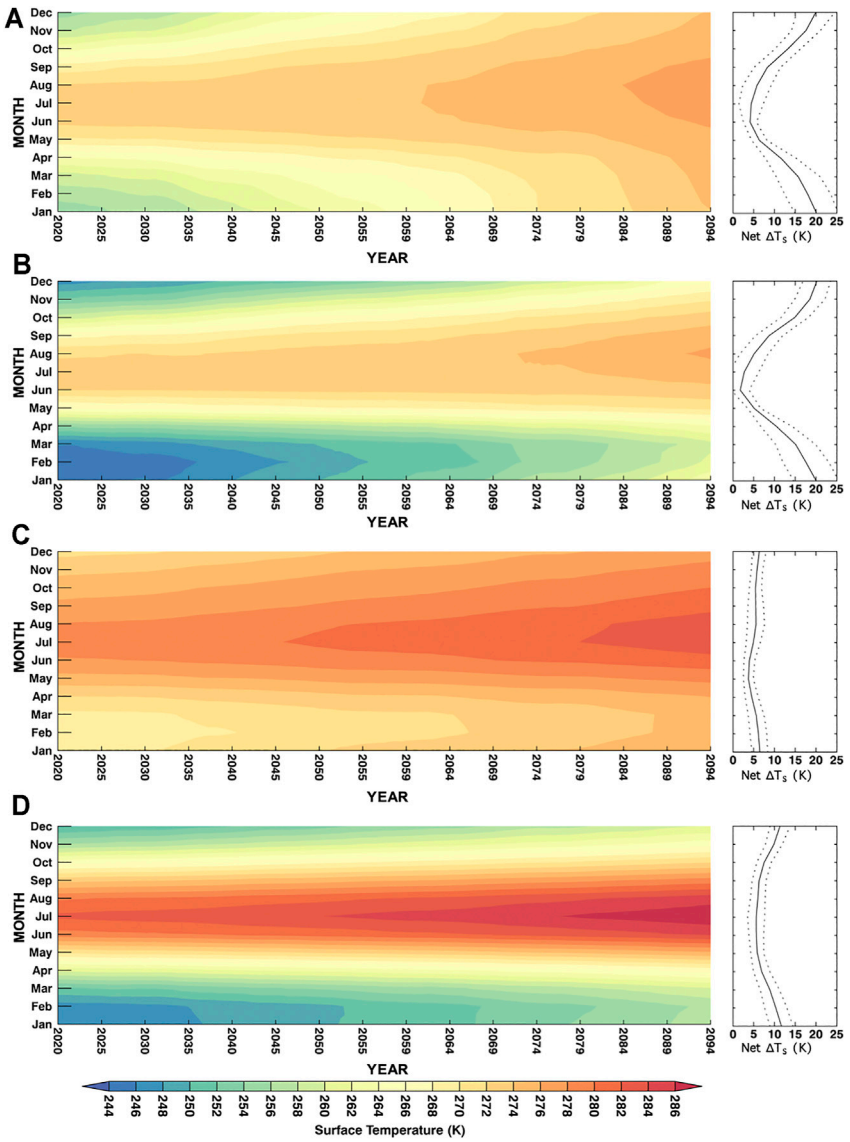

FIGURE 10 | Hovmoller plot of the monthly time series of the CMIP6 ensemble average Arctic surface temperature changes in SSP5-8.5 for **(A)** ice-retreat regions (present-day sea ice concentration >15% and future sea ice concentration <15%), **(B)** ice-covered regions (sea ice concentration >15% in present and future), **(C)** ice-free ocean (present-day sea ice concentration <15%), and **(D)** land. The right panels show the total surface warming (K) by 2100 as the difference between the 2090–2100 and 2015–2025 periods for each surface type (solid black line) and the across-model standard deviation (dotted line).

studies indicate that the cloud masking effect reduced the TOA radiative impact of the observed surface albedo decline by ~50% (Sledd and L'Ecuyer 2019; He et al., 2019; Alkama et al., 2020; Stapf et al., 2020). While not a feedback, the cloud masking effect highlights a mechanism through which present-day cloud properties influence Arctic climate change.

Lastly, microphysical processes influence the evolution of cloud radiative properties and modulate cloud feedback (**Figure 9**). Cloud microphysical processes represent sources and sinks of mixed-phase cloud liquid and ice and modulate the water amount, phase partitioning, and the number and size of hydrometeors (Curry et al., 1996; Beesley and Moritz 1999; Klein et al., 2009; Yang et al., 2015; Tan and Storelvmo 2016; Barrett et al., 2017; Furtado & Field 2017; Wang et al., 2018). However, cloud microphysical processes and their interactions with aerosols are poorly represented in climate models. Ice nucleation mechanisms and ice-nucleating particle (INP) properties and sources are either poorly constrained or not represented in models (Xie et al., 2013; English et al., 2014; Komurcu et al., 2014; Schmale et al., 2021). Mixed-phase cloud INP recycling (Fan et al., 2016; Solomon et al., 2018), secondary ice production (Rangno and Hobbs 2001; Lawson et al., 2017; Sotiropoulou et al., 2020; Zhao et al., 2021) and biological INP-sea ice interactions (Wilson et al., 2015; Irish et al., 2017; Hartmann et al., 2019; Creamean et al., 2020) remain unresolved or unrepresented. In addition, the efficiency of the

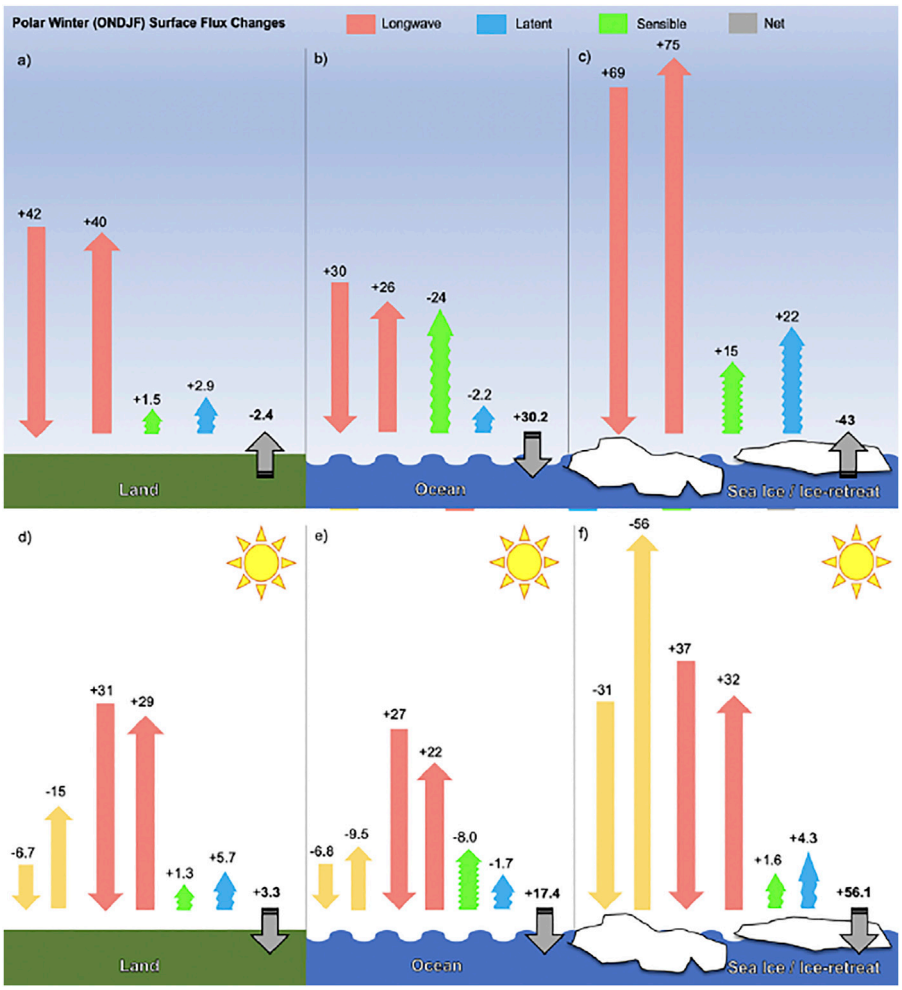

FIGURE 11 | Surface energy budget response by surface type. CMIP6 SSP5-8.5 ensemble mean surface energy budget changes during polar night and day for **(A,D)** land, **(B,E)** ocean, and **(C,F)** sea ice retreat. Surface types are defined as in **Figure 10**. Changes are computed as the difference between the 2080–2100 period and the first 20-years of the simulation (2015–2035).

Wegener-Bergeron-Findeisen process (Tan and Storelvmo 2016), updraft velocity, and ice crystal fall speeds (Ervens et al., 2011; Tan and Storelvmo 2019) are also poorly constrained. These gaps in our understanding of cloud microphysical processes preclude a more quantitative assessment of the Arctic cloud feedback and its influence on AA. Observational constraints that statistically characterize the range of Arctic cloud types are needed to improve parameterized processes and reduce cloud-related uncertainty.

Surface Type Dependence and Seasonality of Arctic Amplification

The diversity of Arctic surface types (e.g., sea ice, ocean, and land) dictates features of the spatial structure and seasonality of AA. Surface-type dependent characteristics and processes such as albedo, surface turbulent fluxes, vertical and horizontal heat transport, and heat capacity control the impact of each surface type. Understanding how specific surface types influence the spatial distribution and seasonality of AA may help reduce the inter-model spread.

Explanations of regional variations in AA must consider the underlying surface. Observed temperature changes indicate that regions with the largest sea ice loss are warming most rapidly (Robock 1983; Screen and Simmonds, 2010a; Bekryaev et al., 2010; Boisvert and Stroeve 2015; **Figure 2**). Moreover, the regional characteristics of warming within a climate model is driven by differences in surface properties and feedbacks (Laîné et al., 2016). **Figure 10** illustrates CMIP6 model projections showing that the magnitude and seasonality of warming is a function surface type: namely, sea ice-retreat, sea ice-covered, ice-free ocean, and land (**Figure 10**; definitions in caption).

Several processes conspire to cause the largest Arctic warming in sea ice-retreat and sea ice-covered regions (**Figure 10**). Surface albedo and sea ice insulation feedbacks strongly enhance surface warming (MS80; Screen and Simmonds, 2010a; Taylor et al., 2013; Pistone et al., 2014; Boeke and Taylor 2018). Cloud feedbacks are also positive in these regions, especially in fall/

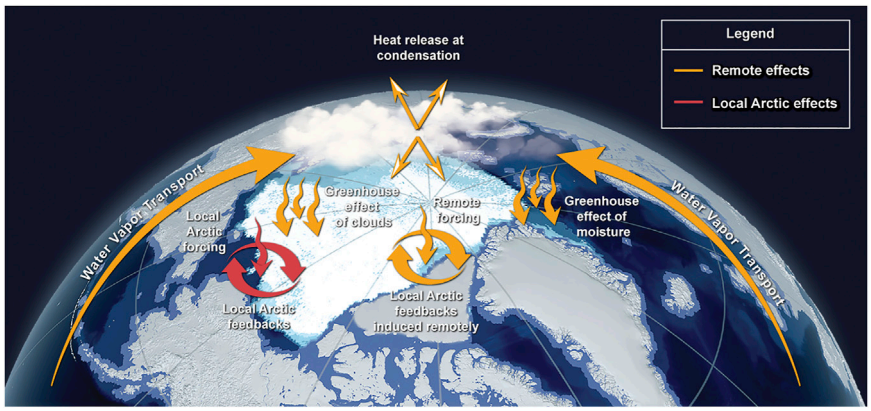

FIGURE 12 | Schematic illustrates how moisture transport from lower latitudes into the Arctic contributes to the *water vapor triple effect* (warming from condensation and the greenhouse effects of moisture and clouds) drives direct Arctic warming and induces additional warming though local feedbacks (yellow arrows). Warming by local Arctic feedbacks induced by local forcing mechanisms (red arrows) is depicted separately.

winter (**Section 5c**). Strong LTS, seasonal ocean energy transfer drive the release of stored ocean heat via SH and LH fluxes (**Figures 11C,F**), and changes in surface thermal inertia contribute to the maximum winter warming in these regions (Robock 1983; Sejas et al., 2014; Laîné et al., 2016; Sejas and Cai 2016; Boeke and Taylor 2018; Feldl et al., 2020).

The characteristics of the warming response in ice-free ocean regions differ from sea ice regions. Ice-free regions have a weaker and almost seasonally uniform warming (**Figure 10**) resulting from the large ocean heat capacity (Dwyer et al., 2012) and weaker positive feedbacks (especially the surface albedo feedback; Boeke and Taylor 2018). Thus, the SEB response is smaller than in sea ice regions and shows an opposite net flux change during winter from differing SH flux responses (**Figures 11B,E**). Additionally, changes in ocean heat transport also influence the warming (**Section 5f**), however it is unclear if these changes affect these regions differently.

While warming in land regions has a similar seasonal structure as sea ice, different surface characteristics indicate that a different set of processes cause this signal. Seasonal differences in the surface albedo feedback occur due to the earlier spring peak in land snowmelt compared to sea ice melt (Taylor et al., 2011b). Additionally, the surface albedo feedback is weaker (smaller increases in surface absorbed SW; **Figure 11D**) over snow-covered land than over sea ice because of smaller albedo differences with the underlying surface, despite being at a lower latitude (Taylor et al., 2011a). Surface turbulent flux changes cool the land during summer as opposed to during winter as in sea ice regions (**Figures 11A,D**; Laîné et al., 2016; Letterly et al., 2018); the summer warming minimum over land results from increased cooling and earlier snowmelt rather than increased heat storage as in sea ice regions (Boeke et al., 2021). The small heat capacity of land combined with the nonlinearity of the temperature dependence of LW surface cooling (Henry and Vallis 2021) and increased local atmospheric heat transport from sea ice loss to land regions (Deser et al., 2010; Burt et al., 2016; Boeke and Taylor 2018) also contribute to the winter amplification over land.

Atmospheric Heat Transport Effects

Despite considerable efforts particularly over the last decade, the role of remote influences on AA is still debated. Here, we define remote impacts on Arctic warming as any warming that occurs due to non-Arctic changes (equatorward of 60°N). Thereby, remote effects are not merely associated with changes in meridional heat transports but include the local feedbacks they initiate or mediate (e.g., water vapor and cloud feedbacks). Understanding the partitioning between local and remotely-induced warming (**Figure 12**) is crucial for reducing uncertainty in the impacts of non-well mixed climate forcings (e.g., aerosols; Chung and Räisänen, 2011). Further, simulated Arctic warming and variability may depend on the models' representation of tropical Pacific variability (e.g., Baxter et al., 2019; Ding et al., 2019) and improving Arctic projections may require improved modeling of teleconnections.

Early EBM studies identified the strong impact of meridional heat transports on polar temperatures (Budyko 1969; Sellers, 1969, North, 1975), and, in GCMs, the opposing responses of dry static energy (DSE) and LH transports due to reductions in the meridional temperature gradient and increases in the moisture gradient (MW80). Flannery (1984) extended the dry EBM approach to include the separate effect of increased LH transport with warming; EBMs continue to be used to study polar warming (e.g., Hwang et al., 2011; Rose et al., 2014; Roe et al., 2015; Merlis and Henry 2018; Armour et al., 2019; Feldl and Merlis 2021).

Despite different meridional shapes of the forcing due to CO_2 and solar constant changes, Wetherald and Manabe (1975) and MW80 found that the meridional shape of the response was similar. Langen and Alexeev (2007) identified a preferred polar amplified response mode whose shape is determined by the strength of the TOA radiative restoring feedback and the DSE

and LH transports (also see Merlis and Henry (2018)). The concept of a preferred mode is strengthened by the linearity between Arctic and global mean temperature change inferred from the paleoclimate record (Miller et al., 2010) and CMIP5 models (Yoshimori et al., 2017).

GCM experiments have been performed to gauge the remote impact on Arctic warming. Some used a direct extra energy term added to the SEB ("ghost forcing", Alexeev et al., 2005; Park et al., 2018), some used latitudinally confined CO_2 increases (Chung and Räisänen, 2011; Shaw and Tan, 2018; Stuecker et al., 2018; Semmler et al., 2020) while others specified SST increases at lower latitudes (Yoshimori et al., 2017). Common to these approaches is that any Arctic warming that occurs, does so due to the indirect effects of the remote warming. Chung and Räisänen (2011) attribute 60–85% of Arctic warming to non-local drivers, Yoshimori et al. (2017) find 60–70%, Park et al. (2018) ~50%, Shaw and Tan (2018) ~60%, and Stuecker et al. (2018) ~50%. These studies indicate that non-Arctic forcing increases non-Arctic temperatures, which in turn increase Arctic temperatures. Local-Arctic feedbacks then amplify this remotely induced Arctic warming (**Figure 12**) to produce a final remotely induced warming that accounts for half or more of the full Arctic warming.

AA therefore arises in part due to an asymmetry between low-to-high and high-to-low latitude impacts: low-latitude warming is efficiently communicated poleward while high-latitude warming is less efficiently communicated equatorward (Alexeev et al., 2005; Chung and Räisänen, 2011; Park et al., 2018; Shaw and Tan, 2018; Stuecker et al., 2018; Semmler et al., 2020). Non-Arctic warming tends to produce a rather uniform meridional warming pattern and thereby does not itself cause AA (Park et al., 2018; Stuecker et al., 2018). Nevertheless, the fact that non-Arctic warming does not stay localized, as opposed to local-Arctic induced warming, implies that remote effects contribute significantly to Arctic warming. Similarly, moist EBMs and idealized GCMs produce polar amplification in the absence of a surface albedo feedback due to the down-gradient transport of moist static energy (Alexeev et al., 2005; Langen and Alexeev 2007; Roe et al., 2015; Armour et al., 2019; Russotto and Biasutti 2020).

Tropical impacts on Arctic warming (e.g., Rodgers et al., 2003) have been elaborated in the "tropically excited Arctic warming mechanism" (TEAM, Lee et al., 2011; Lee 2012; 2014). Enhanced convection in the Pacific warm pool leads to strengthened or more frequent excitement of poleward propagating Rossby waves. Through dynamic heating and increased moisture transport into the Arctic, the wave dynamics increase the DLW radiation and lead to warming. The role of tropical Pacific Rossby wave-driven teleconnections to the Arctic has been highlighted for observed warming over northeastern Canada and Greenland (Ding et al., 2014) and Arctic sea ice trends and variability (Ding et al., 2017; Baxter et al., 2019; Ding et al., 2019; Topál et al., 2020). Planetary waves dominate the transport of heat and moisture into the Arctic and can drive temperature increases (Graversen and Burtu 2016; Baggett and Lee 2017). Synoptic waves also transport heat and moisture to the Arctic, but in smaller amounts and only in conjunction with a background of amplified planetary waves (Baggett and Lee 2017).

Several studies have concluded that atmospheric heat transport changes play a small or negligible role in AA, finding a negative correlation between polar amplification and atmospheric heat transport changes (Hwang et al., 2011; Kay et al., 2012; Boeke and Taylor 2018). However, this conclusion may result from neglecting the amplified warming effect of latent heat transport discussed below. Due to the nearly canceling effects of increased LH transport and decreasing DSE transport, models with high AA tend to simulate only small or even negative net heat transport changes. Similar conclusions of a subsidiary role for atmospheric heat transport were drawn by Pithan and Mauritsen (2014), Stuecker et al. (2018) and Feldl et al. (2020) using a TOA kernel-based approach and Taylor et al. (2013) using CFRAM. The discrepancy between these studies and those showing the importance of low-latitude impacts and LH transports is likely due to 1) the effect of transport-driven increases in LH is amplified by accompanying changes in specific humidity and clouds (i.e., a "water vapor triple effect" **Figure 12**; Cai 2006; Graversen and Burtu, 2016; Baggett and Lee, 2017; Lee et al., 2017; Yoshimori et al., 2017; Graversen and Langen, 2019), 2) differing attribution of warming to local and remote processes, and 3) a focus on vertically-integrated energy transport, which does not account for a disproportionate effect of lower versus upper tropospheric transport on surface temperature (Cardinale et al., 2021).

The "*water vapor triple effect*" represents the multiple influences of water vapor on the Arctic energy budget relating to the misattribution of local and remote Arctic warming (**Figure 12**). Water vapor transport from mid-latitudes into the Arctic has multiple effects on the Arctic energy budget beyond the release of latent heat at condensation; before condensation, the added water vapor increases the greenhouse effect and after condensation it leads to increased cloudiness, which in Arctic winter has a warming effect. We call this the *water vapor triple effect* and it means that, per unit of energy transported into the Arctic, latent heat transport is more efficient than DSE transport at warming the Arctic. Graversen and Burtu (2016) show that LH transport eventually leads to an order of magnitude more Arctic warming than DSE transport per unit of energy. When looking at net heat transport changes, this amplified effect is overlooked and the change in total atmospheric heat transport is an unreliable measure of the full effect of atmospheric dynamics (Yoshimori et al., 2017). In offline feedback diagnostic approaches, the water vapor triple effect is attributed to local feedbacks (e.g., water vapor, cloud, lapse rate). Thus, many local feedbacks, as conventionally defined, are not exclusively local in nature. Attribution of total Arctic warming should be considered as four contributions: 1) the local forcing, 2) local feedbacks activated by the locally-induced warming, 3) the remote impacts/forcing and 4) local feedbacks activated by the remotely-induced warming.

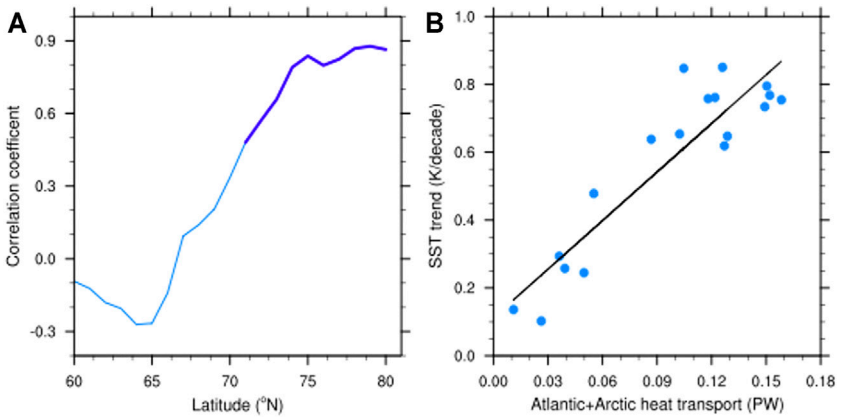

FIGURE 13 | Ocean heat transport and Arctic Warming. **(A)** The correlation between the trend of average SST over 60–90°N during 2015–2,100 and northward ocean heat transport averaged over 2015–2,100 across different latitudes in the Atlantic basin among 18 CMIP6 climate models under the SSP5-8.5 scenario. For each model, only the first ensemble simulation is used to ensure an equal weight among models. Dark blue indicates the latitudes where the correlation is significant with 95% confidence by Pearson's r test. **(B)** The scatter plot of SST trends during 2015–2,100 and northward ocean heat transport averaged over 2015–2,100 across 80°N in the Atlantic sector, with the regression line of the two variables (black).

Impacts 1) and 2) should be counted as locally-induced warming while impacts 3) and 4) should be counted as remotely-induced.

Oceanic Heat Transport Effects

The transport of energy by the oceanic circulation modulates Arctic temperature and sea ice and thus can influence AA. Observations show enhanced ocean heat transports into the Arctic through the Fram Strait and the Barents Sea in recent years (Karcher et al., 2003; Schauer et al., 2004; Dmitrenko et al., 2008; Skagseth et al., 2008; Spielhagen et al., 2011; Årthun et al., 2012). Climate models simulate enhanced high-latitude ocean heat transport under global warming (e.g., Holland and Bitz, 2003; Bitz et al., 2006; Hwang et al., 2011; van der Linden et al., 2019). Several studies suggest that this increased ocean heat transport contributes to Arctic warming (Holland and Bitz, 2003; Hwang et al., 2011; Mahlstein and Knutti, 2011; Singh et al., 2017); in contrast, other studies argue that changes in ocean transport are not correlated with Arctic warming (e.g., Pithan and Mauritsen, 2014; Laîné et al., 2016). This discrepancy mostly comes from the difference of the latitudes where the ocean heat transport is focused (Nummelin et al., 2017). Ocean heat transport increases poleward of 60°N are positively correlated with AA (Holland and Bitz 2003; Hwang et al., 2011; Mahlstein and Knutti 2011).

Several mechanisms contribute to enhanced poleward ocean heat transport under anthropogenic warming. Several studies indicate that increased ocean heat transport in the subpolar North Atlantic is mainly due to warmer Atlantic water (Jungclaus et al., 2014; Koenigk and Brodeau 2014; Nummelin et al., 2017), while other studies highlight ocean circulation changes (Bitz et al., 2006; Rugenstein et al., 2013; Winton et al., 2013; Marshall et al., 2015; Oldenburg et al., 2018; van der Linden et al., 2019). In the latter mechanism, changes in the North Atlantic subpolar gyre or the Atlantic Meridional Overturning Circulation (AMOC) are argued to be important. For example, a strengthened subpolar gyre causes increased oceanic heat transport into the Barents Sea that decreases sea ice and increases oceanic heat release. An anomalous cyclonic circulation is then induced over the Barents Sea that intensifies westerly winds and further promotes oceanic heat transport and warming in the Barents Sea (Ådlandsvik and Loeng, 1991; Goosse et al., 2003; Bengtsson et al., 2004; Arzel et al., 2008; Guemas and Salas-Melia, 2008; Semenov et al., 2009).

Alternatively, the role of AMOC change in high-latitude ocean heat transport and AA is debated. In GFDL models, a stronger AMOC weakening is linked with less high-latitude warming (Rugenstein et al., 2013; Winton et al., 2013). van der Linden et al. (2019) show that changes in the North Atlantic subpolar gyre play a prominent role in modulating ocean heat transport into the Arctic, while AMOC change is a secondary factor in the EC-Earth model. Additionally, the relationship between AMOC and high-latitude ocean heat transport could be different under internal variability and anthropogenic warming (Oldenburg et al., 2018). AMOC is not a one-way forcing on Arctic climate; Arctic sea ice melt under anthropogenic warming may also slow the AMOC after multiple decades (Sévellec et al., 2017; Liu et al., 2019; Li et al., 2021). A recent study (Liu and Fedorov, 2021) reconciles the two-way interaction between Arctic sea ice and the AMOC, which modulates the changes in both variables in a warming climate.

Ocean heat transported into the Arctic from the Atlantic influences Arctic warming and relates to the inter-model spread. Inter-model differences across 18 CMIP6 models (**Figure 13**) illustrate the relationship between Arctic warming and ocean heat transport across different latitudes. The correlation is positive and becomes statistically significant near 70°N and strengthens moving poleward (**Figure 13A**), a result consistent with previous studies (Holland and Bitz 2003; Hwang et al., 2011; Mahlstein and Knutti 2011). At 80°N where much of the Atlantic ocean heat enters the Arctic via the Fram Strait, the correlation between Arctic warming and ocean heat transport reaches 0.91. Thus, models with more (less) ocean heat imported into the Arctic via the Atlantic sector simulate stronger (weaker) warming during 2015–2,100 under SSP5-8.5 (**Figure 13B**).

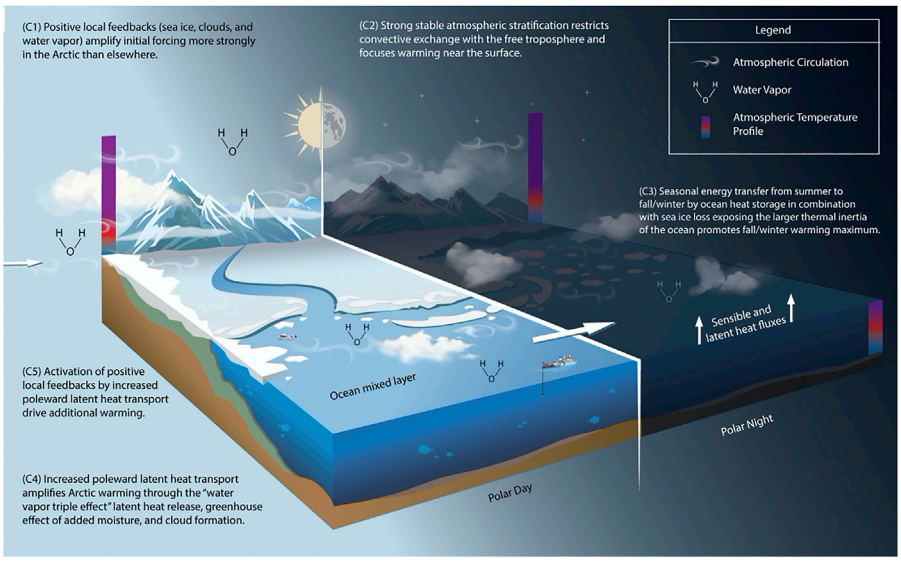

FIGURE 14 | Illustration of the fundamental processes generating AA in the conceptual model.

Role of Episodic Variability: Air Mass Transformation and Moisture Intrusions

Long-term climate change and mean energy budgets symbolize the accumulation of short timescale, episodic events. The nature of episodic events has implications for our understanding and projecting of AA. In the seasonal mean, the wintertime Arctic SEB and lower tropospheric temperature profiles are dominated by radiative cooling and strong stable stratification (Serreze et al., 1992). However, at any point in time and space, the Arctic winter boundary layer over sea ice or land tends to be either in a radiatively clear state with no clouds or ice clouds or a cloudy state with low-level liquid containing clouds (Stramler et al., 2011). In the radiatively clear state over sea ice, surface radiative cooling (~-40 W m^{-2}) drives surface-based temperature inversions with strengths of ~10–15 K. In the radiatively cloudy state, the surface is in approximate radiative balance with the cloud layer and a weaker temperature inversion is elevated to or above the cloud-top (Sedlar et al., 2012; Pithan et al., 2014).

These two states occur at different stages of air-mass transformations (Pithan et al., 2018; Nygård et al., 2019). Following the intrusion of warm, moist air masses from lower latitudes, radiative cooling leads to cloud formation driving the boundary layer into the cloudy state. After several days over Arctic sea ice or land, cooling and drying of the air-mass causes the mixed-phase cloud to glaciate or decay, transitioning to the clear state. The moisture supply aloft and cloud-top radiative cooling lead to cloud top moisture inversions (e.g., increases in specific humidity with height). Given the differences in the thermodynamic profile and the SEB between these states, changes in their frequency of occurrence can impact wintertime sea ice growth, near-surface air temperature and lapse-rate, water vapor and cloud feedbacks.

Episodic variability can influence AA through multiple mechanisms. Changes in the frequency of radiatively clear and cloudy states due to a change in the magnitude or frequency of moist air mass intrusions and atmospheric rivers could alter the SEB and cloud feedback. Observational analyses suggest an increase in the number of moist intrusions has already contributed to wintertime Arctic warming and reduced sea ice growth (Woods and Caballero 2016a; Woods and Caballero 2016b; Graham et al., 2017a; Graham et al., 2017b; Hegyi and Taylor 2018). The initial properties of incoming air-masses could also change, influencing the longevity of mixed-phase clouds; warmer, moister, and potentially more aerosol laden air-masses are possible due to warming at lower latitudes. The potential impact of AA and sea ice loss on the frequency of circulation states with strong meridional advection has been intensely investigated over the past decade and continues to be debated (e.g., Cohen et al., 2020). Lastly, surface turbulent fluxes over the ice-free ocean represent another mechanism by which episodic variability can influence AA as the magnitude of SH and LH fluxes can change by ~100 Wm^{-2} depending upon whether the prevailing winds are from sea ice to ice-free ocean or vice versa (Taylor et al., 2018). A quantitative understanding of the Arctic system response to episodic heat and moisture transport events, air-mass transformation, and cloud formation is needed to reduce uncertainty in Arctic projections.

CONCEPTUAL PICTURE OF ARCTIC AMPLIFICATION

AA results from a collection of interacting processes. Based upon the available evidence, we deduce five fundamental concepts for AA (**Figure 14**): (C1) local positive feedbacks amplify the initial local forcing more strongly in the Arctic than elsewhere, (C2) the

predominance of stable atmospheric stratification (inversion denoted by the color bar in **Figure 14**) restricts convective mixing and focuses warming in a shallow near-surface layer, (C3) the seasonal transfer of energy from summer to fall/winter by ocean heat storage in combination with sea ice loss exposing the larger thermal inertia of the ocean and drives the maximum warming in winter, (C4) increased poleward LH transport amplifies Arctic warming through a "water vapor triple effect", and (C5) activation of local feedbacks by remote atmospheric and oceanic processes drive additional warming. Next, we employ these concepts to describe the AA process.

Initially, rising CO_2 levels increase DLW radiation warming the Arctic surface and overlying air with a surface-based vertical structure. Arctic warming excites a suite of positive local feedbacks (C1; cloud, water vapor, and surface albedo) that lead to further warming. The surface albedo feedback represents the strongest positive local feedback and favors a surface-based warming profile that is further promoted by strong atmospheric stable stratification (C2).

Each local feedback has a unique seasonal signature that shapes its contributions to AA. Sea ice decline is strongest in summer, increasing absorbed solar radiation into the Arctic Ocean; however, summer warming is small due to the Arctic Ocean's large heat capacity and the LH associated with sea ice melt. These processes sequester the surplus energy and transfer it to fall/winter (C3) producing larger warming during these months. The increased upper Arctic Ocean heat content delays fall sea ice freeze onset, exposes the ocean to the atmosphere for a longer time, and increases surface turbulent fluxes from ocean-to-atmosphere. The combination of delayed freeze onset and warmer temperatures promotes less winter sea ice growth and thinner spring sea ice that is more susceptible to earlier summer melt out. This provides more time to accumulate solar radiation in summer, further delaying fall freeze-up.

Simultaneously with these local processes, the rest of the globe warms and moistens in response to increased CO_2 causing the air transported into the Arctic to have a larger moist static energy. The poleward moisture transport contributes not only to the LH release associated with condensation but also to an increased greenhouse effect prior to condensation and subsequent increased cloudiness. Through this water vapor triple effect, increased LH transport (C4) overcomes the countering effect of reduced DSE transports due to a weakened equator-to-pole temperature gradient. As a result, remote atmospheric and oceanic processes drive additional surface warming that triggers interactions with local feedbacks (from C1) that cause further warming (C5).

Our conceptual model describes five overall ideas fundamental to AA. We acknowledge that an improved understanding of individual processes is critical for producing reliable Arctic warming projections and resolving inter-model differences. However, our conceptual model highlights the need to accurately account for local feedback and remote process interactions within the context of the annual cycle to constrain the likelihood that future AA will be on the high-end of model projections.

These five ideas fundamental to AA are not all-encompassing. We acknowledge that the highly coupled nature of the atmosphere, hydrosphere, cryosphere, land, and biosphere means other processes such as permafrost thawing, aerosol-cloud interactions, glacier melt, land use change, among others can influence future AA. These processes, however, are either not included or overly simplified in model simulations or are considered of secondary importance. An improved understanding of individual processes is critical for producing reliable Arctic climate projections and resolving inter-model differences. As model fidelity advances and our knowledge expands, we envision that new knowledge will build upon the fundamentals described in our conceptual model.

CONCLUSION, NEXT STEPS, AND FUTURE WORK

Arctic Amplification is a fundamental aspect of Earth's climate as documented in a range of contexts: paleoclimate, present-day observations, and models of varying complexities. Despite these observations and our current understanding, a complete theory of Arctic Amplification remains elusive. Gaps in our understanding have thwarted reliable surface temperature and sea ice projections due to anthropogenic forcing. After reviewing the current understanding of Arctic Amplification and proposing a conceptual model, we have identified key knowledge gaps and recommendations to accelerate progress.

Recommendations

1. A sustained observing system that resolves key Arctic processes is vital. A pursuit is underway (e.g., integrated Arctic Observing Network (AON)) and this work must continue. In addition, we recommend routine Arctic field expeditions with a MOSAiC-like (https://mosaic-expedition.org) scope to provide the missing data needed to advance understanding (Shupe et al., 2020) for all seasons. Our vision is a permanent, floating Central Arctic observatory.
2. Arctic surface energy budget uncertainties inhibit robust conclusions of critical atmosphere-sea ice-ocean processes with signals <10–20 W m^{-2}. We recommend a focus on advancing satellite-based measurement approaches to obtain Arctic-wide surface energy budget information (e.g., advanced IR sounder radiance assimilation; Smith et al., 2021).
3. A quantitative understanding of how individual physical parameterization schemes influence feedback uncertainty is lacking. We recommend modeling experiments, intercomparison studies, and sophisticated statistical analyses (e.g., data-driven causality discovery methods) to quantify the sensitivity of Arctic feedbacks to physical parameterization schemes. An experimental protocol enabling the community to characterize these links across models and parameterization schemes is needed.
4. Surface turbulent flux schemes vary across climate models, producing fluxes that differ markedly from observations. We recommend a coordinated intercomparison of high-latitude surface turbulent flux parameterizations for "standard" cases

(e.g., on-sea ice flow, off-sea ice flow, ocean with and without sea ice, etc.) with adequate observational constraints to identify the magnitude and source of model bias.
5. Reliable Arctic projections require an accurate accounting of local feedback and remote process interactions within the context of the annual cycle. We recommend that research on how local feedback and remote process interactions influence the sea ice annual cycle should be a near-term research focus. An improved understanding of these energy exchanges and interactions will accelerate our understanding of Arctic Amplification.
6. While energy balance models and feedback diagnostic frameworks are indispensable, these frameworks obscure the episodic nature of time-averaged quantities and the links between small-scale processes and long-term change. We recommend the influence of episodic variability on Arctic Amplification as a key research focus area, complementary to recommendation 5. Specifically, research into how the Arctic system dissipates energy from heat and moisture transport events, air mass transformation, and cloud formation is needed.
7. Regional climate change indicators for policy targets should be adopted to account for the uneven spatial distribution of climate change impacts and risks. The adoption of regional climate change targets would help to raise the priority of Arctic science.
8. Feedback diagnostic frameworks contain ambiguities and inconsistencies that make physical interpretation unclear. For instance, the lapse rate feedback is defensible in the tropics where moist convection couples the surface and upper troposphere, however its interpretation at high latitudes is less clear. We recommend a working group tasked to rethink feedback definitions and diagnostic frameworks, making them more process-oriented.

Polar amplification has been studied in depth for at least 50 years. While the leading explanation for amplified polar warming remains the surface albedo feedback and strong stratification at high latitudes, new details highlight the important role of atmosphere, ocean, and sea ice coupling processes. The highly coupled nature of the polar regions is a source of substantial uncertainty in regional climate projections. Our understanding of polar amplification has been wedded to computational and technological advances that have enabled more complex climate simulations with more detailed physical parameterizations. The role of observations has also evolved from a tool for model tuning to now being used for direct analysis.

While these advances have contributed to our understanding of polar amplification and must continue, an important step remains; to raise Arctic climate sensitivity on the climate modeling priority list, giving it equal priority to global climate sensitivity. Currently, state-of-the-art knowledge of Arctic processes (e.g., surface turbulent flux bulk formula) have not yet been widely implemented in climate models (Bourassa, 2013). Given the rapidly changing Arctic sea ice conditions, older parameterizations developed under thicker, multi-year sea ice conditions are likely to be less applicable in the 'new' Arctic with a predominantly seasonal sea ice cover. Giving Arctic climate sensitivity a high priority ensures the rapid integration of knowledge into climate models and will accelerate the reduction in Arctic climate projection uncertainty.

AUTHOR CONTRIBUTIONS

All authors listed have made a substantial, direct, and intellectual contribution to the work and approved it for publication.

FUNDING

PT, RB, and LB are supported by the NASA Interdisciplinary Studies Program (NNH19ZDA001N-IDS). PT, RB, SS, and YH are support by the NASA Radiation Budget Science Project. IT is funded through the NSERC RGPIN-2021-02720 grant. NF is supported by the US National Science foundation (NSF AGS-1753034). WL is supported by the Alfred P. Sloan Foundation as a Research Fellow, and is also supported by U.S. National Science Foundation (AGS-2053121). Matthew Henry is supported by NERC grant number NE/T00942X/1, under a NERC-NSF partnership named "Dynamics of Warm Past and Future Climates".

REFERENCES

Abe, M., Nozawa, T., Ogura, T., and Takata, K. (2015). Effect of Retreating Sea Ice on Arctic Cloud Cover in Simulated Recent Global Warming. *Atmos. Chem. Phys. Discuss.* 15 (12), 17527–17552. doi:10.5194/acpd-15-17527-2015

Ådlandsvik, B., and Loeng, H. (1991). A Study of the Climatic System in the Barents Sea. *Polar Res.* 10 (1), 45–50. doi:10.3402/polar.v10i1.6726

Alexeev, V. A., Langen, P. L., and Bates, J. R. (2005). Polar Amplification of Surface Warming on an Aquaplanet in "Ghost Forcing" Experiments without Sea Ice Feedbacks. *Clim. Dyn.* 24 (7–8), 655–666. doi:10.1007/s00382-005-0018-3

Alexeev, V. A. (2003). Sensitivity to CO2 Doubling of an Atmospheric GCM Coupled to an Oceanic Mixed Layer: a Linear Analysis. *Clim. Dyn.* 20 (7), 775–787. doi:10.1007/s00382-003-0312-x

Alkama, R., Taylor, P. C., Garcia-San Martin, L., Douville, H., Duveiller, G., Forzieri, G., et al. (2020). Clouds Damp the Radiative Impacts of Polar Sea Ice Loss. *The Cryosphere* 14 (8), 2673–2686. doi:10.5194/tc-14-2673-2020

Armour, K. C., Bitz, C. M., and Roe, G. H. (2013). Time-Varying Climate Sensitivity from Regional Feedbacks. *J. Clim.* 26 (13), 4518–4534. doi:10.1175/JCLI-D-12-00544.1

Armour, K. C., Siler, N., Donohoe, A., and Roe, G. H. (2019). Meridional Atmospheric Heat Transport Constrained by Energetics and Mediated by Large-Scale Diffusion. *J. Clim.* 32 (12), 3655–3680. doi:10.1175/jcli-d-18-0563.1

Arrhenius, S. (1896). XXXI.On the Influence of Carbonic Acid in the Air upon the Temperature of the Ground. *Lond. Edinb. Dublin Phil. Mag. J. Sci.* 41 (251), 237–276. doi:10.1080/14786449608620846

Årthun, M., Eldevik, T., Smedsrud, L. H., Skagseth, Ø., and Ingvaldsen, R. B. (2012). Quantifying the Influence of Atlantic Heat on Barents Sea Ice Variability and Retreat*. *J. Clim.* 25 (13), 4736–4743. doi:10.1175/JCLI-D-11-00466.1

Arzel, O., Fichefet, T., Goosse, H., and Dufresne, J.-L. (2007). Causes and Impacts of Changes in the Arctic Freshwater Budget during the Twentieth and Twenty-First Centuries in an AOGCM. *Clim. Dyn.* 30 (1), 37–58. doi:10.1007/s00382-007-0258-5

Baggett, C., and Lee, S. (2017). An Identification of the Mechanisms that Lead to Arctic Warming during Planetary-Scale and Synoptic-Scale Wave Life Cycles. *J. Atmos Sci* 74 (6), 1859–1877. doi:10.1175/JAS-D-16-0156.1

Barrett, A. I., Hogan, R. J., and Forbes, R. M. (2017). Why Are Mixed-phase Altocumulus Clouds Poorly Predicted by Large-Scale Models? Part 1. Physical Processes. *J. Geophys. Res. Atmos.* 122 (18), 9903–9926. doi:10.1002/2016JD026321

Barton, N. P., Klein, S. A., Boyle, J. S., and Zhang, Y. Y. (2012). Arctic Synoptic Regimes: Comparing Domain-wide Arctic Cloud Observations with CAM4 and CAM5 during Similar Dynamics. *J. Geophys. Res.* 117 (D15), a–n. doi:10.1029/2012JD017589

Baxter, I., Ding, Q., Schweiger, A., L'Heureux, M., Baxter, S., Wang, T., et al. (2019). How Tropical Pacific Surface Cooling Contributed to Accelerated Sea Ice Melt from 2007 to 2012 as Ice Is Thinned by Anthropogenic Forcing. *J. Clim.* 32 (24), 8583–8602. doi:10.1175/JCLI-D-18-0783.1

Beesley, J. A., and Moritz, R. E. (1999). Toward an Explanation of the Annual Cycle of Cloudiness over the Arctic Ocean. *J. Clim.* 12 (2), 395–415. doi:10.1175/1520-0442(1999)012<0395:TAEOTA>2.0.CO;2

Bekryaev, R. V., Polyakov, I. V., and Alexeev, V. A. (2010). Role of Polar Amplification in Long-Term Surface Air Temperature Variations and Modern Arctic Warming. *J. Clim.* 23 (14), 3888–3906. doi:10.1175/2010JCLI3297.1

Bengtsson, L., Semenov, V. A., and Johannessen, O. M. (2004). The Early Twentieth-Century Warming in the Arctic-A Possible Mechanism. *J. Clim.* 17 (20), 40452–44057. doi:10.1175/1520-0442(2004)017<4045:tetwit>2.0.co;2

Bintanja, R., Graversen, R. G., and Hazeleger, W. (2011). Arctic winter Warming Amplified by the thermal Inversion and Consequent Low Infrared Cooling to Space. *Nat. Geosci* 4 (11), 758–761. doi:10.1038/ngeo1285

Bintanja, R., and van der Linden, E. C. (2013). The Changing Seasonal Climate in the Arctic. *Sci. Rep.* 3 (1), 1556. doi:10.1038/srep01556

Bitz, C. M., Gent, P. R., Woodgate, R. A., Holland, M. M., and Lindsay, R. (2006). The Influence of Sea Ice on Ocean Heat Uptake in Response to Increasing CO2. *J. Clim.* 19 (11), 2437–2450. doi:10.1175/JCLI3756.1

Blackport, R., and Kushner, P. J. (2016). The Transient and Equilibrium Climate Response to Rapid Summertime Sea Ice Loss in CCSM4. *J. Clim.* 29 (2), 401–417. doi:10.1175/JCLI-D-15-0284.1

Bliss, A. C., and Anderson, M. R. (2018). Arctic Sea Ice Melt Onset Timing from Passive Microwave-Based and Surface Air Temperature-Based Methods. *J. Geophys. Res. Atmos.* 123 (17), 9063–9080. doi:10.1029/2018jd028676

Boeke, R. C., and Taylor, P. C. (2018). Seasonal Energy Exchange in Sea Ice Retreat Regions Contributes to Differences in Projected Arctic Warming. *Nat. Commun.* 9 (1), 5017. doi:10.1038/s41467-018-07061-9

Boeke, R. C., Taylor, P. C., and Sejas, S. A. (2021). On the Nature of the Arctic's Positive Lapse-Rate Feedback. *Geophys. Res. Lett.* 48 (1), e2020GL091109. doi:10.1029/2020GL091109

Boisvert, L. N., Markus, T., and Vihma, T. (2013). Moisture Flux Changes and Trends for the Entire Arctic in 2003-2011 Derived from EOS Aqua Data. *J. Geophys. Res. Oceans* 118 (10), 5829–5843. doi:10.1002/jgrc.20414

Boisvert, L. N., and Stroeve, J. C. (2015). The Arctic Is Becoming Warmer and Wetter as Revealed by the Atmospheric Infrared Sounder. *Geophys. Res. Lett.* 42 (11), 4439–4446. doi:10.1002/2015GL063775

Boisvert, L. N., Wu, D. L., and Shie, C.-L. (2015). Increasing Evaporation Amounts Seen in the Arctic between 2003 and 2013 from AIRS Data. *J. Geophys. Res. Atmos.* 120 (14), 6865–6881. doi:10.1002/2015JD023258

Bourassa, M. A., Gille, S. T., Bitz, C., Carlson, D., Cerovecki, I., Clayson, C. A., et al. (2013). High-Latitude Ocean and Sea Ice Surface Fluxes: Challenges for Climate Research. *Bull. Amer. Meteorol. Soc.* 94 (3), 403–423. doi:10.1175/BAMS-D-11-00244.1

Broecker, W. S. (1975). Climatic Change: Are We on the Brink of a Pronounced Global Warming? *Science* 189 (4201), 460–463. doi:10.1126/science.189.4201.460

Brown, R. D., and Robinson, D. A. (2011). Northern Hemisphere spring Snow Cover Variability and Change over 1922-2010 Including an Assessment of Uncertainty. *The Cryosphere* 5 (1), 219–229. doi:10.5194/tc-5-219-2011

Bryan, K., Komro, F. G., Manabe, S., and Spelman, M. J. (1982). Transient Climate Response to Increasing Atmospheric Carbon Dioxide. *Science* 215, 56–58. doi:10.1126/science.215.4528.56

Budyko, M. I. (1966). "Polar Ice and Climate," in Proceedings of the Symposium on the Arctic Heat Budget and Atmospheric Circulation (Santa Monica, California: Rand Corporation).

Budyko, M. I. (1969). The Effect of Solar Radiation Variations on the Climate of the Earth. *Tellus* 21 (5), 611–619. doi:10.3402/tellusa.v21i5.10109

Burt, M. A., Randall, D. A., and Branson, M. D. (2016). Dark Warming. *J. Clim.* 29 (2), 705–719. doi:10.1175/jcli-d-15-0147.1

Cai, M. (2005). Dynamical Amplification of Polar Warming. *Geophys. Res. Lett.* 32 (22), a–n. doi:10.1029/2005GL024481

Cai, M. (2006). Dynamical Greenhouse-Plus Feedback and Polar Warming Amplification. Part I: A Dry Radiative-Transportive Climate Model. *Clim. Dyn.* 26 (7–8), 661–675. doi:10.1007/s00382-005-0104-6

Cai, M., and Lu, J. (2009). A New Framework for Isolating Individual Feedback Processes in Coupled General Circulation Climate Models. Part II: Method Demonstrations and Comparisons. *Clim. Dyn.* 32 (6), 887–900. doi:10.1007/s00382-008-0424-4

Caldwell, P. M., Bretherton, C. S., Zelinka, M. D., Klein, S. A., Santer, B. D., and Sanderson, B. M. (2014). Statistical Significance of Climate Sensitivity Predictors Obtained by Data Mining. *Geophys. Res. Lett.* 41 (5), 1803–1808. doi:10.1002/2014GL059205

Cardinale, C. J., Rose, B. E. J., Lang, A. L., and Donohoe, A. (2021). Stratospheric and Tropospheric Flux Contributions to the Polar Cap Energy Budgets. *J. Clim.* 34 (11), 4261–4278. JCLI-D-20-0722.1.xml. doi:10.1175/jcli-d-20-0722.1

Cavalieri, D. J., Parkinson, C. L., Gloersen, P., and Zwally, H. (1996). "Sea Ice Concentrations from Nimbus-7 SMMR and DMSP SSM/I-SSMIS Passive Microwave Data," in *[2003–2016], NASA DAAC at the Natl. Snow and Ice Data Cent.* (Boulder, Colo: NSIDC). [Updated yearly].

Cess, R. D., and Potter, G. L. (1988). A Methodology for Understanding and Intercomparing Atmospheric Climate Feedback Processes in General Circulation Models. *J. Geophys. Res.* 93 (D7), 8305–8314. doi:10.1029/JD093iD07p08305

Cess, R. D., Potter, G. L., Blanchet, J. P., Boer, G. J., Del Genio, A. D., Déqué, M., et al. (1990). Intercomparison and Interpretation of Climate Feedback Processes in 19 Atmospheric General Circulation Models. *J. Geophys. Res.* 95 (D10), 16601–16615. doi:10.1029/JD095iD10p16601

Cess, R. D., Potter, G. L., Blanchet, J. P., Boer, G. J., Ghan, S. J., Kiehl, J. T., et al. (1989). Interpretation of Cloud-Climate Feedback as Produced by 14 Atmospheric General Circulation Models. *Science* 245 (4917), 513–516. doi:10.1126/science.245.4917.513

Cess, R. D., Potter, G. L., Zhang, M.-H., Blanchet, J.-P., Chalita, S., Colman, R., et al. (1991). Interpretation of Snow-Climate Feedback as Produced by 17 General Circulation Models. *Science* 253 (5022), 888–892. doi:10.1126/science.253.5022.888

Chung, C. E., and Räisänen, P. (2011). Origin of the Arctic Warming in Climate Models. *Geophys. Res. Lett.* 38 (21), a–n. doi:10.1029/2011GL049816

Chung, E. S., Ha, K. J., Timmermann, A., Stuecker, M. F., Bodai, T., and Lee, S. K. (2021). Cold-Season Arctic Amplification Driven by Arctic Ocean-Mediated Seasonal Energy Transfer. *Earth's Future* 9 (2), e2020EF001898. doi:10.1029/2020EF001898

Coakley, J. A. (1977). Feedbacks in Vertical-Column Energy Balance Models. *J. Atmos. Sci.* 34, 465–470. doi:10.1175/1520-0469(1977)034<0465:FIVCEB>2.0.CO;2

Cohen, J., Zhang, X., Francis, J., Jung, T., Kwok, R., Overland, J., et al. (2020). Divergent Consensuses on Arctic Amplification Influence on Midlatitude Severe winter Weather. *Nat. Clim. Chang.* 10 (1), 20–29. doi:10.1038/s41558-019-0662-y

Creamean, J. M., Hill, T. C. J., DeMott, P. J., Uetake, J., Kreidenweis, S., and Douglas, T. A. (2020). Thawing Permafrost: an Overlooked Source of Seeds for Arctic Cloud Formation. *Environ. Res. Lett.* 15 (8), 084022. doi:10.1088/1748-9326/ab87d3

Cronin, T. W., and Jansen, M. F. (2016). Analytic Radiative-advective Equilibrium as a Model for High-latitude Climate. *Geophys. Res. Lett.* 43 (1), 449–457. doi:10.1002/2015GL067172

Crook, J. A., Forster, P. M., and Stuber, N. (2011). Spatial Patterns of Modeled Climate Feedback and Contributions to Temperature Response and Polar Amplification. *J. Clim.* 24 (14), 3575–3592. doi:10.1175/2011JCLI3863.1

Curry, J. A., Schramm, J. L., Rossow, W. B., and Randall, D. (1996). Overview of Arctic Cloud and Radiation Characteristics. *J. Clim.* 9 (8), 1731–1764. doi:10.1175/1520-0442(1996)009<1731:OOACAR>2.0.CO;2

Dai, A., Luo, D., Song, M., and Liu, J. (2019). Arctic Amplification Is Caused by Sea-Ice Loss under Increasing CO2. *Nat. Commun.* 10 (1), 121. doi:10.1038/s41467-018-07954-9

Deser, C., Tomas, R., Alexander, M., and Lawrence, D. (2010). The Seasonal Atmospheric Response to Projected Arctic Sea Ice Loss in the Late Twenty-First Century. *J. Clim.* 23 (2), 333–351. doi:10.1175/2009jcli3053.1

Deser, C., Tomas, R. A., and Sun, L. (2015). The Role of Ocean-Atmosphere Coupling in the Zonal-Mean Atmospheric Response to Arctic Sea Ice Loss. *J. Clim.* 28 (6), 2168–2186. doi:10.1175/JCLI-D-14-00325.1

Dickinson, R. E., Meehl, G. A., and Washington, W. M. (1987). Ice-albedo Feedback in a CO2-doubling Simulation. *Climatic Change* 10 (3), 241–248. doi:10.1007/BF00143904

Ding, Q., Schweiger, A., L'Heureux, M., Battisti, D. S., Po-Chedley, S., Johnson, N. C., et al. (2017). Influence of High-Latitude Atmospheric Circulation Changes on Summertime Arctic Sea Ice. *Nat. Clim Change* 7, 289–295. doi:10.1038/NCLIMATE3241

Ding, Q., Schweiger, A., L'Heureux, M., Steig, E. J., Battisti, D. S., Johnson, N. C., et al. (20192019). Fingerprints of Internal Drivers of Arctic Sea Ice Loss in Observations and Model Simulations. *Nat. Geosci* 12, 28–33. doi:10.1038/s41561-018-0256-8

Ding, Q., Wallace, J. M., Battisti, D. S., Steig, E. J., Gallant, A. J. E., Kim, H.-J., et al. (2014). Tropical Forcing of the Recent Rapid Arctic Warming in Northeastern Canada and Greenland. *Nature* 509, 209–212. doi:10.1038/nature13260

Dmitrenko, I. A., Polyakov, I. V., Kirillov, S. A., Timokhov, L. A., Frolov, I. E., Sokolov, V. T., et al. (2008). Toward a Warmer Arctic Ocean: Spreading of the Early 21st century Atlantic Water Warm Anomaly along the Eurasian Basin Margins. *J. Geophys. Res.* 113 (C5). doi:10.1029/2007JC004158

Donohoe, A., Blanchard-Wrigglesworth, E., Schweiger, A., and Rasch, P. J. (2020). The Effect of Atmospheric Transmissivity on Model and Observational Estimates of the Sea Ice Albedo Feedback. *J. Clim.* 33 (13), 5743–5765. doi:10.1175/JCLI-D-19-0674.1

Duan, L., Cao, L., and Caldeira, K. (2019). Estimating Contributions of Sea Ice and Land Snow to Climate Feedback. *J. Geophys. Res. Atmos.* 124 (1), 199–208. doi:10.1029/2018JD029093

Duncan, B. N., Ott, L. E., Abshire, J. B., Brucker, L., Carroll, M. L., Carton, J., et al. (2020). Space-Based Observations for Understanding Changes in the Arctic-Boreal Zone. *Rev. Geophys.* 58 (1), e2019RG000652. doi:10.1029/2019RG000652

Dwyer, J. G., Biasutti, M., and Sobel, A. H. (2012). Projected Changes in the Seasonal Cycle of Surface Temperature. *J. Clim.* 25 (18), 6359–6374. doi:10.1175/JCLI-D-11-00741.1

English, J. M., Kay, J. E., Gettelman, A., Liu, X., Wang, Y., Zhang, Y., et al. (2014). Contributions of Clouds, Surface Albedos, and Mixed-phase Ice Nucleation Schemes to Arctic Radiation Biases in CAM5. *J. Clim.* 27 (13), 5174–5197. doi:10.1175/JCLI-D-13-00608.1

Ervens, B., Feingold, G., Sulia, K., and Harrington, J. (2011). The Impact of Microphysical Parameters, Ice Nucleation Mode, and Habit Growth on the Ice/liquid Partitioning in Mixed-phase Arctic Clouds. *J. Geophys. Res.* 116 (D17). doi:10.1029/2011JD015729

Eyring, V., Bony, S., Meehl, G. A., Senior, C. A., Stevens, B., Stouffer, R. J., et al. (2016). Overview of the Coupled Model Intercomparison Project Phase 6 (CMIP6) Experimental Design and Organization. *Geosci. Model. Dev.* 9, 1937–1958. doi:10.5194/gmd-9-1937-2016

Fan, J., Wang, Y., Rosenfeld, D., and Liu, X. (2016). Review of Aerosol-Cloud Interactions: Mechanisms, Significance, and Challenges. *J. Atmos. Sci.* 73 (11), 4221–4252. doi:10.1175/JAS-D-16-0037.1

Feldl, N., Anderson, B. T., and Bordoni, S. (2017b). Atmospheric Eddies Mediate Lapse Rate Feedback and Arctic Amplification. *J. Clim.* 30 (22), 9213–9224. doi:10.1175/JCLI-D-16-0706.1

Feldl, N., Bordoni, S., and Merlis, T. M. (2017a). Coupled High-Latitude Climate Feedbacks and Their Impact on Atmospheric Heat Transport. *J. Clim.* 30 (1), 189–201. doi:10.1175/JCLI-D-16-0324.1

Feldl, N., and Merlis, T. M. (2021). Polar Amplification in Idealized Climates: The Role of Ice, Moisture, and Seasons. *Geophys. Res. Lett.* 48, e2021GL094130. doi:10.1029/2021GL094130

Feldl, N., Po-Chedley, S., Singh, H. K. A., Hay, S., and Kushner, P. J. (2020). Sea Ice and Atmospheric Circulation Shape the High-Latitude Lapse Rate Feedback. *Npj Clim. Atmos. Sci.* 3 (1), 1–9. doi:10.1038/s41612-020-00146-7

Feldl, N., and Roe, G. H. (2013). Four Perspectives on Climate Feedbacks. *Geophys. Res. Lett.* 40 (15), 4007–4011. doi:10.1002/grl.50711

Flannery, B. P. (1984). Energy Balance Models Incorporating Transport of Thermal and Latent Energy. *J. Atmos. Sci.* 41 (3), 414–421. https://journals.ametsoc.org/view/journals/atsc/41/3/1520-0469_1984_041_0414_ebmito_2_0_co_2.xml.

Furtado, K., and Field, P. (2017). The Role of Ice Microphysics Parametrizations in Determining the Prevalence of Supercooled Liquid Water in High-Resolution Simulations of a Southern Ocean Midlatitude Cyclone. *J. Atmos. Sci.* 74 (6), 2001–2021. doi:10.1175/JAS-D-16-0165.1

GISTEMP Team (2021). *GISS Surface Temperature Analysis (GISTEMP), Version 4*. New York, NY: NASA Goddard Institute for Space Studies. Available at: https://data.giss.nasa.gov/gistemp/ (Accessed 26 April, 2021).

Goosse, H., Kay, J. E., Armour, K. C., Bodas-Salcedo, A., Chepfer, H., Docquier, D., et al. (2018). Quantifying Climate Feedbacks in Polar Regions. *Nat. Commun.* 9 (1), 1919. doi:10.1038/s41467-018-04173-0

Goosse, H., Selten, F., Haarsma, R., and Opsteegh, J. (2003). Large Sea-Ice Volume Anomalies Simulated in a Coupled Climate Model. *Clim. Dyn.* 20 (5), 523–536. doi:10.1007/s00382-002-0290-4

Graham, R. M., Cohen, L., Petty, A. A., Boisvert, L. N., Rinke, A., Hudson, S. R., et al. (2017a). Increasing Frequency and Duration of Arctic winter Warming Events. *Geophys. Res. Lett.* 44 (13), 6974–6983. doi:10.1002/2017GL073395

Graham, R. M., Cohen, L., Petty, A. A., Boisvert, L. N., Rinke, A., Hudson, S. R., et al. (2017b). Increasing Frequency and Duration of Arctic winter Warming Events. *Geophys. Res. Lett.* 44 (13), 6974–6983. doi:10.1002/2017GL073395

Graversen, R. G., and Burtu, M. (2016). Arctic Amplification Enhanced by Latent Energy Transport of Atmospheric Planetary Waves. *Q.J.R. Meteorol. Soc.* 142 (698), 2046–2054. doi:10.1002/qj.2802

Graversen, R. G., Langen, P. L., and Mauritsen, T. (2014). Polar Amplification in CCSM4: Contributions from the Lapse Rate and Surface Albedo Feedbacks. *J. Clim.* 27 (12), 4433–4450. doi:10.1175/JCLI-D-13-00551.1

Graversen, R. G., and Langen, P. L. (2019). On the Role of the Atmospheric Energy Transport in 2 × CO2-Induced Polar Amplification in CESM1. *J. Clim.* 32 (13), 3941–3956. doi:10.1175/JCLI-D-18-0546.1

Graversen, R. G., Mauritsen, T., Tjernström, M., Källén, E., and Svensson, G. (2008). Vertical Structure of Recent Arctic Warming. *Nature* 451 (7174), 53–56. doi:10.1038/nature06502

Graversen, R. G., and Wang, M. (2009). Polar Amplification in a Coupled Climate Model with Locked Albedo. *Clim. Dyn.* 33 (5), 629–643. doi:10.1007/s00382-009-0535-6

Guemas, V., and Salas-Mélia, D. (2008). Simulation of the Atlantic Meridional Overturning Circulation in an Atmosphere-Ocean Global Coupled Model. Part II: Weakening in a Climate Change experiment: a Feedback Mechanism. *Clim. Dyn.* 30 (7), 831–844. doi:10.1007/s00382-007-0328-8

Hahn, L. C., Armour, K. C., Zelinka, M. D., Bitz, C. M., and Donohoe, A. (2021). Contributions to Polar Amplification in CMIP5 and CMIP6 Models. *Front. Earth Sci.* 9, 710036. doi:10.3389/feart.2021.710036

Hall, A., Cox, P., Huntingford, C., and Klein, S. (2019). Progressing Emergent Constraints on Future Climate Change. *Nat. Clim. Chang.* 9 (4), 269–278. doi:10.1038/s41558-019-0436-6

Hall, A., and Qu, X. (2006). Using the Current Seasonal Cycle to Constrain Snow Albedo Feedback in Future Climate Change. *Geophys. Res. Lett.* 33 (3). doi:10.1029/2005GL025127

Hall, A. (2004). The Role of Surface Albedo Feedback in Climate. *J. Clim.* 17 (7), 1550–1568. doi:10.1175/1520-0442(2004)017<1550:trosaf>2.0.co;2

Hansen, J., Lacis, A., Rind, D., Russell, G., Stone, P., Fung, I., et al. (1984). Climate Sensitivity: Analysis of Feedback Mechanisms. *Feedback* 1, 1–3. doi:10.1029/gm029p0130

Hartmann, M., Blunier, T., Brügger, S. O., Schmale, J., Schwikowski, M., Vogel, A., et al. (2019). Variation of Ice Nucleating Particles in the European Arctic over the Last Centuries. *Geophys. Res. Lett.* 46 (7), 4007–4016. doi:10.1029/2019GL082311

He, M., Hu, Y., Chen, N., Wang, D., Huang, J., and Stamnes, K. (2019). High Cloud Coverage over Melted Areas Dominates the Impact of Clouds on the Albedo Feedback in the Arctic. *Sci. Rep.* 9 (1), 9529. doi:10.1038/s41598-019-44155-w

Hegyi, B. M., and Deng, Y. (2017). Dynamical and Thermodynamical Impacts of High- and Low-Frequency Atmospheric Eddies on the Initial Melt of Arctic Sea Ice. *J. Clim.* 30 (3), 865–883. doi:10.1175/JCLI-D-15-0366.1

Hegyi, B. M., and Taylor, P. C. (2018). The Unprecedented 2016-2017 Arctic Sea Ice Growth Season: The Crucial Role of Atmospheric Rivers and Longwave Fluxes. *Geophys. Res. Lett.* 45 (10), 5204–5212. doi:10.1029/2017GL076717

Held, I. M. (2005). The Gap between Simulation and Understanding in Climate Modeling. *Bull. Amer. Meteorol. Soc.* 86 (11), 1609–1614. doi:10.1175/BAMS-86-11-1609

Henry, M., Merlis, T. M., Lutsko, N. J., and Rose, B. E. J. (2021). Decomposing the Drivers of Polar Amplification with a Single-Column Model. *J. Clim.* 34 (6), 2355–2365. doi:10.1175/JCLI-D-20-0178.1

Henry, M., and Merlis, T. M. (2019). The Role of the Nonlinearity of the Stefan-Boltzmann Law on the Structure of Radiatively Forced Temperature Change. *J. Clim.* 32 (2), 335–348. doi:10.1175/JCLI-D-17-0603.1

Henry, M., and Vallis, G. K. (2021). Reduced High-Latitude Land Seasonality in Climates with Very High Carbon Dioxide. *J. Clim.* 1 (aop), 1–38. doi:10.1175/JCLI-D-21-0131.1

Hersbach, H., Bell, B., Berrisford, P., Biavati, G., Horányi, A., Muñoz Sabater, J., et al. (2019). ERA5 Monthly Averaged Data on Pressure Levels from 1979 to Present. Copernicus Climate Change Service (C3S) Climate Data Store (CDS). Available at: https://cds.climate.copernicus.eu/cdsapp#!/dataset/reanalysis-era5-pressure-levels-monthly-means (Accessed March 3, 2021).

Hibler, W. D., III. (1979). A Dynamic Thermodynamic Sea Ice Model. *J. Phys. Oceanogr.* 9 (4), 815–846. doi:10.1175/1520-0485(1979)009<0815:adtsim>2.0.co;2

Hind, A., Zhang, Q., and Brattström, G. (2016). Problems Encountered when Defining Arctic Amplification as a Ratio. *Sci. Rep.* 6 (1), 30469. doi:10.1038/srep30469

Holland, M. M., Bailey, D. A., Briegleb, B. P., Light, B., and Hunke, E. (2012). Improved Sea Ice Shortwave Radiation Physics in CCSM4: The Impact of Melt Ponds and Aerosols on Arctic Sea Ice. *J. Clim.* 25 (5), 1413–1430. doi:10.1175/JCLI-D-11-00078.1

Holland, M. M., and Bitz, C. M. (2003). Polar Amplification of Climate Change in Coupled Models. *Clim. Dyn.* 21, 221–232. doi:10.1007/s00382-003-0332-6

Holland, M. M., Serreze, M. C., and Stroeve, J. (2010). The Sea Ice Mass Budget of the Arctic and its Future Change as Simulated by Coupled Climate Models. *Clim. Dyn.* 34 (2–3), 185–200. doi:10.1007/s00382-008-0493-4

Hu, X., Fan, H., Cai, M., Sejas, S. A., Taylor, P., and Yang, S. (2020). A Less Cloudy Picture of the Inter-model Spread in Future Global Warming Projections. *Nat. Commun.* 11 (1), 4472. doi:10.1038/s41467-020-18227-9

Hu, X., Taylor, P. C., Cai, M., Yang, S., Deng, Y., and Sejas, S. (2017). Inter-Model Warming Projection Spread: Inherited Traits from Control Climate Diversity. *Sci. Rep.* 7 (1), 4300. doi:10.1038/s41598-017-04623-7

Huang, Y., Ding, Q., Dong, X., Xi, B., and Baxter, I. (2021b). Summertime Low Clouds Mediate the Impact of the Large-Scale Circulation on Arctic Sea Ice. *Commun. Earth Environ.* 2 (1), 1–10. doi:10.1038/s43247-021-00114-w

Huang, Y., Dong, X., Bailey, D. A., Holland, M. M., Xi, B., DuVivier, A. K., et al. (2019a). Thicker Clouds and Accelerated Arctic Sea Ice Decline: The Atmosphere-Sea Ice Interactions in Spring. *Geophys. Res. Lett.* 46 (12), 6980–6989. doi:10.1029/2019GL082791

Huang, Y., Dong, X., Xi, B., and Deng, Y. (2019b). A Survey of the Atmospheric Physical Processes Key to the Onset of Arctic Sea Ice Melt in spring. *Clim. Dyn.* 52 (7), 4907–4922. doi:10.1007/s00382-018-4422-x

Huang, Y., Dong, X., Xi, B., Dolinar, E. K., and Stanfield, R. E. (2017b). The Footprints of 16 Year Trends of Arctic Springtime Cloud and Radiation Properties on September Sea Ice Retreat. *J. Geophys. Res. Atmos.* 122 (4), 2179–2193. doi:10.1002/2016JD026020

Huang, Y., Huang, H., and Shakirova, A. (2021a). The Nonlinear Radiative Feedback Effects in the Arctic Warming. *Front. Earth Sci.* 9, 693779. doi:10.3389/feart.2021.693779

Huang, Y., Xia, Y., and Tan, X. (2017a). On the Pattern of CO2 Radiative Forcing and Poleward Energy Transport. *J. Geophys. Res. Atmos.* 122 (2010), 10,578–10,593. doi:10.1002/2017JD027221

Hwang, Y.-T., Frierson, D. M. W., and Kay, J. E. (2011). Coupling between Arctic Feedbacks and Changes in Poleward Energy Transport. *Geophys. Res. Lett.* 38 (17), a–n. doi:10.1029/2011GL048546

Ingram, W. J., Wilson, C. A., and Mitchell, J. F. B. (1989). Modeling Climate Change: An Assessment of Sea Ice and Surface Albedo Feedbacks. *J. Geophys. Res.* 94 (D6), 8609–8622. doi:10.1029/JD094iD06p08609

Irish, V. E., Elizondo, P., Chen, J., Chou, C., Charette, J., Lizotte, M., et al. (2017). Ice-nucleating Particles in Canadian Arctic Sea-Surface Microlayer and Bulk Seawater. *Atmos. Chem. Phys.* 17 (17), 10583–10595. doi:10.5194/acp-17-10583-2017

Jahn, A., Sterling, K., Holland, M. M., Kay, J. E., Maslanik, J. A., Bitz, C. M., et al. (2012). Late-Twentieth-Century Simulation of Arctic Sea Ice and Ocean Properties in the CCSM4. *J. Clim.* 25 (5), 1431–1452. doi:10.1175/JCLI-D-11-00201.1

Jeevanjee, N., Hassanzadeh, P., Hill, S., and Sheshadri, A. (2017). A Perspective on Climate Model Hierarchies. *J. Adv. Model. Earth Syst.* 9 (4), 1760–1771. doi:10.1002/2017MS001038

Jungclaus, J. H., Lohmann, K., and Zanchettin, D. (2014). Enhanced 20th-century Heat Transfer to the Arctic Simulated in the Context of Climate Variations over the Last Millennium. *Clim. Past* 10 (6), 2201–2213. doi:10.5194/cp-10-2201-2014

Karcher, M. J., Gerdes, R., Kauker, F., and Köberle, C. (2003). Arctic Warming: Evolution and Spreading of the 1990s Warm Event in the Nordic Seas and the Arctic Ocean. *J. Geophys. Res.* 108 (C2), a–n. doi:10.1029/2001JC001265

Kato, S., Rose, F. G., Rutan, D. A., Thorsen, T. J., Loeb, N. G., Doelling, D. R., et al. (2018). Surface Irradiances of Edition 4.0 Clouds and the Earth's Radiant Energy System (CERES) Energy Balanced and Filled (EBAF) Data Product. *J. Clim.* 31 (11), 4501–4527. doi:10.1175/jcli-d-17-0523.1

Kay, J. E., Deser, C., Phillips, A., Mai, A., Hannay, C., Strand, G., et al. (2015). The Community Earth System Model (CESM) Large Ensemble Project: A Community Resource for Studying Climate Change in the Presence of Internal Climate Variability. *Bull. Am. Meteorol. Soc.* 96 (8), 1333–1349. doi:10.1175/BAMS-D-13-00255.1

Kay, J. E., and Gettelman, A. (2009). Cloud Influence on and Response to Seasonal Arctic Sea Ice Loss. *J. Geophys. Res.* 114 (D18), 1. doi:10.1029/2009JD011773

Kay, J. E., Holland, M. M., Bitz, C. M., Blanchard-Wrigglesworth, E., Gettelman, A., Conley, A., et al. (2012). The Influence of Local Feedbacks and Northward Heat Transport on the Equilibrium Arctic Climate Response to Increased Greenhouse Gas Forcing. *J. Clim.* 25 (16), 5433–5450. doi:10.1175/JCLI-D-11-00622.1

Kay, J. E., Holland, M. M., and Jahn, A. (2011). Inter-annual to Multi-Decadal Arctic Sea Ice Extent Trends in a Warming World. *Geophys. Res. Lett.* 38 (15), 1. doi:10.1029/2011GL048008

Kim, D., Kang, S. M., Shin, Y., and Feldl, N. (2018). Sensitivity of Polar Amplification to Varying Insolation Conditions. *J. Clim.* 31 (12), 4933–4947. doi:10.1175/JCLI-D-17-0627.1

Kim, K.-Y., Hamlington, B. D., Na, H., and Kim, J. (2016). Mechanism of Seasonal Arctic Sea Ice Evolution and Arctic Amplification. *The Cryosphere* 10 (5), 2191–2202. doi:10.5194/tc-10-2191-2016

Kim, K.-Y., Kim, J.-Y., Kim, J., Yeo, S., Na, H., Hamlington, B. D., et al. (2019). Vertical Feedback Mechanism of Winter Arctic Amplification and Sea Ice Loss. *Sci. Rep.* 9 (1), 1184. doi:10.1038/s41598-018-38109-x

Klein, S. A., McCoy, R. B., Morrison, H., Ackerman, A. S., Avramov, A., Boer, G. d., et al. (2009). Intercomparison of Model Simulations of Mixed-phase Clouds Observed during the ARM Mixed-phase Arctic Cloud Experiment. I: Single-Layer Cloud. *Q.J.R. Meteorol. Soc.* 135 (641), 979–1002. doi:10.1002/qj.416

Koenigk, T., and Brodeau, L. (2014). Ocean Heat Transport into the Arctic in the Twentieth and Twenty-First century in EC-Earth. *Clim. Dyn.* 42 (11), 3101–3120. doi:10.1007/s00382-013-1821-x

Komurcu, M., Storelvmo, T., Tan, I., Lohmann, U., Yun, Y., Penner, J. E., et al. (2014). Intercomparison of the Cloud Water Phase Among Global Climate Models. *J. Geophys. Res. Atmos.* 119 (6), 3372–3400. doi:10.1002/2013JD021119

Kwok, R. (2018). Arctic Sea Ice Thickness, Volume, and Multiyear Ice Coverage: Losses and Coupled Variability (1958-2018). *Environ. Res. Lett.* 13 (10), 105005. doi:10.1088/1748-9326/aae3ec

Laîné, A., Yoshimori, M., and Abe-Ouchi, A. (2016). Surface Arctic Amplification Factors in CMIP5 Models: Land and Oceanic Surfaces and Seasonality. *J. Clim.* 29 (9), 3297–3316. doi:10.1175/JCLI-D-15-0497.1

Langen, P. L., and Alexeev, V. A. (2007). Polar Amplification as a Preferred Response in an Idealized Aquaplanet GCM. *Clim. Dyn.* 29, 305–317. doi:10.1007/S00382-006-0221-X

Lawson, P., Gurganus, C., Woods, S., and Bruintjes, R. (2017). Aircraft Observations of Cumulus Microphysics Ranging from the Tropics to Midlatitudes: Implications for a "New" Secondary Ice Process. *J. Atmos. Sci.* 74 (9), 2899–2920. doi:10.1175/JAS-D-17-0033.1

Laxon, S., Peacock, N., and Smith, D. (2003). High Interannual Variability of Sea Ice Thickness in the Arctic Region. *Nature* 425 (6961), 947–950. doi:10.1038/nature02050

Lee, S. (2014). A Theory for Polar Amplification from a General Circulation Perspective. *Asia-pacific J. Atmos. Sci.* 50, 31–43. doi:10.1007/s13143-014-0024-7

Lee, S., Gong, T., Feldstein, S. B., Screen, J. A., and Simmonds, I. (2017). Revisiting the Cause of the 1989-2009 Arctic Surface Warming Using the Surface Energy Budget: Downward Infrared Radiation Dominates the Surface Fluxes. *Geophys. Res. Lett.* 44, 10654–10661. doi:10.1002/2017GL075375

Lee, S., Gong, T., Johnson, N., Feldstein, S. B., and Pollard, D. (2011). On the Possible Link between Tropical Convection and the Northern Hemisphere Arctic Surface Air Temperature Change between 1958 and 2001. *J. Clim.* 24 (16), 4350–4367. doi:10.1175/2011JCLI4003.1

Lee, S. (2012). Testing of the Tropically Excited Arctic Warming Mechanism (TEAM) with Traditional El Niño and La Niña. *J. Clim.* 25, 4015–4022. doi:10.1175/JCLI-D-12-00055.1

Lenssen, N. J. L., Schmidt, G. A., Hansen, J. E., Menne, M. J., Persin, A., Ruedy, R., et al. (2019). Improvements in the GISTEMP Uncertainty Model. *J. Geophys. Res. Atmos.* 124 (12), 6307–6326. doi:10.1029/2018JD029522

Letterly, A., Key, J., and Liu, Y. (2018). Arctic Climate: Changes in Sea Ice Extent Outweigh Changes in Snow Cover. *The Cryosphere* 12, 3373–3382. doi:10.5194/tc-12-3373-2018

Li, H., Fedorov, A., and Liu, W. (2021). AMOC Stability and Diverging Response to Arctic Sea Ice Decline in Two Climate Models. *J. Clim.* 34 (13), 1–47. doi:10.1175/JCLI-D-20-0572.1

Li, X., Krueger, S. K., Strong, C., Mace, G. G., and Benson, S. (2020). Midwinter Arctic Leads Form and Dissipate Low Clouds. *Nat. Commun.* 11 (1), 206. doi:10.1038/s41467-019-14074-5

Li, Z.-X., and Le Treut, H. (1992). Cloud-radiation Feedbacks in a General Circulation Model and Their Dependence on Cloud Modelling Assumptions. *Clim. Dyn.* 7 (3), 133–139. doi:10.1007/BF00211155

Liu, W., Fedorov, A., and Sévellec, F. (2019). The Mechanisms of the Atlantic Meridional Overturning Circulation Slowdown Induced by Arctic Sea Ice Decline. *J. Clim.* 32 (4), 977–996. doi:10.1175/JCLI-D-18-0231.1

Liu, W., and Fedorov, A. V. (2019). Global Impacts of Arctic Sea Ice Loss Mediated by the Atlantic Meridional Overturning Circulation. *Geophys. Res. Lett.* 46 (2), 944–952. doi:10.1029/2018GL080602

Liu, W., and Fedorov, A. (2021). Interaction Between Arctic Sea Ice and the Atlantic Meridional Overturning Circulation in a Warming Climate. *Clim. Dyn.* doi:10.1007/s00382-021-05993-5

Liu, Y., Key, J. R., Liu, Z., Wang, X., and Vavrus, S. J. (2012). A Cloudier Arctic Expected with Diminishing Sea Ice. *Geophys. Res. Lett.* 39 (5), a–n. doi:10.1029/2012GL051251

Loeb, N. G., Doelling, D. R., Wang, H., Su, W., Nguyen, C., Corbett, J. G., et al. (2018). Clouds and the Earth's Radiant Energy System (CERES) Energy Balanced and Filled (EBAF) Top-Of-Atmosphere (TOA) Edition-4.0 Data Product. *J. Clim.* 31 (2), 895–918. doi:10.1175/jcli-d-17-0208.1

Lu, J., and Cai, M. (2009b). A New Framework for Isolating Individual Feedback Processes in Coupled General Circulation Climate Models. Part I: Formulation. *Clim. Dyn.* 32 (6), 873–885. doi:10.1007/s00382-008-0425-3

Lu, J., and Cai, M. (2009a). Seasonality of Polar Surface Warming Amplification in Climate Simulations. *Geophys. Res. Lett.* 36 (16). doi:10.1029/2009GL040133

Maher, P., Gerber, E. P., Medeiros, B., Merlis, T. M., Sherwood, S., Sheshadri, A., et al. (2019). Model Hierarchies for Understanding Atmospheric Circulation. *Rev. Geophys.* 57 (2), 250–280. doi:10.1029/2018RG000607

Mahlstein, I., and Knutti, R. (2011). Ocean Heat Transport as a Cause for Model Uncertainty in Projected Arctic Warming. *J. Clim.* 24 (5), 1451–1460. doi:10.1175/2010JCLI3713.1

Manabe, S., Spelman, M. J., and Stouffer, R. J. (1992). Transient Responses of a Coupled Ocean-Atmosphere Model to Gradual Changes of Atmospheric CO2. Part II: Seasonal Response. *J. Clim.* 5 (2), 105–126. doi:10.1175/1520-0442(1992)005<0105:TROACO>2.0.CO;2

Manabe, S., and Stouffer, R. J. (1980). Sensitivity of a Global Climate Model to an Increase of CO2concentration in the Atmosphere. *J. Geophys. Res.* 85 (C10), 5529–5554. doi:10.1029/JC085iC10p05529

Manabe, S., Stouffer, R. J., Spelman, M. J., and Bryan, K. (1991). Transient Responses of a Coupled Ocean-Atmosphere Model to Gradual Changes of Atmospheric CO2. Part I. Annual Mean Response. *J. Clim.* 4 (8), 785–818. doi:10.1175/1520-0442(1991)004<0785:TROACO>2.0.CO;2

Manabe, S., and Wetherald, R. T. (1975). The Effects of Doubling the CO2Concentration on the Climate of a General Circulation Model. *J. Atmos. Sci.* 32 (1), 3–15. doi:10.1175/1520-0469(1975)032<0003:TEODTC>2.0.CO;2

Manabe, S., and Wetherald, R. T. (1967). Thermal Equilibrium of the Atmosphere with a Given Distribution of Relative Humidity. *J. Atmos. Sci.* 24 (3), 241–259. doi:10.1175/1520-0469(1967)024<0241:teotaw>2.0.co;2

Markus, T., Stroeve, J. C., and Miller, J. (2009). Recent Changes in Arctic Sea Ice Melt Onset, Freezeup, and Melt Season Length. *J. Geophys. Res. Oceans* 114 (C12). doi:10.1029/2009jc005436

Marshall, J., Scott, J. R., Armour, K. C., Campin, J.-M., Kelley, M., and Romanou, A. (2015). The Ocean's Role in the Transient Response of Climate to Abrupt Greenhouse Gas Forcing. *Clim. Dyn.* 44 (7), 2287–2299. doi:10.1007/s00382-014-2308-0

Maslanik, J., Stroeve, J., Fowler, C., and Emery, W. (2011). Distribution and Trends in Arctic Sea Ice Age through spring 2011. *Geophys. Res. Lett.* 38 (13), a–n. doi:10.1029/2011GL047735

McCoy, D. T., Tan, I., Hartmann, D. L., Zelinka, M. D., and Storelvmo, T. (2016). On the Relationships Among Cloud Cover, Mixed-phase Partitioning, and Planetary Albedo in GCMs. *J. Adv. Model. Earth Syst.* 8 (2), 650–668. doi:10.1002/2015MS000589

McCusker, K. E., Kushner, P. J., Fyfe, J. C., Sigmond, M., Kharin, V. V., and Bitz, C. M. (2017). Remarkable Separability of Circulation Response to Arctic Sea Ice Loss and Greenhouse Gas Forcing. *Geophys. Res. Lett.* 44 (15), 7955–7964. doi:10.1002/2017GL074327

Meehl, G. A., Collins, W. D., Boville, B. A., Kiehl, J. T., Wigley, T. M. L., and Arblaster, J. M. (2000). Response of the NCAR Climate System Model to Increased CO2and the Role of Physical Processes. *J. Clim.* 13 (11), 1879–1898. doi:10.1175/1520-0442(2000)013<1879:rotncs>2.0.co;2

Meredith, M., Sommerkorn, M., Cassotta, S., Derksen, C., Ekaykin, A., Hollowed, A., et al. (2019). "Polar Regions," in *IPCC Special Report on the Ocean and Cryosphere in a Changing Climate*. Editors H.-O. Pörtner, D. C. Roberts, V. Masson-Delmotte, P. Zhai, M. Tignor, E. Poloczanska, et al. (Geneva, Switzerland: Intergovernmental Panel on Climate Change). In press.

Merlis, T. M., and Henry, M. (2018). Simple Estimates of Polar Amplification in Moist Diffusive Energy Balance Models. *J. Clim.* 31 (15), 5811–5824. doi:10.1175/JCLI-D-17-0578.1

Merlis, T. M. (2014). Interacting Components of the Top-Of-Atmosphere Energy Balance Affect Changes in Regional Surface Temperature. *Geophys. Res. Lett.* 41 (20), 7291–7297. doi:10.1002/2014GL061700

Middlemas, E. A., Kay, J. E., Medeiros, B. M., and Maroon, E. A. (2020). Quantifying the Influence of Cloud Radiative Feedbacks on Arctic Surface Warming Using Cloud Locking in an Earth System Model. *Geophys. Res. Lett.* 47 (15), e2020GL089207. doi:10.1029/2020GL089207

Miller, G. H., Alley, R. B., Brigham-Grette, J., Fitzpatrick, J. J., Polyak, L., Serreze, M. C., et al. (2010). Arctic Amplification: Can the Past Constrain the Future? *Quat. Sci. Rev.* 29, 1779–1790. doi:10.1016/j.quascirev.2010.02.008

Mitchell, J. F. B., Senior, C. A., and Ingram, W. J. (1989). C02 and Climate: a Missing Feedback? *Nature* 341 (6238), 132–134. doi:10.1038/341132a0

Morrison, A. L., Kay, J. E., Chepfer, H., Guzman, R., and Yettella, V. (2018). Isolating the Liquid Cloud Response to Recent Arctic Sea Ice Variability Using Spaceborne Lidar Observations. *J. Geophys. Res. Atmos.* 123 (1), 473–490. doi:10.1002/2017JD027248

Morrison, A. L., Kay, J. E., Frey, W. R., Chepfer, H., and Guzman, R. (2019). Cloud Response to Arctic Sea Ice Loss and Implications for Future Feedback in the CESM1 Climate Model. *J. Geophys. Res. Atmos.* 124 (2), 1003–1020. doi:10.1029/2018JD029142

North, G. R. (2007). Theory of Energy-Balance Climate Models. *J. Atmos. Sci.* 32 (11), 2033–2043. https://journals.ametsoc.org/view/journals/atsc/32/11/1520-0469_1975_032_2033_toebcm_2_0_co_2.xml.

Nghiem, S. V., Rigor, I. G., Perovich, D. K., Clemente-Colón, P., Weatherly, J. W., and Neumann, G. (2007). Rapid Reduction of Arctic Perennial Sea Ice. *Geophys. Res. Lett.* 34 (19). doi:10.1029/2007GL031138

Nummelin, A., Li, C., and Hezel, P. J. (2017). Connecting Ocean Heat Transport Changes from the Midlatitudes to the Arctic Ocean. *Geophys. Res. Lett.* 44 (4), 1899–1908. doi:10.1002/2016GL071333

Nygård, T., Graversen, R. G., Uotila, P., Naakka, T., and Vihma, T. (2019). Strong Dependence of Wintertime Arctic Moisture and Cloud Distributions on Atmospheric Large-Scale Circulation. *J. Clim.* 32 (24), 8771–8790. doi:10.1175/JCLI-D-19-0242.1

Oldenburg, D., Armour, K. C., Thompson, L., and Bitz, C. M. (2018). Distinct Mechanisms of Ocean Heat Transport into the Arctic under Internal Variability and Climate Change. *Geophys. Res. Lett.* 45 (15), 7692–7700. doi:10.1029/2018GL078719

Oudar, T., Sanchez-Gomez, E., Chauvin, F., Cattiaux, J., Terray, L., and Cassou, C. (2017). Respective Roles of Direct GHG Radiative Forcing and Induced Arctic Sea Ice Loss on the Northern Hemisphere Atmospheric Circulation. *Clim. Dyn.* 49 (11), 3693–3713. doi:10.1007/s00382-017-3541-0

Park, H.-S., Kim, S.-J., Seo, K.-H., Stewart, A. L., Kim, S.-Y., and Son, S.-W. (2018). The Impact of Arctic Sea Ice Loss on Mid-holocene Climate. *Nat. Commun.* 9 (1), 4571. doi:10.1038/s41467-018-07068-2

Parkinson, C. L., and DiGirolamo, N. E. (2016). New Visualizations Highlight New Information on the Contrasting Arctic and Antarctic Sea-Ice Trends since the Late 1970s. *Remote Sensing Environ.* 183, 198–204. doi:10.1016/j.rse.2016.05.020

Pavelsky, T. M., Boé, J., Hall, A., and Fetzer, E. J. (2011). Atmospheric Inversion Strength over Polar Oceans in winter Regulated by Sea Ice. *Clim. Dyn.* 36 (5), 945–955. doi:10.1007/s00382-010-0756-8

Payne, A. E., Jansen, M. F., and Cronin, T. W. (2015). Conceptual Model Analysis of the Influence of Temperature Feedbacks on Polar Amplification. *Geophys. Res. Lett.* 42 (21), 9561–9570. doi:10.1002/2015GL065889

Pendergrass, A. G., Conley, A., and Vitt, F. M. (2018). Surface and Top-Of-Atmosphere Radiative Feedback Kernels for CESM-CAM5. *Earth Syst. Sci. Data* 10 (1), 317–324. doi:10.5194/essd-10-317-2018

Perovich, D. K., Light, B., Eicken, H., Jones, K. F., Runciman, K., and Nghiem, S. V. (2007). Increasing Solar Heating of the Arctic Ocean and Adjacent Seas, 1979-2005: Attribution and Role in the Ice-Albedo Feedback. *Geophys. Res. Lett.* 34 (19). doi:10.1029/2007GL031480

Persson, P. O. G., Shupe, M. D., Perovich, D., and Solomon, A. (2017). Linking Atmospheric Synoptic Transport, Cloud Phase, Surface Energy Fluxes, and Sea-Ice Growth: Observations of Midwinter SHEBA Conditions. *Clim. Dyn.* 49 (4), 1341–1364. doi:10.1007/s00382-016-3383-1

Pistone, K., Eisenman, I., and Ramanathan, V. (2014). Observational Determination of Albedo Decrease Caused by Vanishing Arctic Sea Ice. *Proc. Natl. Acad. Sci. USA* 111 (9), 3322–3326. doi:10.1073/pnas.1318201111

Pithan, F., and Mauritsen, T. (2014). Arctic Amplification Dominated by Temperature Feedbacks in Contemporary Climate Models. *Nat. Geosci* 7 (3), 181–184. doi:10.1038/ngeo2071

Pithan, F., Medeiros, B., and Mauritsen, T. (2014). Mixed-phase Clouds Cause Climate Model Biases in Arctic Wintertime Temperature Inversions. *Clim. Dyn.* 43 (1), 289–303. doi:10.1007/s00382-013-1964-9

Pithan, F., Svensson, G., Caballero, R., Chechin, D., Cronin, T. W., Ekman, A. M. L., et al. (2018). Role of Air-Mass Transformations in Exchange between the Arctic and Mid-latitudes. *Nat. Geosci* 11 (11), 805–812. doi:10.1038/s41561-018-0234-1

Previdi, M., Janoski, T. P., Chiodo, G., Smith, K. L., and Polvani, L. M. (2020). Arctic Amplification: A Rapid Response to Radiative Forcing. *Geophys. Res. Lett.* 47 (17), e2020GL089933. doi:10.1029/2020GL089933

Rakipova, L. R. (1966). "The Influence of the Arctic Ice Cover on the Zonal Distribution of Atmospheric Temperature," in Proceedings of the Symposium on the Arctic Heat Budget and Atmospheric Circulation (Springer).

Ramanathan, V. (1977). Interactions between Ice-Albedo, Lapse-Rate and Cloud-Top Feedbacks: An Analysis of the Nonlinear Response of a GCM Climate Model. *J. Atmos. Sci.* 34 (12), 1885–1897. doi:10.1175/1520-0469(1977)034<1885:ibialr>2.0.co;2

Rangno, A. L., and Hobbs, P. V. (2001). Ice Particles in Stratiform Clouds in the Arctic and Possible Mechanisms for the Production of High Ice Concentrations. *J. Geophys. Res.* 106 (D14), 15065–15075. doi:10.1029/2000JD900286

Riihelä, A., Manninen, T., and Laine, V. (2013). Observed Changes in the Albedo of the Arctic Sea-Ice Zone for the Period 1982-2009. *Nat. Clim Change* 3 (10), 895–898. doi:10.1038/nclimate1963

Rind, D., Healy, R., Parkinson, C., and Martinson, D. (1995). The Role of Sea Ice in 2×CO2Climate Model Sensitivity. Part I: The Total Influence of Sea Ice Thickness and Extent. *J. Clim.* 8 (3), 449–463. doi:10.1175/1520-0442(1995)008<0449:TROSII>2.0.CO;2

Robock, A. (1983). Ice and Snow Feedbacks and the Latitudinal and Seasonal Distribution of Climate Sensitivity. *J. Atmos. Sci.* 40, 986–997. doi:10.1175/1520-0469(1983)040<0986:iasfat>2.0.co;2

Rodgers, K. B. (2003). A Tropical Mechanism for Northern Hemisphere Deglaciation. *Geochem. Geophys. Geosyst.* 4 (5), 1046. doi:10.1029/2003gc000508

Roe, G. H., Feldl, N., Armour, K. C., Hwang, Y.-T., and Frierson, D. M. W. (2015). The Remote Impacts of Climate Feedbacks on Regional Climate Predictability. *Nat. Geosci* 8, 135–139. doi:10.1038/ngeo2346

Rogers, W. E., Thomson, J., Shen, H. H., Doble, M. J., Wadhams, P., and Cheng, S. (2016). Dissipation of Wind Waves by Pancake and Frazil Ice in the Autumn Beaufort Sea. *J. Geophys. Res. Oceans* 121 (11), 7991–8007. doi:10.1002/2016JC012251

Rose, B. E. J., Armour, K. C., Battisti, D. S., Feldl, N., and Koll, D. D. B. (2014). The Dependence of Transient Climate Sensitivity and Radiative Feedbacks on the Spatial Pattern of Ocean Heat Uptake. *Geophys. Res. Lett.* 41, 1071–1078. doi:10.1002/2013GL058955

Rugenstein, M. A. A., Winton, M., Stouffer, R. J., Griffies, S. M., and Hallberg, R. (2013). Northern High-Latitude Heat Budget Decomposition and Transient Warming. *J. Clim.* 26 (2), 609–621. doi:10.1175/JCLI-D-11-00695.1

Russotto, R. D., and Biasutti, M. (2020). Polar Amplification as an Inherent Response of a Circulating Atmosphere: Results from the TRACMIP Aquaplanets. *Geophys. Res. Lett.* 47, 12. doi:10.1029/2019GL086771

Salzmann, M. (2017). The Polar Amplification Asymmetry: Role of Antarctic Surface Height. *Earth Syst. Dynam.* 8 (2), 323–336. doi:10.5194/esd-8-323-2017

Schauer, U., Fahrbach, E., Osterhus, S., and Rohardt, G. (2004). Arctic Warming through the Fram Strait: Oceanic Heat Transport from 3 Years of Measurements. *J. Geophys. Res.* 109 (C6). doi:10.1029/2003JC001823

Schmale, J., Zieger, P., and Ekman, A. M. L. (2021). Aerosols in Current and Future Arctic Climate. *Nat. Clim. Chang.* 11 (2), 95–105. doi:10.1038/s41558-020-00969-5

Schneider, S. H. (1975). On the Carbon Dioxide-Climate Confusion. *J. Atmos. Sci.* 32 (11), 2060–2066. doi:10.1175/1520-0469(1975)032<2060:OTCDC>2.0.CO;2

Schweiger, A., Lindsay, R., Zhang, J., Steele, M., Stern, H., and Kwok, R. (2011). Uncertainty in Modeled Arctic Sea Ice Volume. *J. Geophys. Res.* 116 (C8), 1. doi:10.1029/2011JC007084

Screen, J. A., Deser, C., and Simmonds, I. (2012). Local and Remote Controls on Observed Arctic Warming. *Geophys. Res. Lett.* 39 (10), a–n. doi:10.1029/2012GL051598

Screen, J. A., Deser, C., Smith, D. M., Zhang, X., Blackport, R., Kushner, P. J., et al. (2018). Consistency and Discrepancy in the Atmospheric Response to Arctic Sea-Ice Loss across Climate Models. *Nat. Geosci* 11 (3), 155–163. doi:10.1038/s41561-018-0059-y

Screen, J. A., and Simmonds, I. (2010a). Increasing Fall-winter Energy Loss from the Arctic Ocean and its Role in Arctic Temperature Amplification. *Geophys. Res. Lett.* 37 (16), a–n. doi:10.1029/2010GL044136

Screen, J. A., and Simmonds, I. (2010b). The central Role of Diminishing Sea Ice in Recent Arctic Temperature Amplification. *Nature* 464 (7293), 1334–1337. doi:10.1038/nature09051

Sedlar, J., Shupe, M. D., and Tjernström, M. (2012). On the Relationship between Thermodynamic Structure and Cloud Top, and its Climate Significance in the Arctic. *J. Clim.* 25 (7), 2374–2393. doi:10.1175/JCLI-D-11-00186.1

Sejas, S. A., Cai, M., Hu, A., Meehl, G. A., Washington, W., and Taylor, P. C. (2014). Individual Feedback Contributions to the Seasonality of Surface Warming. *J. Clim.* 27 (14), 5653–5669. doi:10.1175/JCLI-D-13-00658.1

Sejas, S. A., and Cai, M. (2016). Isolating the Temperature Feedback Loop and its Effects on Surface Temperature. *J. Atmos. Sci.* 73 (8), 3287–3303. doi:10.1175/JAS-D-15-0287.1

Sellers, W. D. (1969). A Global Climatic Model Based on the Energy Balance of the Earth-Atmosphere System. *J. Appl. Meteorol.* 8 (3), 392–400. doi:10.1175/1520-0450(1969)008<0392:AGCMBO>2.0.CO;2

Semenov, V. A., Park, W., and Latif, M. (2009). Barents Sea Inflow Shutdown: A New Mechanism for Rapid Climate Changes. *Geophys. Res. Lett.* 36 (14). doi:10.1029/2009GL038911

Semmler, T., Pithan, F., and Jung, T. (2020). Quantifying Two-Way Influences between the Arctic and Mid-latitudes through Regionally Increased CO2 Concentrations in Coupled Climate Simulations. *Clim. Dyn.* 54 (7), 3307–3321. doi:10.1007/s00382-020-05171-z

Serreze, M. C., Barrett, A. P., Stroeve, J. C., Kindig, D. N., and Holland, M. M. (2009). The Emergence of Surface-Based Arctic Amplification. *The Cryosphere* 3 (1), 11–19. doi:10.5194/tc-3-11-2009

Serreze, M. C., and Barry, R. G. (2011). Processes and Impacts of Arctic Amplification: A Research Synthesis. *Glob. Planet. Change* 77 (1), 85–96. doi:10.1016/j.gloplacha.2011.03.004

Serreze, M. C., Schnell, R. C., and Kahl, J. D. (1992). Low-Level Temperature Inversions of the Eurasian Arctic and Comparisons with Soviet Drifting Station Data. *J. Clim.* 5 (6), 615–629. doi:10.1175/1520-0442(1992)005<0615:LLTIOT>2.0.CO;2

Sévellec, F., Fedorov, A. V., and Liu, W. (2017). Arctic Sea-Ice Decline Weakens the Atlantic Meridional Overturning Circulation. *Nat. Clim Change* 7 (8), 604–610. doi:10.1038/nclimate3353

Shaw, T. A., and Tan, Z. (2018). Testing Latitudinally Dependent Explanations of the Circulation Response to Increased CO 2 Using Aquaplanet Models. *Geophys. Res. Lett.* 45 (18), 9861–9869. doi:10.1029/2018GL078974

Shell, K. M., Kiehl, J. T., and Shields, C. A. (2008). Using the Radiative Kernel Technique to Calculate Climate Feedbacks in NCAR's Community Atmospheric Model. *J. Clim.* 21 (10), 2269–2282. doi:10.1175/2007JCLI2044.1

Shupe, M. D., Persson, P. O. G., Brooks, I. M., Tjernström, M., Sedlar, J., Mauritsen, T., et al. (2013). Cloud and Boundary Layer Interactions over the Arctic Sea Ice in Late Summer. *Atmos. Chem. Phys.* 13 (18), 9379–9399. doi:10.5194/acp-13-9379-2013

Shupe, M. D. (2020). *The MOSAiC Expedition: A Year Drifting with the Arctic Sea Ice*. Washington, DC USA: National Oceanic and Atmospheric Administration. doi:10.25923/9g3v-xh92

Singh, H. A., Rasch, P. J., and Rose, B. E. J. (2017). Increased Ocean Heat Convergence into the High Latitudes with CO2 Doubling Enhances Polar-Amplified Warming. *Geophys. Res. Lett.* 44 (2010), 10,583–10,591. doi:10.1002/2017GL074561

Skagseth, Ø., Furevik, T., Ingvaldsen, R., Loeng, H., Mork, K. A., Orvik, K. A., et al. (2008). "Volume and Heat Transports to the Arctic Ocean via the Norwegian and Barents Seas," in *Arctic–Subarctic Ocean Fluxes: Defining the Role of the Northern Seas in Climate*. Editors R. R. Dickson, J. Meincke, and P. Rhines (Springer Netherlands), 45–64. doi:10.1007/978-1-4020-6774-7_3

Sledd, A., and L'Ecuyer, T. (2019). How Much Do Clouds Mask the Impacts of Arctic Sea Ice and Snow Cover Variations? Different Perspectives from Observations and Reanalyses. *Atmosphere* 10 (1), 12. doi:10.3390/atmos10010012

Smith, D. M., Dunstone, N. J., Scaife, A. A., Fiedler, E. K., Copsey, D., and Hardiman, S. C. (2017). Atmospheric Response to Arctic and Antarctic Sea Ice: The Importance of Ocean-Atmosphere Coupling and the Background State. *J. Clim.* 30 (12), 4547–4565. doi:10.1175/JCLI-D-16-0564.1

Smith, D. M., Screen, J. A., Deser, C., Cohen, J., Fyfe, J. C., García-Serrano, J., et al. (2019). The Polar Amplification Model Intercomparison Project (PAMIP) Contribution to CMIP6: Investigating the Causes and Consequences of Polar Amplification. *Geosci. Model. Dev.* 12 (3), 1139–1164. doi:10.5194/gmd-12-1139-2019

Smith, W., Revercomb, H., Weisz, E., Tobin, D., Knuteson, R., Taylor, J., et al. (2021). Hyperspectral Satellite Radiance Atmospheric Profile Information Content and its Dependence on Spectrometer Technology. *IEEE J. Sel. Top. Appl. Earth Observations Remote Sensing* 14, 4720–4736. doi:10.1109/JSTARS.2021.3073482

Soden, B. J., Broccoli, A. J., and Hemler, R. S. (2004). On the Use of Cloud Forcing to Estimate Cloud Feedback. *J. Clim.* 17 (19), 3661–3665. doi:10.1175/1520-0442(2004)017<3661:OTUOCF>2.0.CO;2

Soden, B. J., and Held, I. M. (2006). An Assessment of Climate Feedbacks in Coupled Ocean-Atmosphere Models. *J. Clim.* 19 (14), 3354–3360. doi:10.1175/JCLI3799.1

Solomon, A., de Boer, G., Creamean, J. M., McComiskey, A., Shupe, M. D., Maahn, M., et al. (2018). The Relative Impact of Cloud Condensation Nuclei and Ice Nucleating Particle Concentrations on Phase Partitioning in Arctic Mixed-phase Stratocumulus Clouds. *Atmos. Chem. Phys.* 18 (23), 17047–17059. doi:10.5194/acp-18-17047-2018

Solomon, A., Shupe, M. D., Persson, O., Morrison, H., Yamaguchi, T., Caldwell, P. M., et al. (2014). The Sensitivity of Springtime Arctic Mixed-phase Stratocumulus Clouds to Surface-Layer and Cloud-Top Inversion-Layer Moisture Sources. *J. Atmos. Sci.* 71 (2), 574–595. doi:10.1175/JAS-D-13-0179.1

Song, X., Zhang, G. J., and Cai, M. (2014). Quantifying Contributions of Climate Feedbacks to Tropospheric Warming in the NCAR CCSM3.0. *Clim. Dyn.* 42 (3), 901–917. doi:10.1007/s00382-013-1805-x

Sotiropoulou, G., Sullivan, S., Savre, J., Lloyd, G., Lachlan-Cope, T., Ekman, A. M. L., et al. (2020). The Impact of Secondary Ice Production on Arctic Stratocumulus. *Atmos. Chem. Phys.* 20 (3), 1301–1316. doi:10.5194/acp-20-1301-2020

Spelman, M. J., and Manabe, S. (1984). Influence of Oceanic Heat Transport upon the Sensitivity of a Model Climate. *J. Geophys. Res.* 89 (C1), 571–586. doi:10.1029/JC089iC01p00571

Spielhagen, R. F., Werner, K., Sørensen, S. A., Zamelczyk, K., Kandiano, E., Budeus, G., et al. (2011). Enhanced Modern Heat Transfer to the Arctic by Warm Atlantic Water. *Science* 331 (6016), 450–453. doi:10.1126/science.1197397

Stapf, J., Ehrlich, A., Jäkel, E., Lüpkes, C., and Wendisch, M. (2020). Reassessment of Shortwave Surface Cloud Radiative Forcing in the Arctic: Consideration of Surface-Albedo-Cloud Interactions. *Atmos. Chem. Phys.* 20 (16), 9895–9914. doi:10.5194/acp-20-9895-2020

Stramler, K., Del Genio, A. D., and Rossow, W. B. (2011). Synoptically Driven Arctic Winter States. *J. Clim.* 24 (6), 1747–1762. doi:10.1175/2010JCLI3817.1

Stroeve, J., Barrett, A., Serreze, M., and Schweiger, A. (2014). Using Records from Submarine, Aircraft and Satellites to Evaluate Climate Model Simulations of Arctic Sea Ice Thickness. *The Cryosphere* 8 (5), 1839–1854. doi:10.5194/tc-8-1839-2014

Stuecker, M. F., Bitz, C. M., Armour, K. C., Proistosescu, C., Kang, S. M., Xie, S.-P., et al. (2018). Polar Amplification Dominated by Local Forcing and Feedbacks. *Nat. Clim Change* 8 (12), 1076–1081. doi:10.1038/s41558-018-0339-y

Susskind, J., Blaisdell, J. M., and Iredell, L. (2014). Improved Methodology for Surface and Atmospheric Soundings, Error Estimates, and Quality Control Procedures: The Atmospheric Infrared Sounder Science Team Version-6 Retrieval Algorithm. *J. Appl. Remote Sens* 8 (1), 084994. doi:10.1117/1.JRS.8.084994

Swart, N. C., Fyfe, J. C., Hawkins, E., Kay, J. E., and Jahn, A. (2015). Influence of Internal Variability on Arctic Sea-Ice Trends. *Nat. Clim Change* 5 (2), 86–89. doi:10.1038/nclimate2483

Swart, N. (2017). Natural Causes of Arctic Sea-Ice Loss. *Nat. Clim Change* 7 (4), 239–241. doi:10.1038/nclimate3254

Tan, I., and Storelvmo, T. (2019). Evidence of Strong Contributions from Mixed-Phase Clouds to Arctic Climate Change. *Geophys. Res. Lett.* 46 (5), 2894–2902. doi:10.1029/2018GL081871

Tan, I., and Storelvmo, T. (2016). Sensitivity Study on the Influence of Cloud Microphysical Parameters on Mixed-phase Cloud Thermodynamic Phase Partitioning in CAM5. *J. Atmos. Sci.* 73 (2), 709–728. doi:10.1175/JAS-D-15-0152.1

Tan, I., Storelvmo, T., and Zelinka, M. D. (2016). Observational Constraints on Mixed-phase Clouds Imply Higher Climate Sensitivity. *Science* 352 (6282), 224–227. doi:10.1126/science.aad5300

Taylor, K. E., Stouffer, R. J., and Meehl, G. A. (2012). An Overview of CMIP5 and the Experiment Design. *Bull. Am. Meteorol. Soc.* 93 (4), 485–498. doi:10.1175/BAMS-D-11-00094.1

Taylor, P. C., Cai, M., Hu, A., Meehl, J., Washington, W., and Zhang, G. J. (2013). A Decomposition of Feedback Contributions to Polar Warming Amplification. *J. Clim.* 26 (18), 7023–7043. doi:10.1175/JCLI-D-12-00696.1

Taylor, P. C., Ellingson, R. G., and Cai, M. (2011a). Geographical Distribution of Climate Feedbacks in the NCAR CCSM3.0. *J. Clim.* 24 (11), 2737–2753. doi:10.1175/2010JCLI3788.1

Taylor, P. C., Ellingson, R. G., and Cai, M. (2011b). Seasonal Variations of Climate Feedbacks in the NCAR CCSM3. *J. Clim.* 24 (13), 3433–3444. doi:10.1175/2011jcli3862.1

Taylor, P. C., Kato, S., Xu, K. M., and Cai, M. (2015). Covariance between Arctic Sea Ice and Clouds within Atmospheric State Regimes at the Satellite Footprint Level. *J. Geophys. Res. Atmos.* 120 (24), 12656–12678. doi:10.1002/2015JD023520

Taylor, P. C., Maslowski, W., Perlwitz, J., and Wuebbles, D. J. (2017). "Ch. 11: Arctic Changes and Their Effects on Alaska and the Rest of the United States. Climate Science Special Report: Fourth National Climate Assessment, Volume I," in *Climate Science Special Report: Fourth National Climate Assessment, Volume I*. Editors D. J. Wuebbles, S. W. Fahey, K. A. Hibbard, D. J. Dokken, B. C. Steward, and T. K. Maycock (Washington, DC, USA: U.S. Global Climate Change Research Program), 303–332. doi:10.7930/J00863GK

Taylor, P., Hegyi, B., Boeke, R., and Boisvert, L. (2018). On the Increasing Importance of Air-Sea Exchanges in a Thawing Arctic: A Review. *Atmosphere* 9 (2), 41. doi:10.3390/atmos9020041

Topál, D., Ding, Q., Mitchell, J., Baxter, I., Herein, M., Haszpra, T., et al. (2020). An Internal Atmospheric Process Determining Summertime Arctic Sea Ice Melting in the Next Three Decades: Lessons Learned from Five Large Ensembles and Multiple CMIP5 Climate Simulations. *J. Clim.* 33 (17), 7431–7454. doi:10.1175/JCLI-D-19-0803.1

Tsushima, Y., Emori, S., Ogura, T., Kimoto, M., Webb, M. J., Williams, K. D., et al. (2006). Importance of the Mixed-phase Cloud Distribution in the Control Climate for Assessing the Response of Clouds to Carbon Dioxide Increase: a Multi-Model Study. *Clim. Dyn.* 27 (2), 113–126. doi:10.1007/s00382-006-0127-7

Uttal, T., Curry, J. A., Mcphee, M. G., Perovich, D. K., Moritz, R. E., Maslanik, J. A., et al. (2002). Surface Heat Budget of the Arctic Ocean. *Bull. Amer. Meteorol. Soc.* 83 (2), 255–275. doi:10.1175/1520-0477(2002)083<0255:shbota>2.3.co;2

van der Linden, E. C., Le Bars, D., Bintanja, R., and Hazeleger, W. (2019). Oceanic Heat Transport into the Arctic under High and Low CO_2 Forcing. *Clim. Dyn.* 53 (7), 4763–4780. doi:10.1007/s00382-019-04824-y

Vargas Zeppetello, L. R., Donohoe, A., and Battisti, D. S. (2019). Does Surface Temperature Respond to or Determine Downwelling Longwave Radiation? *Geophys. Res. Lett.* 46 (5), 2781–2789. doi:10.1029/2019GL082220

Vavrus, S., Holland, M. M., and Bailey, D. A. (2011). Changes in Arctic Clouds during Intervals of Rapid Sea Ice Loss. *Clim. Dyn.* 36 (7), 1475–1489. doi:10.1007/s00382-010-0816-0

Vavrus, S. (2004). The Impact of Cloud Feedbacks on Arctic Climate under Greenhouse Forcing*. *J. Clim.* 17 (3), 603–615. doi:10.1175/1520-0442(2004)017<0603:TIOCFO>2.0.CO;2

Vavrus, S., Waliser, D., Schweiger, A., and Francis, J. (2008). Simulations of 20th and 21st century Arctic Cloud Amount in the Global Climate Models Assessed in the IPCC AR4. *Clim. Dyn.* 33 (7), 1099–1115. doi:10.1007/s00382-008-0475-6

Vignesh, P. P., Jiang, J. H., Kishore, P., Su, H., Smay, T., Brighton, N., et al. (2020). Assessment of CMIP6 Cloud Fraction and Comparison with Satellite Observations. *Earth Space Sci.* 7 (2), e2019EA000975. doi:10.1029/2019EA000975

IPCC (2021). "Climate Change 2021: The Physical Science Basis," in *Contribution of Working Group I to the Sixth Assessment Report of the Intergovernmental Panel on Climate Change*. Editors V. Masson-Delmotte, P. Zhai, A. Pirani, S. L. Connors, C. Péan, S. Berger, et al. (Cambridge: Cambridge University Press). In Press.

IPCC (2018). "Summary for Policymakers," in *Global Warming of 1.5°C. An IPCC Special Report on the Impacts of Global Warming of 1.5°C above Pre-industrial Levels and Related Global Greenhouse Gas Emission Pathways, in the Context of Strengthening the Global Response to the Threat of Climate Change, Sustainable Development, and Efforts to Eradicate Poverty*. Editors V. Masson-Delmotte, P. Zhai, H.-O. Pörtner, D. Roberts, J. Skea, P. R. Shukla, et al. (Geneva, Switzerland: World Meteorological Organization), 32.

Wang, Y., Zhang, D., Liu, X., and Wang, Z. (2018). Distinct Contributions of Ice Nucleation, Large-Scale Environment, and Shallow Cumulus Detrainment to Cloud Phase Partitioning with NCAR CAM5. *J. Geophys. Res. Atmos.* 123 (2), 1132–1154. doi:10.1002/2017JD027213

Warren, S. G., Rigor, I. G., Untersteiner, N., Radionov, V. F., Bryazgin, N. N., Aleksandrov, Y. I., et al. (1999). Snow Depth on Arctic Sea Ice. *J. Clim.* 12 (6), 1814–1829. doi:10.1175/1520-0442(1999)012<1814:SDOASI>2.0.CO;2

Washington, W. M., and Meehl, G. A. (1989). Climate Sensitivity Due to Increased CO2: Experiments with a Coupled Atmosphere and Ocean General Circulation Model. *Clim. Dyn.* 4 (1), 1–38. doi:10.1007/BF00207397

Washington, W. M., and Meehl, G. A. (1986). General Circulation Model CO2 Sensitivity Experiments: Snow-Sea Ice Albedo Parameterizations and Globally Averaged Surface Air Temperature. *Climatic Change* 8 (3), 231–241. doi:10.1007/BF00161596

Washington, W. M., and Meehl, G. A. (1996). High-latitude Climate Change in a Global Coupled Ocean-Atmosphere-Sea Ice Model with Increased Atmospheric CO2. *J. Geophys. Res.* 101 (D8), 12795–12801. doi:10.1029/96JD00505

Washington, W. M., and Meehl, G. A. (1984). Seasonal Cycle experiment on the Climate Sensitivity Due to a Doubling of CO2with an Atmospheric General Circulation Model Coupled to a Simple Mixed-Layer Ocean Model. *J. Geophys. Res.* 89 (D6), 9475–9503. doi:10.1029/JD089iD06p09475

Webster, M. A., Rigor, I. G., Nghiem, S. V., Kurtz, N. T., Farrell, S. L., Perovich, D. K., et al. (2014). Interdecadal Changes in Snow Depth on Arctic Sea Ice. *J. Geophys. Res. Oceans* 119 (8), 5395–5406. doi:10.1002/2014JC009985

Wetherald, R. T., and Manabe, S. (1988). Cloud Feedback Processes in a General Circulation Model. *J. Atmos. Sci.* 45 (8), 1397–1416. doi:10.1175/1520-0469(1988)045<1397:CFPIAG>2.0.CO;2

Wetherald, R. T., and Manabe, S. (1975). The Effects of Changing the Solar Constant on the Climate of a General Circulation Model. *J. Atmos. Sci.* 32 (11), 20442–22059. doi:10.1175/1520-0469(1975)032<2044:teocts>2.0.co;2

Wielicki, B. A., Young, D. F., Mlynczak, M. G., Thome, K. J., Leroy, S., Corliss, J., et al. (2013). Achieving Climate Change Absolute Accuracy in Orbit. *Bull. Am. Meteorol. Soc.* 94 (10), 1519–1539. doi:10.1175/BAMS-D-12-00149.1

Wilson, C. A., and Mitchell, J. F. B. (1987). A Doubled CO2climate Sensitivity experiment with a Global Climate Model Including a Simple Ocean. *J. Geophys. Res.* 92 (D11), 13315–13343. doi:10.1029/JD092iD11p13315

Wilson, T. W., Ladino, L. A., Alpert, P. A., Breckels, M. N., Brooks, I. M., Browse, J., et al. (2015). A marine Biogenic Source of Atmospheric Ice-Nucleating Particles. *Nature* 525 (7568), 234–238. doi:10.1038/nature14986

Winker, D. M., Pelon, J., Coakley, J. A., Jr., Ackerman, S. A., Charlson, R. J., Colarco, P. R., et al. (2010). The CALIPSO Mission. *Bull. Am. Meteorol. Soc.* 91 (9), 1211–1230. doi:10.1175/2010bams3009.1

Winton, M., Griffies, S. M., Samuels, B. L., Sarmiento, J. L., and Frölicher, T. L. (2013). Connecting Changing Ocean Circulation with Changing Climate. *J. Clim.* 26 (7), 2268–2278. doi:10.1175/JCLI-D-12-00296.1

Woods, C., and Caballero, R. (2016a). The Role of Moist Intrusions in Winter Arctic Warming and Sea Ice Decline. *J. Clim.* 29 (12), 4473–4485. doi:10.1175/JCLI-D-15-0773.1

Woods, C., and Caballero, R. (2016b). The Role of Moist Intrusions in Winter Arctic Warming and Sea Ice Decline. *J. Clim.* 29 (12), 4473–4485. doi:10.1175/JCLI-D-15-0773.1

Wu, F., Li, W., Zhang, P., and Li, W. (2021). Relative Contributions of Internal Atmospheric Variability and Surface Processes to the Interannual Variations in Wintertime Arctic Surface Air Temperatures. *J. Clim.* 34 (17), 1–48. doi:10.1175/JCLI-D-20-0779.1

Wuebbles, D. J., Fahey, D. W., Hibbard, K. A., DeAngelo, B., Doherty, S., Hayhoe, K., et al. (2017). "Executive Summary. Climate Science Special Report: Fourth National Climate Assessment, Volume I," in *Climate Science Special Report: Fourth National Climate Assessment, Volume I* (Washington, DC USA: US Global Climate Change Research Program). doi:10.7930/J0DJ5CTG

Xie, S., Liu, X., Zhao, C., and Zhang, Y. (2013). Sensitivity of CAM5-Simulated Arctic Clouds and Radiation to Ice Nucleation Parameterization. *J. Clim.* 26 (16), 5981–5999. doi:10.1175/JCLI-D-12-00517.1

Yang, F., Ovchinnikov, M., and Shaw, R. A. (2015). Long-lifetime Ice Particles in Mixed-phase Stratiform Clouds: Quasi-Steady and Recycled Growth. *J. Geophys. Res. Atmos.* 120 (22), 11,617–11,635. doi:10.1002/2015JD023679

Yoshimori, M., Abe-Ouchi, A., and Laîné, A. (2017). The Role of Atmospheric Heat Transport and Regional Feedbacks in the Arctic Warming at Equilibrium. *Clim. Dyn.* 49 (9), 3457–3472. doi:10.1007/s00382-017-3523-2

Yoshimori, M., Watanabe, M., Abe-Ouchi, A., Shiogama, H., and Ogura, T. (2014). Relative Contribution of Feedback Processes to Arctic Amplification of Temperature Change in MIROC GCM. *Clim. Dyn.* 42 (5), 1613–1630. doi:10.1007/s00382-013-1875-9

Yu, Y., Taylor, P. C., and Cai, M. (2019). Seasonal Variations of Arctic Low-Level Clouds and its Linkage to Sea Ice Seasonal Variations. *J. Geophys. Res. Atmos.* 124 (22), 12206–12226. doi:10.1029/2019JD031014

Zelinka, M. D., Klein, S. A., and Hartmann, D. L. (2012). Computing and Partitioning Cloud Feedbacks Using Cloud Property Histograms. Part II: Attribution to Changes in Cloud Amount, Altitude, and Optical Depth. *J. Clim.* 25 (11), 3736–3754. doi:10.1175/JCLI-D-11-00249.1

Zhang, J., Rothrock, D., and Steele, M. (2000). Recent Changes in Arctic Sea Ice: The Interplay between Ice Dynamics and Thermodynamics. *J. Clim.* 13 (17), 3099–3114. doi:10.1175/1520-0442(2000)013<3099:RCIASI>2.0.CO;2

Zhao, X., Liu, X., Phillips, V. T. J., and Patade, S. (2021). Impacts of Secondary Ice Production on Arctic Mixed-phase Clouds Based on ARM Observations and CAM6 Single-Column Model Simulations. *Atmos. Chem. Phys.* 21 (7), 5685–5703. doi:10.5194/acp-21-5685-2021

Zhu, T., Huang, Y., and Wei, H. (2019). Estimating Climate Feedbacks Using a Neural Network. *J. Geophys. Res. Atmos.* 124 (6), 3246–3258. doi:10.1029/2018JD029223

Conflict of Interest: The authors declare that the research was conducted in the absence of any commercial or financial relationships that could be construed as a potential conflict of interest.

Publisher's Note: All claims expressed in this article are solely those of the authors and do not necessarily represent those of their affiliated organizations, or those of the publisher, the editors and the reviewers. Any product that may be evaluated in this article, or claim that may be made by its manufacturer, is not guaranteed or endorsed by the publisher.

frontiers in Earth Science

ORIGINAL RESEARCH
published: 10 February 2022
doi: 10.3389/feart.2022.765304

Constraining Arctic Climate Projections of Wintertime Warming With Surface Turbulent Flux Observations and Representation of Surface-Atmosphere Coupling

Linette N. Boisvert[1]*, *Robyn C. Boeke*[2,3], *Patrick C. Taylor*[2] and *Chelsea L. Parker*[1,4]

[1]NASA Goddard Space Flight Center, Greenbelt, MD, United States, [2]NASA Langley Research Center, Langley, VA, United States, [3]Science Systems and Applications, Inc., Hampton, VA, United States, [4]Earth System Science Interdisciplinary Center (ESSIC), University of Maryland, College Park, MD, United States

The drivers of rapid Arctic climate change—record sea ice loss, warming SSTs, and a lengthening of the sea ice melt season—compel us to understand how this complex system operates and use this knowledge to enhance Arctic predictability. Changing energy flows sparked by sea ice decline, spotlight atmosphere-surface coupling processes as central to Arctic system function and its climate change response. Despite this, the representation of surface turbulent flux parameterizations in models has not kept pace with our understanding. The large uncertainty in Arctic climate change projections, the central role of atmosphere-surface coupling, and the large discrepancy in model representation of surface turbulent fluxes indicates that these processes may serve as useful observational constraints on projected Arctic climate change. This possibility requires an evaluation of surface turbulent fluxes and their sensitivity to controlling factors (surface-air temperature and moisture differences, sea ice, and winds) within contemporary climate models (here Coupled Model Intercomparison Project 6). The influence of individual controlling factors and their interactions is diagnosed using a multi-linear regression approach. This evaluation is done for four sea ice loss regimes, determined from observational sea ice loss trends, to control for the confounding effects of natural variability between models and observations. The comparisons between satellite- and model-derived surface turbulent fluxes illustrate that while models capture the general sensitivity of surface turbulent fluxes to declining sea ice and to surface-air gradients of temperature and moisture, substantial mean state biases exist. Specifically, the central Arctic is too weak of a heat sink to the winter atmosphere compared to observations, with implications to the simulated atmospheric circulation variability and thermodynamic profiles. Models were found to be about 50% more efficient at turning an air-sea temperature gradient anomaly into a sensible heat flux anomaly relative to observations. Further, the influence of sea ice concentration on the sensible heat flux is underestimated in models compared to observations. The opposite is found for the latent heat flux variability in models; where the latent heat flux is too sensitive to a sea ice concentration anomaly. Lastly, the results suggest that present-day trends in sea ice

OPEN ACCESS

Edited by:
Matthew Collins,
University of Exeter, United Kingdom

Reviewed by:
Alex Crawford,
University of Manitoba, Canada
Jack Reeves Eyre,
University of Washington, United States

***Correspondence:**
Linette N. Boisvert
linette.n.boisvert@nasa.gov

Specialty section:
This article was submitted to Cryospheric Sciences, a section of the journal Frontiers in Earth Science

Received: *26 August 2021*
Accepted: *17 January 2022*
Published: *10 February 2022*

Citation:
Boisvert LN, Boeke RC, Taylor PC and Parker CL (2022) Constraining Arctic Climate Projections of Wintertime Warming With Surface Turbulent Flux Observations and Representation of Surface-Atmosphere Coupling. Front. Earth Sci. 10:765304. doi: 10.3389/feart.2022.765304

retreat regions may serve as suitable observational constraints of projected Arctic warming.

Keywords: turbulent fluxes, Arctic sea ice, CMIP6, AIRS, Arctic warming

INTRODUCTION

Sea ice and its overlying snowpack shape energy flows through the Arctic by reflecting the majority of the solar radiation in the sunlit months and inhibiting the Arctic Ocean and atmosphere from exchanging heat, moisture and momentum year-round (e.g., Screen et al., 2013; Vihma, 2014; Boisvert et al., 2015b; Taylor et al., 2018). As global temperatures rise due to climate change, the Arctic is warming faster than anywhere else on the Earth (IPCC, 2013), known as Arctic Amplification (Serreze et al., 2009; Screen and Simmonds, 2010a; Screen and Simmonds, 2010b). In response, Arctic sea ice has melted and satellite monitoring of sea ice extent has shown that the summer minimum has decreased at a rate of ~14% per decade over the past 4 decades (Cavalieri and Parkinson, 2012; Stroeve and Notz, 2018). From 2009 to 2020, the Arctic saw 11 out of the lowest 13 September sea ice extents of the satellite record. Arctic sea ice extent is decreasing in all months, with the most rapid declines occurring since the early 2000s (Parkinson and DiGirolamo, 2016). In addition to declining sea ice extent, the totality of the changing conditions in the Arctic, including a warming of SSTs and a lengthening of the sea ice melt season, contribute to increases in evaporation and turbulent fluxes (e.g. Steele et al., 2008; Markus et al., 2009; Stroeve et al., 2014; Boisvert et al., 2015a; Taylor et al., 2018; Boeke et al., 2021).

Increased sensible (SHF) and latent (LHF) heat fluxes play an important role in the Arctic Amplification process. Although the Arctic sea ice albedo feedback is largest in the summer months, the strongest warming has occurred in fall and winter (Deser et al., 2010). This wintertime warming maximum has been linked to sea ice loss using observations, meteorological reanalysis, and climate model simulations (Boeke and Taylor, 2018; Screen and Simmonds, 2010a; Screen et al., 2012; Serreze et al., 2009). One way in which sea ice influences the winter warming maximum is that reduced sea ice cover promotes increased turbulent fluxes from the ocean surface to the lower atmosphere and drives atmospheric warming (Screen and Simmonds, 2010b).

Given the multiple mechanisms through which surface-atmosphere coupling processes influence Arctic climate system evolution, one may be surprised to find that the representation of surface turbulent flux parameterizations has not kept up with our understanding. Bourassa et al. (2013) indicate that modern understanding of the physics behind the bulk formula parameterizations and their application over highly stable and heterogeneous sea ice surfaces has not been incorporated into surface flux parameterizations (e.g., Brunke et al., 2006; Grachev et al., 2007; Andreas et al., 2010a; Andreas et al., 2010b; Reeves Eyre et al., 2021). While there have been changes to these parameterizations globally that have produced more accurate surface turbulent fluxes in the mid-latitudes; these changes have not significantly improved estimates in the Arctic (Bourassa et al., 2013). As a result, turbulent fluxes in the Arctic from reanalyses and climate models are inaccurate and often get the magnitude and sign of the fluxes incorrect when compared to in situ and satellite-derived data (Boisvert et al., 2015b; Taylor et al., 2018; Graham et al., 2019; Renfrew et al., 2021).

The large disparities between modeled and observed turbulent fluxes (Cullather and Bosilovich, 2011; Boisvert et al., 2015b; Graham et al., 2019; Taylor et al., 2018; Bourassa et al., 2013) are caused by multiple factors: 1) the specific parameterizations and assumptions used in the bulk formula, 2) discrepancies in sea ice properties, which drive the surface temperature and humidity and drag coefficients, 3) the representation of near surface-air temperature and humidity gradients, and 4) the spatial and temporal resolution. Currently, climate models and reanalyses apply mid-latitude boundary layer parameterizations in the Arctic (Bourassa et al., 2013). However, the boundary layer over sea ice is more stable than the nocturnal boundary layer over land, resulting in substantial flux errors (Grachev et al., 2007). The basic difference between these stable boundary layers is that the surface boundary layer in the Arctic is long-lived. Hence, there is usually no residual layer separating the Arctic surface boundary layer from the free atmosphere, making it more responsive to the influence of gravity waves, an additional source of turbulence (Zilitinkevich and Esau, 2007). Boisvert et al., (2015a) demonstrate that the magnitude of the fluxes in these stable boundary layers in the winter produced with the Grachev et al. (2007) algorithm are on average 24% larger than those calculated with Holtslag and de Bruin (1988), which is widely used in climate models.

Accurate roughness lengths for wind speed, humidity and temperature profiles over the ice are required to determine the transfer coefficients and to calculate the fluxes (Andreas, 2002; Andreas et al., 2010a). These have often been difficult to estimate and there are large inaccuracies especially over the sea ice due to its complex and heterogeneous topography, consisting of ridges and leads. Climate models often represent Arctic sea ice simplistically and cannot reproduce the sea ice extent, thickness and loss from observations and lack arepresentation of surface topography (Schweiger et al., 2011; Stroeve J. et al., 2014; Holland et al., 2010; Jahn et al., 2012). While there have been improvements in representing sea ice properties and seasonality in recent climate models, there are still significant biases compared to observations and a range in future predictions (SIMIP Community, 2020; Smith et al., 2020; Crawford et al., 2021; Watts et al., 2021). These errors in the sea ice can feedback on the near surface atmospheric variables, for example, in a large-eddy simulation model, a 1% variation in sea ice concentration was found to change the surface air temperature by 3.5 K in winter (Lüpkes et al., 2008a). Models and reanalyses also struggle to capture near surface temperature, humidity, and wind speeds

and suffer from a lack of available in situ observations for assimilation (Jakobson et al., 2012; Graham et al., 2019; Davy and Outten, 2020). Finally, models have different temporal, spatial and vertical resolutions and do not resolve changes in the fluxes due to small scale changes in the atmospheric and surface conditions.

It is likely that the patchwork manner in which Arctic surface turbulent schemes have been developed and the incomplete integration of modern understanding are behind some of the substantial inter-model differences in surface turbulent fluxes. Graham et al. (2019) compared six reanalyses with *in-situ* observations and found that reanalyses do not represent turbulent fluxes correctly in any season over sea ice and consistently have the direction of the SHF wrong and the order of magnitude incorrect for LHF. Taylor et al. (2018) found substantial differences in the mean surface turbulent fluxes in the Arctic across Coupled Model Intercomparison Project 5 (CMIP5) models indicating that they did not appropriately simulate that the central Arctic tends to be a heat sink to the Arctic atmosphere. Further, Taylor et al. (2018) found the largest inter-model spread occurring in winter and in regions of the most rapid sea ice retreat. Given the substantial inter-model differences in the representation of surface turbulent fluxes found across recent multi-model ensembles (e.g., Taylor et al., 2018), additional work is needed to evaluate the next generation of climate models from the Coupled Model Intercomparison Project 6 (CMIP6) (Eyring et al., 2016) and better understand the sources of model discrepancies.

The large discrepancies between the model representation of surface-atmospheric coupling processes indicates that this area is prime for the use of observations to understand and constrain the influence of these processes on projected Arctic warming--a goal of this paper. These differences are thought to be caused by how models handle the evolution of the surface albedo and the properties of the sea ice pack (e.g. extent, concentration, thickness, snow) and their representation of surface turbulent fluxes. Previous work suggests that atmospheric coupling processes and in particular surface turbulent fluxes may serve as a meaningful constraint on projected Arctic warming. For example, Boeke and Taylor (2018) indicate that the magnitude of projected Arctic Amplification strongly correlates with the seasonal heat transfer from summer to fall/winter, of which the surface turbulent flux response plays a substantial role. Physically, surface turbulent fluxes directly contribute to Arctic warming via the ice insulation effect and can influence the atmospheric circulation variability (Burt et al., 2016; Zheng et al., 2019). Thus, there is a need to evaluate models and understand the causes of differences with observations.

This study is designed to address two knowledge gaps: 1) continued evaluation of surface turbulent flux representation and inter-model spread across contemporary climate models and 2) exploration of the use of observational constraints of surface turbulent fluxes to constrain projected Arctic warming during the winter, which we define as October-January. To do this we use the observation-derived turbulent flux dataset produced using NASA's Atmospheric Infrared Sounder (AIRS) (Boisvert et al., 2013; Boisvert et al., 2015a; Boisvert et al., 2015b; Taylor et al., 2018) together with CMIP6 models to perform the model evaluation and assess inter-model spread. From the outset, we knew that this comparison would be challenging due to the substantial natural variability in the Arctic not being synced in models and observations, which has not been fully considered in previous assessments of climate model representation of surface turbulent fluxes. To account for this, we adopt a sea ice regime compositing approach to control for the inter-model differences in the natural variability of sea ice (**Section 3a**). By controlling for sea ice trend differences, this approach gives insights into the physical reasons for the errors in the parameterizations and input variables which are driving the intermodal differences. Guided by previous studies (Screen and Simmonds, 2010a; Sejas and Cai, 2016; Boeke and Taylor, 2018), we also hypothesize that models that more efficiently produce larger surface turbulent fluxes produce more winter warming and sea ice loss.

DATA AND MODELS

Atmospheric InfraRed Sounder Surface Turbulent Fluxes

The Atmospheric Infrared Sounder (AIRS) onboard NASA's Aqua satellite was launched in May 2002 and has been collecting twice daily, global data ever since. AIRS has 2,378 infrared channels and a 13.5 km spatial resolution. The AIRS instrument was designed to produce highly accurate temperature and humidity profiles globally (Susskind et al., 2014), which is important in the Arctic where data is sparse and clouds are prevalent. We use version 7, level 3 daily skin temperatures, 925–1,000 hPa air temperatures, 925–1,000 hPa relative humidity and 925–1,000 hPa geopotential heights to derive SHF and LHF. Level 3 data is produced on a $1^{\circ} \times 1^{\circ}$ grid with retrievals from data quality control flagged as best and good quality (Susskind et al., 2014). Unfortunately, the Advanced Microwave Sounding Unit-A2 (AMSU-A2) instrument, used in the creation of AIRS/AMSU combined data products, lost power in September 2016 causing these data products to no longer be produced, thus we use the AIRS-only products for October-January 2002–2020 for consistency. AIRS temperatures and humidity products have been compared with a variety of *in-situ* data and have shown to have modest uncertainty in skin temperature (±2.3 K), 2-m air temperature (±3.41 K) and specific humidity (±0.54 g kg^{-1}) (Boisvert et al., 2015a; Taylor et al., 2018).

Daily 10-m wind speeds are taken from NASA's Modern Era-Retrospective Analysis for Research and Applications, version 2 (MERRA-2) (Gelaro et al., 2017) and are used in the calculations of the surface turbulent fluxes. MERRA-2 winds perform well when compared to radiosonde sounding data over the Arctic Ocean and are deemed reliable for turbulent flux computations over sea ice (Graham et al., 2019).

Sea ice concentrations (I_C) are produced using the Defense Meteorological Satellite Program (DMSP) Special Sensor Microwave Imager (SSMI) on board the F-13 satellite (31 January 2003-31 December 2007), the Special Sensor Microwave Imager/Sounder (SSMI/S) on board the F-17

satellite (1 January 2008- April 1, 2016), and SSMI/S on board the F-18 satellite (April 1, 2016—present). *The daily I_C is derived from the NASA Team sea ice algorith*m (Cavalieri et al., 1996, updated 2020) and is used in the calculations of the surface turbulent fluxes. Accuracy of the I_C product is between 5 (winter)-15 (summer)% (Cavalieri et al., 1992).

The SHF and LHF are calculated via the bulk method using the Monin Obukhov Similarity Theory and are given by

$$\mathrm{SHF} = c_p S_r \left[C_{Sz,i} I_C (T_{S,i} - T_A) + C_{Sz,w} (1 - I_C)(T_{S,w} - T_A)\right] \quad (1)$$

$$\mathrm{LHF} = \rho S_r \left[C_{Ez,i} L_i I_C \left(q_{S,i} - q_A\right) + C_{Ez,w} L_w (1 - I_C)\left(q_{S,w} - q_A\right)\right] \quad (2)$$

where ρ is the air density, c_p is the specific heat of air, L_i (L_w) is the latent heat of sublimation (vaporization) over ice (water), C_{Sz} (C_{Ez}) is the sensible (latent) heat transfer coefficient over ice (i) and water (w), I_C is the sea ice concentration, S_r is the effective wind speed at 10 m (m s^{-1}) (Andreas et al., 2010b), T_S (q_S) is the surface temperature (specific humidity) of either sea ice (i) or water (w), and T_A (q_A) is the air temperature (specific humidity) at 2 m. Extensive *in situ* measurements were made over the Arctic sea ice during the Surface Heat Budget of the Arctic Ocean Experiment (SHEBA) campaign in 1997–1998 and Grachev et al. (2007) used these to create a highly accurate flux profile algorithm for stable conditions over the ice. This algorithm better fits the very stable boundary layer conditions in the Arctic and are used in our calculations over sea ice. Andreas et al. (2010a), Andreas et al., 2010b used roughness lengths measured from the SHEBA campaign to create an algorithm over the sea ice in the winter when the ice is covered with compact, dry snow and in the summer when the ice is covered with wet snow, melt ponds and leads. As these are the most accurate estimates made for the sea ice in different seasons, these new roughness lengths are used in our turbulent flux scheme.

The updated flux profile algorithm from Launiainen and Vihma (1990) includes these changes, which improve the accuracy of the turbulent flux calculations over grid points that contain sea ice (Boisvert et al., 2015a). This method also allows for the input parameters of temperature, humidity and wind speed to be taken at various heights above the surface and uses an iterative calculation that accounts for the stability of the boundary layer in calculating the values at a predetermined reference height (e.g., 2 m) (Launiainen and Vihma, 1990). Readers are referred to Boisvert et al., 2013, Boisvert et al., (2015a) for a full description of the model used to calculate the turbulent fluxes over the sea ice. These Arctic sea ice specific changes made to this algorithm, to the best of our knowledge, have not been adopted in any other climate models or reanalysis products. This algorithm is better suited to simulate turbulent fluxes over the Arctic Ocean and when compared with *in situ* data from the N-ICE2015 campaign, AIRS-derived LHF (SHF) had a root mean square error of 0.74 W m^{-2} (5.32 W m^{-2}) (Taylor et al., 2018). Overall, these comparisons indicate an uncertainty of ~20% in the AIRS-derived surface turbulent fluxes, however we can't say for certain that this uncertainty is the same over all sea ice types and seasons with a lack of *in situ* data. The native resolution of this data set is 25 × 25 km, however these fluxes have been interpolated onto a common 1° × 1° grid for this study.

Coupled Model Intercomparison Project 6

Model results are calculated from 18 CMIP6 models (**Table 1**) participating in the historical and SSP5-8.5 (shared socioeconomic pathway) scenarios (Eyring et al., 2016). To cover the entire 2002–2020 observational time period, monthly data from the historical simulations for the period 2002–2015 is merged with the first 5 years of the SSP5-8.5 future scenario (2015–2020). We just use one ensemble member per model. Model-simulated surface turbulent flux differences are poorly understood due to insufficient observational datasets; further, substantial across-model spread in turbulent fluxes has remained consistent from CMIP5 to CMIP6 (Wild, 2020). Models often lack the complexity required to represent the processes affecting the simulation of surface turbulent fluxes (e.g. evaporation/precipitation, sea ice/snow cover, wind speed) (Wild, 2020). All CMIP6 model output has been interpolated onto a common 1° × 1° grid.

METHODOLOGY

Sea Ice Regimes

Models and observations represent unique perspectives of the climate system, such that differences between them cannot always be interpreted as model error. Meaningful observation-model comparisons require the rectification of these different perspectives. Common challenges include rectifying differences in quantity definitions (e.g., cloud fraction; Bodas-Salcedo et al., 2011) and differences in spatial and temporal resolution. When comparing trends, natural variability differences must also be accounted for.

Coupled, free running atmosphere-ocean models used to simulate the recent climate (**Table 1**) produce their own natural variability that is not synced with observed variability. Thus, a direct comparison of the spatial patterns of modeled and observed trends does not provide a meaningful evaluation. This is a substantial challenge in the Arctic where natural variability is especially large (e.g., Kay et al., 2012). We adopt a sea ice regime compositing approach to control for the effects of Arctic sea ice variability on our comparison.

The sea ice regime compositing approach defines four regimes based upon trends in I_C: persistent sea ice, and slow, moderate, and fast sea ice loss. The four sea ice regimes are defined by the quartiles of observed I_C trends:

- Persistent regime: I_C trends > −0.27% $decade^{-1}$
- Slow sea ice loss: −0.27% $decade^{-1}$ > I_C trends > −2.4% $decade^{-1}$
- Moderate sea ice loss: −2.4% $decade^{-1}$ > I_C trends > −7.5% $decade^{-1}$
- Fast sea ice loss: I_C trends < −7.5% $decade^{-1}$

Figure 1 depicts the sea ice regimes for passive microwave observations and four CMIP6 models. These models highlight the

TABLE 1 | Summary of CMIP6 models used in this study.

Model	Modeling agency	References
ACCESS-CM2	CSIRO, ARCCSS	Dix (2019)
ACCESS-ESMI-5	CSIRO	Ziehn et al. (2019)
BCC.CSM2-MR	Beijing Climate Center, China Meteorological Administration	Wu et al. (2018)
CanESMS	Canadian Centre for Climate Modelling and Analysis	Swart et al. (2019)
CESM2	National Center for Atmospheric Research	Danabasoglu (2019)
CESM2-WACCM	National Center for Atmospheric Research	Danabasoglu (2019)
FIO-ESM-2-0	First Institute of Oceanography, Qingdao National Laboratory for Marine Science and Technology	Song et al. (2019)
FGOALS-f3-L	Chinese Academy of Sciences	Yu et al. (2019)
FGOALS-g3	Chinese Academy of Sciences	Li (2019)
GFDL-ESM4	NOAA/Geophysical Fluid Dynamis Laboratory	Krasting et al. (2018)
INM-CM4-8	Institute for Numerical Mathematics	Volodin et al. (2019)
INM-CM5-0	Institute for Numerical Mathematics	Volodin et al. (2019)
IPSL-CM6A-LR	L'Institut Pierre-S imon Laplace	Boucher et al. (2021)
MIROC6	Japan Agency for Marine Earth Science and Technology, Atmosphere and Ocean Research Institute, National Institute for Environmental Studies, RIKEN Center for Computational Science	Shiogama et al. (2019)
MPI-ESM1-2-HR	Max Planck Institute for Meteorology	Jungclaus (2019)
MPI-ESM1-2-LR	Max Planck Institute for Meteorology	Wieners (2019)
MRI-ESM2-0	Meteorological Research Intitute	Yukimoto et al. (2019)
NESM3	Nanjing University of Information Science and Technology	Cao and Wang (2019)

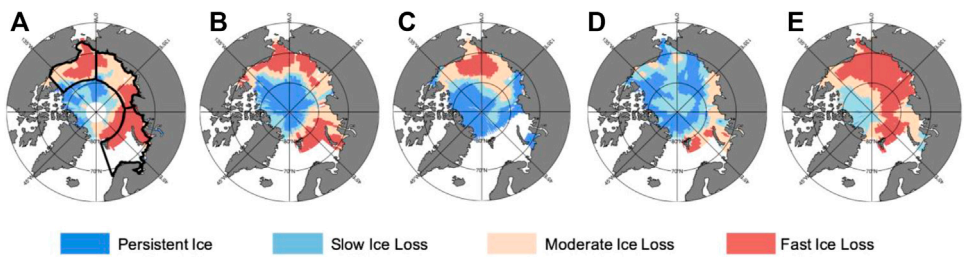

FIGURE 1 | Winter (October-January) sea ice loss regimes for observations **(A)** and four CMIP6 models **(B–E)** ACCESS-CM2, CESM2-WACCM, INM-CM4-8 and MRI-ESM2-0. White and grey (land) portions are areas not included in our discussion. Black lines denote regions of interest (clockwise): Beaufort-Chukchi seas, Laptev-East Siberian seas, Barents-Kara seas and the Central Arctic in the areas around the North Pole.

inter-model range in sea ice loss trends. While ACCESS-CM2 (**Figure 1B**) simulates sea ice retreat regimes similar to observations (**Figure 1A**), the other models vary drastically (**Figures 1C–E**). These differences in I_C trends across the models indicate that the location and number of grid boxes in each sea ice loss regime also differ. Overall, the observed I_C trends are found within the model range. Our approach is to compare SHF and LHF from models and observations within these sea ice loss regimes to control for the large differences in I_C trends.

Diagnostic Approach Assessing Sensitivity of Surface Turbulent Fluxes to Controlling Factors

A multi-linear regression approach is developed to determine the most impactful variables on surface turbulent fluxes (namely, air-sea temperature (T_S–T_A) and moisture (q_S–q_A) gradients, 10-m wind speed ($\bar{U}$), I_C) and to provide a means of consistently intercomparing models without knowing the specific model bulk formula. The full regression equation below is fit to observations and models.

$$SHF = \beta_0 + \beta_{T_S-T_A} \cdot (T_S - T_A) + \beta_{I_C} \cdot I_C + \beta_{\bar{U}} \cdot \bar{U} + \beta_{I_C \cdot T_S - T_A} \cdot [I_C \cdot (T_S - T_A)] + \beta_{\bar{U} \cdot T_S - T_A} \cdot [\bar{U} \cdot (T_S - T_A)] \quad (3)$$

$$LHF = \beta_0 + \beta_{q_S-q_A} \cdot (q_S - q_A) + \beta_{I_C} \cdot I_C + \beta_{\bar{U}} \cdot \bar{U} + \beta_{I_C \cdot q_S - q_A} \cdot [I_C \cdot (q_S - q_A)] + \beta_{\bar{U} \cdot q_S - q_A} \cdot [\bar{U} \cdot (q_S - q_A)] \quad (4)$$

For CMIP6 models, $\bar{U}$ was calculated as $\bar{U} = \sqrt{(u^2 + v^2)}$ where u and v are the 10-m $\bar{U}$ components. All other variables were obtained from the CMIP6 archive except for q_S, which was calculated using the Clausius-Clapeyron equation and model temperature output. Before performing the regression, the linear trend at each grid box was removed for each variable and it was normalized by its standard deviation over the time period of the study. This step is performed to account for the differences in the variability of each of these terms across models. Further, the multi-linear regression model was applied using all available grid boxes within a regime to create a set of Arctic domain coefficients for each model and for observations.

The slopes $\beta_{\text{TS-TA}}$, $-\beta_{I_C}$, and $-\beta_{U}$ represent the linear response of SHF (LHF) to T_S-T_A (q_S-q_A), I_C, and $\bar{U}$. Two covariance terms [$\beta_{I_C \cdot T_S - T_A}$ ($\beta_{I_C \cdot q_S - q_A}$) and $\beta_{\bar{U} \cdot T_S - T_A}$ ($\beta_{\bar{U} \cdot q_S - q_A}$)] are included in the regression due to the strong covariation between T_S-T_A (q_S-q_A) with both I_C and $\bar{U}$. The relationship between T_S-T_A (q_S-q_A) and I_C is because less sea ice coverage potentially allows for a larger air-sea temperature (moisture) gradient; incorporating a product term [$I_C^*(T_S$-$T_A)$; $I_C^*(q_S$-$q_A)$] approximates this interaction. T_S-T_A (q_S-q_A) also covaries with $\bar{U}$, whereby higher $\bar{U}$ tends to occur with a larger air-sea temperature (moisture) gradient. The significance of these terms is tested for each model and in observations by computing the extra sum of squares (ESS) and performing an F-test (Ramsey and Schafer, 2012). ESS is a measure of how much the unexplained variance in SHF (LHF) decreases with the addition of the covariance terms and is calculated as, *ESS = Sum of squared residuals in reduced model–Sum of squared residuals in the full model*, where the reduced model is the regression equation without the covariance term and the full model is the regression equation including the covariance term. The full model variance is used in the denominator of **Eq. 5** because the purpose of this test is to evaluate the statistical significance of adding covariance terms to the regression model. The significance test was performed for observations and each model individually for each ice loss regime.

The F-statistic based on the *ESS* is defined in **Equation 5** and is used to obtain a *p*-value at the desired level of confidence.

$$F - statistc = \frac{\left[\frac{ESS}{\#\ of\ \beta's\ being\ tested}\right]}{\sigma^2\, from\, full\, model} \tag{5}$$

If the *p*-value is small then we can conclude that the reduced model without the covariance terms is incorrect and accept the full model. In **Equation (5)**, $\boldsymbol{\sigma^2}$ is the variance from the full model including covariance terms. The full model is appropriate for all ice regimes for the SHF and LHF regressions. The significance of each term (β) for CMIP6 models and observations are found in **Supplementary Table S1**.

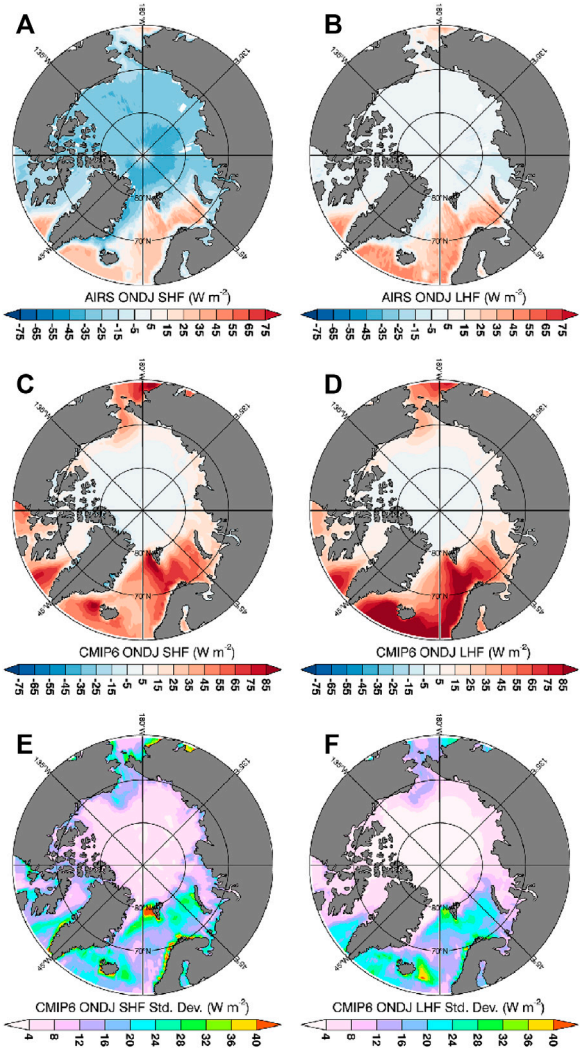

FIGURE 2 | Average winter (ONDJ) SHF and LHF from 2002 to 2020 for AIRS-derived **(A,B)** and CMIP6 **(C,D)** and across-model spread represented as the standard deviation **(E,F)**.

RESULTS

Models that produce a stronger increase in SHF and LHF for the same sea ice loss are hypothesized to warm more over the Arctic. We address this hypothesis by 1) evaluating the SHF and LHF climatological distribution in CMIP6 models against observations, 2) comparing observed and simulated SHF and LHF trends within sea ice retreat regimes, 3) analyzing SHF and LHF sensitivities to controlling factors, and 4) analyzing relationships with projected Arctic warming. We separate the discussion of observed and model-simulated trends deliberately to reduce the temptation to directly compare observed and model-simulated trends and limit observation-model comparison to the appropriate circumstances when the influence of sea ice natural variability is controlled for or small: 20-year mean state and sea ice loss regimes. In the discussion below, positive (negative) fluxes denote energy exchange from the surface to the atmosphere (atmosphere to the surface).

Observed Surface Turbulent Flux Mean State and Trends

The Arctic surface is a net heat sink to the Arctic atmosphere during winter with the strongest sink in the central Arctic and a heat source in the Barents-Kara (B-K) seas region (**Figure 2**). The central Arctic is characterized by a broad region of negative SHF and LHF values that contribute to the Arctic average SHF and LHF values: -31.8 ± 5.19 W m^{-2} and -3.1 ± 1.88 W m^{-2}, respectively (**Table 2** and **3**). The primary mechanism of turbulent heat transfer from the atmosphere to the surface is the SHF; central Arctic LHF values are an order of magnitude smaller than SHF. The magnitude of the heat sink is reduced by the positive SHF and LHF fluxes in the B-K

TABLE 2 | Summary of mean values and their standard deviation (decadal trends and their standard deviations in parenthesis) for AIRS-derived and CMIP6 models SHF for October-January 2002–2020. Values are stratified by Arctic sea ice loss regimes.

	Fast loss	Mod loss	Slow loss	Persistent	All
ACCESS-CM2	23.9 ± 19.2	9.84 ± 14.2	−1.74 ± 6.91	−6.57 ± 2.92	0.77 ± 14.5
—	(8.36 ± 8.07)	(1.97 ± 2.67)	(0.97 ± 1.27)	(0.685 ± 0.653)	(1.96 ± 4.12)
ACCESS-ESM1-5	5.4 ± 7.21	4.83 ± 13.2	−2.28 ± 12.2	−1.23 ± 12.3	−0.395 ± 12.5
—	(3.63 ± 2.27)	(2.07 ± 2.2)	(0.965 ± 1.2)	(−0.212 ± 2.23)	(0.849 ± 2.12)
BCC-CSM2-MR	25.0 ± 17.4	6.46 ± 8.72	2.18 ± 7.07	−1.69 ± 6.94	−0.185 ± 8.31
—	(1.91 ± 2.32)	(0.715 ± 1.56)	(0.874 ± 1.53)	(0.211 ± 1.04)	(0.36 ± 1.23)
CanESM5	17.8 ± 17.2	2.21 ± 12.8	−8.02 ± 7.24	−9.67 ± 2.8	−1.75 ± 14.7
—	(15.2 ± 13.3)	(1.92 ± 3.71)	(1.14 ± 2.13)	(0.544 ± 0.433)	(3.85 ± 8.39)
CESM2	8.32 ± 9.29	11.2 ± 16.2	0.83 ± 6.2	4.46 ± 7.87	4.64 ± 10.2
—	(3.6 ± 1.65)	(1.13 ± 1.51)	(0.649 ± 0.87)	(0.028 ± 1.13)	(0.87 ± 1.59)
CESM2-WACCM	13.8 ± 10.6	10.2 ± 13.7	4.46 ± 8.84	2.90 ± 6.84	4.71 ± 9.2
—	(3.17 ± 1.32)	(0.892 ± 1.18)	(0.039 ± 0.937)	(−0.248 ± 1.04)	(0.14 ± 1.35)
FIO-ESM-2-0	4.09 ± 8.38	6.38 ± 16.7	3.71 ± 16.8	−0.694 ± 14.2	4.47 ± 13.9
—	(3.08 ± 1.42)	(1.0 ± 1.79)	(0.387 ± 1.6)	(-0.131 ± 1.21)	(1.65 ± 1.98)
FGOALS-f3-L	36.8 ± 13.7	16.7 ± 18.1	2.87 ± 10.2	−1.52 ± 6.57	0.392 ± 9.66
—	(4.79 ± 2.5)	(1.91 ± 1.94)	(0.818 ± 1.25)	(-0.19 ± 1.05)	(0.122 ± 1.33)
FGOALS-g3	14.7 ± 21.4	11.9 ± 21.1	−1.98 ± 15.9	−8.43 ± 7.84	−6.21 ± 11.9
—	(3.22 ± 5.0)	(1.03 ± 3.66)	(0.393 ± 2.42)	(0.023 ± 1.22)	(0.206 ± 1.88)
GFDL-ESM4	21.3 ± 12.8	13.6 ± 14.8	5.21 ± 10.5	−0.314 ± 6.32	2.27 ± 9.93
—	(5.35 ± 2.71)	(2.09 ± 2.15)	(0.26 ± 1.47)	(−0.395 ± 1.06)	(0.11 ± 1.84)
INM-CM4-8	33.1 ± 35.9	11.9 ± 21.6	−2.73 ± 8.37	−2.81 ± 8.2	−0.918 ± 12.5
—	(0.403 ± 6.45)	(−1.09 ± 4.03)	(0.095 ± 1.35)	(−0.161 ± 1.18)	(-0.137 ± 1.9)
INM-CM5-0	20.3 ± 8.84	10.9 ± 15.5	−0.581 ± 13.4	−2.12 ± 9.92	-0.39 ± 12.1
—	(4.29 ± 3.28)	(2.31 ± 2.6)	(0.549 ± 1.42)	(−0.398 ± 1.51)	(0.103 ± 1.86)
IPSL-CM6A-LR	7.49 ± 10.3	5.53 ± 15.0	−4.63 ± 5.95	−4.89 ± 6.4	1.22 ± 11.5
—	(4.40 ± 4.06)	(0.306 ± 1.77)	(-0.304 ± 0.987)	(-0.506 ± 1.13)	(1.25 ± 3.3)
MIROC6	4.25 ± 5.45	3.67 ± 9.32	−1.71 ± 6.84	−3.15 ± 6.38	−1.36 ± 7.55
—	(3.55 ± 1.32)	(1.2 ± 1.35)	(0.13 ± 0.907)	(−0.376 ± 1.05)	(0.161 ± 1.39)
MPI-ESM1-2-HR	37.8 ± 27.6	25.2 ± 19.1	12.9 ± 13.1	8.17 ± 7.32	11.5 ± 13.0
—	(4.64 ± 4.14)	(0.769 ± 1.95)	(−0.426 ± 1.38)	(−0.876 ± 1.31	(−0.481 ± 1.84)
MPI-ESM1-2-LR	23.9 ± 17.4	19.9 ± 18.1	4.87 ± 7.87	7.82 ± 9.51	8.2 ± 12.0
—	(4.37 ± 3.28)	(0.835 ± 1.83)	(−0.489 ± 0.948)	(−0.974 ± 1.16)	(−0.252 ± 1.68)
MRI-ESM2-0	7.87 ± 16.0	2.14 ± 14.5	−7.30 ± 6.22	−9.11 ± 5.35	0.151 ± 14.1
—	(5.15 ± 4.41)	(1.22 ± 1.62)	(1.12 ± 0.586)	(0.75 ± 0.319)	(2.41 ± 3.23)
NESM3	15.0 ± 14.4	6.29 ± 12.0	2.47 ± 6.23	−2.03 ± 5.36	8.74 ± 13.2
—	(5.76 ± 2.89)	(2.83 ± 3.28)	(1.7 ± 3.12)	(0.534 ± 1.57)	(3.7 ± 3.51)
ENSEMBLE	17.8 ± 10.8	9.94 ± 6.16	0.474 ± 5.02	−1.72 ± 5.15	1.99 ± 4.34
—	(4.72 ± 3.1)	(1.28 ± 0.90)	(0.492 ± 0.594)	(−0.094 ± 0.492)	(0.937 ± 1.3)
AIRS	−28.2 ± 5.86	−32.8 ± 4.49	−34.6 ± 3.74	−31.5 ± 4.13	−31.8 ± 5.19
—	(3.16 ± 2.46)	(1.51 ± 2.99)	(1.59 ± 2.45)	(1.57 ± 1.73)	(1.96 ± 2.56)

seas, providing a narrow area of surface heat source to the atmosphere. The contributions to the B-K sea heat source are roughly equally distributed between SHF and LHF.

The observed SHF and LHF trends suggest that the changing Arctic surface is altering the character of the atmosphere's heat sink in the winter (**Figure 3**). Turbulent flux trends (**Figure 3F**) show increases across much of the central Arctic, weakening the heat sink. SHF trends, rather than LHF, account for most of this weakening and are driven by a thinning of the multi-year sea ice (Kwok, 2018), which allows for more conduction through the sea ice from the ocean and warming surface temperatures, along with a potential weakening of the surface-based temperature inversion. Additionally, there is a strengthening surface heat source near the sea ice edge in the B-K seas region, roughly evenly distributed between SHF and LHF trends (**Figure 3**). There is also a weakening of the heat source farther south in the North Atlantic potentially related to surface cooling from Greenland melt water (Allan and Allan, 2019). These SHF and LHF trends are consistent with the AIRS-observed changes in T_S–T_A and q_S–q_A (**Figures 3C,D**), and are largest in regions of substantial sea ice loss (**Figure 3E**).

Analysis of trends within the sea ice loss regimes shows that the fast sea ice loss regime exhibits the largest trends, further highlighting the relationship between sea ice and SHF and LHF (**Figure 4**). LHF trends increase from the slow to fast sea ice loss regime (**Figure 4**). The regime-to-regime differences in SHF trends from observations are constant in all regimes and increase for the fast sea ice retreat regime. The SHF trends are positive in all sea ice loss and persistent regimes, whereas the LHF trends are slightly negative in the slow sea ice retreat and persistent regimes. The trends in SHF and LHF are consistent with the trends in T_S–T_A and q_S–q_A. Overall, in the entire Arctic, the SHF and LHF trends in the observations are positive.

The presence of sea ice modifies the SHF and LHF frequency distributions (**Figure 5**). The mode of the AIRS-derived LHF is slightly negative and the SHF is more negative. The SHF distribution shows a broader distribution than LHF. All sea ice

TABLE 3 | Summary of mean values and their standard deviation (decadal trends and their standard deviations in parenthesis) for AIRS-derived and CMIP6 models LHF for October-January 2002–2020. Values are stratified by Arctic sea ice loss regimes regions.

—	Fast loss	Mod loss	Slow loss	Persistent	All
ACCESS-CM2	21.1 ± 14.3	10.2 ± 9.74	1.87 ± 3.92	–0.165 ± 1.32	4.61 ± 10.1
—	(7.56 ± 5.31)	(1.94 ± 1.48)	(0.53± 0.545)	(0.111 ± 0.185)	(1.46 ± 3.23)
ACCESS-ESM1-5	9.13 ± 5.3	9.38 ± 10.6	3.31 ± 9.85	4.77 ± 10.3	5.09 ± 10.2
—	(3.28 ± 1.47)	(1.85 ± 1.73)	(0.45 ± 0.840)	(–0.361 ± 1.61)	(0.522 ± 1.67)
BCC-CSM2-MR	21.9 ± 9.79	8.1 ± 4.95	4.24 ± 3.83	2.07 ± 4.0	3.1 ± 5.06
—	(1.29 ± 0.935)	(0.832 ± 0.756)	(0.341 ± 0.643)	(0.0378 ± 0.435)	(0.156 ± 0.571)
CanESM5	16.3 ± 9.49	7.43 ± 7.03	2.69 ± 3.64	1.61 ± 1.48	5.81 ± 7.83
—	(9.04 ± 7.73)	(1.19 ± 1.82)	(0.70 ± 1.06)	(0.333 ± 0.198)	(2.31 ± 4.87)
CESM2	7.5 ± 7.09	10.3 ± 13.7	1.28 ± 5.04	4.1 ± 5.47	4.46 ± 8.29
—	(3.32 ± 1.2)	(1.34 ± 0.822)	(0.208 ± 0.365)	(–0.657 ± 0.666)	(0.482 ± 1.40)
CESM2-WACCM	10.3 ± 7.6	7.79 ± 11.0	2.6 ± 5.34	1.59 ± 4.75	3.05 ± 6.75
—	(3.42 ± 1.04)	(1.38 ± 0.817)	(0.342 ± 0.475)	(–0.0393 ± 0.501)	(0.402 ± 1.06)
FIO-ESM-2-0	6.44 ± 5.42	7.81 ± 11.4	6.58 ± 13.0	4.40 ± 8.93	6.79 ± 9.65
—	(3.01 ± 1.01)	(1.04 ± 0.845)	(0.278 ± 0.935)	(0.284 ± 0.988)	(1.63 ± 1.51)
FGOALS-f3-L	26.6 ± 8.81	12.6 ± 12.3	4.02 ± 6.2	1.26 ± 3.99	2.47 ± 6.08
—	(2.02 ± 2.65)	(1.05 ± 1.0)	(0.398 ± 0.565)	(–0.0861 ± 0.552)	(0.069 ± 0.689)
FGOALS-g3	13.3 ± 11.7	11.7 ± 11.9	4.13 ± 8.94	0.764 ± 4.07	1.95 ± 6.44
—	(2.1 ± 2.25)	(0.822 ± 1.78)	(0.178 ± 1.04)	(–0.049 ± 0.436)	(0.0808 ± 0.856)
GFDL-ESM4	16.9 ± 9.4	11.7 ± 10.9	5.74 ± 7.17	2.26 ± 4.17	4.0 ± 6.84
—	(3.8 ± 1.51)	(1.76 ± 1.5)	(0.403 ± 0.796)	(–0.125 ± 0.527)	(0.244 ± 1.18)
INM-CM4-8	28.7 ± 22.8	12.8 ± 13.7	1.37 ± 4.49	1.18 ± 4.48	2.71 ± 7.97
—	(3.85 ± 4.53)	(0.291 ± 2.05)	(0.0626 ± 0.580)	(–0.0608 ± 0.383)	(0.0768 ± 1.05)
INM-CM5-0	23.4 ± 12.2	12.7 ± 12.2	3.88 ± 7.66	2.31 ± 6.66	3.78 ± 8.31
—	(3.89 ± 3.24)	(1.95 ± 2.08)	(0.270 ± 0.622)	(–0.277 ± 0.894)	(0.0833 ± 1.26)
IPSL-CM6A-LR	11.1 ± 8.55	9.87 ± 13.1	1.42 ± 4.58	2.53 ± 5.12	6.23 ± 9.52
—	(4.18 ± 3.65)	(0.829 ± 1.73)	(–0.126 ± 0.699)	(–0.433 ± 0.778)	(1.36 ± 2.97)
MIROC6	5.59 ± 2.69	5.55 ± 6.99	2.12 ± 5.67	1.04 ± 4.89	2.25 ± 5.72
—	(3.33 ± 0.840)	(1.47 ± 0.783)	(0.24 ± 0.542)	(-0.0969 ± 0.623)	(0.378 ± 1.03)
MPI-ESM1-2-HR	22.7 ± 14.4	14.9 ± 12.4	6.29 ± 8.09	3.39 ± 3.69	5.54 ± 7.82
—	(4.15 ± 2.58)	(0.798 ± 1.17)	(0.206 ± 0.824)	(–0.388 ± 0.499)	(–0.0293 ± 1.14)
MPI-ESM1-2-LR	13.6 ± 7.99	11.6 ± 10.2	2.99 ± 4.03	4.26 ± 4.85	4.79 ± 6.46
—	(3.06 ± 1.67)	(1.14 ± 0.872)	(0.150 ± 0.327)	(–0.236 ± 0.582)	(0.294 ± 0.902)
MRI-ESM2-0	12.0 ± 11.7	8.18 ± 10.6	1.57 ± 4.66	0.741 ± 3.86	6.72 ± 10.2
—	(4.63 ± 3.57)	(1.14 ± 1.15)	(0.339 ± 0.292)	(0.142 ± 0.136)	(1.91 ± 2.82)
NESM3	9.69 ± 7.87	4.35 ± 5.42	2.09 ± 2.56	0.393 ± 1.1	5.89 ± 6.85
—	(4.1 ± 1.40)	(2.0 ± 1.10)	(1.15 ± 0.796)	(0.289 ± 0.508)	(2.61 ± 1.70)
ENSEMBLE	15.3 ± 7.17	9.83 ± 2.75	3.23 ± 1.68	2.09 ± 1.5	4.40 ± 1.57
—	(3.89 ± 1.83)	(1.27 ± 0.484)	(0.34 ± 0.271)	(–0.104 ± 0.255)	(0.78 ± 0.856)
AIRS	–3.28 ± 2.72	–3.66 ± 1.65	–2.99 ± 1.43	–2.39 ± 1.02	–3.1 ± 1.88
—	(0.823 ± 1.23)	(0.146 ± 0.908)	(–0.154 ± 0.512)	(-0.097 ± 0.489)	(0.179 ± 0.933)

regimes have a similar slightly negative mode of the SHF and LHF, however regions of faster sea ice loss exhibit a broader distribution of SHF and LHF (**Figure 5**). The frequency of slightly negative SHF and the frequency of moderate and strong positive LHF increases as sea ice loss becomes stronger. The fast sea ice loss regime has a much higher frequency of positive LHF values compared to any of the other sea ice regimes. Changes in the SHF and LHF distributions by sea ice regime correspond to differences in the T_S–T_A and q_S–q_A distributions (**Figures 5E,G**) showing that faster sea ice loss regimes correspond to greater T_S–T_A and q_S–q_A values. Thus, faster wintertime sea ice loss corresponds with larger T_S–T_A and q_S–q_A gradients and positive SHF and LHF trends.

CMIP6 Models Surface Turbulent Flux Mean State and Trends

While capturing key features of the observed spatial variations in SHF and LHF (**Figures 2A,B**), models represent the Arctic surface as a heat source, not a heat sink, to the winter Arctic atmosphere (**Figures 2C,D**). The model ensemble shows weak negative SHF and LHF across much of the central Arctic and strong positive SHF and LHF in the B-K seas region. The ensemble mean also shows similar magnitudes of the SHF and LHF across the Arctic suggesting that the two flux terms are of equal importance to the central Arctic surface energy budget, different from observations. The B-K seas region heat source is approximately 34 times stronger than in observations (CMIP6 ensemble average SHF + LHF: 70.1 W m^{-2}; AIRS-derived SHF + LHF: 2.1 W m^{-2}). While **Table 2** indicates that the magnitude of the surface heat source varies strongly, most models simulate the winter Arctic surface as a heat source to the atmosphere indicating a different role of surface-atmospheric coupling in the simulations compared to observations.

CMIP6 SHF and LHF trends indicate a narrowing area of the surface atmospheric heat sink and a broadening of the heat source, as observed, in concert with the declining sea ice cover

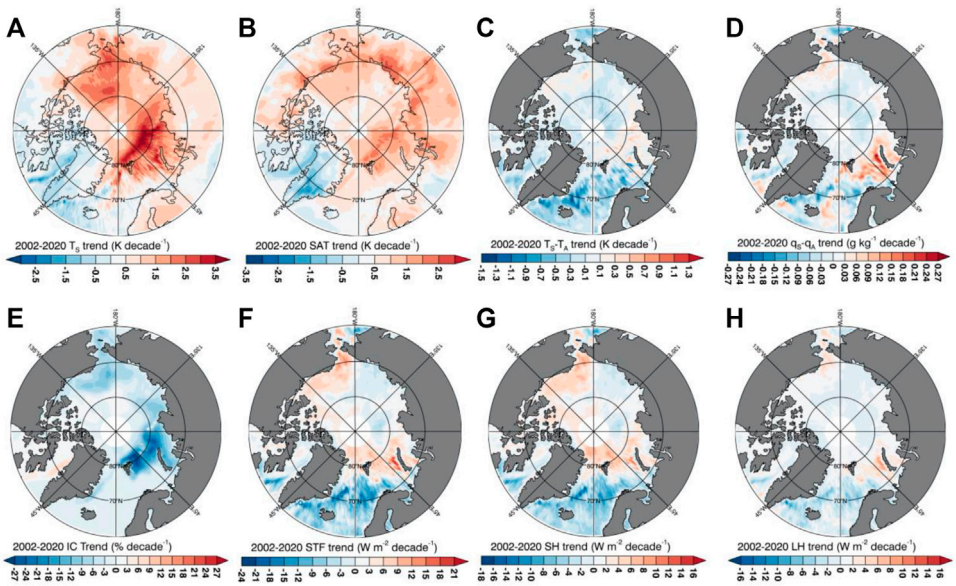

FIGURE 3 | Winter (ONDJ) decadal trends in **(A)** AIRS surface skin temperature, **(B)** AIRS surface air temperature, **(C)** AIRS T_S–T_A, **(D)** AIRS q_S–q_A, **(E)** observed I_C, **(F)** AIRS-derived surface turbulent flux, **(G)** AIRS-derived SHF and **(H)** AIRS-derived LHF.

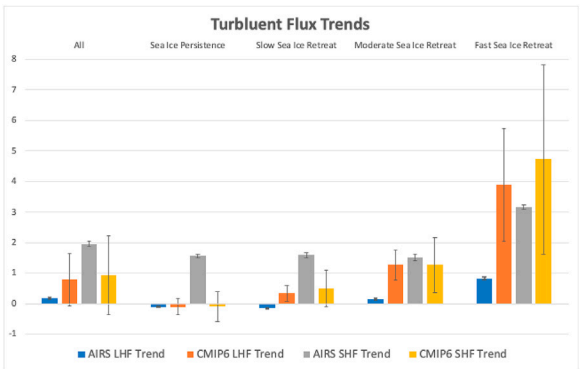

FIGURE 4 | Bar plot summarizing the Arctic winter (ONDJ) surface turbulent flux trends (Wm^{-2} per decade) by sea ice loss regime. Average trends for both AIRS-derived and CMIP6 ensemble-means are shown in the bars. The standard error of the AIRS-derived turbulent flux trends are shown in the error bars and the error bars for the CMIP6 ensemble-mean turbulent flux trends represent the inter-model spread.

(**Figure 6**). Surface temperature, SHF, and LHF trends are strongest in the Beaufort-Chukchi (B-C) and B-K seas regions with the most rapid sea ice decline. While the ensemble mean and observed patterns in the SHF and LHF trends are similar, the magnitudes are weaker than observations due to the averaging over multiple models. Moreover, the correspondence between the observed and ensemble mean spatial patterns of SHF and LHF trends may be misleading as the observations represent only a single realization of natural variability. The inter-model spread of these trends is substantial (**Figures 6F–J**) and is also strongest in the regions of the largest sea ice loss. As a result, the degree of sea ice loss and the resulting surface energy budget changes may serve as a useful observational constraint (**Section 4d**).

Model SHF and LHF trends within sea ice loss regimes tell a story consistent with observations, highlighting the sea ice influence on the inter-model trend differences (**Figure 4**). Model simulated SHF and LHF trends increase with greater sea ice loss and increases in T_S-T_A. The largest discrepancies between models and observations occur in the fast sea ice loss regime. For all sea ice loss regimes, the model ensemble LHF trends are always greater and more than double the observed value. With respect to SHF, there is a large observed trend in the persistent regime not found in models indicating that the models are struggling to capture the observed increase in T_S-T_A. This difference could also result from differences in the conductive heat flux through sea ice in the presence of thinning. The inter-model differences in SHF and LHF trends (**Figure 4**, error bars) are smaller within the sea ice loss regime framework than within the spatial distribution indicating that much of the inter-model differences in SHF and LHF flux trends correspond to differences in sea ice loss.

The SHF and LHF distributions within sea ice regimes indicate that the character of model-observational differences stems in part from different distributions of T_S–T_A and q_S–q_A (**Figure 5**). Model simulated SHF and LHF distributions show similar high frequencies of slightly negative SHF values and near zero LHF values as observations, however do not capture the frequency of negative SHF or LHF values. The dependence of the model-simulated SHF and LHF distributions on the sea ice loss rate exhibits similar behavior as observations. However, the model SHF distributions show moderate negative values for all sea ice regimes, but do not show values that reach < −20 W m^{-2} as in observations. These differences stem from models not simulating

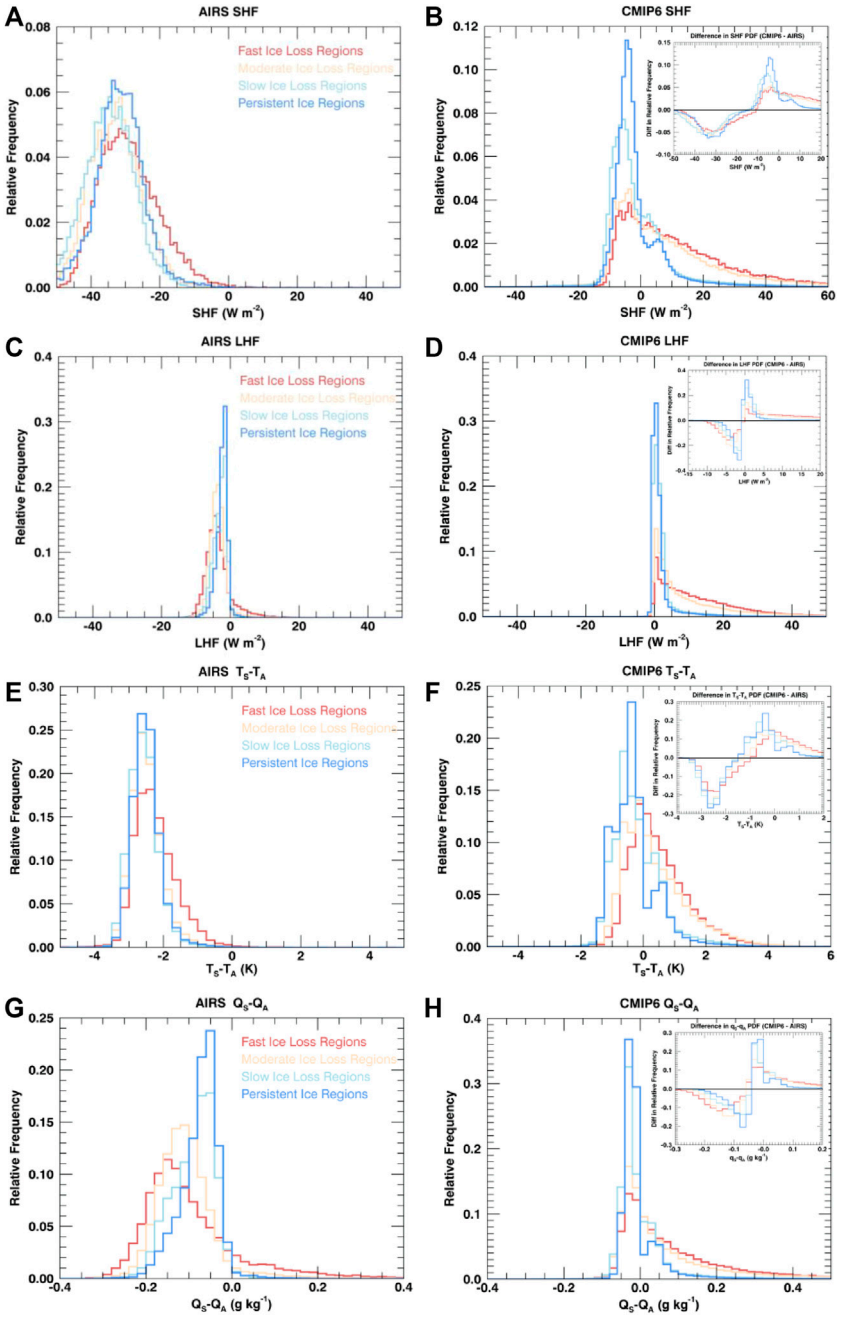

FIGURE 5 | PDFs of surface turbulent fluxes and surface-air temperature and moisture gradients for AIRS **(A,C,E,G)** and CMIP6 **(B,D,F,H)** for the four ice loss regimes for the Arctic winter (ONDJ). Insets represent difference plots (CMIP6—AIRS).

as strongly negative T_S–T_A values. The mode of the observed T_S–T_A distribution is ~ −3 K which is not found in the model simulated range (**Figure 5E**). Similarly, the model LHF distributions for all sea ice regimes show a larger frequency of positive values than observed and rarely produce negative values. These model-observation differences in the LHF distribution are driven by the differences in the q_S-q_A distributions; observations indicate frequent negative q_S–q_A values (**Figure 5G**), whereas the models rarely simulate negative q_S–q_A gradients. Radiosondes taken during the SHEBA campaign showed that specific humidity and temperature consistently increased with height near the surface due to frequent wintertime inversions (Yu., 2019; Yu et al., 2019) and q_S–q_A measurements taken during the Tara drifting station in spring and summer 2007 showed slight negative differences (Boisvert et al., 2015a) when surface-based inversions are weaker than the winter. Thus, these negative gradients in satellite-derived q_S–q_A appear realistic and are not captured in CMIP6 models. The underlying model-observations

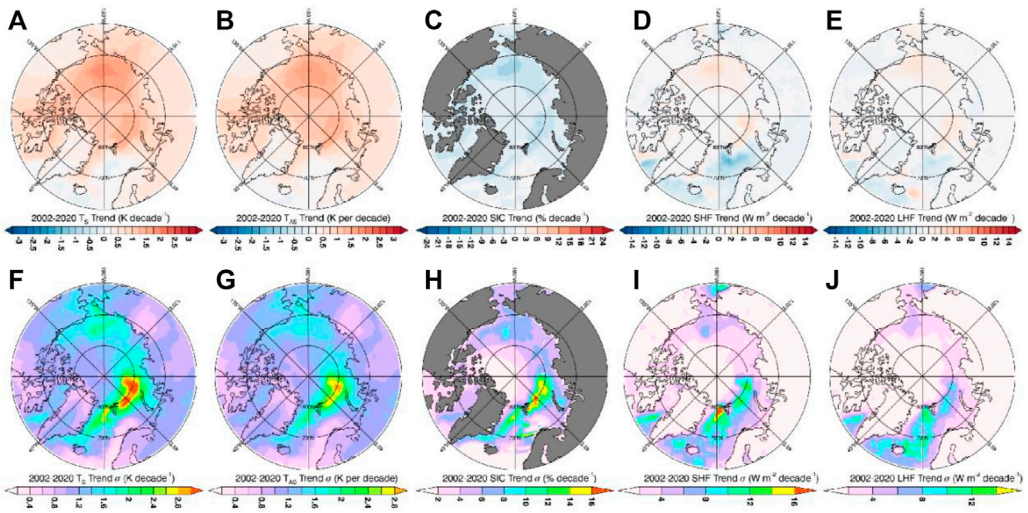

FIGURE 6 | Winter (ONDJ) decadal trends for CMIP6 for **(A)** T_S, **(B)** T_A, **(C)** I_C, **(D)** SHF and **(E)** LHF, and the across model spread for **(F)** T_S, **(G)** T_A, **(H)** I_C, **(I)** SHF and **(J)** LHF.

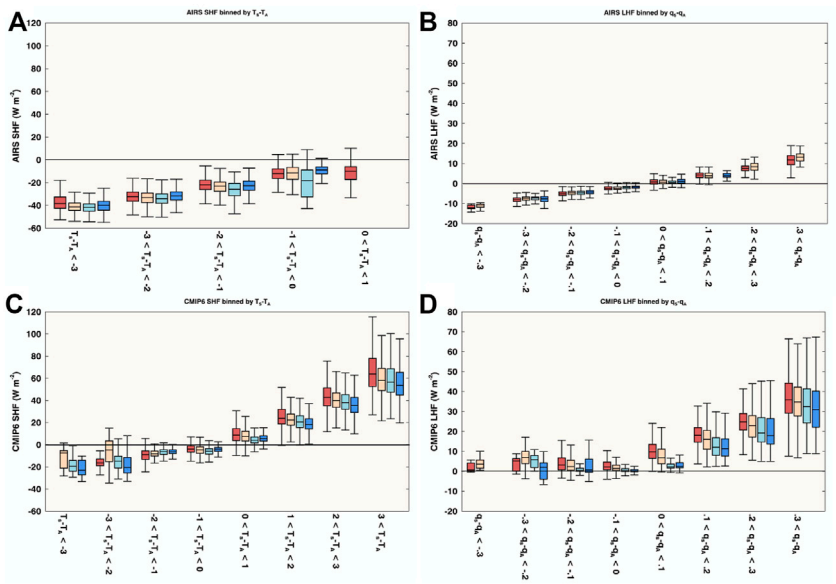

FIGURE 7 | Arctic winter (ONDJ) SHF (LHF) binned by T_S–T_A (q_S–q_A) for AIRS **(A,B)** and CMIP6 **(C,D)**. Data is further separated into the four ice loss regimes, denoted by color: fast loss (red), moderate loss (yellow), slow loss (light blue), and persistent regimes (royal blue). If a given T_S–T_A (q_S–q_A) bin lacked sufficient data points to compute a box and whisker, the bin was omitted (e.g, AIRS SHF for the largest T_S–T_A bin for moderate, slow and persistent ice loss regimes).

differences in the SHF and LHF values are related to the differences in the T_S–T_A and q_S–q_A distributions.

Since it appears that the source of the model and observational differences in SHF and LHF are largely driven by the difference in T_S–T_A and q_S–q_A, the turbulent fluxes are stratified by T_S–T_A, q_S–q_A for each sea ice regime (**Figure 7**). Qualitatively, the dependence of the mean SHF and LHF stratified by T_S–T_A and q_S–q_A is similar between models and observations; however quantitatively, the models show larger SHF values for the same T_S–T_A and much larger values for LHF for the same q_S–q_A. Especially surprising in **Figure 7**, is that models substantially differ from observed SHF and LHF values when the T_S–T_A and q_S–q_A values are the same. Especially troubling is that for negative q_S-q_A gradients, models are largely unable to produce a negative (atmosphere-to-surface) LHF. **Figures 5**, **7** together indicate that the larger SHF and LHF for models is from both more frequent T_S–T_A and q_S–q_A positive values and the larger SHF and LHF values at the same T_S–T_A and q_S–q_A values.

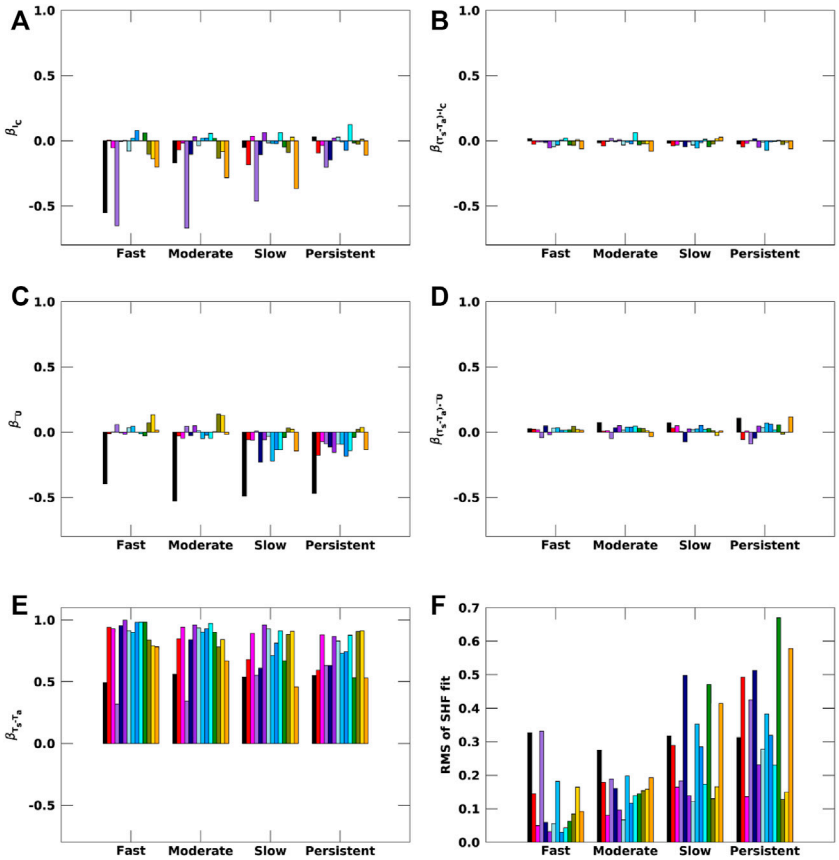

FIGURE 8 | Slopes obtained from the multi-linear regression on SHF **(A–E)** for observations (black) and CMIP6 models (colored) for the four ice loss regimes during Arctic winter (ONDJ). RMS for the fit is shown in **(F)**.

Surface Turbulent Flux Controlling Factors

Understanding which factors are most important for controlling surface turbulent flux variability and which factors contribute most strongly to the differences with observations is needed to improve the model representations of Arctic surface turbulent fluxes. We first considered applying a sensitivity study methodology to surface turbulent flux parameterizations from individual models to quantify the contributions of the component terms. However, compiling a complete set of STF parameterizations used by CMIP6 models would be complex and is beyond the scope of this study. Instead, we develop a multi-linear regression approach (**Section 3b**) to quantify the contributions from individual factors to SHF and LHF variability that can be consistently applied across models.

The multi-linear regression approach reasonably captures the variance in SHF and LHF for observations and models at the monthly mean timescale. The method is applied consistently to observations and models using $1^{\circ} \times 1^{\circ}$ monthly mean fields to create a single, Arctic-wide set of coefficients. The root mean square error of the multi-linear regression (**Figures 8F**, **9F**) shows a range in reliability; root mean square error values range from 5 to ~60% depending upon the model and sea ice regime. In most cases, the root mean square error values are <30% and the approach is better at representing LHF than SHF. While imperfect, the root mean square errors indicate that this approach captures the majority of SHF and LHF variability and captures physically-valid relationships.

Regression model robustness is also supported by the consistency in sign and magnitude across the CMIP6 model results (**Figures 8**, **9**). Error bars are not included in **Figures 8**, **9** since the accurate statistical error analysis is not considered trustworthy enough given the potential for spatial autocorrelation in the residuals. However, the overall consistency across the 18 CMIP6 models in the sign and magnitude of the dominant coefficients (β_{Ts-Ta}, β_{IC}, and β_{qs-qa}; **Figures 8**, **9**) provides confidence that the regression model approach is robust and indicates substantial model-observational disagreements in the importance of specific terms.

Applying the approach yields some expected features, such as the importance of $T_S - T_A$, and some unexpected features, such as the strong negative sign of the wind term for observations. β_{Ts-Ta} is the largest term in the majority of models with values from 0.3 to nearly 1.0 W m^{-2} per unit anomaly (**Figure 8E**). This is the case across all sea ice regimes. β_{Ts-Ta} is also an important term for observed SHF variability; however, most climate models possess a β_{Ts-Ta} nearly double the observational value.

β_{IC}, the largest magnitude observational slope, and $\beta_{\bar{U}}$ terms are associated with negative SHF anomalies. The β_{IC} represents

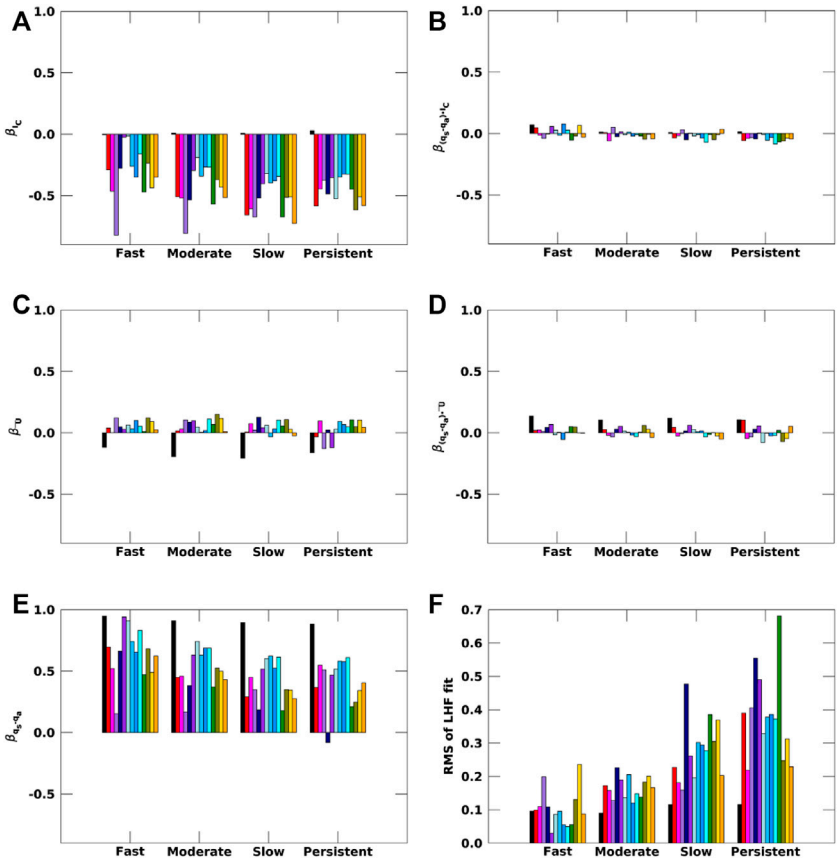

FIGURE 9 | Slopes obtained from the multi-linear regression on LHF **(A–E)** for observations (black) and CMIP6 models (colored) for the four ice loss regimes during Arctic winter (ONDJ). RMS for the fit is shown in **(F)**.

the influence of sea ice surface properties and atmospheric conditions, such as stability, that correlate with I_C. The models show a wider range of β_{IC} and $\beta_{\bar{U}}$ values compared to β_{Ts-Ta} (**Figure 8**). For β_{IC}, the large spread in the values suggests that sea ice surface properties that influence SHF (e.g., surface roughness, atmospheric stability, sea ice topography, etc.) are either represented differently by models and/or their effects on SHFs are parameterized differently. The importance of β_{IC} in producing SHF variability is much larger in observations than in most models.

The observational $\beta_{\bar{U}}$ value may seem slightly counterintuitive when not considering the mean state context. The majority of observational grid boxes have negative mean T_S–T_A values such that months with anomalously strong winds drive a more negative SHF. Stated plainly, this result indicates that a positive monthly mean wind anomaly drives a more negative SHF anomaly. The model $\beta_{\bar{U}}$ values are similarly tied to the background mean SHF value and stronger winds reinforce the background SHF. This explains the model behavior in the overall progression of $\beta_{\bar{U}}$ values to be generally positive over fast loss regime and generally negative over the persistent regime due to the smaller and negative mean state SHF values (**Table 2**).

As opposed to the SHF, observed variability of LHF is dominated by a single term, β_{qs-qa}. The observed β_{qs-qa} exceeds 0.9 W m^{-2} per unit anomaly for all sea ice regimes (**Figure 9E**). All models show a consistent sign of β_{qs-qa}, in line with observations, with a substantial inter-model spread in the magnitude. β_{IC} and $\beta_{\bar{U}}$ (**Figures 9A,C**) are substantially weaker than β_{qs-qa} in observations; specifically, observed β_{IC} is near zero. However, β_{IC} is of equal importance as β_{qs-qa} to explaining variability of LHF in models. $\beta_{\bar{U}}$ is of similar magnitude as β_{IC} and β_{qs-qa} for a few models, but overall accounts for small contributions to LHF variability.

Lastly, the inclusion of covariance terms is compelled by the statistical analysis and improves the explained variance of the model. **Figures 8B,D**, **9B,D** indicate, however, that most of these values are less than 0.1 Wm^{-2} per unit anomaly. The slopes of the covariance terms are small, show a narrower inter-model spread, and contribute little to the variance in SHF and LHF.

As shown in **Figures 5**, **7**, a portion of the discrepancy with the observed and model mean SHF and LHF results from different distributions of surface-air temperature and moisture gradients in models. In this section, we learn that substantial differences exist between the sensitivity of SHFs and LHFs to perturbations in relevant controlling factors (e.g., **Eqs. 1**, **2**. Models are much more efficient, by ~50%, at turning a T_S–T_A anomaly into a SHF anomaly relative to observations. Further, the influence of I_C on SHF is more important in observations than in models. The

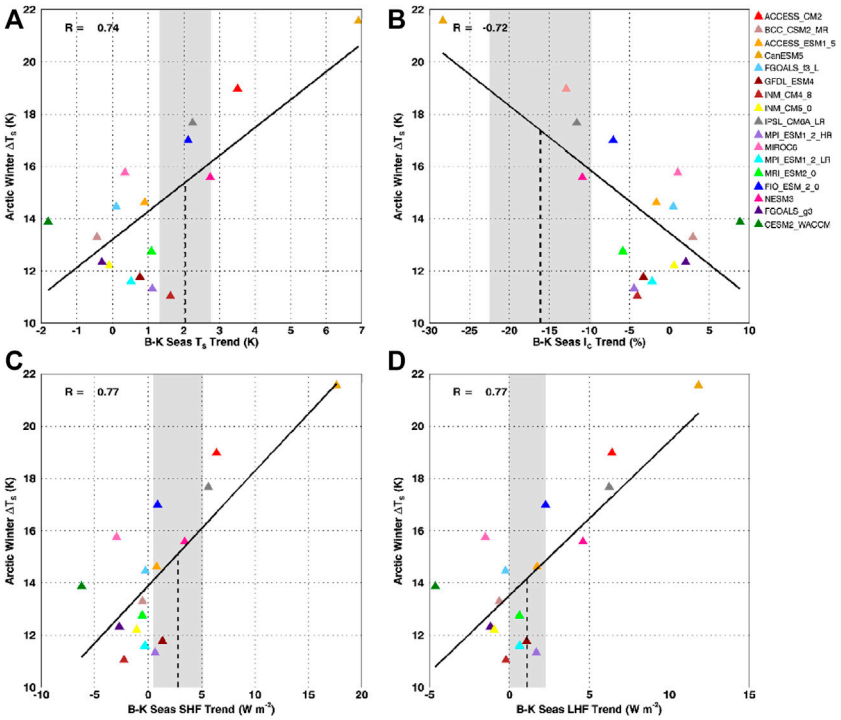

FIGURE 10 | Barents-Kara Seas present-day trends for sea ice gridboxes (>15% I_C) in **(A)** T_S, **(B)** I_C, **(C)** SHF and **(D)** LHF correlated with projected Arctic winter (ONDJ) warming. CMIP6 models are colored triangles while the dashed line indicates the present-day trend found for observations with the grey shading ± the observational standard deviation.

opposite is found for LHF variability in models; LHF is more sensitive to an I_C anomaly. Thus, the sea ice surface property influence on variability in SHF and LHF are inconsistent with observations and with each other. These results (**Figures 8**, **9**) illustrate that the most important terms for the model SHF and LHF flux variability are T_S–T_A and q_S–q_A.

Relationships With Projected Arctic Warming

There is a great deal of interest around constraining Arctic projections with observations to reduce uncertainty and make projections more actionable. We address the possibility of the above analyses being applied in this manner. Boeke and Taylor (2018) found that seasonal energy exchanges in sea ice retreat regions contribute significantly to the spread in model projections of Arctic amplification, whereby models that more efficiently disperse the energy stored in the ocean from summer via surface turbulent fluxes warm more. Dai et al. (2019) also found that increased turbulent heat fluxes from ice-free ocean in sea ice retreat regimes contributes to Arctic amplification. Given the importance of turbulent heat fluxes in recent literature, the SHF (LHF) regression slopes from **Figures 8**, **9** are tested as a possible emergent constraint (EC)--an approach that uses an ensemble of models to connect an observable process from present-day to future climate projections to narrow the uncertainty.

Given the dominance of the $\beta_{Ts\text{-}Ta}$ ($\beta_{qs\text{–}qa}$) terms in determining SHF (LHF), we hypothesized that model capability in turning a strong surface-air temperature (moisture) gradient into SHF (LHF) would correlate with projected Arctic warming and could make a suitable EC. While significant correlations with projected Arctic winter warming are found for some of the regression slopes, none of the regression slopes are good ECs because the observed regression slopes typically fall outside the model range. Despite this, we found that present-day trends in surface turbulent fluxes, I_C and T_S in ice-retreat regions correlate strongly with projected winter warming and could serve as a useful EC (**Figure 10**); for these quantities the observed trends fall within the model range, and the range in model values is large relative to the observational uncertainty (grey shading in **Figure 10**). To ensure that CanESM5 is not driving these relationships, we computed the regression again, removing CanESM5. The slopes and y-intercept values are very similar to those obtained using all the models, and while the correlation coefficient is smaller, it is still significant at the 95% level, therefore this relationship is robust. The relationships in **Figure 10** indicate a constrained Arctic winter warming range of ~14–17 K, substantially smaller than the 10–21 K inter-model range in warming.

DISCUSSION

The results presented in this study are not unique to the current generation of climate models. In fact, the previous generation of

climate models and current reanalyses both have turbulent flux biases when compared with observations in the Arctic. For instance, Taylor et al. (2018) show substantial model-observational differences between CMIP5 models and the previous version of the AIRS-derived SHF and LHF dataset that also indicate that the magnitude of the central Arctic surface heat sink is too weak. However, *in situ* observations show that negative fluxes in the winter over sea ice are a realistic phenomenon (e.g. SHEBA: Persson et al., 2017; N-ICE2015: Walden et al., 2017), and SHF were found to range between −20 and −30 W m^{-2}, consistent with the AIRS-derived SHF magnitudes. Here, we have shown that the unrealistically weak heat sink also persists in the current generation of CMIP6 models and could in part be driven by the poor representation of the stable boundary layer over ice in winter, which can underestimate the magnitude of the fluxes (Grachev et al., 2007; Boisvert et al., 2015a). These results are also consistent with comparisons of reanalyses and *in situ* data. For example, Graham et al. (2019) compared six widely used reanalysis products with *in situ* flux measurements taken during the N-ICE2015 campaign during winter, summer and spring of 2015. They found that the reanalyses got similar magnitudes for SHF and an order of magnitude difference in LHF, however the direction of the fluxes were often wrong. Thus, the inability to represent the sign and magnitude of the SHF and LHF is also present in reanalysis.

Our results have also shown that models have a positive bias in T_S-T_A and q_S-q_A when compared to observations, which may be related to the model representation of the strong wintertime surface-based inversions over sea ice. Arctic temperature inversions and associated near-surface variables are poorly represented in climate models (CMIP3: Medeiros et al., 2011; CMIP5: Pithan et al., 2014) and reanalyses (Serreze et al., 2012), and are influenced by how they simulate the stable boundary layer turbulence, surface energy budget, clouds, radiative transfer, and their vertical resolution (Lammert et al., 2010; Kilpeläinen et al., 2012). However, the accurate representation of these temperature and humidity inversions have important implications for the magnitude and sign of the turbulent fluxes (Bintanja et al., 2011; Devasthale et al., 2011; Vihma, 2014). These misrepresented temperature and humidity inversions could be contributing to biases in T_A and q_A, and would mean that the magnitude of T_S-T_A and q_S-q_A would be smaller and/or greater than zero depending on the situation, thus affecting the direction and magnitude of the fluxes in the Arctic.

Sea ice cover also influences the thermodynamic structure of the Arctic atmosphere by promoting more frequent temperature inversions, particularly in winter (Pavelsky et al., 2011; Taylor et al., 2015). Once sea ice forms in fall and winter, its lower effective heat capacity means the surface can cool more rapidly than the air above it leading to the development of temperature inversions, indicating a downward turbulent flux. Thus, how climate models represent the sea ice is very important, not just for the surface-based inversions, but also T_S and q_S and the boundary layer structure. However, climate models continue to struggle to represent sea ice cover extent and recent decline compared to observations (Schweiger et al., 2011; Stroeve J. et al., 2014; Holland et al., 2010; Jahn et al., 2012; SIMIP Community, 2020, Smith et al., 2020; Crawford et al., 2021; Watts et al., 2021; **Figure 1**), let alone the snow and ice thickness and surface characteristics. These sea ice and snow properties (e.g. location, compactness, roughness, and thickness) affect T_S and q_S, and the drag coefficients and roughness lengths, all which influence the boundary layer representation, and in turn the magnitude of the fluxes.

Observations are not free from bias, and the current limitations of satellite retrievals might contribute to the apparent model biases. For example, the vertical resolution of AIRS is 1 km and the instrument is therefore not able to resolve near surface variables (Susskind et al., 2014). In order to get the 2-m T_A and q_A variables, an iterative technique is used following Launiainen and Vihma (1990) to estimate these values from standard pressure levels using various boundary layer stability assumptions. These estimated T_A and q_A have been compared previously with *in situ* observations and have root mean square errors of 3.41 K and 0.54 g kg^{-1}, respectively, demonstrating that this iterative technique produces realistic results (Boisvert et al., 2015a; Taylor et al., 2018). Future satellite missions, as part of the Decadal Survey Planetary Boundary Layer, will work on having better resolution near the surface (Teixeira et al., 2021), which would improve the near surface temperature and humidity retrievals and reduce some of the errors in the fluxes.

Additionally, the observations might be biased towards clear sky or heterogeneous cloud cover conditions. Accurate retrievals can be derived for all channels under most cloud conditions, except for overcast or near-overcast conditions within the AIRS footprint Susskind et al. (2003), Susskind et al. (2014). Pithan et al. (2014) have shown that surface-based inversions were weaker during cloudy wintertime conditions than during clear conditions, and because under some extreme cloud conditions AIRS cannot retrieve variables, occurrences of smaller gradients in T_S-T_A and q_S-q_A might sometimes be missed. Regardless of these potential biases, AIRS captures wintertime Arctic temperature and humidity inversions well Devasthale et al. (2010), Devasthale et al. (2011).

While some CMIP6 ensemble member modeling groups have not made any changes to the turbulent flux scheme over sea ice (e.g. CESM2, Danabasoglu et al., 2020), others like the BCC-CSM2-MR have specifically made changes to improve these fluxes (Wu et al., 2019). Like the AIRS-derived scheme, they incorporate a gustiness parameterization, have updated the bulk parameterizations, changed the roughness lengths to be different based on season, and adopted the scalar roughness as a function of the Reynolds number. However, the gustiness parameterization used in BCC-CSM2-MR is one computed over the Western Pacific and tropical North Atlantic oceans (Zeng et al., 2002) and is not an Arctic sea ice specific parameterization that is different in stable and unstable conditions (Andreas et al., 2010b), which is adopted in the AIRS-derived scheme. The bulk parameterizations are taken from Zeng et al. (1998), which were produced using data from the tropical ocean, whereas in the AIRS-derived scheme, the bulk parameterizations are taken from Grachev et al. (2007), which were produced using SHEBA data and are specifically for Arctic

sea ice. The roughness lengths do change according to T_S being < or > −2°C in BCC-CSM2-MR, but are fixed numbers and are the same for heat and moisture. The AIRS-derived scheme has varying roughness lengths by season, by ice concentration, and differs for heat and moisture following Andreas et al. (2010a), Andreas et al. (2010b). The sea ice thickness and concentration are simulated using a sea ice simulator (Winton, 2000) in BCC-CSM2-MR, which might not reproduce the same sea ice cycle and trends that are observed in observations. While these adjustments to the BCC-CSM2-MR turbulent flux scheme are an example of climate models trying to improve the flux estimates over sea ice, large differences between BCC-CSM2-MR and the AIRS-derived fluxes still exist (e.g. BCC-CSM2-MR LHF: 3.1 ± 5.06 W m^{-2}, SHF: −0.185 ± 8.31 W m^2; AIRS-derived LHF: −3.1 ± 1.85, SHF: −31.8 ± 5.19 W m^{-2}).

While there are some diagnostic analyses of the sensitivity of surface turbulent fluxes (e.g. Reeves Eyre et al., 2021), multiple studies have compared bulk algorithms over the global oceans (Zeng et al., 1998; Brunke et al., 2002; Brunke et al., 2006; Brodeau et al., 2016), and some bulk algorithm parameterizations have been compared over Arctic sea ice (Andreas, 2002; Brunke et al., 2006; Grachev et al., 2008; Lu et al., 2013), there does not appear to be large-scale sensitivity analysis of these fluxes undertaken specifically over the Arctic sea ice. The multi-linear regression approach described here appears to be a first attempt to consistently evaluate the causes of inter-model differences in the surface turbulent flux calculations. While the approach provides a means of intercomparing models, we think that it represents just the 'tip of the iceberg' and we encourage and are pursuing additional techniques.

CONCLUSION

The Arctic is rapidly warming; this warming is most pronounced near the surface and during the winter months and is expected to continue in the future. Recent works have attributed this surface-based warming to a loss in sea ice cover and an increase in surface turbulent fluxes. Currently, there are large inter-model spreads in present day sea ice loss, turbulent fluxes and wintertime warming. This uncertainty hinders our ability to predict the magnitude of future wintertime warming. Here we use observational AIRS-derived turbulent fluxes computed from an Arctic-specific turbulent flux scheme to assess CMIP6 models in the winter months (October-January) between 2002 and 2020 to constrain future projections of wintertime warming.

The results show that CMIP6 models represent the surface turbulent fluxes in the central Arctic differently from observations, as a heat source rather than a heat sink to the winter Arctic atmosphere like observations. CMIP6 models produce mostly positive fluxes (from the surface to the atmosphere) in winter, meaning that the surface temperature and humidity is consistently larger than that of the overlying air, even in areas of persistent sea ice cover. These biases are likely driven by the models' inability to reproduce the strong surface-based inversions over the sea ice in the winter. The poor representation of these fluxes by climate models is a severe limitation to reducing uncertainties in projected Arctic warming. To evaluate model surface turbulent fluxes, a sea ice loss regime approach was used to account for the natural variability differences between climate models and observations. Both observations and models show that the turbulent fluxes have increased the most in areas of fast ice loss, whereas in areas of persistent ice cover there has been relatively little change.

When using a multiple regression approach to diagnose the influence of various controlling factors on surface turbulent flux variability, it was found that models exhibit much stronger sensitivities to a T_S-T_A anomaly than is found in observations. Models also exhibit a much weaker I_C damping effect than observations, suggesting that specific surface properties and characteristics associated with the sea ice surface type (e.g. strong stability) are represented differently between models compared to observations. Hence, the differences in observed and modeled surface turbulent fluxes is not solely due to parameterization differences. Differences in the air-sea temperature and moisture gradient distributions make a substantial contribution.

The magnitudes of differences of air-sea temperature and moisture gradients between observations and models is large, and is likely a driving factor in the magnitude of differences seen in the turbulent fluxes. One hypothesis for these differences is that models struggle to produce strong surface-based inversions over the sea ice in winter. Another hypothesis is that the models can not accurately parameterize the stable boundary layer characteristics over sea ice. While it remains difficult to pinpoint the exact causes of the differences between the models themselves and observations, due to the different turbulent flux schemes and representation of sea ice, future work should focus on understanding the driving factors for the differences.

There is a clear relationship between modeled trends in turbulent fluxes and sea ice loss with projected wintertime Arctic warming. Models that simulate larger surface turbulent flux trends and more sea ice loss show larger amounts of winter warming. Using trends in the observations to constrain these models, our results indicate that Arctic winter warming could fall within the range of ~14–17 K in the Barents-Kara seas, compared to the unconstrained ~10–21 K intermodel spread.

There is still a long road ahead to improve turbulent flux representation in the Arctic, especially over sea ice. These include: 1) turbulent flux schemes need to use more parameterizations that are 'Arctic specific' in order to represent the very stable boundary layer conditions over sea ice, particularly during the winter, 2) the representation of sea ice and snow properties and characteristics (e.g. snow and ice thickness, roughness, concentration, floe size distribution) need to be improved so that the surface drag coefficients and roughness lengths can be accurately assessed and surface and near surface variables can more closely match observed values, 3) spatial and vertical resolution of climate models and satellite observations need to increase so that the boundary layer and sub-grid scale processes that are not currently resolved can be simulated, and 4) better collaboration between those taking the measurements and those who produce the models.

Recent field campaigns, such as MOSAiC, provide valuable measurements for use in improving these turbulent flux parameterizations in the Arctic. We can use these measurements to build upon what was learned from the SHEBA campaign more than 20 years ago. The future Decadal Survey mission, aimed to improve our understanding of the planetary boundary layer, will increase the vertical resolution from satellites, thus enhancing our retrievals of these near surface variables. These current and future measurements could significantly improve the representation of surface turbulent fluxes in the Arctic and hence Arctic wintertime warming.

DATA AVAILABILITY STATEMENT

The original contributions presented in the study are included in the article/**Supplementary Material**, further inquiries can be directed to the corresponding author. AIRS data can be downloaded from https://airs.jpl.nasa.gov/data/get-data/standard-data/. MERRA-2 data can be downloaded from https://gmao.gsfc.nasa.gov/reanalysis/MERRA-2/data_access/. ERA-5 data can be downloaded from https://www.ecmwf.int/en/forecasts/datasets/reanalysis-datasets/era5. AIRS-derived turbulent heat fluxes can be distributed upon request to L. Boisvert. CMIP6 data can be downloaded from https://esgfnode.llnl.gov/.

AUTHOR CONTRIBUTIONS

LB wrote the paper, edited the paper and provided analysis of the data, RB helped to write and edit the paper, and produce the figures. PT helped in idea development, writing and editing of the manuscript. CP helped in writing and editing of the paper.

FUNDING

The work of LB, RB, PT, and CP was funded by NASA IDS Project "Investigating the Fate of Sea Ice and its Interaction with the Atmosphere in the New Arctic" (grant number 80NSSC21K0264).

ACKNOWLEDGMENTS

We would also like to thank the two reviewers for their feedback and suggestions.

SUPPLEMENTARY MATERIAL

The Supplementary Material for this article can be found online at: https://www.frontiersin.org/articles/10.3389/feart.2022.765304/full#supplementary-material

REFERENCES

Allan, D., and Allan, R. P. (2019). Seasonal Changes in the North Atlantic Cold Anomaly: The Influence of Cold Surface Waters from Coastal Greenland and Warming Trends Associated with Variations in Subarctic Sea Ice Cover. *J. Geophys. Res. Oceans* 124 (12), 9040–9052. doi:10.1029/2019JC015379

Andreas, E. L., Horst, T. W., Grachev, A. A., Persson, P. O. G., Fairall, C. W., Guest, P. S., et al. (2010a). Parametrizing Turbulent Exchange over Summer Sea Ice and the Marginal Ice Zone. *Q.J.R. Meteorol. Soc.* 136, 927–943. doi:10.1002/jq.61810.1002/qj.618

Andreas, E. L. (2002). Parameterizing Scalar Transfer over Snow and Ice: A Review. *J. Hydrometeor* 3, 417–432. doi:10.1175/1525-7541(2002)003<0417:pstosa>2.0.co;2

Andreas, E. L., Persson, P. O. G., Grachev, A. A., Jordan, R. E., Horst, T. W., Guest, P. S., et al. (2010b). Parameterizing Turbulent Exchange over Sea Ice in Winter. *J. Hydrometeorology* 11, 87–104. doi:10.1175/2009JHM1102.1

Bintanja, R., Graversen, R. G., and Hazeleger, W. (20112011). Arctic winter Warming Amplified by the thermal Inversion and Consequent Low Infrared Cooling to Space. *Nat. Geosci* 4, 758–761. doi:10.1038/ngeo1285

Bodas-Salcedo, A., Webb, M. J., Bony, S., Chepfer, H., Dufresne, J.-L., Klein, S. A., et al. (2011). COSP: Satellite Simulation Software for Model Assessment. *Bull. Am. Meteorol. Soc.* 92 (8), 1023–1043. doi:10.1175/2011BAMS2856.1

Boeke, R. C., and Taylor, P. C. (2018). Seasonal Energy Exchange in Sea Ice Retreat Regions Contributes to Differences in Projected Arctic Warming. *Nat. Commun.* 9, 5017. doi:10.1038/s41467-018-07061-9

Boeke, R. C., Taylor, P. C., and Sejas, S. A. (2021). On the Nature of the Arctic's Positive Lapse-Rate Feedback. *Geophys. Res. Lett.* 48, e2020GL091109. doi:10.1029/2020GL091109

Boisvert, L. N., Markus, T., and Vihma, T. (2013). Moisture Flux Changes and Trends for the Entire Arctic in 2003-2011 Derived from EOS Aqua Data. *J. Geophys. Res. Oceans* 118, 5829–5843. doi:10.1002/jgrc.20414

Boisvert, L. N., Wu, D. L., and Shie, C.-L. (2015b). Increasing Evaporation Amounts Seen in the Arctic between 2003 and 2013 from AIRS Data. *J. Geophys. Res. Atmos.* 120, 6865–6881. doi:10.1002/2015JD023258

Boisvert, L. N., Wu, D. L., Vihma, T., and Susskind, J. (2015a). Verification of Air/surface Humidity Differences from AIRS and ERA-Interim in Support of Turbulent Flux Estimation in the Arctic. *J. Geophys. Res. Atmos.* 120, 945–963. doi:10.1002/2014JD021666

Boucher, O., Denvil, S., Levavasseur, G., Cozic, A., Caubel, A., Foujols, M.-A., et al. (2021). *IPSL IPSL-Cm6a-LR-INCA Model Output Prepared for CMIP6 CMIP Historical*. Version r1i1p1f1 [1]. Earth System Grid Federation. doi:10.22033/ESGF/CMIP6.13601

Bourassa, M. A., Gille, S. T., Bitz, C., Carlson, D., Cerovecki, I., Clayson, C. A., et al. (2013). High-Latitude Ocean and Sea Ice Surface Fluxes: Challenges for Climate Research. *Bull. Amer. Meteorol. Soc.* 94 (3), 403–423. doi:10.1175/BAMS-D-11-00244.1

Brodeau, L., Barnier, B., Gulev, S. K., and Woods (2017). Climatologically Significant Effects of Some Approximations in the Bulk Parameterizations of Turbulent Air-Sea Fluxes. *J. Phys. Oceanogr.* 47, 5–28. doi:10.1175/JPO-D-16-0169.1

Brunke, M. A., Zeng, X., and Anderson, S. (2002). Uncertainties in Sea Surface Turbulent Flux Algorithms and Data Sets. *J. Geophys. Res.* 107, 5–1–5–21. doi:10.1029/2001JC000992

Brunke, M. A., Zhou, M., Zeng, X., and Andreas, E. L. (2006). An Intercomparison of Bulk Aerodynamic Algorithms Used over Sea Ice with Data from the Surface Heat Budget for the Arctic Ocean (SHEBA) experiment. *J. Geophys. Res.* 111. doi:10.1029/2005JC002907

Burt, M. A., Randall, D. A., and Branson, M. D. (2016). Dark Warming. *J. Clim.* 29 (2), 705–719. doi:10.1175/JCLI-D-15-0147.1

Cao, J., and Wang, B. (2019). *NUIST NESMv3 Model Output Prepared for CMIP6 CMIP Historical*. Version r1i1p1f1[1]. Earth System Grid Federation. doi:10.22033/ESGF/CMIP6.8769

Cavalieri, D. J., Crawford, J., Drinkwater, M., Emery, W. J., Eppler, D. T., Farmer, L. D., et al. (1992). *NASA Sea Ice Validation Program for the DMSP SSM/I: Final Report, NASA Technical Memorandum 104559*. Washington, D. C.: National Aeronautics and Space Administration, 126.

Cavalieri, D. J., and Parkinson, C. L. (2012). Arctic Sea Ice Variability and Trends, 1979-2010. *The Cryosphere* 6, 881–889. doi:10.5194/tc-6-881-2012

Cavalieri, D. J., Parkinson, C. L., Gloersen, P., and Zwally, H. (1996). *Sea Ice Concentrations from Nimbus-7 SMMR and DMSP SSM/I-SSMIS Passive Microwave DataNASA DAAC at the Natl. Snow and Ice Data Cent*. Boulder, Colo. [Updated yearly.

Community, D. S. (2020). Arctic Sea Ice in CMIP6. *Geophys. Res. Lett.* 47. doi:10.1029/2019gl086749

Crawford, A., Stroeve, J., Smith, A., and Jahn, A. (2021). Arctic Open-Water Periods Are Projected to Lengthen Dramatically by 2100. *Commun. Earth Environ.* 2, 109. doi:10.1038/s43247-021-00183-x

Cullather, R. I., and Bosilovich, M. G. (2012). The Energy Budget of the Polar Atmosphere in MERRA. *J. Clim.* 25, 5–24. doi:10.1175/2011JCLI4138.1

Dai, A., Luo, D., Song, M., and Liu, J. (2019). Arctic Amplification Is Caused by Sea-Ice Loss under Increasing CO2. *Nat. Commun.* 10, 121. doi:10.1038/s41467-018-07954-9

Danabasoglu, G., Lamarque, J. F., Bacmeister, J., Bailey, D. A., DuVivier, A. K., Edwards, J., et al. (2020). The Community Earth System Model Version 2 (CESM2). *J. Adv. Model. Earth Syst.* 12 (2). doi:10.1029/2019MS001916

Danabasoglu, G. (2019). *NCAR CESM2 Model Output Prepared for CMIP6 CMIP Amip*. Earth System Grid Federation. doi:10.22033/ESGF/CMIP6.7522

Davy, R., and Outten, S. (2020). The Arctic Surface Climate in CMIP6: Status and Developments since CMIP5. *J. Clim.* 33 (18), 8047–8068. doi:10.1175/JCLI-D-19-0990.1

Deser, C., Tomas, R., Alexander, M., and Lawrence, D. (2010). The Seasonal Atmospheric Response to Projected Arctic Sea Ice Loss in the Late Twenty-First Century. *J. Clim.* 23, 333–351. doi:10.1175/2009JCLI3053.1

Devasthale, A., Sedlar, J., and Tjernström, M. (2011). Characteristics of Water-Vapour Inversions Observed over the Arctic by Atmospheric Infrared Sounder (AIRS) and Radiosondes. *Atmos. Chem. Phys.* 11, 9813–9823. doi:10.5194/acp-11-9813-2011

Devasthale, A., Willén, U., Karlsson, K.-G., and Jones, C. G. (2010). Quantifying the clear-sky Temperature Inversion Frequency and Strength over the Arctic Ocean during Summer and winter Seasons from AIRS Profiles. *Atmos. Chem. Phys.* 10, 5565–5572. doi:10.5194/acp-10-5565-2010

Dix, M. (2019). *CSIRO-ARCCSS ACCESS-CM2 Model Output Prepared for CMIP6 CMIP Historical*. Version r1i1p1f1[1]. Earth System Grid Federation. doi:10.22033/ESGF/CMIP6.4271

Eyring, V., Bony, S., Meehl, G. A., Senior, C. A., Stevens, B., Stouffer, R. J., et al. (2016). Overview of the Coupled Model Intercomparison Project Phase 6 (CMIP6) Experimental Design and Organization. *Geosci. Model. Dev.* 9, 1937–1958. doi:10.5194/gmd-9-1937-2016

Gelaro, R., Suárez, W. M. J., Todling, R., Molod, A., Takacs, L., Randles, C. A., et al. (2017). The Modern-Era Retrospective Analysis for Research and Applications, Version 2 (MERRA-2). *J. Clim.* 30, 5419–5454. doi:10.1175/JCLI-D-16-0758.1

Grachev, A. A., Andreas, E. L., Fairall, C. W., Guest, P. S., and Persson, P. O. G. (2007). SHEBA Flux-Profile Relationships in the Stable Atmospheric Boundary Layer. *Boundary-layer Meteorol.* 124, 315–333. doi:10.1007/s10546-007-9177-6

Grachev, A. A., Andreas, E. L., Fairall, C. W., Guest, P. S., and Persson, P. O. G. (2008). Turbulent Measurements in the Stable Atmospheric Boundary Layer during SHEBA: Ten Years after. *Acta Geophys.* 56 (1), 142–166. doi:10.2478/s11600-007-0048-9

Graham, R. M., Cohen, L., Ritzhaupt, N., Segger, B., Graversen, R. G., Rinke, A., et al. (2019). Evaluation of Six Atmospheric Reanalyses over Arctic Sea Ice from Winter to Early Summer. *J. Clim.* 32 (14), 4121–4143. doi:10.1175/JCLI-D-18-0643.1

Holland, M. M., Serreze, M. C., and Stroeve, J. (2010). The Sea Ice Mass Budget of the Arctic and its Future Change as Simulated by Coupled Climate Models. *Clim. Dyn.* 34, 185–200. doi:10.1007/s00382-008-0493-4

Holtslag, A. A. M., and de Bruin, H. A. R. (1988). Applied Modeling of the Nighttime Surface Energy Balance over Land. *J. Appl. Meteorol.* 27, 689–704. doi:10.1175/1520-0450(1988)027<0689:amotns>2.0.co;2

Intergovernmental Panel on Climate Change (IPCC) (2013). *Annex I: Atlas of Global and Regional Climate Projections*.

Jahn, A., Sterling, K., Holland, M. M., Kay, J. E., Maslanik, J. A., Bitz, C. M., et al. (2012). Late-Twentieth-Century Simulation of Arctic Sea Ice and Ocean Properties in the CCSM4. *J. Clim.* 25 (5), 1431–1452. doi:10.1175/JCLI-D-11-00201.1

Jakobson, E., Vihma, T., Palo, T., Jakobson, L., Keernik, H., and Jaagus, J. (2012). Validation of Atmospheric Reanalyses over the central Arctic Ocean. *Geophys. Res. Lett.* 39, a–n. doi:10.1029/2012GL051591

Jungclaus, J. (2019). *MPI-M MPI-ESM1.2-HR Model Output Prepared for CMIP6 CMIP Historical*. Version r1i1p1f1[1]. Earth System Grid Federation. doi:10.22033/ESGF/CMIP6.6594

Kay, J. E., Holland, M. M., Bitz, C. M., Blanchard-Wrigglesworth, E., Gettelman, A., Conley, A., et al. (2012). The Influence of Local Feedbacks and Northward Heat Transport on the Equilibrium Arctic Climate Response to Increased Greenhouse Gas Forcing. *J. Clim.* 25 (16), 5433–5450. doi:10.1175/JCLI-D-11-00622.1

Kilpeläinen, T., Vihma, T., Manninen, M., Sjöblom, A., Jakobson, E., Palo, T., et al. (2012). Modelling the Vertical Structure of the Atmospheric Boundary Layer over Arctic Fjords in Svalbard. *Q.J.R. Meteorol. Soc.* 138, 1867–1883. doi:10.1002/qj.1914

Krasting, J. P., John, J. G., Blanton, C., McHugh, C., Nikonov, S., Radhakrishnan, A., et al. (2018). *NOAA-GFDL GFDL-ESM4 Model Output Prepared for CMIP6 CMIP Historical*. Version *YYYYMMDD*[1]. Earth System Grid Federation. doi:10.22033/ESGF/CMIP6.8597

Kwok, R. (2018). Arctic Sea Ice Thickness, Volume, and Multiyear Ice Coverage: Losses and Coupled Variability (1958-2018). *Environ. Res. Lett.* 13 (10), 105005. doi:10.1088/1748-9326/aae3ec

Lammert, A., Brümmer, B., Haller, M., Müller, G., and Schyberg, H. (2010). Comparison of Three Weather Prediction Models with Buoy and Aircraft Measurements under Cyclone Conditions in Fram Strait. *Tellus A* 62, 361–376. doi:10.1111/j.1600-0870.2010.00460.x

Launiainen, J., and Vihma, T. (1990). Derivation of Turbulent Surface Fluxes - an Iterative Flux-Profile Method Allowing Arbitrary Observing Heights. *Environ. Softw.* 5, 113–124. doi:10.1016/0266-9838(90)90021-W

Li, L. (2019). *CAS FGOALS-G3 Model Output Prepared for CMIP6 CMIP Historical*. Version *YYYYMMDD*[1]. Earth System Grid Federation. doi:10.22033/ESGF/CMIP6.3356

Lu, Y., Zhou, M., and Wu, T. (2013). Validation of Parameterizations for the Surface Turbulent Fluxes over Sea Ice with CHINARE 2010 and SHEBA Data. *Polar Res.* 32, 20818. doi:10.3402/polar.v32i0.20818

Lüpkes, C., Vihma, T., Birnbaum, G., and Wacker, U. (2008a). Influence of Leads in Sea Ice on the Temperature of the Atmospheric Boundary Layer during Polar Night. *Geophys. Res. Lett.* 35, L03805. doi:10.1029/2007GL032461

Markus, T., Stroeve, J. C., and Miller, J. (2009). Recent Changes in Arctic Sea Ice Melt Onset, Freezeup, and Melt Season Length. *J. Geophys. Res.* 114 (C12). doi:10.1029/2009JC005436

Medeiros, B., Deser, C., Tomas, R. A., and Kay, J. E. (2011). Arctic Inversion Strength in Climate Models. *J. Clim.* 24 (17), 4733–4740. doi:10.1175/2011JCLI3968.1

Parkinson, C. L., and DiGirolamo, N. E. (2016). New Visualizations Highlight New Information on the Contrasting Arctic and Antarctic Sea-Ice Trends since the Late 1970s. *Remote Sensing Environ.* 183, 198–204. doi:10.1016/j.rse.2016.05.020

Pavelsky, T. M., Boé, J., Hall, A., and Fetzer, E. J. (2011). Atmospheric Inversion Strength over Polar Oceans in winter Regulated by Sea Ice. *Clim. Dyn.* 36, 945–955. doi:10.1007/s00382-010-0756-8

Persson, P. O. G., Shupe, M. D., and Solomon, A. (2017). Linking Atmospheric Synoptic Transport, Cloud Phase, Surface Energy Fluxes, and Sea-Ice Growth: Observations of Midwinter SHEBA Conditions. *Clim. Dyn.* 49, 1341–1364. doi:10.1007/s00382-016-3383-1

Pithan, F., Medeiros, B., and Mauritsen, T. (2014). Mixed-phase Clouds Cause Climate Model Biases in Arctic Wintertime Temperature Inversions. *Clim. Dyn.* 43 (1-2), 289–303. doi:10.1007/s00382-013-1964-9

Ramsey, F., and Schafer, D. (2012). *The Statistical Sleuth: A Course in Methods of Data Analysis*. 2nd Edition. Pacific Grove: Wadsworth Group.

Reeves Eyre, J. E. J., Zeng, X., and Zhang, K. (2021). Ocean Surface Flux Algorithm Effects on Earth System Model Energy and Water Cycles. *Front. Mar. Sci.* 8. doi:10.3389/fmars.2021.642804

Renfrew, I. A., Barrell, C., Elvidge, A. D., Brooke, J. K., Duscha, C., King, J. C., et al. (2021). An Evaluation of Surface Meteorology and Fluxes over the Iceland and Greenland Seas in ERA5 Reanalysis: The Impact of Sea Ice Distribution. *Q. J. R. Meteorol. Soc.* 147, 691–712. doi:10.1002/qj.3941

Schweiger, A., Lindsay, R., Zhang, J., Steele, M., Stern, H., and Kwok, R. (2011). Uncertainty in Modeled Arctic Sea Ice Volume. *J. Geophys. Res.* 116 (C8). doi:10.1029/2011JC007084

Screen, J. A., Deser, C., and Simmonds, I. (2012). Local and Remote Controls on Observed Arctic Warming. *Geophys. Res. Lett.* 39 (10), a–n. doi:10.1029/2012GL051598

Screen, J. A., Simmonds, I., Deser, C., and Tomas, R. (2013). The Atmospheric Response to Three Decades of Observed Arctic Sea Ice Loss. *J. Clim.* 26 (4), 1230–1248. doi:10.1175/JCLI-D-12-00063.1

Screen, J. A., and Simmonds, I. (2010b). Increasing Fall-winter Energy Loss from the Arctic Ocean and its Role in Arctic Temperature Amplification. *Geophys. Res. Lett.* 37 (16), a–n. doi:10.1029/2010GL044136

Screen, J. A., and Simmonds, I. (2010a). The central Role of Diminishing Sea Ice in Recent Arctic Temperature Amplification. *Nature* 464, 1334–1337. doi:10.1038/nature09051

Sejas, S. A., and Cai, M. (2016). Isolating the Temperature Feedback Loop and its Effects on Surface Temperature. *J. Atmos. Sci.* 73 (8), 3287–3303. doi:10.1175/JAS-D-15-0287.1

Serreze, M. C., Barrett, A. P., Stroeve, J. C., Kindig, D. N., and Holland, M. M. (2009). The Emergence of Surface-Based Arctic Amplification. *The Cryosphere* 3, 11–19. doi:10.5194/tc-3-11-2009

Serreze, M. C., Barrett, A. P., and Stroeve, J. (2012). Recent Changes in Tropospheric Water Vapor over the Arctic as Assessed from Radiosondes and Atmospheric Reanalyses. *J. Geophys. Res.* 117, a–n. doi:10.1029/2011jd017421

Shiogama, H., Abe, M., and Tatebe, H. (2019). *MIROC MIROC6 Model Output Prepared for CMIP6 ScenarioMIP Ssp585*. Earth System Grid Federation. doi:10.22033/ESGF/CMIP6.898

Smith, A., Jahn, A., and Wang, M. (2020). Seasonal Transition Dates Can Reveal Biases in Arctic Sea Ice Simulations. *The Cryosphere* 14, 2977–2997. doi:10.5194/tc-14-2977-2020

Song, Z., Qiao, F., Bao, Y., Shu, Q., Song, Y., and Yang, X. (2019). *FIO-QLNM FIO-ESM2.0 Model Output Prepared for CMIP6 CMIP piControl*. Version *YYYYMMDD*[1]. Earth System Grid Federation. doi:10.22033/ESGF/CMIP6.9205

Steele, M., Ermold, W., and Zhang, J. (2008). Arctic Ocean Surface Warming Trends over the Past 100 Years. *Geophys. Res. Lett.* 35 (2). doi:10.1029/2007GL031651

Stroeve, J., Barrett, A., Serreze, M., and Schweiger, A. (2014a). Using Records from Submarine, Aircraft and Satellites to Evaluate Climate Model Simulations of Arctic Sea Ice Thickness. *The Cryosphere* 8, 1839–1854. doi:10.5194/tc-8-1839-2014

Stroeve, J. C., Markus, T., Boisvert, L., Miller, J., and Barrett, A. (2014). Changes in Arctic Melt Season and Implications for Sea Ice Loss. *Geophys. Res. Lett.* 41 (4), 1216–1225. doi:10.1002/2013GL058951

Stroeve, J., and Notz, D. (2018). Changing State of Arctic Sea Ice across All Seasons. *Environ. Res. Lett.* 13 (10), 103001. doi:10.1088/1748-9326/aade56

Susskind, J., Barnet, C. D., and Blaisdell, J. M. (2003). Retrieval of Atmospheric and Surface Parameters from AIRS/AMSU/HSB Data in the Presence of Clouds. *IEEE Trans. Geosci. Remote Sensing* 41 (2), 390–409. doi:10.1109/TGRS.2002.808236

Susskind, J., Blaisdell, J. M., and Iredell, L. (2014). Improved Methodology for Surface and Atmospheric Soundings, Error Estimates, and Quality Control Procedures: The Atmospheric Infrared Sounder Science Team Version-6 Retrieval Algorithm. *J. Appl. Remote Sens* 8 (1), 084994. doi:10.1117/1.JRS.8.084994

Swart, N. C., Cole, J. N. S., Kharin, V. V., Lazare, M., Scinocca, J. F., Gillett, N. P., et al. (2019). *CCCma CanESM5 Model Output Prepared for CMIP6 ScenarioMIP Ssp126*. Version YYYYMMDD[1]. Earth System Grid Federation. doi:10.22033/ESGF/CMIP6.3683

Taylor, P. C., Kato, S., Xu, K. M., and Cai, M. (2015). Covariance between Arctic Sea Ice and Clouds within Atmospheric State Regimes at the Satellite Footprint Level. *J. Geophys. Res. Atmos.* 120 (24), 12656–12678. doi:10.1002/2015JD023520

Taylor, P., Hegyi, B., Boeke, R., and Boisvert, L. (2018). On the Increasing Importance of Air-Sea Exchanges in a Thawing Arctic: A Review. *Atmosphere* 9 (2), 41. doi:10.3390/atmos9020041

Teixeira, J., Piepmeier, J. R., Nehrir, A. R., Ao, C. O., Chen, S. S., Clayson, C. A., et al. (2021). *Toward a Global Planetary Boundary Layer Observing System: The NASA PBL Incubation Study Team Report*. NASA PBL Incubation Study Team, 134.

Vihma, T. (2014). Effects of Arctic Sea Ice Decline on Weather and Climate: A Review. *Surv. Geophys.* 35 (5), 1175–1214. doi:10.1007/s10712-014-9284-0

Volodin, E., Mortikov, E., Gritsun, A., Lykossov, V., Galin, V., Diansky, N., et al. (2019). *INM INM-CM4-8 Model Output Prepared for CMIP6 CMIP piControl*. Version *YYYYMMDD*[1]. Earth System Grid Federation. doi:10.22033/ESGF/CMIP6.5080

Walden, V. P., Hudson, S. R., Cohen, L., Murphy, S. Y., and Granskog, M. A. (2017). Atmospheric Components of the Surface Energy Budget over Young Sea Ice: Results from the N-Ice2015 Campaign. *J. Geophys. Res. Atmos.* 122 (16), 8427–8446. doi:10.1002/2016JD026091

Watts, M., Maslowski, W., Lee, Y. J., Kinney, J. C., and Osinski, R. (2021). A Spatial Evaluation of Arctic Sea Ice and Regional Limitations in CMIP6 Historical Simulations. *J. Clim.*, 1–54. doi:10.1175/jcli-d-20-0491.1

Wieners, K.-H. (2019). *MPI-M MPI-ESM1.2-LR Model Output Prepared for CMIP6 CMIP Historical*. Version r1i1p1f1[1]. Earth System Grid Federation. doi:10.22033/ESGF/CMIP6.6595

Wild, M. (2020). The Global Energy Balance as Represented in CMIP6 Climate Models. *Clim. Dyn.* 55, 553–577. doi:10.1007/s00382-020-05282-7

Winton, M. (2000). A Reformulated Three-Layer Sea Ice Model. *J. Atmos. Oceanic Technol.CO* 17 (4), 5252–5531. doi:10.1175/1520-0426(2000)017<0525:ARTLSI>2.010.1175/1520-0426(2000)017<0525:artlsi>2.0.co;2

Wu, T., Chu, M., Dong, M., Fang, Y., Jie, W., Li, J., et al. (2018). *BCC BCC-Csm2mr Model Output Prepared for CMIP6 CMIP Historical*. Version r1i1p1f1 [1]. Earth System Grid Federation. doi:10.22033/ESGF/CMIP6.2948

Wu, T., Lu, Y., Fang, Y., Xin, X., Li, L., Li, W., et al. (2019). The Beijing Climate Center Climate System Model (BCC-CSM): the Main Progress from CMIP5 to CMIP6. *Geosci. Model. Dev.* 12, 1573–1600. doi:10.5194/gmd-12-1573-2019

Yu, L., Yang, Q., Zhou, M., Zeng, X., Lenschow, D. H., Wang, X., et al. (2019). The Intraseasonal and Interannual Variability of Arctic Temperature and Specific Humidity Inversions. *Atmosphere* 10 (4), 214. doi:10.3390/atmos10040214

Yu, Y. (2019). *CAS FGOALS-F3-L Model Output Prepared for CMIP6 CMIP Historical*. Version *YYYYMMDD*[1]. Earth System Grid Federation. doi:10.22033/ESGF/CMIP6.3355

YukimotoKoshiro, S. T., Kawai, H., Oshima, N., Yoshida, K., Urakawa, S., et al. (2019). *MRI MRI-ESM2.0 Model Output Prepared for CMIP6 CMIP Historical.* Version r1i1p1f1 [1]. Earth System Grid Federation. doi:10.22033/ESGF/CMIP6.6842

Zeng, X., Zhang, Q., Johnson, D., and Tao, W.-K. (2002). Parameterization of Wind Gustiness for the Computation of Ocean Surface Fluxes at Different Spatial Scales. *Mon. Wea. Rev.* 130 (8), 2125–2133. doi:10.1175/1520-0493(2002)130<2125:powgft>2.0.co;2

Zeng, X., Zhao, M., and Dickinson, R. E. (1998). Intercomparison of Bulk Aerodynamic Algorithms for the Computation of Sea Surface Fluxes Using TOGA COARE and TAO Data. *J. Clim.* 11 (10), 2628–2644. doi:10.1175/1520-0442(1998)011<2628:iobaaf>2.0.co;2

Zheng, J., Zhang, Q., Li, Q., Zhang, Q., and Cai, M. (2019). Contribution of Sea Ice Albedo and Insulation Effects to Arctic Amplification in the EC-Earth Pliocene Simulation. *Clim. Past* 15, 291–305. doi:10.5194/cp-15-291-2019

Ziehn, T., Chamberlain, M., Lenton, A., Law, R., Bodman, R., Dix, M., et al. (2019). *CSIRO ACCESS-ESM1.5 Model Output Prepared for CMIP6 ScenarioMIP Ssp245*. Version YYYYMMDD[1]. Earth System Grid Federation. doi:10.22033/ESGF/CMIP6.4322

Zilitinkevich, S. S., and Esau, I. N. (2007). "Similarity Theory and Calculation of Turbulent Fluxes at the Surface for the Stably Stratified Atmospheric Boundary Layer," in *Atmospheric Boundary Layers*. Editors A. Baklanov and B. Grisogono (New York, NY: Springer). doi:10.1088/0143-0807/27/4/007

Conflict of Interest: RB was employed by the company Science Systems and Applications, Inc.

The remaining authors declare that the research was conducted in the absence of any commercial or financial relationships that could be construed as a potential conflict of interest.

Publisher's Note: All claims expressed in this article are solely those of the authors and do not necessarily represent those of their affiliated organizations, or those of the publisher, the editors and the reviewers. Any product that may be evaluated in this article, or claim that may be made by its manufacturer, is not guaranteed or endorsed by the publisher.

Frontiers in Earth Science

Investigates the processes operating within the major spheres of our planet

Advances our understanding across the earth sciences, providing a theoretical background for better use of our planet's resources and equipping us to face major environmental challenges.

Discover the latest Research Topics

See more →

Frontiers

Avenue du Tribunal-Fédéral 34
1005 Lausanne, Switzerland
frontiersin.org

Contact us

+41 (0)21 510 17 00
frontiersin.org/about/contact